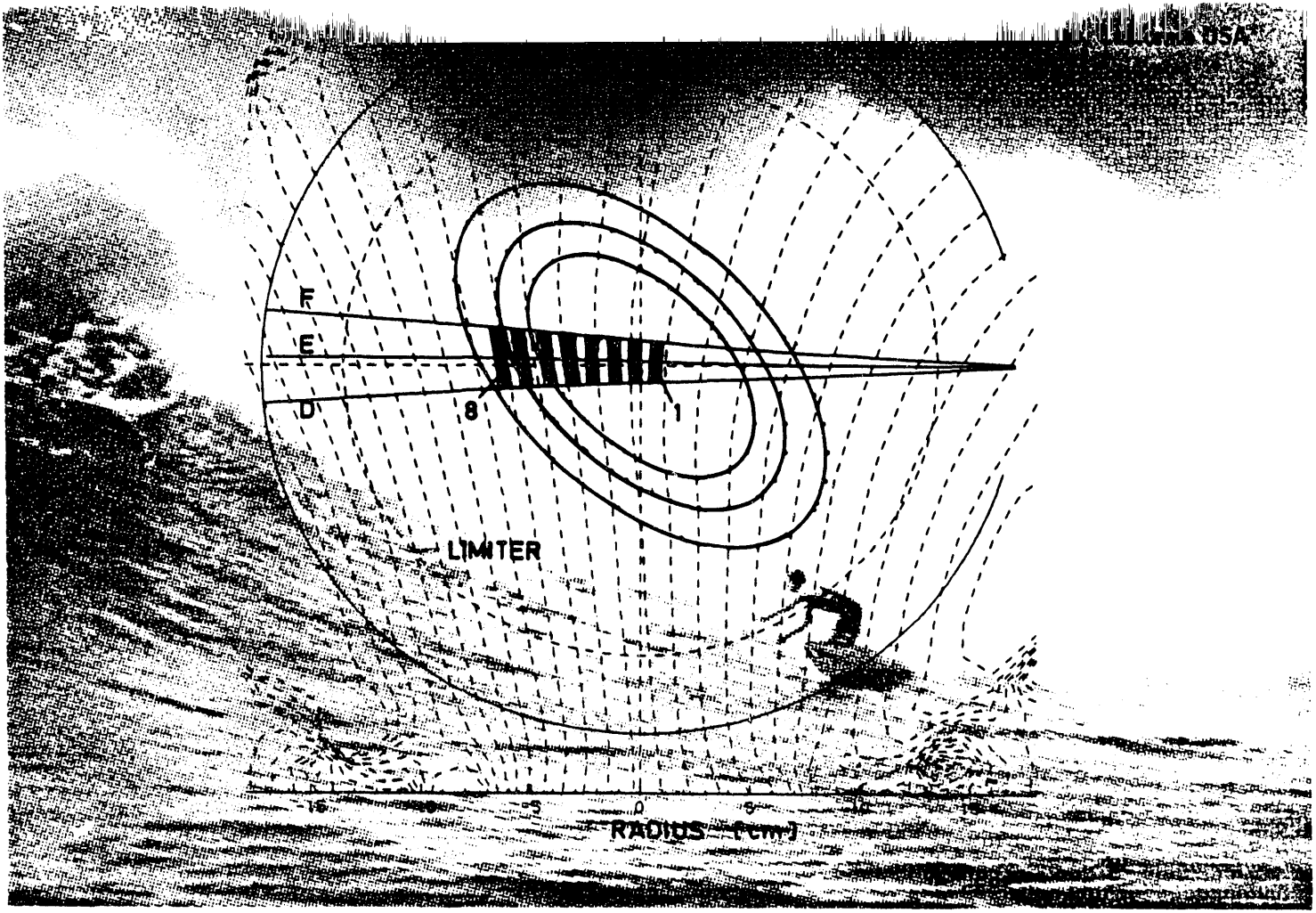


MASTER

GA-A--18294

DE93 000677

# EC–5
# Fifth International Workshop on Electron Cyclotron Emission and Electron Cyclotron Heating

November 9,11,12, 1985

San Diego, California USA

EDITED BY:
RONALD PRATER and JOHN LOHR

GA PROJECT NO. 4991

*The Proceedings of EC–5, the Fifth International Workshop on Electron Cyclotron Emission and Electron Cyclotron Heating, were produced by GA Technologies Inc., Post Office Box 85608, San Diego, CA 92038, USA. Additional copies may be obtained by contacting the GA Technologies Document Center and referencing report number GA–A18294.*

# Preface

A joint workshop on Electron Cyclotron Emission (ECE) and Electron Cyclotron Resonance Heating (ECH) was held in San Diego, California, on November 9 and 11, 1985. This meeting was sponsored by GA Technologies Inc. On November 12, 1985, the Gyrotron User's Meeting was held under U.S. Department of Energy sponsorship. Papers presented at both meetings are included in this volume because of the close relation of the work involved.

The aim of these workshops was to provide a forum for discussion of recent experimental and theoretical progress in the areas of ECE, ECH, and their associated technologies, and an opportunity for specialists in each area to exchange information and ideas. A total of 43 papers was presented. The papers presented here are reproduced directly from the authors' manuscripts.

We would like to thank D. Remsen and A. Valverde for their help with the management of the meeting and P. Turner for assistance with this publication. We would also like to thank the session chairmen (D. Boyd, S. Tamor, A. Cavallo, A. Kritz, and T.V. George) for their help and support.

R. Prater

J. Lohr

# Contents

## Electron Cyclotron Emission Measurements

*First Measurements of Two Dimensional Electron Temperature Profiles on JET,* A.E. Costley, E.A.M. Baker, D.V. Bartlett, D.J. Campbell, M.G. Kiff, S.E. Kissel, G.F. Neill, and P.F. Roach . . . . . 3

*Simulation of JET ECE Spectra Along Multiple Chords and Comparison with Experiment,* G. Ramponi, A. Airoldi, D.V. Bartlett, M. Brusati, S. Nowak, and A. Orefice . . . . . 10

*Electron Cyclotron Emission Measurements on TFTR,* F.J. Stauffer, P.C. Efthimon, G. Taylor, V. Arunasalam, D.A. Boyd, R.C. Cutler, M.P. McCarthy, D.A. Rasmussen, and J. Wilgen . . . . . 18

*Electron Cyclotron Emission Measurements During Electron Cyclotron Heating in the Wendelstein VII-A Stellarator at 1 Tesla and 2.5 Tesla,* H.J. Hartfuß, M. Tutter, and the W VII-A Team . . . . . 37

*Central Power Balance in Sawtoothing Ohmically Heated Tokamak Discharges in the Princeton Large Torus,* A. Cavallo, J. Hosea, R. Bell, and D. McNeill . . . . . 45

*The Transmission System for the DIII–D ECE Radiometer,* C. Moeller, J. Lohr, and R. Prater . . . . . 56

*A Comparison of Three Different Methods for Calibrating ECE Measurement Systems,* S.E. Kissel, B.J.D. Tubbing, E.A.M. Baker, D.V. Bartlett, D.J. Campbell, A.E. Costley, D.G. Moss, R.M. Niestadt, Th. Oyevaar, and H.W. Piekaar . . . . . 65

## Electron Cyclotron Emission Theory

*What is the Limiting Polarization of Electron Cyclotron Emission Leaving a Fusion Plasma?,* D.A. Boyd . . . . . 77

*Study of the Electron Cyclotron Maser Instability,* M. Bornatici, U. Ruffina, and E. Westerhof . . . . . 88

*Electron Runaway Effects Induced by Electron Cyclotron Waves,* L. Demeio and F. Englemann . . . . . 97

*The Stability of Electron Cyclotron Waves in the Presence of Strong Electron Cyclotron Heating,* J.Y. Hsu and C.N. Lashmore-Davies . . . . . 105

*NOTEC, A Code for the Calculation of Non-Thermal ECE Spectra Emitted from Tokamak Plasmas,* R.M.J. Sillen . . . . . 113

*Perpendicular Electron Cyclotron Emission for Relativistic Loss-Cone Type Momentum Distributions,* M. Bornatici and U. Ruffina . . . . . 123

## Electron Cyclotron Heating

*ECRH Studies in CLEO Tokamak,* A.C. Riviere, N.R. Ainsworth, B. Alper, D. Atkinson, S.G.F. Blewett, P.R. Collins, A.N. Dellis, T. Edlington, B. Lloyd, F. Ma, M.R. O'Brien, B.J. Parham, D.C. Robinson, D.F.H. Start, and T.N. Todd . . . . . 135

*Experiments on Heat Transport Applying the Modulation and Correlation Technique to Electron-Cyclotron-Heated Plasmas in the Wendelstein VII-A Stellarator,* H.J. Hartfuß, H. Maaßberg, M. Tutter, W VII-A Team, Universität Stuttgart ECRH Group . . . . . 145

*Experimental Results of Electron Cyclotron Heating in TFR,* TFR Group J.A. Hoekzema, H.P.L. de Esch, R.W. Polman, and W.J. Schrader . . . . . 154

*Heating Effectiveness in Elecytron Cyclotron Heating Experiments in the Doublet III Tokamak,* R. Prater and A.J. Lieber . . . . . 168

*The 2 MW ECRH System for COMPASS,* A.C. Riviere, M.W. Alcock, A.N. Dellis, M. Hughes, M. O'Brien, D.C. Robinson, and T.N. Todd . . . . 181

*Proposed Fundamental Heating on the TARA Tandem Mirror,* W.C. Guss, M.E. Manuel, R. Myer, and D.K. Smith . . . . . 189

*Observation of Ti XXI Line Radiation in ECH Plasmas,* P. Lee, A.J. Lieber, A.K. Pradhan, and X. Yueming . . . . . 196

*Dependence of ECH Deposition Profile on the Modeling of Incident Wave Energy,* A.H. Kritz, H. Hsuan, and K. Matsuda . . . . . 213

*Accessibility Study on a High Density Noncircular Tokamak by Ray Tracing,* K. Matsuda, V.S. Chan, R.W. Harvey, and A.H. Kritz . . . . . 223

*Simulation of the Effect of Electron Cyclotron Heating on Tearing Modes,* E. Westerhof and W. Goedheer . . . . . 228

*Velocity Space Diffusion of Electrons Induced by a Beam of Electron Cyclotron Waves of Finite Size in Toroidal Geometry,* L. Demeio and F. Englemann . . . . . 238

*Propagation of a Gaussian Wave Packet in an Absorbing Medium and Generalization of a Group Velocity,* M. Tanaka . . . . . 246

*On the Application of Whistler Waves to Toroidal Discharges,* C.N. Lashmore-Davies . . . . . 264

## Gyrotron Development

*Varian Gyrotrons for Electron Cyclotron Heating Applications,* H. Jory . . . 275

*Progress on the Varian 140 GHz Gyrotron,* K. Felch . . . . . 276

*Varian Gyrotron Production and Reliability Improvement Progress,* L.J. Craig . . . . . 277

*Research on High Power, CW Relevant Gyrotrons at the Naval Research Laboratory,* M.E. Read and R. Rhinewine . . . . . 278

*Prospects for High Power Gyrotrons,* K.E. Kreischer, B.G. Danly, H. Saito, R.J. Temkin, and T.M. Tran . . . . . 286

*The 120 GHz Quasi-Optical Gyrotron at the Centre de Recherches en Physique des Plasmas,* M.Q. Tran, and the Quasi-Optical Gyrotron Development Group . . . . . 294

*Design and First Experimental Results of Components for ERCH at Thomson-CSF,* A. Benshimhon, P. Garin, E. Jedar, G. Mourier, A. Thevenot . . . . . 300

## ECH Systems and Waveguide Development

*Technical Aspects of the Joint FOM/CEA ECH Experiment on TFR,* A.G.A. Verhoeven, A.F. van der Grift, J. de Hoop, M. van der Kaay, L. Kroonenburg, A.B. Sterk, J.P. Crenn, L. Rebuffi, and B. Tournesac . . . 303

*Microwaves for ECRH in Milano C.N.R. Laboratory,* S. Cirant and G. Falciasecca . . . . . 313

*Optimization of Wall Perturbations in Rippled Wall Mode Converters for Overmoded Circular Waveguide,* M. Thumm, G.A. Müller, and R. Wilhelm . . . . . 321

*Mode Converters for Generating the $HE_{11}$ (Near-Gaussian) Mode from Gyrotron $TE_{ON}$ Modes at 140 GHz,* M. Thumm and H. Strum . . . . . 329

*Methods of Designing Higher Efficiency, Shorter Length Periodic-Perturbation Mode Converters for Over-Moded Waveguides,* R.J. Vernon, U. Rhee, and K. Audenaerde . . . . . 337

*Waveguide Elliptic Polarizers for ECH at Down Shifted Frequencies on PLT,* J.L. Doane . . . . . 345

*Pure Mode Swept Frequency $TE_{02}$ Measurements in 6.35 cm Circular Waveguide,* T.S. Bigelow, T.L. White, and H.D. Kimrey . . . . . 353

Author Index . . . . . 363

# Electron Cyclotron Emission Measurements

# First Measurements of Two Dimensional Electron Temperature Profiles on JET

A.E. Costley, E.A.M. Baker,* D.V. Bartlett, D.J. Campbell,
M.G. Kiff,* S.E. Kissel, G.F. Neill, and P.F. Roach
*JET Joint Undertaking, Abingdon, Oxon, OX14 3EA, UK*
**National Physical Laboratory, UK*

ABSTRACT

The Spatial Scan ECE System on JET is briefly described. The employed method of calibration is outlined. The first results obtained with some of the oblique viewing channels are presented, and these confirm that the emission is localised in the vertical direction as well as in the radial direction. Full interpretation of the results requires the use of an interpretation/simulation code which is presently being developed.

## 1. Introduction

Electron cyclotron emission (ECE) is an established diagnostic for measuring the spatial dependence of the electron temperature along a diameter of tokamak and stellarator plasmas. By viewing the plasma along different lines of sight, however, there exists the possibility of obtaining the full spatial dependence of the electron temperature in the poloidal cross section. From such measurements it should be possible to construct the lines of constant temperature (isothermals) and these can be compared with, for example, magnetic flux contours determined independently from equilibrium code calculations. The Spatial Scan ECE System on JET has been designed and constructed with this aim in view. During the last operating period of JET (January - June 1985) some preliminary results were obtained with four channels of the measurement system. These first results are presented in this paper. A brief description of the measurement system and an outline of the method of calibration employed are also given.

## 2. Measurement System

The Spatial Scan ECE System on JET was described at the last ECE/ECRH workshop /1/. Briefly, it consists of ten antennae mounted inside the JET vacuum chamber which view the plasma along different lines of sight in the poloidal cross-section. Crystal quartz windows form the vacuum break, and a ten channel, ~ 40 m long, oversized S band waveguide run containing ~ 12 mitre bends tansmits the radiation to the measurement instruments. These are located on the shielded side of the biological protection wall. A free-standing wire grid polarizer is mounted in each channel near the vacuum vessel so that the emission in either the extraordinary or the ordinary mode can be selected. The measurement instruments are four low resolution rapid-scan Michelson interferometers, six Fabry-Perot interferometers and one high resolution Michelson interferometer. Each instrument is fitted with a liquid helium cooled indium antimonide detector (QMC type). The low resolution Michelsons are capable of measuring the emission in the range $90 < f < 600$ GHz with a frequency resolution ~ 10 GHz and a time resolution ~ 15 ms, while the high resolution Michelson can measure the emission in the range $40 < f < 600$ GHz with a frequency resolution ~3 GHz and a time resolution ~15 ms. The Fabry-Perots can be operated in either of two modes: scanning or static. In the scanning mode they measure the emission in limited regions of the spectrum, eg. $100 < f < 180$ GHz with a frequency resolution ~5 GHz and a time resolution $\lesssim$ 3 ms, while in the static mode they measure the time dependence of the emission at fixed frequencies with a time resolution limited only by the detector bandwidth (~500 kHz) and signal to-noise considerations. The system is controlled and monitored through the JET Control and Data Acquisition System (CODAS), and is fully compatible with the planned D-T phase of JET operation.

Thus far four channels have been used routinely to make measurements of extraordinary mode ECE: a horizontal channel 13 cm below the mid-plane and three channels which view the upper half of the plasma at different angles with respect to the mid-plane (17.5°, 25.5°, 33°), Figure 3(A). These channels are equipped with the four low resolution Michelson interferometers and the interferometers are operated synchronously, to give simultaneous measurements. In addition, some measurements have been made

with a channel exactly on the mid-plane using a Fabry-Perot interferometer operating in the static mode.

From the emission measured in the second harmonic of the electron cyclotron frequency, the time and spatial dependence of the electron temperature is determined using frequency to space and intensity to temperature transformations. Full account is taken of the internal magnetic fields (poloidal field, diamagnetism) because they are significant in JET plasmas. For the second harmonic, overlap with the third harmonic limits the region over which the temperature can be determined unambiguously to $2.8 < R < 4.2$ m (R is the major radius), and since a full size JET plasma fills the region $1.7 < R < 4.2$ m, just over half the electron temperature profile is obtained. Antenna pattern width and spectral resolution average the temperature information over a volume ~15 cm (FWHM) along the line of sight and ~15 cm (FWHM) perpendicular to the line of sight. The signal to noise in the measurements is $\gtrsim$ 100:1.

## 3. Calibration

The four Michelson observation channels were calibrated with a portable source developed specially for this purpose by the National Physical Laboratory, UK /2/. Briefly, this source consists of a large area (20 x 20 $cm^2$) hot plate (~ 750 K) with an emissivity > 0.8 in the frequency range of interest. During the summer shutdown of JET (July-September 1985), the source was mounted inside the vacuum vessel close to the end of the antennae. For each observation channel, interferograms were recorded with and without (ambient temperature) the source. By taking the differences between these interferograms the contribution due to room temperature background radiation was removed. Coherent addition was used to give good signal to noise and typically $10^6$ interferograms per channel were averaged. The channel 13 cm below the mid-plane was also calibrated with a microwave absorber immersed in liquid nitrogen (77 K). This calibration was also carried out with the source mounted inside the vacuum vessel.

The result of the calibration process is a determination, for each channel, of the responsivity of the whole measurement chain, i.e. the system response. The uncertainties in the determination of the system response

are the dominant source of uncertainty in the measured electron temperature - it is therefore important to estimate these uncertainties. For the measurements made on JET, we believe the uncertainty on the absolute level of the measured response, and therefore the uncertainty on the level of the measured temperature, is about ± 10%. The uncertainty on the frequency dependence, and therefore the uncertainty on the shape of the temperature profile, is believed to be about ± 5%. For the two dimensional measurements the uncertainty on the relative channel to channel response is also important, and we believe this also to be about ± 5%. In all cases the dominant uncertainties are systematic.

Because access to the vacuum vessel can be gained only very rarely, the long term stability of the system has also to be considered. Steps to ensure the system is stable have been taken: it is mechanically rigid, no components are moved or changed, and the detectors are kept permanently at liquid helium temperature. Measurements made on one observation channel over a period of nine months show that the response of the system external to the vacuum vessel is constant to within a few percent.

Techniques for calibrating Fabry-Perot interferometers independently are not yet available, and so the Fabry-Perot was calibrated against the nearest Michelson observation channel (13 cm below the mid-plane). Techniques for calibrating Fabry-Perot interferometers are presently under development /3/.

## 4. Results

Many measurements have been made with the observation channel 13 cm below the midplane and these have been used extensively in studies of plasma physics phenomena on JET. For example, ECE measurements have played a central role in studies of energy confinement, sawteeth and the related phenomenon of heat pulse propagation, major disruptions, and plasma start-up. Some examples are shown in Figures 1 and 2.

Measurements have also been made with the four calibrated channels of the Spatial Scan System but thus for only a few measurements have been processed. An example is shown in Figure 3. In the figure we show the

projection on the mid-plane of the measured electron temperature along the four different lines of sight for a plasma with $B_T$=3.4T, $I_p$=4.0MA, $n_{eo}$=4.2x10$^{19}$m$^{-3}$, and elongation (height/radial diameter) = 1.44. The measurements are made at one particular time in the discharge during the current flat top.

For the two-dimensional measurements, the first important point to establish is that the temperature information is localised in the vertical direction as well as in the radial direction. Information on this can be obtained by observing the time and spatial dependence of the measured temperature profiles through a single sawtooth oscillation. In this case it is expected that the temperature in the centre of the plasma changes substantially while the temperature in the outer plasma regions changes relatively much less. Measurements on sawteeth have been made, and in Figure 4 we show the time and space dependence of the temperature through a single sawtooth oscillation. Note that only the temperature in the central channels changes substantially, confirming that the temperature information in indeed localised in the vertical direction. To clarify this point, the profiles measured immediately before and after the sawtooth collapse are shown in Figure 5.

In the deduction of the temperature profiles shown in Figure 3, 4 and 5 account is taken of the internal magnetic fields in the plasma. A cylindrical model with elongation is assumed. However, the proper interpretation of the two-dimensional measurements requires that effects such as refraction, harmonic overlap, line broadening, the polarization state of the radiation, and instrumental effects such as the finite antenna pattern and frequency resolution, be properly taken into account. In order to do this a simulation/interpretation code is required. A suitable code is being developed and this is described in a companion paper /3/. The combination of the measurements and the interpretation code will allow us to determine the isothermals in the poloidal cross-section and this will be the next significant development in this work.

## 5. Conclusions

A system capable of measuring the temporal and spatial dependence of the electron temperature in the poloidal cross-section of JET has been designed

and constructed. Four of the ten channels have been absolutely calibrated and some preliminary measurements have been made. These confirm that the temperature information is localised in the vertical direction as well as in the radial direction. Full interpretation of the data requires the use of a code to take into account effects such as refraction, harmonic overlap, and instrumental effects, and this will be the next significant step in this work.

## REFERENCES


/1/ A.E. Costley et al 'First Measurements of ECE from JET'. Proceedings EC-4 Fourth International Workshop on ECE and ECRH, 1-10, Rome (1984).

/2/ Further details on the source can be obtained from Dr. E. Baker, NPL.

/3/ G. Ramponi et al 'Simulation of JET ECE Spectra Along Multiple Chords And Comparison with Experiment.' This conference.


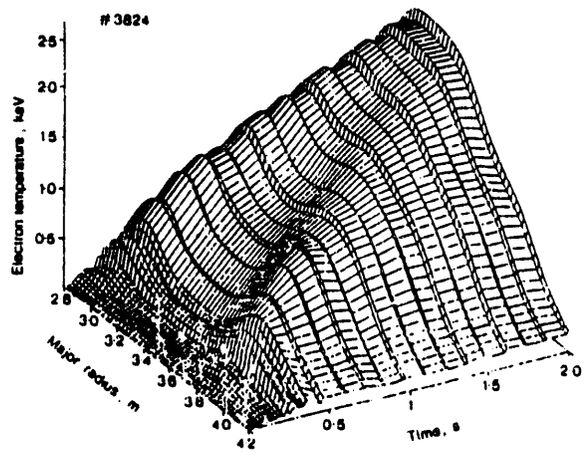


FIG.1 Measured temperature profiles during the start-up phase of a typical JET pulse. At the end of the start up phase the plasma current is 1.6MA and the plasma density ~2 x $10^{19}m^{-3}$.

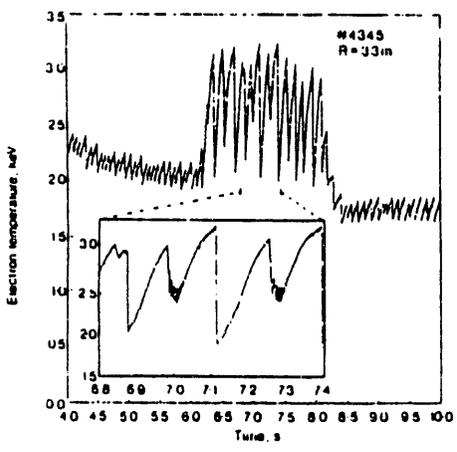


FIG.2 Measured time dependence of the electron temperature close to the plasma centre during 6s of a JET discharge. Measurements made with a Fabry-Perot interferometer operating in the static mode. The increase in the amplitude of the sawteeth during the period 6-8s is due to the addition of 2MW of ICRH.

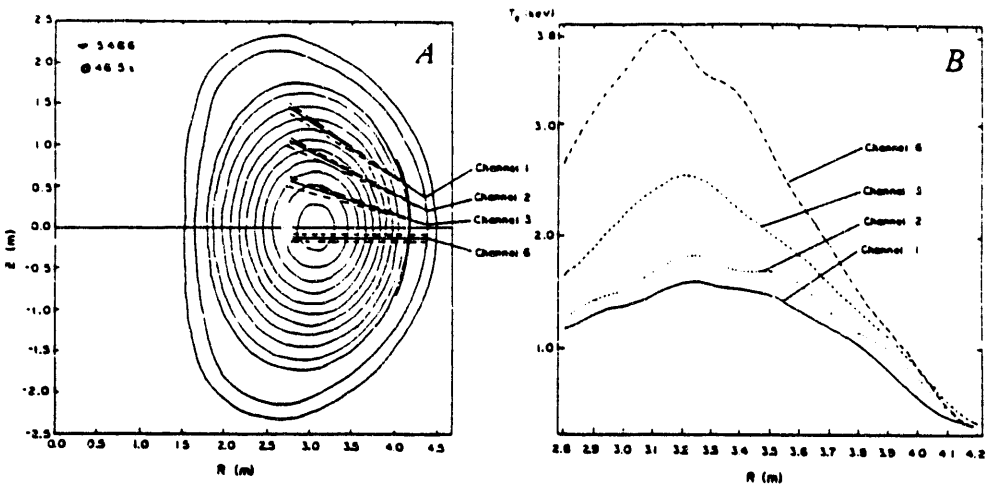


FIG.3 Viewing directions (A) and measured $T_e$ profiles (B) along four different lines of sight in the poloidal cross-sections. The viewing directions are calculated for the frequency corresponding to the centre of the second harmonic including the effect of refraction. The $T_e$ profiles are plotted as a function of major radius.

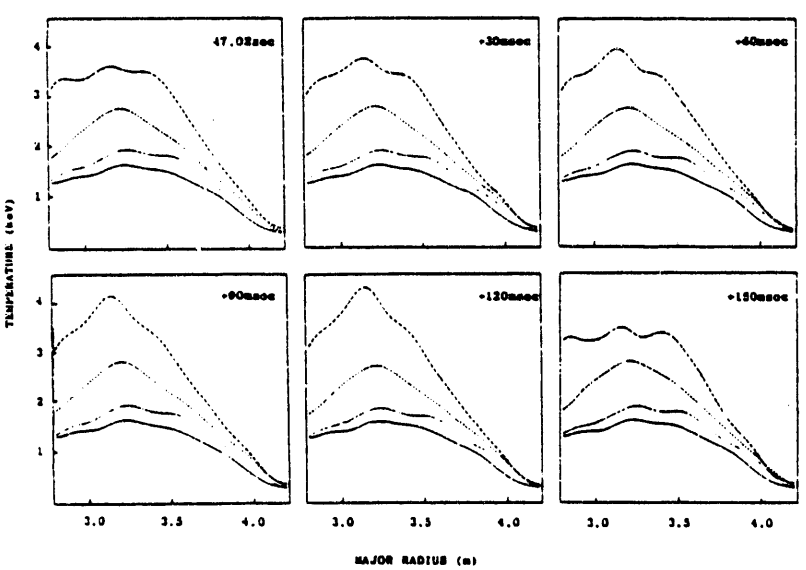


FIG.4 Measured $T_e$ profiles along four different lines of sight during an individual sawtooth oscillation. Note the profiles in the outer channel remain approximately constant while those in the centre channel change substantially confirming that the emission is localised in the vertical direction.

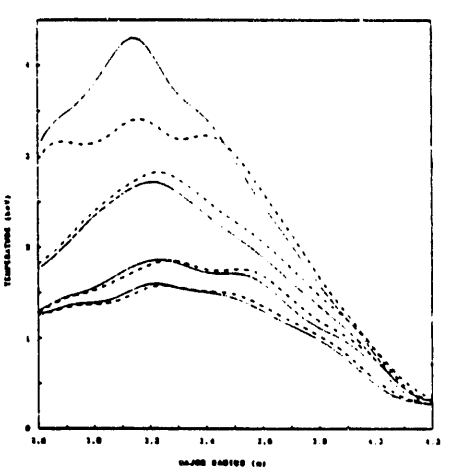

FIG.5 Measured $T_e$ profiles immediately before (solid line) and after (dashed line) the sawtooth crash.

# Simulation of JET ECE Spectra Along Multiple Chords and Comparison with Experiment

G. Ramponi,* A. Airoldi,* D.V. Bartlett, M. Brusati,
S. Nowak, and A. Orefice*
*JET Joint Undertaking, Abingdon, Oxon, OX14 3EA, UK*
**EURATOM-CNR Fusion Association, Milan, Italy*

ABSTRACT

This paper describes the current status and most recent developments in the JET ECE simulation code. Simulated spectra generated by the code are compared with those which have been measured in the four operational channels of the diagnostic. The motivation for measuring two dimensional electron temperature profiles, and the techniques employed, are discussed in the companion paper by Costley et al. at this workshop.

## INTRODUCTION

To exploit fully the possibilities offered by the multi-channel ECE system, account must be taken of various physical effects not generally important in ECE measurements. Some of these effects will be of added significance at the high electron temperatures expected in JET. The first step in the interpretation of two-dimensional temperature profiles is the simulation of measured spectra: if a reasonable agreement can be obtained between calculated and measured spectra, then information generated as a part of the calculations (eg. look-up tables of refraction) can be used with confidence for routine interpretation of the measurements.

The simulation is designed to be as complete as possible. All the relevant physics related to the generation and propagation of the radiation are modelled, and the important aspects of the measurement system are also included. The operation of the code is reviewed in the next section. In the last section the results of the first comparison with multi-channel experimental data are presented.

## THE SIMULATION CODES

The present work is aimed principally at the interpretation of temperature measurements. While it is useful to be able to simulate the entire ECE spectrum (as a check on the behaviour of the models) the spectral regions of most interest are the second harmonic extraordinary mode and the first harmonic ordinary mode, since it is here that the plasma is generally optically thick. Only at the plasma edges (ie. particularly in the outer oblique channels) do we expect to see any influence of wall reflections. It follows that the wall reflected intensity is, for temperature measurements, only a perturbation and it is not necessary to seek an exact model.

The approach taken for these codes is to treat wall reflections with a simplified model and to attempt detailed and accurate calculations only for a single-pass of the radiation through the plasma. Where the plasma is not entirely opaque, this leads to a considerable saving in computation time compared to a method which attempts a full ray tracing calculation in realistic geometry. The outputs of the two computations, "single-pass" and "reflections" are simply combined by taking account of the plasma optical depth calculated by the single-pass code, as well as the emission intensities generated by the two models.

Instrumental effects may also be taken into consideration. The most important of these is probably the antenna pattern width which is modelled, in this geometrical optics approach, by calculating a group of rays for each antenna and making a weighted average over them. The instrument function of the spectrometer can also be included if necessary.

### The Wall Reflection Model

Most previous calculations of ECE in tokamaks have used one of two models of wall reflections: the "plane-parallel" model (eg. [1]) or a "ray-tracing" model (eg. [2]). These represent two extremes of complexity. The plane-parallel model, which supposes a slab plasma lying between plane, parallel reflecting walls, leads to a straightforward analytic solution at the cost of physically unrealistic assumptions. In particular, it is not reasonable to assume for the oblique channels in JET that the radiation propagates back-and-forth through the same region of plasma. At the other extreme, some authors have attempted to trace rays (perhaps with refraction included) through many reflections and passes through the plasma. Apart from the obvious computational cost, there must be doubt about whether the geometry of the wall can be included with sufficient detail, and the density profile be known with sufficient precision, to justify this approach for more than a couple of passes through the plasma.

The model developed for the JET simulations [3] attempts to by-pass these problems by describing the walls as "diffuse reflectors". This is similar to a technique used to evaluate black-body cavities at optical wavelengths: the interchange of energy between all the points on the walls of the cavity is written as a set of integral equations which are solved (generally numerically) to give the intensity distribution at the exit aperture. In the case of a plasma, the calculation is complicated by the presence of the

resonance layers. To keep the computation reasonable (they will be repeated for many different plasma conditions) we make the following assumptions:

1) The plasma is taken to be two dimensional, ie. limited to the poloidal cross-section. This assumption could be avoided, at some computational cost. (For optically thin emission, an analytic integration over the toroidal angle can be made [4]).
2) Refraction is ignored.
3) The wall reflections are assumed completely diffuse (in the poloidal plane), but polarization "scrambling" is included. There are two diffuse reflection coefficients, one for the intensity reflected in the same polarization ($r_D$) and the other for reflection into the opposite polarization ($r_C$).

4) The emission and absorption are calculated using the single space-localized expressions of Bornatici et al [5].

The vacuum vessel wall (a line rather than a surface in this 2-D model) is divided into a set of N sectors, assumed small enough that the incident intensity will be constant across each one. The power transfer between every pair of sectors (taking into account both the geometry and plasma absorption) is incorporated into an N x N matrix. The emission received directly from the plasma onto each sector forms a 1 x N vector. Using the assumed wall reflectivity (including "polarization scrambling" if desired) a matrix equation describes the evolution of the intensities on the wall at each reflection.

This matrix equation is most easily solved by iteration. In practice, it is found that 40 sectors are enough and 20 to 30 iterations give good convergence.

## The Single-Pass Emission Calculation

The code operates within the framework of the geometrical optics approximation. The limitations that this implies are discussed below. It calculates the emitted intensities and optical depths for the two characteristic modes (E- and O- mode) in the frequency range from the first to the fourth harmonic. These quantities may be calculated along ray trajectories with an arbitrary direction of propagation in the plasma. The following physical effects are taken into account:

1) refraction in three dimensions,
2) a relativistic treatment of all the signficant line broadening mechanisms,
3) the presence of the poloidal and diamagnetic (or paramagnetic) fields in the plasma,
4) overlap between the different harmonics,
5) the state of the polarization leaving the plasma.

Much of the essential physics of the single-pass emission calculation has already been described [6,7]. It is reviewed briefly here and the recent additions to the code are described in more detail.

The trajectory of each ray is obtained by solving the Hamiltonian system of geometrical optics equations in full toroidal geometry [8]. The cold plasma dispersion relations are used, since any departures from these expressions due to warm plasma effects are expected to be limited to the core of strongly absorbing cyclotron resonance layers. Emission from these regions should be re-absorbed before escaping the resonance and therefore not observable.

While the cold plasma dispersion relations are both convenient and adequate for ray tracing, weakly relativistic warm plasma theory [9] is required to evaluate the local absorption coefficient. Numerical solution of these expressions gives results valid for arbitrary directions of propagation with respect to the magnetic field. This is essential to the JET simulations, since for typical values of the electron temperature $T_e$, and parallel component of the refractive index $n_{//}$(ie. the propagation direction with respect to the magnetic field), analytic approximations are not accurate. An example which illustrates this is shown in Figure 1. For propagation exactly perpendicular to the magnetic field, the analytic solution (assuming only relativistic broadening) is valid and the results agree with our numerical calculations. At large angles (Figure 1c), the numerical results are close to the non-relativistic analytic formula (Doppler broadening). However, in the intermediate region (Figure 1b) where most calculations for JET are made (see next section) the analytic formulae are not accurate.

The present version of the code assumes a Maxwellian (thermal) plasma. Kirchhoff's law is used to obtain the local emission coefficient, and the radiation intensity leaving the plasma in each of the two polarization modes is computed by using the well known integral solution of the radiation transport equation [10].

Finally, harmonic overlap is taken into account by combining the intensities and optical depths calculated, at a given frequency, for all the harmonics present in the plasma. For the present simulations, it is sufficient to allow for three harmonics in the plasma at any frequency. If these harmonics are numbered $(\ell-1)$, $\ell$ and $(\ell+1)$ with corresponding radiation temperatures $T_r(\ell-1)$, $T_r(\ell)$, $T_r(\ell+1)$ and optical depths $\tau(\ell-1)$, $\tau(\ell)$ and $\tau(\ell+1)$, then the total single-pass emission is given by:

$$T = T_r(\ell+1) + T_r(\ell).\, e^{-\tau(\ell+1)} + T_r(\ell-1).\, e^{-(\tau(\ell+1)+\tau(\ell))} \quad ....(1)$$

Any change in polarization of the radiation between the point of emission and the receiving antenna is of crucial importance to the diagnostic since only in the "local extraordinary mode" in the plasma is sure to be optically thick (for the second harmonic). In JET the antennae select vertically polarized radiation, which may not correspond exactly with the extraordinary mode.

For the single-pass emission calculations, it is assumed that the two characteristic modes propagate independently of each other. This condition, which forms part of the geometrical optics approximation [11] is true when:

$$\left| k_2(\omega) - k_1(\omega) \right| .\ L_2 \gg 1 \quad ....(2)$$

where $k_1(\omega)$ and $k_2(\omega)$ are the wavenumbers of the two characteristic modes, of frequency $\omega$ and L is a typical length scale. Equation 2 is satisfied across most of the second harmonic for typical JET conditions. Hence the polarization of the waves leaving the plasma edge will be that of the local extraordinary (or ordinary) mode at the edge, as determined by the local dispersion relation.

To determine the intensities in the linear polarization received by the antenna, we first evaluate the polarization vector for the two modes in the "intrinsic" coordinate system (whose 3 axes are: along the component of the wave vector perpendicular to the total magnetic field, along the magnetic field, and perpendicular to these two). The expressions for the polarization in this system are given, for example, in [8]. These coordinates are transformed into a system defined by the antenna axis and polarization. Components of the resulting (generally elliptical) polarization then give the fractions, $p_x$ of E-mode emission and $(1-p_x)$ of the O-mode emission collected by the antenna in one of its linear modes. The total intensity received is the sum of these two components.

The important parameter in determining $p_x$ is $F_b = (|n_{//}|.B_p/B_T)_b$ where the suffix b denotes that the parallel refractive index $n_{//}$, the poloidal field $B_p$, and the toroidal field $B_T$, are evaluated at the plasma boundary. For very small $n_{//}$ ($< 10^{-2}$) the polarization of the E-mode is almost linear and the result reduces to:

$$p_x = \cos^2 (\arctan (B_p/B_T) )_b \qquad ...(4)$$

When $n_{//}$ is larger (the typical case in JET, particularly for the oblique antennae) the E-mode is elliptically polarized and $p_x$ is related to $B_p/B_T$ in a less simple way, showing also a frequency dependence.

These features are illustrated in Figure 2 where the results of the numerical calculation are shown for a horizontal antenna (part a) and one inclined at an angle of 33° to the horizontal (part b). The polarization effects can be seen to be quite important, especially at low plasma q and in the oblique antennae.

## RESULTS

The plasma data required for the simulations comes from several sources. The temperature profile is taken from the ECE spectrum measured by the near mid-plane antenna (second harmonic E-mode in the outer half of the plasma, with corrections for the internal magnetic fields), while the density profile is derived from Abel inversion of the data from a multi-channel interferometer. The two dimensional spatial variation of these quantities is obtained by assuming that they are constant on the magnetic flux surfaces derived from equilibrium code calculations based on the magnetics measurements outside the plasma. Other parameters required include the vacuum vessel wall reflectivity, which is adjusted to give the best fit in the optically thin parts of the spectrum, and the instrumental antenna pattern. Convolution of the spectra with the instrument function of the spectrometers has not been included in the calculations presented here.

Figure 3 is a typical refraction calculation for the four antennae currently used for measurements. For this plasma, $B_T$=3.4T, $I_p$=4.0MA, $n_{eo}$=4.2x10$^{19}$m$^{-3}$, $T_{eo}$=3.5keV and the elongation = 1.44. In this case, the refraction is small in both the poloidal and toroidal directions.

Figure 4 shows the first attempts at matching the simulated spectra to those obtained in the experiment. The simulated spectra include the contributions of both E-mode and O-mode intensities to the linear vertical polarization transmitted by the antennae. The plasma chosen is the same as that of Figure 3. For each of the four antennae, the experimental spectra are plotted with simulations obtained using two different sets of reflectivity parameters.

The simulations show that the second harmonic is optically thick in the E-mode for all antennae and, as expected, largely insensitive to the choice of reflectivity coefficients. Therefore, valid temperature measurements can be made over most of the poloidal cross-section. For the most accurate work, account will have to be taken of the small fraction of optically thin O-mode radiation coupled into the antennae, but the necessary correction will not be strongly dependent on the reflectivity coefficients.

The comparisons with the measured spectra show that the model is accurately predicting the emission spectrum for optically thick low frequencies and viewing directions near the mid-plane, but significant discrepancies exist between simulated and measured spectra for other conditions. At low frequencies these discrepancies could be due to simplifications in the present calculations of some instrumental effects (in particular the antenna patterns), while at the optically thin higher frequencies they could be due to simplifications in the present reflectivity model (eg. wall reflectivity independent of poloidal location). Better agreement between simulated and measured spectra is required before the code can be used to build the look-up tables required for temperature measurement interpretation, and so work on both these points is in progress.

Acknowledgements

It is a pleasure to acknowledge all the members of JET who contributed to the measurements shown in this paper. Particular thanks are due to Drs A Costley, D Campbell and S Kissel.

References

[1] A E Costley et al, Phys. Rev. Letts 33 758 (1974)
[2] S Tamor, Nucl, Fusion 18 229 (1978)
[3] D V Bartlett, CEA-Fontenay report EUR-CEA-FC-1187 (1983)
[4] L Laurent and D Bartlett, EC-4 Workshop Proceedings (1984)
[5] M Bornatici et al, Nucl. Fusion 23 1153 (1983)
[6] A Airoldi, A Orefice, G Ramponi, CNR-Milan Report FP 83/15 (1983)
[7] A Airoldi, A Orefice, G Ramponi, EC-4 Workshop Proceedings (1984)
[8] T H Stix, The Theory of Plasma Waves, McGraw Hill (1962)
[9] V Krivenski, A Orefice, J. Plasma Phys. 30 125 (1982)
[10] G Bekefi, Radiation Processes in Plasmas, J Wiley (1966)
[11] V L Ginzburg, Propagation of Electromagnetic Waves in Plasma, Gordon and Breach (1961)

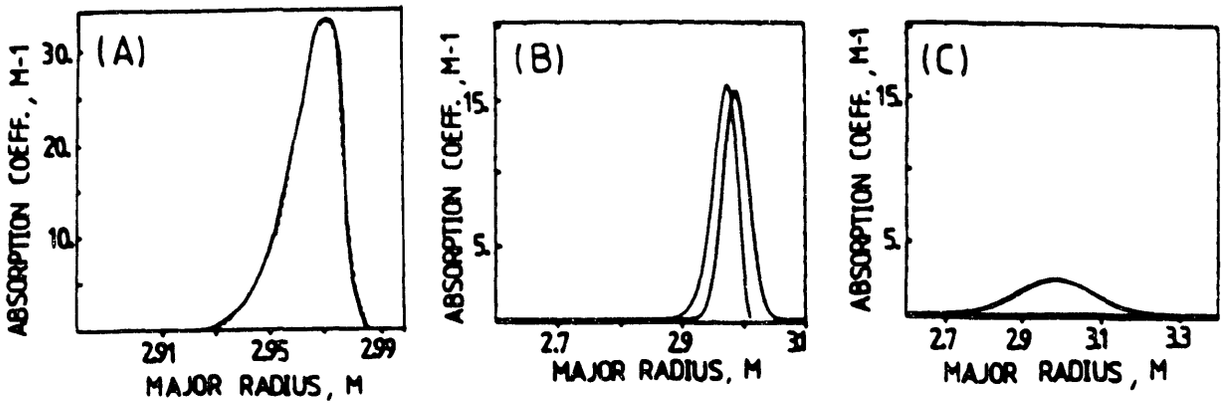


Figure (1): Plots of absorption coefficient at fixed frequency F=191 GHz (E-mode), as a function of major radius for the plasma conditions: $T_{eo}$=1 keV, $B_o$=3.4T, $n_{eo}$=2.5x$10^{19}m^{-3}$. The output of the numerical calculation is compared with the analytic formulae of Ref. 5. The three cases shown correspond to different angles of propagation with respect to the magnetic field: (a) $n_{//}$=0. ($\Theta$=90°); (b) $n_{//}$=.16 ($\Theta$=81°); (c) $n_{//}$=0.73 ($\Theta$=43°).

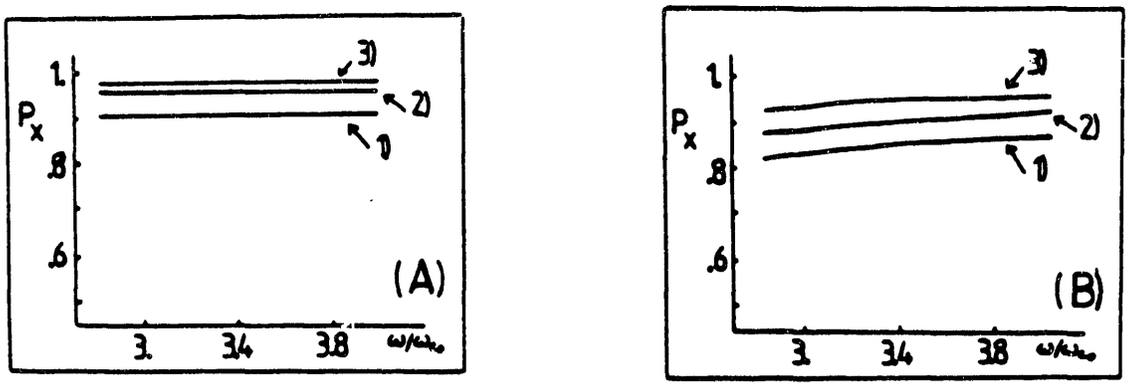


Figure (2): The fraction of E-mode intensity received by the ECE antennae ($p_x$) for three different plasma conditions and two different antennae: (a) Antenna 6, (Horizontal): 1)Pulse 2037, $F_b$=3.7x$10^{-3}$; 2) Pulse 3047, $F_b$=2x$10^{-3}$; 3) Pulse 1327, $F_b$=1.7x$10^{-3}$; (b) Antenna 1 (oblique): 1) Pulse 2037, $F_b$=5.5x$10^{-2}$; 2) Pulse 3047, $F_b$=2.5x$10^{-2}$; 3) Pulse 1327, $F_b$=1.3x$10^{-2}$.

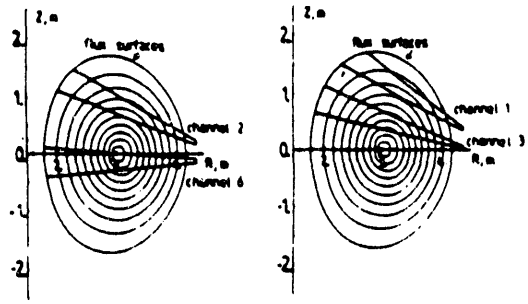

Figure (3): Ray traces for the four antennae with which measurements have been made. The antenna pattern is illustrated by calculating rays at ± 4.5°. For each antenna the plasma data is that of pulse 5486, The radiation frequency, 190 GHz (E-mode), corresponds to about the plasma centre at 3.4 Tesla toroidal field.

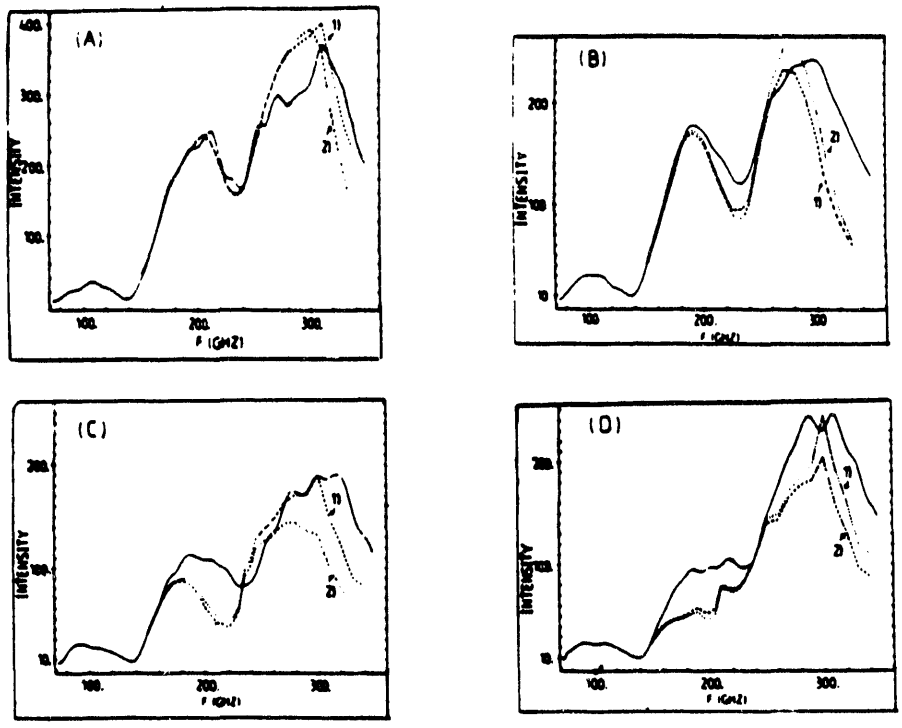


Figure (4): Comparison of simulated and measured spectra for pulse 5486. The unbroken lines are the experimental spectra and the broken lines are the two simulations with different reflectivities:

(A) Antenna 6: 1) $r_c$=0, $r_D$=0.65 and 2) $r_c$=0.32, $r_D$=0.33
(B) Antenna 3: 1) $r_c$=0, $r_D$=0.65 and 2) $r_c$=0.38, $r_D$=0.39
(C) Antenna 2: 1) $r_c$=0, $r_D$=0.89 and 2) $r_c$=0.42, $r_D$=0.46
(D) Antenna 1: 1) $r_c$=0, $r_D$=0.925 and 2) $r_c$=0.41, $r_D$=0.52

# Electron Cyclotron Emission Measurements on TFTR

F.J. Stauffer,[1] P.C. Efthimion, G. Taylor, V. Arunasalam,
D.A. Boyd,[1] R.C. Cutler, M.P. McCarthy, D.A. Rasmussen,[2]
and J. Wilgen[2]
*Princeton University, Princeton, New Jersey 08544, USA*
[1] *University of Maryland, College Park, Maryland 20742, USA*
[2] *Oak Ridge National Laboratory, Oak Ridge, Tennessee 37830, USA*

ABSTRACT

The latest generation of tokamaks (TFTR, JET, JT-60) with their large major radii (R > 2.5 M) and toroidal fields ($B_T$ > 3.5 T) are well suited for electron cyclotron emission (ECE) diagnostics. A fast scanning heterodyne receiver (radiometer) and a Michelson interferometer have been developed and operated to support the plasma confinement studies in the Tokamak Fusion Test Reactor (TFTR). This paper will examine some of the issues important to ECE diagnostics on TFTR, review the instruments, and show examples of measurements made during a variety of plasma experiments.

## 1. Electron Cyclotron Emission on TFTR

An examination of the emission properties of a high density ohmically heated helium plasma in TFTR illustrates some of the important aspects of the electron cyclotron emission. Figure 1 shows the location of the electron cyclotron resonant frequency for the first three harmonics, the frequency cutoffs, and other resonant frequencies in a ($\bar{n}$ = 6 x $10^{19}m^{-3}$, $T_e$ = 3 keV, $B_T$ = 4.8 T, a = 0.83 m) TFTR plasma. The three harmonics of the electron cyclotron frequency have the usual inverse major radius dependence (f $\alpha$ 1/R). Because of the large dimensions of TFTR there is an overlap of all the harmonics except in the case of the first harmonic. In the figure, the second harmonic emission from the high magnetic field side of the plasma has the same frequency as the low magnetic field side of the third harmonic. This prevents the determination of the temperature or density (see Section 7) for certain locations in the plasma. Overlap of the harmonics tends to be a problem for all of the large plasmas. The overlap can be seen in the emission spectrum

measured by the Michelson interferometer in Fig. 11(a). Figure 1 also shows the upper hybrid resonance ($f_{UH}$), the plasma frequency ($f_{pe}$) and the cutoffs for the extraordinary mode ($f_{CO1}$, $f_{CO2}$). With a line averaged plasma density ($\bar{n}_e$) of $6 \times 10^{19} m^{-3}$ there is no problem with the accessibility of the ordinary mode at the first harmonic.

Because the optical thickness of emission in a tokamak is a linear function of the major radius, large tokamaks such as TFTR have substantially high values of optical thickness. For the same high density helium discharge the single-pass optical thickness[1] of the first harmonic ordinary mode and the second and third harmonic extraordinary modes are plotted versus radial position in Fig. 2. As in many smaller tokamaks, the first harmonic ordinary mode and the second harmonic extraordinary mode are optically thick, but the magnitude of the optical depth now is very large as a result of the larger major radius and the higher electron temperature due to the better thermal confinement. The emission from the first harmonic ordinary mode and second harmonic extraordinary mode is at the blackbody level ($\tau \gtrsim 2$) without the aid of reflections from the vessel wall for a minor radius less than 0.65 m and 0.75 m respectively. Note that even the third harmonic extraordinary mode has a substantial optical depth ($\tau \sim 1$) in the plasma center.

The determination of an accurate temperature profile from ECE requires corrections to the vacuum magnetic field due to the poloidal field and plasma diamagnetism[2]. The magnitude of the total field correction ($\delta B$) is given by:

$$\frac{\delta B}{B_o} = \frac{\tilde{B}}{B_o} + \frac{1}{2} b_\Theta^2$$

where $B_o$ is the vacuum field, $\tilde{B}$ is the diamagnetic contribution and is given by

$$-\frac{1}{B_o} \frac{d\tilde{B}}{dr} = \frac{1}{2} \left[ \frac{d\beta_\perp}{dr} + \frac{db_\Theta^2}{dr} \right] + \frac{b_\Theta^2}{r} ,$$

$\beta_\perp$ is the normalized plasma perpendicular pressure, and $b_\Theta(r)$ is the normalized poloidal field and is derived from the plasma current density $j(r)$:

$$b_\Theta = \frac{\mu_o}{B_o} \int_o^r \frac{j(r')\, r'\, dr'}{r} .$$

Although the magnitude of the corrections is relatively small (~ $(r/R)^2$), the corrections are noticeable because of the size of the plasma in TFTR. Figure 3 shows a comparison of temperature profiles measured with the ECE diagnostics and with Thomson scattering for a full-size (a = 0.83 m) ohmically heated deuterium plasma. Both the profiles measured with ECE include the field correction. In addition, the temperature profile measured by the Michelson interferometer without the corrections is shown. The field correction broadens and shifts the temperature profile ~ 8-10 cm for this 1.4 MA plasma. The contributions of the poloidal field and diamagnetism to the correction are of nearly equal magnitude. The radiometer measured the first harmonic ordinary mode, and the Michelson interferometer measured the second harmonic extraordinary mode.

## 2. Radiometer

Figure 4 shows an overall schematic of the TFTR radiometer, in which three heterodyne receivers allow observation of emission between 75 and 220 GHz[3,4]. A periscope attached to the vacuum vessel was designed so that there is no direct path to the fused silica vacuum windows for impurities from the discharge. A rotatable aluminum alloy toroidal mirror can be directed either to collect ECE from the horizontal midplane of the TFTR plasma or to view a liquid-nitrogen-cooled blackbody. The periscope optics determine the spatial resolution transverse to the major radial direction at the TFTR vacuum vessel center, which is typically 15-20 cm depending on the frequency of the emission. The major radial resolution, 2.5 - 5 cm, is determined by the bandwidth of the receivers. A horn antenna and lens arrangement collects radiation from the periscope and directs it down 8 meters of J-band waveguide to three frequency-swept microwave receivers in the TFTR diagnostic basement. To distribute incident power to the receivers, a four-port power splitting network, which has a smooth frequency response without significant moding or resonances, has been designed. This network has good isolation between receivers so that local oscillator leakage power and reflected incident power do not couple from one receiver to another. The total front end loss between the periscope and each receiver due to all these components is typically 7-8 dB. Gaussian tapers are used to transfer to and from fundamental guide in order to minimize losses.

Each receiver design is a development of the radiometer described by Efthimion et al.[5]. A simplified schematic for one of the receivers is shown in Fig. 5. A power-leveled backward-wave oscillator (BWO) provides a frequency swept local oscillator for a millimeter wave mixer. The three receivers operate at 75-110, 110-170 and 170-220 GHz. A programmable sweep generator provides a ramp voltage to a high voltage amplifier, which generates a 2 kV ramp to modulate the BWO cathode. In the 170-220 GHz receiver a second harmonic mixer is used so that a BWO operating at 75-110 GHz can be employed. Each of the BWO's can be swept every 4 ms with a sweep time of 2 ms. This determines the time resolution in swept mode. Ramp voltage comparators with preset reference voltages are used to provide triggers for a transient digitizer connected to the video amplifier at the output of the receiver. The output from each receiver is sampled 24 times during a sweep. In total the output of the radiometer is sampled at 72 frequencies between 75 and 220 GHz every 4 ms and is stored in memory for later analysis. A verification of the BWO cathode voltage and mixer bias current for each of the 72 samples is stored also, just prior to the start of each plasma discharge. In "dwell mode", each BWO can be set to dwell at one of the 24 preset frequencies and output is then digitized at 24 kHz, in order to measure the temperature at selected locations with better time resolution.

The radiometer is calibrated absolutely in-situ to an accuracy of 10% by using a chopped blackbody and a Dicke switching technique[6]. An eccosorb-covered chopping drum with two holes rotates at approximately 3000 rpm so that the radiometer alternately views the cold source and room temperature source about 100 times per second. Then, one of the receivers is set to dwell at one of its 24 sample frequencies and the receiver output signal is measured with a lock-in amplifier.

## 3. Michelson Interferometer

The Fast-Scanning Michelson Inteferometer (FMI) measures the ECE spectrum 72 times per second with a time resolution of 11 ms. Although it has less time resolution than the radiometer, it has a broader spectral range. Currently, the FMI can measure over the range 75-540 GHz with a resolution of 3.6 GHz. This is adequate for measuring at least the first three cyclotron

harmonics at all available TFTR magnetic fields. The range could be extended to include more harmonics if it were desired. In order to take advantage of the intrinsic multi-mode capability of the FMI, which makes it comparatively easy to calibrate, its optical system was designed to use imaging components and free-space propagation. In particular, it was decided to design a system that could efficiently transport only the fundamental Gaussian beam-mode for a spectral frequency of 75 GHz and that would make a smooth transition to an efficient geometric optics system as the spectral frequency increases.[7]

The front end (periscope) of the optical system is shown in Fig. 6. The light-collecting component is a 90° off-axis ellipsoidal mirror that views the TFTR plasma inward along a major radius line. The light is deflected by a plane mirror and passes from vacuum into air through a wedged z-cut crystal quartz window. The primary means for controlling the field of view in the TFTR plasma is the field stop aperture that is mounted outside the crystal quartz window. It is located at the short focal point of the ellipsoidal mirror. In the geometric optics limit, the mirror focuses a magnified image of the field stop to its long focal point, close to the back wall of TFTR. The working diameter of the mirror and the diameter of the field stop (15 cm and 5 cm respectively) were determined by the sizes of TFTR and the periscope and by the choice of 75 GHz as the long wavelength limit of the FMI spectral range. The resulting vertical extent of the field of view is approximately 15-25 cm. For a typical range of central toroidal field values in TFTR (2.6 - 5.2 T), the radial spatial resolution for the measurement of electron temperature using the second harmonic varies between 1.5 and 11 cm, depending upon the radial position.

Following the field stop, a plane mirror directs the collected light into a TPX lens relay, which transports the light over a distance of approximately 8.5 meters to the input of the FMI, which is located in the basement underneath TFTR. As shown in Fig. 7, the light that is output from the FMI is refocussed by a TPX lens and then reflects off two diffraction gratings which act as spectral low-pass filters that restrict the spectral range to 540 GHz. When ECE is being measured, a wire grid is placed after the second filter to attenuate the light before it is focussed into the liquid helium-cooled detector by a 90° off-axis paraboloidal mirror. The attenuator rejects over 98% of the ECE into an eccosorb dump to prevent saturating the sensitive

detector.

In order to calibrate the FMI system in-situ, a vacuum feedthru is used to rotate the ellipsoidal mirror away from the vacuum vessel so that it can view the calibration source (type CV eccosorb immersed in LN) through a 20 cm clear aperture fused silica window as shown in Fig. 6. Typically, the detector signal produced by a single scan of the FMI is averaged over 32,000 scans. Since the wire grid attenuator is removed for measuring the calibration source spectrum, a separate measurement of the spectrally flat attenuation factor has to be made in order to compute the absolute level of the ECE spectra. Moreover, the transmissivity of the fused silica calibration window must be taken into account for this computation. The uncertainties in the measurement of the calibration source spectrum, the wire grid attenuation factor, and the fused silica window transmissivity combine to yield an uncertainty of ± 8% in the measured ECE spectral intensity (and hence in the measured electron temperatures). Thus, the efficiency of the optical system has been adequate to achieve a good calibration. The predicted loss between the calibration source and the input lens of the FMI is 4 dB at 75 GHz, but this has not been experimentally confirmed.

## 4. Studies of Sawteeth

With its 2 ms scan time and 4 ms scan period, the radiometer is particularly well suited to study electron temperature sawtooth fluctuations on TFTR, where typical sawtooth periods range from 40 to 120 ms. After the radiometer data has been converted to temperature vs. radius and time, constant-radius slices can be used to measure the sawtooth period and to follow heat pulse propagation outward in the same way that fixed frequency ECE diagnostics are used on smaller tokamaks. Constant-time slices reveal the evolution of the temperature profile, and overlapping these profiles offers a convenient way to locate the inversion radius. For finer time scale studies at fixed locations in the plasma, the radiometer can be switched to dwell mode, for which the time resolution is less than 50 μs.

The Michelson collects data on both the forward and reverse strokes of its scanning mirror. The time assigned to each scan is taken to be the time of occurrence of the "centerburst" of the interferogram. Since the

centerburst occurs close to one end of the mirror stroke, the nominal time between successive scans alternates between 6 ms and 22 ms. Therefore, the Michelson does not sample the temperature profile frequently enough to follow the sawtooth waveform, except in the case of the longer period sawteeth. However, when it does sample the profile, its time resolution appears to be adequate to reveal the profile shape.

Together with the TFTR soft X-ray imaging system, the radiometer has been used to identify two basic types of temperature sawteeth - the simple type, with a period of about 40 ms, and the compound sawtooth, with a period of up to 120 ms.[8,9] Examples of the latter type are shown in Fig. 8. Figure 8(a) shows three consecutive compound sawteeth and four profiles for one of them, as measured with the radiometer. Profiles C and D show that the profile actually becomes hollow at the time of the sawtooth "crash". This remarkable feature is corroborated by two profiles (E and F) that were measured with the Michelson for another similar discharge, as shown in Fig. 8(b). Profiles A and B of Fig. 8(a) illustrate the characteristic feature of a compound sawtooth, i.e. an intermediate relaxation, which appears to be a partial reconnection that leaves the center of the plasma unaffected. Note that profiles E and F in Fig. 8(b) have not been corrected for the slight deviation of the magnetic field from the simple $R^{-1}$ dependence that it has in vacuum.

## 5. Parametric Dependence of the Temperature Profile

Both the radiometer and the Michelson have been used to study the parametric dependence of the peak electron temperature and the shape of the profile in ohmically heated plasmas. A multiple linear regression analysis was applied to data from over 200 plasma discharges, including some from PLT, to characterize the dependence of the peak electron temperature upon various plasma parameters.[8] The result was:

$$T_{eo} \sim B_T^{0.78} R^{-0.31} a^{1.1} Z_{eff}^{0.45} I_p^{-0.24}$$

This scaling is similar to those predicted by the models of Perkins[10] and Tang et al.[11], in the sense that the peak temperature is independent of the average density for fixed effective Z. The scaling also suggests that the confinement time is a function of the major radius, which is consistent with

the TFTR confinement scaling found by Efthimion et al.[12]

The radiometer has been used to study the shape of the temperature profile for a range of minor radii and plasma currents in ohmically heated discharges.[8] As illustrated by Fig. 9, the radius of the q = 1 surface, normalized to the minor radius, was found to be approximately inversely proportional to the edge q. Moreover, when the profile shape was characterized by the ratio of the volume-averaged temperature divided by the central temperature, this quantity also was found to be approximately inversely proportional to the edge q. Recently, temperature profiles measured with the Michelson during TFTR discharges with neutral beam auxiliary heating have been shown to exhibit the same trends.[13]

## 6. Temperature Evolution During Discharge Startup

The TFTR ECE diagnostics provide valuable support for the effort to optimize the startup of the TFTR discharge. It has been found that poloidal flux consumption can be reduced and current penetration can be facilitated by growing the plasmas inward from the outer limiter during the startup phase, instead of keeping the major radius constant. In order to produce model computations of the current density profile evolution during startup, the transport analysis code TRANSP requires measurements of the electron temperature profile evolution, starting as early in the discharge as possible. A recent report included an analysis of a 1.0 MA plasma startup that used temperatures measured by the radiometer[14]. Naturally, under these conditions of comparatively low electron temperature and density, the optical thickness of the plasma becomes an issue. While the parametric scaling of the optical thickness of the ordinary mode first harmonic and the extraordinary mode second harmonic is the same, the absolute magnitude of the optical thickness is approximately twice as large for the second harmonic. Since the wider spectral range of the Michelson allows it to use the second harmonic for all available TFTR toroidal field levels, it has become the preferred instrument for studying startup.

Fig. 10(a) shows three temperature profiles measured with the Michelson during a constant radius startup. It is interesting to note that the shape and magnitude of the outer portion of the final profile appears to act like a

limiting envelope for the earlier profiles. Figure 10(b) shows three profiles measured during a "grown" startup. Note that the early profiles are not hollow in this case. The inward shift of the major radius and the gradually growing minor radius are evident. Current profiles computed by TRANSP for these two cases indicate that the current penetrated to the center faster for the "grown" case. The temperature profiles in Fig. 10 have not been corrected for the deviation of the magnetic field from its value in vacuum.

## 7. The Attempt to Measure the Electron Density Profile

To date, attempts to use measurements of optically thin ECE to measure the electron density profile in a tokamak[15,16] have been thwarted by the inability to control the field of view for the optically thin portion of the spectrum. Due to the reflective walls of the vacuum vessel, the emission intensity at each optically thin spectral frequency represents some unknown type of average of the intensity from a vertical slab of plasma. The effect of the reflective TFTR vacuum vessel is evident in Fig. 11(a), which compares measurements of the ECE spectrum using the Michelson in the two polarization directions for two essentially identical discharges. Following Hutchinson and Komm[17], the measured intensities of the optically thin third harmonic, extraordinary and ordinary modes, can be used together with the calculated value of the single pass optical depth for the extraordinary mode to compute two parameters that are related to the effect of the vacuum vessel upon the spectrum. In that model, the observed shape of the optically thin portion of the spectrum results from the fraction q of the incident intensity that is reflected without changing the polarization direction, and the fraction p of the incident intensity that is reflected into the orthogonal polarization direction. The spectra in Fig. 11(a) yield $q = .57$ and $p = .18$, and these values are essentially the same, considering the experimental uncertainties, as the results that were obtained by Stauffer and Boyd on PLT and by Hutchinson and Komm on Alcator.

Recently, a viewing target for the Michelson has been installed into TFTR as part of the graphite bumper limiter on the back wall of the vessel. The target consists of a 15 cm diameter concave spherical reflector. The surface of the graphite was highly polished, and a laser was employed to align it so as to re-image the Michelson viewing port onto itself. The choice of a

smaller field stop should allow the reflector to fill the field of view of the Michelson. Under these conditions, the averaging effect of multiple reflections upon the optically thin spectrum should be eliminated. Then it should be possible to use the optically thin extraordinary mode third harmonic or the optically thin ordinary mode second harmonic to measure the density profile. The required measurement of the electron temperature can be achieved in either polarization direction, as is illustrated by the two profiles in Fig. 11(b), which were derived from the spectra in Fig. 11(a). These profiles have not been corrected for the deviation of the magnetic field from its value in vacuum.

Acknowledgement

This work was supported by U.S. DoE Contract No. DE-AC02-76-CHO-3073.

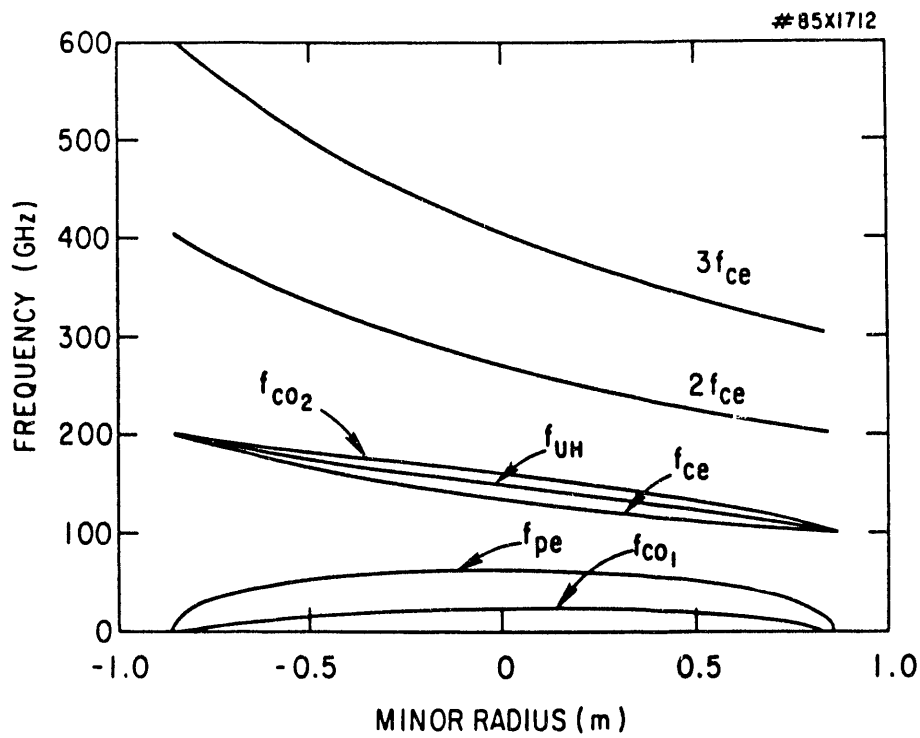


Figure 1

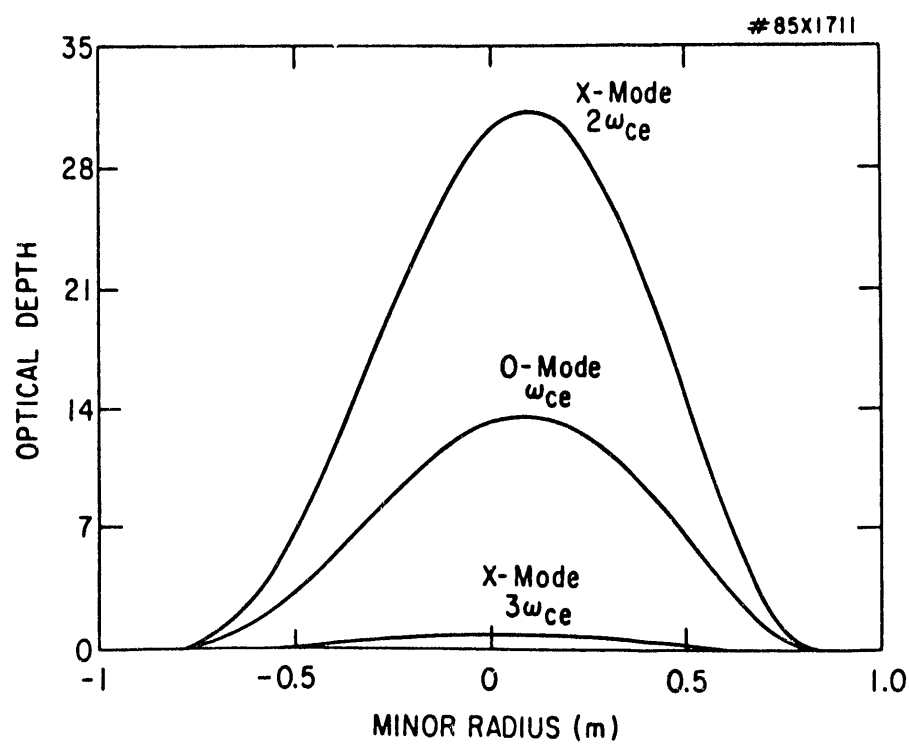


Figure 2

## REFERENCES


[1] M. Bornatici, Plasma Physics 24, 629 (1982).

[2] W.H. Clark, Plasma Physics 25, 1501 (1983).

[3] G. Taylor, P.C. Efthimion, M.P. McCarthy, V. Arunasalam, R. Bitzer, J. Bryer, R.C. Cutler, E. Fredd, M.A. Goldman, and D.A. Kaufman, Rev. Sci. Instr. 55, 1739 (1984).

[4] G. Taylor, P.C. Efthimion, M.P. McCarthy, E. Fredd, M.A. Goldman, and D.A. Kaufman, Rev. Sci. Instr. 56, 928 (1985).

[5] P.C. Efthimion, V. Arunasalam, R. Bitzer, L. Campbell, and J.C. Hosea, Rev. Sci. Instr. 50, 949 (1979).

[6] M.P. McCarthy, G. Taylor, P.C. Efthimion, E. Fredd, M.A. Goldman, R.C. Cutler, F.J. Stauffer, and D.A. Boyd, in Proc. of 8th Intl. Conf. on Infrared and Millimeter Waves, (Miami, Florida) Paper M4.5 (1983).

[7] F.J. Stauffer, D.A. Boyd, R.C. Cutler, and M.P. McCarthy, Rev. Sci. Instrum. 56, 925 (1985).

[8] G. Taylor, et al., Princeton University, Plasma Physics Laboratory Report, PPPL-2221 (1985) (Submitted to Nuclear Fusion for publication.)

[9] H. Yamada, et al., Princeton University, Plasma Physics Laboratory Report, PPPL-2213 (1985).

[10] F.W. Perkins, Proc. 3rd Intl. Symp. on Heating in Toroidal Plasmas, (Rome, Italy) Vol. II, 977 1984.

[11] W.M. Tang, et al., 10th Intl. Conf. on Plasma Physics and Controlled Nucl. Fus. Research (London, UK) 1984.

[12] P.C. Efthimion, et al., 10th Intl. Conf. on Plasma Physics and Controlled Nucl. Fus. Research (London, UK) 1984.

[13] M. Murakami, et al., Proc. 12th Europ. Conf. on Controlled Fusion and Plasma Physics (Budapest, Hungary) 1985.

[14] D. Mueller et al., Proc. of Erice Workshop on Tokamak Startup (1985).

[15] F. Engelmann and M. Curatolo, Nucl. Fusion 13, 497 (1973).

[16] D.A. Boyd, Int. J. Infrared Millimeter Waves 1, 45 (1980).

[17] I.H. Hutchinson and D.S. Komm, Nucl. Fus. 17, 1077 (1977).

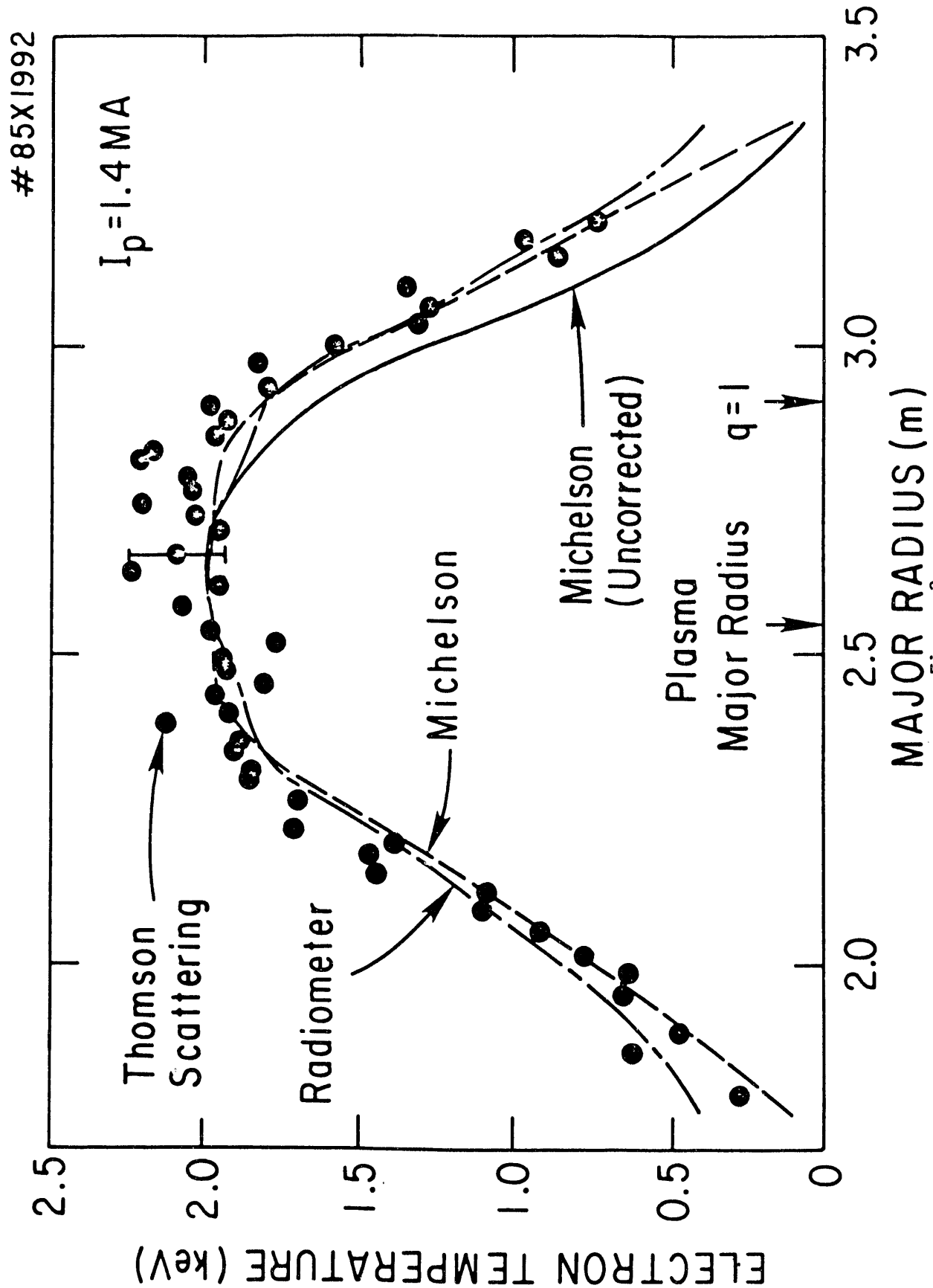
#85X1992
$I_p$=1.4 MA
Thomson Scattering
Radiometer
Michelson
Michelson (Uncorrected)
Plasma Major Radius
q=1
ELECTRON TEMPERATURE (keV)
MAJOR RADIUS (m)
2.5
2.0
1.5
1.0
0.5
0
2.0
2.5
3.0
3.5

Figure 3

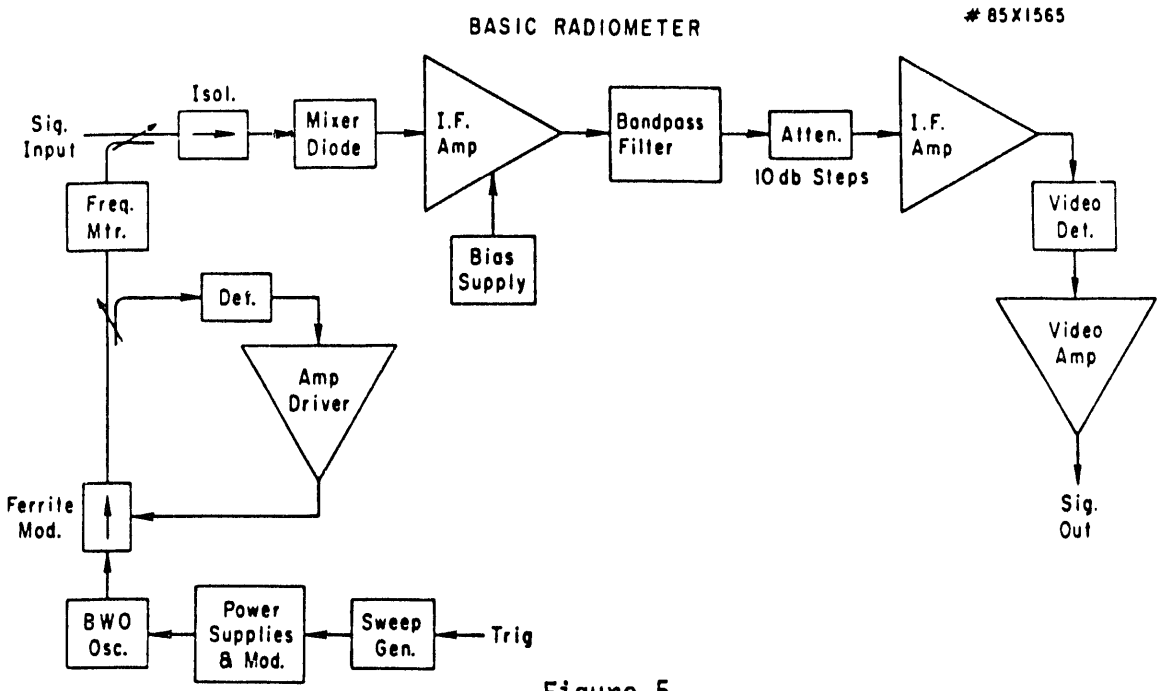


Figure 5

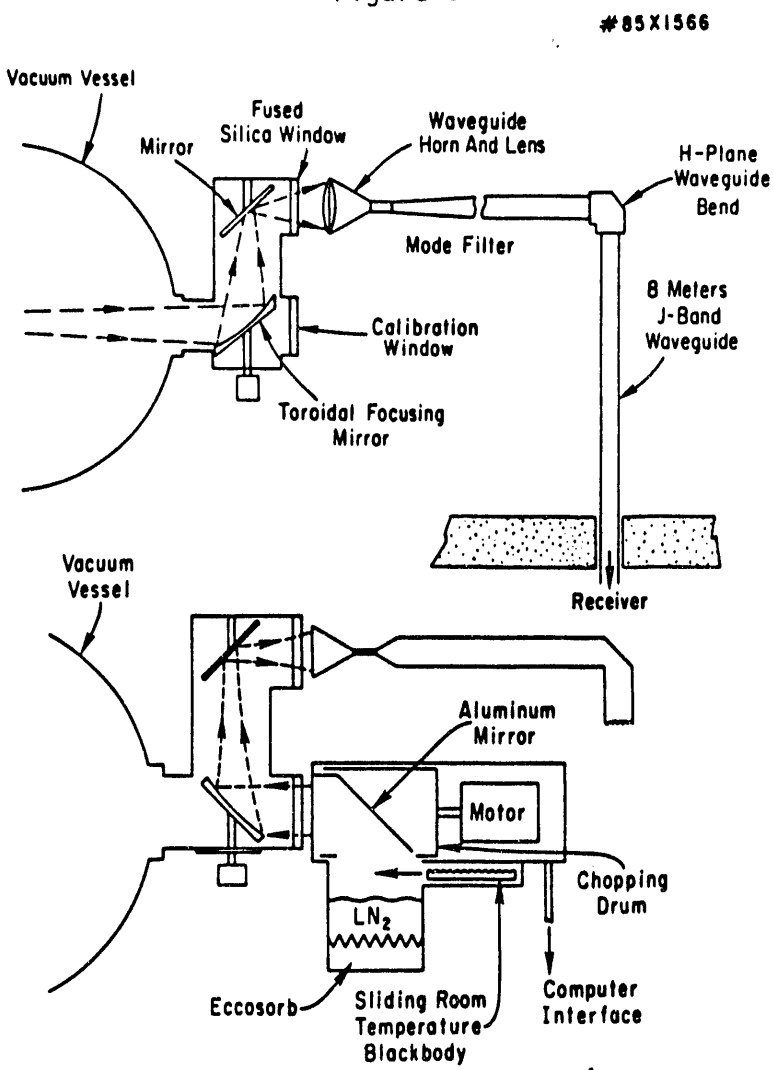


CALIBRATION SETUP

Figure 4

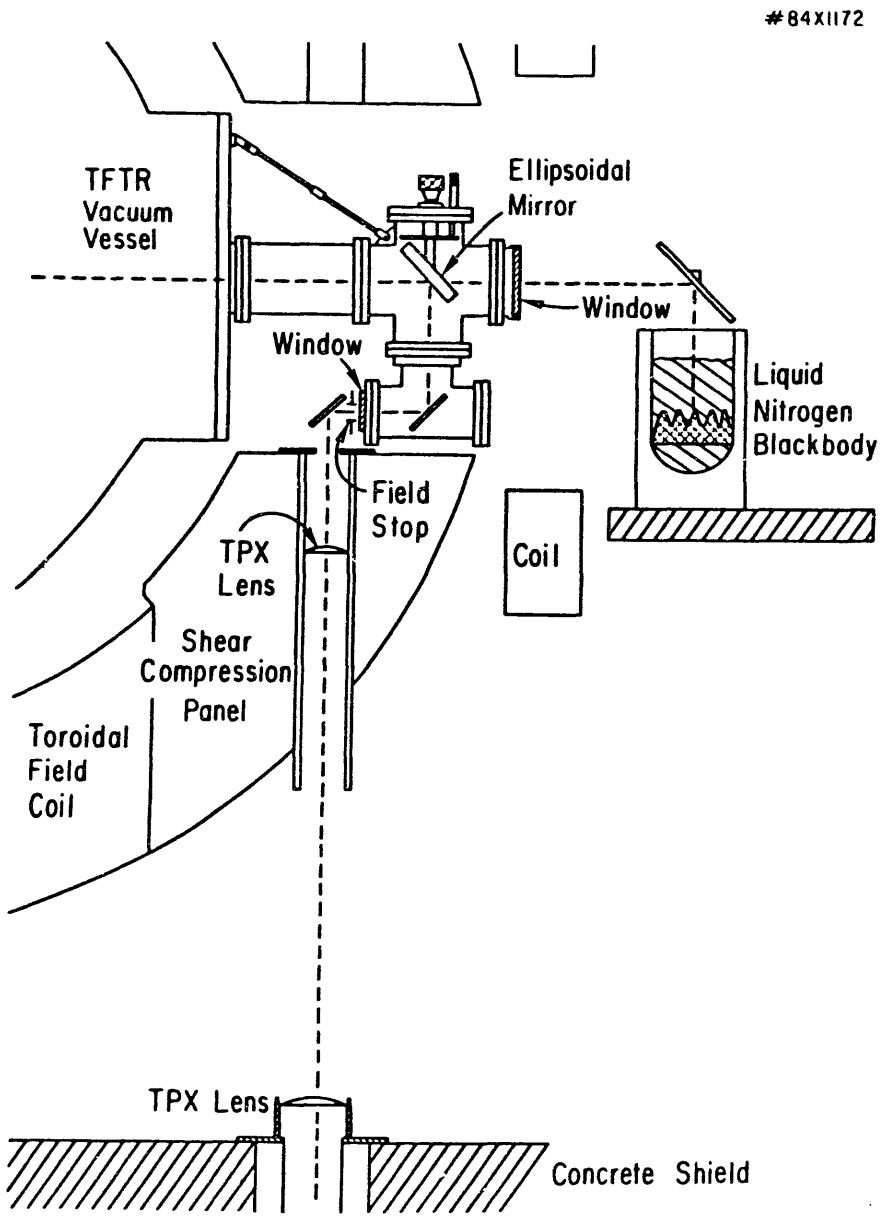


Figure 6

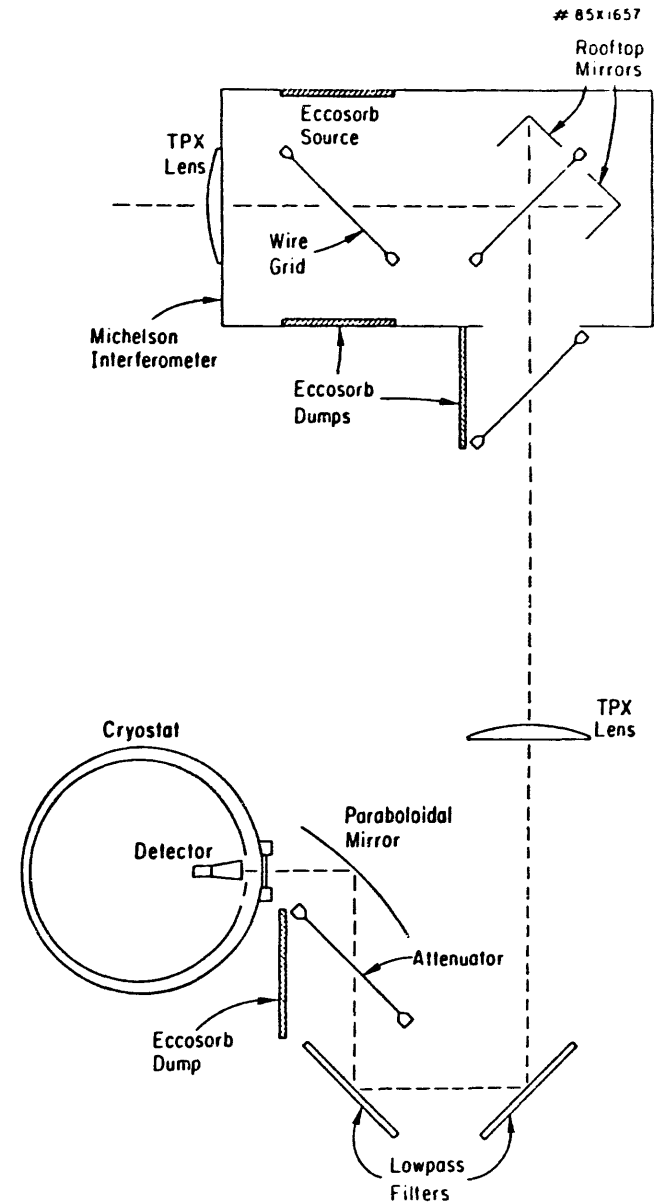


Figure 7

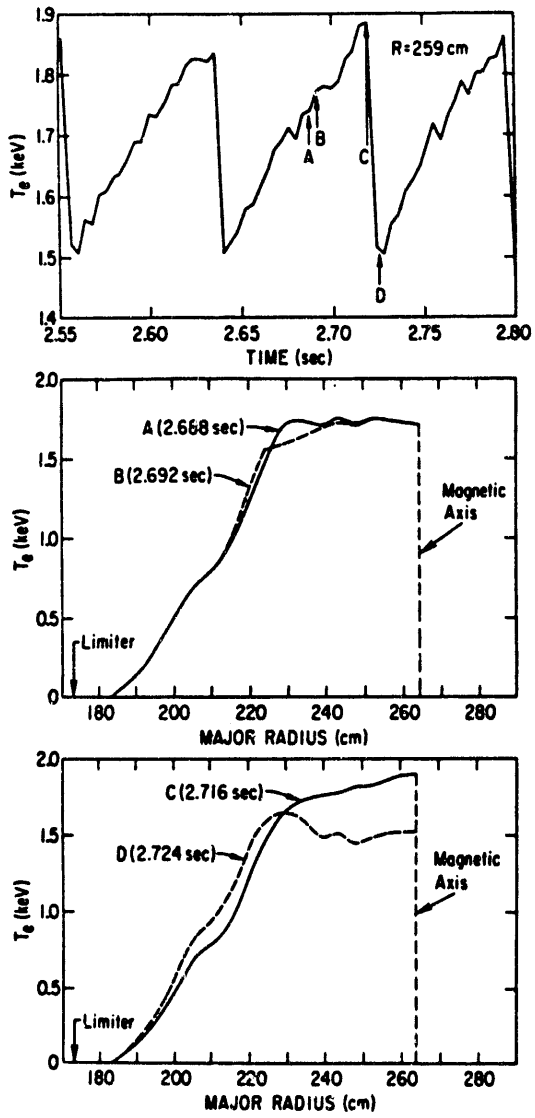


Figure 8 (a)

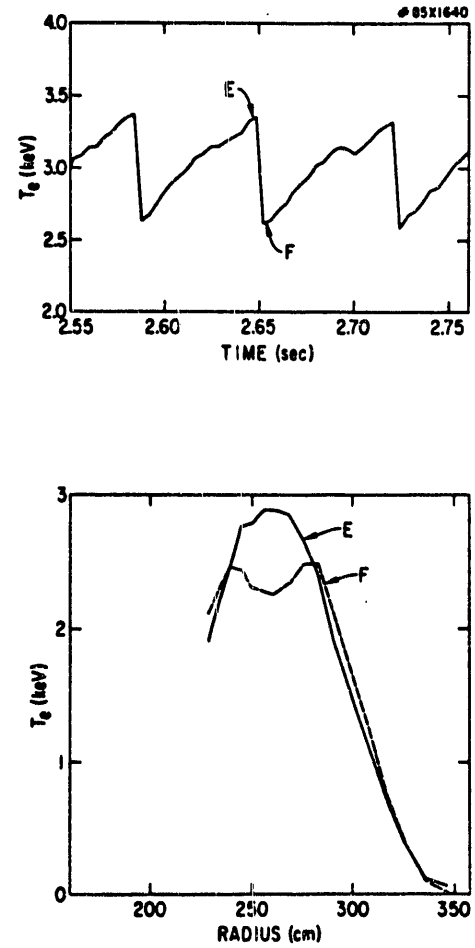


Figure 8 (b)

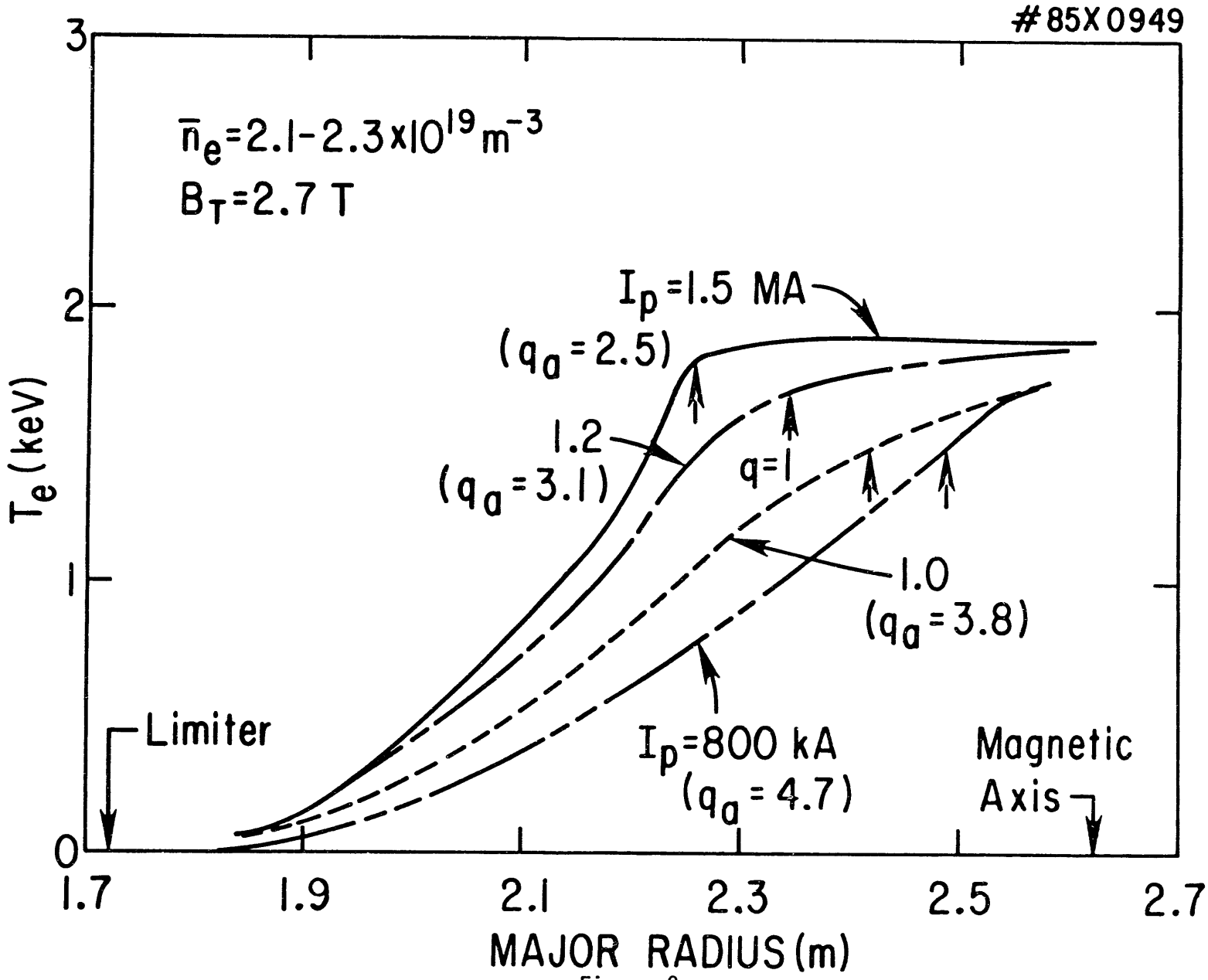
#85X0949
$\bar{n}_e$=2.1-2.3x10$^{19}$m$^{-3}$
$B_T$=2.7 T
$I_p$=1.5 MA
($q_a$=2.5)
1.2
($q_a$=3.1)
q=1
1.0
($q_a$=3.8)
$I_p$=800 kA
($q_a$=4.7)
Limiter
Magnetic
Axis
$T_e$(keV)
MAJOR RADIUS(m)
0
1
2
3
1.7
1.9
2.1
2.3
2.5
2.7
Figure 9

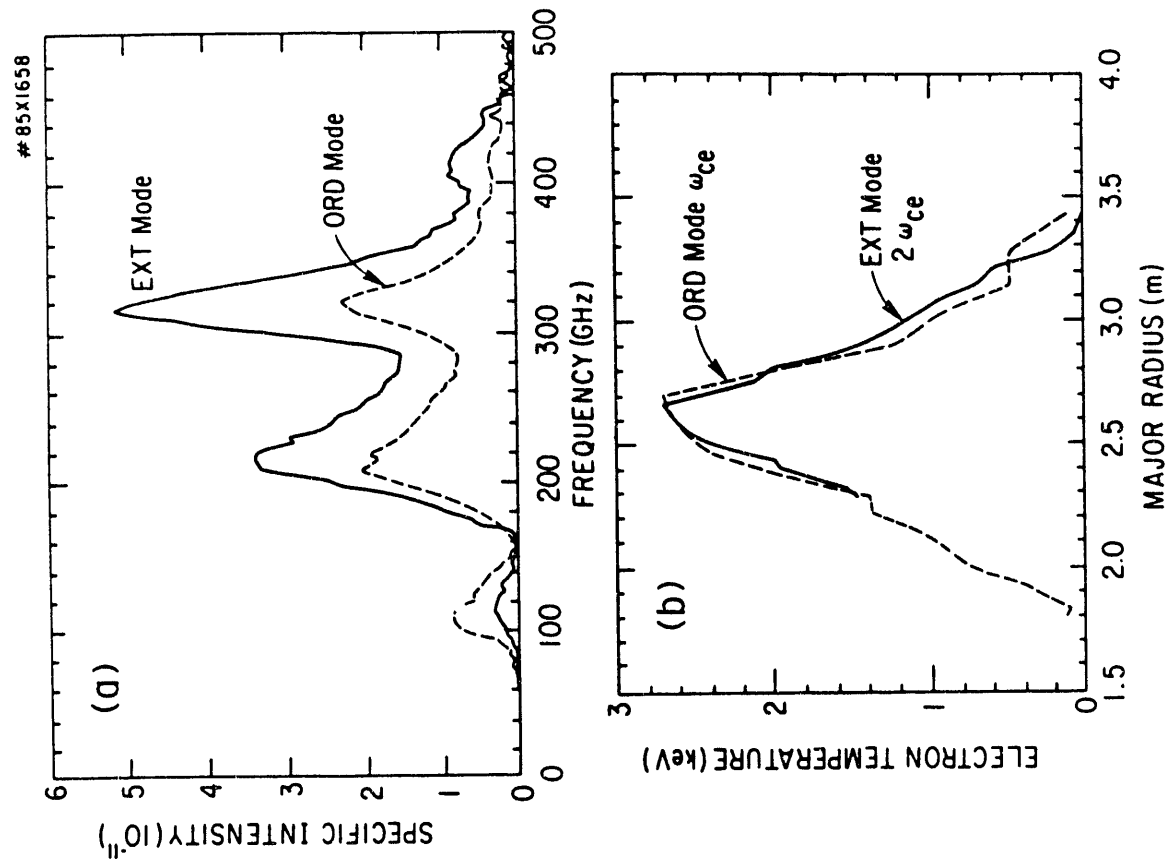


Figure 11

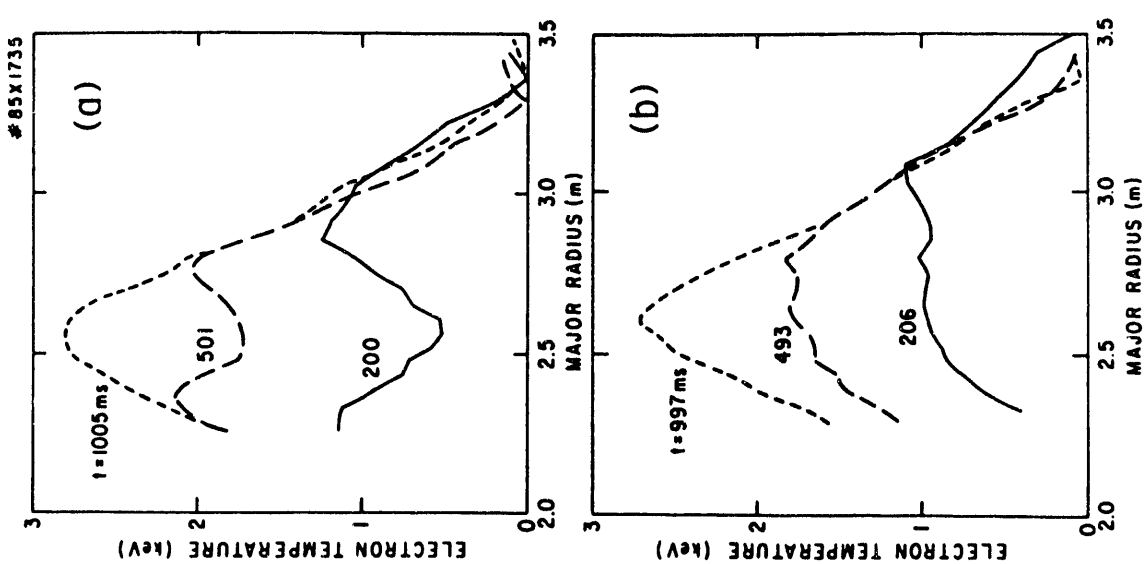


Figure 10

# Electron Cyclotron Emission Measurements During Electron Cyclotron Heating in the Wendelstein VII–A Stellarator at 1 Tesla and 2.5 Tesla

H.J. Hartfuß, M. Tutter, W VII–A Team*
*Max-Planck-Institut für Plasmaphysik*
*EURATOM Association, D-8046 Garching*
*Federal Republic of Germany*

*ECRH Group***
*Institut für Plasmaforschung der Universität Stuttgart*
*D-7000 Stuttgart*
*Federal Republic of Germany*

ABSTRACT

Second harmonic electron cyclotron emission measurements were performed with an eight-channel heterodyne receiver on the WENDELSTEIN VII-A Stellarator (R = 2.0 m, a = 0.1 m, l = 2, m =5) during electron cyclotron heated discharges at 1 T (28 GHz) and 2.5 T (70 GHz). Characteristic deviations in the shape of the electron temperature profile compared to Thomson scattering results have been found which are explained assuming a small amount of mildly relativistic suprathermal electrons in addition to the thermalized bulk. Code simulations were carried out from which the suprathermal energy and density can be estimated.

## 1. Introduction

Electron cyclotron heating (ECH) was extensively studied in WENDELSTEIN VII-A Stellarator using a single gyrotron for plasma build up and heating. The experiments were carried out at 1 T main toroidal field on axis with a 28 GHz/200 kW/40 ms gyrotron, and at 2.5 T with a 70 GHz/200 kW/100 ms one. The power was launched as a linearly polarized wave in O-mode polarization ($E \parallel B$, $k \perp B$). Different circular waveguide modes ($TE_{02}$, $TE_{01}$, $TE_{11}$, $HE_{11}$) resulting in various degrees of polarization were tested /1/.

---

* G. Cattanei, D. Dorst, A. Elsner, V. Erckmann, G. Grieger, P. Grigull H. Hacker, H.J. Hartfuß, H. Jäckel, R. Jaenicke, J. Junker, M. Kick, H. Kroiss, G. Kuehner, H. Maaßberg, C. Mahn, S. Marlier, G. Müller, W. Ohlendorf, F. Rau, H. Renner, H. Ringler, F. Sardei, M. Tutter, A. Weller, H. Wobig, E. Würsching, M. Zippe

** W. Kasparek, G. Müller, P.G. Schüller, K. Schwörer, M. Thumm, R. Wilhelm

In each of the different types of discharges investigated, characteristic deviations in ECE temperature profiles compared to Thomson scattering results are found. They are most pronounced on the low field side and exhibit a clear correlation with electron density. The deviations are explained assuming an energetic tail in the Maxwell distribution of the electrons.

## 2. Electron cyclotron emission measurements

ECE measurements were carried out at the 2nd harmonic electron cyclotron frequency in X-mode polarization viewing along a major radius from the low-field side. Two different circular horn antennas are used with an estimated aperture angle of $\pm 4^{o}$. Fundamental mode rectangular waveguide pieces are incorporated acting as polarization filters. A fixed tuned eight-channel heterodyne receiver is used /2/. It has different front ends tuned to 56 GHz and 140 GHz respectively. The back end contains eight six-pole filters covering the intermediate frequency (IF) band of 5 to 10.04 GHz. The 56 GHz version of the receiver is absolutely calibrated applying the hot/cold technique. The different channels of the 140 GHz receiver are only relatively calibrated with the aid of a wide band plasma noise source whose radiation

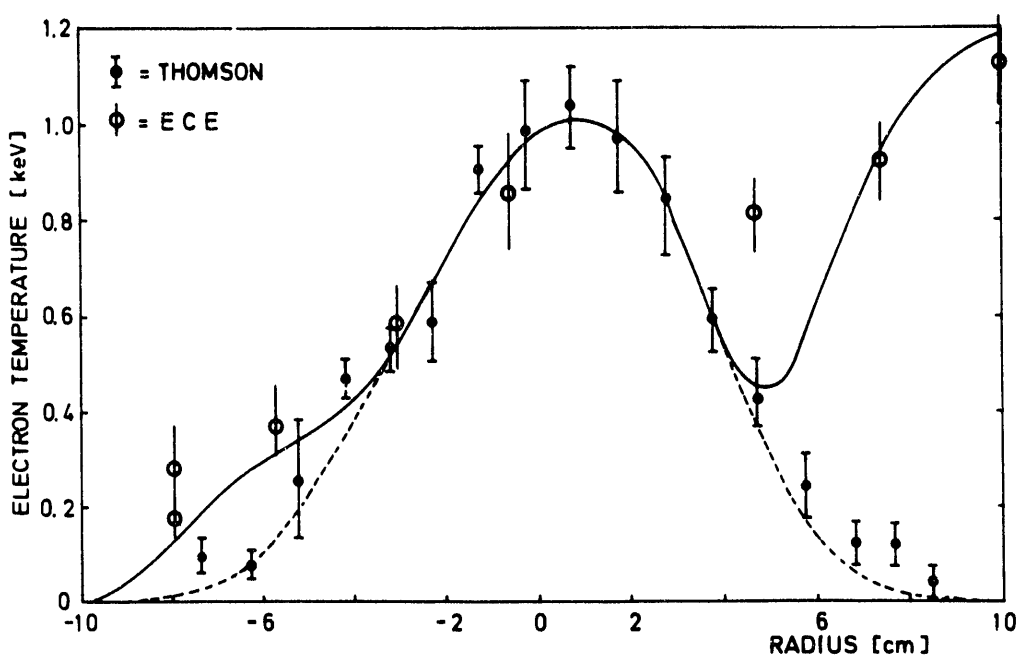


Fig. 1: Electron temperature as measured by Thomson scattering in comparison to the "profile" from 2nd harmonic ECE measurements during a 1 T electron cyclotron heated discharge. The solid line gives the "profile" from code calculations assuming $E_o = 5.3$ keV, $E_{co} = 0$, $n_{ST} = 1 \times 10^{16}/m^3$.

temperature was not known exactly. They are brought to absolute scale relating the central channel to a Thomson scattering measurement during a neutral beam heated discharge.

Due to the different absolute bandwidths of the 2nd harmonic ECE spectrum at 1 T and 2.5 T, the receiving channels cover different plasma radii: at 1 T the complete profile is covered with 4 channels on either side ranging from - 8.6 to + 9.4 cm. At 2.5 T two different local oscillator (LO) frequencies, 151 and 129 GHz respectively (including sideband changes) are necessary to cover the high field side from - 8.2 to - 1.4 cm and the low field side from + 1.4 to 9 cm with 8 channels separately. To avoid interference with the 2nd harmonic emission of the gyrotron itself, sharp notch filters tuned to 56 and 140 GHz are introduced which effectively suppress ( > 40 dB) direct radiation. Additional bandfilters with about 10 % relative bandwidth in front of the receiver suppress any out of band signal. The bandfilters are essential during the calibration procedure.

## 3. Results

A few examples are given representative for a large number of measurements. Each of the figures combine the electron profile measurements from Thomson scattering and ECE. The common feature of all the figures is the occurence of an additional maximum on the low field side of the profile which is interpreted as due to the presence of a thin suprathermal population.

Emission spectra calculations were carried out (see next chapter) for the combined thermal and suprathermal electron populations and the results are included in the figures, too. To make this direct comparison possible, the measured and calculated emission intensities are given in equivalent black body radiation temperatures. Figure 1 gives a measurement with 1 T toroidal field and ECH power irradiation in the $TE_{11}$ mode. Here in addition clear deviations are obvious also on the high field side (radius $r < 0$, $-a \leq r \leq +a$) of the profile.

Figures 2a and 2b give the profiles measured during a 2.5 T discharge at two different times, 30 ms and 70 ms. Wave-launching is in the $HE_{11}$ mode. During this discharge the electron density increases from $1.6 \times 10^{19}/m^3$ to $2.1 \times 10^{19}/m^3$, significantly changing both the electron temperature profile and the suprathermal content. Finally Figures 3a and 4a give as a further

Fig. 2a:

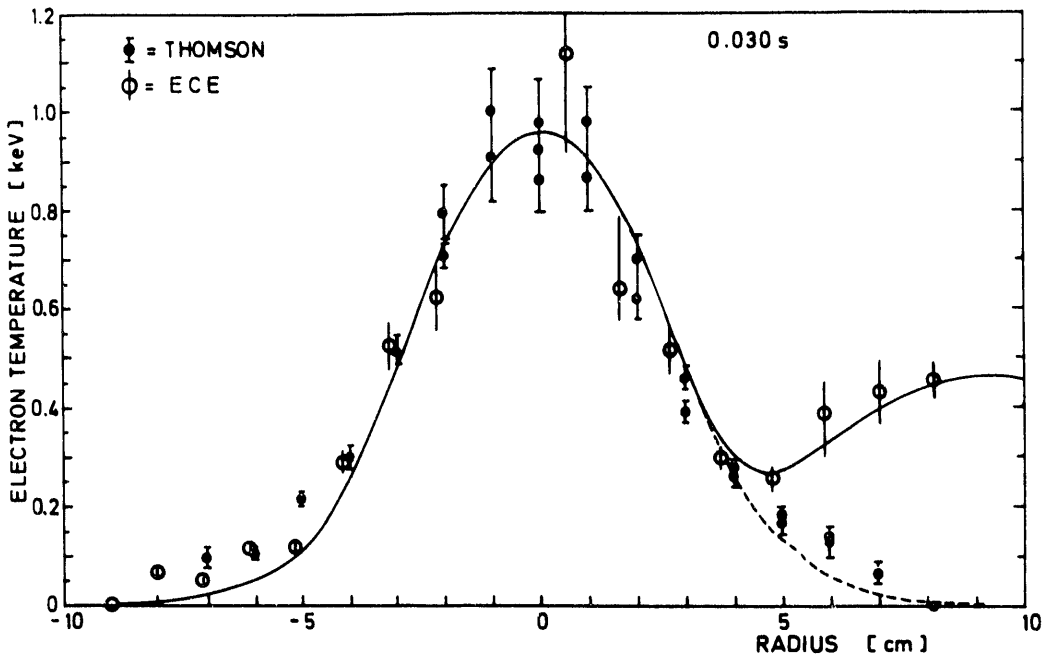


Fig. 2b:

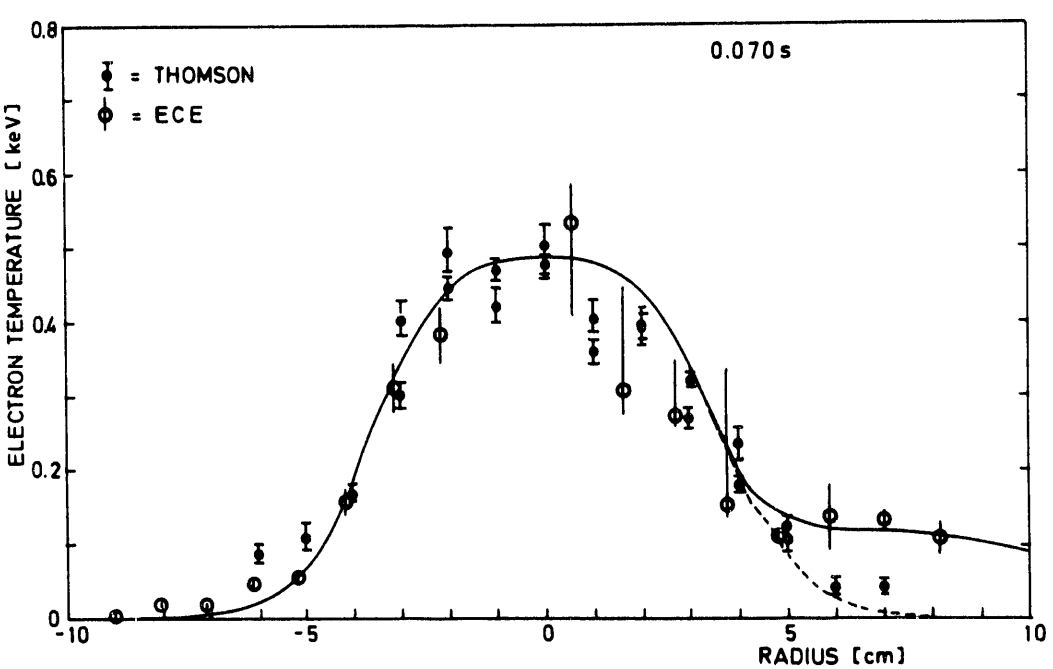


a) Profile information from Thomson scattering and 2nd harmonic ECE measurements at 40 ms, Fig. 2a, and 70 ms, Fig. 2b, during a 2.5 T EC-heated discharge. Increasing electron density reduces the suprathermal content. Solid line results from code simulations:

a) $E_0$ = 10 keV, $E_{CO}$ = 0, $n_{ST} = 2 \times 10^{16}/m^3$, $n_{TH} = 1.6 \times 10^{19}$.

b) $E_0$ = 7 keV, $E_{CO}$ = 3 keV, $n_{ST} = 5 \times 10^{15}/m^3$, $n_{TH} = 2 \times 10^{19}/m^3$.

Fig. 3a:

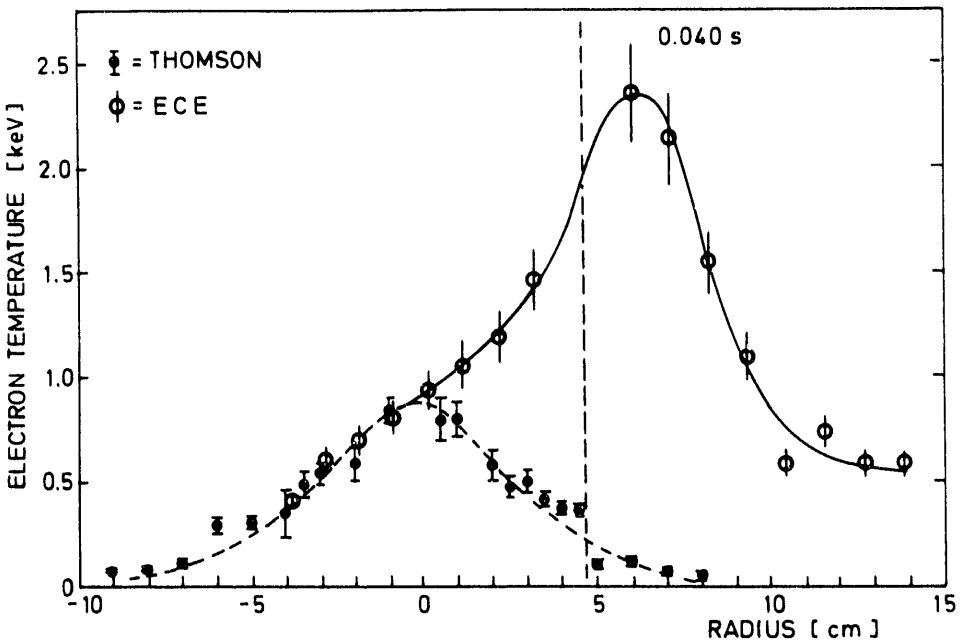


Fig. 3b:

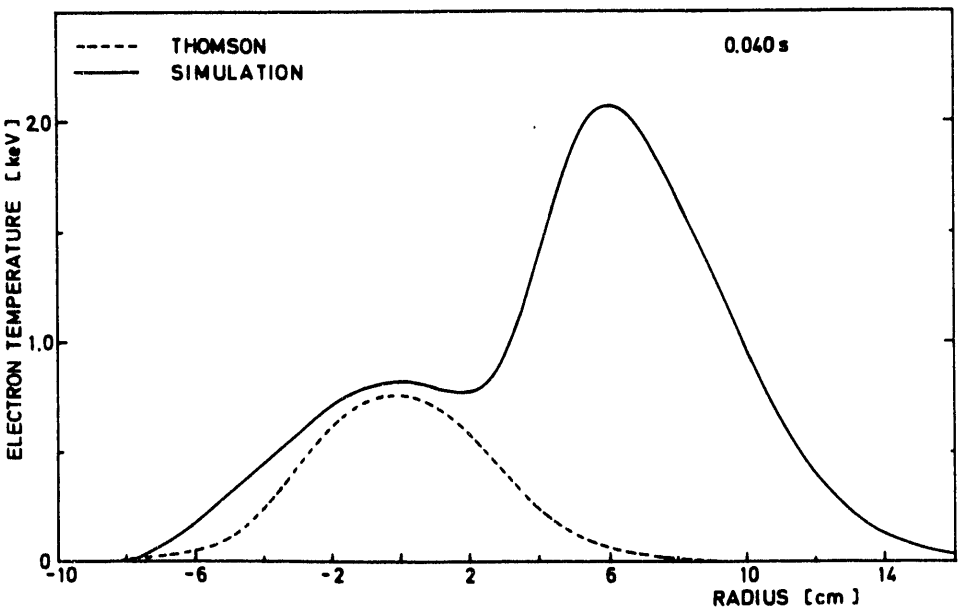


a) Thomson scattering and ECE measurements during an off axis 70 GHz EC-heating experiment. The resonance zone is shifted outwards by nearly 5 cm (vertical dashed line).

b) Code calculation to simulate the ECE "profile" of Fig. 3a. $E_o$ = 3 keV, $E_{CO}$ = 0, $n_{ST}$ = 3 x $10^{17}/m^3$, $n_{TH}$ = 7.9 x $10^{18}/m^3$.

Fig. 4a:

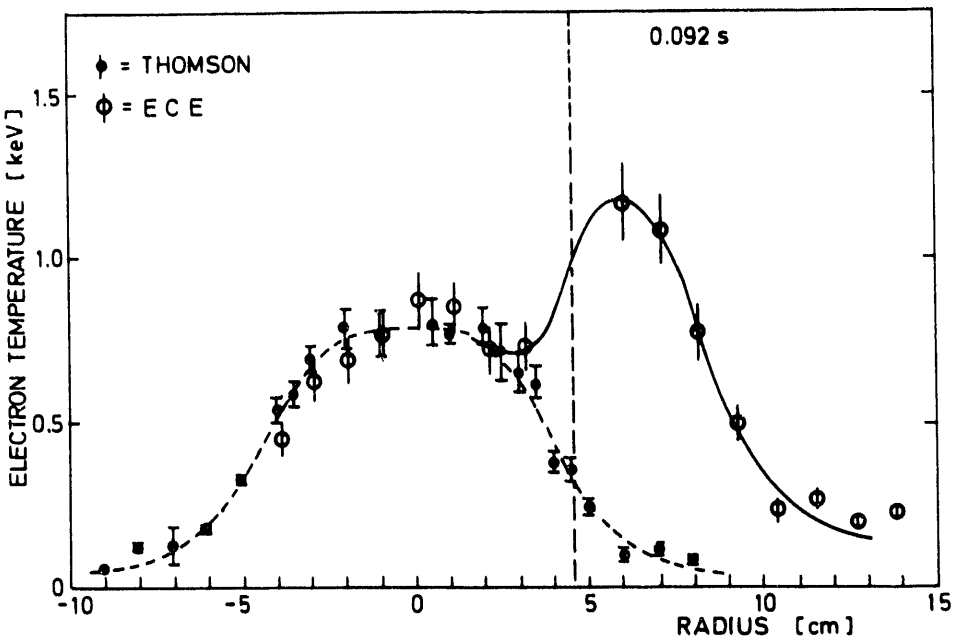


Fig. 4b:

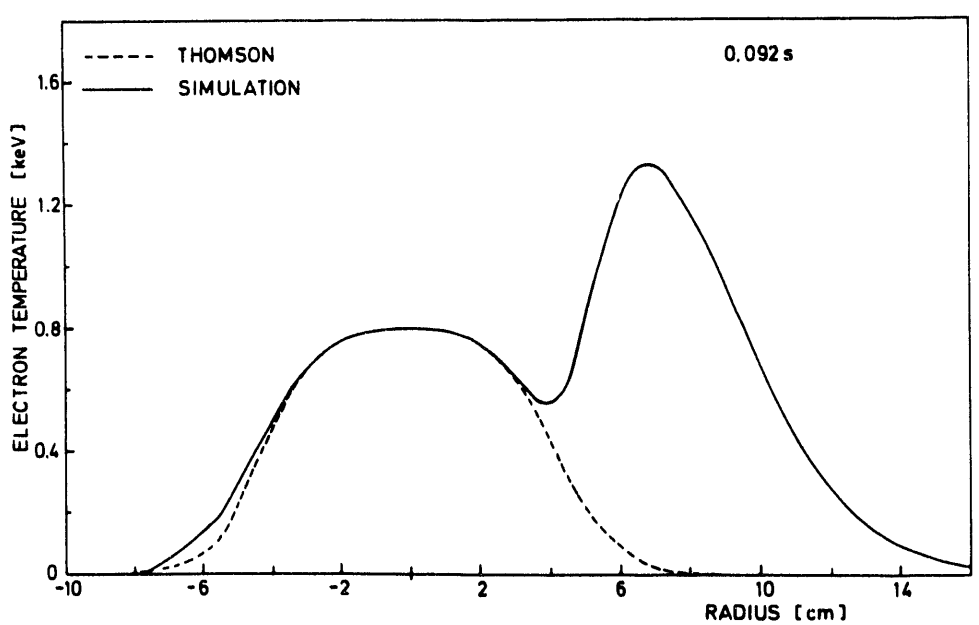


a) Same experiment as given in Figs. 3, but profiles measured at later time during the discharge where density is increased, resulting in reduced suprathermal emission

b) Code calculation with $E_0 = 3$ keV, $E_{CO} = 0$, $n_{ST} = 2 \times 10^{17}$, $n_{TH} = 1.6 \times 10^{19}/m^3$.

example the profiles measured at two different times, 40 ms and 92 ms, of a 2.5 T discharge. But in this experiment the resonance zone was shifted outwards by about 4.5 cm owing to an 2 % increase of the toroidal field. Extreme deviations between the Thomson and ECE measurements are obvious, but again the effect is diminished by the increase of electron density which is 8 x $10^{18}/m^3$ at 40 ms and 1.6 x $10^{19}/m^3$ at 92 ms.

Practically no change in the suprathermal content (width and height of the low field side hump) is observed during constant density discharges, and no significant systematic deviations from the Thomson profiles are found in high density neutral beam heated discharges.

## 4. Simulation

The one dimensional model used to simulate the experimentally observed profiles or spectra is similar to one described earlier /3/. An optically thin suprathermal population of density $n_{ST}$ is assumed with a radial distribution equal to the calculated ECH power deposition profile. The energy distribution is assumed to be purely exponential, $f(E) \sim \exp - (E/E_0)$ with a lower cut-off, $E_{CO}$ and the parallel velocity $v_{\parallel}$ to be neglegible compared to the perpendicular velocity $v_{\perp}$. The code calculations are based on measured temperature and density profiles. They make use of the Schott-Trubnikov formula to calculate the emission intensity. The diamagnetic correction to the magnetic field is considered as well as both linear and quadratic Doppler effects.

The results as given in the figures are calculated omitting completely any wall reflections. Recently these have been included into the code as well as polarization scrambling /4, 5/. Considering both, the estimated suprathermal energy, $E_0$, and the density $n_{ST}$ must be decreased within a factor of 2 to 3 to simulate the observed spectra.

REFERENCES

/1/ V. Erckmann et al., "Recent Results in the WENDELSTEIN VII-A Stellarator" in "Radio Frequency and Plasma Heating" ed. D.G. Swenson, AIP Conference, Proc. No. 129, pp 189-203, New York 1985.

/2/ H.J. Hartfuß, M. Tutter, Rev. Sci, Instr. 56, 1703 (1985).

/3/ C.M. Celata, D.A. Boyd, Nucl. Fus., 17, 735 (1977).

/4/ A.E. Costley et al., Phys. Rev. Lett., 33, 758 (1974).

/5/ R.M.J. Sillen et al., "Electron Cyclotron Measurements on T-10 with a Grating Polychromator", submitted to Nucl. Fus..

# Central Power Balance in Sawtoothing Ohmically Heated Tokamak Discharges in the Princeton Large Torus

A. Cavallo, J. Hosea, R. Bell, and D. McNeill
*Princeton Plasma Physics Laboratory, Princeton, New Jersey 08544, USA*

ABSTRACT

The central energy balance for sawtoothing ohmically heated discharges has been calculated by two different methods. The first uses Z-effective (average effective ion charge) measurements, and the other uses the rate of rise of central stored electron energy as observed on temperature and density sawteeth. The two methods are in reasonable agreement at moderate ($\sim 1.5 \times 10^{13}$ $cm^{-3}$) densities.

If bolometric data is available which can confirm that central radiated power is negligible, then the central Z-effective may be computed from the temperature and density sawteeth.

## INTRODUCTION

The internal disruption, or sawtooth,[1] is a feature of most tokamak discharges. Details of its behavior, especially those which immediately preceed the central density and temperature drop, are quite complicated, and several theories[2-6] have been proposed to explain them.

However, if one looks at the central region immediately after an internal disruption, it is quite simple. The central electron density ($N_{eo}$), central electron temperature ($T_{eo}$) and plasma current profiles are flattened, and the safety factor [$q \equiv rB_T/RB_p$] is equal to one over a large region ($\rho \equiv r/a \lesssim 0.25$) of the discharge. [Here $B_T$ is the toroidal field $B_p$ is the poloidal

field, R is the major radius and a the minor radius of the torus and r is the distance from the magnetic axis.] Thus, immediately after a sawtooth collapse, the central ohmic power deposition to the electrons[7] is:

$$P_\Omega = 4.43 \times 10^3 \frac{Z_e}{T_{eo}^{3/2}} \frac{B_T^2}{R^2} \ln \Lambda \left(\frac{w}{m^3}\right) \qquad (1)$$

Here $Z_e$ is the central effective ion charge, and $\ln\Lambda$ has its usual definition. The electron power balance at the center of the discharge can also be written as:

$$P_\Omega = P_{ei} + \frac{d}{dt}\left(\frac{3}{2} N_{eo} T_{eo}\right) + P_{rad} + P_{TR} \qquad (2)$$

Here $P_{ei}$ is the central electron to ion power transfer, $P_{RAD}$ is the central radiated power and $P_{TR}$ is the central heat loss due to conduction and convection. For tokamak discharges is well conditioned machines with carbon limiters, the power radiated from the central of the discharge is very small: $P_{RAD}$ will be ignored. It will also be assumed that $P_{TR}$ is very small compard to $P_\Omega$, since density and temperature profiles are flattened after a disruption and conduction and convection should be negligible.

Given these assumptions, the central power balance can be written as

$$P_\Omega = P_{ei} + \frac{3}{2} N_{eo} \frac{dT_{eo}}{dt} + \frac{3}{2} T_o \frac{dN_{eo}}{dt} \qquad (3)$$

Thus, central $Z_e$ can be calculated by measuring central power deposition using Eq. 3 and solving Eq. 1 for $Z_e$. This has been verified on PLT (Princeton Large Torus) where we have independently measured $Z_e$ as well as the quantities necessary to measure the central power balance in Eq. 3.

## EXPERIMENTAL PROCEDURES AND RESULTS

On PLT, central electron temperatures and its rate of rise are measured with a grating polychromator[8] which measures second harmonic electron cyclotron emission. This instrument can be calibrated absolutely[9] or by using laser Thomson scattering data. A typical trace of $T_{eo}$ vs time in an ohmic discharge is shown in Fig. 1; the rate of rise of central electron temperature can be measured directly as indicated.

Time average density, $\bar{N}_e$, is measured along the major radius using a single channel 2 mm interferometer. The behavior of the line average density during a typical ohmic discharge is shown in Fig. 3, which illustrates the density sawteeth as well. The amplitude of the density sawteeth ($\delta\bar{N}_e/\bar{N}_e \simeq 0.01$) is much less than the amplitude of the temperature sawteeth ($\delta T_{eo}/T_{eo} \simeq 0.1$) since only changes in line average density are observed.

From Thomson scattering data, for moderate densities ($\bar{N}_e \lesssim 3 \times 10^{13}$ $cm^{-3}$), the density profile is parabolic: $N_{eo} \simeq 1.5\ \bar{N}_e$.

The rate of rise of central density, $dN_{eo}/dt$, is estimated in the following manner. An internal disruption flattens the density and temperature profiles out to some radius m:

Top of sawtooth: $N_T = N_1\ (1-\rho^2)\ -1 < \rho +1$

Bottom of sawtooth:

$$N_B = N_2 \qquad -m < \rho < +m$$

$$= N_1\ (1 - \rho^2) \qquad \begin{matrix} -1 < \rho < -m \\ +m < \rho < +1 \end{matrix}$$

The change in line average density in a sawtooth collapse is given by:

$$\int N_T\, d\rho - \int N_B d\rho = \Delta\bar{N} = N_1 m\ [1 - \frac{m^2}{3}] - N_2 m \qquad (4)$$

Since there is no loss of electrons from the discharge during a sawtooth,

$$\int N_T \, \rho d\rho = \int N_B \, \rho d\rho \tag{5}$$

This plus Eq. 4 yields

$$\Delta\bar{N}/\bar{N} = m^3/4 \tag{6}$$

Grating polychromator measurements indicate that the q=1 surface is at $\rho \approx 0.35$ ($\pm 0.04$). Thus, for $m \approx 0.35$, $\Delta\bar{N}/\bar{N} = 0.01$ and the central electron density changes by about 6% during an internal disruption. The rate of rise of central electron density is then approximately:

$$\frac{dN_{eo}}{dt} \approx 0.06 \, \frac{N_{eo}}{\tau} \, . \tag{7}$$

Here $\tau$ is the period of the sawtooth.

Central ion temperature is obtained from neutron emission measurements; electron to ion power transfer is a small part (<20%) of the power balance for densities $\bar{N}_e < 3 \times 10^{13} \, m^{-3}$.

In order to monitor the impurity content of the discharge, a calibrated Z meter[10] has been installed on PLT. This measures the line average Z-effective ($\bar{Z}_e$) along a major radius:

$$\bar{Z}_e = KV_B \left[ \int_{-1}^{1} \frac{N_e^2(\rho)}{T_e^{1/2}(\rho)} \, d\rho \right]^{-1} \, .$$

Here $V_B$ is the output of the photomultiplier tube which measures the intensity of the visible bremsstrahlung emission at a wavelength of 5235 Å and K is a calibration constant. For the discharges which we have considered, $N_e = N_{eo}(1-\rho^2)$ and $T_e = T_{eo}(1-\rho^2)^3$. It is assumed that $\bar{Z}_e$ is constant across the discharge, so that $\bar{Z}_e = Z_e(\rho=o)$.

Plotted in Fig. 4 is the central ohmic power deposition as calculated from Z-meter measurements versus central power deposition as calculated from the rate of rise of density and temperature sawteeth (using Eq. 3). Agreement is reasonably good for most of the discharges; those farthest from the line $P_\Omega(\bar{Z}_e) = P_\Omega$ are low density discharges ($\bar{N}_e \lesssim 10^{13}$ cm$^{-3}$). At these densities the Z-meter tends to overestimate the central $Z_e$: this is actually to be expected[10] as the signal levels are quite low.

However, at low densities even with carbon limiters, it cannot necessarily be assumed that central radiated power is negligible. Under these conditions it would be best to confirm this assumption using bolometric or spectroscopic data. If this can be verified, then Eq. 3 should prove to be a more reliable way of measure $\bar{Z}_e$ in this regime of tokamak operation.

One problem with using Eq. 3 to measure power deposition (and $\bar{Z}_e$) is that a substantial fraction of the increase in central electron stored energy is due to the rise in $N_{eo}$. From Eq. 7, the contribution from the $dN_{eo}/dt$ term in Eq. 3 is about half the $dT_{eo}/dt$ term. This is quite substantial, and the reliability of this method could be improved if the rate of rise of central density could be measured directly instead of using assumptions about the shape of the density profile before and after the sawtooth collapse.

This could be accomplished using electron cyclotron emission measurements at the third harmonic, extraordinary mode (wave E-field perpendicular to $B_T$) which is optically thin. This would require the use of a viewing dump inside the vacuum vessel.

We have attempted to use third harmonic emission to measure $dN_{eo}dt$ on PLT, but can only affirm that a viewing dump is essential for the success of this method.

## Conclusion

The rate of rise of density and temperature sawteeth can be used under a large variety of tokamak discharge conditions to calculate central $Z_e$. This may be simpler, more direct and more accurate than Z-meter measurements.


## Acknowledgment

We would like to thank R. Fonck and A. Ramsey for their help in the installation and calibration of the Z-meter.


## LIST OF FIGURES

1. Electron temperature ($T_e$) vs time for a typical PLT discharge. The sawteeth are shown on an expanded scale, and $dT_{eo}/dt$ is illustrated.

2. Line average density ($\bar{N}_e$) vs time for a PLT discharge. The density sawteeth are shown in the expanded scale.
3. Illustration of the density profile flattening during an internal disruption.
4. Central power deposition from Z-meter measurements ($P_\Omega(Z_e)$) vs central power deposition $P_\Omega$ from Eq. 3 in the text. For these discharges $q(a) = 3.3$, $B_T \approx 3.2T$, $1 < \bar{Z}_e < 8$, $0.9 \times 10^{13}$ cm$^{-3}$ $< \bar{N}_e < 3 \times 10^{13}$ cm$^{-3}$, 12 eV/ms $< dT_e/dt <$ 78 eV/ms.

## REFERENCES


1. Von Goeler, S., Stodiek, W., and Sauthoff, N., Phys. Rev. Lett., 33 (1974) 1201.
2. Kadomtsev, B.B., Sov. J. Plasma Physics, 1 (1975) 389.
3. Waddell, B.V., Rosenbluth, M.N., Monticello, D.A., and White, R.B., Nucl. Fusion, 16 (1976) 528.
4. Sykes, A. and Wesson, J.A. Phys. Rev. Lett., 37 (1976) 140.
5. Jahns, G.L., Soler, M., Waddell, B.V., Callen, J.D., and Hicks, H.R., Nucl. Fusion 18 (1978) 609).
6. Samain, A., Plasma Physics, 18, 551 (1976).
7. Gross, R.A., Fusion Energy, p138, 1984 (Wiley).
8. Fischer, J., Boyd, D.A., Cavallo, A., Benson, J., Rev. Sci. Inst., 54, 1085 (1983).
9. Cavallo, A., Cutler, R. Rev. Sci. Inst., 56, 931 (1985).
10. Kadota, K., Otsuka, M., Fujito, J. Nuc. Fusion 20, 209 (1980).

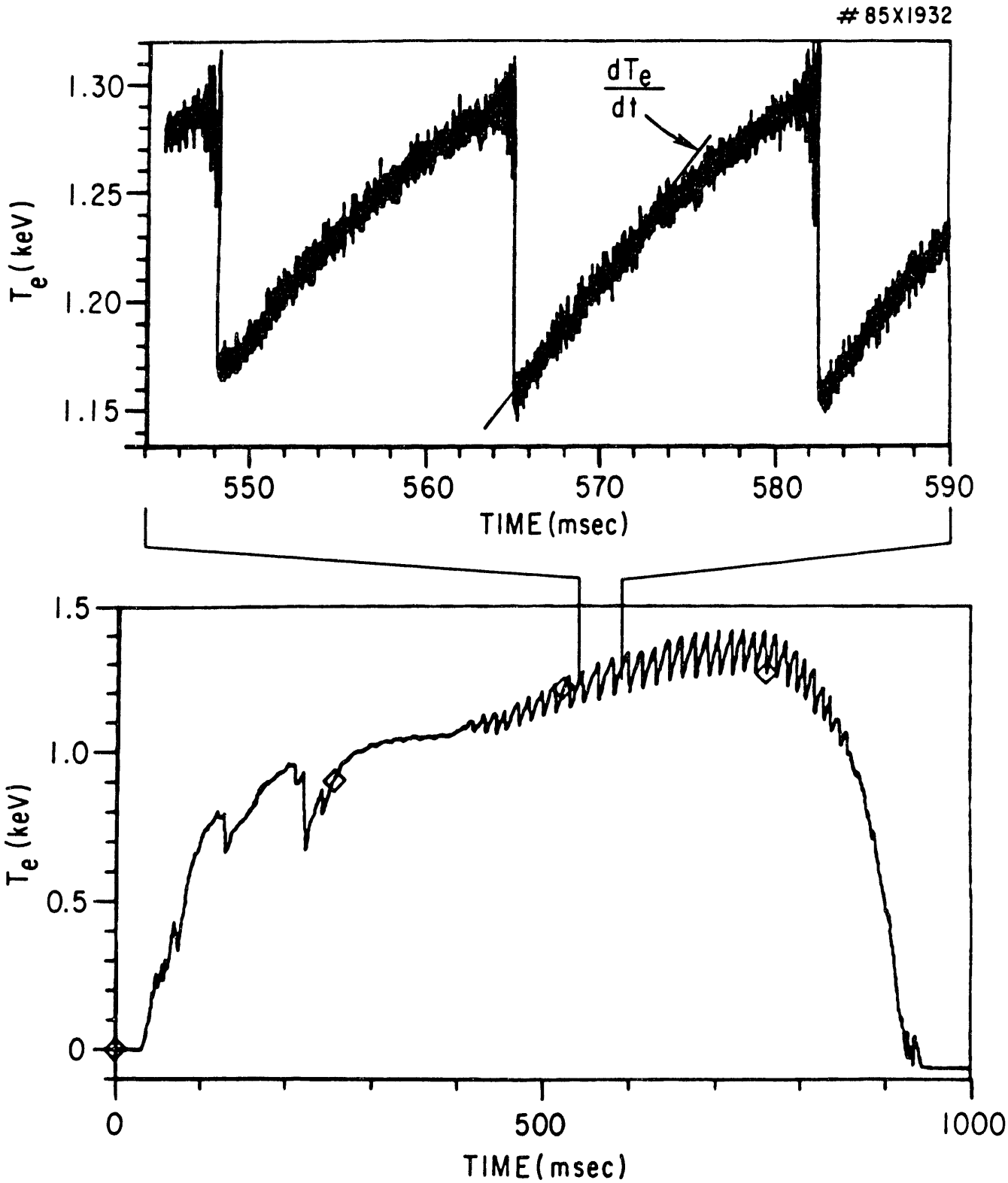
#85X1932
1.30
1.25
1.20
1.15
$T_e$ (keV)
$\frac{dT_e}{dt}$
550
560
570
580
590
TIME (msec)
1.5
1.0
0.5
0
$T_e$ (keV)
0
500
1000
TIME (msec)

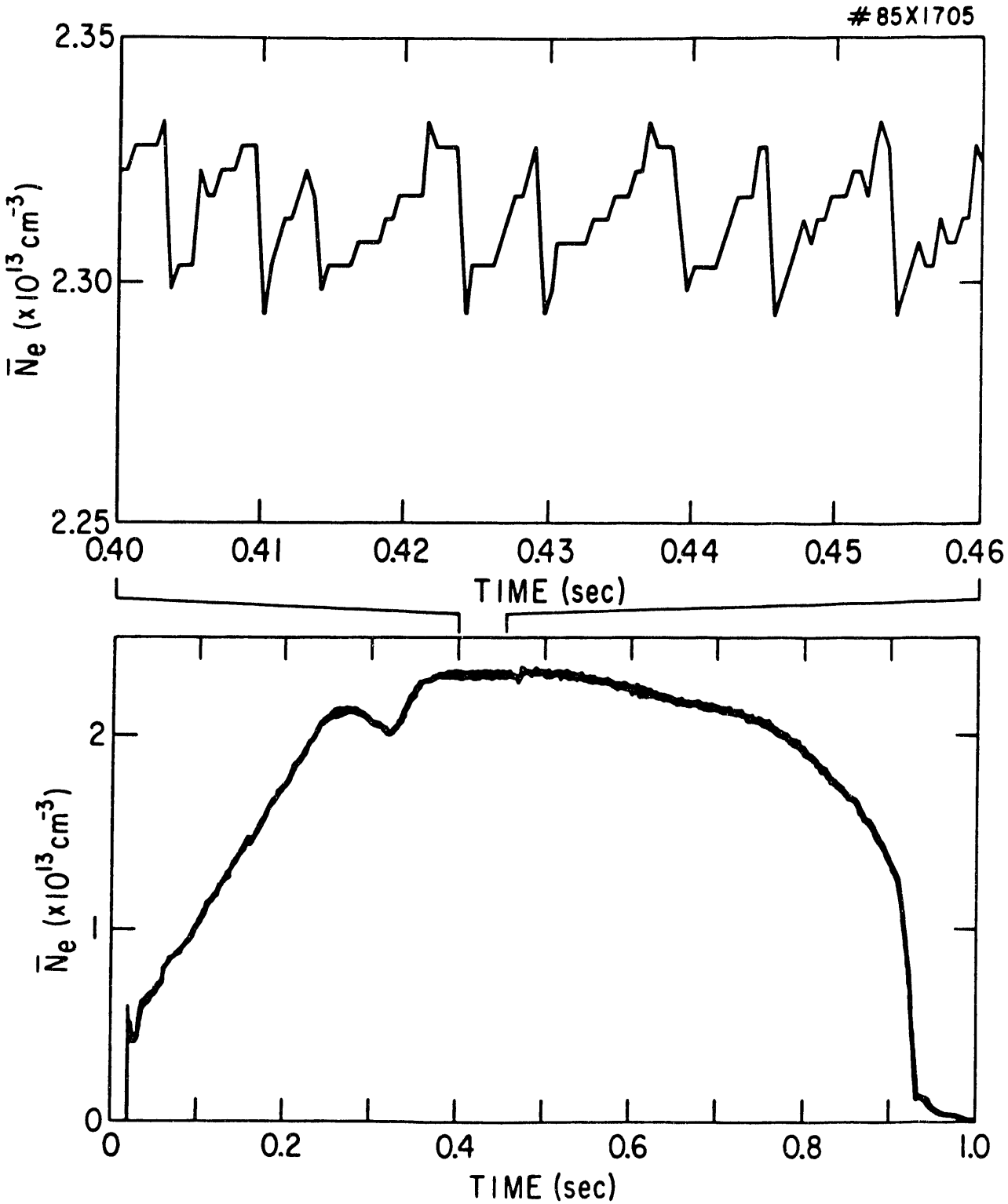
#85X1705
2.35
2.30
2.25
$\bar{N}_e$ (x10$^{13}$cm$^{-3}$)
0.40
0.41
0.42
0.43
0.44
0.45
0.46
TIME (sec)
2
1
0
$\bar{N}_e$ (x10$^{13}$cm$^{-3}$)
0
0.2
0.4
0.6
0.8
1.0
TIME (sec)

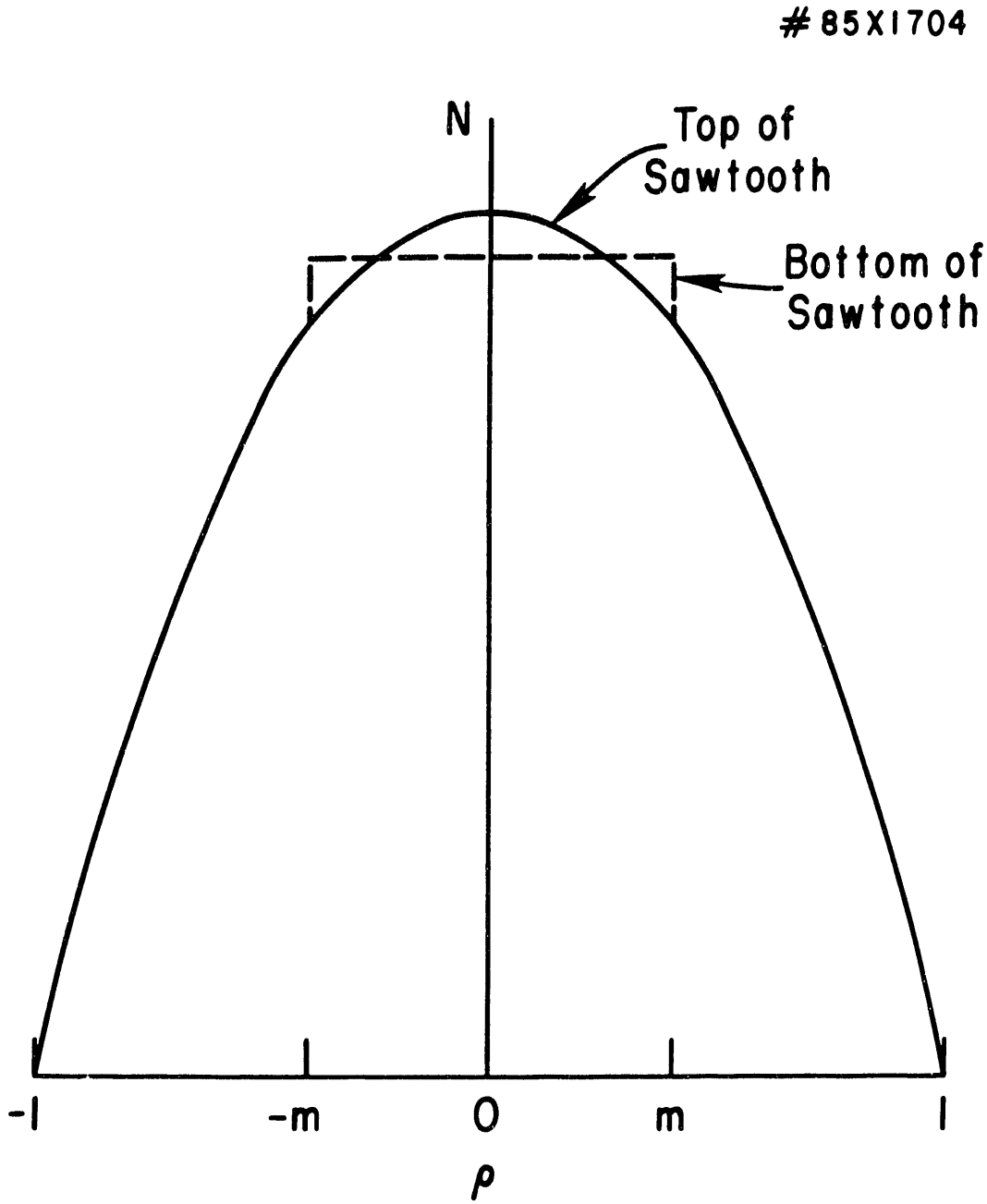


——— $N_1 = (1-\rho^2)$

— — — $N_2 \begin{cases} = (1-\rho^2) & -1 \le \rho \le -m; \quad m \le \rho \le 1 \\ = K & -m \le \rho \le +m \end{cases}$

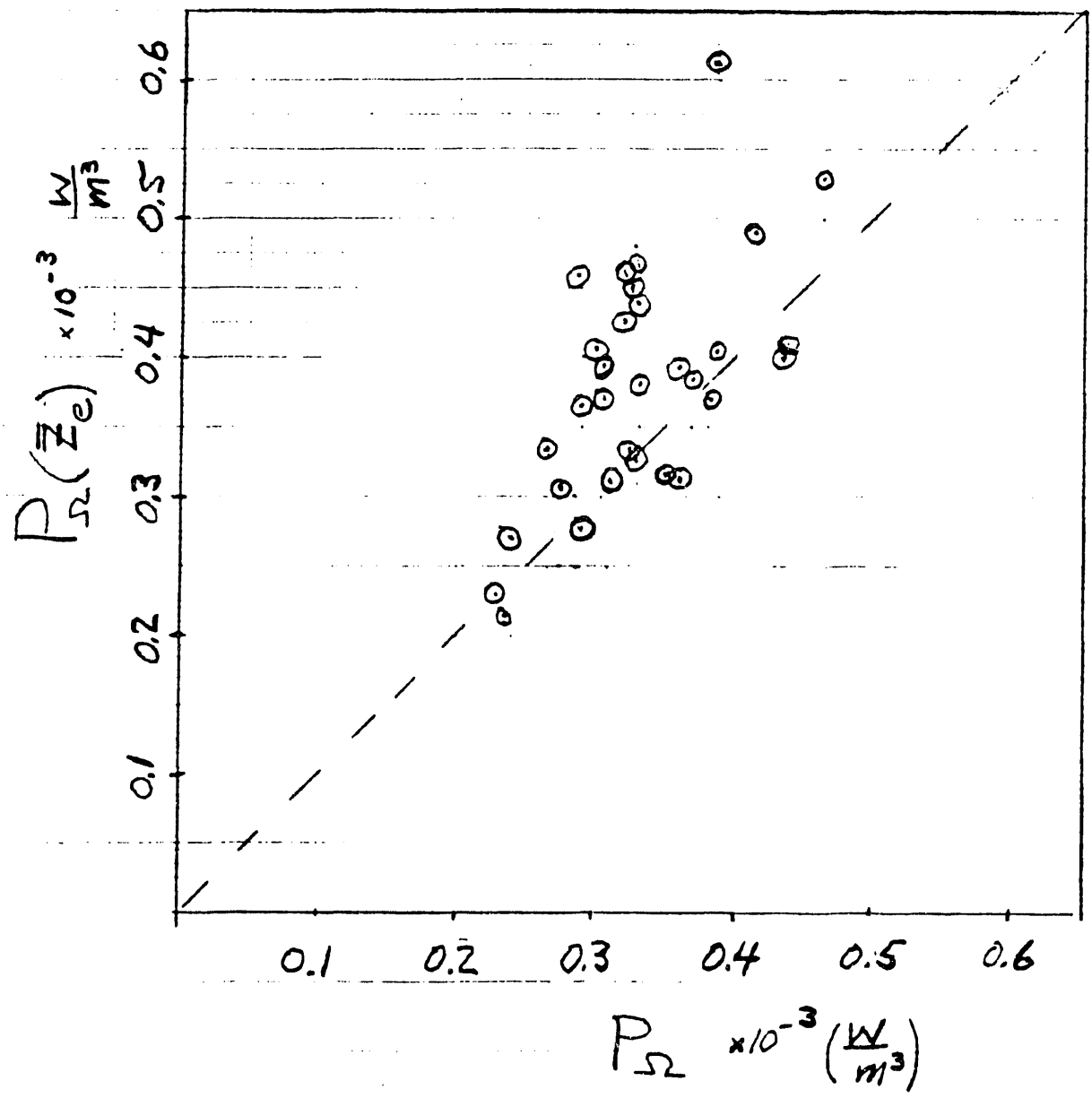
0.6
0.5
0.4
0.3
0.2
0.1
$P_\Omega(\Xi_e)$ $\times 10^{-3}$ $\frac{W}{m^3}$
0.1
0.2
0.3
0.4
0.5
0.6
$P_\Omega$ $\times 10^{-3}$ $\left(\frac{W}{m^3}\right)$

# The Transmission System for the DIII-D ECE Radiometer*

Charles Moeller, John Lohr, and Ron Prater
*GA Technologies, Inc., San Diego, California 92138, U.S.A.*

*In order to improve the noise immunity and increase the availability of the DIII-D ECE radiometer, the radiometer receiver will be located outside the radiation shield wall. Further noise immunity is obtained by the use of a 50 kHz rf modulator, which is compatible with the 90 to 140 GHz low loss, single mode transmission system, the design and expected performance of which will be discussed. The testing of microwave components and the absolute calibration of the system is also discussed.*

## Introduction

Several improvements are being made to the DIII–D ECE radiometers to reduce their susceptability to interference and increase their availability. They are also to be absolutely calibrated using hot and cold black body sources. Both the grating [1] and Michelson [2] radiometers are being located outside the radiation shield wall so that they will be accessible during machine operation. Also, the input to the grating instrument will be chopped at 50 kHz, permitting synchronous detection and giving considerable immunity to both electrical noise and neutron interference. The absolute calibration is greatly facilitated by low transmission loss, while the only high frequency choppers available are in fundamental mode waveguide.

*This is a report of work sponsored by the Department of Energy under Contract No. DE-AC03-84ER51044.

## Transmission System

Possible low loss transmission schemes use (1) highly overmoded rectangular guide, (2) hollow dielectric waveguide, (3) the $HE_{11}$ mode in corrugated waveguide, and (4) the $TE_{01}$ mode in smooth wall circular guide with corrugated guide bends. The chosen approach must be compatible with a transition to fundamental mode guide.

This last requirement is consistent with our intention of propagating a single mode in order that the antenna pattern be as narrow and well defined as possible. Given the small area of the ultimate detectors, there would appear to be no increase in received power to be obtained by propagating multiple modes, even if the antenna pattern were of no concern. With a single incident mode, any subsequent mode conversion represents a power loss, since the detector is single moded.

Oversized rectangular guide has the disadvantage that the losses decrease only as $1/b$, $b$ the waveguide height, so that low loss requires rather large guide, in which mode conversion is difficult to avoid. It is therefore inferior to the remaining schemes, in which the loss varies as $1/a^3$, "$a$" the circular guide radius.

The hollow dielectric guide [3] is potentially attractive at very short wavelengths, but in the 90 to 140 GHz range, to propagate the $HE_{11}$ mode, an inside diameter of 13 cm is required assuming an optimum dielectric constant to keep the losses to less than 1 dB in 15 m, the required length of run. Making a transition to that diameter from fundamental mode guide is awkward. We therefore favor metallic guide, which can achieve a similar loss in $<1/10$ the diameter.

The $HE_{11}$ mode in corrugated wall guide can achieve <1 dB in 15 m in 1.25 cm diameter, at least at the optimum frequency. Furthermore, the polarization is already linear, so that the $HE_{11}$ mode is suitable both for the receiving antenna (using a corrugated horn) and for radiating into the radiometer receiver. However, it is necessary to make a broad band transition to fundamental guide, in order to use the chopper. Also, the entire run must be in the corrugated guide, and guide with rather deep corrugations at that, which is expensive.

We therefore have chosen to use the $TE_{01}$ mode, which can be propagated in straight smooth-wall guide, only requiring corrugated guide at bends.

All the elements of the system can cover the required 1.55:1 bandwidth. A broad band transition, the Marié transducer, is available to convert from fundamental rectangular guide to the $TE_{01}$ mode in circular guide. The corrugated bends are also broad band. If the corrugation depth and length are optimized for the highest frequency, they continue to be adequate at lower frequencies, as can be seen from the following argument.

The amplitude converted to a particular mode due to curvature is proportional to $C/(\Delta\beta^2 a^2)$, where $C$ is the coupling coefficient between the $TE_{01}$ mode and the undesired mode and $\Delta\beta$ is the difference in their propagation constants [4]. The undesired mode of concern is the $TM_{11}$ ($HE_{11}$ in corrugated guide), which has the same cutoff wavenumber as the $TE_{01}$ at zero corrugation depth. If the corrugation depth is optimized for the highest frequency, the difference in the cutoff wavenumbers, $\Delta k_\perp$, decreases with decreasing frequency. This is shown in Fig. 1, which is based on a surface impedence model [4]. The optimum corrugation depth $\ell$ is about $\ell/\lambda = 0.07$ or $\ell/a = 0.024$ at 140 GHz [5]. Then $\Delta k_\perp a = 1.23$ at 140 GHz and 0.83 at 90 GHz. But $\Delta\beta \simeq (c/\omega)k_\perp \Delta k_\perp$ is in fact larger at 90 GHz than at 140 GHZ, because the reduced value of $\omega$ more than compensates for the reduced $\Delta k_\perp$. Since the $TE_{01}$–$TM_{11}$ coupling coefficient is just proportional to $\omega$, the mode conversion loss decreases with decreasing $\omega$ for a fixed corrugation depth. The values of $\Delta k_\perp$ for other interfering modes actually increase as $\omega$ decreases, and the coupling coefficients have higher (positive) power dependence on $\omega$, and therefore also decrease with decreasing $\omega$. We have also confirmed experimentally that bends for 60 GHz work equally well at 35 GHz.

A block diagram of the transmission system is shown in Fig. 2. The part of the run propagating the $TE_{01}$ mode, which has a total length of approximately 15 m, is in circular waveguide of 1.25 cm diameter, giving a theoretical ohmic loss of 0.3 dB at 150 GHz and 0.6 dB at 90 GHz. Our experience at 60 GHz suggests we might expect a total loss of about twice the theoretical ohmic loss. The d.c. break at the receiver end

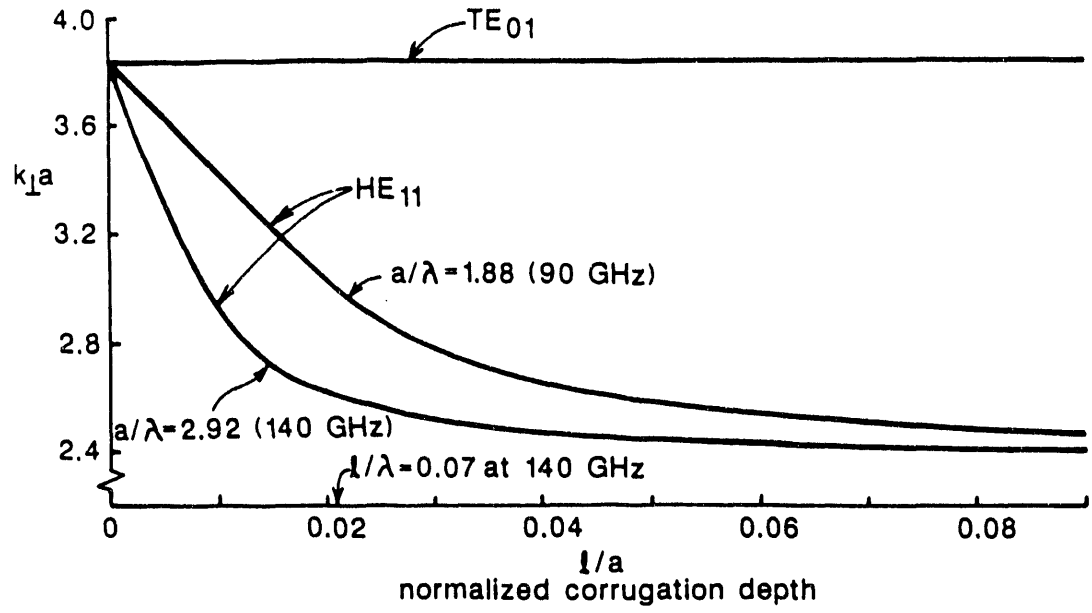


FIG. 1. Normalized cutoff wavenumber versus corrugation depth for corrugated waveguide.

of the run consists of a series of alternating polystyrene and aluminum disks. A 20 cm long stack of such disks easily provides the required 30 kV isolation with <0.05 dB loss.

At each end of that part of the run propagating the $TE_{01}$ mode, there is a non-linear taper from 1.25 to 0.4 cm, followed by a Marié converter. The anticipated loss per converter is <0.5 dB.

At the receiver end of the system, there is a 90° bend in WR-8 waveguide, followed (in the case of the grating instrument) by the chopper, which will be discussed below. Following the chopper is a standard (25 dB gain) horn, which radiates into the receiver.

At the tokamak end of the system, there is, following the Marié converter, a transition from WR-8 waveguide to 2.4 mm diameter circular guide. Beyond this transition is the vacuum window, which is a 0.013 mm thick mica disk sealed by a Viton o-ring. The expected voltage reflection coefficient from this window is then ≤0.065 (or VSWR <1.13) over the band. The window has been found to withstand 10 atmospheres of pressure without failure.

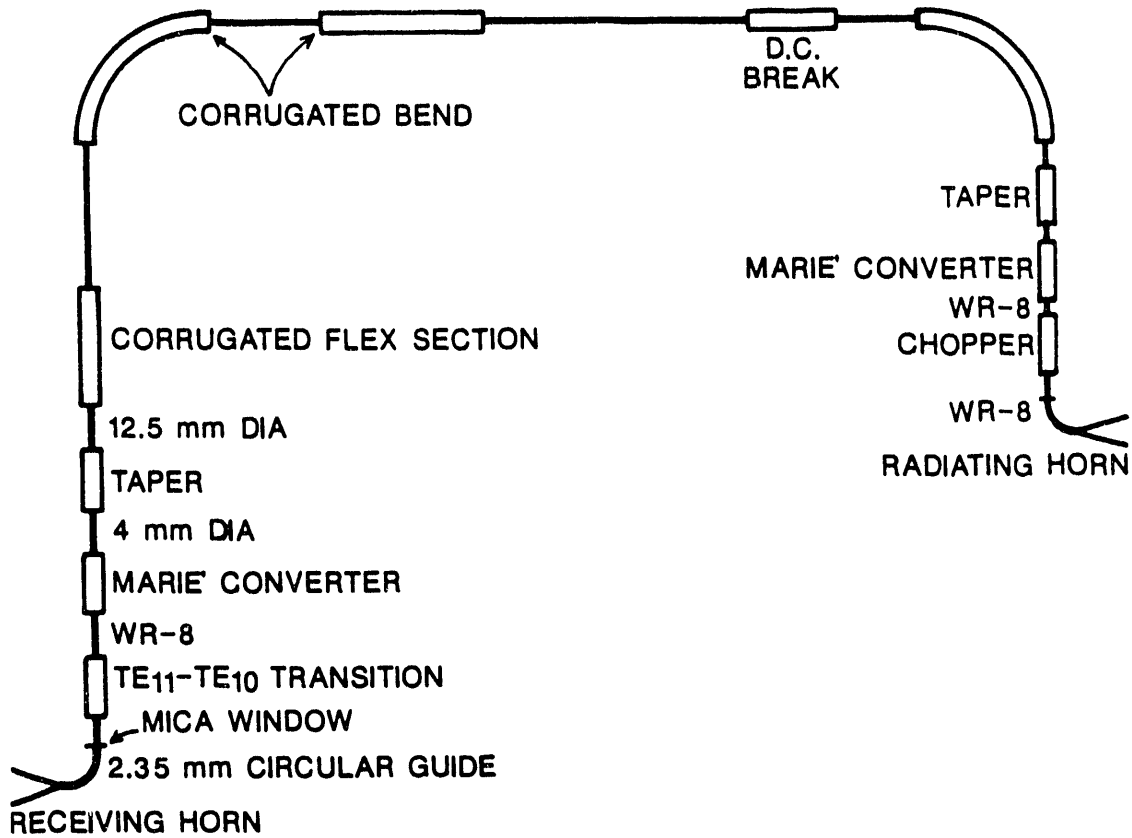


FIG. 2. Block diagram of the transmission system.

Beyond the window is a 90° bend in 2.4 mm circular guide, followed, in the initial installation, by a conical horn. This horn views the plasma radially through a 3.8 cm gate valve which is only 30 cm beyond the vacuum vessel inner surface. The entire assembly can therefore be disconnected from the vacuum vessel and rotated 180° for calibration without venting the machine. The use of circular guide allows us to examine both polarizations by simply rotating the rectangular to circular transition on the atmospheric side of the window.

The overall attenuation of this system is primarily determined by the fundamental mode components at the ends, since the $TE_{01}$ mode loss should be <1 dB. The theoretical attenuation of WR-8 guide ranges from 5 dB/m at 90 GHz to 3 dB/m at 140 GHz, while the values for 2.4 mm circular guide are about 2/3 of those numbers. The total length of such guide is only 0.2 m, however, contributing less than 1 dB. The horns should give less than 0.25 dB total, while the Marié converters should each

contribute 0.5 dB loss. The worst single element is the chopper. A full waveguide bandwidth chopper [6] has an insertion loss of $\leq 3$ dB. We are also developing an electro-optical chopper which has an insertion loss of $<1$ dB. The total transmission loss should therefore be 6.25 dB with the ferrite chopper or 4.25 dB for the electro-optical chopper. There is one remaining unknown, but possibly serious loss, that is due to coupling inefficiencies within the radiometers themselves. For plasma operation, the attenuation is not of great consequence if stable, but it greatly effects the ease of calibration.

## Calibration

We are most interested in the calibration of the grating instrument. The system will contain low pass filters, the effectiveness of which can be tested by placing in the fundamental mode section a piece of waveguide cutoff at 140 GHz when using our hot source.

Circuit models of our system for different chopper locations (which are rigorously correct when dealing with any single mode) are shown in Figs. 3a and 3b. The attenuator may represent a distributed loss. The elements of the system are assumed reflectionless (*i.e.*, matched to the transmission line). The difference in noise temperature at the receiver between the on and off states of the chopper is just $\Delta T = A(T_s - T_c)$ for Fig. 3a and $\Delta T = A(T_s - T_c) + (T_a - T_c)$ for Fig. 3b, where $A$ is the attenuation factor of the attenuator, and $T_a$, $T_c$, and $T_s$ are the temperatures of the attenuator, chopper, and noise source, respectively. If the chopper and other dissipative elements of the system are all at the same temperature, the location of the chopper is irrelevant. If $|T_a - T_c|$ is not $\ll A(T_s - T_c)$, as might be the case with a system having high loss and temperature gradients, it then is necessary to have the chopper near the noise source.

We will initially locate the chopper where it is most accessible, at the receiver, and relocate it only if the system losses require it. Even if the system has high loss, but much of the loss is within the receiver, the chopper could still remain at the receiver end of the system.

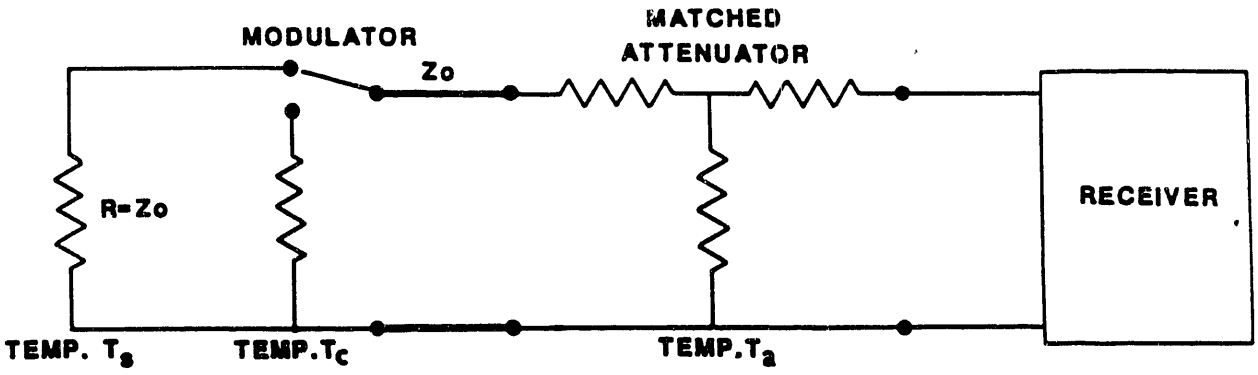


FIG. 3a. Equivalent circuits of the system with the chopper near the noise source. $T_s$, $T_c$, and $T_a$ refer to the noise temperatures of the source, chopper, and attenuator, respectively.

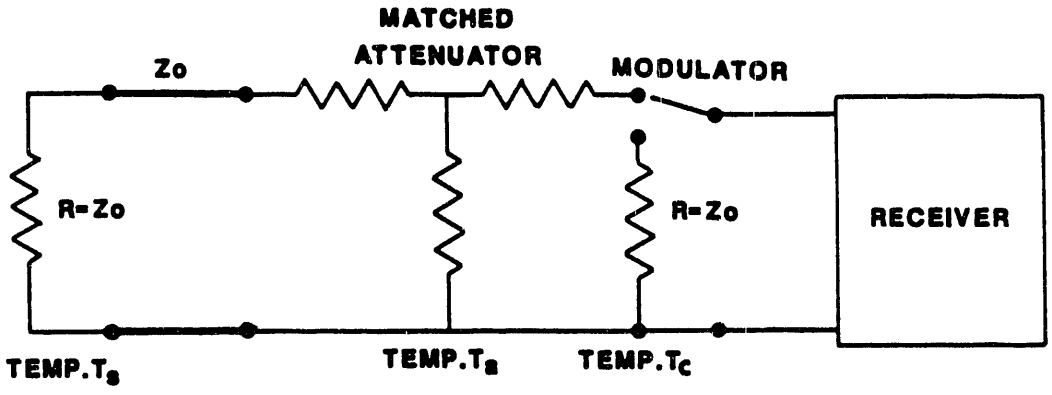


FIG. 3b. Same as for Fig. 3a, with the chopper near the receiver.

The $\Delta T$ values at the receiver for the 77°K and 1300°K loads we propose to use for calibration are 53°K and 237°K, respectively, with the ferrite chopper and 84°K and 376°K, respectively, for the electro-optical chopper, assuming in both cases a 300°K ambient. The noise power into the receiver is also proportional to the bandwidth per channel, which varies from 0.8 to 2 GHz.

The receiver noise comes primarily from the intrinsic detector [6] noise and the equivalent input noise of the amplifier input stage, which are specified in terms of the

RMS noise voltage to be $2.7\times10^{-9}$ V/$\sqrt{\text{Hz}}$ and $1.5\times10^{-9}$ V/$\sqrt{\text{Hz}}$, respectively. The latter number is for a low noise FET at 50 kHz.

The radiometer detector response is given as $>4\times10^{3}$ volts per watt of incident radiation [7]. When $\Delta T > 100$ eV, the microwave power per channel $>5\times10^{-8}$ watts, giving a fundamental component at the modulation frequency of 0.099 mV RMS. For the 10 kHz I.F. bandwidth we are interested in, the RMS noise voltage is $3.1\times10^{-7}$, so that the signal to noise ratio >300 (we will be using synchronous detection).

For calibration, however, $\Delta T \sim 273°$K for the 1300°K hot source, assuming 6.25 dB of rf attenuation, giving a $2.5\times10^{-8}$ V RMS signal. To get a 100:1 S/N ratio, we then require an IF bandwidth of $6\times10^{-3}$ Hz giving a signal risetime of 100 sec. In comparison, if we had a 13 dB rf loss and a 1300°K noise source, $\Delta T$ is only 50°, giving a required risetime of $3.3\times10^{3}$ sec for a 100:1 S/N ratio.

A block diagram for testing the waveguide components is shown in Fig. 4. The only sweepable sources that cover 90 to 140 GHz directly are a pair of extremely expensive B.W.O.'s. We chose instead to use a broad band harmonic mixer driven by a YIG oscillator as a harmonic generator. By also using a harmonic mixer as a receiver, with the local oscillator detuned by $\Delta f$ and an IF filter centered at $n\,\Delta f$, only the n$^{\text{th}}$ harmonic will be detected.

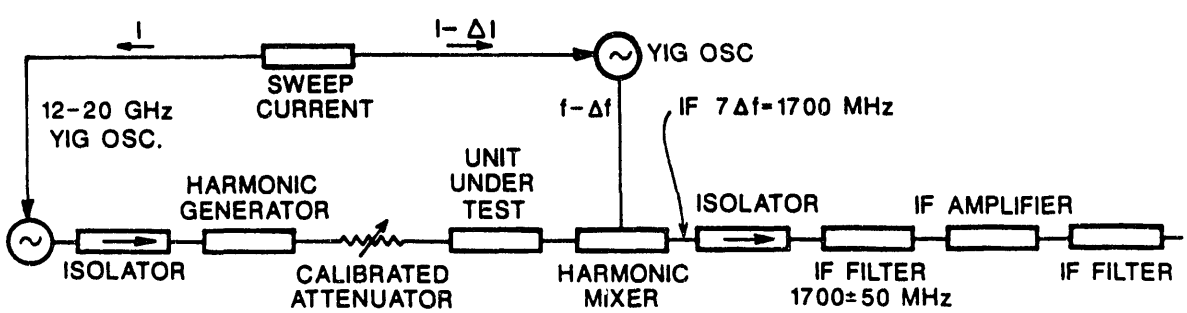


FIG. 4. Block diagram of the sweepable transmission test system.

The harmonic generator has a minimum output of 3 $\mu$W, the harmonic mixer has a conversion loss of <35 dB, and the IF amplifier a noise figure of 4 dB. If the unit

under test has no loss, the signal to noise ratio, assuming a 100 MHz IF bandwidth, is >200, so no special signal processing would be required.

## Summary

A low loss transmission system for single mode propagation has been designed for the 90 to 140 GHz band. Combined with a high temperature black body source, only a few minutes per channel should be required for calibration. Location of the radiometers outside the shield wall and modulation of the microwave signal should greatly reduce electrical and neutron interference during plasma operation.

## References


[1] J. Fischer, D. Boyd, A. Cavallo, J. Benson, Ref. Sci. Inst. **54**, 1085 (1983)

[2] D.H. Martin and E. Puplet, Infrared Physics **10**, 105 (1970).

[3] E.A.J. Marcatili and R.A. Schmeltzer, Bell System Tech. J. **43**, 1783 (1964).

[4] Hans-Georg Unger, Bell System Tech. J. **37**, 1599 (1958).

[5] J.L. Doane, Proc. 10th Symp. on Problems in Fusion Engineering, Philadelphia, December 1983.

[6] Hughes Aircraft Co., P.O. Box 7940, Torrance, CA 90509.

[7] QMC Instruments, Ltd., 229 Mile End Road, London, U.K.

# A Comparison of Three Different Methods for Calibrating ECE Measurement Systems

S.E. Kissel, B.J.D. Tubbing,* E.A.M. Baker,** D.V. Bartlett, D.J. Campbell, A.E. Costley, D.G. Moss,** R.M. Niestadt,* Th. Oyevaar,* and H.W. Piekaar*

*JET Joint Undertaking, Abingdon, Oxon, OX14 3EA, UK*

**FOM Instituut voor Plasmafysica, Netherlands*

***National Physical Laboratory, UK*

ABSTRACT

An ECE measurement system has been calibrated using three different methods: a conventional thermal source, an untuned cavity, and a system of antenna pattern integration. The last two techniques employ a coherent microwave source and produce signal levels comparable with those measured from a tokamak plasma. The measured system responses agree within the estimated experimental uncertainties.

## 1. Introduction

The accuracy of ECE measurements of plasma electron temperature is currently dominated by uncertainties in the calibration process. The most commonly used method employs a large surface area thermal emitter, such as a heated plate, or an absorber placed in liquid nitrogen. Special techniques for measuring small signals must be used which introduce uncertainties and are usually tedious and time consuming. In some cases the method fails because the radiation intensity is just too weak, or because too much power is emitted at high frequencies. Alternative calibration methods are desirable and, in some cases, essential.

To investigate alternative methods we have calibrated an ECE system using three methods: a thermal source, an untuned cavity, and an antenna pattern integration technique. In this paper we discuss each method and present a comparison of the calibration results.

The comparison made here covers the frequency interval 110-170GHz, corresponding to 2nd harmonic ECE from a plasma with 2 to 3T magnetic field.

## 2. Method

A standard polarising Michelson interferometer, operating with rooftop mirrors was coupled to a liquid helium cooled InSb hot electron detector via a focussing lens, circular waveguide and F4 winston cone. The input to the Michelson was a 30mm by 40mm rectangular waveguide which tapered up to S band, 34mm by 72mm. The polarisation was linear with the electric vector parallel to the long side of the waveguide, that is , opposite to the conventional definition of the fundamental mode. The S-band waveguide was 30 m long with 10 H-plane and 7 E-plane bends.

Interferograms were collected by a signal averager under control of a micro processor which also operated additional equipment. The reference and clock signals to the averager were generated through a moire fringe system attached to the vibrating arm of the interferometer which was driven at 30Hz with a 16mm amplitude.

With each method of calibration a characterised radiation source is placed in front of the S-band antenna filling the entire field of view. The corresponding interferogram is measured and Fourier transformed to give a spectrum. The system response is then defined as the ratio of the known source to the measured spectrum:

| | | |
|---|---|---|
| CHARACTERISED SOURCE | $I(f)$ | $\frac{\text{watts}}{m^2 \cdot \text{ster} \cdot df}$ |
| MEASURED INTERFEROGRAM | $V(x)$ | volts |
| MEASURED SPECTRUM | $S(f)$ | $\frac{\text{volts}}{df}$ |
| SYSTEM RESPONSE | $R(f) = \frac{S(f)}{I(f)}$ | $\frac{\text{volts} \cdot m^2 \text{ster}}{\text{watt}}$ |

where f is frequency and x is the interferometer path difference. An identical Fourier transform routine was used for each method, producing spectra with 10GHz resolution (apodised). The methods differed only in the manner of measuring the interferogram and of characterising the source.

## 3. Thermal Source

Calibration with a thermal source is fairly common and is only briefly outlined here.

The source is characterised by a black-body emission function and a characteristic temperature which may have weak frequency dependence. This temperature is expressed as the difference between the radiation temperature of the source and the background room temperature:

$$I(\omega) = \frac{K(T_{rad}(\omega)-T_{BG})f^2}{c^2} \qquad \frac{\text{watts}}{m^2 \cdot \text{ster} \cdot df}$$

The "measured interferogram", V(x), is the difference of interferograms obtained with the source present and with the source removed:

$$V(x) = V_{SOURCE}(x) - V_{BG}(x)$$

The source used has been developed by the National Physical Laboratory, UK, to be compact, convenient, and able to achieve high temperature. The surface area is 400mm² and has a radiation temperature >~370K above room temperature. This temperature and its frequency dependence is determined by surface reflectivity and thermocouple/infrared camera measurements. The characterisation is validated by comparison with an absorber immersed in liquid nitrogen. The characterisation produces a 10% systematic uncertainty.

Because of the weak signal, coherent averaging for 6 hours (50% duty cycle) was necessary to measure the interferogram. The resulting spectrum has less than 10% statistical error in the frequency band of interest.

The entire measurement system has been shown to have no polarisation

mixing, so only the single appropriate linear polarisation is considered. The system response determined by this method is shown in Fig.3(a).

## 4. Untuned Cavity

To fill the antenna pattern of the measurement system, the calibration source must excite all relevant modes in the receiving antenna. This is the function of the untuned cavity: production of constant power in all the modes which the system accepts. The cavity (designed and constructed by the FOM Institute, Holland) is shown schematically in Fig.1. A backward wave oscillator V(BWO) injects power at a single frequency into an irregularly shaped volume. Two equivalent apertures are connected to the measurement system and to a fundamental mode power meter (Anritsu type MP83B/ML83A) respectively. The power meter has been absolutely calibrated by NPL with a 20% uncertainty. Rotation of half the surface of the cavity and jittering the BWO frequency helps destroy any spatial coherence, so that the output modes will have time averaged equal power. A broadband source was simulated by stepping the BWO frequency by 1GHz from 110GHz to 170GHz and superposing the results. Each intermediate value was scaled to the corresponding fundamental mode power since the output power of the BWO was not constant with frequency. The source characterisation is thus determined by the assumption that every mode has equal power and by the frequency step interval $\Delta f$:

$$I(f) = \frac{f^2}{c^2 \Delta f}$$

$$V(x) = \sum_i \left(\frac{V_i(x)}{P_i}\right)$$

where $V_i(x)$ is the interferogram for BWO frequency $f_i$ and $P_i$ is the measured fundamental mode power at that frequency. The values of $P_i$ were typically a few μW, while the BWO output was several mW. $P_i$ of 1μW corresponds to an effective temperature of $7.2 \times 10^7$K, which is close to the plasma temperature being measured. Approximately 2 minutes was required at each frequency setting for leveling of the power meter. The resulting system response is shown in Fig.3(b).

## 5. Antenna Pattern Integration

A large area source can be simulated by a two-dimensional array of microwave sources. The overall dimensions of the array should be such that the antenna-pattern of the instrument under calibration is fully filled. Fig.2 shows a schematic of this method. Each element of the array occupies an angular area $\Delta Y_1$ by $\Delta Y_2$.

If a spherical surface is chosen with the distribution of microwave sources uniform in solid angle the effective surface brightness becomes

$$I = \frac{PG}{4\pi r^2 \Delta Y_1 \Delta Y_2} \qquad \frac{\text{Watts}}{\text{m}^2\text{ster}}$$

where:

P is the emitted power (~3mW), G the launch antenna-gain (~50), and r the distance between launch and receiving antennae (~1m).

In the experiment the BWO is moved from point to point by a mechanical arm driven by stepper motors (designed and constructed by FOM), which are interfaced to the controlling computer. The detector output at every gridpoint must be added, which is equivalent to integrating the antenna pattern. The method is outlined in detail by Tubbing [1].

A broadband source was simulated by stepping the BWO frequency and superposing the resulting interferograms. Again, each individual interferogram was scaled according to the output power:

$$I(f) = \frac{G}{4\pi r^2 \Delta Y_1 \Delta Y_2 \Delta f}$$

$$V(x) = \sum_i \frac{V_i(x)}{P_i}$$

where a frequency step size of $\Delta f$=2.5GHz was used. The effective temperature of this composite source is ~$10^{10}$K.

To save time, the movement of the source was synchronised with the data sampling so that antenna pattern integration was automatically obtained. Typically, scanning through a 10° square requires about 20 minutes per frequency.

The power measurements (P) were taken at the end of the BWO's launch horn (3.5mm x 7mm) with the aid of a similar horn tapering to the input waveguide of the meter. The antenna-gain of the launch horn was calculated, including a correction for the tapering.

Fig.3(c) shows the system response from this method. Difficulties with automation restricted the frequency range over which these measurements were made, thus the relatively smaller frequency range of this measurement. Given more time, a wider range could have been measured.

## 6. Comparison of Calibration Methods

In comparing the three methods the possible sources of errors must be considered.

The thermal source method has a 10% statistical error and a similar systematic error resulting from uncertainties in source characterisation. The two microwave techniques are dominated by systematic errors. For the untuned cavity, the number of excited modes is unknown, as is the effect of a necessary taper from 10mm by 10mm to S band (1 meter). Qualitative evidence suggests that the cavity is adequate - we can make no quantitative statements about its performance. For the antenna pattern integration, it is not certain that the grid spacing was optimal, nor is it known that the power remained constant during the integration period or that the antenna gain was correct. Both methods suffer from uncertainty in power measurement. A systematic error of 20% is likely. The comparison of responsivities may indicate a problem at low frequency - but in general the agreement must be considered good. The weakest area at the moment is the absolute power measurement of the microwave source. Presently, this measurement is being automated.

## 7. Conclusions

Although the thermal source method required the greatest amount of time, no substantial error resulted. The stability of both the source and the measurement system allows the use of long integration periods to overcome weak signal levels. Automation reduces the human impact of such long times. However, a dynamic range of 50dB minimum is needed.

Given an ideal microwave source - one that has both frequency and power stability - that operated over a broad band, both microwave techniques would be suitable. The untuned cavity is a compact system which could be used for calibration in tokamak vacuum vessels. However, the physics of the cavity and the resulting modes is not simple, so that every cavity will be different. The cavity couples radiation to the receiving antenna completely in waveguide - whereas the desired coupling is free space.

The physics of the antenna pattern method is readily understood, and different mechanical systems should produce the same result. Only one polarisation is excited, and this could have some consequence. Errors in antenna gain, radial distance and grid spacing will be systematic only - and these parameters are not difficult to measure. Although this method is time consuming, it does produce useful extra information - the antenna pattern. In this study, drifts in power, particularly those resulting from moving the BWO, made this technique the most unreliable and difficult.

The choice of which system to employ should be decided by external factors - such as available space and system sensitivity. Whichever route is chosen, some degree of automation is essential, and the equipment should be flexible enough to allow, for example, this kind of comparison. As more experience with these techniques is gained, it is likely that the agreement will improve. For first measurements, the present result is considered encouraging and suggests that refinement of the coherent source calibration techniques be continued.

## Reference

[1] B.J.D. Tubbing, Rijnhuizen Report 83-149.

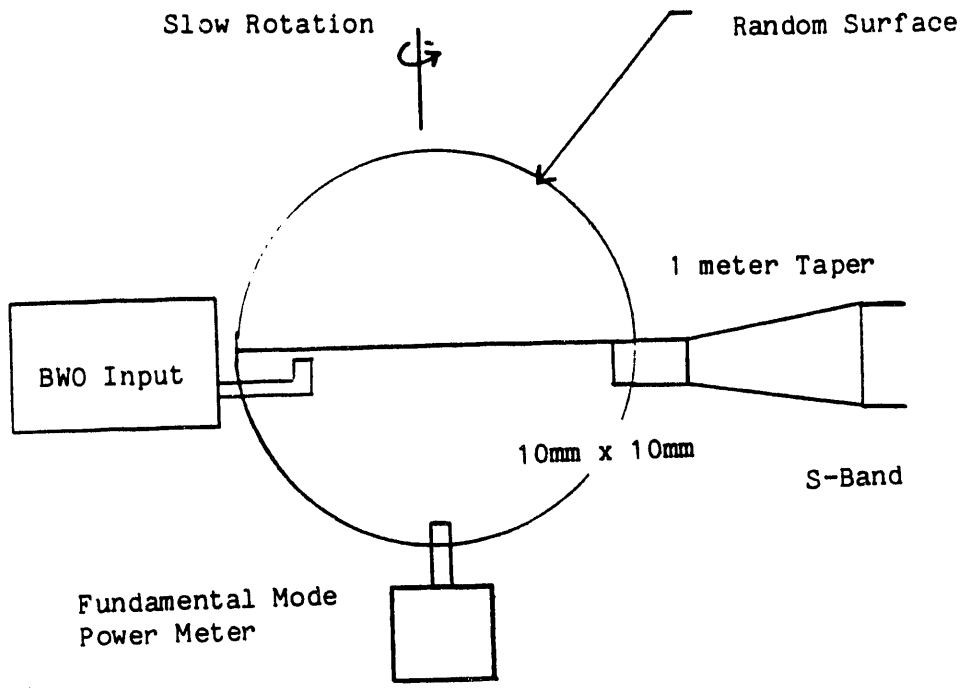


FIG.(1): Untuned Cavity.

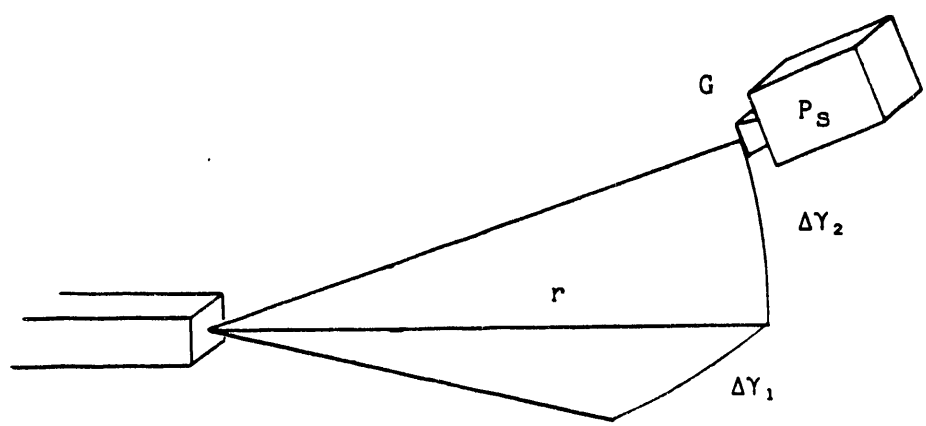


FIG.(2): Antenna Pattern Integration. The antenna pattern was normally integrated over ±10° in both planes, with grid size $\Delta\Upsilon_1$=0.3° $\Delta\Upsilon_2$=0.03°.

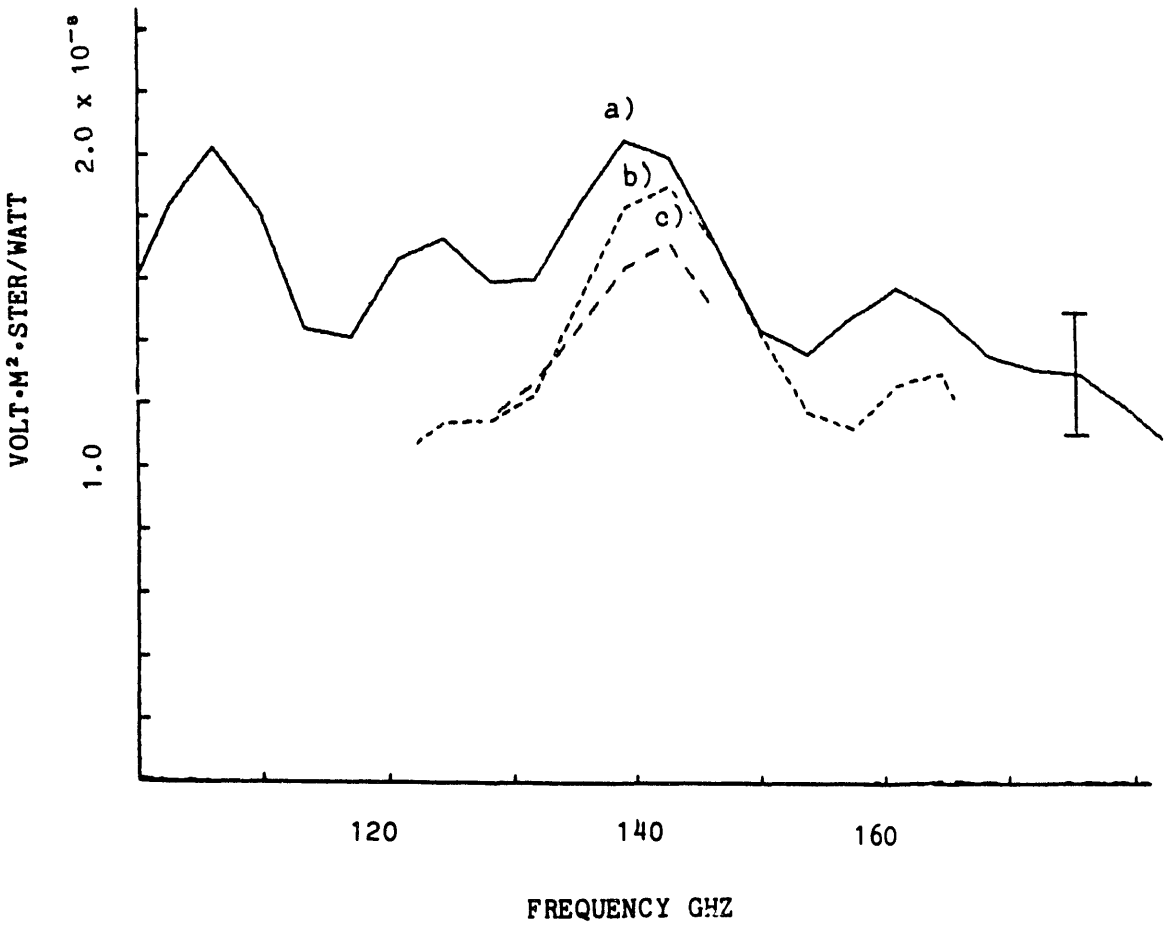


FIG.(3): A comparison of ECE system response measured by three methods:

a) Thermal Source
b) Untuned Cavity
c) Antenna Pattern Integration

The 10% error bar refers to the statistical error of method a) which may also have an additional 10% systematic error. Methods b) and c) may contain a 20% systematic error and probably have a similar statistical error. Systematic errors will shift the curves relative to each other without altering their shape, while statistical error may influence the shape.

# Electron Cyclotron Emission Theory

# What is the Limiting Polarization of Electron Cyclotron Emission Leaving a Fusion Plasma?

D.A. Boyd
*Laboratory for Plasma and Fusion Energy Studies*
*University of Maryland, College Park, Maryland 20742, USA*

The propagation of electron cyclotron emission perpendicular to a sheared magnetic field is considered. Coupled equations for the ordinary and extraordinary modes of polarization are used to deduce the emerging state of polarization: the limiting polarization. Tokamaks have a limiting polarization characterized by the edge plasma conditions, but certain spheromaks for cyclotron harmonics above $\ell = 3$ will preserve the polarization of the emission at the source.

## I. INTRODUCTION

In the case for which the radiation propagates perpendicular to the magnetic field, the electron cyclotron emission is generated in two modes of polarization; the extraordinary mode with its electric vector perpendicular to the local magnetic field and the ordinary mode with its electric vector parallel to the magnetic field. This fact was noted by Engelmann and Curatolo[1] and they suggested that it be used to measure the orientation of the magnetic at the source of the radiation. Clearly if the radiation emerged from the plasma with the same orientation of the electric vector as it started, an experimental determination of its orientation would fix the orientation of the magnetic field at the

source. This would give us one of those elusive poloidal field diagnostics.

Unfortunately, as the radiation propagates from its source through the plasma across an, in general, sheared magnetic, there is a tendency for the electric vector to rotate with the magnetic field. Thus, in general, the electric vector will not emerge from the plasma with the orientation that it had at its source, but at some angle given by the direction of the magnetic field in some low plasma density region near the plasma edge.

The orientation of the emergent electric vector is given by the "limiting polarization". It is the purpose of this paper to examine the problem of determining the limiting polarization of electron cyclotron emission emitted from fusion plasmas generated in contemporary devices.

## II. THE EQUATIONS DESCRIBING THE PROPAGATION WAVES

The formulation of Fidone and Granata[2] is used to describe the propagation of the radiation in a plane stratified plasma. The radiation propagates in the z-direction which is along the density gradient and perpendicular to the magnetic field which is sheared in the x-y plane (see Fig. 1).

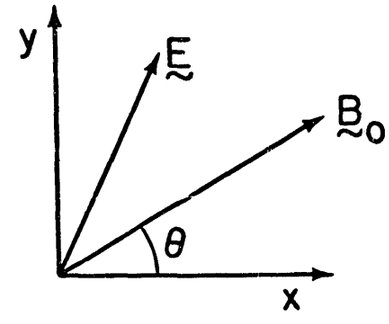


Fig. 1. The coordinate system. E is the wave electric field and $B_0$ the confining magnetic field.

For this case Maxwell's equations can be written in matrix form,

$$d/dz \begin{bmatrix} B_x \\ E_x \\ -B_y \\ E_y \end{bmatrix} = i \frac{\omega}{c} \begin{bmatrix} 0 & \beta & 0 & \gamma \\ 0 & 0 & 1 & 0 \\ 0 & \alpha & 0 & \beta \\ 1 & 0 & 0 & 0 \end{bmatrix} \begin{bmatrix} B_x \\ E_x \\ -B_y \\ E_y \end{bmatrix} \tag{1}$$

where

$$\alpha = N_0^2 \cos^2\theta + N_x^2 \sin^2\theta$$

$$\beta = (N_0^2 - N_x^2) \sin\theta \cos\theta$$

$$\gamma = N_0^2 \sin^2\theta + N_x^2 \cos^2\theta$$

$$N_0^2 = 1 - X$$

$$N_x^2 = \frac{(1 - X)^2 - Y^2}{1 - X - Y}$$

where $N_0$ and $N_x$ are the refractive indices for the ordinary and extraordinary modes respectively. $X \equiv \omega_p^2/\omega^2$; $Y = \omega_c^2/\omega^2$ and $\theta$ is the angle that the confining magnetic field makes with the x-axis.

A set of coupled equations are then derived for the propagating waves, i.e.,

$$\frac{df_i}{dz} + i \frac{\omega}{c} q_i f_i = \Gamma_{i1} f_1 + \Gamma_{i2} f_2 + \Gamma_{i3} f_3 + \Gamma_{i4} f_4 \tag{2}$$

where i = 1, 2, 3, 4 and

$$\Gamma_{12} = -\Gamma_{21} = -i(1/2N_0)(dN_0/dz) \ ,$$

$$\Gamma_{34} = -\Gamma_{43} = -i(1/2N_x)(dN_x/dz) \ ,$$

$$\Gamma_{13} = -\Gamma_{31} = \Gamma_{24} = -\Gamma_{42} \frac{N_0 + N_x}{2\sqrt{N_0 N_x}} \phi \ ,$$

$$\Gamma_{14} = -\Gamma_{41} = -\Gamma_{23} = \Gamma_{32} = -i \frac{N_0 - N_x}{2\sqrt{N_0 N_x}} \phi \ ,$$

$$\Gamma_{11} = \Gamma_{22} = \Gamma_{33} = \Gamma_{44} = 0 \ ; \qquad \phi = d\theta/dz \ .$$

$$q_1 = -q_2 = N_0 \ ; \qquad q_3 = -q_4 = N_x \ .$$

If the coupling parameters $\Gamma_{ij}$ are set equal to zero then the four waves propagate independently. In this case $f_1$ and $f_3$ represent the forward going ordinary and extraordinary waves and $f_2$ and $f_4$ the backward going ordinary and extraordinary waves respectively.

The components of the electric field in the x, y coordinate system are given by

$$E_x = -i \frac{\cos\theta}{\sqrt{2N_0}} f_1 - \frac{\cos\theta}{\sqrt{2N_0}} f_2 + i \frac{\sin\theta}{\sqrt{2N_x}} f_3 + \frac{\sin\theta}{\sqrt{2N_x}} f_4 \ ,$$

$$E_y = -i \frac{\sin\theta}{\sqrt{2N_0}} f_1 - \frac{\sin\theta}{\sqrt{2N_0}} f_2 - i \frac{\cos\theta}{\sqrt{2N_x}} f_3 - \frac{\cos\theta}{\sqrt{2N_x}} f_4 \ . \qquad (3)$$

The components of the electric field in the coordinate system rotating with the sheared magnetic field are given by

$$E_{\parallel} = E_x \cos\theta + E_y \sin\theta \ ,$$

$$E_{\perp} = - E_x \sin\theta + E_y \cos\theta \ . \tag{4}$$

$\parallel$ and $\perp$ indicate the direction parallel and perpendicular to the local magnetic field direction respectively.

## III. SOLVING THE EQUATIONS

Second order and fourth order equations can be derived from the set of Equations (2) which can then be integrated along the propagation path to find the orientation of the electric field of the propagating wave when it leaves the plasma. In general this can only be done numerically although an analytic solution does exist for the case of constant shear.[3] However, crudely, two extreme cases occur; one in which the electric vector rotates with the magnetic field and the other when the orientation of the electric field remains fixed in configuration space. What I am interested in finding is the boundary between these two cases so the approximate solutions of Fidone and Granata are significant.

When $\phi$ is small and $N_0 \sim N_x \sim 1$, then $\Gamma_{14} \sim 0$. If in addition the backward waves $f_2$ and $f_4$ are neglected, the Eqs. (2) become

$$\frac{df_1}{dz} + i \frac{\omega}{c} N_0 f_1 = \phi f_3 \ ,$$

$$\frac{df_3}{dz} + i \frac{\omega}{c} N_x f_3 = - \phi f_1 \ . \tag{5}$$

Equations (3) give us

$$E_x = -i/\sqrt{2}(f_1 \cos\theta - f_3 \sin\theta) ,$$

$$E_y = -i/\sqrt{2}(f_1 \sin\theta + f_3 \cos\theta) ,$$

and

$$E_y/E_x = \frac{\sin\theta}{\cos\theta} \frac{u_x + \cos\theta/\sin\theta}{u_x - \sin\theta/\cos\theta} ;$$

$$E_x/E_y = \frac{\sin\theta}{\cos\theta} \frac{\cos\theta/\sin\theta - u_0}{\sin\theta/\cos\theta + u_0} , \tag{6}$$

where $u_x = f_1/f_3$; $u_0 = f_3/f_1$. Equations (4) become

$$E_{\parallel} = -\frac{i}{\sqrt{2}} f_1 ,$$

$$E_{\perp} = -\frac{i}{\sqrt{2}} f_3 .$$

The equations (5) can be transformed to

$$\frac{du_x}{dz} + i \frac{\omega}{c} (N_0 - N_x)u_x - \phi(1 + u_x^2) = 0 ,$$

$$\frac{du_0}{dz} - i \frac{\omega}{c} (N_0 - N_x)u_0 + \phi(1 + u_0^2) = 0 . \tag{7}$$

First we consider the solution when the anisotropy $A = N_0 - N_x$ is approximately zero. Then the solutions to Eq. (7) are

$$u_x = \tan[\theta(z) + \delta] \ ,$$

$$u_0 = \cot[\theta(z) + \delta] \ , \tag{8}$$

where $\delta$ is the angle between the y-axis and the initial orientation of the E-field. Substituting these solutions into the Eqs. (6) shows that $E_y/E_x = \cot\delta$ and $E_x/E_y = \tan\delta$ which are constant. Thus the orientation of the electric vector is fixed in configuration space when the anisotropy is approximately zero that is at very low density.

Next we consider the case where the anisotropy is dominant. However, $\phi$ is sufficiently small to still make $\Gamma_{14}$ negligible. Then if $d\phi/dz$ is negligible, we can define two new variables $v_x$ and $v_0$,

$$-\phi u_x = \frac{1}{v_x}\frac{dv_x}{dz} - \frac{i}{2}\frac{\omega}{c}(N_0 - N_x) \ ,$$

$$-\phi u_0 = \frac{1}{v_0}\frac{dv_0}{dz} + \frac{i}{2}\frac{\omega}{c}(N_0 - N_x) \ . \tag{9}$$

Then Eqs. (7) become

$$\frac{d^2 v_x}{dz^2} + \frac{\omega^2}{c^2}\left[\frac{1}{4}(N_0 - N_x)^2 + \left(\frac{c\phi}{\omega}\right)^2 - \frac{i}{2}\frac{c}{\omega}\frac{d(N_0 - N_x)}{dz}\right] v_x = 0 \ ,$$

$$\frac{d^2 v_0}{dz^2} + \frac{\omega^2}{c^2}\left[\frac{1}{4}(N_0 - N_x)^2 + \left(\frac{c\phi}{\omega}\right)^2 + \frac{i}{2}\frac{c}{\omega}\frac{d(N_0 - N_x)}{dz}\right] v_0 = 0 \ . \tag{10}$$

If the anisotropy is much greater than the shear, $A \gg S$, i.e.,

$$A = |N_0 - N_x| >> \frac{2c\phi}{\omega} = S \ . \tag{11}$$

Then the solution to Eqs. (10) are

$$v_x = \exp\left[\frac{i}{2}\frac{\omega}{c}\int (N_0 - N_x)dz\right] ,$$

$$v_0 = \exp\left[-\frac{i}{2}\frac{\omega}{c}\int (N_0 - N_x)dz\right] . \tag{12}$$

Substitution of these solutions into Eqs. (9) give the physically acceptable results

$$u_x = 0$$

$$u_0 = 0 \ . \tag{13}$$

Substitution of these results into Eqs. (6) give

$$\frac{E_y}{E_x} = -\cot\theta \quad \text{and} \quad \frac{E_x}{E_y} = \cot\theta \ . \tag{14}$$

These equations tell us that the extraordinary mode rotates with the magnetic field to keep the electric vector perpendicular to the magnetic field and that the ordinary mode also rotates to keep the electric vector parallel to the magnetic field. Thus at higher density when the anisotropy overwhelms the shear the electric vector rotates with the magnetic field.

## IV. DECIDING WHICH CASE APPLIES

The boundary between these two regimes is given approximately by

$$|N_0 - N_x| = \frac{2c}{\omega}\frac{d\theta}{dz} \quad \text{or} \quad |A| = S \ . \tag{15}$$

Since $N_0 \sim N_x \sim 1$ and if we set $X = \omega_p^2/\omega^2$ and $Y = \omega_c^2/\omega^2$, the left-hand side of Eq. (15) becomes,

$$\left|\frac{N_0}{2}\left(1 - \frac{N_x^2}{N_0^2}\right)\right| = \frac{1}{\sqrt{1 - X}}\left(\frac{XY}{1 - X - Y}\right) \ .$$

If we set $\omega = \ell\omega_c$ then Eq. (15) becomes

$$\frac{1}{\sqrt{\ell^2 - X'}}\left(\frac{X'/\ell}{\ell^2 - 1 - X'}\right) = S \ , \tag{16}$$

where $X' = \omega_p^2/\omega_c^2$ .

Equation (16) gives us a cubic equation for the critical density $X'$,i.e., that density above which the anisotropy overwhelms the shear,

$$0 = \ell^2(\ell^2 - 1)^2 - (\ell^2 - 1)(3\ell^2 - 1)X' + (3\ell^2 - 2 - 1/\ell^2 s^2)X'^2 - X'^3 \ . \tag{17}$$

This relationship is plotted in Fig. 2.

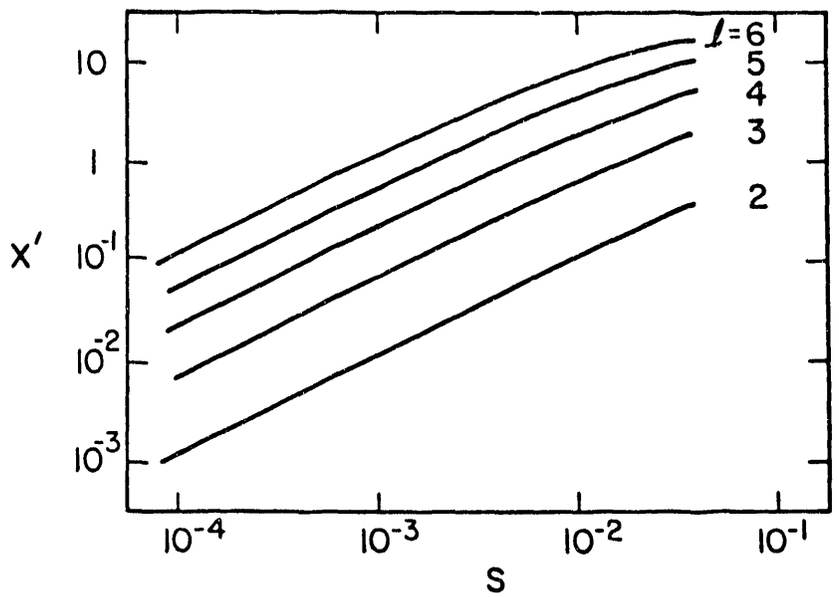


Fig. 2. The critical density as a function of shear for harmonics 2 and larger.

As the lines are almost straight in Fig. 2, the critical density $\omega_p^2/\omega_c^2$ is nearly directly proportional to the shear, S.

Now we need to estimate S for fusion devices,

$$S = \frac{2c}{\omega}\frac{d\theta}{dr} \approx 2\frac{\lambda_0}{a}\frac{\psi}{\pi}, \tag{18}$$

where $\lambda_0$ is the vacuum wavelength of the emission, a the radius of the plasma and $\psi$ is the maximum value of $\theta$.

For circular cross section tokamaks $\psi \sim \pi/30$, $\lambda_0 \sim 2 \times 10^{-3}$m, a ~ 0.5 m, and therefore $S \sim 3 \times 10^{-4}$.

For a high magnetic field spheromak $\psi \sim \pi/2$, $\lambda_0 \sim 2 \sim 10^{-3}$m, a ~ 0.1 m, and therefore $S \sim 2 \times 10^{-2}$.

These values of S cover the range for fusion devices and it is clear that for tokamaks the critical density is very low and will only occur near the edge,perhaps within the shadow of the limiter, even for the

fifth harmonic. The spheromak example shows that the higher harmonics, $\ell = 3, 4, 5$ could emerge unrotated depending on the operating density of the plasma.

## V. CONCLUSIONS

1. The equation delineating the boundary between the two regions is

$$1/N_0(1 - N_0^2/N_x^2) = \frac{2\lambda_0}{\pi}\frac{d\theta}{dz} .$$

2. If anisotropy wins (LHS > RHS) the polarization rotates with the magnetic field. If shear wins (LHS < RHS) the polarization is fixed in configuration space.

3. The critical density $\omega_p^2/\omega_c^2$ is nearly directly proportional to the shear $S = \frac{2\lambda_0}{\pi}\frac{d\theta}{dz}$ .

4. In tokamaks anisotropy wins and the polarization rotates even for higher harmonics like $\ell = 5$.

5. In a high field spheromak at moderate densities $\ell = 3$ and at higher densities $\ell = 4$, shear wins and the polarization does not rotate.

## ACKNOWLEDGMENTS

This work was supported by the Department of Energy.

## REFERENCES

1. F. Engelmann and M. Curatolo, Nucl. Fusion 13, 497 (1973).
2. I. Fidone and G. Granata, Nucl. Fusion 11, 133 (1971).
3. G. C. McCormick, IEEE Trans. MTT.15, 433 (1967).

# Study of the Electron Cyclotron Maser Instability

M. Bornatici,[a] U. Ruffina,[a] and E. Westerhof[b]
[a]*Physics Department "A. Volta," University of Pavia, Pavia, Italy*
[b]*Association Euratom-FOM, FOM-Instituut voor Plasmafysica Rijnhuizen, Nieuwegein, The Netherlands*

**ABSTRACT**. The fully relativistic dispersion relation for the extraordinary mode around the electron cyclotron frequency is investigated, both analytically and numerically, for propagation perpendicular to the magnetic field and a (relativistic) loss-cone distribution. Both the wave dispersion and the (spatial) absorption, which can be positive or negative, as well as the $(\omega_p/\omega_c)$-range for the absolute maser instability are evaluated and discussed.

## INTRODUCTION

Recently fully relativistic investigations of the electon cyclotron maser instability driven by a loss-cone distribution have been performed numerically for propagation both parallel [1,2], and perpendicular [3] to the magnetic field. These studies mainly deal with the evaluation of the temporal growth rate of the instability which is appropriate for cases of wave propagation where time dependences are the dominant feature. On the other hand, for situations of practical interest in laboratory plasmas, the problem of cyclotron absorption and emission is more properly treated as a space-dependent problem [4]. Here we investigate analytically the fully relativistic dispersion relation of the extraordinary mode around the electron cyclotron frequency $\omega_c$, for propagation perpendicular to the magnetic field in a (relativistic) loss-cone plasma and analyse numerically both the dispersion (i.e., real wavenumber as a function of frequency) and the positive and negative (spatial) wave absorption. Furthermore, the $(\omega_p/\omega_c)$-range for the occurrence of the absolute maser instability is obtained.

## FULLY RELATIVISTIC DISPERSION RELATION

For propagation perpendicular to the magnetic field $B_o = \hat{z} \mid B_o \mid$, the (local) dispersion relation for the extraordinary (X) mode yields $N_\perp^2 = \varepsilon_{yy} + \varepsilon_{xy}^2/\varepsilon_{xx}$, where $N_\perp = ck_\perp/\omega$ is the refractive index and $\varepsilon_{ij}$ are the ij-elements of the dielectric tensor. For $|N_\perp| \leq 1$, the dominant features of the mode dynamics around the resonance $\omega = \omega_c$ are appropriately described by taking the finite Larmor radius effects in $\varepsilon_{ij}$ to lowest order, and evaluating the corresponding non-resonant contribution to the dispersion relation in the cold plasma limit. The dipersion equation thus reduces to

$$N_\perp^2 = \left[ 1 - \frac{\omega_p^2}{\omega(\omega + \omega_c)} \right] \frac{\varepsilon_{xx} + i\varepsilon_{xy}}{\varepsilon_{xx}} \tag{1}$$

with

$$\varepsilon_{xx} + i\varepsilon_{xy} = 1 - \frac{1}{2} \left( \frac{\omega_p}{\omega} \right)^2 I \left( \frac{\omega}{\omega_c}, f_o \right) \tag{2}$$

$$\varepsilon_{xx} = 1 - \frac{\omega_p^2}{2\omega(\omega + \omega_c)} - \frac{1}{4} \left( \frac{\omega_p}{\omega} \right)^2 I \left( \frac{\omega}{\omega_c}, f_o \right) \tag{3}$$

where

$$I \left( \frac{\omega}{\omega_c}, f_o \right) \equiv - \int d^3p \frac{p_\perp}{\gamma - (\omega_c/\omega)} \frac{\partial f_o}{\partial p_\perp} \tag{4}$$

accounts for the resonant contribution around $\omega = \omega_c$; $\gamma = [1 + (p/mc)^2]^{1/2}$, p being the electron momentum, with $p_\perp$ the corresponding component perpendicular to $B_o$, and $f_o$ is the electron distribution. In the cold plasma limit, (4) reduces to $I = 2\omega/(\omega - \omega_c)$, and from (1) the well-known dispersion equation for the perpendicular X-mode is recovered. Because of the relativistic resonance $\gamma - \omega_c/\omega = 0$, which is present for $\omega \lesssim \omega_c$, the integral in (4) has an imaginary part given by

$$\mathrm{Im}\, I = \pi \int d^3p\, p_\perp \times (\partial f_o/\partial p_\perp)\, \delta\left(\gamma - (\omega_c/\omega)\right),$$

whose sign depends on the sign of $\partial f_o/\partial p_\perp$ in the resonant p-domain. From (2) and (3), assuming $\omega$ to be real, it is $\mathrm{Im}(\varepsilon_{xx} + i\varepsilon_{xy}) = 2\mathrm{Im}(\varepsilon_{xx}) = -(1/2)(\omega_p/\omega)^2\, \mathrm{Im}\, I$.

We consider specifically a **relativistic loss-cone distribution** of the form

$$f_o = C_j(\mu) \left( \frac{p_\perp}{mc} \right)^{2j} e^{-\mu\gamma} \tag{5}$$

where $C_j(\mu) \equiv \mu^{j+1}[4\pi(mc)^3\, 2^j\, j!\, K_{j+2}(\mu)]^{-1}$, $\mu \equiv mc^2/T$ is an inverse temperature variable, j is the loss-cone index (j = 0 corresponds to the re-

lativistic Maxwellian) and $K_\nu(z)$ is the modified Bessel function of the second kind with index $\nu$ and argument z. The average particle kinetic energy $\langle W \rangle = (\langle \gamma \rangle - 1)mc^2$ connected with (5) is

$$\langle W \rangle = \left[ \frac{3 + 2j}{\mu} + \frac{K_{j+1}(\mu)}{K_{j+2}(\mu)} - 1 \right] mc^2 \tag{6}$$

which reduces to $\langle p^2 \rangle / 2m = (3/2 + j)T$ to lowest order in $\mu^{-1} (= T/mc^2 \ll 1)$.

To perform the integration occurring in (4) it is convenient to use the variables $\gamma$, $x \equiv p_{\|}^2 / (\gamma^2 - 1)$ and the azimuthal angle of p, this latter integration being readily carried out, whereas the integration over x can be expressed in terms of the $\Gamma$-function. The result obtained for the quantity defined in (4) is thus

$$I\left( \frac{\omega}{\omega_c} ; j \right) = 2\mu a_{j+2}(\mu) \left[ - \frac{1}{a_{j+1}(\mu)} \frac{j}{\mu} + (j+1)\tilde{F}_{j+3/2} - j \frac{\omega_c}{\omega} \tilde{F}_{j+3/2} \right] \tag{7}$$

where $a_q(\mu) \equiv (\pi/2\mu)^{1/2} e^{-\mu}/K_q(\mu)$ ($= 1$, to lowest order in $\mu^{-1}$),

$$\tilde{F}_q \equiv \tilde{F}_q\left[\mu\left(\frac{\omega_c}{\omega} - 1\right)\right] = \left(\frac{\mu}{2}\right)^{q-1} \frac{e^\mu}{\Gamma(q)} \int_1^\infty d\gamma \frac{(\gamma^2-1)^{q-1}}{\gamma - (\omega_c/\omega)} e^{-\mu\gamma} \tag{8a}$$

$$= -i \int_0^\infty d\tau \frac{\left[\frac{2\mu}{\pi}(1-i\tau)\right]^{1/2} e^{\mu(1-i\tau)}}{(1-i\tau)^q} K_{q-1/2}(\mu(1-i\tau))\, e^{-i\mu\left(\frac{\omega_c}{\omega} - 1\right)\tau}. \tag{8b}$$

Referring to (8b), by making use of the asymptotic expansion of the Bessel function $K_{q-1/2}$, one can express $\tilde{F}_q$ as

$$\tilde{F}_q(z) = \sum_{k=0}^{n-1} \frac{\Gamma(q+k)}{k!\,\Gamma(q-k)} \frac{1}{(2\mu)^k} F_{q+k}(z) + O\left(\frac{1}{\mu^n}\right) \tag{8c}$$

with

$$F_q(z) \equiv -i \int_0^\infty d\tau \frac{e^{-iz\tau}}{(1-i\tau)^q}, \tag{9}$$

the series representation (8c) of $\tilde{F}_q$ being particularly convenient for the numerical evaluation of I as the properties of the $F_q$-functions are well established [4].

As for the quantity (7), one notes that i) the lowest order in $\mu^{-1}$, i.e., in the weakly relativistic limit, from (8c), $\tilde{F}_q = F_q$, so that

$$I\left(\frac{\omega}{\omega_c};j\right) = 2\mu[(j+1)F_{j+5/2} - jF_{j+3/2}] \tag{10}$$

where $F_q \equiv F_q[\mu((\omega_c/\omega) - 1)]$; ii) exactly at resonance $\omega = \omega_c$, the function $\tilde{F}_q$, in the form (8a), can be expressed in terms of the Whittaker's function $W_{k,\nu}$, with the result that

$$I(\omega=\omega_c;j) = 2\mu a_{j+2}(\mu)\left[-\frac{1}{a_{j+1}(\mu)}\frac{j}{\mu} + \frac{j+1}{j+3/2}\tilde{W}_{j+3/2}(2\mu) - \frac{j}{j+1/2}\tilde{W}_{j+1/2}(2\mu)\right] \tag{11}$$

where $\tilde{W}_q(2\mu) \equiv W_{1/2,q}(2\mu)/(2\mu)^{1/2}e^{-\mu}$ (= 1, to lowest order in $\mu^{-1}$). Quantity (11) is a real quantity, which, to lowest order in $\mu^{-1}$, reduces to $I(\omega = \omega_c;j) = \mu[(j + 1/2)(j + 3/2)]^{-1}$; iii) as mentioned before, the quantity I has a non-zero imaginary part for $\omega < \omega_c$; by noting that, from (8a), one has

$$\mathrm{Im}\,\tilde{F}_q = -\frac{\pi}{\Gamma(q)}\left\{\frac{\mu}{2}\left[\left(\frac{\omega_c}{\omega}\right)^2 - 1\right]\right\}^{q-1} e^{-\mu\left(\frac{\omega_c}{\omega}-1\right)}, \tag{12}$$

from (7) it follows

$$\mathrm{Im}\,I\left(\frac{\omega}{\omega_c};j\right) = -2\mu a_{j+2}(\mu)\frac{\pi(j+1)}{\Gamma(j+5/2)}\left\{\frac{\mu}{2}\left[\left(\frac{\omega_c}{\omega}\right)^2 - 1\right]\right\}^{j+1/2} \times$$
$$\times\left\{\frac{\mu}{2}\left[\left(\frac{\omega_c}{\omega}\right)^2 - 1\right] - \frac{j(j+3/2)}{j+1}\frac{\omega_c}{\omega}\right\} e^{-\mu\left(\frac{\omega_c}{\omega}-1\right)}, \quad \omega < \omega_c \tag{13}$$

From (13) it appears that either $\mathrm{Im}\,I < 0$, corresponding to positive absorption ($\mathrm{Im}\,N_\perp > 0$, stability) or $\mathrm{Im}\,I > o$, corresponding to negative absorption ($\mathrm{Im}\,N_\perp < 0$, instability) depending on whether $\omega < \omega_j(\mu)$ or ($\omega_c >$) $\omega > \omega_j(\mu)$, respectively, with $\omega_j(\mu)$ the frequency at which the quantity within the curly brackets in (13) is zero, i.e.,

$$\frac{\omega_j(\mu)}{\omega_c} = \left\{1 + \left[\frac{j(j+3/2)}{j+1}\frac{T}{mc^2}\right]^2\right\}^{1/2} - \frac{j(j+3/2)}{j+1}\frac{T}{mc^2}. \tag{14}$$

Hence, $\omega_j(\mu)$ is a decreasing function of both the loss-cone index j and the temperature T, the decrease in T being the faster the larger j is.

Correspondingly, also the width of the unstable frequency range increases.

**(Absolute) maser instability.** For $N_\perp = 0$ and considering frequencies around the right-hand cutoff the dispersion equation (1) reduces to $\varepsilon_{xx} + i\varepsilon_{xy} = 0$, or, with (2), to

$$1 - \frac{1}{2}\left(\frac{\omega_p}{\omega}\right)^2 I\left(\frac{\omega}{\omega_c}, f_0\right) = 0; \tag{15}$$

I being given by (7) for a relativistic loss-cone distribution. Equation (15) is to be solved for complex $\omega$ and, as said above, one finds that $\mathrm{Im}\,\omega \geq 0$ for $\omega_j(\mu) \leq \omega' \equiv \mathrm{Re}\,\omega \leq \omega_c$, which corresponds to the (absolute) electron- cyclotron maser instability recently considered by a number of authors [1-3]. Here, we just note that taking $\omega' = \omega_c(\mu)$ and $\omega' = \omega_j(\mu)$ in (15) yields, respectively, the upper and lower limit of $(\omega_p/\omega_c)^2$ for the excitation of the maser instability, i.e.,

$$\left(\frac{\omega_p}{\omega_c}\right)^2_{max} = \frac{2}{I(\omega=\omega_c;j)}, \quad \left(\frac{\omega_p}{\omega_c}\right)^2_{min} = \frac{2}{I(\omega=\omega_j(\mu);j)}\left(\frac{\omega_j(\mu)}{\omega_c}\right)^2, \tag{16}$$

$\omega_j(\mu)$ being given by (14), whereas $I(\omega=\omega_j(\mu);j)$ is to be obtained from (7) and $I(\omega=\omega_c;j)$ is given by (11), both I's being real and positive. In particular, in the weakly relativistic limit, $(\omega_p/\omega_c)^2_{max} = (2j+1)(3/2+j)T/mc^2$. Whereas $(\omega_p/\omega_c)_{max}$ is an increasing function of both j and T, $(\omega_p/\omega_c)_{min}$ is a weakly increasing function of T and a weakly decresing function of j, (e.g., for T = 20 keV, $(\omega_p/\omega_c)_{min} \simeq 0.20$ for j = 1 and 2, whereas $(\omega_p/\omega_c)_{max} \simeq 0.5$ for j = 1 and 0.8 for j = 2; for T = 100 keV, $(\omega_p/\omega_c)_{min} \simeq 0.45$ for j = 1 and 0.37 for j = 2, whereas $(\omega_p/\omega_c)_{max} \simeq 1.1$ for j = 1 and 1.5 for j = 2).

**Numerical analysis.** As is well-known, in the cold plasma limit, the dispersion relation (1) predicts a stop band for $\omega_\infty < \omega \leq \omega_0$, with $\omega_\infty$ the upper hybrid frequency that corresponds to a resonance for the slow X-branch ($N_\perp > 1$) and $\omega_0$ the right-hand (RH) cutoff for the fast X-branch ($N_\perp < 0$). This picture is significantly modified by the effects of both temperature, as shown in [5] for a Maxwellian distribution, and loss-cone. A sample of a numerical analysis performed for a loss-cone distribution is given in Figs. 1 and 2 for a loss-cone index j = 1 and $(\omega_p/\omega_c)^2 = 0.2$. More specifically, in Fig. 1a $\mathrm{Re}\,k_\perp$ (normalized to $\omega_c/c$) is shown as a function of $\omega/\omega_c$, for different temperatures, namely

T = 15; 18.33 and 20 keV. For the moderately high values of T considered it appears that it is in the frequency range $\omega \geq \omega_c$ that we wave dispersion senses the thermal effects. More specifically, i) for T = 15 keV, there are two disconnected branches, the corresponding stop band being bounded by the right-hand cutoff downshifted by the relativistic effects and a low-frequency cutoff occuring at $\omega = \omega_c$ ; ii) for T = 18.33 keV, the two branches get connected through a pronounced dip around a frequency which is very nearly a cutoff; iii) for T = 20 keV, the single branch connection is more complete and one tends towards the single branch of the tenous-plasma limit with just a wiggle around $\omega = \omega_c$. It has to be noted that the merging into a single branch occurs at temperatures which are lower than those corresponding to a Maxwellian distribution [5] (which has to do with the fact that a loss-cone distribution is connected with a higher average particle kinetic energy). As for Im $k_\perp$, this is shown in Fig. 1b for the same parameters as in Fig. 1a. The peak values of | Im $k_\perp$ | for negative absorption (Im $k_\perp \leq 0$, for $\omega_j(\mu) \leq \omega \leq \omega_c$, corresponding to instability) are about a factor 3 larger than the peak values for positive absorption ($Imk_\perp \leq 0$, for $\omega \leq \omega_j(\mu)$), while the unstable frequency range is narrower than that corresponding to stability.

As the temperature increases further, the wave dispersion is dominated by the relativistic downshift in frequency along with the strong (positive and/or negative) absorption occurring at $\omega < \omega_c$. As shown in Fig. 2a, the single branch at 100 keV differs remarkably from that at 20 keV, the main feature being a pronounced dip around $\omega = \omega_j(\mu)(< \omega_c)$, extending down to nearly zero and due to Re$(N_\perp^2)$ becoming negative (note that Re $k_\perp = [\mathrm{Re}(k_\perp^2) + (\mathrm{Im}\, k_\perp)^2]^{1/2}$, so that Re $k_\perp = 0$ when either Re$(k_\perp^2) = (\mathrm{Im}\, k_\perp)^2 = 0$, or Re$(k_\perp^2) = -(\mathrm{Im}\, k_\perp)^2$). As the temperature increases, the dip both shifts towards lower frequencies, as a result of the relativistic downshift, and reduces its depth, as shown by the 150 keV-curve. For the corresponding Im $k_\perp$, shown in Fig. 2b, one notes that in the low temperature range the (magnitude of the) peak of negative absorption is higher than that corresponding to positive absorption, both peaks increasing with T, cf. also Fig. 1b (this latter scaling being the same as that of the absorption for a Maxwellian distribution in the finite-density regime [4]), whereas the opposite is true for the high temperature range, cf. the curves for 100 and 150 keV in Fig. 2b (again, the scaling with

respect to T is the same as the one for a Maxwellian distribution in the tenuous-plasma regime [4]).

Finally, we note that i) the effects on both $\mathrm{Re}\, k_\perp$ and $\mathrm{Im}\, k_\perp$ due to increasing the loss-cone index j and/or decreasing $(\omega_p/\omega_c)^2$ have the same main features as the ones connected with increasing the temperature; ii) no threshold in $(\omega_p/\omega_c)$ exists for the excitation of the instability, in contrast with what happens for the absolute instability, cf. (15).

**ACKNOWLEDGEMENTS**

Useful discussions with F. Engelmann are gratefully acknowledged. This work was performed under the Euratom-FOM association agreement with financial support from ZWO, Euratom and Ministero Pubblica Istruzione.

**REFERENCES**

1. Y.Y. Lau, and K.R. Chu, Phys. Rev. Lett. **50**, 243 (1983).
2. K.T. Tsang, Phys. Fluids **27**, 1659 (1984).
3. P.L. Pritchett, Phys. Fluids **27**, 2393 (1984).
4. M. Bornatici, R. Cano, O. De Barbieri, and F. Engelmann, Nucl. Fusion **23**, 1153 (1983).
5. D.B. Batchelor, R.C. Goldfinger, and H. Weitzner, Phys. Fluids **27**, 2835 (1984).

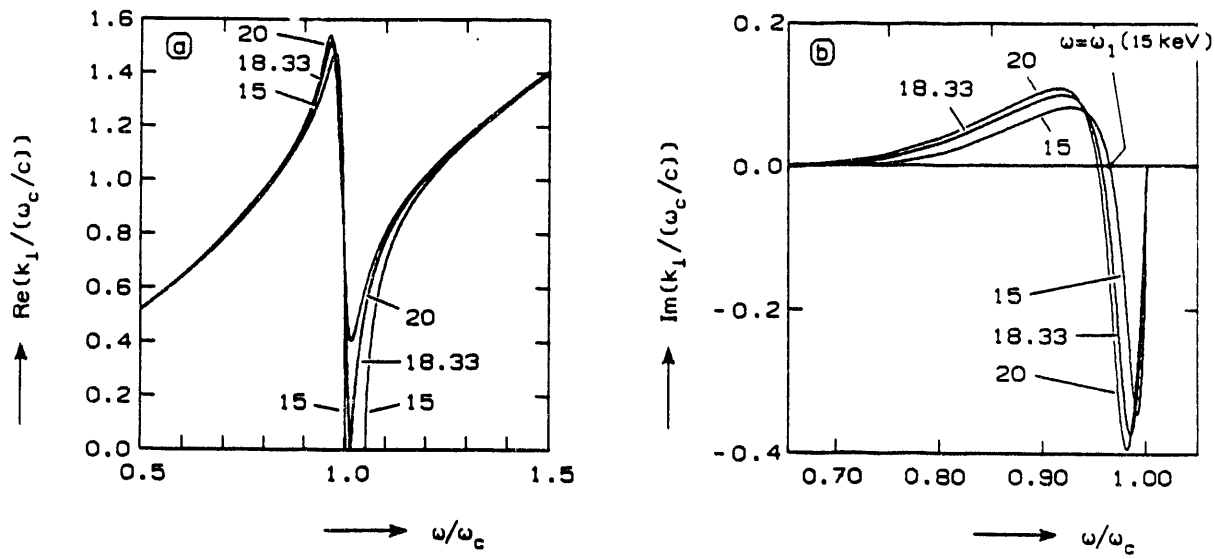


Fig. 1a. The (normalyzed) real part of the perpendicular wave number vs. $\omega/\omega_c$, for $(\omega_p/\omega_c)^2 = 0.2$, $j = 1$ and $T = 15$; 18.33; and 20 keV.

Fig. 1b. The (normalized) imaginary part of the perpendicular wave number vs. $\omega/\omega_c$ for the same parameters as in Fig. 1a. $\omega_1(\mu)$ is given by (14) with $j = 1$.

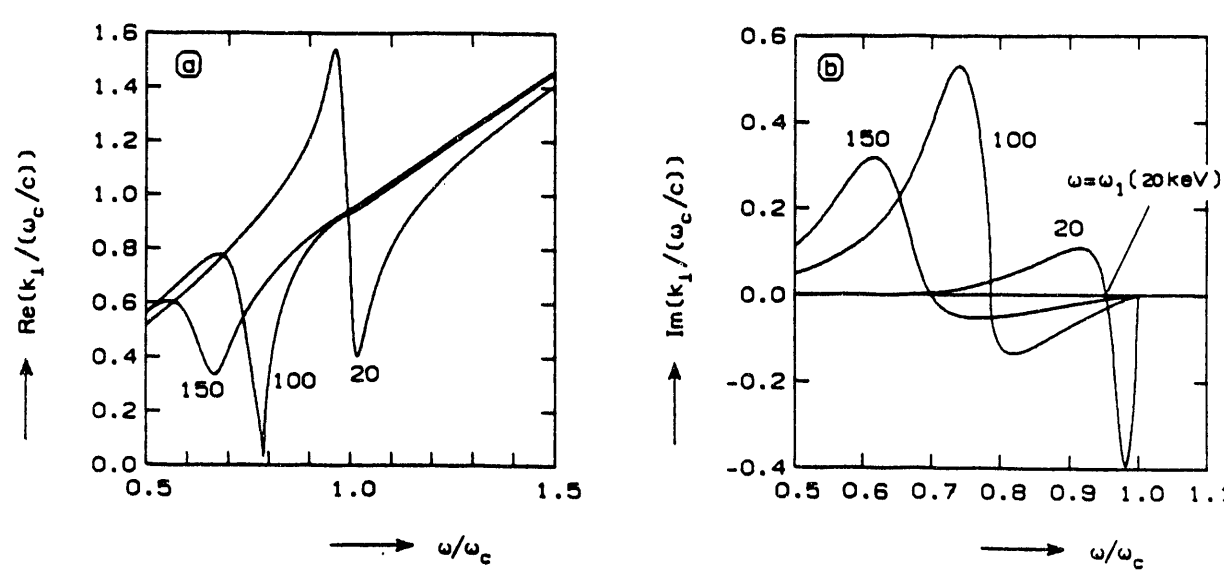


Fig. 2a. Same as Fig. 1a for $T = 20$; 100; and 150 keV.

Fig. 2b. Same as Fig. 1b for $T = 20$; 100; and 150 keV.

# Electron Runaway Effects Induced by Electron Cyclotron Waves

L. Demeio* and F. Engelmann
*Association Euratom-FOM, FOM-Instituut voor Plasmafysica*
*Rijnhuizen, Nieuwegein, The Netherlands*

ABSTRACT

Runaway effects perpendicular to the confining magnetic field, induced by electron cyclotron waves, were investigated, adopting a quasi-uniform model. Using the results of [4], the conditions for the quasi-uniform model to be satisfactory for tokamak plasmas of practical interest are discussed.

## 1. Introduction

The motion of electrons in velocity space induced by the combined effect of collisions and electron cyclotron waves around the fundamental frequency and in the ordinary mode polarization, was investigated in [1], adopting a model in which both the magnetoplasma and the wave field were taken to be homogeneous. When applying this model to a practical situation in a tokamak in which the magnetic field is space-dependent and the plasma is in interaction with a wave beam of finite size, the only adjustment was the reduction of the quasilinear diffusion coefficient [2] by the ratio of the beam cross section and the area of the flux surface considered. This "quasi-uniform" model indicated that runaway effects in the component of the velocity vector perpendicular to the confining magnetic field, in a certain range of the parameter $\Delta\bar{\omega} \equiv (\omega-\omega_c)/\omega_c$, can occur at relatively low levels of the power flux of the waves. Here, $\omega$ is the wave frequency and $\omega_c \equiv |eB/mc|$ is the electron cyclotron frequency (e and m are, respectively, the charge and the relativistic mass of the electron, c is the speed of light and B the confining magnetic field) which, in tokamak geometry, is dependent on the distance from the main axis of the torus. Recently, the quasilinear diffusion coefficient has been re-derived for freely circulating electrons

* Euratom fellow; Commission of the European Communities, Brussels, Belgium

confined in tokamak geometry, in the presence of a wave beam of finite size [3,4]. From this, the limits of validity of the homogeneous model can be derived.

Starting from the results given in [1], we discuss here to which extent the quasi-uniform model is able to describe runaway effects in practical situations.

## 2. The conditions for runaway occurrence

We briefly recall the model developed in [1]. There, the test-particle method introduced by Dreicer [5] was used to investigate the electron motion in velocity space, analyzing the topology of the flow lines corresponding to the total force, $\underline{\delta F} = \underline{\delta F}_d + \underline{\delta F}_w$ which acts on the test particles. Here, $\underline{\delta F}_d$ is the drag force due to collisions and $\underline{\delta F}_w$ the force due to the interaction with the waves. From the kinetic equation for the test electrons, we have

$$\underline{\delta F}_d = -6mA\delta N \frac{\underline{v}}{v^3} \text{ and}$$

$$\underline{\delta F}_w = m\delta N \left\{\frac{\partial}{\partial v_\perp}(v_\perp D)\right\}\frac{\underline{v}_\perp}{v_\perp^2} ;$$

here $A = 2\pi e^4 n \ln\Lambda/m^2$, n being the plasma density and $\ln\Lambda$ the Coulomb logarithm, $\delta N$ is the density and $\underline{v}$ is the average velocity of the test particles with $v \gg v_t$, $v_t$ being the thermal velocity of the bulk electrons. The quasilinear diffusion coefficient D is given by

$$D = \frac{e^2\omega_c^2}{4\pi^2 m^2 V} \int d^3k \frac{|\theta_{\underline{k}}|^2}{\omega^2} \delta(\omega - k_\parallel v_\parallel - \omega_c/\gamma) ,$$

where $\gamma \equiv \{1-(v/c)^2\}^{-1/2}$, $\underline{k}$ is the wave vector and V is the plasma volume, whose linear dimensions are assumed to be large compared to the wavelengths of the wave spectrum excited. The function $\theta_{\underline{k}}$ is given in [2]; for the ordinary mode, both at oblique and perpendicular propagation, it takes the form

$$|\theta_{\underline{k}}|^2 = \frac{1}{4} |\varepsilon''_{\underline{k}}|^2 \{1-(\omega_p/\omega_c)^2\}(v_\parallel/c)^2 ,$$

where $\omega_p = \{4\pi ne^2/m\}^{1/2}$ is the electron plasma frequency and $\varepsilon''_{\underline{k}}$ the component of the wave electric field parallel to the confining magnetic field.

This simple model was applied to a number of different wave spectra, yielding qualitatively similar results in all cases. In Fig. 1, the flow lines and the resonant domain of velocity space are shown for waves propagating obliquely with respect to $\underline{B}$, having a fixed frequency $\omega$ and a "rectangular" spectrum in $k_{||}$,

$$|\varepsilon''_{\underline{k}}|^2 = |E_o|^2 f(k_{||}),$$

with $f(k_{||}) = 1$ for $k\cos\theta - \Delta k_{||} \leq k_{||} \leq k\cos\theta + \Delta k_{||}$, and $f(k_{||}) = 0$ elsewhere, $\theta$ being the average angle of propagation. For simplicity, the condition $\Delta k_{||} << |k\cos\theta|$ is assumed to be valid and in the angular range under consideration relativistic effects are taken not to be important in the wave propagation properties. The equation of the flow lines in velocity space, defined by $dv/\delta F_v = vd\xi/\delta F_\xi$, then is

$$v = \{2\,\frac{c+v_o^2\,\cos\xi}{\cos^2\xi}\}^{1/2},$$

where polar coordinates $v$, $\xi$ are used in the $v_{||}$, $v_\perp$ plane, $v_o^2 \equiv 6A|v_{||}|/D$ and $c$ is an integration constant distinguishing different flow lines. The diffusion coefficient D, in this particular case, is given by

$$D = \frac{\pi^2 e^2}{m^2 c^2 \omega_c N}\,\frac{[1-(\omega_p/\omega_c)^2]\sin\theta}{\{1+[1-(\omega_p/\omega_c)^2]\cos^2\theta\}^{1/2}}\,\frac{\Pi}{\Delta N_{||}}\,|v_{||}|,$$

where $\Pi$ is the Poynting flux, $N \equiv kc/\omega$ is the refractive index and $\Delta N_{||} \equiv \Delta k_{||}c/\omega$.

The parameter $v_o$ measures the critical velocity for the occurrence of runaway effects; in the region $v \leq v_o$ collisions are dominant, while at larger velocities wave effects are large and high-energy particles can be produced. The two regions typically correspond to closed (i.e. converging rapidly to $v = 0$) and open (i.e. diverging to large $v$) flow lines,

respectively. In which range the conditions for the generation of runaway electrons are fulfilled can, therefore, be seen by direct inspection of the flow lines in the resonant domain. Effectively, runaway effects occur if the resonance domain covers velocities larger than $v_o$. They are particularly strong if $v_o$ is a few times $v_t$, because then they are present in the vicinity of the bulk of the electrons.

## 3. Applicability of the model and discussion of practical cases

The condition for the quasi-uniform model to be applicable to a tokamak discharge (major radius: R) into which a finite wave beam (toroidal size: L; vertical size: 2b) is injected around the equatorial plane, is (see Ref. 4)

$$\left(\frac{v_{\parallel}}{c}\right)^2 \{1+[g(r)]^{-2}\} + \left(\frac{v_{\perp}}{c}\right)^2 > 1 \ ,$$

where

$$g(r) \equiv \frac{1}{\sqrt{2\pi}} \frac{\omega_c L}{c} \frac{r}{R} \{1-[1-(\frac{b}{r})^2]^{1/2}\} \ ,$$

for $r > b$, and

$$g(r) = \frac{1}{\sqrt{2\pi}} \frac{\omega_c L}{c} \frac{r}{R} \ ,$$

for $r \leq b$, r being the distance from the minor axis of the torus. The corresponding region in velocity space is the exterior of the ellipse centered at $v = 0$, intersecting the coordinate axis at the points

$$v_{\parallel} = 0, \ \frac{v_{\perp}}{c} = 1 \quad \text{and}$$

$$\frac{v_{\perp}}{c} = \pm \{1+[g(r)]^{-2}\}^{-1/2} \ , \ v_{\perp} = 0.$$

Therefore, for the quasi-uniform model to be a good approximation for electron velocities $v \ll c$, the value of $g(r)$ must be small compared to 1. Furthermore, for this model to cover the interesting range of velocities v somewhat above $v_t$, one needs $g(r) \approx v_t/c$.

The properties of the function g(r) are shown in Fig. 2. It has a maximum for r = b, whose value

$$g(b) = \frac{1}{\sqrt{2\pi}} \frac{\omega_c L}{c} \frac{b}{R}$$

depends on the cross section of the beam and on the characteristic of the device. It is readily seen that the most favourable case for the quasi-uniform model to be applicable would be that of a large machine with a low magnetic field and a well-collimated beam, which is a parameter combination of little practical importance. As an illustration, in Table I the values of g(b) are given for three different cases, a "reactor-like" tokamak, a small device and a compact high-field tokamak, taking for the beam parameters b = 5 cm and L = 10 cm throughout. As a result, the quasiuniform model is never satisfactory for flux surfaces with r = b, while it tends to be applicable where g(r) << 1, i.e. in a (small) range around the magnetic axis and, usually, in the exterior part of the plasma column, at least close to the injection port of the wave beam. Effectively, for waves propagating obliquely with respect to the magnetic field, then the runaway region is given by

$$v_{\parallel} > v_o ,$$

$$\frac{v_{\perp}}{c} \geq g(r) ,$$

$$v_{\parallel}^{-} \leq v_{\parallel} \leq v_{\parallel}^{+} ,$$

$v_{\parallel}^{-}$ and $v_{\parallel}^{+}$ being the lower and the upper limit of the (non-relativistic) resonant domain.

**TABLE I**

| tokamak | R | B | g(b) |
|---|---|---|---|
| Reactor-like | 5 m | 4 T | ~ 1 |
| Small | 1 m | 2 T | $\gtrsim$ 3 |
| Compact | 1 m | 8 T | ~ 10 |

Let us illustrate the situation by an example. The quasi-uniform model predicts the occurrence of runaway effects at relatively low values of the power fluxes of the waves [1], of the order of 0.1 kW/cm$^2$ averaged over a magnetic surface. For small devices, this is achieved with relatively low powers ($\lesssim$ 1 MW); on the other hand, in the case of a reactor-like device, the corresponding powers tend to be quite large. In Fig. 3 and 4, the limits of the runaway region are shown for $v_\perp = 0$ as a function of $X_{res}$, the position of the resonant cylinder where $\omega = \omega_c(v = 0)$. The two examples refer to a reactor-like device (see Table I) and flux surfaces with, respectively, r = 1 and 50 cm. For r = 1 cm and a plasma temperature T = 10 keV one has $g(r) = 2\, v_t/c = 0.3$. This shows explicitely that in the limit $r \ll b$ the domain in velocity space, where the quasi-uniform model is valid, tends to approach the bulk electrons only in a very limited range around the magnetic axis. In the opposite limit, r = 50 cm $\gg$ b, one even has $g(r) < v_t/c$. Note that in this case a power of the order of 100 MW is required to achieve power fluxes leading to runaway production. In both cases runaway production is most efficient if the resonance is situated about 30 cm beyond the magnetic surface considered.

In a small device with a central temperature of T = 1 keV the condition $g(r) \lesssim 2v_t/c$ would be met only for $r \lesssim 2$ mm and in the outer region of the plasma in front of the injection port of the beam. In contrast, in the other regions of the plasma, large modifications of the results of the quasi-uniform model are found if proper account is taken of the effects of toroidal geometry and finite beam size [4]. E.g., for r = b = 5 cm only about 20% of the beam interacts resonantly with particles having $|v_\parallel| = 2v_t$. Hence, in total a 5 times higher power, typically 5 MW, must be injected to actually create a situation similar to that of Fig. 1, where a strong production of runaway electrons occurs.

Similar results are obtained for perpendicular propagation. But since in this case the waves couple to suprathermal electrons only beyond the range where absorption due to the bulk electrons occurs, only in small devices, under very special conditions, runaway generation can occur and be described by the quasi-uniform model.

In conclusion, while for special cases the quasi-uniform model is suitable for analyzing the appearance of runaway effects induced by electron cyclotron waves in a tokamak plasma, in situations of practical interest this is in general not the case. Rather the diffusion coefficient [3,4], which takes proper account of the effect of the finite beam size and magnetic field inhomogeneity in the wave-particle interaction, has to be used for obtaining quantitatively satisfactory results throughout. This applies in particular to most of the plasma core. These effects, on the one hand, tend to reduce the strength of quasilinear diffusion and, on the other, widen the resonant domain. Hence, the region where collisional effects dominate, for a given power flux, is enlarged, while the upper boundary of the runaway region, if there is any, is shifted towards higher energies.

Acknowledgement

This work was performed under the Euratom-FOM association agreement with financial support from ZWO and Euratom.

References

[1] Demeio, L., Engelmann, F., Proc. Workshop on Math. Aspects of Fluid and Plasma Dynamics, Trieste, May 30-June 2 (1984) p. 201.

[2] Kennel, C.F., Engelmann, F., Phys. Fluids 9 (1966) 2377.

[3] Cairns, R.A., Lashmore-Davies, C.N., Proc. IVth Int. Symp. on ECE and ECRH, Rome, March 28-30 (1984) p. 71.

[4] Demeio, L., Engelmann, F., this Workshop.

[5] Dreicer, H., Phys. Rev. 117A (1960) 329.

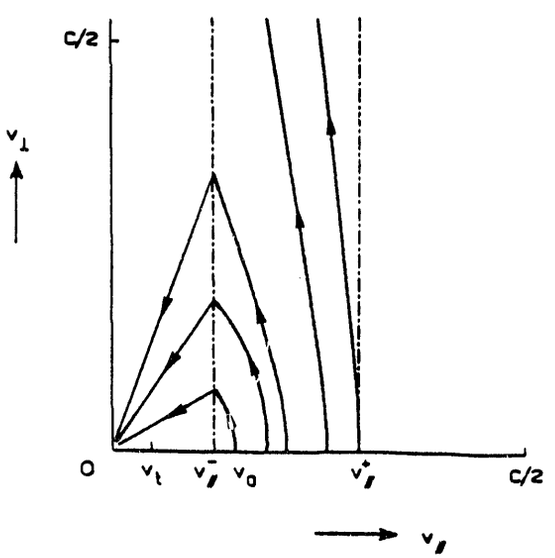


Fig. 1.

Flow lines and resonant domain, delimited by $v_\parallel = v_\parallel^{\pm}$, for a rectangular spectrum in $k_\parallel$, with $v_t/c = 5\times10^{-2}$, $n = 1.3\times10^{13}$ cm$^{-3}$, $R = 1$ m, $B = 2$ T, $\Delta\bar{\omega} = 5\times10^{-2}$, $\Pi = 5\times10^{-2}$ kW/cm$^2$, $\theta = 70$ degrees and $\Delta N_\parallel = 0.1$.

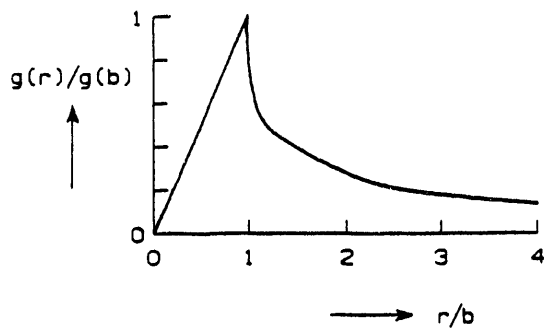


Fig. 2.
The function g(r), normalized to its maximum, versus r/b.

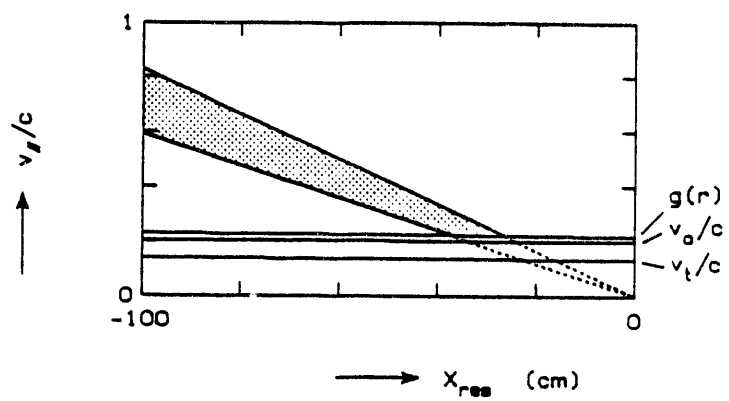


Fig. 3. Range of parallel velocities, $v_{\parallel}/c$, in which runaway effects in $v_{\perp}$ are induced, for r = 1 cm, R = 5 m, B = 4 T, T = 10 keV, $n = 5\times10^{13}$ $cm^{-3}$, $\Pi$ = 0.1 kW/$cm^2$, $\theta$ = 70 degrees, $\Delta N_{\parallel}$ = 0.05; the relevant range is shaded, and the values of g(r), $v_o/c$ as well as $v_t/c$ are shown.

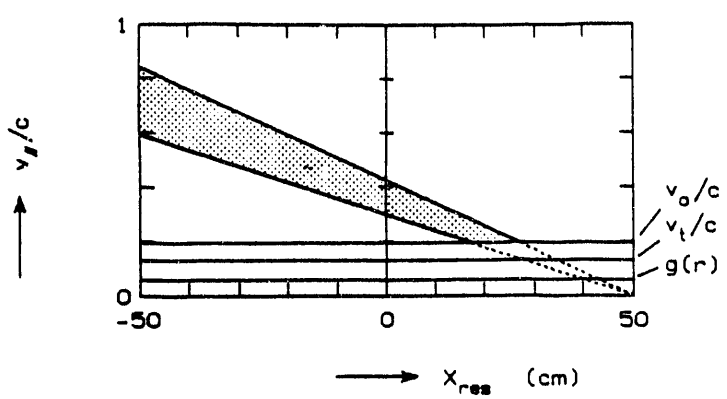


Fig. 4. As Fig. 3, but r = 50 cm.

# The Stability of Electron Cyclotron Waves in the Presence of Stong Electron Cyclotron Heating*

J.Y. Hsu
*GA Technologies, Inc., San Diego, California, 92138, U.S.A.*
and
C.N. Lashmore-Davies
*Culham Laboratory, Abingdon, Oxfordshire OX14 3DB, U.K.*
*EURATOM/UKAEA Fusion Association*

*We examine the stability of the O-mode for perpendicular propagation when a certain fraction of the electrons form a hot electron ring. We consider the case of a sharp ring simpler to analyze and a diffuse ring which may occur under conditions of strong electron cyclotron heating. In both cases the parallel distribution of velocities is assumed to be Maxwellian. We find that both distributions can be unstable to the O-mode. For the diffuse ring we estimate the temperature of the background thermal plasma required to stabilize the instability.*

## 1. INTRODUCTION

Recently, effects of energetic particles on MHD stability have been of great interest [1]. It has been suggested that an energetic component may help the plasma to reach the second stability regime of the ballooning mode. A ring structure of hot electrons may also act like a limiter to stabilize the kink instabilities by forcing the kink perturbations to vanish at the ring location.

The X-mode at the second harmonic of the electron cyclotron frequency is particularly suitable to create such an energetic ring since more energetic particles can be preferentially heated. These particles then collapse toward the weak magnetic field side

*This is a report of work sponsored by the Department of Energy under Contract No. DE-AC03-84ER53158.

where the resonance layer may be placed. The collapse to the resonance point by way of resonance localization [2] only stops due to the effect of relativistic detuning. The relativistic detuning eventually moves the resonance point outside the particle bounce orbit, thus allowing a steady-state ring structure.

The distribution function of the ring can therefore be constructed by allowing a fraction of the electrons to be heated up to the energy such that the resonance poloidal angle $\theta_r$ coincides with the angle at the "banana tip" $\theta_t$ in a circular tokamak. Assuming that the magnetic field is given by $B = B_0(1 - \varepsilon\cos\theta)$, where $\varepsilon \equiv r/R$, that the particle energy at $\theta = 0$ is $E = \frac{1}{2}m(v_\perp^2 + v_\parallel^2)$ and using the invariance of the magnetic moment $\mu$, we find that at the "banana tip" $E = \frac{1}{2}mv_\perp^2(1-\varepsilon\cos\theta_t)/2(1-\varepsilon)$ with the result that

$$1 - \cos\theta_t = \frac{(1-\varepsilon)v_\parallel^2}{\varepsilon v_\perp^2} \,. \tag{1}$$

Choosing the second harmonic resonance to be at $\theta = 0$ for $\gamma = 1$ fixes the applied frequency $\omega = 2\Omega_0(1-\varepsilon)$. Using the resonance condition for a heated particle $\omega = 2\Omega_0[(1-\varepsilon\cos\theta_r)/\gamma]$, we then obtain

$$1 - \cos\theta_r = \frac{(\gamma-1)(1-\varepsilon)}{\varepsilon} \,. \tag{2}$$

The condition $\theta_t = \theta_r$ then gives $v_\parallel^2/v_\perp^2 = \gamma - 1$, which in the weakly relativistic limit can be written as $v_\perp^2 = \sqrt{2}\,c|v_\parallel|$. Assuming that the distribution of parallel velocities is Maxwellian, we can therefore write the distribution function for the hot electron ring as

$$f_R(v_\parallel, v_\perp) = \frac{1}{\pi^{3/2}v_e}\, e^{-v_\parallel^2/v_e^2}\, \delta\left(v_\perp^2 - \sqrt{2}\,c|v_\parallel|\right) \,, \tag{3}$$

where the $J$-invariant has been approximated to justify the constancy of $v_\parallel$ during the heating. The above distribution represents a diffuse ring due to the thermal spread of the parallel velocities.

## 2. STABILITY OF HOT ELECTRON RING TO ELECTRON CYCLOTRON WAVES

The hot electron ring distribution discussed above is similar to those used in gyrotrons to generate electromagnetic waves. For these devices, the distribution is usually taken to be a sharp ring, *i.e.*, $f(v_\perp) = (1/2\pi v_{\perp 0})\,\delta(v_\perp - v_{\perp 0})$. If such rings are to be of use in a tokamak, it is important that they should not radiate away the energy stored in them due to the occurrence of a cyclotron instability. We shall therefore analyze the stability of the above distribution to electron cyclotron waves. The plasma will be viewed as consisting of a thermal background plasma with a non-thermal population of electrons which form the ring. We shall consider two non-thermal distributions. The first is a sharp ring given by

$$f_0(\beta_\perp, \beta_\parallel) = \frac{1}{2\pi\beta_{\perp 0}}\,\delta\left(\beta_\perp - \beta_{\perp 0}\right)\frac{1}{\sqrt{\pi}\,\beta_e}\,e^{-\beta_\parallel^2/\beta_e^2}\ , \tag{4}$$

where $\beta_\perp \equiv P_\perp/m_0c$, $\beta_\parallel = P_\parallel/m_0c$, and $\beta_e \equiv \gamma v_e/c$. The second is the diffuse ring which may arise under strong electron cyclotron heating, as discussed in the introduction.

$$f_0\left(\beta_\perp, \beta_\parallel\right) = \frac{1}{\pi^{3/2}\beta_e}\,e^{-\beta_\parallel^2/\beta_e^2}\,\delta\left(\beta_\perp^2 - \sqrt{2}\,|\beta_\parallel|\right)\ . \tag{5}$$

Before analyzing the stability of the above distributions we note the following points. Zayed and Kitsenko [3] have analyzed the stability of the distribution

$$f_0 = \delta\left(\beta_\perp - \beta_{\perp 0}\right)\frac{\delta\left(\beta_\parallel - \beta_{\parallel 0}\right)}{2\pi\beta_{\perp 0}}\ , \tag{6}$$

and found that for perpendicular propagation ($k_\parallel = 0$) the X-mode was unstable even for $\beta_{\parallel 0} = 0$, whereas the O-mode was only unstable if $\beta_{\parallel 0} \neq 0$. Secondly, Farina, Lontano, and Pozzoli [4] have shown that for an anisotropic distribution where $T_\perp \neq T_\parallel$ the O-mode absorption coefficient, $\alpha_0 \Rightarrow 0$ as $T_\parallel \Rightarrow 0$ for perpendicular propagation.

This indicates that the thermal electron gyro-motion is coupled to the cold plasma O-mode through the parallel thermal motion. The question therefore arises as to whether the O-mode could become unstable in the presence of a hot electron ring through the parallel thermal motion tapping the free energy in the ring.

The distribution given in Eq. (4) might also be relevant to gyrotron work since it includes the effect of the parallel thermal spread, which is usually ignored. In the present work, we shall only discuss the case of perpendicular propagation ($k_{\|} = 0$) for which the thermal effects are thought to be absent. We shall show, however, that even in this case the parallel thermal spread can introduce additional effects.

In the rest of this paper we shall discuss the stability of the O-mode. The question of the stability of the X- and Whistler modes will be considered elsewhere. The O-mode dispersion relation for perpendicular propagation is

$$\frac{c^2 k_\perp^2}{\omega^2} = \varepsilon_{zz} \,, \tag{7}$$

where $\varepsilon_{zz}$ is the relevant element of the hot plasma dielectric tensor. Since we shall be dealing with cyclotron resonance of the non-thermal ring electrons, we assume that we can represent the thermal electrons by the cold plasma dielectric tensor, *i.e.*, we assume that the ring electrons are decoupled from the bulk. We shall include the damping effect due to the thermal electrons of a Maxwellian distribution later. The dispersion relation can now be written

$$\frac{c^2 k_\perp^2}{\omega^2} = 1 - \frac{\omega_{pe}^2}{\omega^2} - \varepsilon'_{zz} \,, \tag{8}$$

where

$$\varepsilon'_{zz} = -\sum_\ell \frac{2\omega_{pe}'^2}{\omega^2} \iint \beta_{\|}^2 \frac{J_\ell^2(\lambda_\perp)}{X_\ell} f_2 \, 2\pi\beta_\perp \, d\beta_\perp \, d\beta_{\|} \,, \tag{9}$$

and $\varepsilon'_{zz}$ represents the non-thermal ring electrons. $\omega_{pe}'^2/\omega_{pe}^2$ is the ratio of the density of non-thermal to thermal electrons, $X_\ell = \ell\Omega_e/\omega - \gamma$ where $\Omega_e$ is the cyclotron frequency

referred to the next mass ($\Omega_e > 0$), $\gamma = (1 + \beta_\parallel^2 + \beta_\perp^2)^{1/2}$, and $\lambda_\perp = n_\perp \beta_\perp \omega / \Omega_e$. The quantity $f_2$ is given by $f_2 = (1 - \ell\Omega_e/\omega\gamma)\, \partial f_0/\partial\beta_\parallel^2 + [(\ell\Omega_e/\omega\gamma)(\partial f_0/\partial\beta_\perp^2)]$. We only include the second term of $f_2$ since it is only this one which contains a cyclotron resonance. Using the sharp ring distribution [Eq. (4)] and taking $\ell = 1$, we obtain for $\varepsilon'_{zz}$

$$\varepsilon'_{zz} \simeq \frac{1}{\sqrt{\pi}} \frac{\omega_{pe}'^2}{\omega^2} \frac{n_\perp^2 \omega}{2\Omega_e} \left(2 + \beta_{\perp 0} \frac{\partial}{\partial \beta_{\perp 0}}\right) \int_{-\infty}^{\infty} \frac{X^2 e^{-X^2}}{X_0^2 - X^2}\, dX \,, \tag{10}$$

where $X = \beta_\parallel/\beta_e$, $X_0^2 = (\Omega_e/\omega - 1 - \frac{1}{2}\beta_{\perp 0}^2)/\frac{1}{2}\beta_e^2$ and we have only included the (weakly) relativistic correction in the resonance term, assuming $v_{\perp 0}^2/c^2 \ll 1$. For the sharp ring distribution the analysis could be carried out for $v_{\perp 0} \sim c$. Note that the integration in Eq. (10) follows an integral path to ensure damping in Maxwellian plasmas. Assuming $X_0 \ll 1$ we obtain the dispersion relation

$$n_\perp^2 \simeq 1 - \frac{\omega_{pe}^2}{\omega^2} + \frac{\omega_{pe}'^2}{\omega^2} \frac{n_\perp^2 \omega}{2\Omega_e} \left(2 + \beta_{\perp 0} \frac{\partial}{\partial \beta_{\perp 0}}\right) i\sqrt{\pi}\, X_0\, e^{-X_0^2} \,, \tag{11}$$

where the imaginary part in $\varepsilon'_{zz}$ gave the dominant contribution. Equation (11) becomes, after differentiation,

$$\omega^2 - \omega_{pe}^2 - c^2 k_\perp^2 = -i\sqrt{\pi}\, \omega_{pe}'^2 \frac{c^2 k_\perp^2}{\omega\Omega_e} \left(X_0 - \frac{\beta_{\perp 0}^2}{2\beta_e^2 X_0} + \frac{\beta_{\perp 0}^2 X_0}{\beta_e^2}\right) e^{-X_0^2} \,. \tag{12}$$

We note that the second term on the right-hand-side becomes resonant as $X_0 \Rightarrow 0$. This resonance corresponds to a cyclotron harmonic wave supported by the non-thermal ring electrons. Its frequency is $\omega \simeq \Omega_e/(1 + \beta_{\perp 0}^2/2)$. The condition for the non-thermal electron cyclotron mode to couple to the cold plasma O-mode is $(\omega_{pe}^2 + c^2 k_\perp^2)^{1/2} = \Omega_e/(1 + \beta_{\perp 0}^2/2)$. Imposing this condition, we look for a solution to Eq. (12) of the form $\omega = (\omega_{pe}^2 + c^2 k_\perp^2)^{1/2} + \delta\omega$, obtaining

$$(\delta\omega)^{3/2} \simeq -\left(\frac{\pi}{2}\right)^{1/2} \omega_{pe}'^2 \frac{c^2 k_\perp^2}{\omega\Omega_e} \frac{\beta_{\perp 0}^2}{2\beta_e} \frac{\Omega_e^{1/2}}{2(\omega_{pe}^2 + c^2 k_\perp^2)^{1/2}} \,, \tag{13}$$

where we included only the resonant term on the right-hand-side of Eq. (12). Equation (13) gives instability with growth rate $\gamma_i$ given by

$$\gamma_i = \frac{\sqrt{3}}{2}\left[\left(\frac{\pi}{2}\right)^{1/2} \frac{1}{4}\frac{\omega_{pe}'^2}{\Omega_e^2}\frac{c^2k_\perp^2}{\Omega_e^{1/2}}\frac{\beta_{\perp 0}^2}{\beta_e}\right]^{2/3} . \tag{14}$$

The growth rate increases with the number of non-thermal electrons, as expected. As the parallel thermal spread increases, the growth rate decreases but only as $T_\parallel^{-1/3}$. As $T_\parallel$ decreases, the growth rate increases but the bandwidth becomes narrower. $T_\parallel$ cannot be made vanishingly small without violating the small $X_0$ approximation.

Let us now consider the stability of the O-mode to the distribution given by Eq. (5) — the diffuse ring. We again start from Eqs. (8) and (9). Taking only the second term in $f_2$ as before we can write

$$\varepsilon_{zz}' \simeq -\frac{4}{\sqrt{\pi}}\frac{\omega_{pe}'^2}{\omega^2}\frac{\ell\Omega_e}{\omega}\frac{\beta_e}{\sqrt{2}}\int_0^\infty \frac{J_\ell^2(\lambda_\perp)}{\gamma X_\ell}\frac{\partial}{\partial X}\left(X^2 e^{-X^2}\right) dX , \tag{15}$$

where we have singled out the $\ell^{\text{th}}$ harmonic. Note that the integration is from 0 to $\infty$ due to the dependence of $\delta(\beta_\perp^2 - \sqrt{2}\,|\beta_\parallel|)$ on $|\beta_\parallel|$. $X$ is again $\beta_\parallel/\beta_e$, $\lambda_\perp = (n_\perp\omega/\Omega_e)(\sqrt{2}\,\beta_e X)^{1/2}$ and $X_\ell = \ell\Omega_e/\omega - \gamma$, where $\gamma = (1 + \sqrt{2}\,\beta_e X + \beta_e^2 X^2)^{1/2}$. Assuming $\ell = 1$ and making the small Larmor radius expansion, $\varepsilon_{zz}'$ becomes

$$\varepsilon_{zz}' \simeq -\frac{\omega_{pe}'^2}{\omega\Omega_e}\left(\frac{2}{\pi}\right)^{1/2}\beta_e n_\perp^2 \int_0^\infty \frac{X\frac{\partial}{\partial X}(X^2 e^{-X^2})}{X_0 - X}\, dX , \tag{16}$$

where $X_0 = \sqrt{2}\,(\Omega_e/\omega - 1)/\beta_e$. Note that we have neglected the quadratic term in the denominator of the integrand since this only gave a negative root for the zeros of the denominator. Since the integration is only for $X \geq 0$ this root could not therefore give rise to a pole of the integrand. The only important contribution to the dispersion relation of $\varepsilon_{zz}'$ is its imaginary part which is obtained by taking the integral path to ensure damping in Maxwellian plasmas. We therefore write

$$\varepsilon'_{zz} \simeq -i\sqrt{2\pi}\,\frac{\omega'^2_{pe}}{\omega\Omega_e}\,2\beta_e n_\perp^2 X_0^2\,(1-X_0^2)\,e^{-X_0^2}\,. \tag{17}$$

Substituting Eq. (25) into Eq. (13) we obtain the dispersion relation for the O-mode in the presence of a diffuse hot electron ring

$$n_\perp^2 = 1 - \frac{\omega_{pe}^2}{\omega^2} - i\,2\sqrt{2\pi}\,\frac{\omega'^2_{pe}}{\omega\Omega_e}\,\beta_e n_\perp^2 X_0^2\,(1-X_0^2)\,e^{-X_0^2}\,. \tag{18}$$

This time the cold O-mode is coupled to a set of resonant hot electrons instead of a resonant mode. We again solve Eq. (18) by assuming $\omega \simeq (\omega_{pe}^2 + c^2k_\perp^2)^{1/2} + \delta\omega$, giving

$$\delta\omega \simeq i\sqrt{2\pi}\,\frac{\omega'^2_{pe}}{\Omega_e}\,\beta_e\,\frac{c^2k_\perp^2}{\omega_0^2}\,X_0^2\,(1-X_0^2)e^{-X_0^2}\,, \tag{19}$$

where $\omega_0 \equiv (\omega_{pe}^2 + c^2k_\perp^2)^{1/2}$. Clearly for instability we require $X_0 < 1$. The maximum growth occurs for $X_0^2 \simeq 0.38$. This gives the condition $\Omega_e/\omega - 1 = 0.44\,v_T/c$ where $v_T$ corresponds to the parallel thermal velocity.

## 3. CONCLUSION

We are now in a position to return to the question of the decoupling of the non-thermal ring electrons from the thermal electrons. We previously assumed that the relativistic shift of the cyclotron resonance of the non-thermal electrons was large enough to move all thermal electrons out of resonance. We now examine this condition quantitatively. For the O-mode, the contribution to the imaginary part of $\omega$ from the thermal electrons is given by [5]

$$(\delta\omega)_{\text{thermal}} \simeq -i\sqrt{\pi}\,\tfrac{2}{15}\,\frac{\omega_{pe}^2}{(\omega_{pe}^2 + c^2k_\perp^2)^{1/2}}\,\frac{c^2k_\perp^2}{\Omega_e^2}\,|Z|^{5/2}\,e^{-|Z|}\,, \tag{20}$$

where $Z = c^2(\omega - \Omega)/v_T^2\omega$ and we assume $v_T$ is the same for bulk and ring electrons. We may now obtain a criterion for a diffuse hot electron ring to be unstable to the O-mode. For the purposes of illustration we consider two cases. In the first example, we

assume that the ratio of the density of non-thermal electrons to thermal electrons is 0.1. Under these conditions the O-mode is unstable when $v_T/c \lesssim 0.03$. For a lower density of ring electrons with a ratio of 0.01, the condition for the O-mode to be unstable is $v_T/c \lesssim 0.026$. Evidently the stability of the diffuse ring does not depend very strongly on the number density of electrons in the ring. However, the above conditions suggest that such a ring will be stable to O-mode in a plasma whose bulk temperature is of the order of several hundred eV but unstable for lower temperatures.

## 4. ACKNOWLEDGMENTS

This is a report of work sponsored by the Department of Energy under Contract No. DE-AC03-84ER53158 and by the EURATOM/UKAEA Fusion Association.

## 5. REFERENCES

[1] M.N. Rosenbluth, S.T. Tsai, J.W. Van Dam, and M.G. Engquist, Phys. Rev. Lett. **51**, 1969 (1983); L. Chen, R.B. White, and M.N. Rosenbluth, Phys. Rev. Lett. **52**, 1122 (1984); J.Y. Hsu, C.S. Liu, R. Prater, and S.H. Lin, GA Technologies Report GA-A17731 (1984), to be published in Phys. Fluids.

[2] J.Y. Hsu, V.S. Chan, R.W. Harvey, R. Prater, and S.K. Wong, Phys. Rev. Lett. **53**, 564 (1984).

[3] K.E. Zayed and A.B. Kitsenko, Plasma Phys. **10**, 147 (1968).

[4] D. Farina, M. Lontano, and R. Pozzoli, in *Proc. Symposium on Heating in Toroidal Plasmas* ( Grenoble, 1982), Vol. II, p. 749.

[5] R.A. Cairns and C.N. Lashmore-Davies, Phys. Fluids **25**, 1605 (1982).

# NOTEC, A Code for the Calculation of Non-Thermal ECE Spectra Emitted from Tokamak Plasmas

R.M.J. Sillen
*Association Euratom-FOM, FOM-Instituut voor Plasmafysica, Rijnhuizen, Nieuwegein, The Netherlands*

ABSTRACT

A 3-D code, NOTEC, has been developed to calculate ECE spectra for the JET tokamak plasma allowing for a large class of non-thermal populations. Because bulk densities up to $10^{20}$ $m^{-3}$ are expected in JET, refraction as well as high-density effects on the absorption and emission coefficients are included. The thermal and non-thermal absorption and emission coefficients are calculated using fully relativistic expressions. The modular structure of the code makes it possible to use the code for any tokamak plasma. Results of a comparison with other numerically simulated ECE spectra are given.

## 1. Introduction

In many cases the electron cyclotron emission (ECE) spectra exhibit non-thermal features [1]. Especially in plasmas heated by lower hybrid-, ion cyclotron- and electron cyclotron waves these features are observed, but also in low density discharges as well as when trapped particles are important. The basic tool for studying the relation between the emission spectrum and the electron distribution is a code which can calculate the ECE spectrum for a given distribution. Non-thermal features can be modelled with electron distribution functions that include drifting maxwellians, temperature anisotropy, loss- and anti-loss cones etc. Because non-thermal emission spectra do not uniquely correspond to one electron distribution function, one usually has to simplify strongly when describing the non-thermal features. In practice, one is forced to consider a limited class of distributions only.

Such a code, NOTEC, [2], has been developed for JET, to assist the interpretation of the measured ECE spectra. Because of its modular structure it is easy to adapt the code to any toroidal geometry both with respect to the plasma equilibrium and to the liner. Properties such as the reflectivity and the shape of the liner as well as the details of the antenna pattern, can be essential for the emitted spectrum. The code is kept flexible with respect to the modelling of these properties. In Section 2, the model underlying the code is described. In Section 3 the results of preliminary tests of the code are given.

## 2. Description of the model

To determine the intensity of the radiation emitted by a plasma in a certain direction, $\vec{k}$, the absorption and emission coefficient have to be calculated locally as a function of the angular frequency $\omega$, the density $n_e$, the temperature $T_e$, the absolute value of the magnetic field $|\vec{B}|$ and the angle $\theta$ between the wave-vector and the magnetic field. The receiving antenna is only sensitive to a narrow solid angle $d\Omega$ viewing the plasma. To calculate whether the emitted intensity from a given location will reach the antenna within this solid angle, refraction has to be taken into account for regimes with $\omega_p/\omega_c > 1$. Thus ray tracing , as the approximation of geometrical optics is in general valid, is required. In NOTEC, ray tracing is done in the same way as in RAYS, a code developed by Batchelor and Goldfinger [3]. For the dispersion relation the cold plasma approximation is used. Physically, the problem of following the radiation emitted locally by a plasma along a ray toward the antenna is equivalent to calculating the emitted radiation along a ray starting from the antenna (except of course, if the electron population has a drift velocity). Numerically, the latter is of great advantage. The total intensity $I_\omega^A$ can then be found by solving along these rays the equation of radiative transfer [4],

$$I_\omega^A = \frac{I_\omega^B e^{-\tau^B}}{(n_r^B)^2} + \int_{\tau^A}^{\tau^B} S_\omega(\tau) e^{-\tau} d\tau \ . \qquad (1)$$

Here, $S_\omega$ is the source function of the plasma $n_r$ is the ray refractive index, and $\tau$ is the optical depth. A is located at the antenna and B is the endpoint of integration in the plasma where a stop criterion is met, e.g. a preset value of $\tau$ is reached. This criterion has to be chosen in such a way that the first term on the right-hand side of Eq. (1) is negligible.

The integral in Eq. (1) reflects the way the intensity is calculated numerically. After determining the stepsize required, the path of the ray in a given plasma is calculated, and simultaneously the contribution in each step to the emitted intensity as well as to $\tau$. By summation, one then finds the total intensity reaching the antenna.

The source function $S_\omega$ is related to the ratio of the emission coefficient $j_\omega$ and the absorption coefficient $\alpha_\omega$,

$$S_\omega = \frac{1}{n_r^2}\frac{j_\omega}{\alpha_\omega} . \tag{2}$$

For a thermal plasma this becomes

$$S_\omega = \frac{\omega^2 kT}{8\pi^3 c^2} ,$$

where T is the temperature of the medium, and the other symbols have their usual meaning. The thermal absorption and emission coefficients are calculated similarly as in SNECTR, an ECE code, valid only for low densities, developed by S. Tamor [5]. The values obtained with NOTEC were checked against SNECTR values for the regimes where both codes are applicable, see Fig. 1. The agreement is very satisfactory.

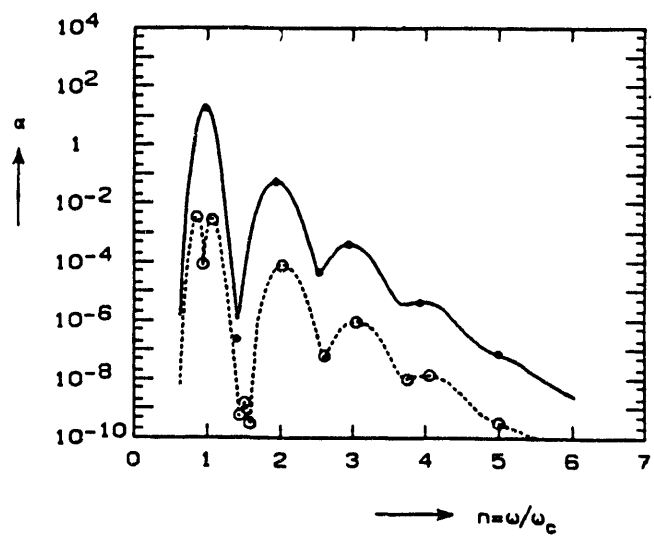


Fig. 1. The absorption coefficient $\alpha$ of a thermal plasma ($T_e$ = 3 keV, $n_e$ = 5 × $10^{19}$ $m^{-3}$, and $\theta$ = 30°.) calculated by NOTEC, as a function of the normalized frequency $n = \omega/\omega_c$, X-mode (solid line), O-mode (dashed line). The values calculated by SNECTR are also given: X-mode (•), O-mode (o).

If the electron distribution function is not maxwellian, the formalism given above cannot be used. For an electron distribution function $f(p_{||}, p_{\perp})$ where the indices $_{||}$ and $_{\perp}$ refer to parallel and perpendicular with respect to the magnetic field, respectively, the absorption and emission coefficients for electron cyclotron emission can be calculated, following [4], from

$$j_\omega = \int_0^\infty \int_{-\infty}^\infty \eta_\omega(p_{||}, p_{\perp}) f(p_{||}, p_{\perp}) 2\pi p_{\perp} \, dp_{\perp} \, dp_{||} , \tag{3}$$

$$\alpha_\omega = - \frac{8\pi^3 c^2}{n_r^2 \omega^2} \int_0^\infty \int_{-\infty}^\infty \eta_\omega(p_{||}, p_{\perp})$$

$$\left| \frac{E}{c^2} \frac{\partial f}{\partial p_{\perp}} - N_{||} \left( \frac{p_{||}}{c} \frac{\partial f}{\partial p_{\perp}} - \frac{p_{\perp}}{c} \frac{\partial f}{\partial p_{||}} \right) \right| 2\pi p_{\perp} \, dp_{\perp} \, dp_{||} , \tag{4}$$

where E is the total relativistic energy of an electron, $N_{||}$ is the parallel component of the refractive index and $\eta_\omega$ is the differential rate of emission. This differential rate is given by Freund et al. [6]. Assuming that the density of non-thermal electrons is small one can write the total electron distribution function as the sum of a thermal population $f_{th}$ and a number of non-thermal populations $f^h_{nth}$ with

$$f = (1 - \sum_h \varepsilon_h) f_{th} + \sum_h \varepsilon_h f^h_{nth} ,$$

where $\varepsilon_h$ ($\ll 1$), is the ratio of the density of a specific non-thermal population to the total density. The property $\sum_h \varepsilon_h \ll 1$ also implies that the ray refractive index is determined by the thermal population only. The source function S then can be written as:

$$S = \frac{1}{n_r^2} \left| \frac{j_{th} + \sum_h j_{nth}}{\alpha_{th} + \sum_h \alpha_{nth}} \right| , \tag{5}$$

where, the j's and α's can be calculated from Eqs. (3) and (4) for each population h. However, for this more general form of $f_{nth}$, the integrals cannot be evaluated using a recursion scheme similar as done for the thermal case [5], and have to be done numerically [6]. For the non-thermal populations $f_{nth}$ we use the model distribution function:

$$f_{nth}(u_{\|},u_{\perp}) = Cu_{\perp}^{k}(u_{\|}-u_{o})^{\ell}\exp\{-\frac{m_e c^2}{T_{\perp}}\sqrt{1+(\frac{u_{\perp}}{c})^2+\frac{T_{\perp}}{T_{\|}}(\frac{u_{\|}-u_o}{c})^2}\} .$$

Here C is a normalization constant, given by

$$C = \frac{(k+2)(\frac{m_e c^2}{2T_{\perp}})^{\frac{k+1}{2}}(\frac{m_e c^2}{2T_{\|}})^{\frac{\ell+1}{2}}}{4\sqrt{\pi}\,\Gamma(\frac{\ell+1}{2})\Gamma(2+\frac{k}{2})(c)^{k+\ell+3}K_{2+\frac{\ell+k}{2}}(\frac{m_e c^2}{T_{\perp}})} ,$$

where $\vec{u} = \gamma\vec{v}$ is the momentum per unit of rest mass and $\vec{u}_o$ is the momentum per unit of rest mass related to the drift velocity. Γ denotes the gamma function, $K_m$ the modified Bessel function of order m and $T_{\perp,\|}$ are the perpendicular and parallel temperatures expressed in eV. Anti-loss- and loss-cone distributions are obtained for $\ell \neq 0$, $k=0$, and $\ell=0$, $k\neq 0$, respectively. The absorption and emission coefficients depend on the values of k, ℓ, $u_o$, $T_{\perp}$, $T_{\|}$ and ε chosen for the non-thermal populations.

As a test, absorption and emission coefficients for a thermal plasma have been calculated with the non-thermal modules of NOTEC and compared with the coefficients calculated with the thermal modules. As can be seen in Fig. 2 the results coincide, except for frequencies below the gyrofrequency $\omega_c$ where the results of NOTEC are not valid.

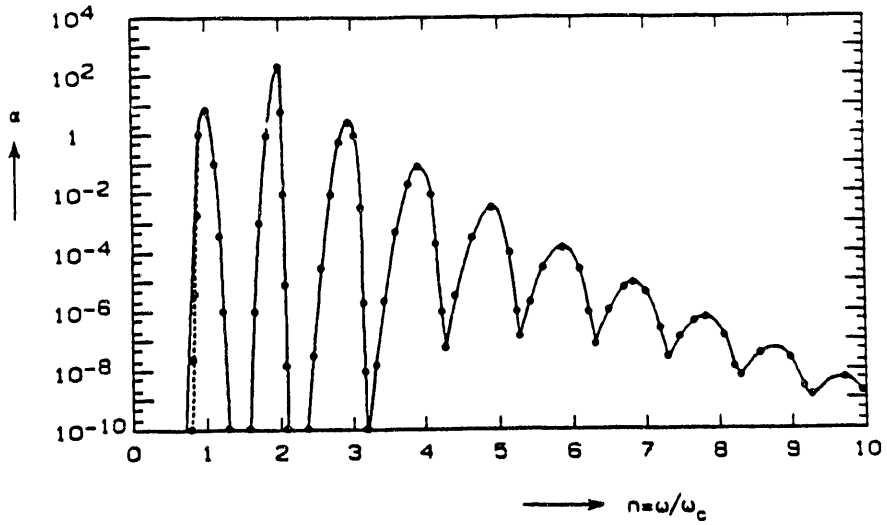


Fig. 2. Absorption coefficients α for the X-mode calculated by NOTEC, as a function of the normalized frequency for a thermal homogeneous plasma ($T_e$ = 2 keV, $n_e$ = $5\times10^{19}$ $m^{-3}$, the angle of observation θ is 70° with respect to the direction of the magnetic field). The solid line is calculated with the thermal modules and the dotted line (---•---•---) with the non-thermal modules.

Taking the density of the non-thermal populations as a fraction of the total density would imply that the non-thermal populations have the same profile characteristics as the "bulk" density. Additionally to the specification of the number of particles of a non-thermal population in NOTEC, one also has to specify, for every non-thermal population the inner and outer flux surfaces in which this population is situated. Furthermore, to enable NOTEC to simulate trapped-particle populations, one also has the possibility to limit the range of poloidal angles in which there is a non-thermal population.

For a thermal tokamak plasma the relation for the spatial line width for a specific frequency can be found in Ref. [8] and is, for a JET plasma (R = 3 m) and for temperatures ranging from 1 to 5 keV, of the order of 5 to 25 cm. For a non-thermal population this line width can become appreciably larger. The combined appearance of thermal and non-thermal populations generally results in different scale lengths for the thermal and non-thermal absorption and emission coefficients. These different scale lengths required special numerical care.

While NOTEC is a 3-D code, some three-dimensional effects are treated in a simplified way. Toroidal symmetry of the liner is assumed, so that one has to specify the wall characteristics for one poloidal plane only. For frequencies for which the plasma is optically thin, the optical depth along a ray will not reach the preset $\tau$-stop criterion in a single transit. A reflection of the ray then will occur. Although for a fully realistic simulation of reflections, a complete 3-D description of the vessel, its ports and bellows, etc., would be necessary, in practice this will be too time consuming. To model reflection effects NOTEC provides three options. Geometrically the vessel wall is described as a torus having a smooth surface reflecting like a mirror. To describe the reflection process one has to give the reflectivity of the wall material and also the reflection matrix elements which account for polarization scrambling.

In the "plane-slab" option, a reflection modelling similar to the plane-slab approximation of a tokamak is used, but these model parameters are then the same for every reflection occurring in the torus and they have to be specified as input parameters. The angle of reflection is determined by specular reflection and calculated by the code. In the option of "specular reflection" the reflectivity is still an input parameter but the matrix elements and the angle of reflection are calculated by the code for an electromagnetic wave reflected on a conducting surface (Ref. [8]). In the option of "diffuse reflection", the angle of reflection is chosen at random out of a cone which gives the probability that a specific direction occurs. The width of this cone is determined by an input parameter. The limits of the cone function yield the complete diffuse reflection and specular reflection cases. Once the incoming and outgoing direction of the wave are specified, the code calculates the reflection matrix elements. The reflectivity of the wall is again an input parameter. To be able to account for the existence of ports, etc., which are additional sinks of radiation, the reflectivity of the wall can be specified as a function of the poloidal angle.

The actual running time of the code depends strongly on the number of rays which have to be followed. This number is determined by three effects. Firstly, the total number of frequencies which are

necessary to build up a spectrum and which have to be followed on independent rays. Secondly, the number of rays necessary to account for the antenna pattern, and thirdly the existence of the already mentioned polarization scrambling and the fact that the O- and X-mode have different ray paths. Because of these effects the total number of rays can become very large; more than $10^5$ is not exceptional. To reduce the number due to the latter effect, several options were built into the code. If refraction effects are small (in the high frequency part of the spectrum), the possibility exists to solve the equation of radiative transfer for more than one frequency along a ray and to prescribe that, after a reflection, only one ray path must be traced for X- and O-mode. Even if refraction effects are appreciable, splitting up of the ray is still not always necessary. The calculation of the absorption and emission coefficients for an O-mode, along the ray path of an X-mode, will still give a reasonable estimate of the O-mode contribution to the X-mode intensity. The case of the X-mode contribution to the O-mode intensity is of course more delicate. If polarization scrambling is high, the intensity of the O-mode for optically thin frequencies is largely determined by the X-mode. Both modes have to be traced separately for the optically thick part of the spectrum, but then reflections are usually not important.

## 3. Results of preliminary tests

Apart from a number of internal consistency checks, NOTEC results were compared with spectra calculated with SNECTR. In Ref. [9] spectra calculated for TFR runaway discharges are presented and two models are proposed. Model b was considered by Tamor to be the more realistic one. With NOTEC the spectrum was calculated adapting Tamor's model b. The total number of particles of all the three non-thermal populations, has been equal for both calculations. The reflection coefficient for the identical polarization was 0.93, as in Tamor's model b. The coefficient for polarization scrambling was 0.04. In Fig. 3, both spectra are compared. The agreement between the two results is satisfactorily.

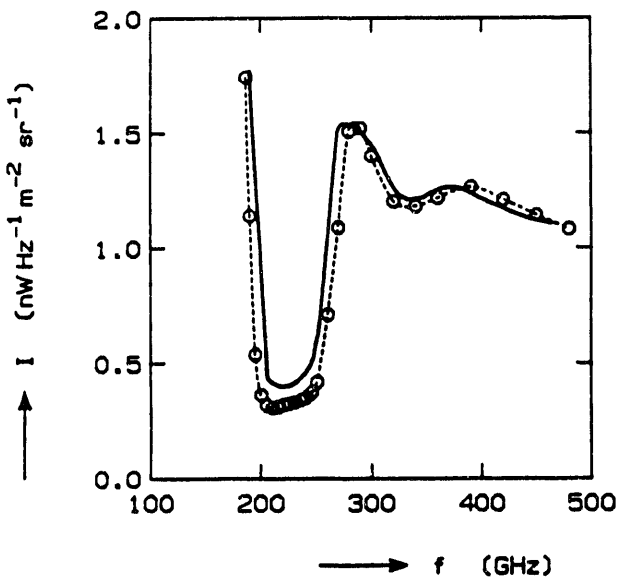


Fig. 3. Comparison of calculations of emission spectra of TFR done with NOTEC (....o....o....) and with SNECTR (————) (see Ref. 10).

In Ref. [9] Tamor finds that one still has the freedom to adjust in an appropriate way both the temperature and the drift velocity (i.e. the parameter $\gamma$) for one of the populations in his model. In fact $\gamma = 1.1$ and $T_e = 450$ keV gives the same results as $\gamma = 1.25$ and $T_e = 700$ keV in SNECTR. This result is reproduced by the NOTEC calculations.

## 4. Conclusions

A code to calculate ECE spectra for JET for thermal as well as non-thermal populations has been developed. The results of the code NOTEC, for thermal populations, have been checked against simple analytical expressions. The comparison of the thermal absorption and emission coefficients derived with NOTEC, with the absorption and emission coefficients calculated by SNECTR, gave excellent agreement. The cross-check of the results for thermal calculations done with the non-thermal modules agree well. As a further check of the code as a whole, non-thermal calculations as done by Tamor [9] were reproduced with NOTEC, and the agreement was good. After a complete check of the numerical modelling used to simulate the effects of reflections, antennae patterns and non-thermal features, additional to those present in the SNECTR code, the code will be put in operation at JET.

Acknowledgements

The author wishes to thank Prof.Dr. H. de Kluiver, Prof.Dr. F. Engelmann and Dr.Ir. H.W. Piekaar for their valuable comments on the manuscript. The author is very grateful to S. Tamor for giving him the opportunity of using a copy of SNECTR.

This work was performed as part of the research programme of the association agreement of Euratom and the "Stichting voor Fundamenteel Onderzoek der Materie" (FOM) with financial support from the "Nederlandse Organisatie voor Zuiver-Wetenschappelijk Onderzoek" (ZWO) and Euratom.

References

[1] Brossier, P., Costley, A.E., Komm, D.S., Ramponi, G. and Tamor, S., Plasma Phys. and Contr. Nucl. Fusion Research (Proc. 6th Int. Conf. Berchtesgaden 1976) Vol I, IAEA, Vienna (1977) 409.
Piekaar, H.W., Rutgers, W.R., Rijnhuizen Report RR 80-128, Nieuwegein, The Netherlands (1980).
Melin, G., How, J.A., Girard, A., et al., Proc. 4th Int. Symp. on Heating in Toroidal Plasmas, Rome, March (1984), p. 628.
Boyd, D.A., EC-4 Workshop on ECE and ECRH, Rome, March 1984 and references therein.

[2] Sillen, R.M.J., Allaart, M.A.F., Goedheer, W.J., Kattenberg, A., to be published.

[3] Batchelor, D.B., Goldfinger, R.C., Oak Ridge National Laboratory, Oak Ridge, U.S.A., ORNL/TM-6844.

[4] Bekefi, G., Radiation Processes in Plasmas, J. Wiley and Sons, New York, U.S.A., 1966.

[5] Tamor, S., Nucl. Fusion, 18 (1978) 229.
Tamor, S., LAPS-26, SAI-77-593-LJ, Science Appl. Int. Corp., La Jolla, U.S.A., April 1977.

[6] Freund, H.P., Wu, C.S., Gaffey Jr., J.D., Phys. Fluids 27 (1984) 1396.
Goedheer, W.J., to be poublished.
Bornatici, M., private communication.

[7] Bornatici, M., Cano, R., De Barbieri, O., Engelmann, F., Nucl. Fusion 23 (1983) 1153.

[8] Tamor, S., Nuclear Technology /Fusion, Vol. 3, March 1983, p.293.
Stratton, J.A., Electromagnetic Theory, McGraw Hill, New York, U.S.A., 1941.

[9] Tamor, S., Nucl. Fusion 19 (1979) 455.

# Perpendicular Electron Cyclotron Emission for Relativistic Loss-Cone Type Momentum Distributions

M. Bornatici and U. Ruffina
*Physics Department, "A. Volta," University of Pavia, Pavia, Italy*

ABSTRACT

The electron cyclotron emission of both the extraordinary and ordinary mode is calculated, both analytically and numerically, for two classes of relativistic loss-cone distributions, for propagation perpendicular to the magnetic field and accounting for both finite-density and finite Larmor radius effects. The effects of varying both the strength of the loss-cone and the temperature on the frequency dependence of the emissivity are investigated and discussed with reference to the case of an isotropic Maxwellian.

## Introduction

Electron cyclotron emission perpendicular to the magnetic field is of practical interest as a diagnostic tool in both tokamak and non-tokamak configurations (Bornatici et al., 1983). As for the latter configurations, with reference in particular to the bumpy-torus and mirror devices, a key role is played by hot electron rings whose velocity distribution is likely to be of the loss-cone type. This paper is devoted to the calculation and discussion of the emissivity of two possible relativistic loss-cone distributions, namely, a modified Maxwellian having a loss-cone with a sharp edge and a DGH distribution (Dory et al., 1965). Previous calculations of the emission from loss-cone plasmas have been mainly numerical (Uckan and Uckan, 1982; Tamor, 1983) or subject to a number of simplifying approximations; e.g., finite-density effects are disregarded (Winske and Boyd, 1983). Here we present analytical calculations for the fully relativistic case.

Sharp-edged loss-cone distribution. The electron distribution is assumed to be a relativistic Maxwellian of temperature T with a step function in pitch angle $\psi = \cos^{-1}(p_{\parallel}/p)$, i.e.,

$$f(p,\cos\psi) = C(\psi_o)\, e^{-\mu\gamma}\, H(\cos^2\psi_o - \cos^2\psi) \qquad (1)$$

where $C(\psi_o) \equiv \mu\,[4\pi(mc)^3\, K_2(\mu)\cos\psi_o]^{-1}$ is the normalization constant, with $\mu \equiv mc^2/T$ ($mc^2$ being the electron rest mass), $\psi_o$ the angle of the loss-cone and $K_\nu(z)$ the modified Bessel function of the second kind with index $\nu$ and argument z; $\gamma \equiv [1 + (p/mc)^2]^{1/2}$, with p the electron momentum ($p_{\parallel}$ and $p_{\perp}$ denoting the components, respectively, parallel and perpendicular to the equilibrium magnetic field); $H(\cos^2\psi_o - \cos^2\psi)$ is the Heaviside step function, that is $H = 1$ for $\psi_o < \psi < \pi-\psi_o$ and $H = 0$ otherwise. The limit $\psi_o \to \pi/2$ corresponds to a two-dimensional distribution with no motion along the magnetic field, whereas $\psi_o = 0$ yields the isotropic relativistic Maxwellian distribution. The average kinetic electron energy $\langle W \rangle = (\langle \gamma \rangle - 1)\, mc^2$ connected with (1) is

$$\langle W \rangle = \left(\frac{3}{\mu} + \frac{K_1(\mu)}{K_2(\mu)} - 1\right) mc^2$$

that is the same as for a Maxwellian distribution.

As for the evaluation of the emission (absorption) coefficient connected with the distribution (1), one has to deal with an integration over the momentum space for which it is convenient to use the variables $\gamma, \chi \equiv \cos\psi$ and the azimuthal angle of $\underline{p}$, this latter integration being readily carried out. Referring to wave propagation perpendicular to the magnetic field, the integrations over $\gamma$ and $\chi$ are uncoupled; the former is carried out simply by using the $\delta$-function contained in the integrand and describing the relativistic resonance condition $\gamma - n\omega_c/\omega = 0$, with $n \geq 1$ the harmonic number. As for the $\chi$-integration, we make use of the series representation of the Bessel functions entering the integrand, with the result that the integration can be carried out analytically term by term (Bornatici and Ruffina, 1984).

For the extraordinary (X) mode, the emission coefficient for perpendicular radiation around the n-th harmonic, $n \geq 2$, is found to be

$$\frac{j_n^{(X)}}{J_o} = \left[\left(\frac{\pi}{2\mu}\right)^{1/2} \frac{e^{-\mu}}{K_2(\mu)}\right] \frac{n^{2n}}{2^n (n-1)!} \left[1+A(\omega)\right]^2 \left[N_r^{(X)}\right]^2 \left[N_\perp^{(X)}\right]^{2n-3} \left(\frac{T}{mc^2}\right)^{n-1} \times$$

$$\times \sum_{k=0}^{\infty} c_{n,k}\, f_{n,k}\, b_{n+k}^{(X)}(\psi_o) \left[(n\, N_\perp^{(X)})^2 \frac{T}{mc^2}\right]^k G_{n+k-1}\,, \quad n \geq 2 \qquad (2)$$

where $j_o \equiv \omega_p^2 \omega_c m/8\pi^2 c$. The summation over k originates from the series expansion of the Bessel functions, the terms with $k \geqslant 1$ accounting for the higher order finite Larmor radius (FLR) effects. In eq. (2),

$$C_{n,k} \equiv (-1)^k \frac{n!\left[2(n+k)\right]!}{2^k\, k!\,(2n+k)!\;(n+k)!} \quad (=1 \text{ for } k=0) \tag{3}$$

$$f_{n,k} \equiv 1 + \frac{2k}{n\left[1+A(\omega)\right]} + \frac{2k(k-1)(n+k)}{n^2\left[2(n+k)-1\right]\left[1+A(\omega)\right]^2} \quad . \tag{4}$$

The effect of the loss-cone is described entirely by the quantity

$$b_{n+k}^{(X)}(\psi_o) \equiv \frac{2}{\sqrt{\pi}(n+k)!} \sum_{s=0}^{n+k} (-1)^s \binom{n+k}{s} \frac{(\cos\psi_o)^{2s}}{2s+1} \quad . \tag{5a}$$

This is an increasing function of $\psi_o$, such that

$$\frac{1}{\Gamma(n+k+3/2)} = b_{n+k}^{(X)}(\psi_o=0) \leqslant b_{n+k}^{(X)}(\psi_o) \leqslant b_{n+k}^{(X)}(\psi_o=90^o) = \frac{2}{\sqrt{\pi}(n+k)!} \tag{5b}$$

The function $G_{n+k-1} \equiv G_{n+k-1}(\frac{\omega}{n\omega_c}, \mu \equiv \frac{mc^2}{T})$, to be referred to as the profile function, is defined by

$$G_q \equiv (\frac{\omega}{n\omega_c})^{2q+1} \left[\frac{\mu}{2}\left((\frac{n\omega_c}{\omega})^2 - 1\right)\right]^{q+3/2} e^{-\mu(\frac{n\omega_c}{\omega} - 1)} \tag{6}$$

for $\omega < n\omega_c$, whereas $G_q = 0$, for $\omega \geqslant n\omega_c$; it exhibits a maximum for $\omega/n\omega_c \simeq (1 + qT/mc^2)^{-1}$. In eq.(2) the quantity $A(\omega) \equiv -i\varepsilon_{xy}/\varepsilon_{xx} = i\,\tilde{E}_x/\tilde{E}_y$ (the equilibrium magnetic field being in the z-direction and the wave vector in the x-direction) is connected with the longitudinal (x) component of the mode polarization and is taken in the cold plasma limit, this being in general an appropriate approximation for all the harmonics except the first one (Bornatici et al., 1983). The same applies to both the wave refractive index $N_\perp^{(X)}$ and the ray refractive index $N_r^{(X)}$.

To lowest order in $\cos^2\psi_o$, the series appearing in (2) can be summed up in terms of the Bessel functions $J_n = J_n(b)$ and $J_n' = dJ_n/db$, with $b = N_\perp^{(X)}\left[n^2 - (\omega/\omega_c)^2\right]^{1/2}$, with the result that

$$\frac{j_n^{(X)}}{j_o} = \left[\left(\frac{\pi}{2\mu}\right)^{1/2} \frac{e^{-\mu}}{K_2(\mu)}\right] \frac{2}{\sqrt{\pi}} \left[N_r^{(X)}\right]^2 \left[N_\perp^{(X)}\right]^{-3} \frac{mc^2}{T} \frac{\omega_c}{\omega} \times$$

$$\times \; n^2 \left[\frac{\mu}{2}\left(\left(\frac{n\omega_c}{\omega}\right)^2 - 1\right)\right]^{1/2} \left[A(\omega) J_n + \frac{b}{n} J_n'\right]^2 e^{-\mu\left(\frac{n\omega_c}{\omega} - 1\right)} \equiv \frac{j_n^{(X)}(\psi_o = 90^o)}{j_o}, \quad n \geq 2 \tag{2'}$$

As for the <u>ordinary (0) mode</u>, the emission coefficient around the n-th harmonic, $n \geq 1$, can be obtained from (2), with $X \to 0$, by multiplying the right-hand-side by $T/mc^2$ and replacing both $\left[1+A(\omega)\right]^2 \left[N_r^{(X)}/N_\perp^{(X)}\right]^2$ and $f_{n,k}$ by 1, whereas $G_{n+k-1}$ is to be replaced with $G_{n+k}$. Explicitly, one has (Bornatici and Ruffina, 1984)

$$\frac{j_n^{(0)}}{j_o} = \left[\left(\frac{\pi}{2\mu}\right)^{1/2} \frac{e^{-\mu}}{K_2(\mu)}\right] \frac{n^{2n}}{2^n (n-1)!} \left[N_\perp^{(0)}\right]^{2n-1} \left(\frac{T}{mc^2}\right)^n \times$$

$$\times \sum_{k=0}^{\infty} c_{n,k}\, b_{n+k}^{(0)}(\psi_o) \left[(nN_\perp^{(0)})^2 \frac{T}{mc^2}\right]^k G_{n+k}, \quad n \geq 1 \tag{7}$$

where

$$b_{n+k}^{(0)}(\psi_o) \equiv \frac{4}{\sqrt{\pi}(n+k)!} \sum_{s=0}^{n+k} (-1)^s \binom{n+k}{s} \frac{(\cos\psi_o)^{2(s+1)}}{2s+3} \left(< b_{n+k}^{(X)}(\psi_o)\right) \tag{8}$$

is the function that accounts for the effect of the loss-cone on the emission of the 0-mode. Unlike the corresponding function (5) for the X-mode, as $\psi_o$ increases from 0, $b_{n+k}^{(0)}(\psi_o)$ increases only slightly above the value for a Maxwellian distribution, $b_{n+k}^{(0)}(\psi_o=0) = \left[\Gamma(n+k+5/2)\right]^{-1}$, and reaches a maximum for values of $\psi_o$ which are the higher the larger (n+k) is, the maximum being a decreasing function of (n+k) (e.g., $b_{1,max}^{(0)} \simeq 0.3$ for $\psi_{o,max(1)} \simeq 24^o$, whereas $b_{2,max}^{(0)} \simeq 0.2$ for $\psi_{o,max(2)} \simeq 38^o$). As $\psi_o$ tends to $90^o$, $b_{n+k}^{(0)}(\psi_o)$ tends to 0 as $\cos^2\psi_o$. Such a non-monotonous dependence on $\psi_o$ has to do with the fact that the emission (absorption) of the 0-mode is connected with the particle velocity parallel to the magnetic field, in addition to FLR effects, with the result that the emission (absorption) tends to decrease whenever the decrease of the parallel velocity tends to prevail over the increase of the perpendicular velocity, as it occurs at significantly high values of the loss-cone angle. The dependence on the mode polarization of the effect of the loss-cone might

be of practical relevance for determining the underlying anisotropy of the electron distribution (Tamor, 1983; Winske and Boyd, 1983).

DGH loss-cone distribution. Another distribution of the loss-cone type is (Dory et al., 1965)

$$f(p,\psi) = C_{\ell m}\, p^{\ell}\, |\sin\psi|^{m}\, e^{-\mu\gamma} \tag{8a}$$

where

$$C_{\ell m} \equiv \frac{\mu^{\ell/2+1}}{2^{\ell/2}(4\pi)(mc)^{\ell+3}K_{\ell/2+2}(\mu)}\;\frac{\Gamma(\frac{m+3}{2})}{\Gamma(\frac{\ell+3}{2})\Gamma(\frac{m}{2}+1)} \tag{8b}$$

with $\ell$ and m the loss-cone indexes ($\ell$=m=0 yields the isotropic relativistic Maxwellian). The average kinetic energy connected with the DGH distribution (8) is

$$< W > = \left[\frac{3+\ell}{\mu} + \frac{K_{\ell/2+1}(\mu)}{K_{\ell/2+2}(\mu)} - 1\right] mc^2$$

which is independent of the index m and to lowest order in $\mu^{-1}$ ($=T/mc^2 << 1$) reduces to $< p^2>/2m = [(3+\ell)/2]T$. Following the same procedure as for the sharp-edged loss-cone, the emissivity coefficient of the X-mode can be evaluated analytically; for perpendicular propagation one finds

$$\frac{j_n^{(X)}}{j_o} = \left[\left(\frac{\pi}{2\mu}\right)^{1/2}\frac{e^{-\mu}}{K_2(\mu)}\right]\frac{n^{2n}}{2^n(n-1)!}\left[1+A(\omega)\right]^2\left[N_r^{(X)}\right]^2\left[N_\perp^{(X)}\right]^{2n-3}\left(\frac{T}{mc^2}\right)^{n-1} \times$$

$$\times\; a_{\ell m}(\mu)\sum_{k=0}^{\infty} c_{n,k}\, f_{n,k}\, b_{n+k,m}^{(X)}\left[(nN_\perp^{(X)})^2\frac{T}{mc^2}\right]^k G_{n+k-1,\ell}\;,\quad n \geq 2 \tag{9}$$

where

$$a_{\ell m}(\mu) \equiv \frac{\Gamma(\frac{m+3}{2})}{\Gamma(\frac{\ell+3}{2})\Gamma(\frac{m}{2}+1)}\;\frac{K_2(\mu)}{K_{\ell/2+2}(\mu)}\quad (= 1,\ \text{for } m=\ell=0) \tag{10}$$

$$b_{n+k,m}^{(X)} \equiv \frac{\Gamma(n+k+m/2+1)}{(n+k)!\,\Gamma(n+k+\frac{m+3}{2})} \tag{11}$$

and

$$G_{q,\ell} \equiv \left[\frac{\mu}{2}\left(\left(\frac{n\omega_c}{\omega}\right)^2-1\right)\right]^{\ell/2} G_q \qquad (12)$$

with $G_q$ defined by (6). Note that, unlike the case of the sharp-edged loss--cone, the profile function (12) is itself affected by the loss-cone feature, namely, it depends on the loss-cone index $\ell$ connected with the momentum distribution in (8a). In particular, the maximum of (12) occurs at $\omega/n\omega_c \simeq \left[1+(n+k+\frac{\ell+3}{2})\frac{T}{mc^2}\right]^{-1}$, that is downshifted as $\ell$ increases.

As for the 0-mode, the corresponding emission coefficient around the n-th harmonic, $n \geq 1$, can be obtained from (9) with $X \to 0$ and $b^{(0)}_{n+k,m}=(n+k+\frac{m+3}{2})^{-1}b^{(X)}_{n+k,m}$, by multiplying the right-hand-side by $T/mc^2$ and replacing both $[1+A(\omega)]^2$ $[N_r^{(X)}/N_\perp^{(X)}]^2$ and $f_{n,k}$ by 1, whereas $G_{n+k-1,\ell}$ is to be replaced with $G_{n+k,\ell}$.

Numerical Analysis. On the basis of (2) and (9) and the corresponding expressions of the emissivity for the 0-mode, a numerical analysis of the emissivity spectra of both the X-mode, $j^{(X)}=\sum_{n=2}^{\infty} j_n^{(X)}$, and the 0-mode, $j^{(0)}=\sum_{n=1}^{\infty} j_n^{(0)}$, has been performed and sample results are shown for both a sharp-edged loss-cone distribution, Fig.s 1-3, and a DGH loss-cone distribution, Fig. 4, taking $(\omega_p/\omega_c)^2= 0.1$ and varying the loss-cone strength and temperature. More specifically, the dependence on the loss-cone angle of the emissivity spectra of the X-mode at fixed temperature, is shown in Fig. 1 for $\psi_o= 0$; $30^o$; $65^o$ and $90^o$, and T = 100 keV. It appears that i) the loss-cone enhances the emission with respect to that corresponding to a Maxwellian distribution ($\psi_o= 0$), which has to do with the fact that the emission of the harmonics $n \geq 2$ of the perpendicular X-mode is entirely connected with FLR effects, these latter being enhanced with respect to the Maxwellian case since, for a loss-cone distribution, the kinetic particle energy is preferentially stored in the degree of freedom perpendicular to the magnetic field; ii) the emissivities at $\psi_o= 0$ and $\psi_o= 90^o$, respectively, constitute the lower and upper bound, in agreement with conditions (5b); iii) the peaks in the emission profile occur at frequencies that are independent of the value of $\psi_o$, which readily follows from the fact that the profile function (6) and, as a consequence, the corresponding maximum is independent of the angle of the loss--cone; iv) the cutoff at the low-frequency side of the emissivity spectrum is due to the (cold) right-hand cutoff of the (fast) X-mode; v) whereas the low-frequency part of the spectrum exhibits a line structure, the main peak

corresponding to the 2.nd harmonic downshifted by relativistic effects, the corresponding high-frequency part is continuous as a result of the overlapping of neighbouring harmonics. In Fig.2, the emission spectrum of the X-mode is shown for a fixed loss-cone angle $\psi_o = 90^o$ and different temperatures, i.e., T(keV) = 100; 200; 300; 511 ($T=mc^2$) and $10^3$. As the temperature increases, it appears that i) the line structure turns into a continuous profile; ii) the high-frequency part of the profile is weakly dependent on the frequency, with the tendency to develop a broad maximum around frequencies that are the higher the larger the temperature is.

Turning now to the O-mode, the emissivity spectrum is shown in Fig. 3 for a fixed temperature T = 100 keV, and three different values of the loss-cone angle, $\psi_o = 0;\ 24^o;\ 65^o$. One sees that i) the non-monotonous dependence on $\psi_o$ is more significant around the first two harmonics; ii) for $0 \lesssim \psi_o \lesssim \psi_{o,max(1)} = 24^o$ the line structure of the spectrum is dominated by the peak around the first harmonic, downshifted by relativistic effects. The comparison of Fig.1 and 3 shows that for 100 keV the emissivity of the O-mode is typically an order of magnitude smaller than that of the X-mode.

As for the DGH distribution, the emissivity spectrum of the X-mode is shown in Fig.4 for T = 100 keV and three different values for the loss-cone index, $\ell = m = 0;1;2$. The main features of the spectrum are the same as the ones for the sharp-edged loss-cone distribution, cf. Fig.1. A noticeable difference, however, relates to the line structure of the spectrum, i.e., the corresponding peaks tend to be shifted toward lower frequencies as the loss-cone index increases, which is connected with the profile fuction (12) as mentioned previously.

Acknowledgements. Useful discussion with F. Engelmann are gratefully acknowledged. This work was performed under the Euratom-FOM association agreement with financial support from ZWO and Euratom and the Ministero della Pubblica Istruzione of Italy.

References

Bornatici M., Cano R., De Barbieri O. and Engelmann F., Nucl. Fusion. 23, 1153 (1983)

Bornatici M. and Ruffina U., Proceed. Int. Conf. Plasma Phys., Lausanne 1984, Contributed Papers, Vol. II, p. 339

Dory R.A., Guest G.E. and Harris E.G. Phys. Rev. Lett. 14, 131 (1965)

Tamor S., Phys. Fluids 26, 1335 (1983)

Uckan T. and Uckan N.A., Phys. Fluids 25, 2372 (1982)

Winske D and Boyd D.A., Phys. Fluids 26, 755 (1983).

Figure Captions

Fig. 1 - Frequency dependence of the emissivity of the extraordinary mode for a sharp-edged loss-cone distribution, for $(\omega_p/\omega_c)^2=0.1$, T=100 keV and angles of the loss-cone equal to $\psi_o=30^o$; $65^o$ and $90^o$. The dashed curve refers to the Maxwellian distribution ($\psi_o=0$).

Fig. 2 - Same as Fig.1 for a fixed loss-cone angle $\psi_o=90^o$ and different temperatures, T = 100; 200; 300; 511; $10^3$ keV.

Fig. 3 - Frequency dependence of the emissivity of the ordinary mode for a sharp-edged loss-cone distribution, for $(\omega_p/\omega_c)^2=0.1$, T=100 keV and angles of the loss-cone equal to $\psi_o=24^o$; $65^o$. The dashed curve refers to the Maxwellian distribution ($\psi_o=0$).

Fig. 4 - Frequency dependence of the emissivity of the extraordinary mode for a DGH loss-cone distribution, for $(\omega_p/\omega_c)^2=0.1$, T=100 keV and loss-cone index $\ell = m = 1$; 2. The dashed curve refers to the Maxwellian distribution ($\ell = m = 0$).

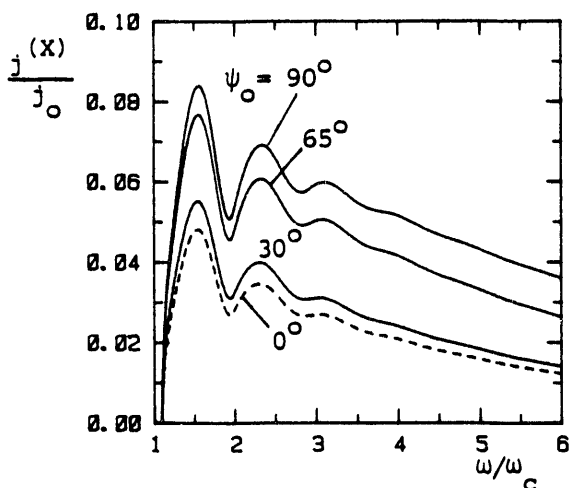


Fig. 1

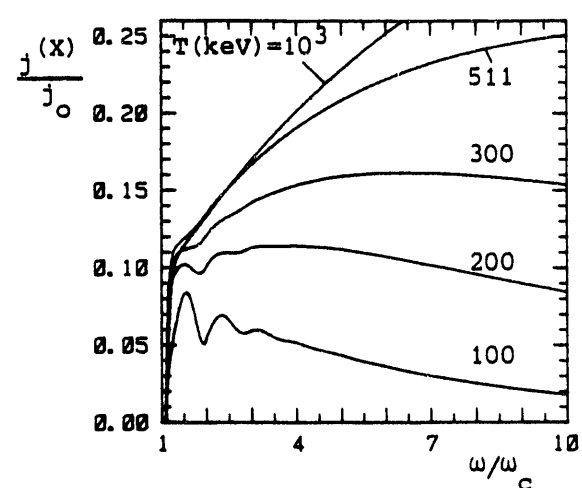


Fig. 2

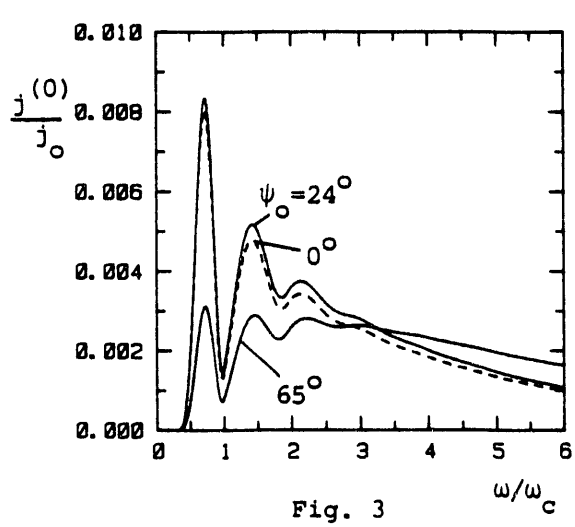


Fig. 3

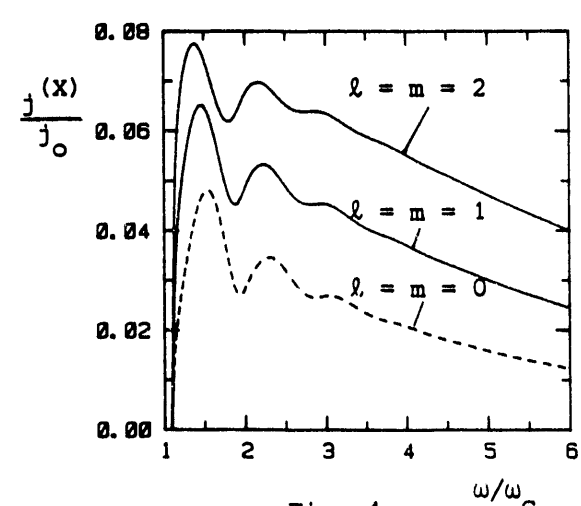


Fig. 4

# Electron Cyclotron Heating

# ECRH Studies in CLEO Tokamak

A.C. Riviere, N.R. Ainsworth, B. Alper, D. Atkinson, S.G.F. Blewett, P.R. Collins, A.N. Dellis, T. Edlington, B. Lloyd, F. Ma,* M.R. O'Brien, B.J. Parham, D.C. Robinson, D.F.H. Start, and T.N. Todd
*UKAEA/Euratom Fusion Association*
*Culham Laboratory, Abingdon, Oxon, OX14 3DB, UK*

* People's Republic of China

## INTRODUCTION

Electron cyclotron resonance heating (ECRH) has been studied in the CLEO tokamak at 28 GHz and 60 GHz at the second harmonic, as well as at the fundamental resonance at 28 GHz [1,2]. Substantial bulk heating has been observed in all cases and the variation of heating efficiency with electron density, toroidal magnetic field and plasma current has been investigated. The measured soft X-ray (SXR) spectra and those deduced from a Fokker Planck calculation of the electron distribution function during ECRH at both 28 and 60 GHz agree when the effects of both ECRH and the loop voltage are included.

ECRH assisted start-up at 28 GHz has resulted in the production of well-controlled discharges with loop voltage $V_\ell < 2V$ throughout. The average loop voltage during the current rise was ~ 1.1V corresponding to an electric field of 0.19 V/m and giving a current rise of 0.44 MA/s.

The effect of second harmonic heating at 60 GHz on the operational density limit in CLEO has also been studied. It was possible to lower the I/N limit ($N \equiv \bar{n}_e \pi a^2$) from $1.7 \times 10^{-14}$ to $1.0 \times 10^{-14}$ A m during ECRH.

## TECHNICAL DETAILS

The CLEO device has been described in detail elsewhere[3]. Although originally designed as an $\ell$=3 stellarator it now operates primarily as an iron core tokamak of major radius $R_0$ = 0.9m and minor radius a = 0.13m as defined by two poloidal tungsten limiters placed 180° apart toroidally. Feedback control of plasma current, line-averaged electron density and both vertical and horizontal plasma position allows well-controlled reproducible plasmas to be established with pulse durations up to 0.5s. For most of the work to be described here the RF power at both 60 and 28 GHz was injected along a major radius from the low field side of the torus through open-ended oversized circular waveguide, with the power transmitted to the antenna in the form of the circularly polarised $TE_{01}$ mode. Hence both the ordinary (O) and extraordinary (X) modes were excited in the plasma.

## SECOND HARMONIC HEATING

Second harmonic heating at 60 GHz has been studied over a wide range of plasma parameters ($5\ kA \lesssim I_p \lesssim 30\ kA$, $0.3 \times 10^{19} m^{-3} \lesssim \bar{n}_e \lesssim 1.6 \times 10^{19} m^{-3}$, $1.0T \lesssim B_{\phi o} \lesssim 1.15T$). The typical characteristics of on-axis heating in a

clean well-conditioned vacuum vessel are illustrated in Fig. 1. During the rf, $V_\ell$ is reduced to < 0.5 V so that the ohmic heating becomes a small fraction of the total power input (< 10%). There is a substantial increase in soft X-ray emission across the whole plasma (Fig. 2) together with a broadening of the emission profile (FWHM (ohmic) ~ 5.3 cm, FWHM (ECRH) ~ 7.7 cm). For optimum heating a fast change in the vertical field is necessary to maintain the plasma well centred during the rf. Magnetic measurements indicate $\Delta(\beta_p + \ell_i/2) \sim 0.7$ in agreement with the change in $\beta_p$ deduced from the diamagnetic loop. The central electron temperature, $T_{eo}$, increases from 425 eV to 1250 eV (from a fit to the spectrum of Fig 3a below $h\nu \lesssim 5$ keV) and there is a small non-thermal tail formation. The density scaling of $\Delta\beta_p$ is shown in Figure 4a.

A prominent feature of Fig. 1 is the large fall in $\bar{n}_e$ during the rf. The gas injection rate is maintained constant from t = 70ms onwards and it should be noted that the particle recycling coefficient from the CLEO vacuum vessel is small as a result of titanium gettering between shots. The density decrease can be countered by strong gas puffing. There is even an increase shortly after a vacuum break. Figure 4b shows the density scaling of the density decrease in a clean torus. Attempts to self-consistently explain the measurements of $V_\ell$, $I_p$, $\bar{n}_e$, $T_{eo}$, $\beta_p + \ell_i/2$, $\beta_p$ and the soft X-ray emission profiles reveal that a consistent picture can be established only if the density profile undergoes a substantial broadening when the rf is on. The decrease in $\bar{n}_e$ can then be explained with only a ~ 10% fall in the total number of particles. Ray tracing indicates that for these discharges refraction of the rays away from the inaccessible region where the density exceeds the X-mode cut-off density (~ $2.2 \times 10^{19} m^{-3}$) becomes more significant as $\bar{n}_e$ increases. This leads to a strongly localised off-axis power deposition which may be responsible for causing the density redistribution and/or particle loss.

The heating efficiency is sensitive to the resonance position with the stored energy increase, $\Delta E$, reduced to half its maximum value when the resonance is at r/a ~ 0.5. At low plasma current, where the energy balance is dominated by the rf ($P_{rf}/P_{OH} \sim 10$), $\Delta E$ increases linearly with plasma current. From ~ 15 kA ($q_a \sim 7$) to 30 kA ($q_a \sim 3.5$) a saturation in $\Delta E$ is observed as the ohmic power becomes comparable to the absorbed rf power.

Assuming that the energy confinement time, $\tau_E$, is identical before and during rf injection, it is calculated that up to 60% of the rf power is absorbed by the plasma during 60 GHz second harmonic heating. Multiple-pass ray tracing calculations indicate that after the initial temperature increase and density profile evolution the absorption should be > 90% implying a fall in $\tau_E$. However, bearing in mind the decrease in $\bar{n}_e$, the energy confinement time during the rf with this absorption efficiency is still of the same order as would be attained in an ohmically heated plasma of similar line-averaged density.

Results of second harmonic heating on CLEO at 28 GHz have been reported extensively elsewhere [4,5,6]. The cut-off density is ~ 0.49 x $10^{19}m^{-3}$ so the experiments were necessarily carried out at rather low density where significant tail formation occurs in contrast to the 60 GHz results (see Fig 3b). The maximum plasma energy at fixed rf power was proportional to $I_p$ up to ~ 20 kA. At very low densities ($\bar{n}_e$ < 2 x $10^{18}m^{-3}$) the electron energy distribution was anisotropic and there was an increase in the energy confinement time over the value attained in ohmic plasmas of similar density.

## MODELLING OF SXR SPECTRA WITH A FOKKER-PLANCK CODE

A code called BANDIT ("Bounce Averaged Non-Maxwellian Distributions In Tokamaks"), has been developed to solve the flux-averaged Fokker-Planck equation for tokamak magnetic field geometry using an implicit finite difference algorithm[7,8]. The time evolution of the electron distribution function for a given flux surface, f, may be written schematically for this code as

$$\frac{\partial f}{\partial t} = \left\langle \left(\frac{\partial f}{\partial t}\right)_c \right\rangle + \left\langle \frac{-eE}{m_e}\frac{\partial f}{\partial v_\parallel} \right\rangle + \left\langle \frac{1}{v^2}\frac{\partial}{\partial v}\left(\frac{v^3 f}{2\tau_E}\right) \right\rangle + \left\langle \left(\frac{\partial f}{\partial t}\right)_{ECRH} \right\rangle \qquad (1)$$

Here < > indicates the flux-averaging, the first, second and third terms on the right hand side represent the effect of e-e and e-i collisions, the steady toroidal electric field, E, and a finite energy confinement time, $\tau_E$, respectively, v is the electron speed and $v_\parallel$ the component of velocity parallel to the magnetic field. The fourth term represents the additional heating, in this case ECRH, and has been derived from a quasilinear diffusion model [7]. Fig 3a shows a comparison between the soft X-ray spectrum obtained during second harmonic 60 GHz experiments and that predicted by the code for the conditions shown. The best fit with the model is obtained with a bulk temperature of 1.1 keV, but the distortions due to the ECRH in this case are small. Experiments at lower densities and higher temperatures with second harmonic 28 GHz ECRH give larger distortions in the electron distribution function as the spectrum in Fig 3b indicates, and these larger distortions are predicted by the code. The predicted spectrum depends to some extent on the choice of flux surface but neither the ECRH alone nor the electric field alone were sufficient to produce such distortions.

## FUNDAMENTAL HEATING

Initial fundamental heating studies at 28 GHz have yielded encouraging results. Injection of 70 kW into target plasmas with $I_p$ ~ 11 kA, $\bar{n}_e$ ~ 3.6 x $10^{18}m^{-3}$, $B_\phi$ = 1.015T resulted in a central electron temperature increase from ~ 450 eV to 1 keV with no significant tail production. As illustrated in

Fig. 5 a modest decrease in $\bar{n}_e$ (~ 7%) was observed together with a large drop in loop voltage ($V_\ell$ = 1.6V to $V_\ell$ = 0.5 V). Equilibrium field measurements indicated an increase in ($\beta_p + \ell_i/2$) of ~ 0.64. A modest broadening of the soft X-ray profiles was observed comparable to that measured during 60 GHz second harmonic heating. On-axis second harmonic heating of similar target plasmas at 60 GHz resulted in a central electron temperature increase to ~ 1.15 keV for ~ 70 kW of injected power. Thus, for similar target plasmas, fundamental and second harmonic heating produced comparable increases in the central electron temperature. However, in general, fundamental heating was found to be effective in a more restricted region of parameter space.

## COMBINED 60GHZ AND 28GHZ HEATING

For a large aspect ratio torus such as CLEO (R/a ~ 7) the fundamental resonance at 28 GHz and the 2nd harmonic resonance at 60 GHz are well separated (~ 6cm ≈ 0.5a). For combined heating either one or both of the resonant surfaces will be at a non-optimum position. If the fundamental resonance is too close to the launch antenna, reflected power causes early termination of the 28 GHz rf pulse. Nevertheless for a restricted range of toroidal fields combined heating at moderate power levels has been attempted and clear resonance position-dependent modifications to the soft X-ray emission profile demonstrated. For $B_\phi$=1T (Fig 6(a)) the 60GHz resonance is inwardly displaced by ~ 6cm (r/a ~ 0.46). During the initial 2nd harmonic heating the soft X-ray emission profile is slightly broadened and the peak amplitude falls suggesting a loss of particles from the plasma centre. A consistent , spatially localised enhancement is observed on the low field side of the profile. Subsequent addition of rf at 28 GHz (resonance on axis) produced an overall increase in emission with no further broadening. In contrast for $B_\phi$=1.05T (Fig 6(b)) with the two resonances either side of the machine axis the X-ray emission is increased everywhere and the profile broadens during 60 GHz injection. Addition of the 28 GHz power results in a further general increase in emission with no further broadening.

## ECRH-ASSISTED START-UP

Studies of ECRH-assisted start-up, using an 80 kW, 20 ms rf pulse at 28 GHz, have resulted in the production of well controlled discharges with $I_p$ ~ 13 kA, $\bar{n}_e \sim 5 \times 10^{18} m^{-3}$ in the presence of a loop voltage $V_\ell$ < 2V throughout. The rf was injected at a time t = 4ms (Figure 7) into an initial prefill of deuterium at $B_{\phi o}$ = 0.895T the plasma formed had a central line-averaged electron density of $\bar{n}_e \sim 0.9 \times 10^{18} m^{-3}$. At this field the fundamental cyclotron resonance is inwardly displaced ~ 0.09m from the minor axis (ie at $(R-R_o)/a \sim -0.7$).

The plasma current feedback system is triggered at t = 13ms and provides the initial rate of current rise of 0.75 MA/s. The plasma current reaches its programmed flat-top level of 13.2 kA at 42.8ms representing an average rate of current rise of ~ 0.44 MA/s. Throughout this phase the loop voltage is typically ~ 1.1V corresponding to an electric field of E ~ 0.19 V/m.

In Fig. 7 the discharge under consideration is compared with the best (ie lowest voltage at breakdown) yet achieved in the absence of rf power. The final current level and the rate of current rise are the same in the two cases. The preionisation results in a ~ 50% reduction in the volt-second consumption during the current rise phase and a ~ 50% increase in the fraction of electromagnetic energy input from the poloidal field system which is converted to stored magnetic energy. The voltage required at the initiation of the current ramp is reduced by a factor of 5.

## MODIFICATION OF THE DISRUPTIVE DENSITY LIMIT

The disruption of tokamak discharges at the density limit (at $I/N \lesssim 1.5 \times 10^{-14}$Am, where $N=\pi ab\bar{n}_e$) is widely believed to be primarily a consequence of peripheral losses eroding the current density profile to the point where a steep current-density gradient appears just inside the q=2 surface. The disruption follows the ensuing destabilisation of the (m=2, n=1) mode, either directly as an ideal kink mode, or via the overlap of islands of this and higher order tearing modes which develop subsequently. Thus the density limit should be raised by any technique which permits higher peripheral losses while maintaining the stability of the 2,1 surface, eg (i) increasing the power arriving there (core or local heating), (ii) directly affecting the current gradient (local current drive, externally induced islands [9]) or (iii) adding vacuum rotational transform, $\bar{\iota}_{vac}$. Both methods (i) and (iii) have been studied on CLEO. Here we present the results for method (i) using ECRH.

The study was performed with 60 GHz second harmonic heating where X-mode absorption dominates. The cut-off density is $2.2 \times 10^{19}/m^3$, corresponding to critical $\bar{n}_e$ of $\lesssim 1.6 \times 10^{19}/m^3$ for core heating with moderately peaked profiles. Thus for interestingly low values of I/N in CLEO the plasma current has to be $\lesssim$ 11 kA. At the resonant field of 1.07T this corresponds to a high q (10 at 10 kA for example), and hence a tendency towards rather narrow temperature profiles. For strong absorption an initial electron temperature $\gtrsim$ 150 eV is required which is unlikely to be achieved in CLEO in the vicinity of the q=2 surface close to the high density limit. Accordingly, the best I/N limits were found with the resonance placed at or near the hot core of the plasma (~ 350 eV under OH only) although ray tracing calculations show that refractive effects displace the heating zone as $\bar{n}_e$ is increased. Such an ECRH assisted shot is compared with its OH equivalent in

Fig 8. An rf power of 120 kW is injected at $B_{\phi o}$ = 1.07T (corresponding to second harmonic resonance on axis) and results in a lowering of the operational $I_p/N$ limit from 1.7 x $10^{-14}$ to 1.0 x $10^{-14}$Am. Since the initial effect of the ECRH is to cause a drop in $\bar{n}_e$ (probably mostly due to profile flattening), a downward step in plasma current was programmed to facilitate the fall in I/N while the density was forced back up. It should be noted that the close shell ($\tau \sim$ 3ms) and powerful feedback systems of CLEO make it very rare for hard disruptions to fully quench the plasma current.

When the plasma current was programmed to fall below ~ 7 kA (ie $q \gtrsim 14$) then both OH and ECRH discharges would evolve without major disruptions to cool, quiescent plasmas which were of very low I/N but were not considered relevant to conventional tokamak operation. An interpretation of this is that there is some critical poloidal Lundquist number (~ $10^3$ here) below which MHD activity is suppressed (as is evidenced by decreasing Mirnov coil signals) and no disruptions can occur.

ACKNOWLEDGEMENTS

This work could not have been accomplished without the support of the CLEO technical team. We are also grateful for the loan of a 60 GHz gyrotron from GA Technologies and for the help and advice of Ron Prater with its installation and commissioning.

REFERENCES

[1] Edlington T E et al, Proc 12 Eur Conf on Contr Fus & Plasma Phys, Vol Budapest, 1985

[2] LLoyd B et al, Proc of workshop on Application of RF waves to tokamak plasmas, Varenna, 1985

[3] Reynolds P et al, Plasma Phys & Contr Nuc Fus Res, Proc 5th Int Conf, Tokyo, Vol II, 13, IAEA, Vienna, 1975

[4] Alcock M W et al, Proc 11th Eur Conf on Contr Fus & Plasma Phys, Vol I, 401, 1983

[5] Riviere A C et al, Proc 4th Int Symp on Heating in Toroidal Plasmas, Vol II, 795, 1984

[6] Robinson D C et al, Plasma Phys & Contr Nuc Fus Res, Proc 10th Int Conf, London, Vol I, 205, 1985

[7] O'Brien M R, Cox M and Start D F H, Proc 12 Eur Conf on Contr Fus & Plasma Phys, Budapest 1985, Vol II, p76

[8] O'Brien M R, Cox M and Start D F H, Proc 3rd Eur Wkshop on the Numerical Modelling of Plasmas (NUMOP85) to be published in Comp Phys Comm.

[9] Morris A W et al, Workshop on Magnetic Reconnection and Turbulence, Corsica, 1985.

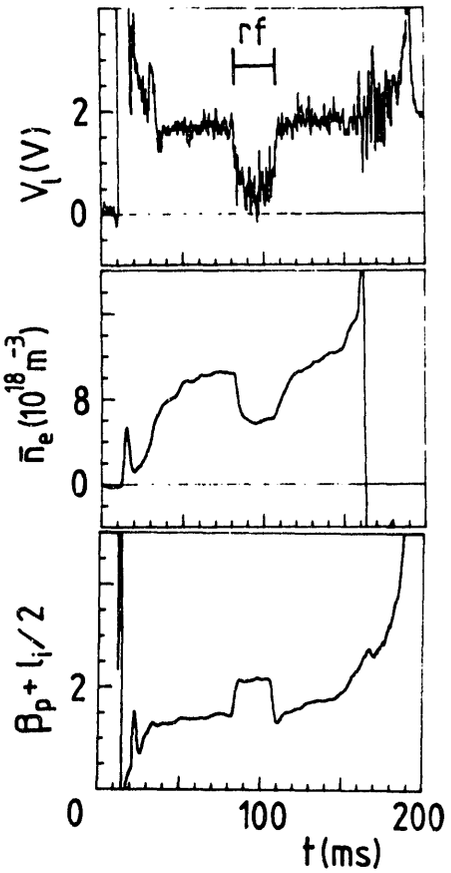


Fig 1. 60 GHz 2nd harmonic heating

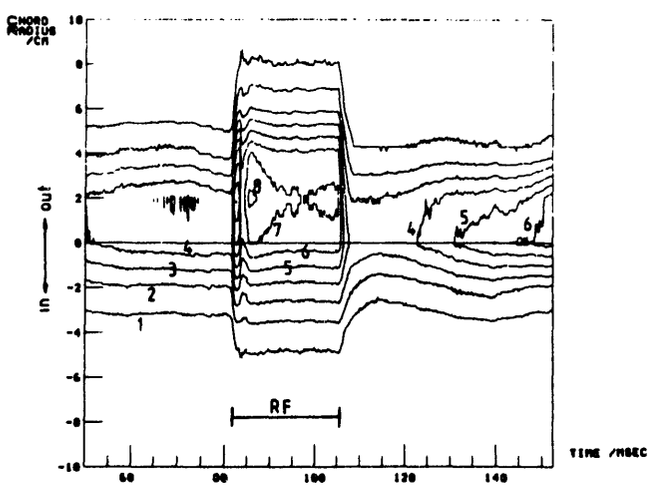


Fig 2. Time-dependence of soft X-ray emission contours for discharge in Fig 1. (Contours are linearly spaced at intervals of $I_m/10$ where $I_m$ is max intensity at any radius during the discharge.)

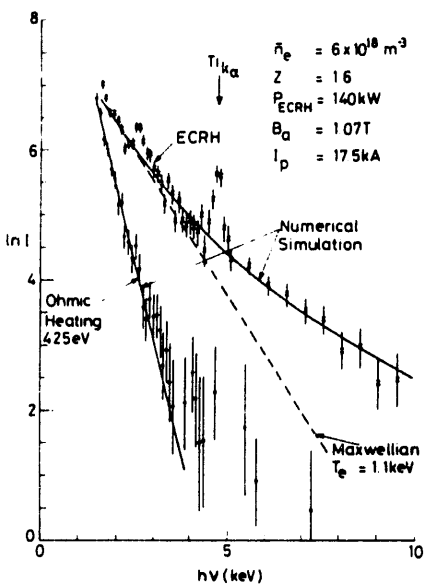


Fig 3a Soft X-ray spectrum measured during 2nd harmonic 60 GHz ECRH experiments. The radius of the flux surface chosen for the numerical simulation was 2.0 cm.

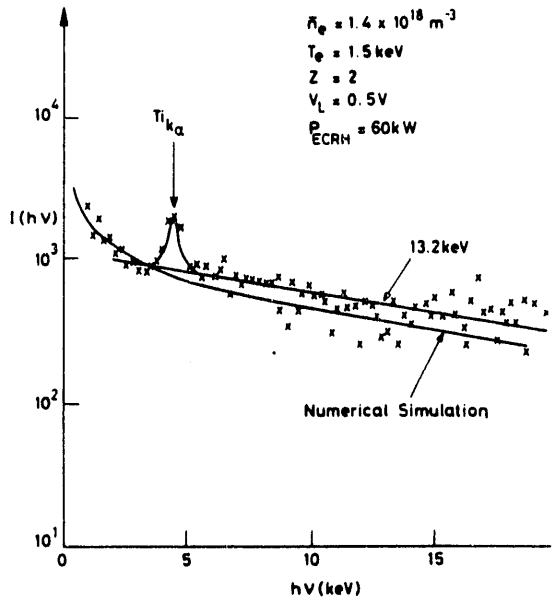


Fig 3b As Fig 3a but for 2nd harmonic 28 GHz ECRH. The radius of the flux surface chosen for the numerical simulation was 2 cm and here $V_\ell$ = 0.75V.

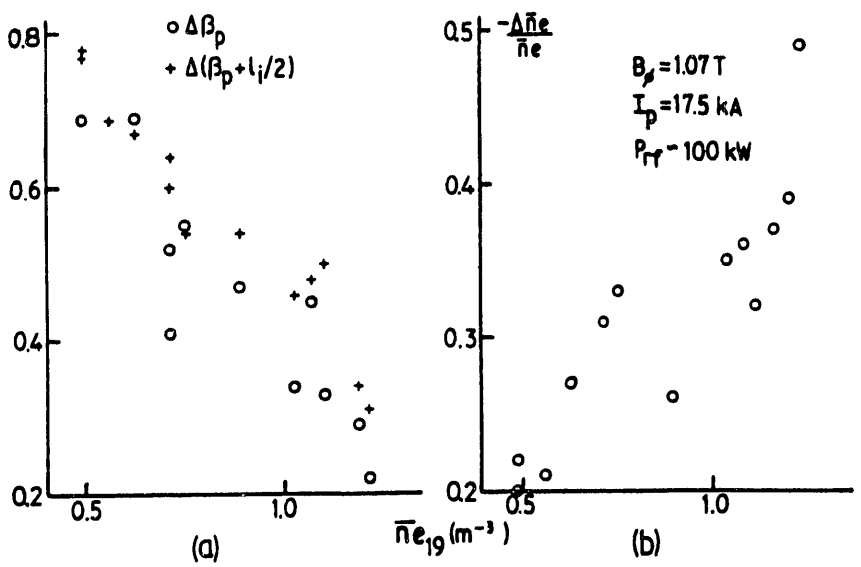


Fig 4. Density scaling of 60 GHz second harmonic heating

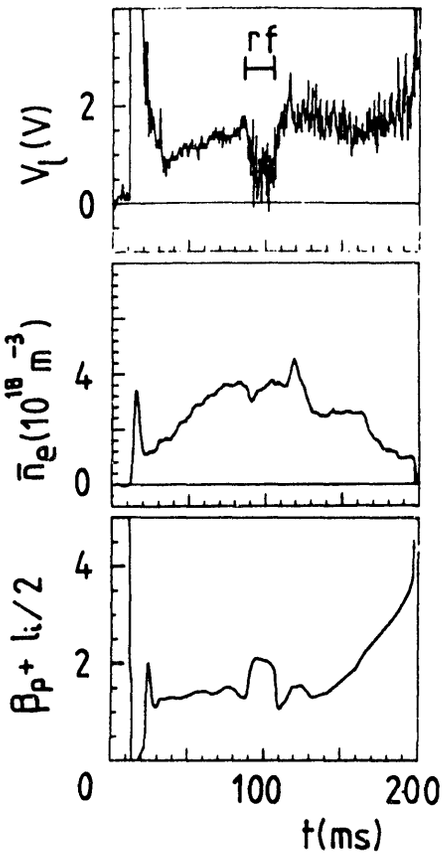


Fig 5. 28 GHz fundamental heating

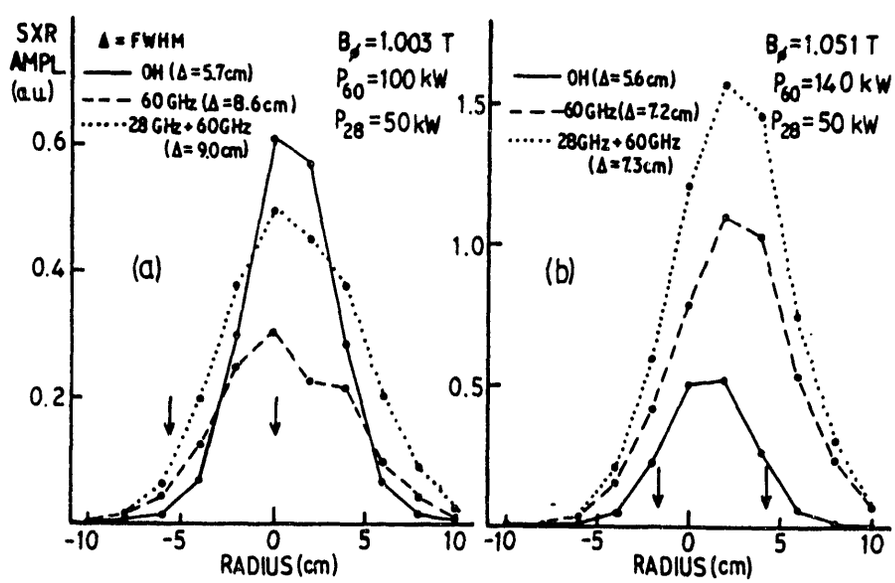


Fig 6. Changes in line integrated soft X-ray emission profiles due to 2nd harmonic (60 GHz) and combined (60 GHz + 28 GHz) heating at two different toroidal fields. The arrows indicate the resonance locations.

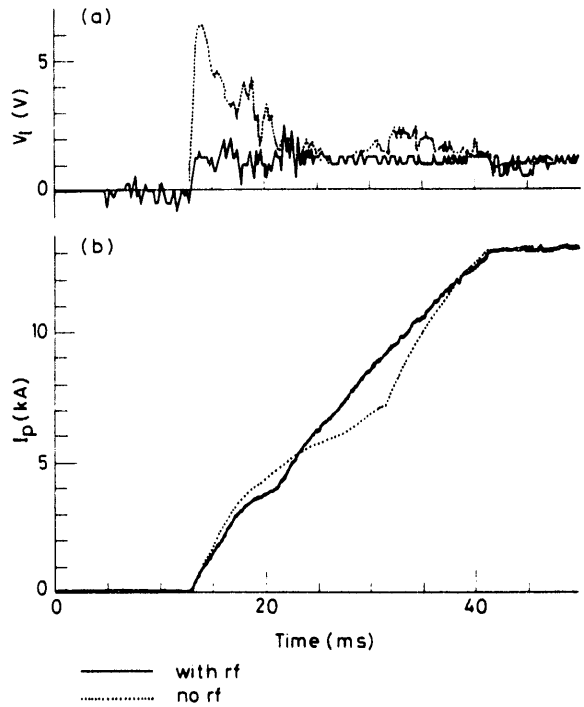


Fig 7. Comparison of ohmic and ECRH-assisted start-up

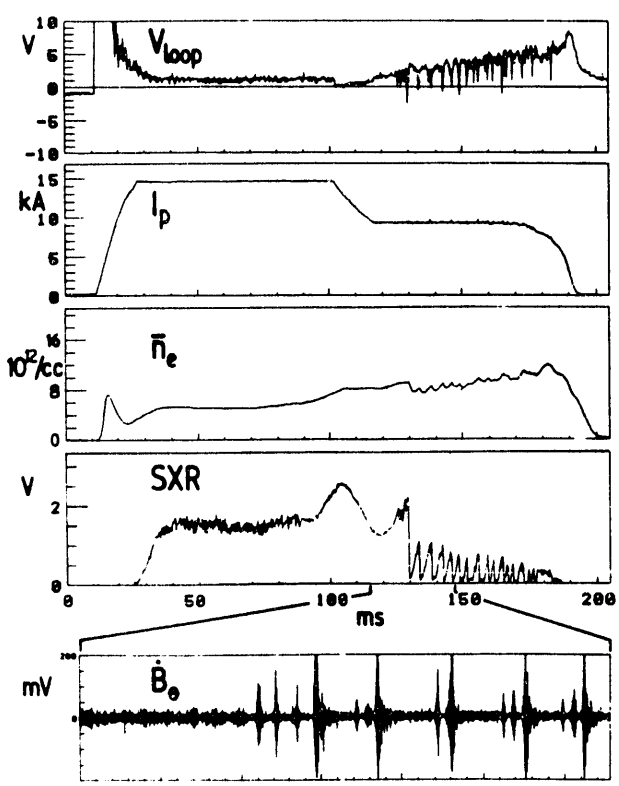


Fig 8(a) Density limit behaviour in OH tokamak

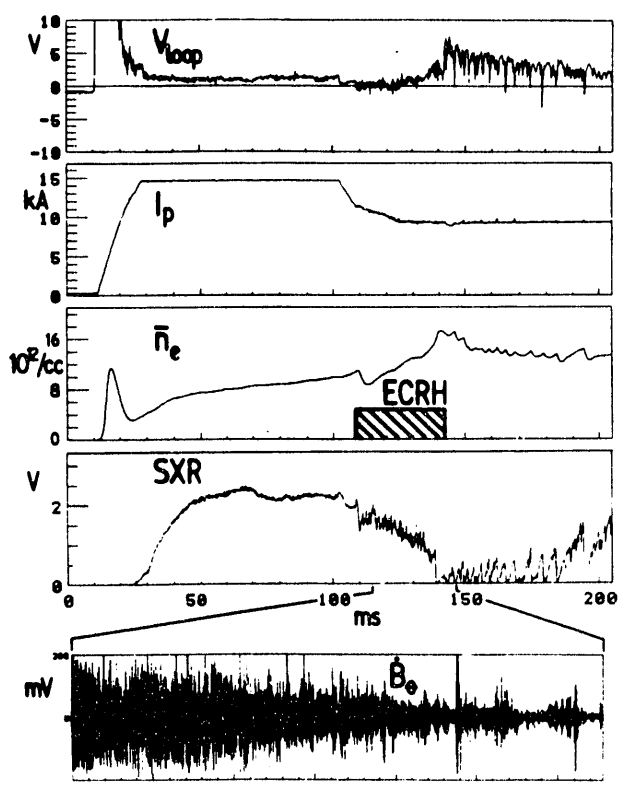


Fig 8(b) Higher densities are achieved with ECRH

# Experiments on Heat Transport Applying the Modulation and Correlation Technique to Electron-Cyclotron-Heated Plasmas in the Wendelstein VII-A Stellarator

H.J. Hartfuß, H. Maaßberg, M. Tutter, W VII-A Team*
*Max-Planck-Institut für Plasmaphysik*
*EURATOM Association, D-8046 Garching*
*Federal Republic of Germany*
and
*ECRH Group***
*Institut für Plasmaforschung der Universität Stuttgart*
*D-7000 Stuttgart*
*Federal Republic of Germany*

ABSTRACT

The electron temperature response to square-wave-modulated electron cyclotron heating power is measured by means of a multichannel system via electron cyclotron emission. The experimental data are evaluated to determine the local heat conductivity coefficient $\chi_e(r)$. An example is given, and the theoretical model and the data evaluation are briefly outlined.

## 1. Introduction

The existence of a well-defined heating zone in an electron-cyclotron-heated (ECH) plasma allows direct experiments on heat wave propagation perpendicular to the magnetic surfaces from which the local heat transport coefficient $\chi_e(r)$ can be derived /1, 2/. We carried out such experiments in the WENDELSTEIN VII-A Stellarator (R = 2.0 m, a = 0.1 m, l = 2, m = 5) in which the heating power $P^{ECH}$ was modulated by periodic reduction by $2\Delta P^{ECH}$, ($2\Delta P^{ECH}/P^{ECH} = 0.3$) and the temperature response to this perturbation, resolved in both time and space, was measured by means of electron cyclotron emission (ECE).

## 2. Experimental set-up

We use a 70 GHz/170 kW/100 ms gyrotron for plasma build-up and heating. The

* G. Cattanei, D. Dorst, A. Elsner, V. Erckmann, G. Grieger, P. Grigull, H. Hacker, H.J. Hartfuß, H. Jäckel, R. Jaenicke, J. Junker, M. Kick, H. Kroiss, G. Kuehner, H. Maaßberg, C. Mahn, S. Marlier, G. Müller, W. Ohlendorf, F. Rau, H. Renner, H. Ringler, F. Sardei, M. Tutter, A. Weller, H. Wobig, E. Würsching, M. Zippe

** W. Kasparek, G. Müller, P.G. Schüller, K. Schwörer, M. Thumm, R. Wilhelm

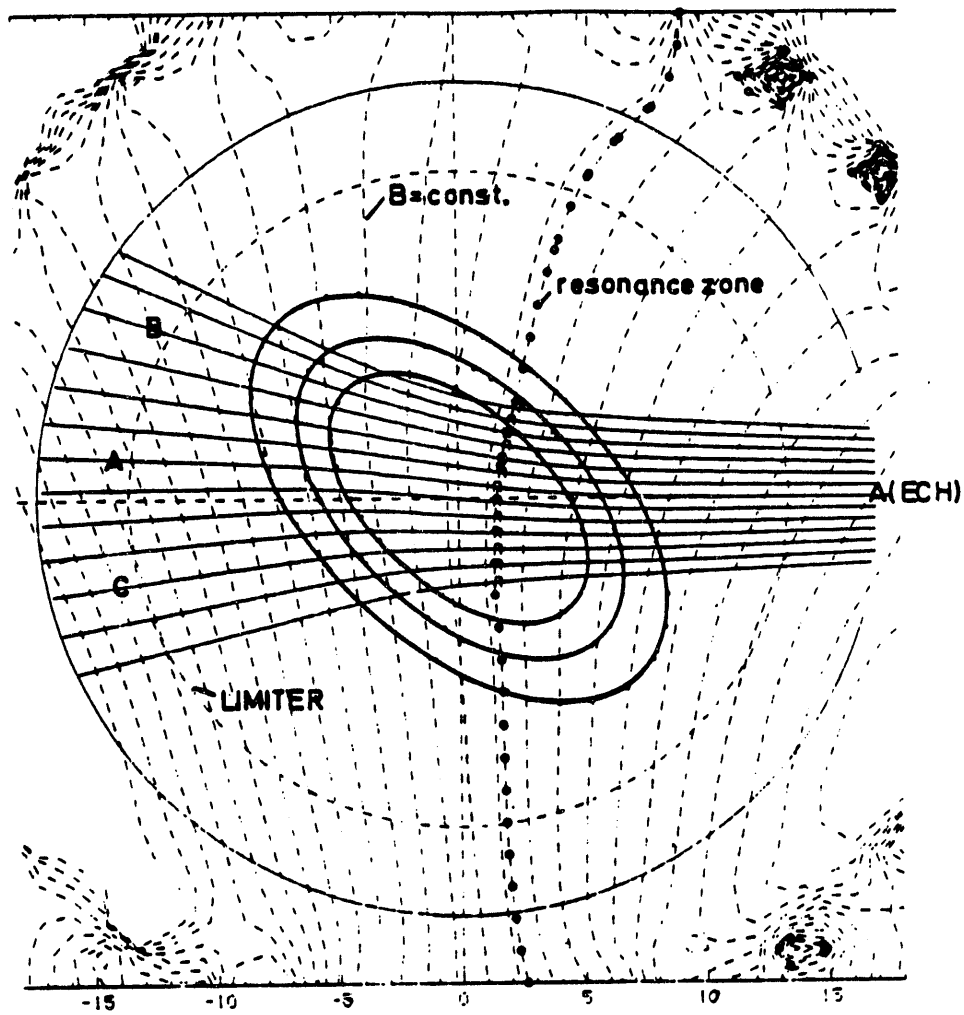


Fig. 1a:

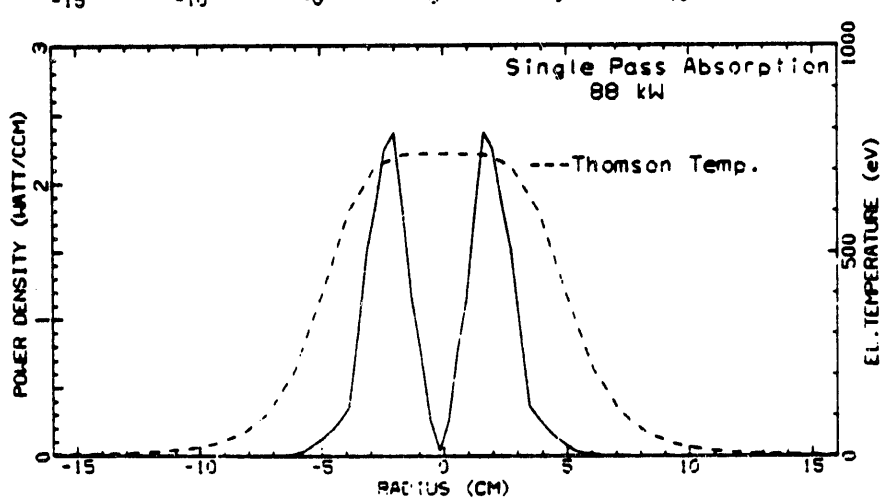


Fig. 1b:

a) ECH launching geometry from ray tracing calculations.

b) The calculated power deposition profile (solid line) and the measured electron temperature profile (dashed line). The resonance zone is shifted outwards resulting in the splitted deposition profile.

toroidal field on axis is 2.5 T. The ECH wave ($HE_{11}$-mode) is launched from the low-field side in O-mode orientation. Figure 1a gives the launching geometry. A circular corrugated waveguide (Ø = 2.5 inches) acts as the antenna A (ECH). Rays B, C are - 3 dB below the power level of the central ray A. The rays are calculated on the assumption of a pure toroidal field within the cold plasma model. Figure 1b gives the power deposition profile. It is calculated on the basis of temperature and density profiles as determined by Thomson scattering, and of a power density distribution across the radius d of the circular horn A (ECH) like exp $(-(d/2.12)^2)$, (d in cm). The resonance is calculated with allowance for both linear and quadratic Doppler shifts as well as diamagnetic correction to the magnetic field and relativistic shift of the gyration frequency. The ECH power absorbed in the

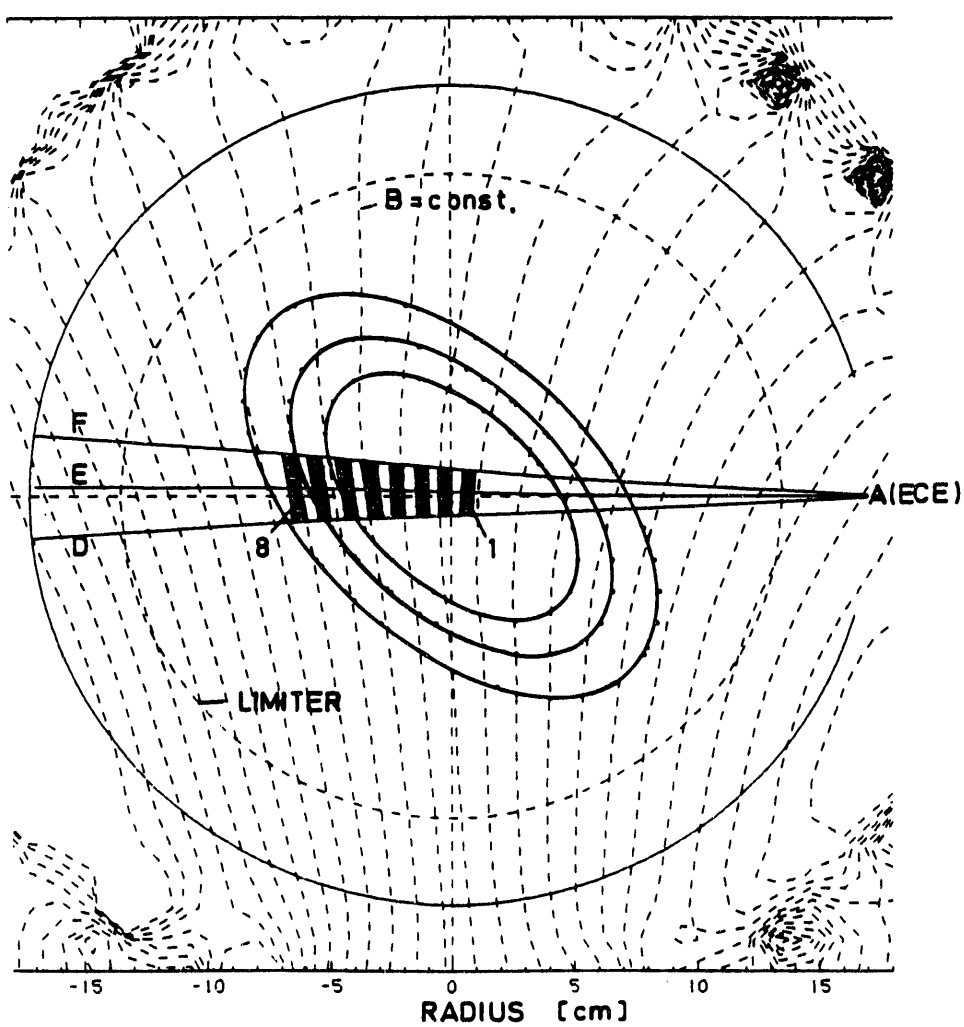


Fig. 2: Observation geometry: A (ECE) is the receiver antenna. The dashed areas indicate the zones (1...8) monitored by the eight channel receiver.

resonance layer is distributed within the magnetic flux surfaces, thus resulting in a symmetric ECH power deposition. The results reported are obtained for a quasistationary discharge characterized by the following parameters: total energy content about 400 J, electron density on axis 2 x $10^{19}/m^3$, electron temperature on axis 740 eV, ion temperature about 150 eV.

## 3. ECE measurements

The simultaneous measurement of the transient electron temperature at 8 different radii $r_i$ on the high-field side of the temperature profile was carried out by means of a multichannel heterodyne radiometer /2/ tuned to monitor the band ranging from 140.96 to 146.00 GHz within the second-harmonic electron cyclotron emission spectrum. The band corresponds to radii between + 0.6 and - 6.3 cm ($-a \leq r \leq +a$). The distance $r_i - r_{i-1}$ is about 1 cm, the spatial resolution $\Delta r$ about 0.5 cm. The temporal resolution is determined by the sampling rate of the data acquisition system which is 13.6 kHz.

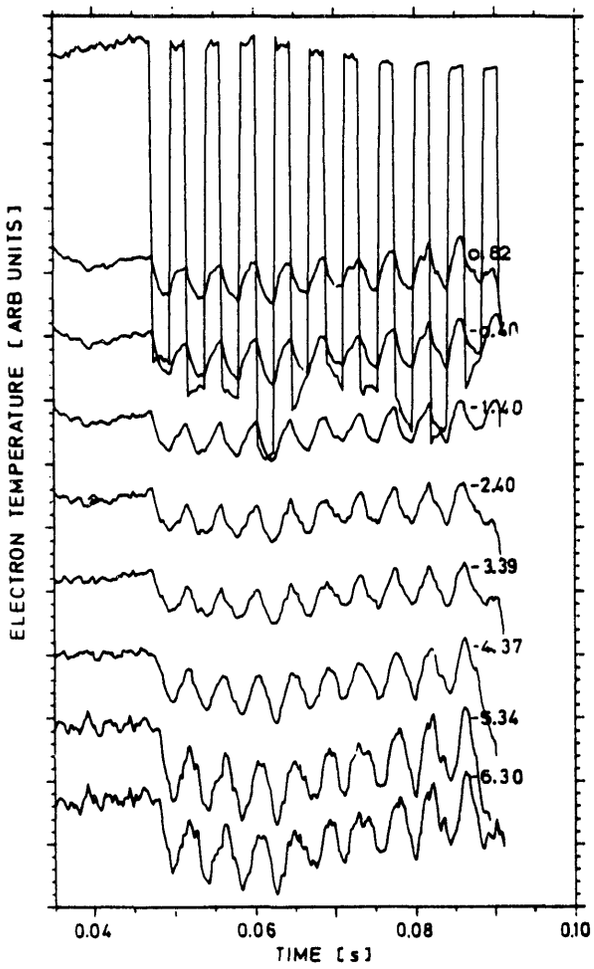


**Fig. 3a:**
The transient electron temperature as measured by the individual channels. The signals are normalized to channel 4 at 40 ms to enhance the modulation. On the right hand side the position of the obser vation zone is given in cm of radius as defined in the text. Channel 1 corresponds to 0.62 cm, channel 8 to - 6.30 cm. Channels displaced for easier comparison. Included is the square wave ECH power signal.

Figure 2 gives the observation geometry: as before, 3 rays D, E, F characterize the circular receiving horn A (ECE). Behind the horn a D-band rectangular waveguide acts as a high-pass and X-mode polarization filter. An oversized circular waveguide (Ø = 23 mm, 5 m long) transports the radiation to the receiver.

The dashed areas in the figure indicate the position of the 8 observation channels. The $T_e$-profile information obtained is in good agreement with the Thomson scattering results.

Figure 3a gives as an example the transient electron temperature $T_e$ ($r_i$, t), i = 1...8, during 230 Hz modulation of the heating power. To enhance the modulation $\Delta T_e$ ($r_i$, t) of the electron temperature ($\Delta T_e/T_e \leq 5$ %), the signals are normalized to have the same magnitude at t = 0.40 s as the channel 4 signal. Figure 3b gives the signals of channels 1 and 6 separately during the modulation phase to demonstrate the time delay.

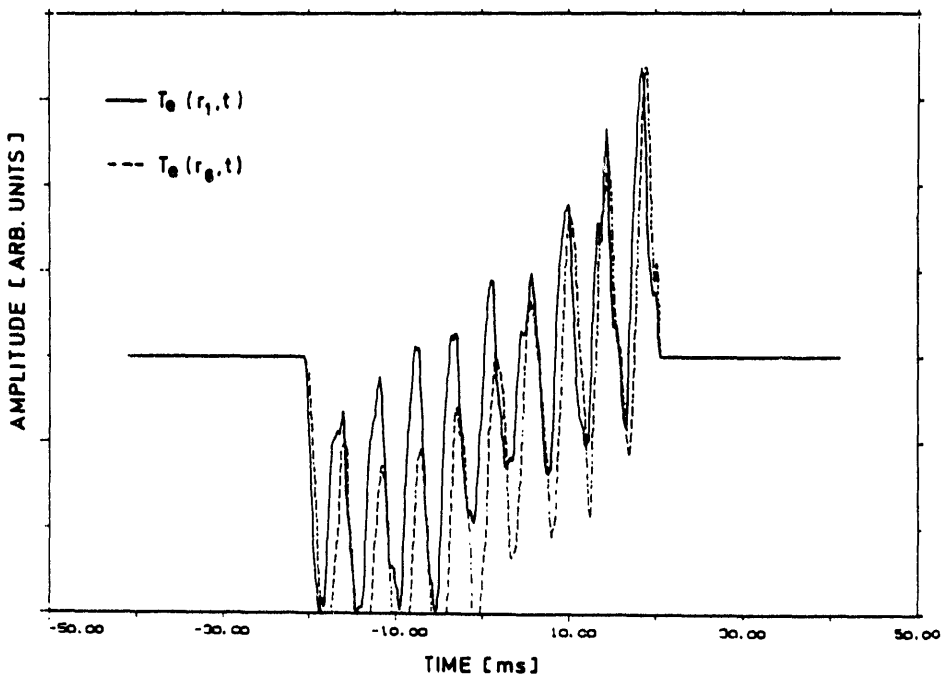


Fig. 3b: The enhanced channel 1 (0.62 cm) and channel 6 (-4.37 cm) signals during the modulation phase clearly exhibit a phase shift.

## 4. Evaluation of the experimental data

The transient electron temperature $T_e$ ($r_1$, t) is measured well within the power deposition zone, and so it is necessarily in phase with the ECH power

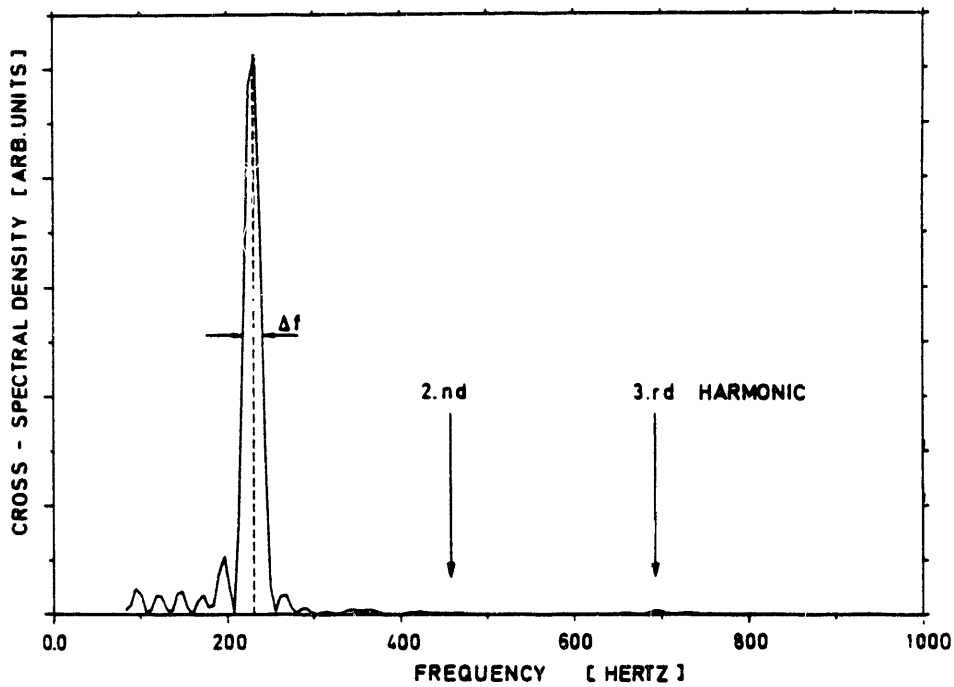


Fig. 4: The Fourier transform of the cross-correlation function of the two signals of figure 3b.

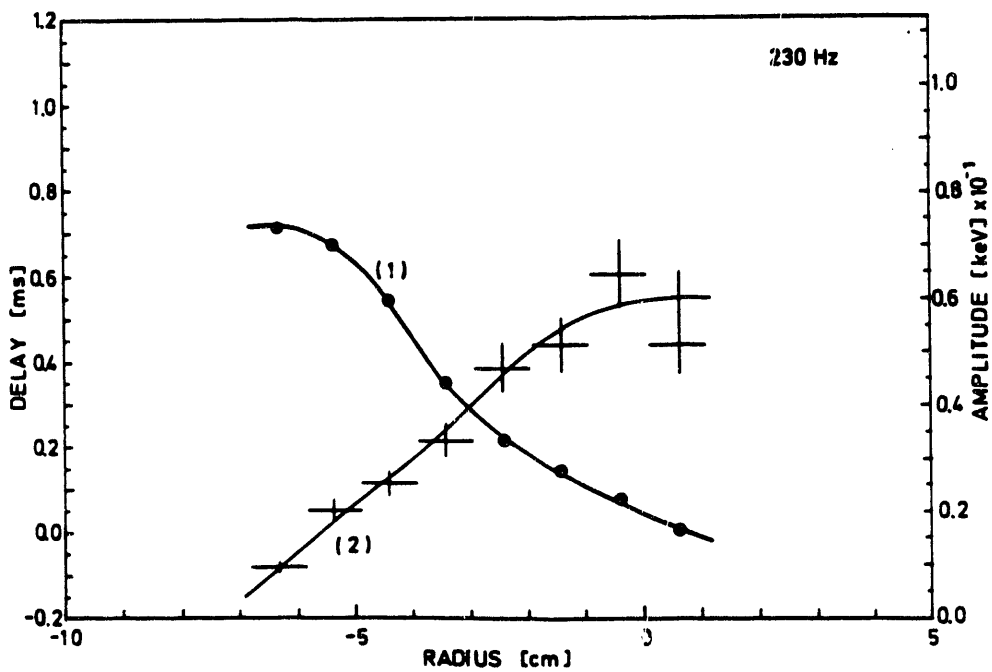


Fig. 5: The time delay as function of radius, curve (1), with left hand side scale and the modulation amplitude, curve (2), with corresponding scale at the right.

modulation. It is used to construct the cross-correlation function

$$R_{1i}(\tau) = (1/T) \int_0^T T_e(r_1\ t) \cdot T_e(r_i,\ t+\tau)\, dt\ , \qquad i = 2...8$$

from which by Fourier transform the complex cross spectral function is obtained, which directly yields the time delay $\Delta t\ (r_i)$ of $T_e\ (r_i, t)$ related to $T_e\ (r_1,\ t)$. Figure 4 gives the cross-spectrum for the two signals of Figure 3b. Besides the modulation frequency, its weak harmonics can be seen. The width $\Delta f$ of the spectral line is mainly due to the short observation interval T of only about 40 ms ($\Delta f \cdot T \approx 1$).

Figure 5 gives $\Delta t\ (r_i)$ within $-7$ cm $< r <$ 0.5 cm together with the modulation amplitude $|\Delta T_e\ (r_i)|$. Owing to the increasing heat capacity of the plasma with increasing $|r|$, the modulation amplitude decreases. The time delay increases monotonically owing to the finite time necessary for electron heat transport (as long as the power deposition at greater radii can be neglected).

## 5. Theoretical model

To evaluate the experimental data, a simplified transport model is used. We consider only processes related to the electron temperature gradient in an axisymmetric model. The modulated power $P^{ECH}\ (r,t)$, which is assumed to be purely sinusoidal with angular frequency $\omega$ and amplitude $\Delta P^{ECH}$, causes the temperature modulation with complex amplitude $\Delta T_e\ (r)$, which includes the phase shift or time lag effect. The time dependence of $\chi_e$ and n is of higher order and thus neglected. The volume electron power loss $P^L$ which contains radiation loss and energy transfer to the background ions depends on $T_e$. In lowest order of expansion, the modulated part is given by $(\partial P^L/\partial T_e) \cdot \Delta T_e(r) \cdot e^{i\omega t}$. In first order of expansion, the electron energy balance equation:

$$(\Delta T_e)'' + \frac{(rn\chi_e)'}{rn\chi_e} \cdot (\Delta T_e)' + P^{ECH} - \left[\frac{1}{n\chi_e} \cdot \frac{\partial P^L}{\partial T_e} + \frac{3}{2}\, i\, \frac{\omega}{\chi_e}\right] \cdot \Delta T_e = 0 \quad ,$$

which has to be solved numerically. $\Delta T_e$ is fitted to the experimental data yielding $\chi_e(r)$.

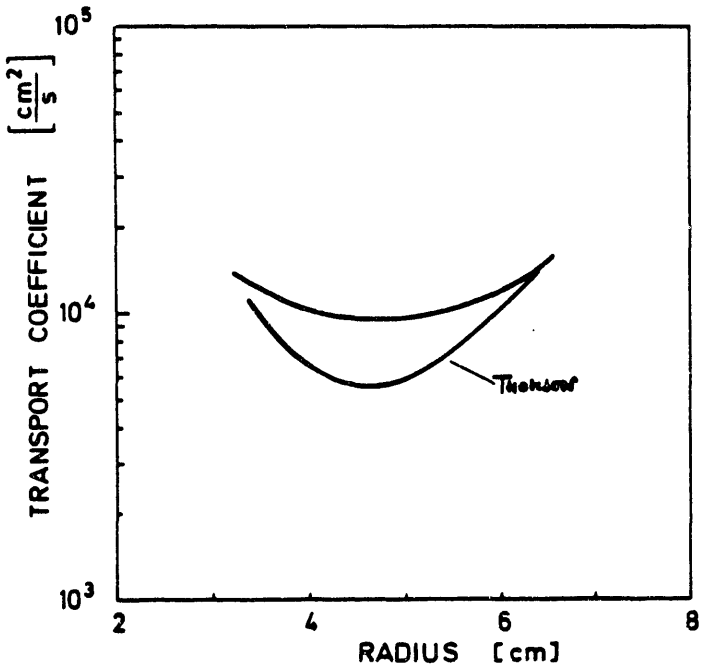


Fig. 6: The local heat conductivity coefficent as derived from the experiment. The curve labelled Thomson is derived from the stationary energy balance, with $T_e$ taken from Thomson scattering.

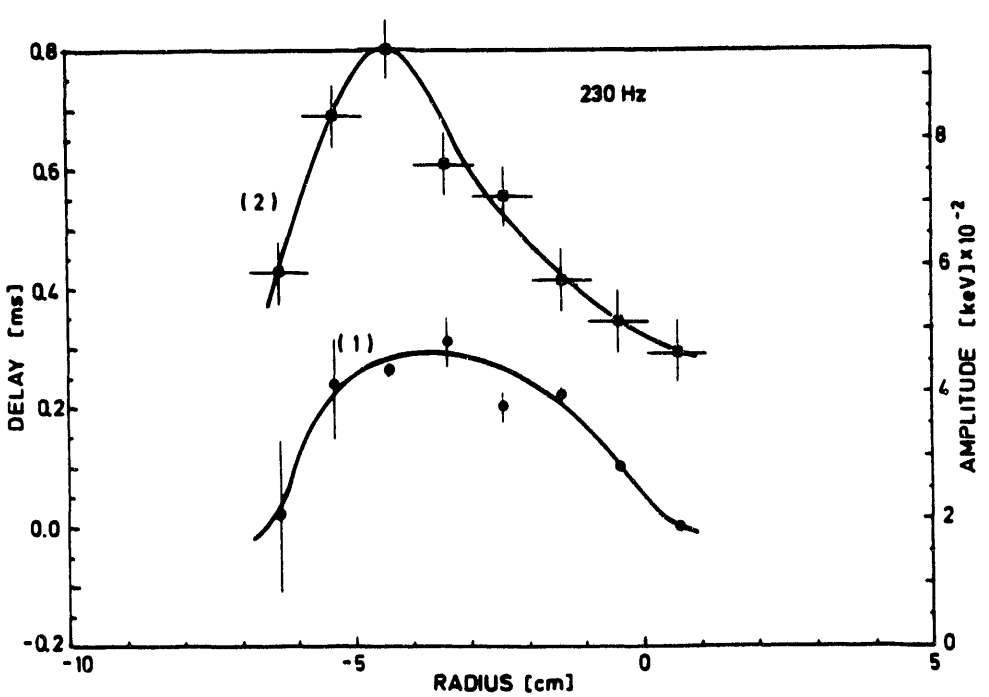


Fig. 7: Time delay (1) and modulation amplitude (2) for an example without clear separation of power deposition and observation zones.

## 6. Results and error discussion

We restrict the evaluation of the electron heat conductivity coefficient to outer regions ($|r| > 3$ cm) where the power deposition is negligible, $P^{ECH}$ ($r > 3$ cm) = 0. Figure 6 gives $\chi_e(r)$ as obtained from this modulation-correlation experiment. It is within a factor of two in agreement with results obtained from the stationary energy balance and theoretical predictions /4/.

The accuracy of the method is crucially determined by the extend to which the power deposition and observation zones can be separated. Incomplete single-pass absorption of the ECH wave followed by wall reflections can cause power deposition in the boundary layers of the plasma column, that completely compensates the phase delay. Figure 7 gives an example. Because boundary layer deposition cannot be completely excluded, the result given in Figure 6 is more an upper limit to the real radial transport coefficient profile.

## REFERENCES


/1/ G.L. Jahns et al., "Measurement of thermal transport by synchronous detection of modulated electron cyclotron heating in Doublet III tokamak", GA Technologies, Internal Report GA-A 17858.

/2/ H.J. Hartfuß et al., "Evaluation of local heat conductivity coefficient by power-modulated electron cyclotron heating in the WENDELSTEIN VII-A stellarator", submitted to Nucl. Fusion.

/3/ H.J. Hartfuß et al., Rev. Sci. Instr. 56, 1703 (1985).

/4/ H. Wobig, to be published

# Experimental Results of Electron Cyclotron Heating in TFR

TFR Group
*Association Euratom-CEA sur la Fusion, DRFC, CEN,*
*Boîte Postale No.6,*
*92260 Fontenay-aux-Roses, France*
and
J.A. Hoekzema, H.P.L. de Esch, R.W. Polman, and W.J. Schrader
*Association Euratom-FOM, FOM-Instituut voor Plasmafysica*
*Rijnhuizen, Nieuwegein, The Netherlands*

ABSTRACT

The ECRH facility on TFR uses three 60 GHz, 200 kW, 100 ms gyrotrons. The power is launched from the low-field side of the torus in the ordinary mode polarization. Introductory experiments were performed with one gyrotron connected to TFR. Approximately 100 kW of microwave power was injected into the plasma at 30 ms pulse length. The full system with three transmission lines connected to TFR has recently come into operation. Heating experiments at full power show electron temperature increase up to 2 keV and a limited degradation of confinement. MHD-stabilization experiments demonstrate suppression of the m=2 mode up to the maximum ECRH pulse length (300 ms). The first experiments on current drive with oblique injection of microwave power and frozen primary loop voltage do not show a current increase that cannot be explained by a thermal decrease of resistivity.

## 1. Introduction

The joint effort of the Associations Euratom-CEA and Euratom-FOM on electron cyclotron resonant heating, current drive, and pre-ionization in TFR [1] was initiated in 1982, and was given its technical basis in 1983 and 1984. The ECR heating system, on which a technical companion paper [2] will be more explicit, consists of a high-voltage supply, a regulator modulator, three 60 GHz, 200 kW, 100 ms assemblies, each with a separate transmission line to TFR, and a data acquisition and control system. The first assembly delivered power into TFR in March 1985 and full operation of the whole system was reached in August 1985.

The microwave power is launched into the plasma through open oversized waveguide antennae and has a horizontal polarization ($TE_{11}$-mode) to couple to the ordinary (O-)mode in the plasma. Figure 1 shows the disposition of the one oblique and the two perpendicular launchers and of the two types of mirror that can be placed on the inboard side of the torus wall. The polarization-twisting reflector allows interaction from the inboard side

with the X-mode in regimes with a high transmitted power fraction. Also, because of the 20° deflection, absorption at a Doppler-shifted resonance can be studied. The oblique antenna allows this also and can be used moreover at plasma densities above cut-off because reflection of power into the antenna is avoided.

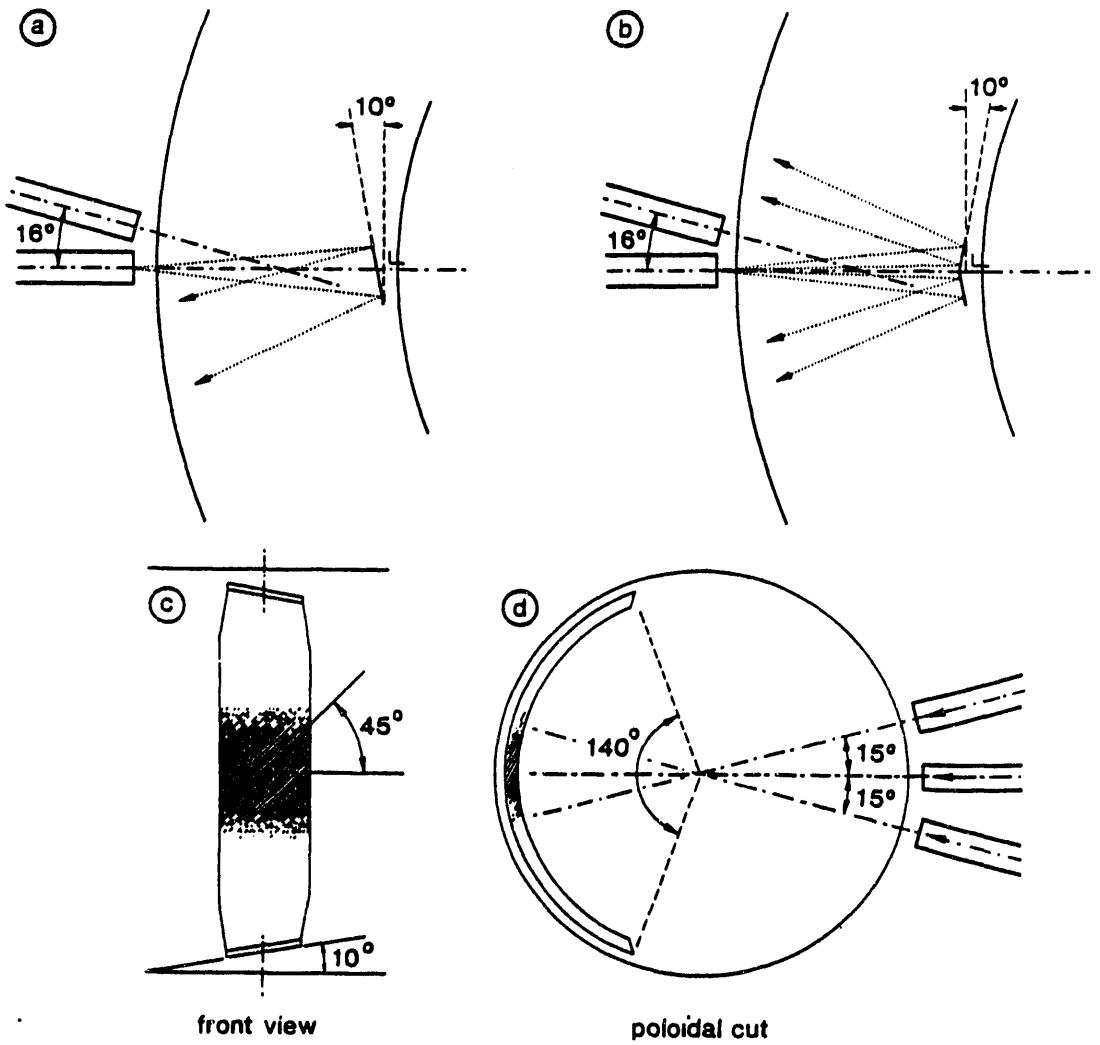


Fig. 1. Positions of the antennae and of the reflecting mirrors:
a), c), and d): the one-sided polarization-twisting mirror.
b) : the symmetric, roof-top, smooth mirror.

TFR (major radius 0.98 m) was operated with carbon limiters, generally at 0.20 m minor radius. The ohmically heated target plasmas had the following characteristics:

| | | | |
|---|---|---|---|
| $n_e$ (o) | = $(1\div3)\times10^{19}$ $m^{-3}$ | $I_p$ | = 100÷150 kA |
| $T_e$ (o) | = 800÷1200 eV | $V_\ell$ | = 1.2÷1.5 V |
| $T_i$ (o) | = 300 eV | $\Delta H$ | = -2÷-4 cm |
| B(o) | = 20 - 27 kG | q(a) | = 2.8÷4. |

The first results, pertaining to one-gyrotron operation (the antenna in the horizontal plane, 100 kW into the plasma during 30 ms) and obtained on heating, suprathermal effects, and control of MHD activity, were published at the Budapest Conference [3]. They were obtained with the smooth roof-top mirror. The present paper is a first report on full power, full pulse lengths, three-gyrotron operation, using the polarization-twisting reflector.

## 2. Heating

During the introductory ECRH experiments with one gyrotron connected to TFR [3], two ohmic regimes were explored with a different value of the plasma current, $I_p$. For low values of $I_p$ (< 110 kA), no MHD activity was observed and the electron energy confinement time, $\tau_E$, decreased from 6.5 to 4.5 ms during central ECRH (100 kW). A quite different behaviour was found at higher values of $I_p$, where strong MHD activity developed (especially m=2), giving rise to a strongly peaked temperature profile. Here $\tau_E$ increased slightly from 3.7 to 4.3 ms during central ECRH.

The two regimes were again explored with full ECRH power. A discharge with high current (130 kA) is illustrated in Figs. 2-4. The temperature profile is less peaked than in the high-current case of Ref. [3]. This can be attributed to a higher value of $I_p$ and therefore a larger radius of the q=2 surface. In this type of discharge, large scale MHD activity is observed. ECRH power was applied in a staged way by switching on the three gyrotrons with 25 ms intervals. The heating was focussed at the magnetic axis.

During ECRH, the loop voltage drops gradually from 1.8 to 1.1 V. The ion temperature remains constant with a central value $T_i$(o) = 350 eV. Contrary to the previous experiments with one gyrotron, the central-chord line density does not show a pump-out. It is quite difficult to maintain the plasma position ($\Delta H$ = -2 cm) with full ECRH power. The line density, after an initial tendency to pump out, often shows an increase during ECRH which

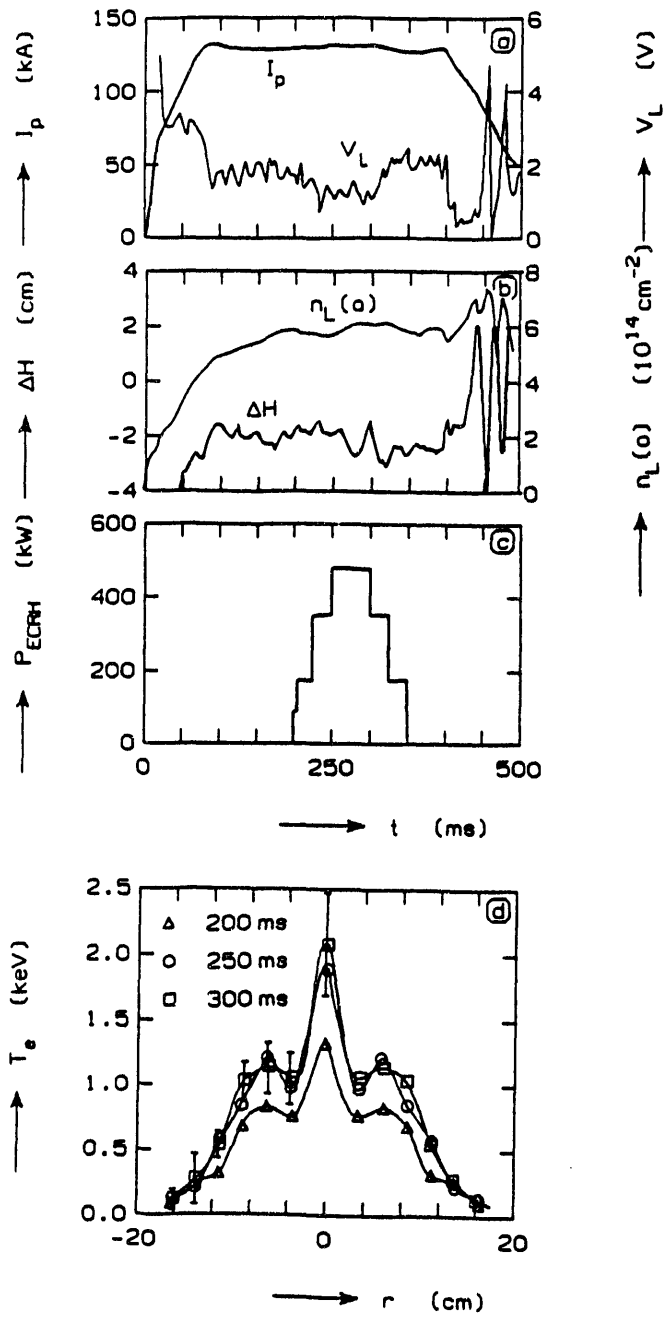


is correlated with the variation of the position of the plasma and which is therefore probably due to enhanced plasma-wall interaction.

The electron temperature profile, as obtained from Thomson scattering, gives an indication of a gradual disappearance of the q=2 islands with ECRH power, but the statistics are not good enough to draw a conclusion.

Central heating is, however, often accompanied by a reduction of m=2 activity. This may be caused by a change of the current density profile due to heating which leads to an m=2 stable configuration. It may also be connected with a small displacement of the plasma, which increases the q-value at the limiter slightly, and reduces the interaction of the q=3 island with the wall. Due to a displacement of the magnetic axis, the electron temperature profiles obtained from

Fig. 2. High-current case. Plasma current $I_p$, loop voltage $V_\ell$, horizontal displacement ΔH, central-chord line density $n_L(o)$, and injected 60-GHz microwave power $P_{ECRH}$ as functions of time (a,b,c).

Fig. 2d. Electron temperature profiles at different times during the discharge as measured in a vertical plane with Thomson scattering. $B_t(o)$ = 21.4 kG (resonance layer at the magnetic axis).

Thomson scattering can be pessimistic because they are measured on a vertical chord centered on the torus axis.

Figure 3 shows the $T_e$ profiles in the horizontal plane of the plasma as obtained from second harmonic ECE recorded with a scanning Michelson interferometer (spatial resolution = 6 cm, scanning time 15 ms). They indicate a much broader $T_e$ profile during ECRH than is deduced from Thomson scattering although suprathermal effects cannot be completely ruled out.

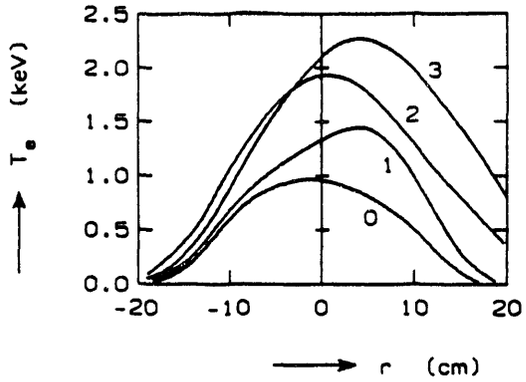


Fig. 3.
Electron temperature, measured from $2\omega_{ce}$ emission using a scanning Michelson interferometer, in the horizontal plane of the torus. The numbers refer to the number of gyrotrons switched on during the time of measurement.

The dependence of the energy confinement time on the amount of ECRH power for this discharge is given in Fig. 4. Figure 5 shows the density fluctuation spectrum measured at intermediate radii with $k_\perp = 6\ cm^{-1}$ (using microwave scattering).

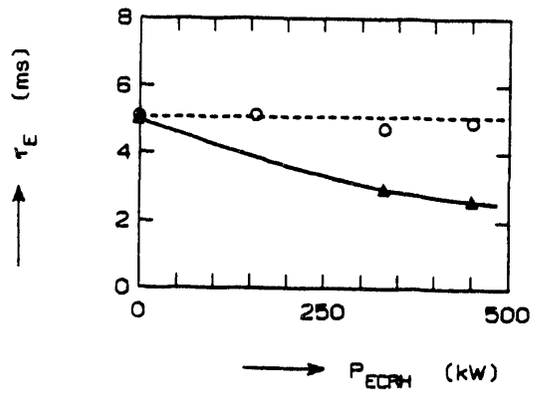


Fig.4.
Energy confinement time as a function of injected ECRH power for the high-current discharge of Fig. 2. The straight curve was obtained using the Thomson-scattering $T_e$ profiles; the dashed curve using the ECE temperatures.

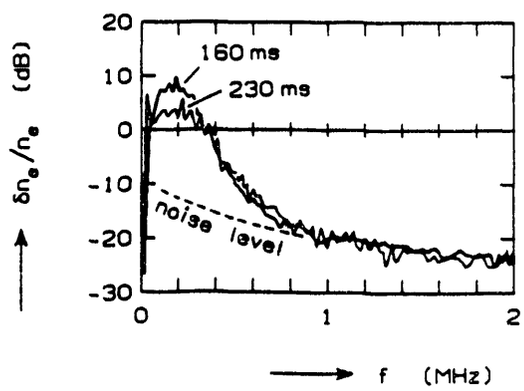


Fig. 5.
Density fluctuation spectra before (160 ms) and during ECRH (230 ms).

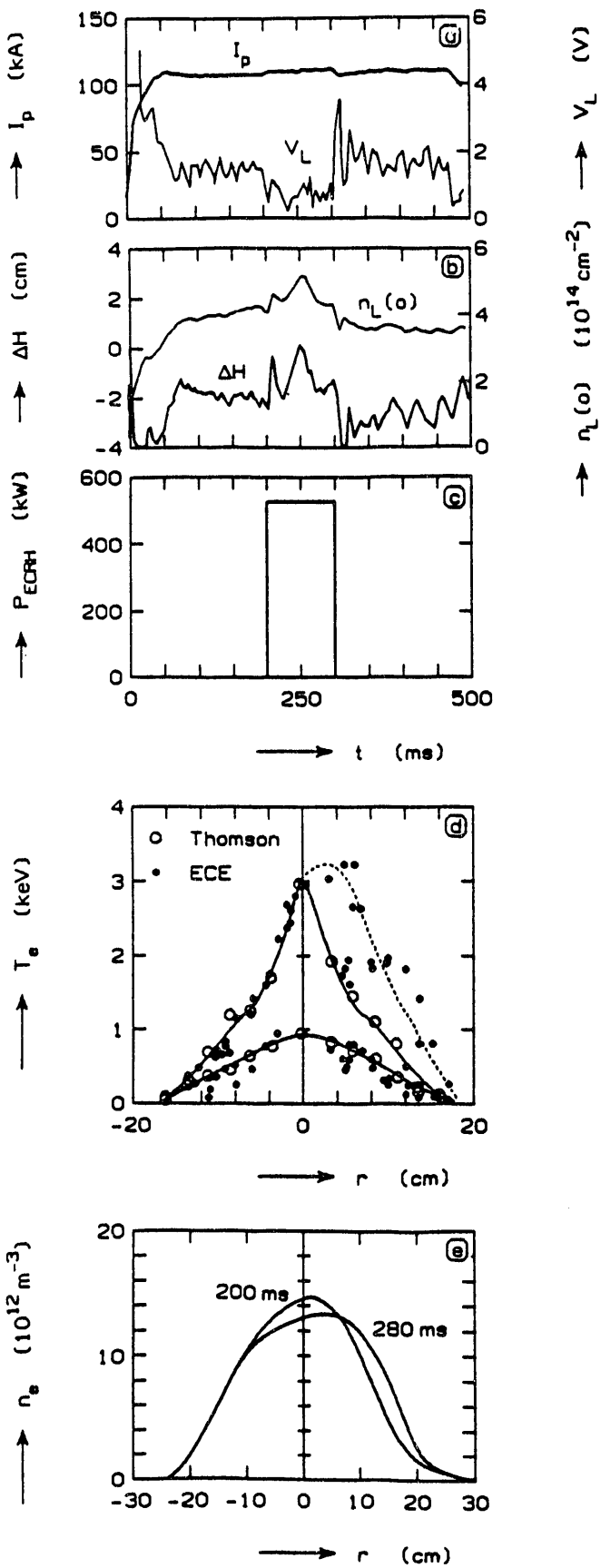


Fig. 6.

Low-current case. Plasma current $I_p$, loop voltage $V_\ell$, horizontal displacement ΔH, central chord-line density $n_L(o)$ and injected ECRH power as functions of time (a,b,c). Electron temperature profiles before (200 ms) and during (280 ms) ECRH as measured by Thomson scattering and ECE (superheterodyne detection) (d).

$B_T$ = 21.4 kG (central heating). Electron density profiles before and during ECRH (e).

Some high-current discharges at higher magnetic fields were also studied. They confirm the conclusion of Ref. [3] that the heating efficiency is reduced when the resonance layer is displaced outward.

A discharge with relatively low plasma current is illustrated in Figs. 6,7. In this case $I_p$ is slightly below 110 kA and ECRH heating is central. The loop voltage drops during ECRH by a factor of 3 (1.5 to 0.5 V). The horizontal position of the plasma is much more difficult to control than in the high-current cases and the displacements give rise to an influx of gas, as is apparent from the line-density signal. The electron density is rather low, but the discharge is still thermal. The central ion temperature, as measured by charge-exchange neutrals energy analysis, shows a very fast (and unexplained) increase during ECRH from ≈ 300 eV to ≈ 400 eV. Also in this case, a difference is found between the vertical $T_e$ profile measured by Thomson scattering and the horizontal ECE profile, which is here measured with a superheterodyne system on a shot-to-shot basis. This difference is probably due again to a displacement of the magnetic axis, which is also seen on the density profile.

Using the Thomson $T_e$-profile, the energy confinement time during ECRH is found to be reduced by a factor of 2 (from 5 to 2.5 ms). A smaller reduction of $\tau_E$ is found using the sketched ECE-profile (3.5 ms). A transport code produces the electron heat-conductivity profile given in Fig. 7, when the Thomson $T_e$-profile and other experimental profiles are used.

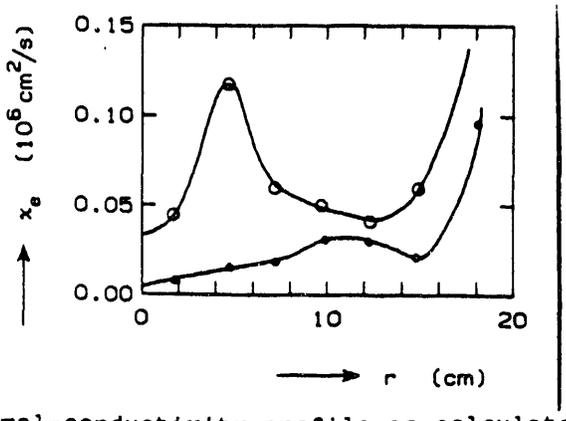


Fig. 7. Electron thermal-conductivity profile as calculated with a transport code, using the experimental $n_e$, $T_e$ and $T_i$ values.

## 3. MHD control experiments

The reduction of m=2 activity by ECRH has already been shown (e.g. [3], [4]). More extensive experiments have now been done on TFR, using the local heating scheme: by deposing ECRH power outside the q=2 surface, the temperature gradient - and therefore the current gradient - is locally reduced, leading to a stabilization of the mode through $\Delta'_{NL}$ reduction. It was found that the efficiency is higher when the energy is deposited outside the q=2 surface on the low-field side rather than on the high-field side (i.e. at $R = R_o + r_{q=2} + \delta_r$ rather than at $R = R_o - r_{q=2} - \delta_r$) because of the better localization. Maximum efficiency is observed at $\delta_r = 2$ cm, but the exact position of the q=2 surface is presently not known with a precision better than ± 1 cm. Two different types of experiments were performed. In the first one continuous ECRH power was applied (200 kW during up to 300 ms) on a target plasma which - without ECRH - exhibits strong MHD activity. Figure 8 shows suppression of both the m=2 and the m=3 activity.

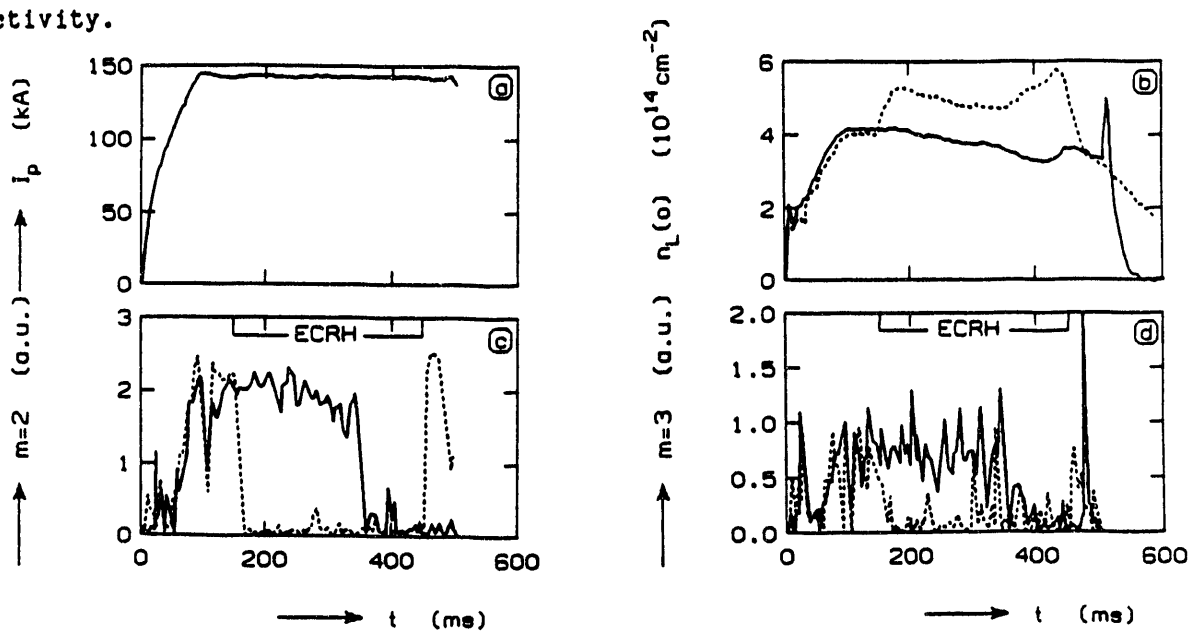


Fig. 8. Plasma current (a), central-chord line density (b), m=2, n=1 (c), and m=3, n=1 (d) amplitudes as a function of time, without and with (dashed curve) ECRH. q(a) = 3.45, $r_{ECRH}$ = 15.1 cm, $r_{q=2}$ = 12.7 cm, $r_{q=3}$ = 18 cm.

A second type of experiments used a simple feedback loop, where ECRH was on when and only when the m=2 amplitude exceeded a preset level. Of course this is a very coarse regulation, and the interest is mainly to show the effect of ECRH on m=2 rather than to obtain a practical MHD regulation.

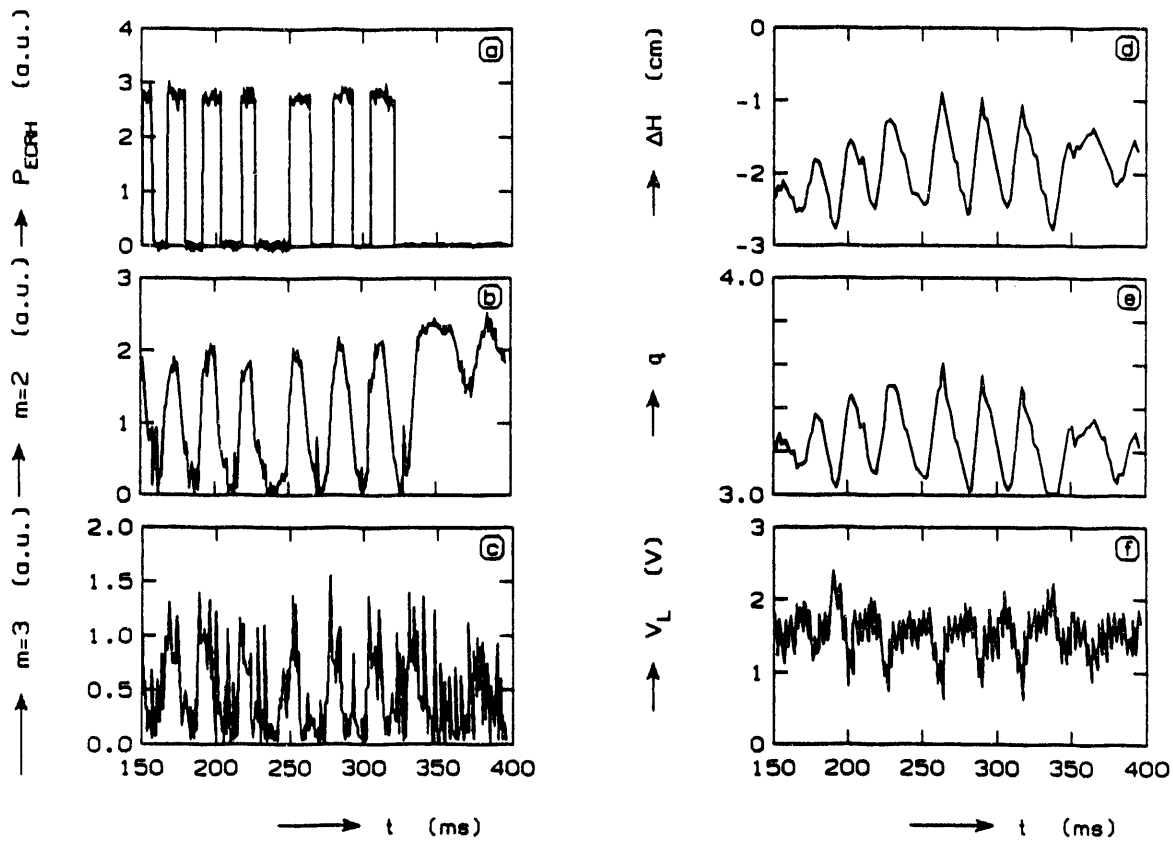


Fig. 9. Feedback MHD control. The following signals are shown as functions of time: a) rf-power (at the plasma), b) m=2 amplitude, c) m=3 amplitude, d) horizontal displacement, e) safety factor and f) loop voltage . $r_{ECRH}$ = 13.3 cm, $r_{q=2}$ = 12.7 cm, $r_{q=3}$ = 18 cm.

Figure 9 shows the repeated suppression of MHD activity with ECRH. The horizontal displacement, the safety factor and the loop voltage are also given as a function of time. From their behaviour arises the question whether the stabilization is due to the mechanism described just above or to a displacement induced by heating: increase of plasma energy leads to a displacement away from the inner limiter and hence to reduction in recycling and impurity inflow, (and also minor radius increase) hence to stabilization.

In fact the observation of MHD-activity reduction in central heating experiments may be due to this mechanism (see Sect. 2). When the heating layer is located at larger radii, both phenomena contribute, but the sensitivity to the respective positions of $r_{ECRH}$ and $r_{q=2}$ shows that the predominant mechanism is the first one, i.e. local j(r) modification due to local $T_e(r)$ modification.

Experiments are planned using ECRH power phase-locked to the mode rotation, following a suggestion by H. Hsuan et al. [5]

## 4. Experiments on current drive

TFR is usually run with a regulated flat top current value. To be able to study current drive effects, we froze the primary-winding loop voltage at the value it had at a preset time (200 ms in Fig. 10). The plasma current then decayed at a slow rate. Adding ECRH during the decay, we could look for differences in I(t) behaviour. Three series of experiments were done, with toroidal field values of 21.4, 24.0, and 27.0 kG. At the high value of the magnetic field the first-pass absorption of rf-power is negligible and two-thirds of the ECRH power is essentially injected from the inboard side of the torus in the X-mode at a 70° angle to the magnetic axis (via the mode converting mirror).

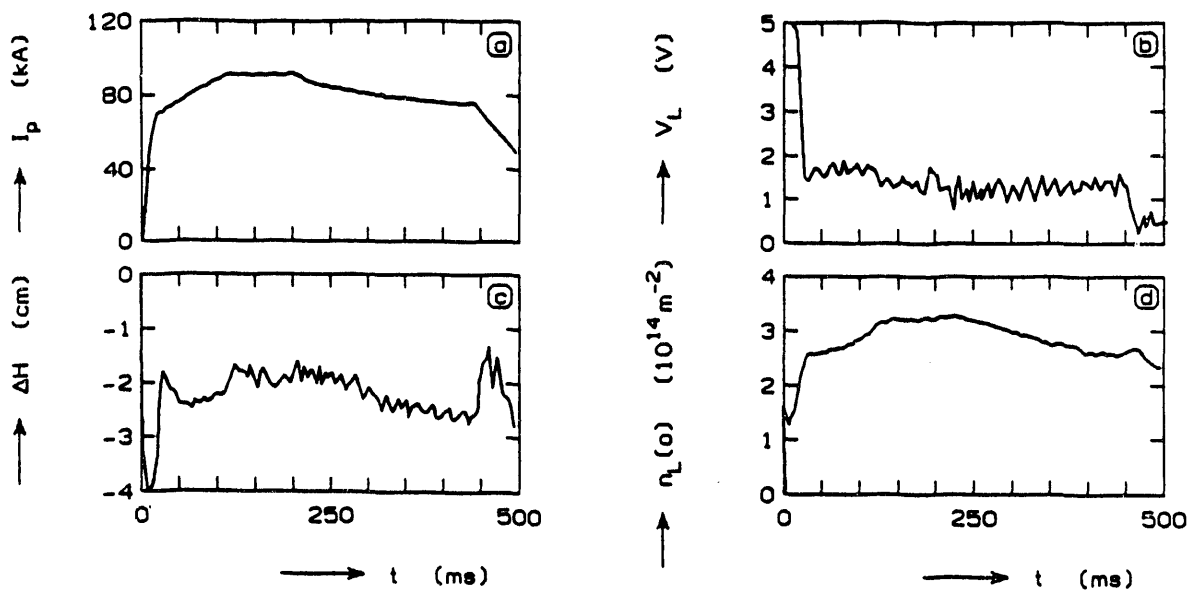


Fig. 10. Plasma current (a), loop voltage (b), horizontal displacement (c), and line density (d) as a function of time for a discharge with frozen primary loop voltage after 200 ms.

### a) B(o) = 21.4 kG

The microwave power heats the bulk of the maxwellian: one expects a decrease in resistivity (seen on the loop voltage when the current is feedback controlled, see Sect. 2). Figure 10 shows a discharge without ECRH. Figure 11 shows the plasma current I(t) behaviour without and with (dashed curve) 600 kW of ECRH from 250 to 350 ms. The difference between the current value at 350 ms, ΔI, is approximately 13%. Taking $\sigma(r) \sim T_e(r)^{3/2}$, and using the

temperature measurements, the expected difference in plasma current is about 20%. The experimental value of ΔI is inferior to this expected value.

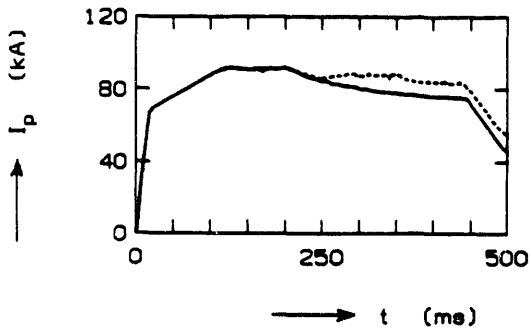


Fig. 11.
Plasma current without and with (dashed curve) ECRH (600 kW).
B(o) = 21.4 kG.

b) B(o) = 24 kG

The microwave frequency is resonant with bulk electrons at r = 12 cm and with electrons in the centre with energies around 40-60 keV. This shift is due to the relativistic effect alone for microwave propagation perpendicular to the magnetic axis: Fig. 12 shows I(t) without and with (dashed) ECRH (400 kW with perpendicular injection). The plasma current difference is again ΔI = 13%. The computed ΔI using measured temperature-profile changes is in good agreement with this value. If microwaves are injected at an angle both the relativistic effect and the Doppler effect are important. When 200 kW is injected at a $74^{o}$ angle to the magnetic axis the plasma current difference is ΔI = 7%, which is also in good agreement with computed resistive values.

This means that the current difference can be attributed to a change of resistivity of the bulk without any non-inductive current drive effect. A complementary test was done by changing the plasma current direction: in the case of oblique injection, the Doppler-effect term would have the wrong sign. In fact, the results were exactly the same, which indicates that the Doppler-shifted interaction with tail electrons was negligible.

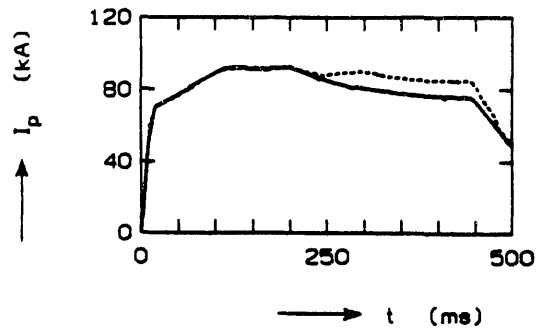


Fig. 12.
Plasma current without and with (dashed curve) ECRH (400 kW, perpendicular injection).
B(o) = 24 kG.

c) B(o) = 27 kG

The microwave frequency is not resonant with bulk electrons within the vacuum vessel, but only with electrons with energies ≈ 90-140 keV. The target plasma used in these experiments had a low density and a high level of runaway electrons. No significant difference could be detected on the plasma current with and without ECRH power for both directions of plasma current (actually there was, in both cases, a slight tendency for a negative value of $\Delta I_r$ but the obvious explanation was enhanced sputtering in the edge due to the non-absorbed microwave power flux on the vacuum vessel wall, leading to impurity increase).

d) Discussion

These results are preliminary in the sence that the target plasmas used do not cover the whole range of possible interest. The possibility of non-inductive current drive effects at fields > 21.4 kG could arise only if a suprathermal tail is present. Figures 13a and 13b show the electron energy spectrum measured with a Si(Li) detector (energy cut-off below 1.6 keV) on a 21.4 kG plasma without and with ECRH. The target plasma is obviously maxwellian, and Fig. 13b shows the heated plasma to be also essentially maxwellian.

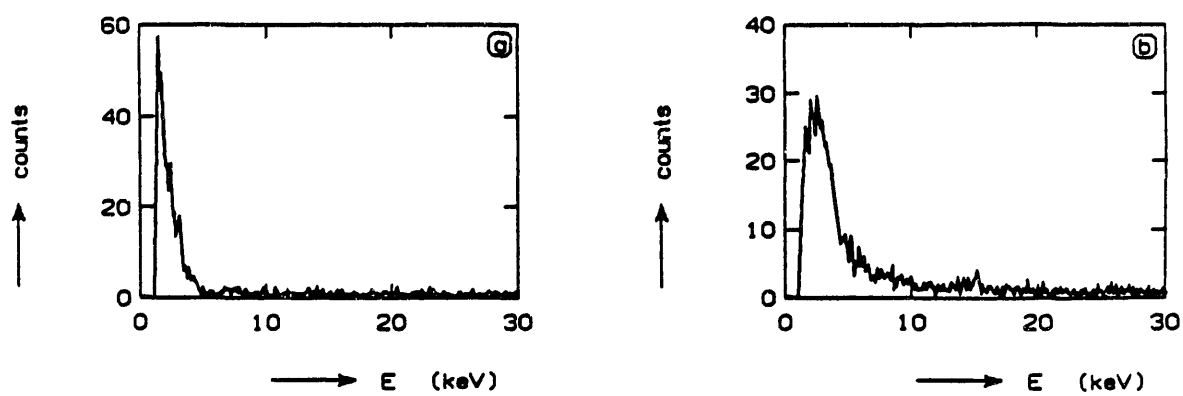


Fig.13. Electron energy spectrum without (a) and with (b) ECRH (600 kW). B(o) = 21.4 kG.

Figures 14a and 14b show the spectra at 24 kG. In both figures a tendency to non-maxwellian is detectable. No obvious difference can be seen: the spectra are strongly reflecting the central behaviour and at 24 kG heating is much less peaked than at 21.4 kG.

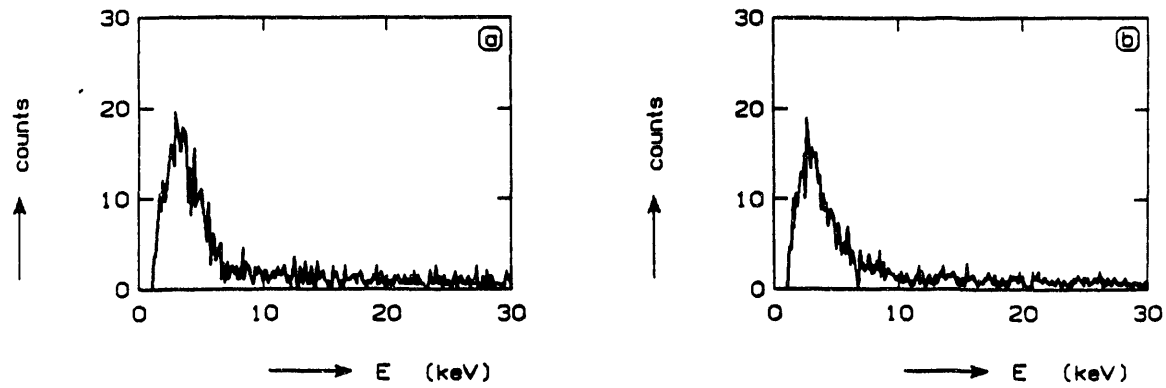


Fig.14. Electron energy spectrum without (a) and with (b) ECRH.
B(o) = 24 kG.

Figures 15a,b show the same at 27 kG: here the target plasma exhibits a significant high energy tail and Fig. 15b is strongly non-maxwellian: even in this case no non-maxwellian inductive current drive effect was detectable.

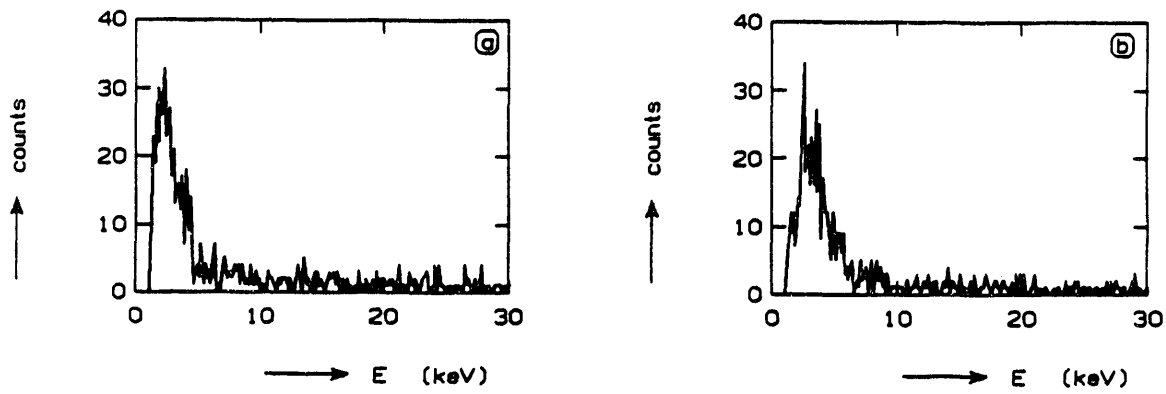


Fig.15. Electron energy spectrum without (a) and with (b) ECRH.
B(o) = 27 kG.

## Acknowledgment

Discussions with T. Schep and E. Westerhof are gratefully acknowledged. The FOM activities were performed under the Euratom-FOM association agreement with financial support from ZWO and Euratom.

## References

[1] R. Cano et al., Proc. 4th Int. Symp. on Heating in Toroidal Plasmas, Rome (1984) Vol. II, p. 853.

[2] A.G.A. Verhoeven et al., this workshop.

[3] FOM-ECRH Team and TFR Group, Proc. 12th Eur. Conf. on Contr. Fusion and Plasma Phys., Budapest, (1985) Vol. II. p. 60.

[4] V.V. Alikaev et al., 10th Int. Conf. on Plasma Phys. and Contr. Nucl. Fusion Res., London (1984) Vol. 1, p. 419.

[5] H. Hsuan, private communication.

# Heating Effectiveness in Electron Cyclotron Heating Experiments in the Doublet III Tokamak

R. Prater and A.J. Lieber
*GA Technologies Inc., San Diego, California USA*

## I. Introduction

A wide range of variability has been found in the heating effectiveness of electron cyclotron heating (ECH) in the Doublet III tokamak, both using the outside quasi-perpendicular launch of the ordinary mode and the inside oblique launch of the extraordinary mode. Although the confinement time for ECH discharges has been found to depend systematically on plasma parameters like plasma current, density, and toroidal field, a range of confinement times is observed even when these macroscopic parameters are held fixed. It is this variability within the systematic framework of the global confinement time scaling for auxiliary heated discharges that is the subject of this paper.

The experimental heating efficiency of outside launch ECH using the ordinary mode in Doublet III has been studied previously [1]. These experiments, which were performed at power levels of 250 kW incident on the plasma, were intended to determine the ECH heating efficiency as a function of plasma density. The density was varied by changing the level of the injection of deuterium gas under otherwise fixed conditions of plasma current (320 kA) and toroidal field (21.7 kG). The unexpected result was that although the density increased only 25% for a factor five increase in the gas injection level, it was found that the total energy increase of the plasma, the density behavior during ECH, and the central electron temperature increase due to ECH changed dramatically.

In particular, it was found that at low gas injection rates the net increase in plasma energy when the ECH was applied was very small (low heating efficiency), while at higher gas injection rates the net increase was as large as 6 kJ (much higher heating efficiency) for plasmas with total energy of 30 kJ. Measurements of the central electron temperature revealed the reverse behavior: the largest increases were found at low gas injection rates. These observations are made consistent by noting that the plasma line-averaged density drops a relatively large amount (up to 40%) upon the application of ECH at low gas injection rate, but that the density drop decreases to less than 10% at the larger gas injection rates.

These results were obtained from discharges made during a single day. When the entire Doublet III outside launch ECH data base was examined for these trends, the results were much less clear. Experimentally, it was found that simply increasing the gas injection level would not necessarily yield improved heating efficiency. It seemed that some other condition of the plasma was involved, possibly having to do with the plasma interaction with the wall since the $D_\alpha$ emission tended to drop in the high heating efficiency cases and increase in the poor efficiency cases.

The experiments described here extend the heating efficiency measurements to the case of inside launch of the extraordinary mode. They also make use of an x-ray spectrometer for measurements of bulk ion rotation speeds; this device was not available at the time of the outside launch experiments.

## II. Apparatus

These experiments were carried out on the Doublet III tokamak using the 60 GHz ECH system. The characteristic parameters of Doublet III under which these experiments were performed are shown in Table 1. The toroidal magnetic field was held close to 21.4 kG, which keeps the gyroresonance for 60 GHz power near the plasma center. For the moderate electron temperature (1–3 keV) and underdense conditions used in these experiments, most of the microwave power incident on the plasma is absorbed within a few centimeters of the gyroresonance, so all the data described here may be considered to be central heating.

**Table 1**
**Doublet III Parameters used in this Study**

| | |
|---|---|
| Major radius (m) | 1.43 |
| Minor radius (m) | 0.38 – 0.41 |
| Elongation | 1.5 – 1.6 |
| Plasma current (kA) | 345 |
| Toroidal field (kG) | 21.4 – 22.7 |
| Plasma density ($10^{19}$ $m^{-3}$) | 3.1 – 4.1 |
| Gas | D |
| ECH frequency (GHz) | 60 |
| ECH power (kW), incident | 450 – 600 |
| Mode | X |

For plasmas heated by ECH or by neutral beam injection, the confinement time $\tau_E$ for Doublet III for discharges with relatively high heating efficiency is consistent with the global scaling

$$\tau_E \propto I_p \, P_{aux}^{-\alpha}$$

where $\alpha$ is between 0.3 and 0.4. The most sensitive parametric dependence is on plasma current $I_P$, and the auxiliary heating power level $P_{aux}$ is also important. The confinement time is independent of plasma density for $2.0 \leq \bar{n}_e \leq 6.0 \times 10^{19} m^{-3}$ and independent of toroidal field provided the resonance is kept within half the minor radius of the center, $17 \leq B_T \leq 25$ kG. In order to keep the systematic variation in confinement time to a minimum, discharges were selected with plasma current very close to a constant value, 345 kA, and with ECH power incident on the plasma within the range 450 to 600 kW.

The experiments were carried out in expanded boundary divertor discharges with elongations of 1.5 to 1.6. Discharges were selected for those which have a minimum of 3 cm between the separatrix flux surface and the closest material limiter; this gap was found to provide the full confinement benefit of the expanded boundary divertor configuration in Doublet III [2]. The working gas in all cases was deuterium.

The ECH power was launched from the inboard wall as a pure extraordinary wave. The geometry of the launcher is shown in Fig. 1. The wave is launched in the plasma median plane at a 30° angle to the radial, in the direction of the toroidal field and plasma current. Calculations using the TORAY ray tracing code [3] indicate that for this geometry the single pass damping of the wave is strong up to a line-averaged density of $\bar{n}_e = 5.6 \times 10^{19}$ $m^{-3}$, at which density refraction effects become important and the rays are refracted away from the plasma center. Typical pulse lengths are 200 msec, which is long enough for the plasma to obtain steady state conditions.

In addition to the usual set of diagnostics available on Doublet III, this work makes use of a curved-crystal Bragg x-ray spectrometer for measurement of the Doppler shift of impurity ion emission lines [4]. Since the momentum transfer between the impurity ions and the main plasma ions is strong, the bulk plasma toroidal rotation speed may be inferred from the Doppler shift measurements of the impurity lines. The determination of plasma rotation speed has an uncertainty of about 1.5 km/sec. The spectrometer views a chord tangent to the plasma axis in the plasma midplane, so its measured spectra are strongly weighted by emission from the plasma center and insensitive to poloidal velocity. The high optical speed of the spectrometer provides a spectrum every 20 msec during the discharge. In this experiment, the impurity line used is the helium-like line from Ti XXI.

## III. Experimental Results

Experimental data from a discharge with poor heating efficiency is shown in Fig. 2 and from a discharge with high efficiency in Fig. 3. The discharges have about the same incident ECH power levels, but in the discharge of Fig. 2 the injected gas

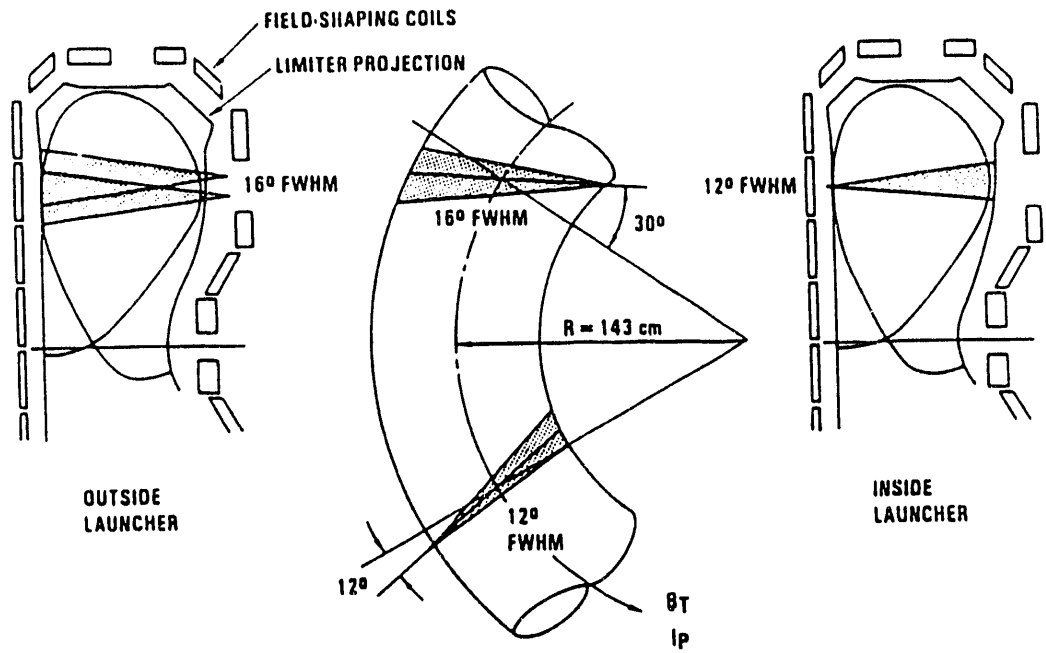


FIG. 1. ECH launcher geometry for Doublet III

level is decreased from 80 Torr-liters/sec to 0 at a time of 370 msec into the discharge, while in the discharge of Fig. 3 the gas injection is held constant at 66 Torr-liters/sec from 400 msec until the end of the discharge.

The behavior of the loop voltage for the two cases is about the same. The voltage drops from about 0.9 V prior to ECH to about 0.5 V during ECH. The loop voltage increase for a period of 20 msec at the start of the ECH pulse and the similar decrease at the end of the ECH pulse are due to plasma motion in the radial direction caused by the change in the plasma stored energy when the input power changes; similar behavior is found for neutral beam heating as well.

The behavior of the line-averaged density for the two discharges is quite different. In the poor heating case, Fig. 2b, the density decreases by 40% during the heating, while in the good heating case the density increases slightly during the heating. In Fig. 2b the density has not attained a steady-state condition at the time of the application of ECH, but clearly the heating causes a strong acceleration in the rate of decrease of the density. Density decrease during ECH has often been observed on experiments in tokamaks [1,5-8], and some conjectures have been put forward concerning cause [6,9], but a definitive study of the density drop has not been made.

The soft x-ray (SXR) emission behavior of the two shots is also quite different, Figs. 2c and 3c. The discharge of Fig. 2, like the other discharges of this study

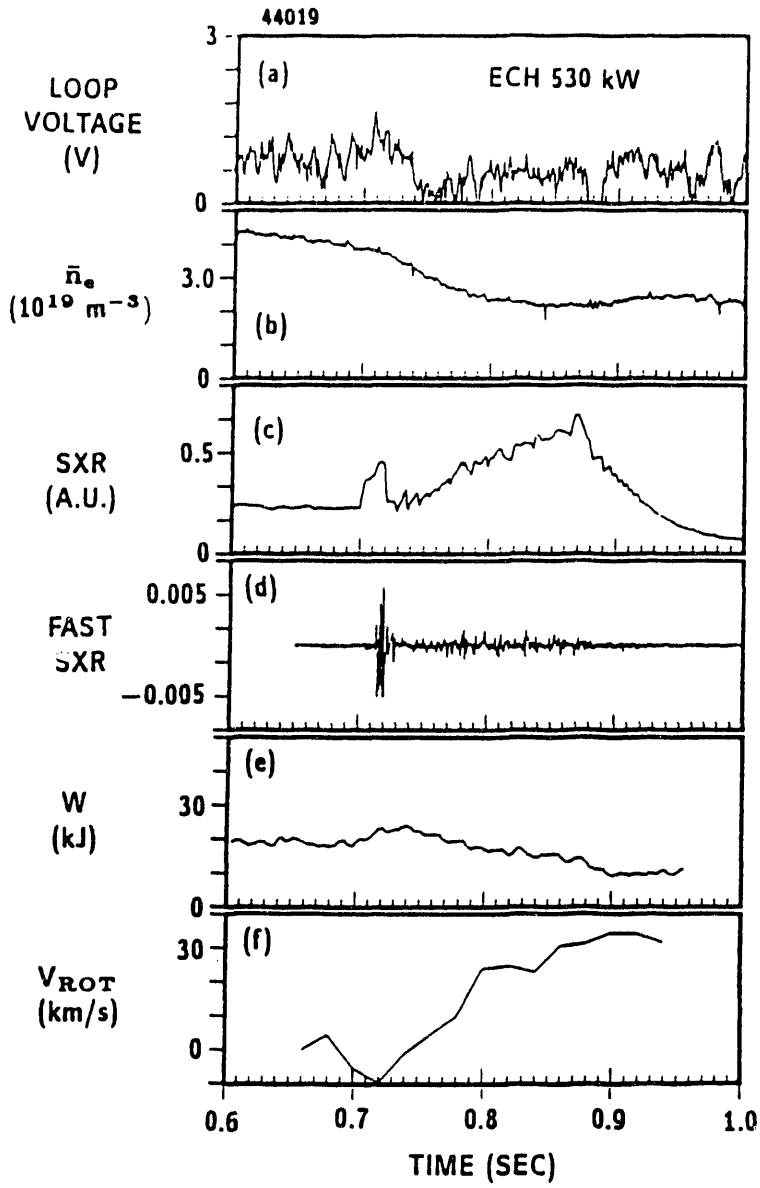


FIG. 2. Plasma behavior for a discharge with poor ECH heating efficiency. (a) Loop voltage and ECH power incident on the plasma; (b) plasma line-averaged electron density; (c) soft x-ray emission along a chord looking radially through the plasma center, with a bandwidth of d.c.-0.5 kHz; (d) SXR emission as measured by the same diode used in (c), but with a bandwidth of 1-50 kHz; (e) plasma energy; (f) rotational speed of plasma core, with positive rotation being in the direction of plasma current; as a function of time. Plasma current is 345 kA, toroidal field is 21.4 kG (parallel to $I_p$), and no deuterium gas is injected after 370 msec.

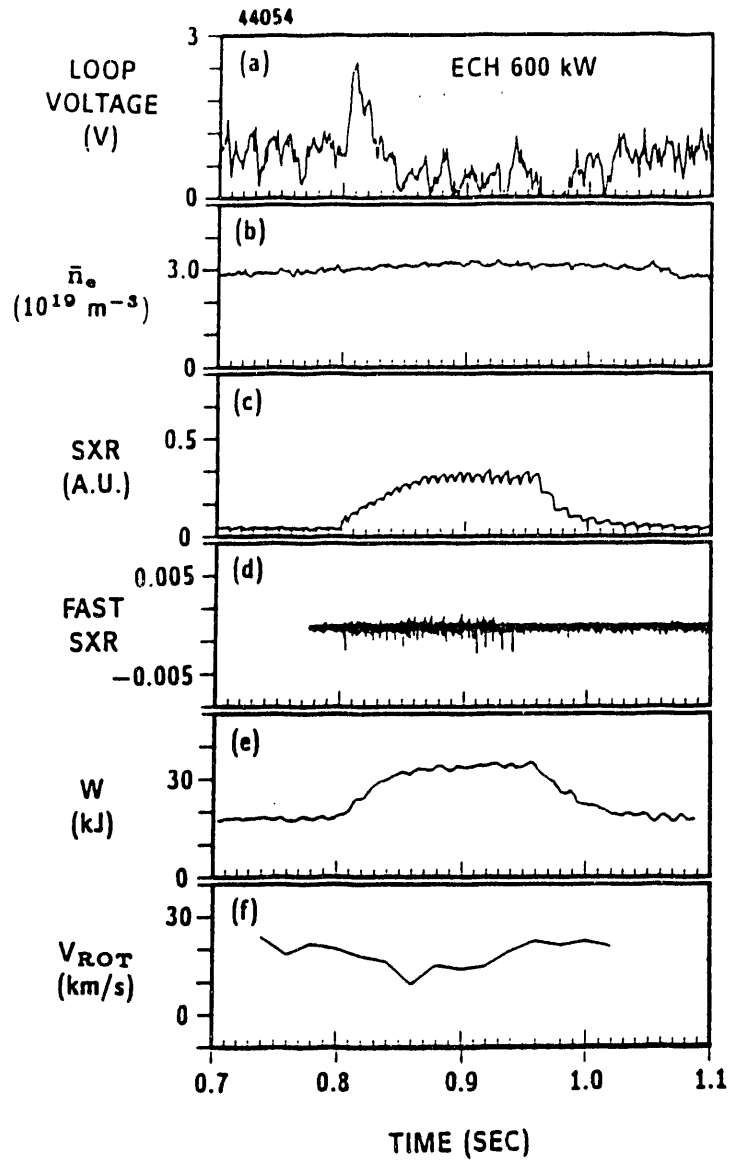


FIG. 3. Plasma behavior for a discharge with good ECH heating efficiency. Quantities plotted are the same as those of Fig. 2. Plasma current is 345 kA, toroidal field is 21.8 kG, and the deuterium gas injection level is 51 Torr-liters/sec.

with poor efficiency, is characterized during the ohmic phase by a relatively high level of SXR emission and a lack of sawteeth. At the inception of the heating the SXR emission level increases rapidly, but after 15 msec a burst of large amplitude m=1 oscillations occurs near the plasma center, as shown in Fig. 2d. The burst of

MHD activity coincides with the turnover in SXR emission. Following the burst, the SXR emission increases during the ECH pulse. In some discharges with poor heating efficiency, the plasma breaks into sawteeth during this phase of the discharge, but the behavior of the discharge is otherwise the same.

The burst of MHD activity also coincides with the turnover in the increase in plasma stored energy, Fig. 2e. Prior to the burst, the energy starts to increase at a rate close to that of a discharge with good heating efficiency, but after the burst it decreases gradually to a level lower than that at which it started.

The plasma rotation speed for the discharge with poor heating (Fig. 2f) starts near zero (stationary plasma) in the ohmic state, and then at the start of the ECH pulse it begins to rotate in the direction counter to the plasma current. After about 50 msec, following the burst of MHD activity near the plasma center, the plasma turns around and begins rotating in the same direction as the plasma current, ending up at a velocity near 25 km/sec, which is about a tenth of the ion sound speed. Following the end of the application of ECH, the plasma typically does not slow back down to its original state, but it continues to rotate.

The behavior of the SXR emission, plasma energy, and plasma rotation are quite different for the plasma with good heating efficiency, Fig. 3. The SXR emission starts out at a lower level in the ohmic phase, where it exhibits sawteeth (Fig. 3c). The sawteeth continue throughout and following the ECH pulse. The fast SXR emission, Fig. 3d, shows little activity other than the usual m=1 activity that immediately precedes the sawtooth fall. In all cases, this m=1 activity is much smaller in amplitude than the MHD activity that accompanies the start of ECH in a poor heating discharge.

The plasma energy increases during the ECH pulse to a new steady state with 70% higher energy content ($\Delta W$=16 kJ) than the initial ohmic state. Following the ECH, the plasma energy decays to its initial level. For the discharges with good heating, for which the data of Fig. 3 are typical, the behavior of the plasma energy is as expected for a plasma heating experiment.

The plasma rotation speed for the high heating efficiency case starts out in the ohmic phase at 20 km/sec in the direction of the plasma current, and during the ECH phase it slows somewhat to 10 km/sec, Fig. 3f. Following the ECH, the plasma returns to its original rotation speed. This behavior is quite distinct from that in the poor heating case. These rotation speed histories are quite characteristic of the two heating modes.

Data for a set of discharges taken over a period of two consecutive days are shown in Table 2. As mentioned earlier, these data have been selected for constant plasma current, centrally localized ECH power deposition, moderate plasma density, and availability of plasma rotation speed measurements. These data are plotted in Fig. 4 as a function of gas injection rate.

Table 2
Discharges used in this Study

| Shot No. | $I_p$ (kA) | $B_T$ (kG) | $P_{rf}$ (kW) | Gas (T-ℓ/s) | $\bar{n}_e$[a] ($10^{19}$ $m^{-3}$) | $V_{rot}$[b] (km/sec) | $V_{rot}$ History | ΔW (kJ) | $T_e(0)$[c] (keV) | Sawteeth[a] | m=1 Burst |
|---|---|---|---|---|---|---|---|---|---|---|---|
| 44005 | 344 | 21.4 | 530 | 0 | 3.4/1.9 | 0 | 2[d] | −0.8 | - | N/Y[f] | - |
| 44019 | 345 | 21.4 | 530 | 0 | 3.1/1.6 | 0 | 2 | 5.1 | 3.7 | N/N | Y |
| 44022 | 345 | 21.4 | 530 | 26 | - | 0 | 2 | 1.8 | - | N/N | N |
| 44027 | 345 | 21.4 | 530 | 21 | 3.7/2.5 | 0 | 2 | 3.0 | - | N/Y | Y |
| 44028 | 345 | 21.4 | 530 | 20 | 4.1/3.1 | 0 | 2 | 1.6 | 2.2 | N/Y | Y |
| 43983 | 345 | 21.4 | 520 | 66 | 3.6/3.6 | 23 | 3[e] | - | 1.25 | Y/Y | N |
| 44051 | 345 | 21.8 | 495 | 33 | 3.1/2.9 | 17 | 3 | 15.4 | 1.9 | Y/Y | N |
| 44054 | 345 | 21.8 | 600 | 51 | 3.2/3.7 | 24 | 3 | 16.1 | 1.6 | Y/Y | N |
| 44055 | 345 | 22.7 | 600 | 65 | 3.0/2.8 | 25 | 3 | 13.8 | 1.7 | Y/Y | N |
| 44056 | 344 | 22.7 | 600 | 65 | - | 25 | 3 | 8.4 | - | Y/Y | N |
| 44073 | 344 | 21.4 | 450 | 65 | 3.1/3.3 | 25 | 3 | 10.2 | 1.5 | Y/Y | N |
| 44145 | 346 | 21.4 | 550 | 65 | 3.5/3.8 | 26 | 3 | 18.7 | 1.3 | Y/Y | N |

[a] Before/during ECH.
[b] Before ECH.
[c] During ECH.
[d] $V_{rot}$ behavior is similar to Fig. 2f.
[e] $V_{rot}$ behavior is similar to Fig. 3f.
[f] "N" means no; "Y" means yes.

Figure 4a shows that, as before in the outside launch experiments, the initial plasma density is only very weakly dependent on the gas injection rate over the range 0 to 70 Torr-liters/sec, but that the final density attained during ECH is much more sensitive to the gas injection rate due to the large density drop found when the gas injection rate is low. Figure 4b shows that the relative density drop can be as large as 40% when ECH is applied and no gas is injected, and that for intermediate gas injection levels the density can actually increase 15% from the level during ohmic heating due to the effect of the ECH.

The maximum increase in central electron temperature as measured by Thomson scattering occurs at the lowest gas injection levels where the density drop is largest, Fig. 4c. Under these conditions, the central temperature increase is as large as 3 keV. At the higher gas injection rates, the increase in central electron temperature becomes much more modest, about 0.6 keV.

The plasma energy increase from the ohmic phase to the ECH phase shows a clear transition from poor heating efficiency below 30 Torr-liters/sec to high heating efficiency above that gas injection rate. The poor heating efficiency cases are characterized by nearly no net increase in plasma energy, while the energy increase is consistently about 15 kJ above the transition.

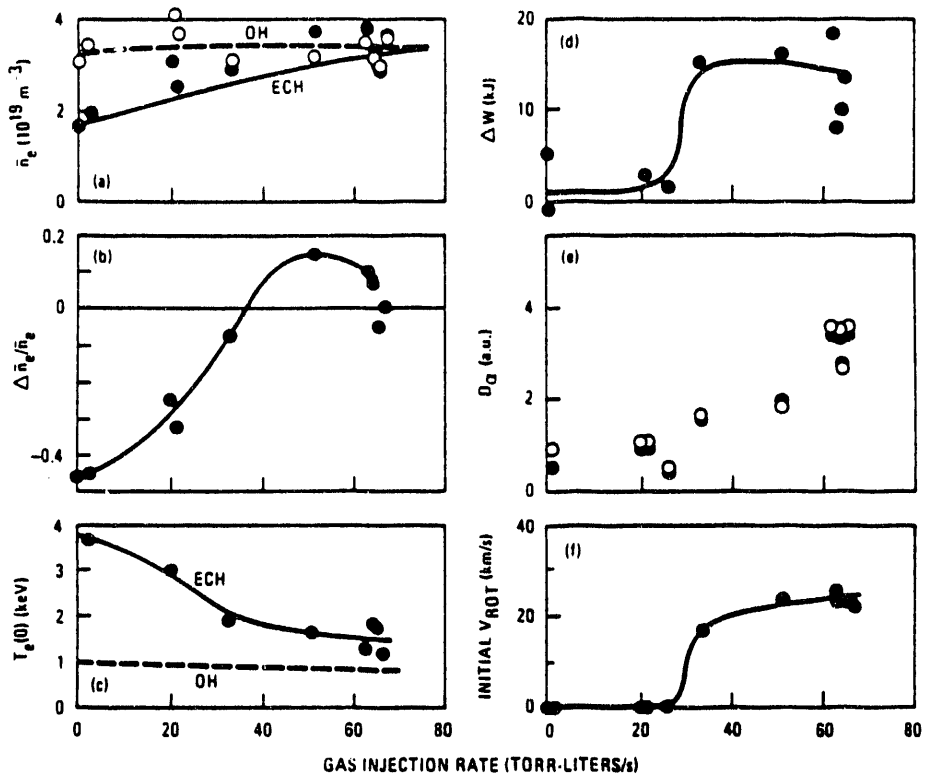


FIG. 4. (a) Plasma density before (o) and during ECH (•); (b) change in line-averaged density relative to initial density; (c) central electron temperature measured by Thomson scattering, before and during ECH; (d) change in plasma energy from before ECH to during ECH, where the plasma energy is an average of the energy change determined from analysis of diamagnetism and from MHD analysis; (e) $D_\alpha$ emission from the plasma, before ECH (o) and during ECH (•); and (f) plasma rotation velocity prior to application of ECH; as a function of the gas injection rate. The plasma current is 345 kA and the toroidal field is 21.4 kG.

In the earlier outside launch experiments, the behavior of the $D_\alpha$ emission at the start of the ECH pulse was found to be predictive of the heating efficiency [1]. It was found that for those discharges for which the $D_\alpha$ emission dropped upon application of ECH, the heating efficiency would be high, and conversely. For the discharges of this study, the $D_\alpha$ emission was found to vary very little from the ohmic phase to the ECH phase irrespective of the heating efficiency. This behavior is shown in Fig. 4e.

The behavior of the plasma rotation during the ohmic phase immediately preceding the application of ECH, Fig. 4f, follows the same pattern as the plasma energy. Figures 4d and 4f show a clear correlation of heating effectiveness with initial rotation velocity, since the discharges without initial rotation are characterized by little increase in plasma energy, while the discharges which are co-rotating prior to the ECH experience energy increases of 15 kJ.

## Discussion

The correlation between $\Delta W$ with ECH and the initial state of the plasma prior to ECH is striking. It is clear from Table 2 and Fig. 4 that the relative heating effectiveness is determined by the plasma conditions prior to application of the ECH. What is unclear from this data set is whether the plasma rotation or the presence of sawteeth is the deciding condition, since all rotating discharges in Table 2 also have sawteeth before ECH.

The discharges presented in Table 2 include all the discharges in the Doublet III ECH data bank for which the plasma rotation has been analyzed and for which the plasma parameters lie within the bounds shown in Table 1. It is possible that further analysis of other discharges will distinguish the factor which determines the relative heating efficiency. For example, discharge #44004, which was described in some detail in previous publications [10,11] as representative of discharges with good heating, does not exhibit sawteeth prior to application of ECH. After about 50 msec of ECH, it breaks into sawtooth activity. For this discharge, the plasma energy determined from analysis of plasma diamagnetism rises from an initial value of 31 kJ to 45 kJ during the ECH with a waveform very similar to that of Fig. 3e. This data shows that discharges without sawteeth in the ohmic phase may still have good relative heating efficiency. The rotation velocity of this discharge has not yet been determined.

The role of the m=1 burst in the development of the discharges with poor heating efficiency seems to be to cause expulsion of the high-Z impurities from the plasma core. Expulsion of high-Z impurities is indicated in discharges like that of Fig. 2 since the SXR emission dramatically falls immediately after the burst, and the vacuum ultra-violet spectrometer typically shows a decrease in the emission from the usual high-Z impurities like Ti and Ni correlated with the drop in SXR emission during the first 30 to 50 msec of the ECH pulse. This effect takes place whether or not sawtooth activity follows the m=1 burst.

In the poor heating discharges which do not experience the m=1 burst, such as discharge #44022 in Table 2, the VUV does not indicate any change in impurity radiation following the start of the ECH. The SXR emission increases to relatively large levels during the ECH, but following the ECH the SXR emission decays only to the level at which it started; this behavior may be distinguished from that of discharges of either Fig. 2, for which the SXR emission decays to a level much lower

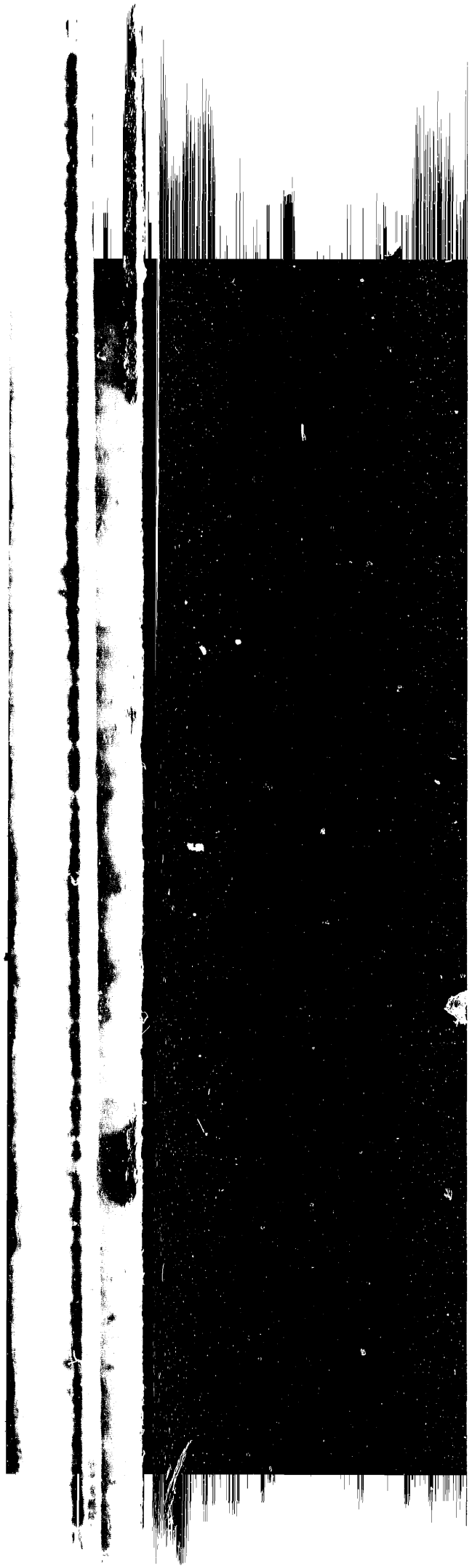

than that at which it began, or Fig. 3, for which the sawtoothing SXR emission starts out at a low level initially. Discharges which are sawtoothing prior to the application of ECH are already low in high-Z impurities, and these discharges tend to have high heating efficiency.

For all the discharges of Table 2 which have high heating efficiency, the plasma is rotating in the direction of plasma current with a velocity of a few tens of km/sec, of order a tenth the ion sound speed, prior to ECH. Application of ECH causes a slight drop in the rotation speed. Co-rotation corresponds to a positive charging of the plasma with a resultant toroidal drift velocity $\mathbf{E_r} \times \mathbf{B_p}$. For all discharges of Table 2 which have poor heating efficiency, the plasma is nearly stationary prior to ECH, and application of ECH results in a rapidly co-rotating plasma which does not slow back down to its original nonrotating state at the end of the ECH. With regard to rotation, the final state of the poor heating discharge is quite similar to the initial state of the good heating discharge.

Recent previous studies of plasma rotation in tokamaks have been performed using neutral beam heating [12-14], for which the introduction of external momentum is large in comparison to that from ECH. The plasma rotation induced by neutral beam injection is found to be larger for tokamaks with toroidally symmetric divertors than for tokamaks with asymmetric material limiters [14], perhaps because the rotation is not required to vanish at the separatrix. For tangential neutral beam injection at power levels of order 1 MW, rotational speeds were found of a factor 10 larger than observed in these ECH experiments. Any correlation between rotation of the plasma core and electron transport (which is the dominant loss channel in the Doublet III ECH experiments) has not been identified in the PDX neutral beam injection experiments [14], even though toroidal rotation in the ohmic heating discharges was divided into two categories, one with rotation speed below 3 km/sec and one with rotation speed about 10 km/sec.

## Summary

High heating efficiency using ECH in divertor discharges in Doublet III is correlated with the presence of sawteeth and with co-rotation of the plasma prior to the heating. Sawteeth are important for reducing levels of high-Z impurities in the plasma, but the burst of m=1 activity which usually accompanies the start of ECH in plasmas without sawteeth is also effective in reducing the level of high-Z impurities, whether or not it is followed by sawteeth. However, good confinement is not restored by either the expulsion of the impurities or by the generation of sawteeth following the m=1 burst. Some discharges without sawteeth in the ohmic phase still have good heating efficiency. Plasma rotation prior to ECH is correlated with good heating efficiency, but discharges with both good and poor heating efficiency end up with the same rotation velocity. These results are summarized in Table 3.

Table 3
Summary of Results

| | Good | | Poor |
|---|---|---|---|
| | Table 2 | #44004 | Table 2 |
| Initial rotation | Y | ? | N |
| Initial sawteeth | Y | N | N |
| Initial High-$Z$ | N | Y | Y |
| Density drop | N | N | Y |
| Final rotation | Y | ? | Y |
| m=1 Burst | N | ? | Y N |
| Final sawteeth | Y | Y | Y/N N |
| Final high-$Z$ | N | N | Y |

## References


1. R. Prater, S. Ejima, S. H. Lin, C. P. Moeller, J. Y. Hsu, K. Matsuda, and R. Stockdale, in Proc. 4th Internat. Symposium on Heating in Toroidal Plasmas, Roma (Internat. School of Plasma Physics, Varenna, 1984), v. II, p. 763.
2. N. Ohyabu, K. H. Burrell, J. DeBoo, S. Ejima, R. Groebner, et al., Nucl. Fusion **25**, 49 (1985).
3. A. H. Kritz, H. Hsuan, R. C. Goldfinger, D. B. Batchelor, Proc. 3rd Joint Varenna-Grenoble Internat. Symposium on Heating in Toroidal Plasmas, Grenoble (Euratom roport EUR7979 EN, 1982), v. II, p. 707.
4. A. J. Lieber, S. S. Wojtowicz, and K. H. Burrell, "Single Shot Time Resolved Crystal X-Ray Spectrometer," *Nuclear Instruments and Methods*, in press.
5. R. M. Gilgenbach, M. E. Read, K. E. Hackett, R. Lucey, B. Hui, et al., Phys. Rev. Letters **44**, 647 (1980).
6. R. J. LaHaye, C. P. Moeller, A. Funahashi, T. Yamamoto, K. Hoshino, et al., Nucl. Fusion **21**, 1425 (1981).
7. D. C. Robinson, M. W. Alcock, N. R. Ainsworth, B. Lloyd, and A. W. Morris, Proc. 3rd Joint Varenna-Grenoble Internat. Symposium on Heating in Toroidal Plasmas, Grenoble (Euratom report EUR7979 EN, 1982), v. II, p. 647.
8. V. V. Alikaev et al., Fiz. Plasmy **2**, 390 (1976) [Sov. J. Plasma Phys. **2**, 212 (1976)].
9. J. Y. Hsu, et al., GA Technologies Report GA-A17386 (1983).
10. R. Prater, K. H. Burrell, S. Ejima, G. L. Jahns, S. H. Lin, et al., GA Technologies report GA-A17939 (1985).
11. R. Prater, GA Technologies report GA-A18149 (1985); to be published in the

Proceedings of the Course and Workshop on Application of RF Waves to Tokamak Plasmas, Varenna, Italy, 1985.
12. S. Suckewer, H.P. Eubank, R.J. Goldston, E. Hinnov, N.R. Sauthoff, Phys. Rev. Lett. **43**, 207 (1979).
13. R.C. Isler, L.E. Murray, Appl. Phys. Lett. **42**, 355 (1983).
14. K. Brau, M. Bitter, R.J. Goldston, D. Manos, K. McGuire, S. Suckewer, Nucl. Fusion **23**, 1643 (1983).

# The 2 MW ECRH System for COMPASS

A.C. Riviere, M.W. Alcock, A.N. Dellis, M. Hughes,
M. O'Brien, D.C. Robinson, and T.N. Todd
*UKAEA/Euratom Fusion Association*
*Culham Laboratory, Abingdon, Oxon, OX14 3DB, UK*

## INTRODUCTION

The new tokamak COMPASS[1] (R = 0.56m, a = 0.23m, b = 0.38m, B =2.1T, $I_p$ = 400 kA) now being constructed at Culham is designed to study and optimise the MHD behaviour of the tokamak configuration in both circular and non-circular cross sections. Additional heating and profile control for this experiment will be provided by an ECRH system with a power of 2 MW at 60 GHz and a pulse length at full power of 5 sec. The experiments will study the active control of disruptive instabilities (by helical external windings which resonate with specific rational q surfaces and by profile modification), operation at low q (< 2), optimisation of $\beta$ in various non-circular plasmas and long pulse ECRH current drive. The localised and efficient nature of ECRH make it ideally suited to these studies. In the case of bulk current drive, calculations indicate that a plasma current of 300 kA might be driven with the full rf power[2]. Low field side (LFS) launch of the X-mode for heating and current drive at the second harmonic will be used initially for optimisation of the plasma at high $\beta$, but high field side (HFS) launch of the X-mode for heating and current drive at the fundamental resonance will be used to access higher plasma densities and allow for example density limit studies in non-circular plasmas.

Some of the 2MW of power will be available before COMPASS is completed and will be used for experiments in the DITE tokamak (R=1.17m, a=0.26m, B = 2.1T, Ip $\lesssim$ 200kA). The ECRH physics programme in this case will be directed at trying to improve the energy confinement during neutral beam heating and at studies of the density limit. This work will start with HFS antennae to access the widest possible range of densities.

## PHYSICS PROGRAMME

The results to be expected with ECRH in COMPASS have been studied by a ray tracing [3], 1 and 1½ D diffusion and stability codes. The calculations show that quite modest rf powers (<0.5MW) can be used for effective profile

control. At the highest rf powers it should be possible to reach plasma $\beta$ values at least as high as the maximum presently achieved. The limit can be written as[4]

$$\bar{\beta}_{max} \simeq \frac{2.8\ Ip\ (MA)}{a(m)\ B(T)}\ \%$$

for an INTOR-like plasma shape and where a(m) is the horizontal minor radius. At the appropriate electron density for ECRH at $2\omega_{ce}$, $\bar{T}e \simeq 5$ KeV is required to reach $\bar{\beta}_{max}$ for Ip = 0.3MA. At such temperatures the plasma conductivity is high and the current distribution is frozen in. The time constant for the current profile to reach equilibrium ($\delta E_\phi/\delta r = 0$) assuming classical resistivity is given by ($Z_{eff}$=1)

$$\tau_{L/R}(sec) \simeq 4.10^{-4}\ \ell_i\ a(m)^2\ \bar{T}e(ev)^{3/2}$$

For $\bar{T}e \simeq 5$ KeV this gives $\tau_{L/R} \simeq 8$s. If the heat deposition and pressure profiles are such that the current profile, j(r), is not changed by the heating there will of course be no current redistribution delay in reaching the final equilibrium. In general the experiments will be concerned with optimising j(r) for stability at high Ip, $\beta$ or $\bar{n}_e$ and the final distribution will differ significantly from the initial one.

To speed up the approach to equilibrium a two stage heating scenario may be used whereby a low power initial heating phase establishes a j(r) close to that finally required. The temperature remains low and resistivity high so the required profile is quickly formed. The full heating power with appropriate spatial distribution is then applied. Results from computer modelling of this scenario are shown in Figure 1 for heating a D shaped plasma with inside launch in COMPASS at $\omega_{ce}$. The initial tailoring of the profile is very successful, q(o) adjusting to ~ 1.8 in 100 ms, which is close to the final value. From 0.1s to 1s there is almost no change in q(o) though there is a substantial change in the electric field profile with $E_{\phi(wall)}/E_{\phi(axis)}$ decreasing from 3 to about unity in 1s. Figure 2 shows the evolution of the plasma with two stage heating from the LFS at $2\omega_{ce}$. Although equilbrium is not fully reached by t = 1 sec in this case, the time scale could be shortened further by delaying the main heating phase beyond the t = 100 ms chosen or by adjustment of the heating profile. In the case shown $\bar{\beta}$ of 6% is reached with $P_{rf}$ = 1.6MW and a section of the pressure profile exceeds the local ballooning mode limit.

In the case of the DITE experiment ECRH will be applied in conjunction with neutral beam heating (NBH). The beam energy, $E_b$, is 27 KeV and four beam lines provide tangential injection in a common direction with a total power

of up to 2 MW. During the slowing down of the fast ions, energy is transferred preferentially to the thermal ions or electrons according to whether Te is above or below the value given by [5]

$$Te(keV) = \frac{E_b(keV)}{30} \left(\frac{A_{th}^{2/3}}{A_f}\right)$$

The critical Te for DITE is therefore approximately 1.4 KeV for an H beam into a D plasma. Thus independent control of Te by ECRH can control the sharing of beam power between the two plasma components and may also provide the unusual condition Te > Ti during NBH. In addition profile control can be used to stabilise modes enhanced by the beam deposition profile. The results obtained in DIII [6] and in FT1 [7] show that with HFS launch quite efficient heating is possible at or even above the X-mode cut off density ($8.8 \times 10^{19}$ $m^{-3}$ for 60 GHz). Since high electron densities ensure rapid energy transfer from beam ions and negligible charge exchange losses, HFS launch provides an attractive advantage over LFS launch when using NBH. For the first DITE experiments HFS antennae will be installed. Power deposition profiles predicted by the ray tracing code for HFS launch (see Fig 5) in DITE are shown in Figure 3 for several values of line average density. Good central heating is found for a wide range of densities even without the extension of efficient heating to higher densities observed in the DIII and FT1 experiments.

## THE RF POWER SYSTEM

The 2MW of microwave power is to be provided by 10 gyrotrons installed in two groups close to the COMPASS experiment. The location is also close to the DITE experiment so that waveguides are readily connected to either facility. Two regulator units will switch the supply on and off to their respective banks of gyrotrons, stabilise the voltage levels and act as protection switches. The control-anode voltage for each gyrotron is separately stabilised to a preset value or to a value which can be programmed to provide a given time sequence of power levels to the plasma. Direct feedback control of the output power from particular gyrotrons - corresponding to particular antennae and therefore heating locations - will be possible using suitably processed diagnostic signals to control the anode voltages.

As discussed above heating or current drive will have to be maintained for several seconds in some cases to allow sufficient time for equilibrium to be established. Gyrotrons with a pulse length capability of 5 sec will be used, equal to the toroidal field pulse length. The evolution of the current profile and the electron velocity distribution over these long periods together with the development and control of the MHD activity will be of central interest.

## THE WAVEGUIDE SYSTEM

The average distance from gyrotron to plasma is ~ 40 m and for most of this the power will be transmitted in the low loss $TE_{01}$ mode. Because of the $O_2$ absorption peak at 60 GHz the atmosphere in the guides will be purged with $N_2$. The sequence of components in a typical transmission line is shown schematically in Figure 4.

At the gyrotron output window more than 95 per cent of the power will be in the $TE_{02}$ mode in circular guide with a diameter of 63.5 mm. Conversion from $TE_{02}$ to $TE_{01}$ is readily achieved by sinusoidally modulating the guide diameter with a period equal to their beat wavelength. To keep the length of this and other mode converters and the arc length of bends short, the waveguide diameter is reduced to 30 mm by using an optimised non-linear taper [8] above the gyrotron. A resistive-wall mode filter is used to damp out trapped modes between this taper and the up-taper within the gyrotron at the output of the cavity.

A number of waveguide bends are needed in each transmission line. Since the need for low loss requires the use of greatly oversized waveguide these bends are designed to minimise mode conversion using corrugated-wall waveguide [8,9]. The arc lengths in 30 mm diameter waveguide are 1.5 m and 2.6 m for the $TE_{02}$ and $TE_{01}$ modes respectively at 60 GHz. The corrugation depth is 0.6 mm with a 1:1 mark-space ratio, corresponding to an electrical depth of ~ $\lambda/14$.

The $TE_{02}$ to $TE_{01}$ 6-beat-period converter and the $TE_{01}$ to $TE_{11}$ 10-beat-period converter have theoretical efficiencies of 98 and 95 per cent respectively including resistive losses, figures which are consistent with low power measurements. Although the $TE_{11}$ mode possesses the linear polarization required for launching, the low-mode-conversion compact bends needed close to the COMPASS and DITE machines are not feasible with this mode. The problem is overcome by further converting the $TE_{11}$ mode to the hybrid $HE_{11}$ mode which propagates in corrugated waveguide. The length of the $TE_{11}$ to $HE_{11}$ converter is 0.22 m, consisting of a straight section of 30 mm diameter corrugated circular waveguide in which the corrugation depth varies smoothly from $\lambda/2$ at the input to $\lambda/4$ at the output. The subsequent $HE_{11}$ waveguide has a corrugation depth of $\lambda/4$. Bends in this 30mm diameter corrugated guide for $HE_{11}$ mode near COMPASS will have angles of 70°, 90° and 110° to match the port angles. With a central curvature radius of 30cm a mode conversion power loss below 1% is predicted from the theory of Doane[10]. Low power tests of an $HE_{11}$ bend showed less than one per cent power loss to be achieved in practice.

The attenuation due to bends, converters and mode filters is expected to be ~ 17% with an additional 7% in the straight waveguide sections. The overall transmission is thus about 75% so that 1.5MW should be available for plasma heating.

Where space permits the vacuum-barrier windows will be commercial units with a diameter of 63.5mm but in the case of HFS launch it is necessary to use a smaller diameter. Present plans are to use single silica discs 38 mm in diameter mounted as shown in Fig.5 for DITE and to cool these between pulses with nitrogen gas. A similar approach was used successfully on D III [11] for pulse lengths up to 0.5s. Window designs suitable for longer pulses are being developed.

The arrangement of ports available for installing antennae on the D shaped vessel in COMPASS is shown in Figure 6. It can be seen that by launching some power on the mid-plane and some at a distance off-axis it will be possible to perform central and off-axis heating simultaneously with a common gyrotron frequency. Additional flexibility can be provided using angled launch in some cases.

## SUMMARY

A 2MW system for ECRH experiments on the COMPASS and DITE tokamaks is described. The facility will allow a wide range of plasma control studies to be carried out up to the operating limits in I , $\beta$ and $\bar{n}_e$.

## REFERENCES

[1] D V Bayes et al, 11th Symp of Fusion Engineering at Austin, Texas, 18-22 Nov 1985.

[2] M R O'Brien, M Cox and D F H Start, Proc 12 Eur Conf on Cont Fus and Plasma Phys, Budapest, 1985, Vol II, p 76 (1985)

[3] T Edlington et al, 3rd Varenna-Grenoble Symp on Heating in Toroidal Plasmas, III (1982) 869

[4] F Troyon et al, Plasma Phys and Controlled Fusion (1984) 209

[5] J G Cordey, Phys of Plasmas Close to Thermonulcear conds, Varenna, I (1979) 359

[6] K H Burrell et al, 10th IAEA Conf Plasma Physics and Controlled Nuc Fus, London, I(1985) 131

[7] Yu F Baranov et al, Sov J Plasma Physics 8 (1962) 383

[8] M Thumm et al, Proc 3rd ECRH Trans System Workshop, US Dept of Energy (1983) 220

[9] C P Moeller, 3rd Varenna-Grenoble Int Symp on Heating in Toroidal Plasmas, III (1982) 1085

[10] J L Doane, IEEE Trans Microwave Theory and Techniques MTT-32 (1984) 1362

[11] R Prater et al, 4th Varenna-Grenoble Int Symp on Heating in Toroidal Plasmas II (1984) 1454

Fig 1

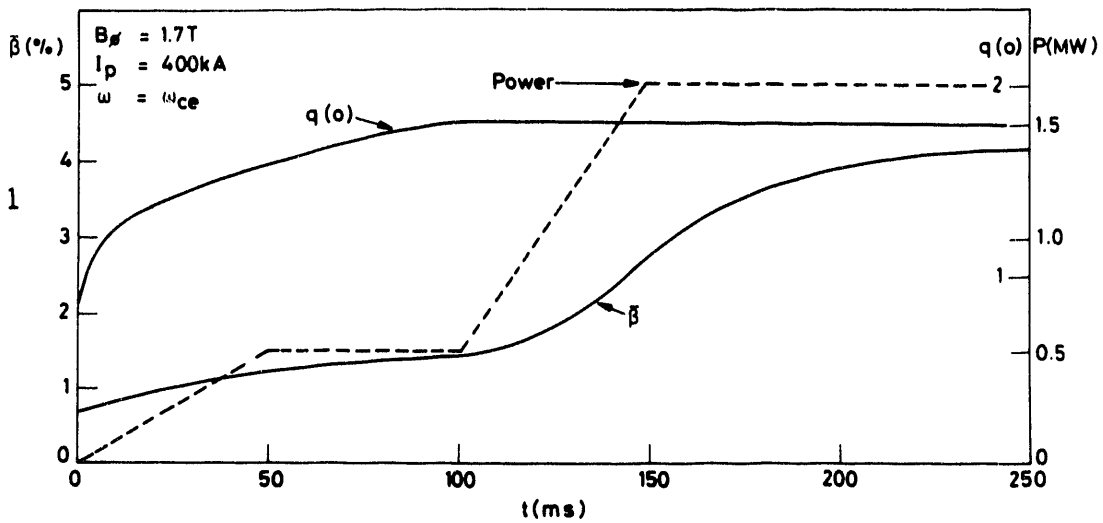


Fig 2 (a)

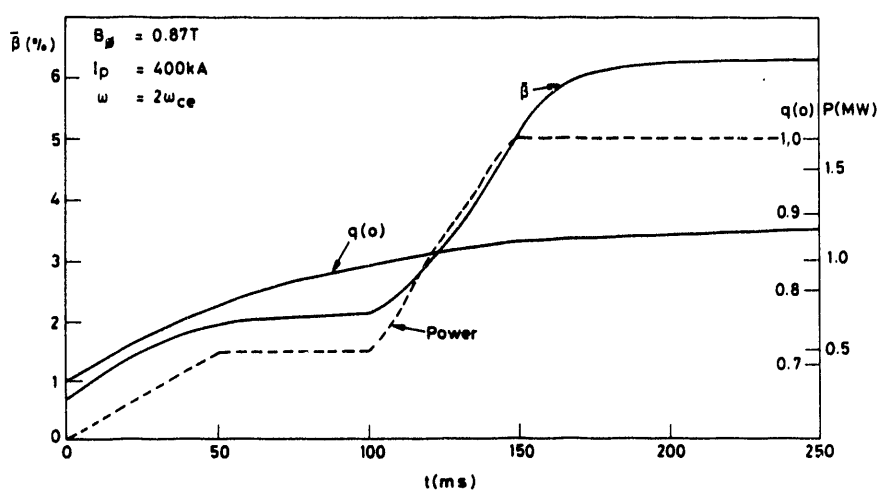


Fig 2 (b)

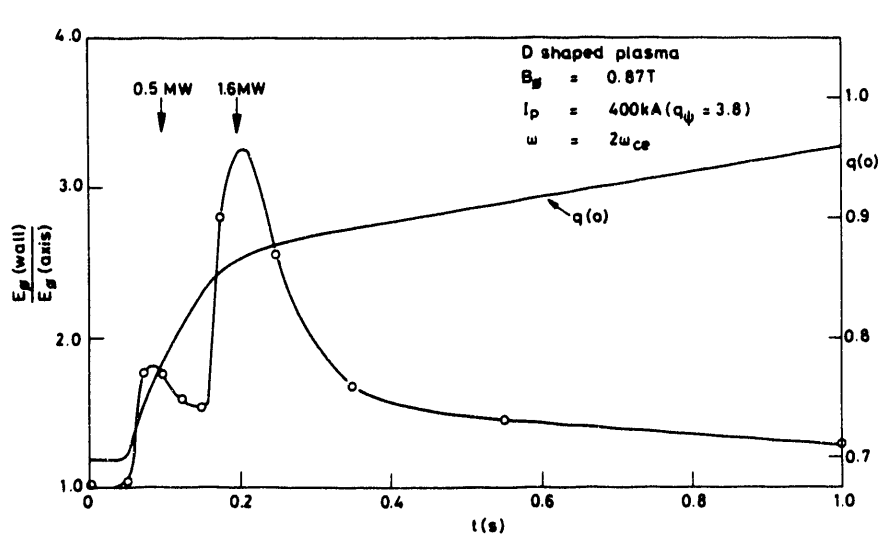


Results from model calculations for two-stage heating in COMPASS

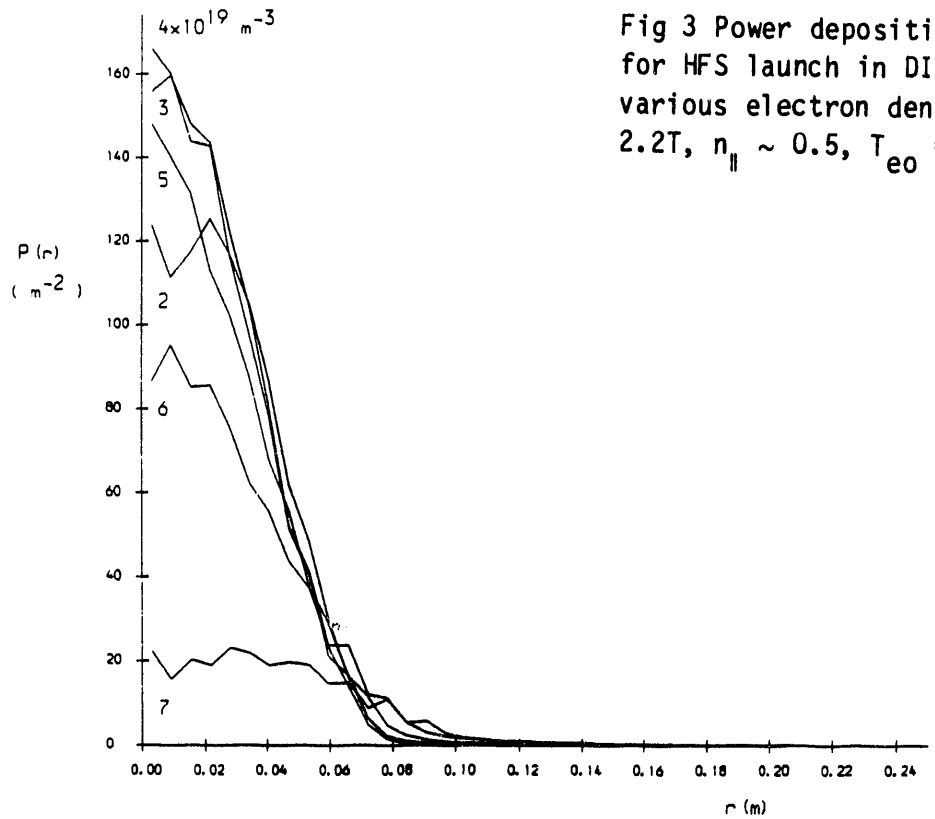


Fig 3 Power deposition profile for HFS launch in DITE for various electron densities (B = 2.2T, $n_{\parallel} \sim 0.5$, $T_{eo}$ = 1 keV).

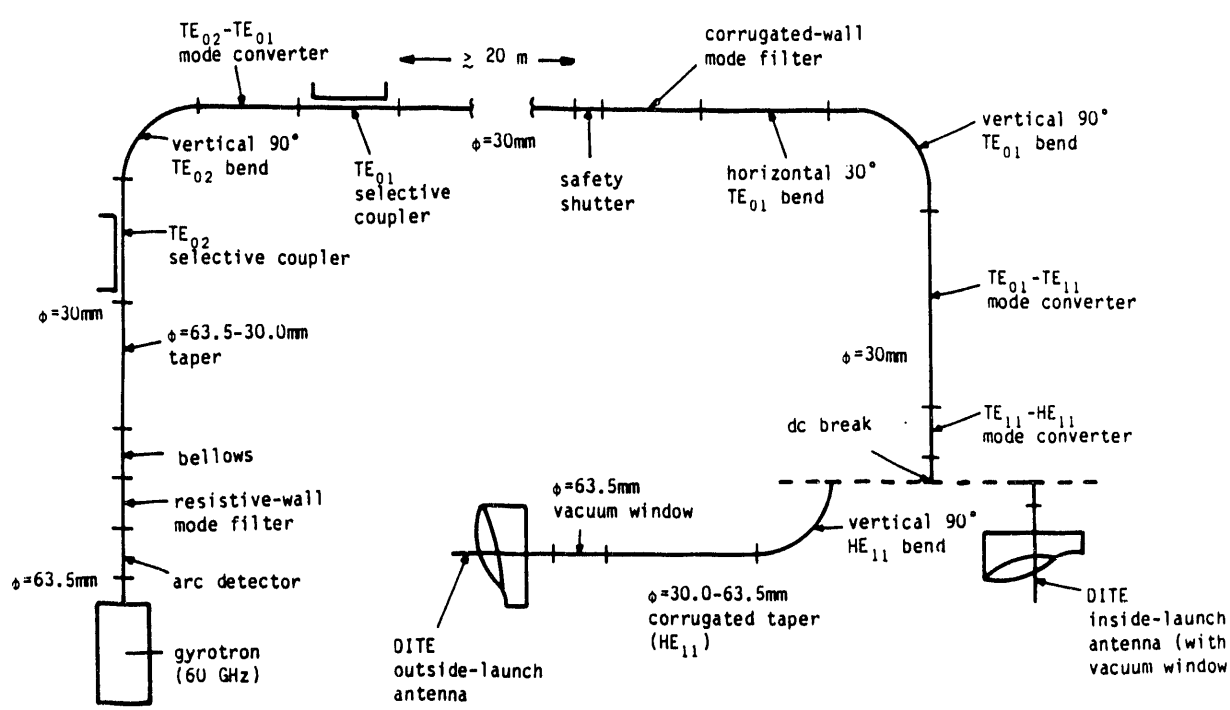


Fig 4 ECRH Waveguide Run for DITE

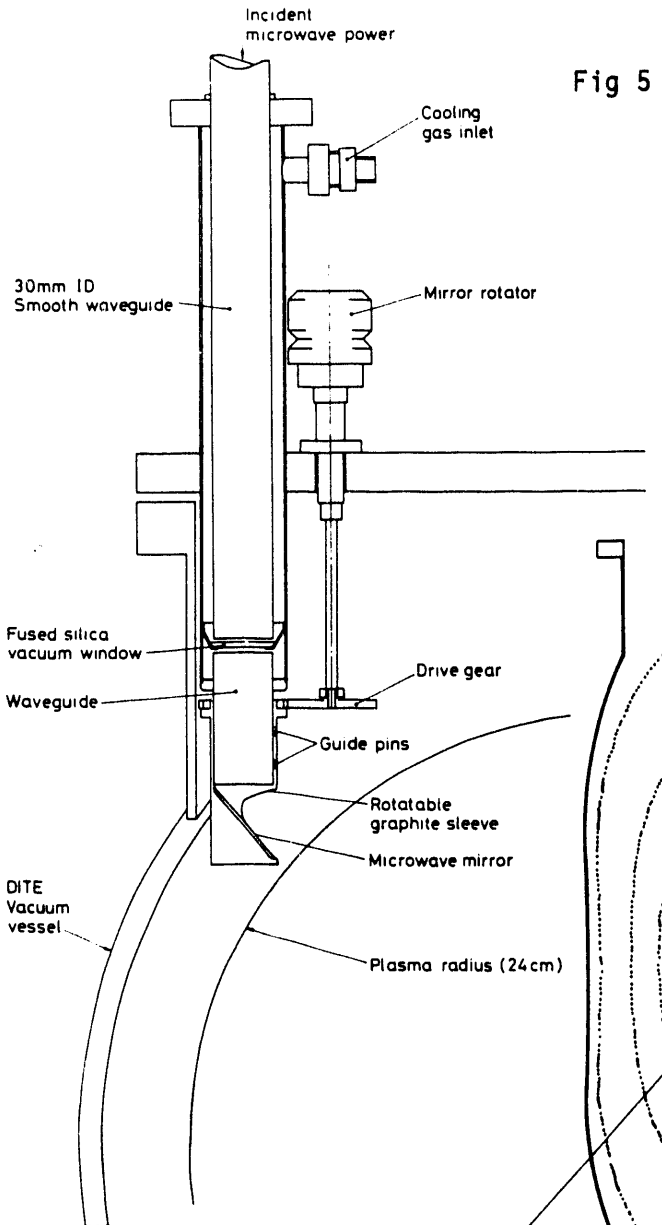


Fig 5 HFS Antenna design for DITE

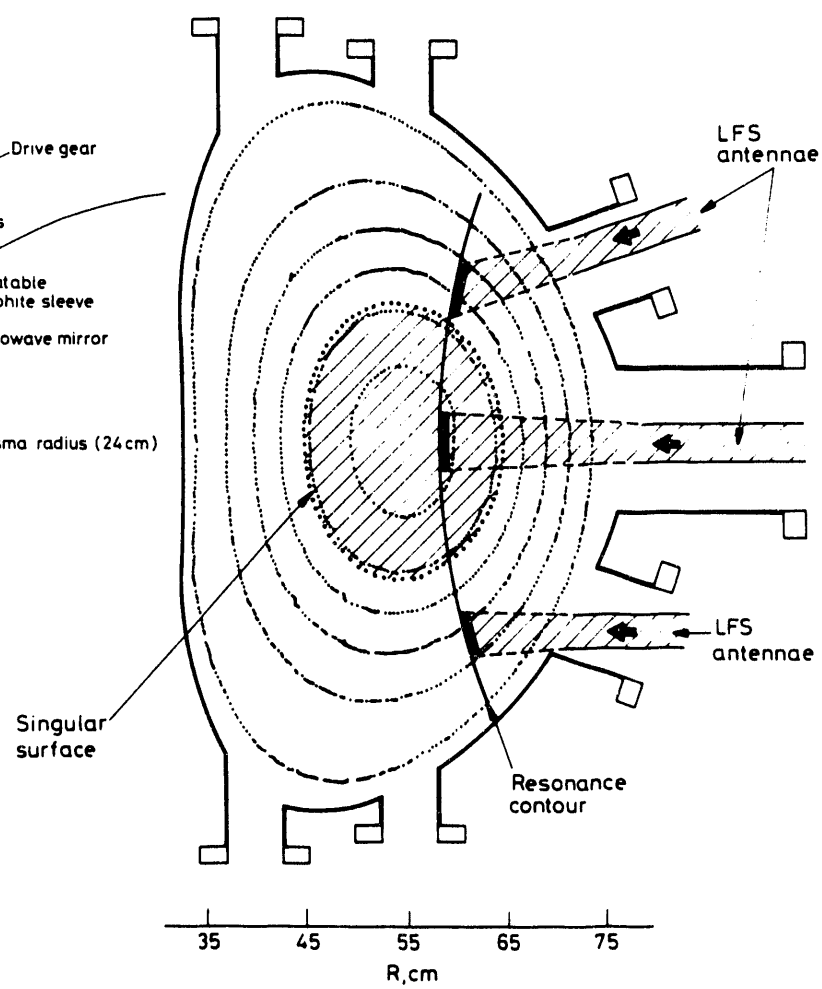


Fig 6 An example of the multiple heating zones simultaneously available in COMPASS

# Proposed Fundamental Heating on the TARA Tandem Mirror*

W.C. Guss, M.E. Manuel, R. Myer, and D.K. Smith
*MIT Plasma Fusion Center, Cambridge, Massachusetts 02139, USA*

Abstract

From experiments completed in the fall of 1984, the absorption efficiency for heating at the fundamental resonance in the plug was found to be rather low ($\lesssim$5%) and low hot electron fraction ($\lesssim$10%). The unpolarized and unfocused microwave radiation was launched from the high field side of the resonance surface. We are proposing a system for launching polarized and focused radiation from the low field side with an option for changing the polarization and launching from the high field side. A comparison of ordinary and extraordinary mode heating is then possible.

Introduction

The concept of tandem mirrors is based on the electrostatic plugging of end losses from the center cell where the plasma is magnetically confined. A positive potential of sufficient magnitude in the end cells (also called axicells) will reflect ions lost from the center cell. In tandem mirrors this potential is generated at the outer plug magnetic field gradient by heating electrons with ECRH at the fundamental to high perpendicular energy and generating a charge separation. Cold electrons also tend to accumulate at the location of the plug potential and must be continuously heated to remove them. One consideration in the viability of mirror reactors is the efficiency of this heating.

Two other considerations are the generation of low cavity power and small $k_{||}$ for the incident radiation. Cavity power can produce low density runaway electrons outside the bulk plasma. This represents a loss of temperature control of the bulk electrons, and the resulting absorption and refraction can further reduce the heating efficiency. Small $k_{||}$ is desired so that spatially localized heating of cold electrons trapped in the plug potential is maintained.

Our previous experience with unfocused and unpolarized Vlasov antennas is that they provide relatively inefficient coupling ($\lesssim$5%) to the plasma. Space restraints prevent the addition of the curved reflector which would localize the radiation and increase the power density. The geometry of the plug suggests launching the microwaves from larger radius at the resonant magnetic field surface.

## Present System

The present fundamental and second harmonic launching systems are shown in Fig. 1. The fundamental heating microwaves are launched from between the split high field coils at the anchor (outer) plug mirror peak. The antenna produces a radiation pattern that is polarized in a half cone shape so that the direction of polarization is not constant along the conical circumference. After bouncing off the vacuum chamber walls both polarizations are expected to be of equal magnitude. Measurements indicate that the aperature of the vacuum manifold leading to the plug chamber is roughly uniformly filled with microwave power. By adding a reflector as shown on the second harmonic antenna, the radiation pattern would become linearly polarized and focused. Unfortunately, the proximity of the plasma to the fundamental antenna prohibits its use. The present system is inefficient in that the plasma does not fill the aperature to the vacuum manifold containing the antenna and that only half the power is in the polarization (x-mode) which would allow absorption at the fundamental resonance.

## Proposed System

The efficiency of the present system could be improved by polarizing and focusing the microwaves, however a new location for the launch point is required. One possibility is perpendicular to the plasma column near the end of the axicell chamber. The behavior of waves launched perpendicularly varies with the mode. In particular, x-mode waves with initial $k_{||} = 0$ change as they approach the resonance zone. Refractive effects cause the propagation vector to approach the resonance zone nearer the normal so a finite $k_{||}$ results. During a discharge, the magnitude of this plasma effect would have the time dependence of the density and would not be controlled. The o-mode does not suffer from this problem. On the other hand, the absorption of this mode is generally smaller. For the finite density regime and quasi-perpendicular propogation in a uniform plasma one finds[1] for a uniform magnetized plasma

$$\frac{\alpha_1^0}{\alpha_1^x} = \frac{1}{4}\,\frac{\omega_p^4}{\omega_c^4}\,\frac{1}{\cos^2\theta}\,\frac{1}{\left(1-\frac{\omega_p^2}{\omega_c^2}\right)^2\left(1+\frac{\omega_p^2}{\omega_c^2}\right)}$$

where $\alpha$ is the attenuation coefficient and $\omega_p$ and $\omega_c$ are the electron plasma and cyclotron frequencies. The angle $\theta$ is the direction cosine of k relative to B. For some plasma conditions ($\omega_p \lesssim \omega_c$) and some angles of incidence ($\sim\pi/2$) the absorption for the two modes is comparable. The actual experiment however, is not well modeled by these equations because of magnetic and density gradients. Predictions of actual wave behavior require a ray tracing code.

*Supported by the U.S. Department of Energy under contract DE-AC0Z-78T51013.

The ray tracing code used for this purpose (NRAY) is a three dimensional geometric optics code based upon a modified cold plasma dispersion relationship to include two electron populations. Relativistic effects are included through the mass term. Finite Larmor radius effects are also included to model effects at the harmonics. The plasma parameters used in our absorption study correspond to those anticipated when both neutral beams and ECRH are applied to the axicell plasma. A hot electron temperature of 30 keV and fraction of 5% were assumed for all the cases of cold plasma temperature and density. The code gives the power absorbed in a cylindrical valume $r < 7$ cm with an axial extent of 10 cm on either side of the resonant surface. In the vicinity of the fundamental resonance surface the plasma radius is about 10 cm. At the edge of the plasma the beam diameter was taken to be 5 cm and at the machine axis 2 cm. A comparison of the x and o mode absorption for several different launch points is shown in Fig. 3 and 4. The o-mode is comparable in its absorption to the x-mode absorption which is qualitatively consistent with the simple theory. The difference in launch points is only 5.0 cm for the two cases which makes antenna location important.

Hardware

The objectives for the hardware were twofold. First it must produce a polarized and focused microwave beam and secondly it must have the flexibility to allow both x-mode and o-mode launch. The method which appeared to offer the best solution was a combination of waveguide mode convertors with a focusing mirror and a plane reflector to allow two-pass absorption. The Tara gyrotrons output predominately $TE_{02}$ which would be converted to $TE_{11}$ using "bumpy" and "snake" converters based on the work of Schelkanoff[2]. The "bumpy" converter has m = 0 radial wall perturbations and transforms $TE_{02}$ into $TE_{01}$. The tentative design parameters are r = 1.905 cm, dr/r = 16% with four periods of length d = 7 cm with a predicted efficiency of 96%. Then the snake convertor with m =1 radial wall perturbations transforms the $TE_{01}$ to $TE_{11}$. Again, the design parameters are r = 1.905 cm, dr/r = 10% with six beat wavelengths for a total length of ~120 cm and a predicted efficiency of ~94%. To reduce the cross polarization component, the $TE_{11}$ mode would be converted to a $HE_{11}$ mode[3]. For a length of 20 cm, the cross polarization component is down more than 25 dB from the desired component.

Because of the less efficient coupling for the o-mode at low electron temperatures and density, start-up may be difficult. To accommodate this possibility, a two pass geometry would be implemented with a Wengenroth[4] plate reflector. After the first pass with o-mode the reflector would rotate the polarization plane so as to return x-mode from the high field side of the resonant surface. Then as the electron parameters increased the first pass absorption would improve. The new hardware would be as shown in Fig.5.

The flexibility to allow launching of both x and o modes is easily achieved by rotating the waveguide by $\pi/2$ plus building in the capability for translation of the waveguide and mirror parallel to the axis of the machine.

## Conclusions

It is important to have heating localized to the vicinity of the plug potential in tandem mirror axicells. Currently x-mode heating is used however, the restriction of vanishing $k_{||}$ may be violated. Ray tracing results suggest that reasonable first pass absorption is possible for perpendicular o-mode propogation. However, hot electron characteristics play an important part in the absorption process. The polarized microwave power can be produced using well known techniques for waveguide converters.

## References


[1] M. Bornatici, et.al., Nucl. Fusion 23, 1153(1983).
[2] S.H. Schelkunoff, Bell. Sys. Tech. J. 34, 995(1955).
[3] M. Thumm, Int. J. IR & MM Waves 6, 577(1985).
[4] R. D. Wengenroth, IEEE MIT 26, 332(1978).

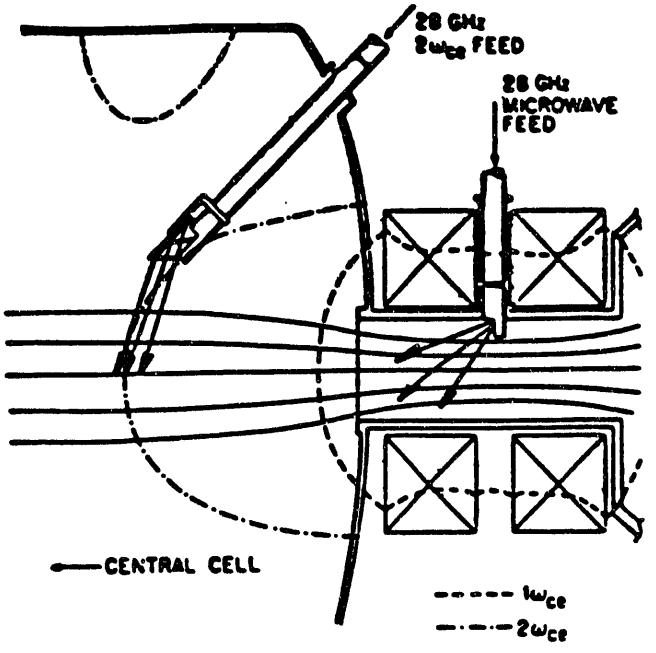


Fig. 1. Present antenna system in the Tara axicell. The fundamental is launched from between the magnets to create the plug potential. And the second harmonic is launched from inside the cell to assist in the thermal barrier formation. The fundamental antenna is a stepped waveguide without a reflector which gives only an unfocused, unpolarized beam.

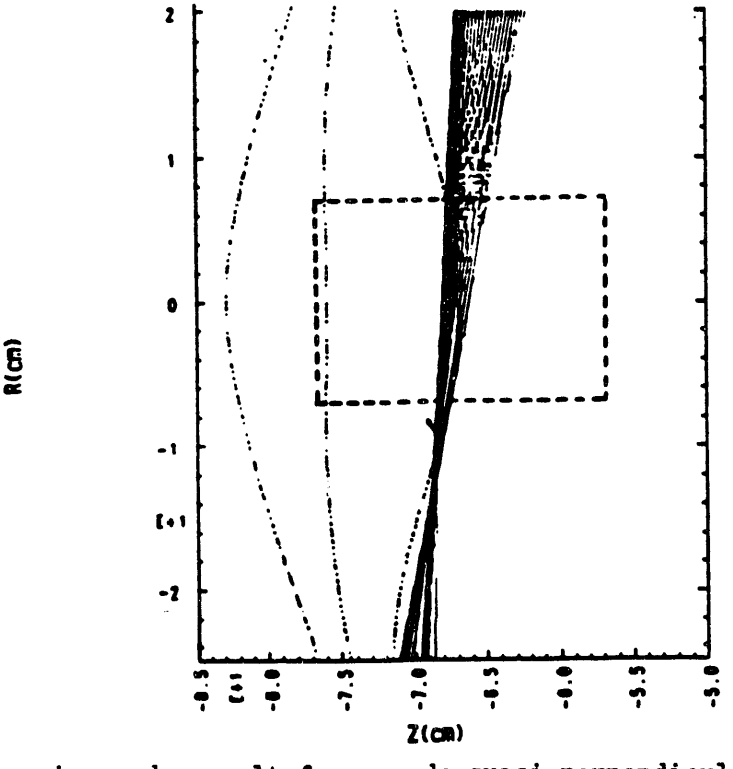


Fig. 2. Ray tracing code result for o-mode quasi-perpendicular launch. The 'scoring' region for absorbed power is indicated by the box. The plasma redius is about 50% larger than that of the box.

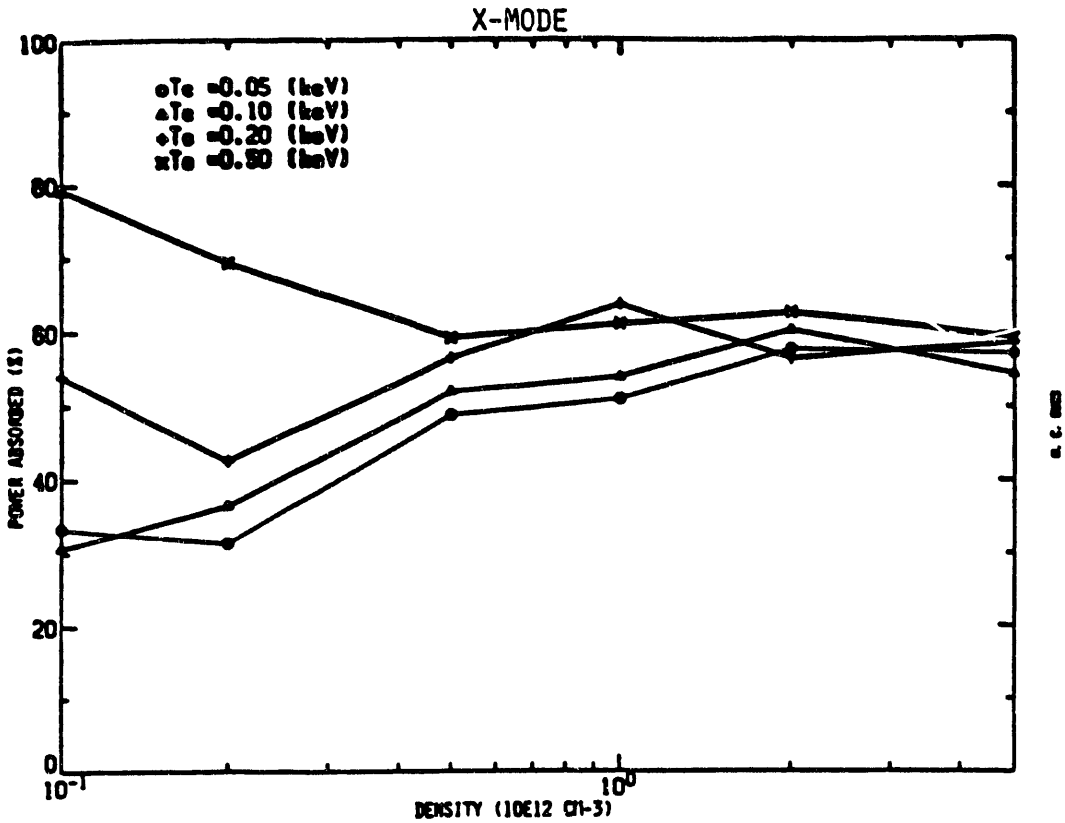


Fig. 3. Absorbed power (x-mode) for varius cold plasma densities and temperatures.

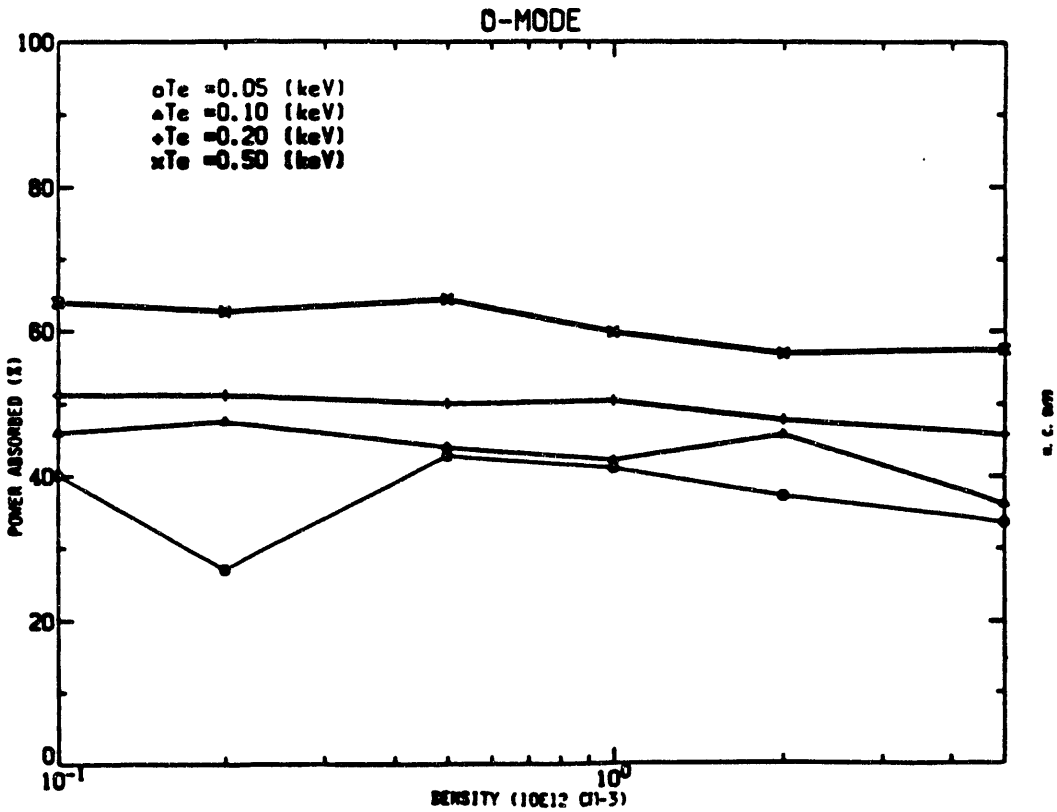


Fig. 4. Absorbed power (o-mode) for varius cold plasma densities and temperatures.

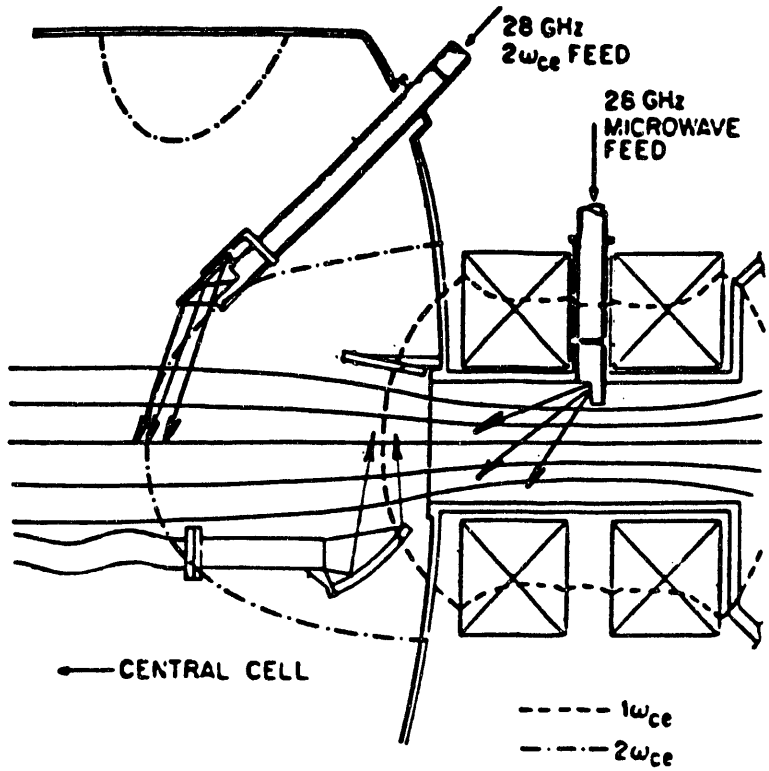


Fig. 5. Proposed fundamental waveguide and antenna system. For the scale of the drawing only part of the snake converter and the focusing mirror are shown.

# Observation of Ti XXI Line Radiation in ECH Plasmas*

P. Lee and A.J. Lieber
*GA Technologies, Inc., San Diego, California 92138, U.S.A.*
and
A.K. Pradhan and X. Yueming
*University of Colorado, Boulder, Colorado 80309, U.S.A.*

*Helium-like titanium line radiation in the x-ray region from 2.60 to 2.64 Å has been measured with a high resolution spectrograph ($\lambda/\Delta\lambda > 19,000$) during electron cyclotron heating (ECH) experiments on the Doublet III tokamak. The intensity of the resonance line (i.e., $1s^2\ ^1S_o - 1s2p\ ^1P_1$) is found to be much more sensitive to the applied ECH power than the intensities of the satellite lines. A qualitative picture which accounts for the observed line intensities is the presence of non-Maxwellian electrons in the ECH plasma.*

## I. Introduction

Electron cyclotron heating (ECH) of tokamak plasmas has received considerable interest in recent years as an auxiliary method of heating plasmas to thermonuclear conditions. Much of the effort in the study of ECH, both experimental and theoretical, is in the area of bulk plasma effects [1,2], such as energy confinement times, parameter scaling, and comparison of ECH to neutral beam heated plasmas. Theoretical models and computer simulations of ECH plasmas have predicted non-Maxwellian electron distributions [3], and measurements of the higher harmonics of the electron cyclotron resonance frequency on various plasma devices have qualitatively supported the theoretical predictions [4].

*This is a report of work sponsored by the Department of Energy under Contract Nos. DE-AC03-84ER51044 and DE-FG02-84ER53189.

High resolution spectroscopy of prominent impurity radiation can measure the ion temperature, bulk plasma rotation, electron temperature, and plasma ionization equilibria. For hot plasmas, the spectra emitted in the x-ray region are sensitive not only to the plasma temperature and density but also the superthermal components of the electron distribution. Reports of high resolution x-ray spectra generated during ECH of tokamak plasmas are scarce. Bryzgunov *et al.* [5] have obtained data on helium-like chromium line radiation in the wavelength region of 2.19 Å (spectral resolution $\lambda/\Delta\lambda$ of 3300) on the T-10 tokamak. For these experiments 500 kW of ECH power was applied for 50 ms with typical discharge parameters of 250 kA of plasma current and electron density of $2\text{–}3\times10^{19}$ m$^{-3}$. The chromium x-ray emission was summed over nine discharges during the 50 ms ECH pulse to produce a chromium spectrum. The reported electron temperatures deduced from the chromium line ratios were in reasonable agreement with Thomson scattering measurements.

We report here high resolution spectroscopy of the helium-like titanium radiation produced during ECH experiments on the Doublet III tokamak with typical temporal resolution of 20 ms.

## II. Experimental Setup

The ECH experiments reported here were carried out in the following parameter ranges: toroidal magnetic fields of 1.8 T $< B_T <$ 2.4 T, plasma current of 200 kA $< I_p <$ 800 kA, plasma elongation of $1.4 < \kappa < 1.6$, and average electron density of $1\times10^{19}$ m$^{-3}$ $< \bar{n}_e < 10\times10^{19}$ m$^{-3}$. Six VGE-8006 gyrotrons operating at 60 GHz are used to launch up to 1 MW of rf power in the extraordinary mode from the vessel inner wall with a pulse duration of up to 500 ms (typical pulse length 250 ms). The plasma cutoff density calculated from ray tracing is $\bar{n}_e = 5.6 \times 10^{19}$ m$^{-3}$ and the resonant magnetic field is 2.14 T. The wave propagates at an angle of 30° to the radial, and the rf power is fully absorbed in an area about 10 cm in height and 5 cm width in the radial direction [6].

The spectrometer used in this experiment is a Bragg crystal spectrograph with a curved quartz crystal (2d = 2.75 Å) in Johann geometry constrained along a 3 m Rowland circle. A position sensitive delay line gas proportional counter with 200 $\mu$m spatial resolution limits the instrument resolution $\lambda/\Delta\lambda$ to 19,000. A detailed description of the instrument can be found elsewhere [7]. A plan view of the spectrometer and its relation to the tokamak is shown in Fig. 1.

## III. Experimental Results

A comparison of the titanium spectra measured during ohmic and ECH discharges is shown in Fig. 2. Each spectrum is obtained with an integration time of 200 ms and is normalized to the resonance line w amplitude. The prominent helium-like lines are the resonance line w, the intercombination lines x and y, and the forbidden line z; they derive from the transitions $1^1S_0$–$2^1P_1$, $1^1S_0$–$2^3P_{2,1}$, and $1^1S_0$–$2^3S_1$, respectively. The stronger $n$=2 satellite lines are t, q, unresolved (a,r), k, and j. Also identified are the $n$=3 dielectric recombination satellite lines $h_{15}$, $d_7$, and $d_{13}$. With the w line in both ECH and ohmic shots normalized in Fig. 2, the other lines may be seen to be of considerably lower intensity in the ECH plasma, by about a factor of 4 for the $z$ and 1.5 for the q lines. The measured electron temperatures for the cases shown here are similar for these shots, 1.54 keV with ECH and 1.49 keV for ohmic heating only. (Note the factor of 3 higher density for the ohmic discharge.)

The temporal response of Ti XXI line radiation during high power ECH is shown in Fig. 3. The directions of increasing wavelength and time (20 ms temporal resolution) are indicated. The prominent emission lines are identified in the figure. The onset of ECH is clearly evident by the sudden increase in the intensities of all lines. As will be shown later, the relative increase in the resonance line intensity is greater than that of the satellite lines. An increase in the resonant line w intensity by a factor of 5 upon application of ECH to the plasma is observed for this discharge.

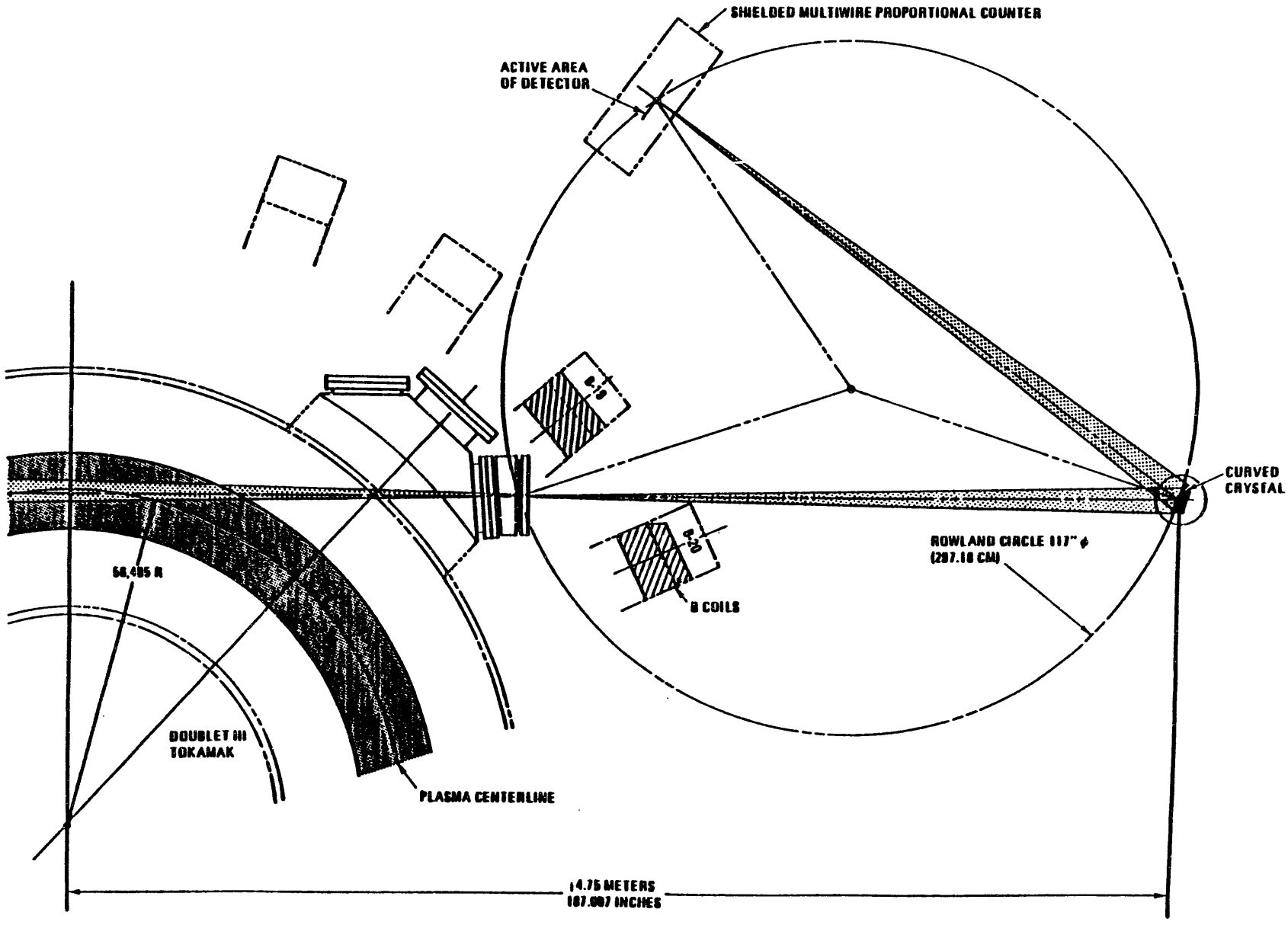


FIG. 1. Plan view of crystal x-ray spectrometer relative to Doublet III tokamak.

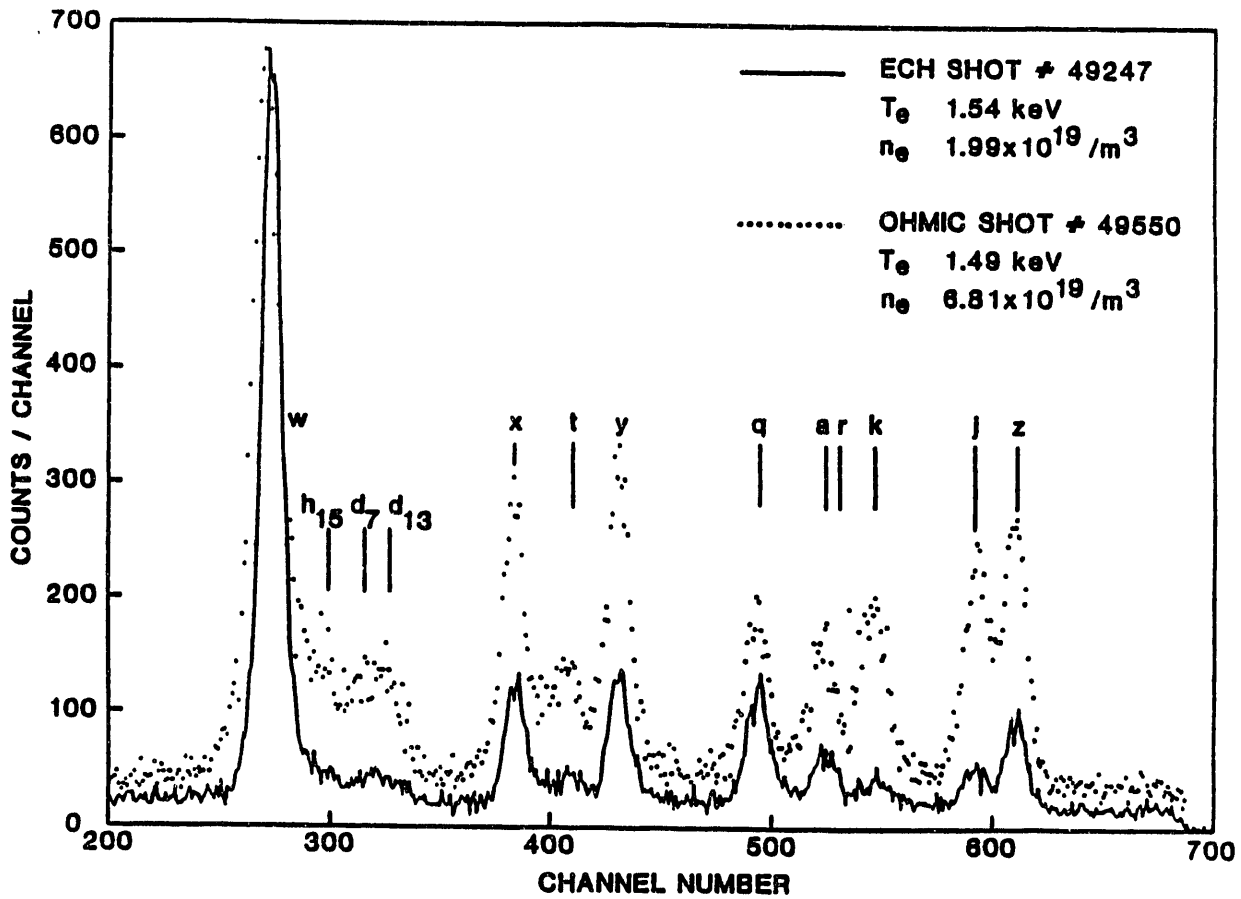


FIG. 2. Comparison of ohmically heated and electron-cyclotron-heated tokamak discharges. Each spectrum was acquired in a 200 ms period and normalized to the same peak value of the resonance line w, for comparison purposes. The prominent lines have been identified according to the usual notation [7]. The measured electron temperatures for the two cases are nearly identical; however, the spectra are dramatically different. The ECH spectrum has notably lower intensities for the nondipole lines, *e.g.*, x, y, and z.

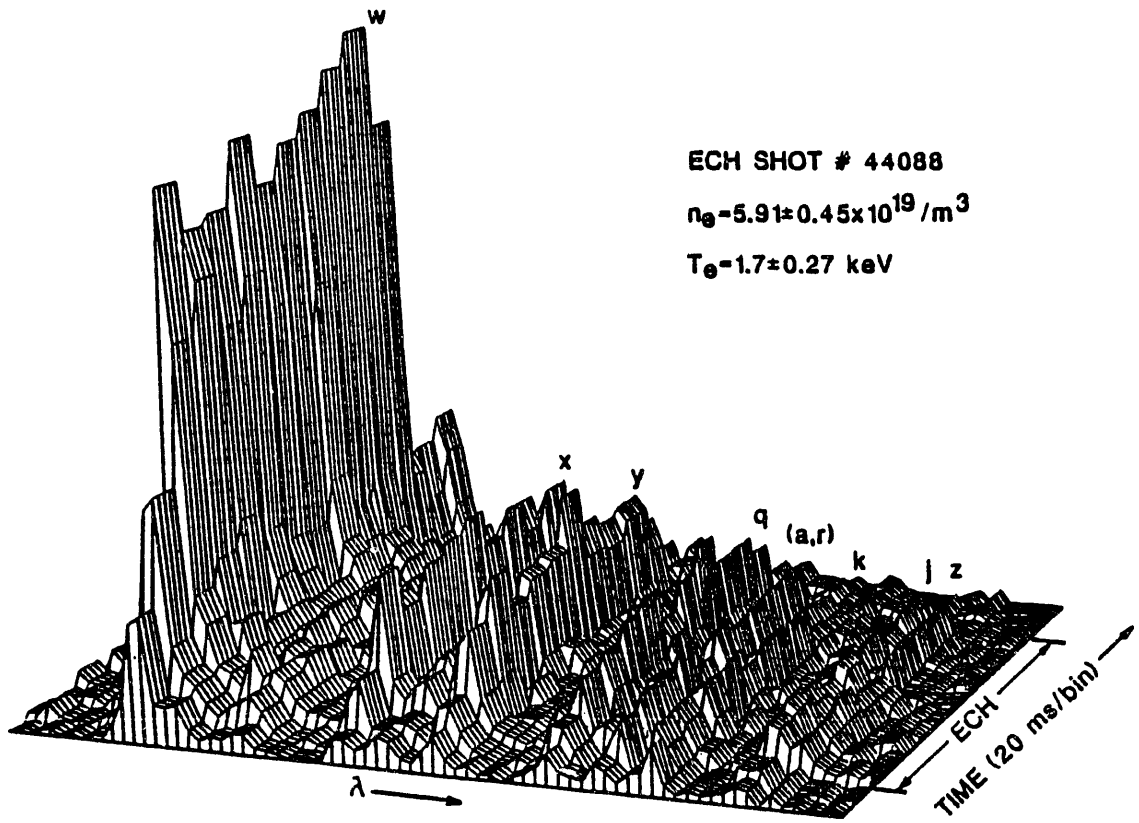


FIG. 3. Temporal evolution of Ti XXI spectra during ECH. The central electron density and temperature are $5.91\times10^{19}$ m$^{-3}$ and 1.7 keV, respectively.

Experimental line intensity ratios can be used to deduce fundamental plasma parameters when the approximation of coronal equilibrium is valid. For example, the following line intensity ratios are commonly used [8]:

| | |
|---|---|
| j/w | Electron temperature |
| $d_{13}/w$ | Electron temperature |
| $G = (x + y + z)/w$ | Ionization equilibria |
| $R = z/(x + y)$ | Electron density |

In earlier reports [9-12] good agreement was found between the line intensities observed in ohmically heated plasmas and theoretical values calculated assuming coronal equilibrium with Maxwellian averaged rates for excitation, ionization, and recombination processes. The rates are calculated for a given temperature characterizing the Maxwellian distribution. Figure 4a shows the dependence of the line ratio $G$ on measured electron temperature in both ohmic and ECH discharges. The titanium spectra were measured within 20 ms of the Thomson scattering measurements mentioned above. Note that nearly all $G$ ratios for the ECH discharge are less than 0.7, which, on theoretical grounds, indicates an ionizing plasma [13]. A plot of the ratio $R$ as a function of measured central electron density is given in Fig. 4b for ECH and ohmic plasmas. At high electron densities (*i.e.*, $n_e < 10^{21}$ m$^{-3}$ for Ti), the collisional excitation from $2^3$D to $2^3$P is expected to deplete the z line relative to the x and y lines and hence to lead to a decrease in $R$. For ECH, the decrease in $R$ is observed to occur at densities 2 orders of magnitude smaller than predicted; hence the decrease in $R$ may be ruled out as a density effect (the ohmic $R$ ratio, although measured for a small range of densities, is observed to be consistent with theory). The temperature dependence of the j/w ratio is shown in Fig. 4c. The solid line is the theoretical prediction [14], and the experimental data are shown as open circles and solid triangles for ohmic and ECH discharges, respectively. Typical error bars for the electron temperatures and line ratios are also given. The ohmic data are distributed about the theoretical value with the scatter in the data larger than the errors in the measurements. The ECH line ratios, however,

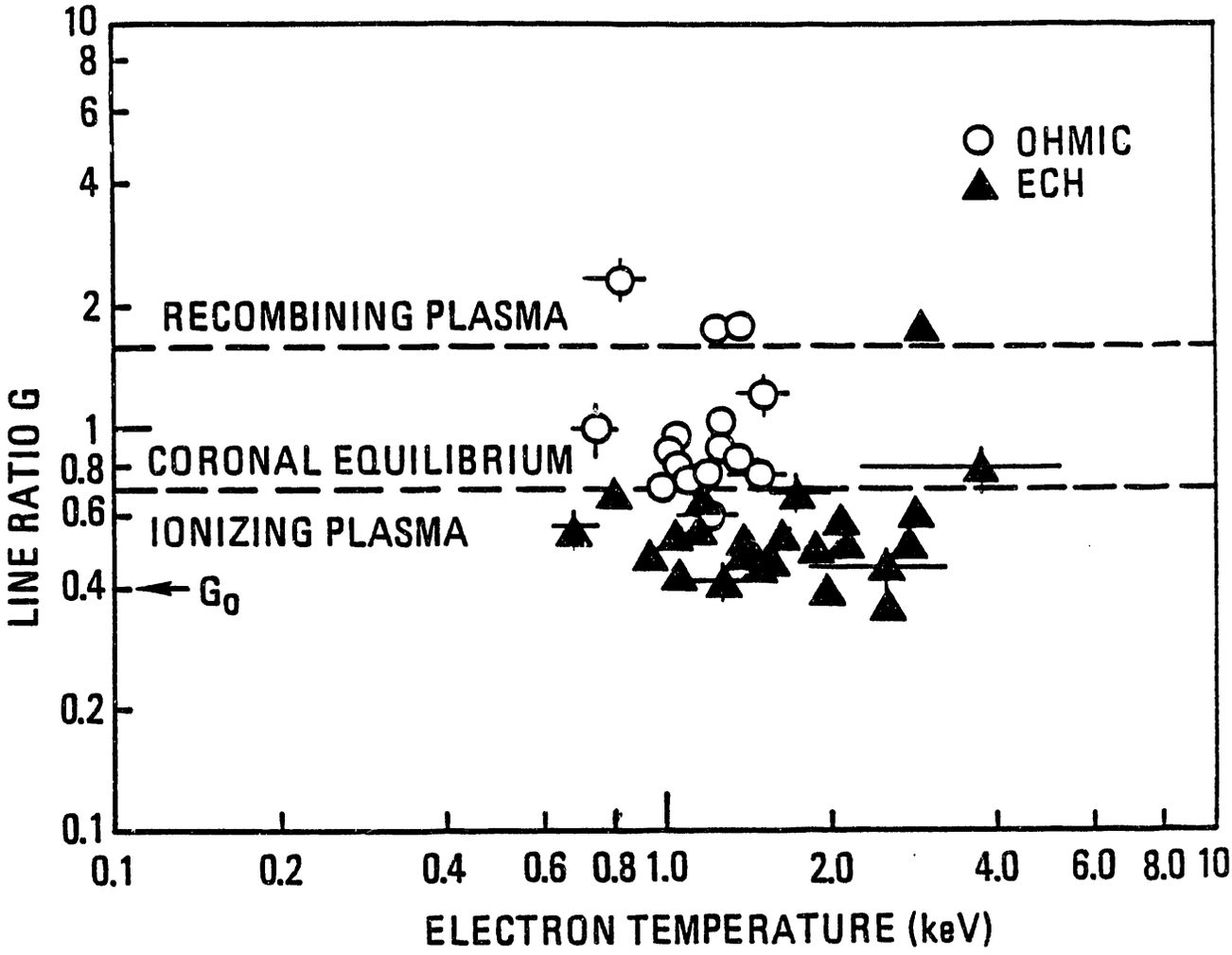


FIG. 4a. Plot of the line ratio $G = (x+y+z)/w$ as a function of Thompson-scattering electron temperature for ohmically heated and ECH plasmas. Most of the ohmic shots are in the coronal equilibrium region, *e.g.*, $0.7 < G < 1.8$, while most of the ECH shots indicate ionizing plasma. Also shown is the value $G_0$, the lower limit determined by the electron impact excitation rates, below which no data points should be found.

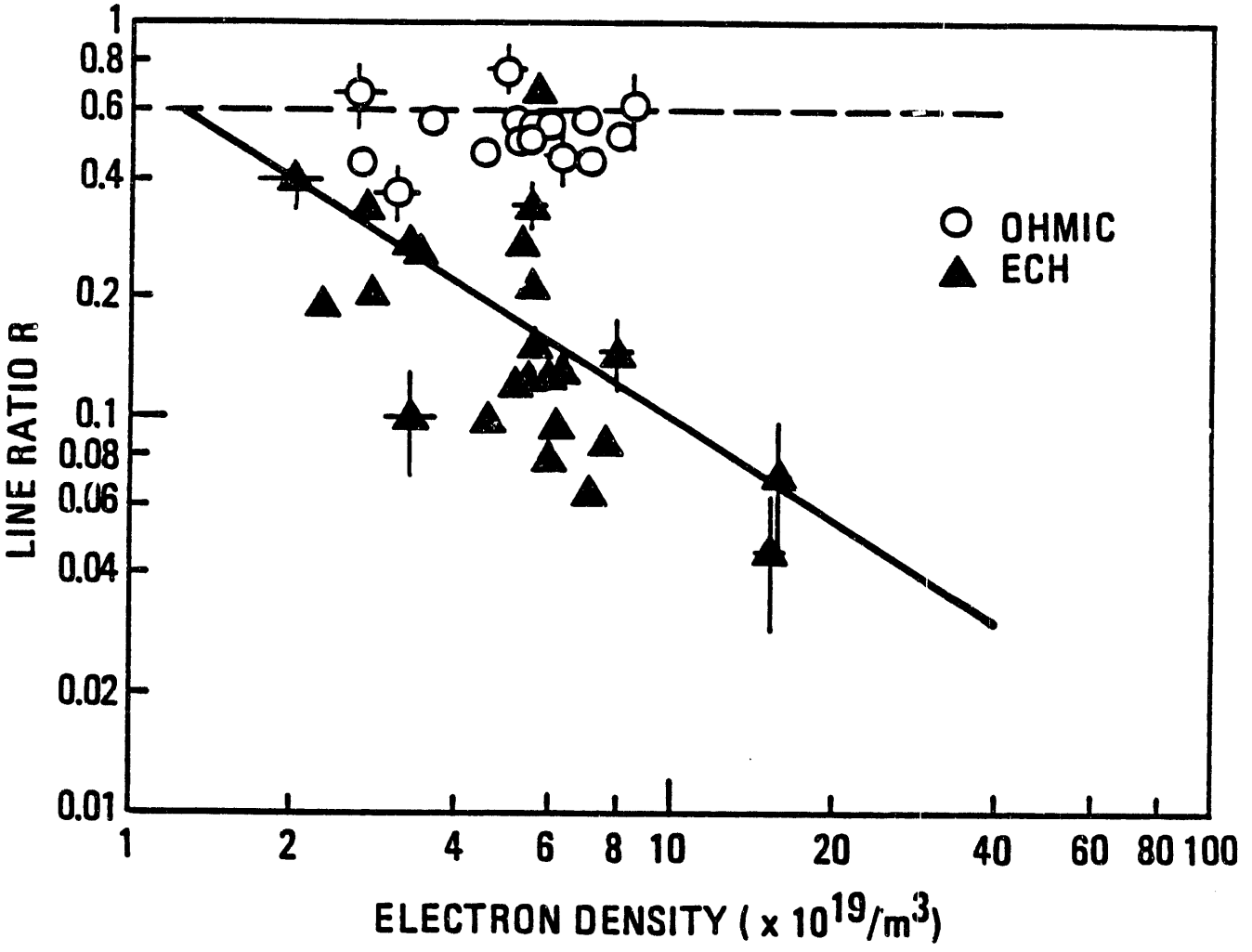


FIG. 4b. Line ratio $R = z/(x+y)$ dependence on electron density for ohmically heated and ECH plasmas. The dashed and solid lines show trends in the data.

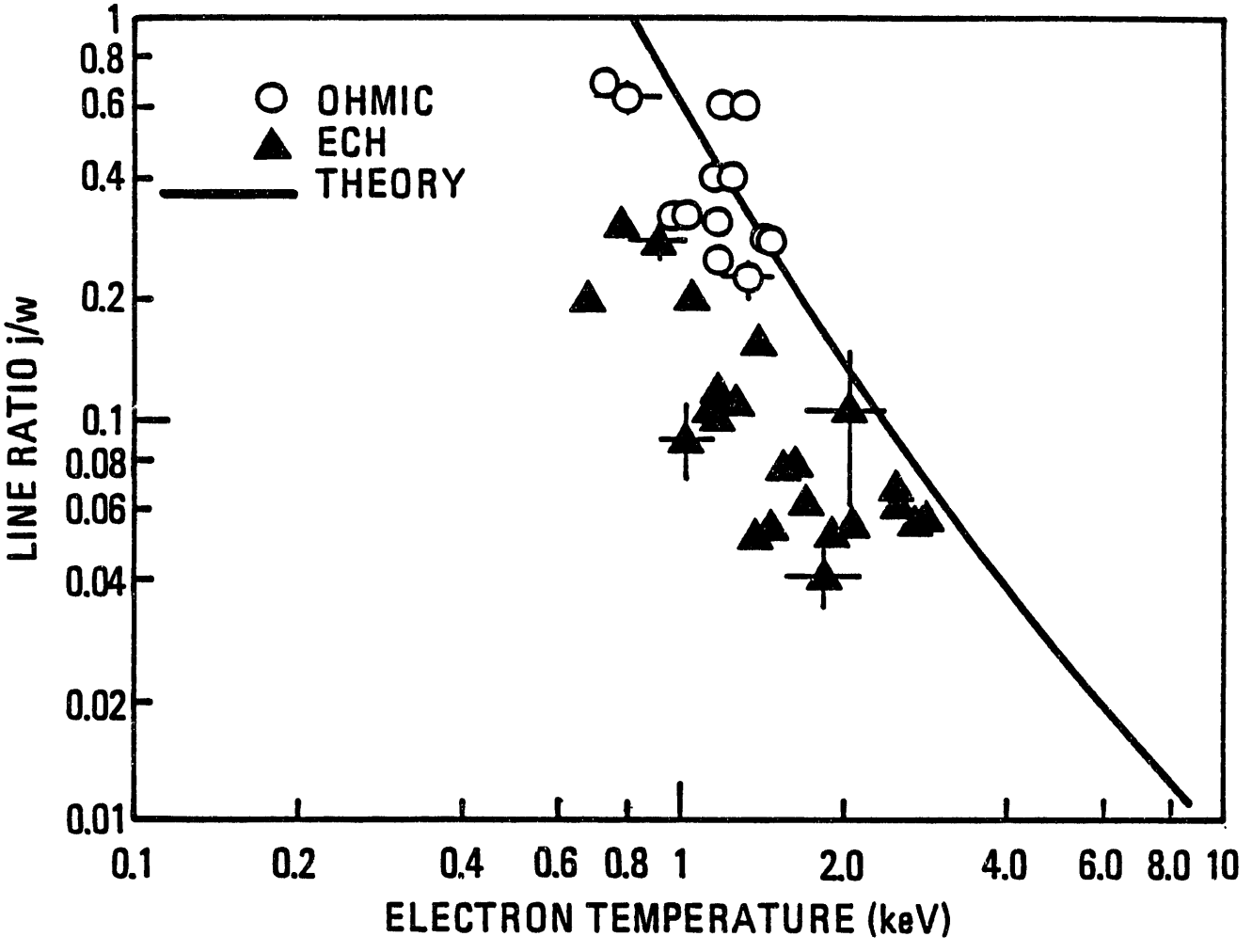


FIG. 4c. The temperature-sensitive line ratio j/w is shown for ohmic and ECH discharges. The solid line is the theoretically predicted curve based on the rate coefficients given by Bely-Dubau *et al.* [13]. The ohmic data are clustered about the solid line with scattering greater than the errors in the measurements. The ECH data, by contrast, are systematically below the theoretical values.

are significantly lower than predicted and considerably lower than the corresponding ohmic line ratio (at the same electron temperature).

Finally, the temporal behavior of the line ratio j/w is plotted in Fig. 5. The decrease in j/w ratio during ECH is consistent with the presence of superthermal electrons. Similar results have been observed by Bartiromo *et al.* [15] during lower-hybrid heating of the Frascati tokamak FT.

## IV. Theoretical Outline

The effects of a nonthermal electron distribution on the line intensity ratios has been outlined by Gabriel and Phillips [16] for the iron satellite lines $d_{13}$ and j, and observed by Apicella *et al.* [17] for the $d_{13}$ line of chromium on the Frascati tokamak FT, and interpreted by Gabriel *et al.* [18] on the observed line ratio $G$ of O VII lines from Puppis-A supernova remnant.

The qualitative picture which emerges from ECH experiments is that the nonthermal portion of the electron distribution enhances the intensity of the resonance line relative to that of the satellite lines. The excitation mechanisms for the resonance line and dielectric satellite lines (*i.e.*, $d_{13}$ and j lines) are:

$$\begin{aligned}
\text{w:}\quad & \text{Ti XXI}\ \ 1s^2\ {}^1S_o + e \rightarrow \text{Ti XXI}\ \ 1s2p^1P_1 + e \quad E_e \geq 4.75\ \text{keV} \\
\text{j:}\quad & \text{Ti XXI}\ \ 1s^2\ {}^1S_o + e \leftrightarrow \text{Ti XX}\ \ 1s^22p^2\ {}^2D_{5/2} \quad E_e = 3.31\ \text{keV} \\
\text{d}_{13}\text{:}\quad & \text{Ti XXI}\ \ 1s^2\ {}^1S_o + e \leftrightarrow \text{Ti XX}\ \ 1s2p3p^2D_{5/2} \quad E_e = 4.14\ \text{keV}
\end{aligned}$$

The excited state in each case is produced by free electron impact of the 1s ground state of the helium-like titanium ion. For the resonance line, excitation is possible for any electron with kinetic energy above a threshold level of 4.75 keV for titanium (*i.e.*, energy of the resonance line photon) as indicated by the shaded region in Fig. 6. For the case of d and j lines, however, the process is that of electron capture and hence the dielectronically captured electrons must have energies very close (*i.e.*, $\Delta E_e \sim 10^{-4}$ keV) to the excitation energies. Thus, the presence of superthermal electrons with kinetic energy above 4.75 keV can significantly increase the intensity of the resonance line w and at the same time have relatively little effect on the satellite lines.

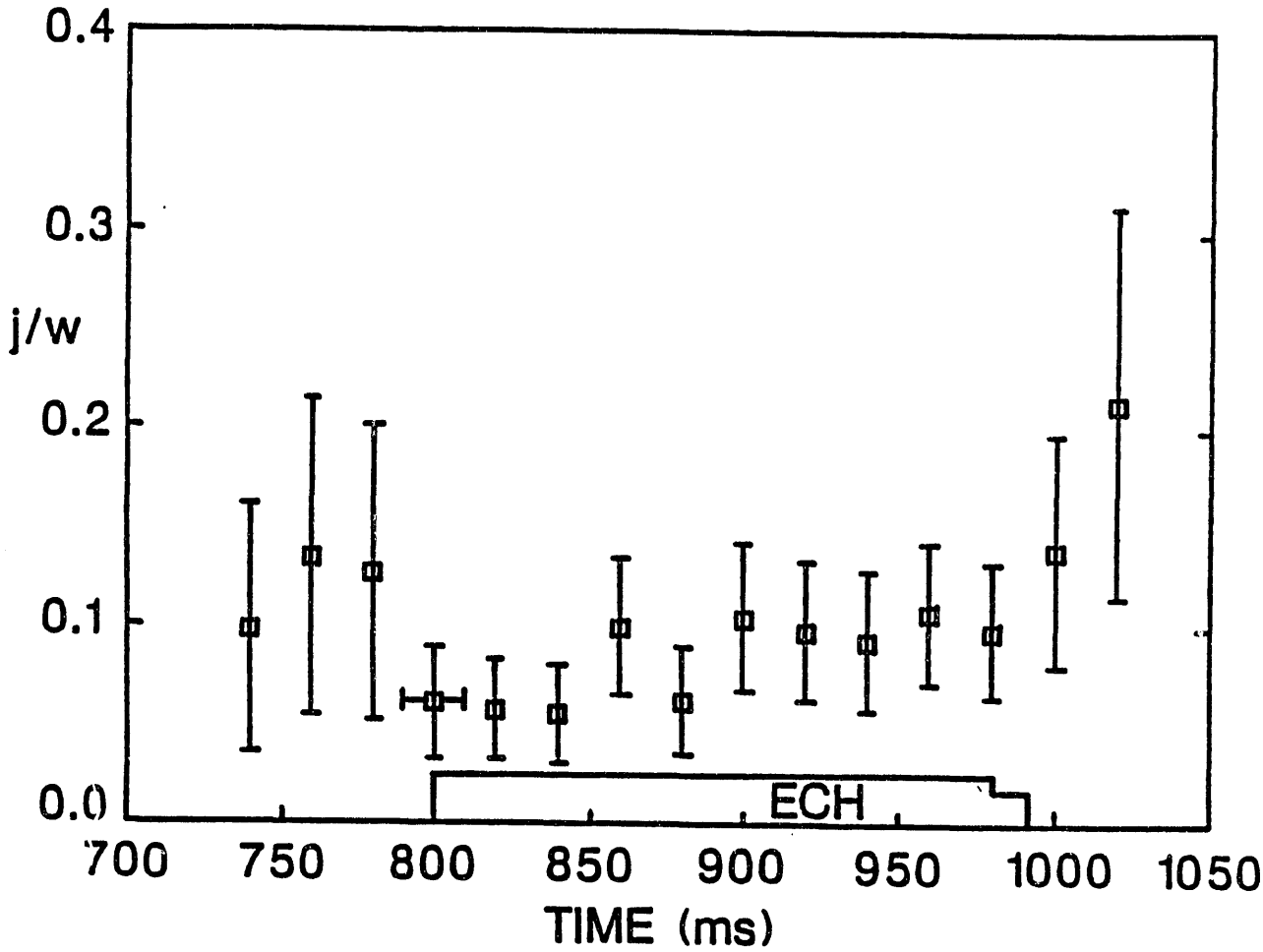


FIG. 5. Time dependent measurement of the line ratio j/w. The duration of the ECH pulse is also indicated.

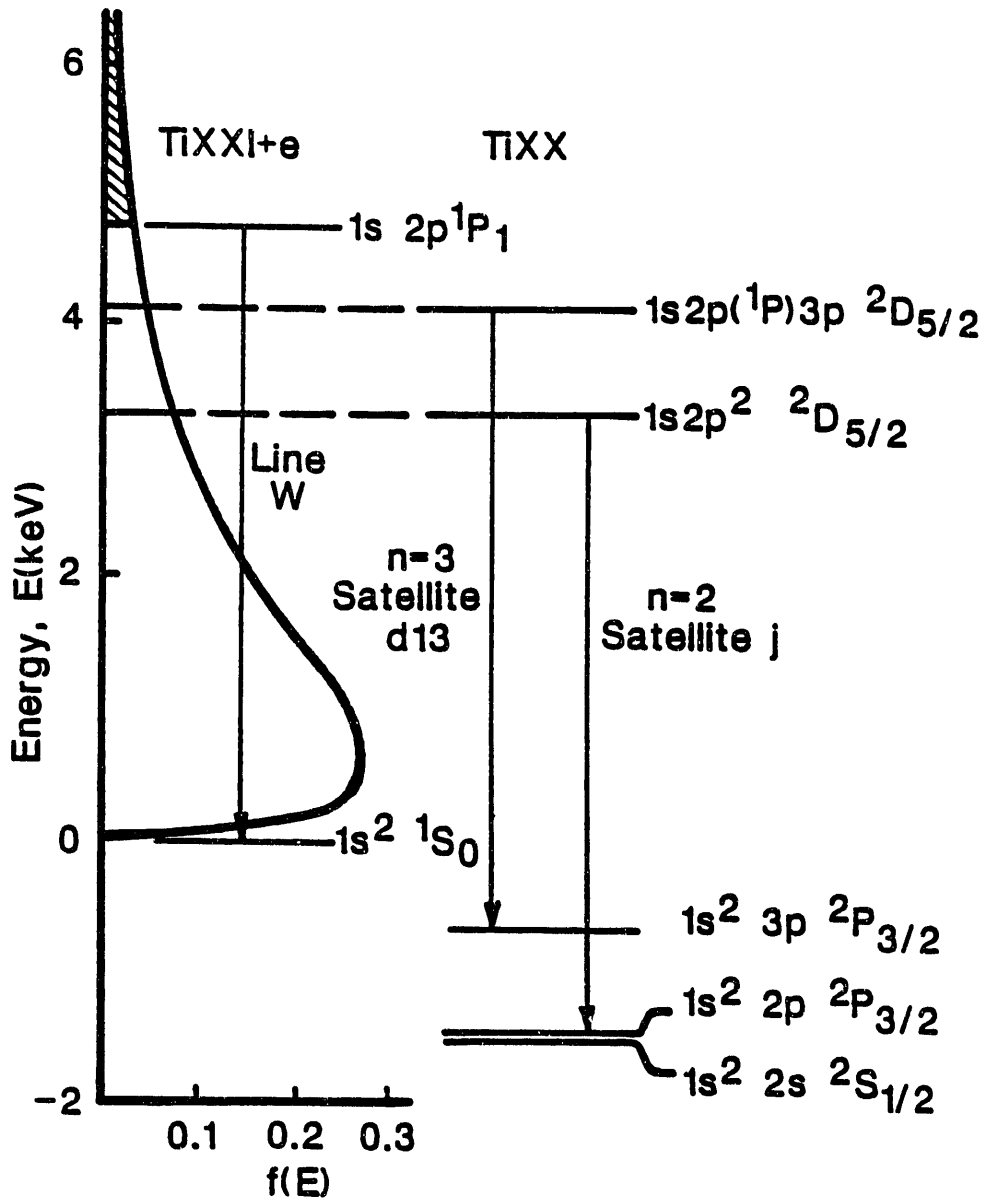


FIG. 6. Energy level diagram for the transitions w, j, and $d_{13}$ lines of titanium. The Ti XXI energy level are shown together with a free electron Maxwellian distribution function.

A simple estimate of the kinetic energy gained by an electron passing through the resonance region is

$$\varepsilon = \frac{1}{4}\,\frac{(eE_{-}\tau)^2}{m} \quad ,$$

here $E_{-} \sim k_{\perp}\rho_e E_0$ is the resonant component of the ECH electric field (typically $k_{\perp}\rho_e \sim 1/10$) [19] and $\tau$ is the time duration spent by an electron in the resonance zone. For a plasma with $T_e \sim 1$ keV and 1 MW ECH injection, $E_{-} \sim 400$ V/cm and $\tau \sim 5$ ns (the resonant dimension is taken to be 5 cm $\times$ 10 cm). Thus an electron acquires $\sim$1.8 keV per pass and hence within a few transit periods ($\sim$3 $\mu$s) the kinetic energy of some electrons will be in the tens of keV range.

It has been pointed out by Inokuti [20] that for electron inpact excitation with energies greater than about 5 keV one should account for the relativistic effects in the calculation of the cross sections. The relativistic Coulomb-Bethe formula given by Fano is used by Bartiromo *et al.*, [15] in order to calculate the rate coefficient for the $w$ transition in Fe XXV. A very useful fact discussed by Bartiromo *et al.*, is that the rate coefficient can be considered to be approximately a constant for the electrons in the high energy tail of the distribution ($E > 20$ keV for Fe XXV).

The usual expression for the ratio of the dielectronic satellite to the resonance line for the nonrelativistic, Maxwellian case is

$$D_{\rm th} = \frac{q(s)}{q(w)} = 3.3(-24)\left(\frac{E_H}{kT}\right)^{3/2} F_2(s)e^{-E_s/kT}/q_w \quad , \tag{1}$$

where the rate coefficient for the satellite line $q(s)$ is given in terms of the parameter $F_2(s)$ which is determined by the autoionization and radiative decay rates for the dielectronic level $s$, i.e., $F_2(s) = A_a(s)A_r(s)/[A_a(s) + A_r(s)]$. The $q(w)$ is the nonrelativistic, Maxwellian averaged rate coefficient for the $w$ line, and $E_H = 13.6$ eV. Now, if we assume that a departure from the Maxwellian implies the excitation of the $w$ line by relativistic electrons in the high energy tail, then, following Bartiromo *et al.*, one may define the fractional deviation from the Maxwellian as

$$\eta = \frac{q(w)}{q_{\rm rel}(w)} \left[ \frac{D_{\rm th}}{D_{\rm ex}} - 1 \right] \quad , \tag{2}$$

where $q_{\rm rel}(w)$ is the relativistic excitation rate coefficient [Eq. (2) is a reformulation of the expression given by Bartiromo *et al.*]. As mentioned above, the assumption implicit in Eq. (2) is that the excitation of the $w$ line depends only on the high energy relativistic electrons [i.e., $\eta = \int_{v_0}^{\infty} f_{\rm ECH}(v) d^3v / \int_{v_0}^{\infty} f_T(v) d^3v^{-1}$, where $f_{\rm ECH}(v)$ and $f_T(v)$ are the electron distribution functions for ECH and thermal plasmas, respectively, and $\frac{1}{2}mv_0^2 = 10$ keV]. Estimates of the relativistic excitation rate coefficient $q_{\rm rel}(w) = \langle \sigma v \rangle_w \sim 6.5(-12)$ cm$^3$/s for T>10 keV using the Coulomb-Bethe formula for Ti XXI. Table I gives the estimates of the fraction of superthermal electrons $\eta$ for various observed plasma temperatures with $F_2(j) = 3.53$ (+14) (from Ref. 14) and $E_j = 3325.2$ eV. It is evident from Table I that the fractional nonthermal component may be quite considerable. As a comparison, Bartiromo *et al.*, had found that for the lower-hybrid rf heating used in the Frascati tokamak, the nonthermal component was <5%, whereas in the ECH case, fractions as high as 20% to 30% may be present.

In summary, we have presented helium-like titanium spectra measured on the Doublet III tokamak during high power ECH discharges. The observed line intensity ratios are consistent with non-Maxwellian electron distributions. Further theoretical analysis is being carried out in an attempt to obtain quantitative information on the non-Maxwellian distributions using line ratio technique.

The authors (P.L. and A.J.L.) would like to acknowledge the cooperation and support from R. Stambaugh and the Doublet III group.

## References

[1] R. Prater, "A Review of Electron Cyclotron Heating Experiments in Toroidal Devices," GA Technologies Report GA-A18149 (1985). Summary," GA Technologies Report GA-A17810 (1985).

[2] H. Hsuan *et al.*, Princeton Plasma Physics Laboratory Report PPPL-2114 (1984).

[3] D. Farina, M. Lontano, and R. Pozzoli, in *Proceedings of EC-4 Fourth International Workshop on Electron Cyclotron Emission and Electron Cyclotron Resonance Heating,* Roma (1984), p. 77.

[4] D.A. Boyd, in *Proceedings of EC-4 Fourth International Workshop on Electron Cyclotron Emission and Electron Cyclotron Resonance Heating,* Roma (1984), p. 145.

[5] V.A. Bryzgunov, S. Yu. Luk'yanov, M.T. Pakhomov, A.M. Potapov, and S.A. Chuvatin, *Sov. Phys. JETP* **55**, 1095 (1982).

[6] R. Prater *et al.*, "Doublet III Electron Cyclotron Heating Physics Summary," GA Technologies Report GA-A17810 (1985).

[7] A.J. Lieber, S.S. Wojtowicz, and K.H. Burrell, *Nucl. Instr. Meth.* **A235**, 565 (1985).

[8] Line ratio techniques are discussed in the following references: A.H. Gabriel, *Mont. Nat. R. Ast. Soc.* **160**, 99 (1972); M. Bitter *et al.*, *Phys. Rev. Lett.* **47**, 921 (1981); E. Källne, J. Källne, E.S. Marmar, and J.E. Rice, *Physica Scripta* **31**, 551 (1985).

[9] M. Bitter *et al.*, *Phys. Rev. Lett.* **42**, 304 (1978); *Phys. Rev. Lett.* **43**, 129 (1979).

[10] E. Källne, J. Källne, and J.E. Rice, *Phys. Rev. Lett.* **49**, 330 (1982); E. Källne *et al.*, *Phys. Rev. Lett.* **52**, 2245 (1984).

[11] TFR Group, J. Dubau, and M. Loulergue, *J. Phys. B* **15**, 1007 (1982).

[12] P. Lee, A.J. Lieber, and S.S. Wojtowicz, *Phys. Rev. A* **31**, 3996 (1985).

[13] A.K. Pradham, *Astrophys. J.* **288**, 824 (1985).

[14] F. Bely-Dubau *et al.*, *Phys. Rev. A* **26**, 3459 (1982).

[15] R. Bartiromo, F. Bambarda, and R. Giannella, *Phys. Rev. A* **32**, 531 (1985).

[16] A.H. Gabriel and K.J.H. Phillips, *Mon. Nat. R. Astr. Soc.* **189**, 319 (1979).

[17] M.L. Apicella, R. Bartiromo, F. Bombarda, and R. Giannella, *Phys. Lett.* **99**, 174 (1983).

[18] A.H. Gabriel, L.W. Acton, F. Bely-Dubau, and P. Faucher, ESA report SP239 (1986)

[19] J.Y. Hsu, V.S. Chan, R.W. Harvey, R. Prater, and S.K. Wong, *Phys. Rev. Lett.* **53**, 564 (1984).

[20] M. Inokuti, *Rev. Mod. Phys.* **43**, 297 (1971).

Table I

Calculated Fraction of

Superthermal Electrons for Experimental Cases

| $T_1$ (keV) | $q_w(T_1)$ cm$^3$/s | $(j/w)_{ex}$ | $(j/w)_{th}$ | $\eta$ |
|---|---|---|---|---|
| 0.8 | 3.16 (−14) | 0.30 | 1.28 | 0.016 |
| 1.0 | 9.76 (−14) | 0.20 | 0.68 | 0.036 |
| 1.2 | 2.01 (−13) | 0.10 | 0.44 | 0.105 |
| 2.0 | 9.06 (−13) | 0.05 | 0.14 | 0.250 |
| 3.0 | 1.90 (−12) | 0.03 | 0.062 | 0.310 |

Note: The relativistic rate coefficient $q_{w_{rel}}(T)$ for Ti XXI is $\approx 6.5(-12)$ cm$^3$/s ($T_2 > 10$ keV).

# Dependence of ECH Deposition Profile On The Modeling of Incident Wave Energy*

A.H. Kritz, Hunter College/CUNY
H. Hsuan, Princeton University
K. Matsuda, GA Technologies

The ray tracing code, TORAY, is used to investigate the importance of modeling assumptions utilized in describing ECH. In particular, we examine the dependence of the ECH deposition profile on the antenna pattern. We demonstrate that different assumptions for representing the incident wave energy by a finite number of rays lead to significantly different results for the energy deposition profile.

## GENERAL BACKGROUND

Correct modeling of the incident electron cyclotron energy is particularly important since knowledge and control of the deposition profile is necessary to achieve many of the goals envisioned for ECH. For example, stabilization of tearing mode instabilities, current drive resulting from deposition of electron cyclotron wave energy and understanding electron transport all depend on controlled localized deposition. The electron cyclotron wave energy propagates from outside the plasma chamber into the plasma with the distribution of incident power determined by the antenna pattern of the launcher. It will be shown that the computed energy deposition profile may sensitively depend on the modeling of the incident power.

The amplitude of the incident wave energy is a continuous function over a solid angle. However, before ray tracing can be used to model ECH deposition, we must determine how to utilize the measured angular pattern of the launcher in choosing a finite number of rays to represent the incident electron cyclotron wave energy. In particular we must decide what algorithm should be used so that a relatively small number of rays properly describes the launched power profile.

One approach is to locate a point source at the plasma boundary (or at the antenna location) and to represent the antenna pattern of the incident energy by a number of rays with each ray being assigned an appropriate fraction of the incident energy. However, it is computationally inefficient to carry out the ray tracing, with the associated energy deposition, and then to weight the result with a small relative weight. A better approach would be to use an appropriate angular distribution of rays. The question that remains to be answered is how many rays and at what angles.

From the examples of case studies presented, we will see that the answer is not simple since the energy deposition profile may be a sensitive function of the angular distribution chosen to represent the incident power. In this paper we compare the energy deposition profiles that result when different assumptions are made in modeling the launch pattern. For example, we compare the deposition profile that results when gaussian beam theory is used to describe the launched antenna power with the deposition profile that results when a uniform pattern of rays is assumed. In part, the interest in gaussian beam theory stems from the fact that the HE11 mode used at the launcher in ECH experiments on the PDX and PLT tokamaks results in an antenna pattern that is properly described by gaussian beam theory. Moreover, the TE11 mode used at the launcher in the D3 and TFR experiments yields a pattern that is gaussian in one direction. Below, we develop the procedure used in choosing the set of rays that describe the power distribution launched from a gaussian antenna in free space.

## GAUSSIAN BEAM ANTENNA

A gaussian beam antenna produces a power density [1-3]

$$P(r,z) = P_o \exp[-2r^2/w(z)^2] \tag{1}$$

where r is the radial displacement from the antenna center line and z is the distance between the antenna center line and the plane where the power density is computed. The beam contour is given by

$$w(z) = w_o \left[ 1 + \left( \frac{\lambda z}{\pi w_o^2} \right)^2 \right]^{1/2} \tag{2}$$

where $\lambda$ is the wavelength. The gaussian beam contracts to a minimum diameter $2w_o$ at the beam waist where the phase front is plane. From the equation for w(z) it follows that the beam contour is a hyperbola with asymptotes inclined to the axis at an angle $\alpha$ where

$$\alpha = \frac{\lambda}{\pi w_o} \tag{3}$$

It follows from Eqs. 1 and 2 that on the plane a distance z from the antenna, the power I, within the radius r is given by:

$$I(r) = \int_o^r P_o \exp[-2u^2/w^2]\, 2\pi u\, du \tag{4}$$

Carrying out the integration and solving for r, we find

$$r = \frac{w}{\sqrt{2}} \left[ - \ln \left( 1 - \frac{I(r)}{I_\infty} \right) \right]^{1/2} \tag{5}$$

where $I_\infty = P_o \pi w^2/2$. By considering average values of $I(r)/I_\infty$ in the various radial zones, we obtain the value of r associated with each zone.

In order to obtain the angular displacement associated with a ray that has radial displacement r from the center of the antenna beam at a distance z from the antenna, we require the effective radius of curvature, R(z), of the wave front. The quantity R(z) is then the distance from where the power density is calculated to effective launch point of the rays. In practice, we find that the effective launch point of the rays may be located well behind the physical location of the antenna. From gaussian beam theory, R(z) is given in terms of the parameters $w_o$ and $\lambda$ by:

$$R(z) = z\left\{1 + \left(\frac{\pi w_o^2}{\lambda z}\right)^2\right\} \tag{6}$$

The angular displacement from the center of the gaussian beam, $\psi$, is expressed in terms of r and R(z) by the equation

$$\psi = \sin^{-1}[r/R(z)] \tag{7}$$

Once $\psi$ is known, we can determine $\Delta\phi$ and $\Delta\vartheta$, the toroidal and poloidal angular displacements for the rays used to describe the antenna pattern of the power launched in the ECH studies.

A problem that remains is to determine the appropriate value of z, that is the location of the plane where the incident radiation pattern is to be computed. For example, should z be chosen so that we compute the gaussian beam pattern near the edge of the plasma or should z be chosen so that the antenna pattern is computed near the location of the resonance layer. We have considered both of these possibilities in our studies and have found that, for the range of plasma parameters examined, the ECH energy deposition profiles do not sensitively depend on our choice of z. In the studies presented here z is chosen so that antenna power profile is computed 5 cm into the plasma from the edge. Below we illustrate the dependence of the power deposition on the representation of the incident angular power spectrum.

## EXAMPLES OF POWER DEPOSITION PROFILES

In order to examine the dependence of the power deposition profile on the incident angular power spectrum, we consider PDX/PLT type plasmas with outside (low field) O-mode launch and D3 tokamak plasmas with inside (high field) X-mode launch. In Figures 1 and 2, we present the results for an antenna of the type used previously on PDX and now on FLT, i.e., an antenna 6.35 cm wide emitting ECH power in the HE11 mode [4,5]. O-mode power is launched from the low field side of a PDX/PLT like plasma with major radius, R, equal to 136 cm; plasma radius, a, equal to 35 cm; and central toroidal field, 21 kG. The frequency of the incident wave power is 60 GHz and the density, temperature and q profiles are given by

$$n_e\,(\mathrm{cm}^{-3}) = 1.4 \times 10^{13}\,[1 - (r/a)^2] \tag{8}$$

$$T_e\,(\mathrm{keV}) = 1.4\,[1 - (r/a)^2]^2 \tag{9}$$

$$q = 1.5 + 2.5(r/a)^2 \tag{10}$$

In each Figure, poloidal and toroidal views of the ray paths are presented along with the plots of deposited power density and integrated deposited power as a function of radius.

In Figure 1, the launched ECH power is represented by a uniform array of 42 rays -- six angles in in the poloidal plane and for each poloidal angle, there are seven angles in the toroidal plane. The rays are taken to be uniformly spaced in both directions over a total angular width of 7.74°, the same angular width that is obtained when gaussian beam theory is used to describe the antenna pattern. The x's along each ray indicates a 10% or more additional power deposition along that ray path. The deposition location depends mainly on the poloidal angle. Since the six poloidal angles are symmetric about the plasma center line, the deposition pattern associated with the chosen uniform ray pattern is peaked at three radial locations. Clearly, this deposition pattern can not properly represent the deposition associated with the continuous, centrally peaked radiation pattern that is emitted by the antenna. In Figure 2, the ray paths and ECH deposition is presented for the case where 40 rays are chosen using the gaussian beam theory described above. The value of $w_o$ for the antenna is 2.032 cm and z was taken equal to 35 cm. R(z) is then equal to 54.2 cm and the effective location of the antenna is 19.2 cm behind the physical location of the antenna. The incident power is represented in terms of five radial zones about the central direction of the antenna.

Comparing the results presented in Figures 1 and 2, one finds that the deposition profile of the ECH power sensitively depends on the antenna modeling assumptions. Moreover, the choice of launch angles for the incident rays based on gaussian beam theory which properly describes the launch pattern results in a more realistic power deposition pattern than when a uniform array of incident rays is used to represent the incident ECH power.

Next we consider different antenna modeling procedures and the resulting power deposition profiles for ECH X-mode power launched into a D3 tokamak plasma from the high field side. The tokamak major radius is 143 cm and the plasma radius is 46 cm. The antenna was located two cm from the edge of the plasma. The plasma density, temperature and q profiles are given by

$$n_e\,(\mathrm{cm}^{-3}) = 4.9 \times 10^{13}\,[1 - (r/a)^{0.6}] \tag{11}$$

$$T_e\,(\mathrm{keV}) = 1.0\,[1 - (r/a)^2] \tag{12}$$

$$q = 1.0 + 3.0(r/a)^2 \tag{13}$$

and the cyclotron resonance is located on the plasma axis.

In Figure 3, we present results for the antenna pattern that was *assumed* in analyzing data taken during the ECH experiments on D3. Eleven rays are launched from the edge of the plasma and the angular range of the rays launched in the poloidal plane is taken to be 9.4° in the poloidal plane and 10.8° in the toroidal plane. In Figures 4 and 5 are results obtained using gaussian beam theory to provide the angular distribution of twenty rays used to model the antenna launch pattern. For the results in Figure 4 the antenna diameter is taken equal to 2.1 cm, the actual D3 antenna diameter. This corresponds to a beam waist radius, $w_o$ equal to 0.68 cm. The effective

launch point is 2.2 cm from the edge of the plasma and the angular range of the launched rays in the poloidal and toroidal planes is 20.5°. Clearly, when gaussian beam theory is used to model the power launched from the 2.1 cm antenna, power deposition occurs over a much broader radial range than when the assumed antenna pattern is used. The plots in Figure 5, show the ray paths and deposition profile that would result if an antenna of the type used on PLT were used on D3. Because of the larger antenna size, the effective launch point is 29.2 cm from the plasma edge and the angular range of the launched rays is 4.7°. Comparing Figures 3 and 5, we find that if this larger size antenna would have been used in the D3 ECH experiment, then the power deposition profile would have been closer to the one used in the analysis of the D3 data, i.e., the one shown in Figure 3.

In our study of ECH deposition profiles, we find that the radial range over which deposition takes place is not as localized as might be desired for some of the applications envisioned for ECH in toroidal geometry. Typically, in our studies the radial range of deposition is 10 to 15% of the plasma radius when the diameter of the wave guide that launches the power is 6.3 cm. When the launching wave guide diameter is smaller, for example 2.1 cm, or when the plasma is dense, the radial range over which power deposition takes place may be as large as 40%.

## CONCLUSIONS

The ECH energy depositions profiles presented above clearly indicate that care must be taken in choosing the ray pattern that represents the launched power. To develop confidence that a reasonable representation of the launched power distribution is being used, one should determine if the energy deposition profile changes when either the number of rays is increased or when some reasonable modification of the launched pattern of antenna power is assumed. Clearly, increased refraction of the rays, associated with higher plasma density, makes the deposition profile more dependent on the antenna modeling. The deposition range depends on the plasma density as well as on the antenna size. We find that when deposition is near the plasma center, the wave energy per unit volume is dependent on what fraction of our chosen antenna pattern happen to pass near the plasma center.

*Supported by DoE Contracts DE-FG02-84-ER5-3187, No. DE-AC02-76-CHO-3073, DE-AT03-84-ER5-3158 and by the CUNY Faculty Research Award Program.

## REFERENCES

1. H. Kogelnik and T. Li, Proceedings of the IEEE, **54**, 1312 (1966).

2. P. Goldsmit, Gaussian Beam Optics in *Infrared and Millimeter Waves* Volume **6**, Chapter 5, Edited by Kenneth Button.

3. R. L. Abrams, IEEE Journal of Quantum Electronics, **8**, 838 (1972).

4. H. Hsuan et al., Plasma Physics and Controlled Fusion **26**, 123 (1985).

5. J. Doane, Infrared and Millimeter Waves **13**, 123 (1985).

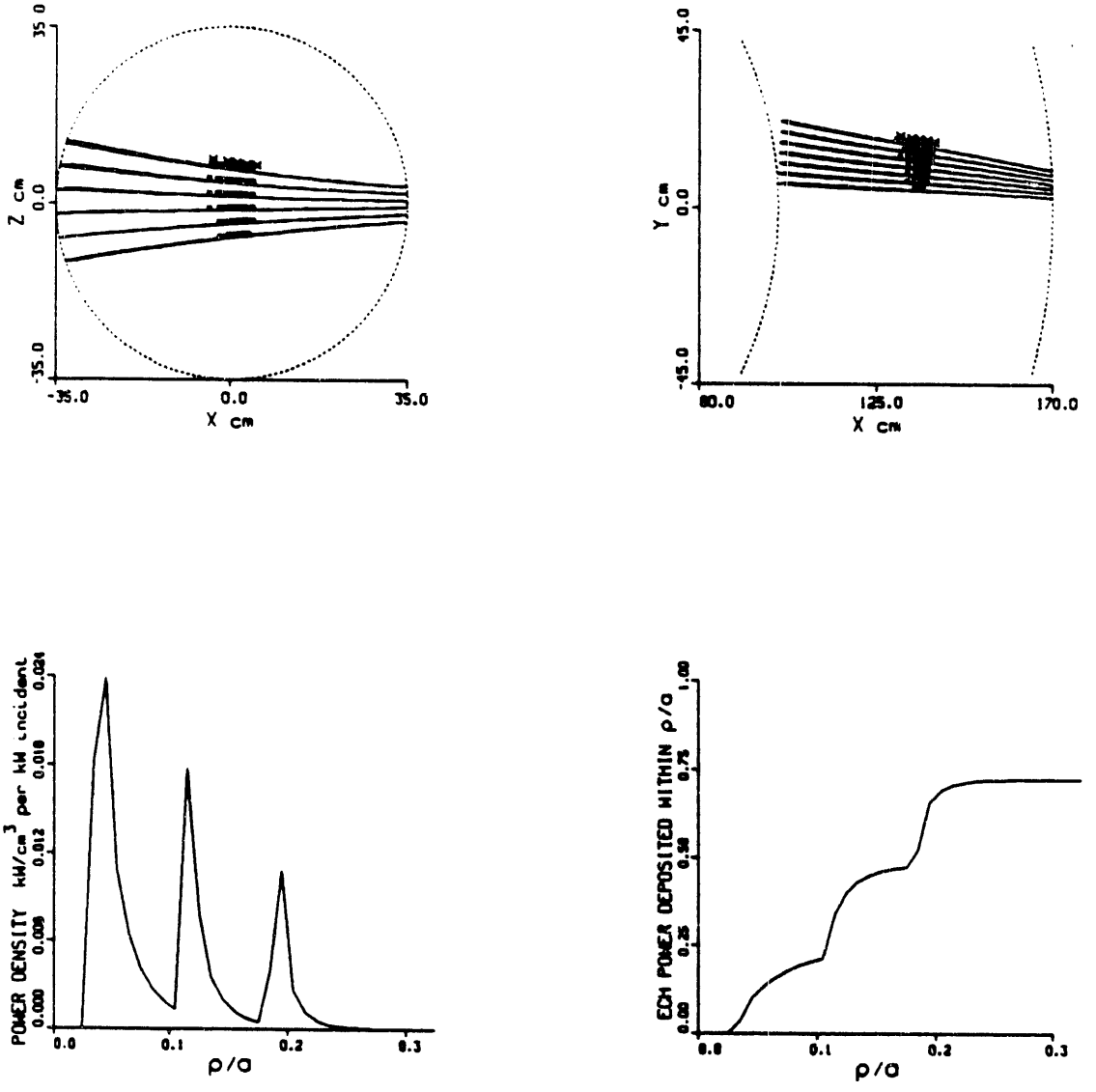


Figure 1. O-mode launched from the low magnetic field side. The antenna pattern is taken to be uniform.

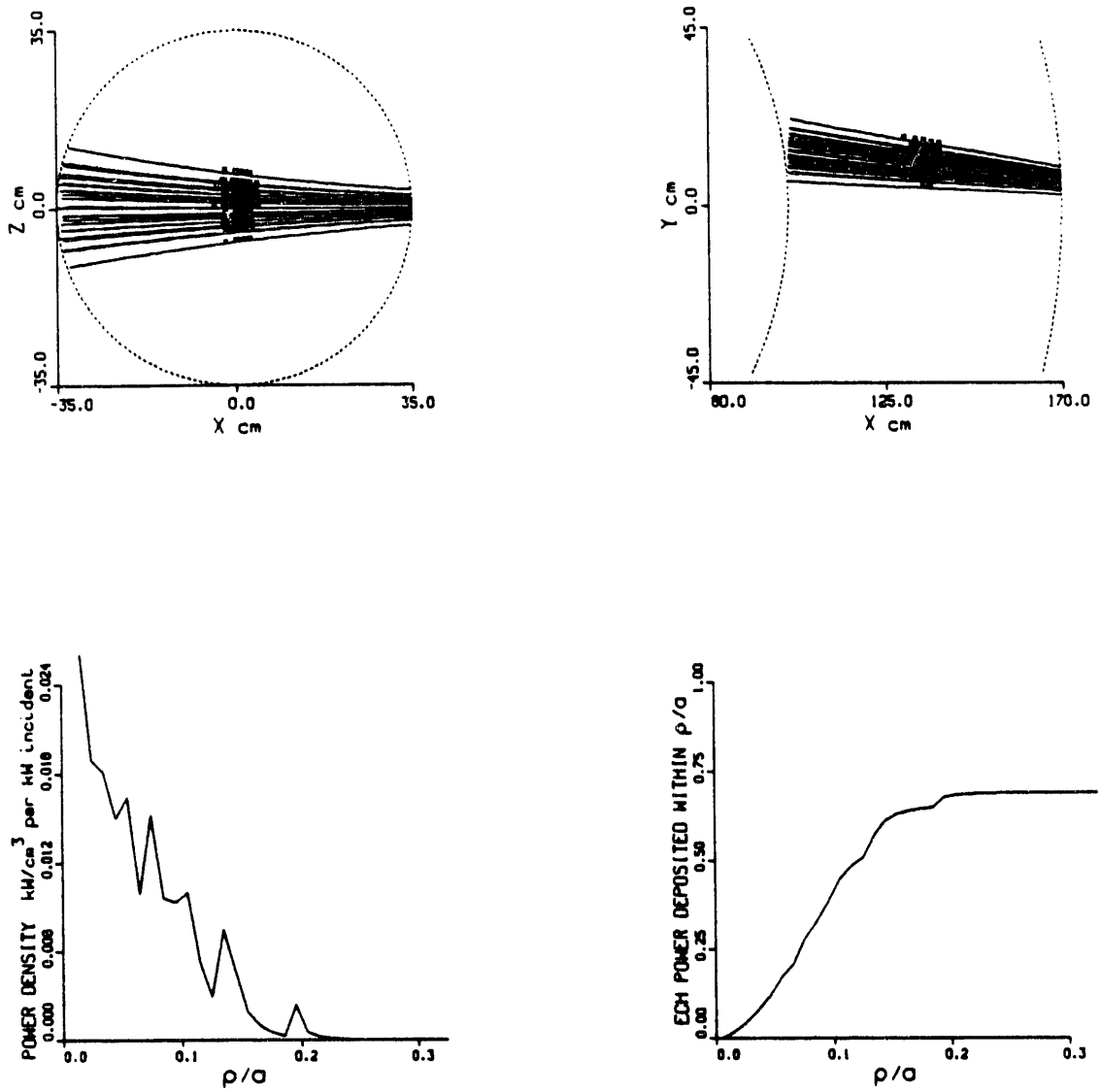


Figure 2. O-mode launched from the low magnetic field side. The antenna pattern is taken to be gaussian.

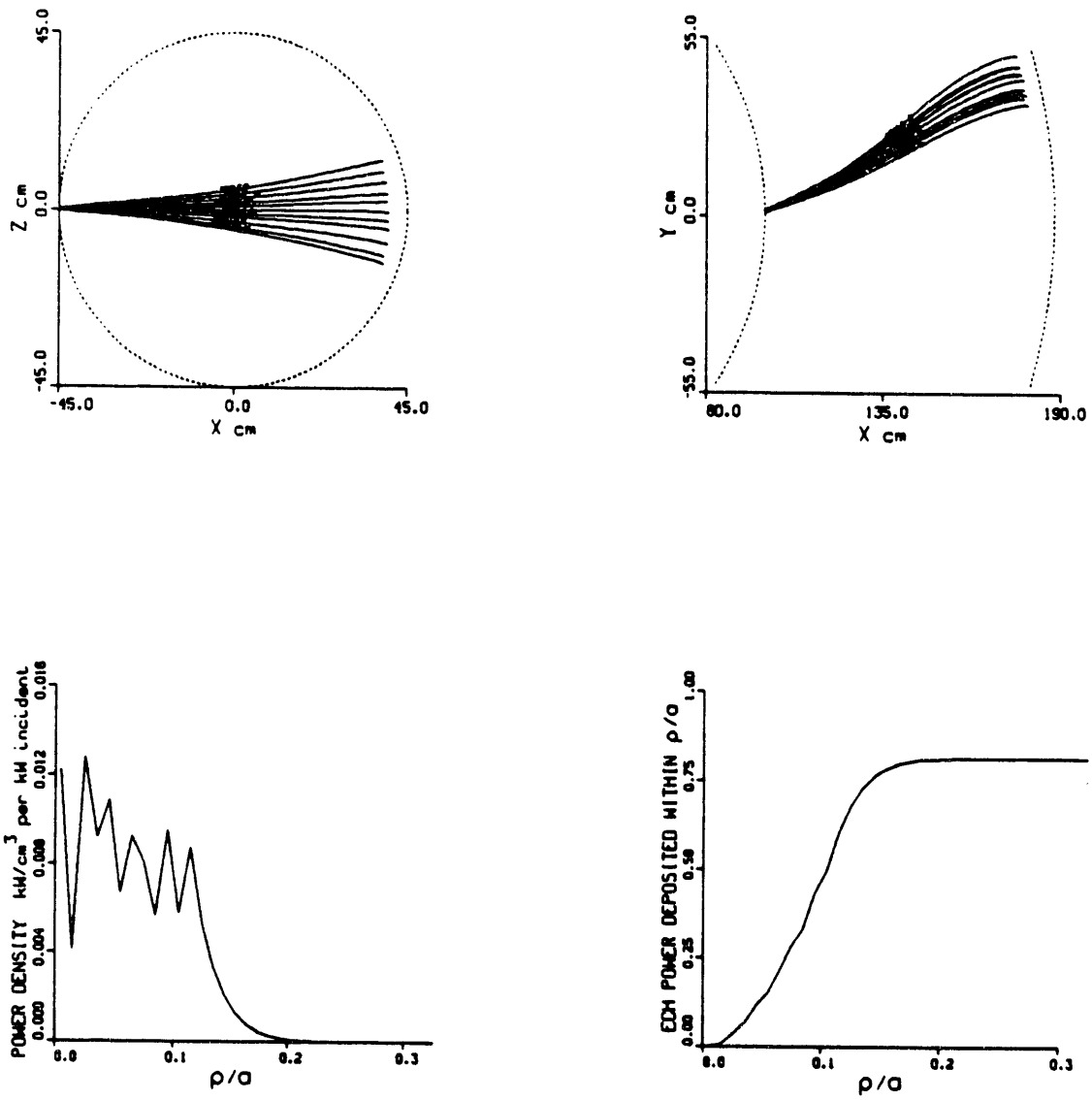


Figure 3. X-mode launched from the high magnetic field side. The antenna pattern is that used in the analysis of ECH data from experiments on D3.

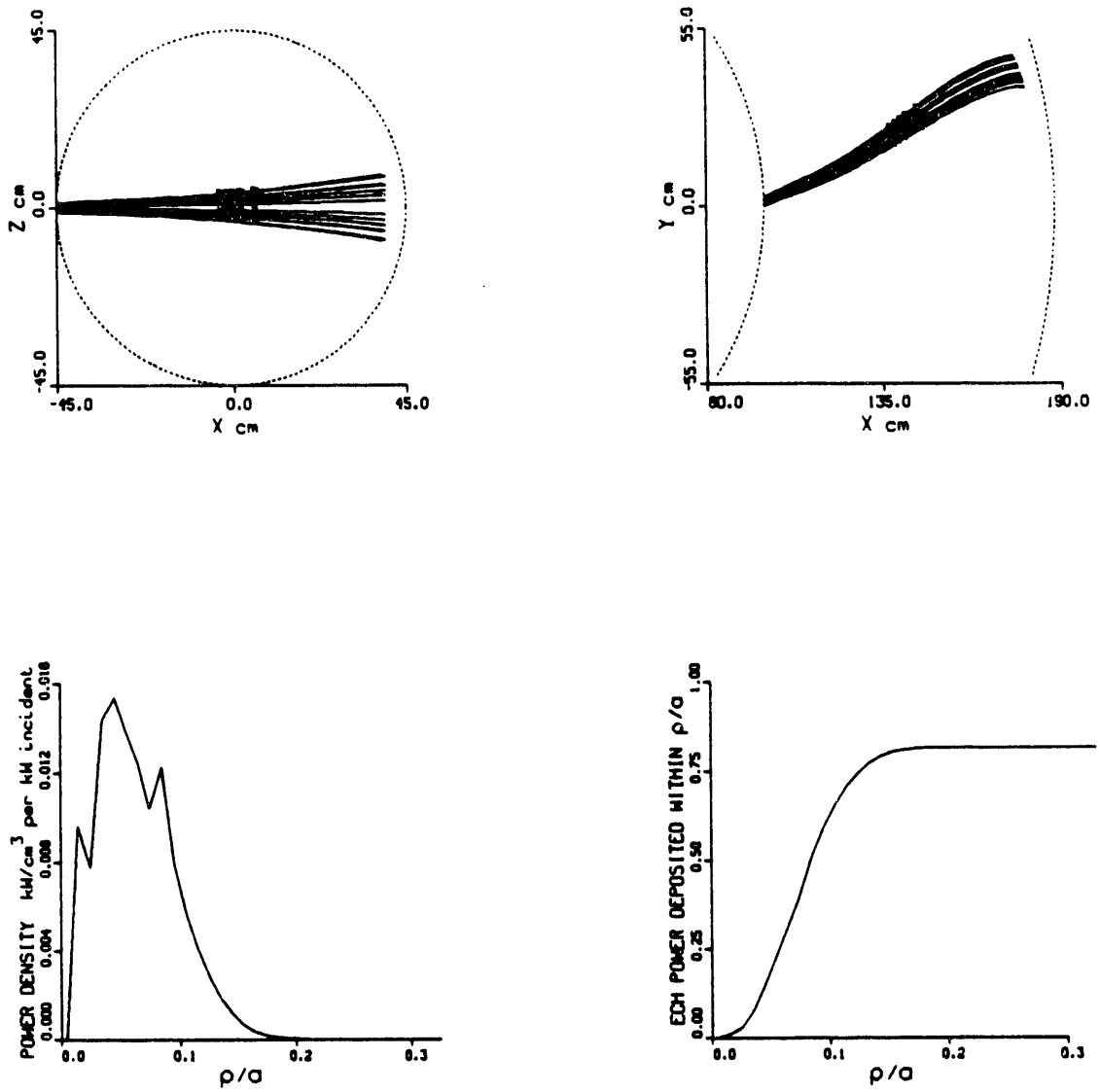


Figure 4. X-mode launched from the high magnetic field side. The antenna pattern is taken to be gaussian for an antenna 2.1 cm in diameter.

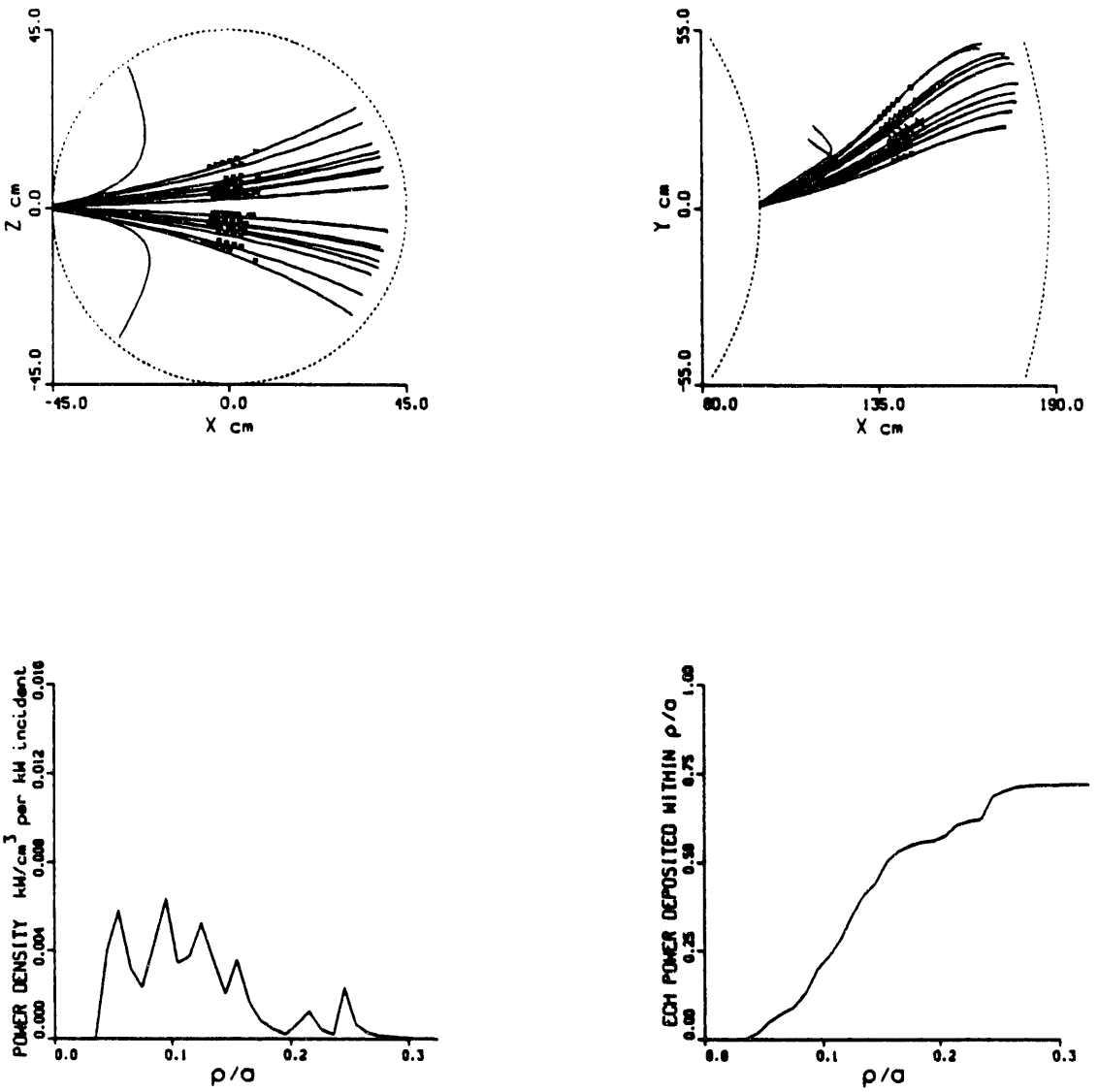


Figure 5. X-mode launched from the high magnetic field side. The antenna pattern is taken to be gaussian for an antenna 6.35 cm wide.

# Accessibility Study on a High Density Noncircular Tokamak by Ray Tracing*

K. Matsuda, V.S. Chan, R.W. Harvey, and A.H. Kritz†
*GA Technologies, Inc., San Diego, California 92138, U.S.A.*

*Using a ray tracing code which works for numerically given, two dimensional distributions of magnetic field and plasma pressure, we have studied the optimum injection angle for a given density profile and a given antenna location at the weaker field side, in a tokamak where the resonance is located at the magnetic axis or on the high field side of it.*

The things which we are going to present here are very simple and probably very obvious. However, we intend to talk about them, because they might be overlooked.

We have modified TORAY [1] which is a ray tracing code for a tokamak of circular cross section to be applicable for a tokamak of an arbitrarily shaped cross section. The code takes output from a MHD equilibrium code. With the help of other diagnostics, the pressure profile is divided into a density profile and a temperature profile. Then, the rest of the job is done by TORAY.

If we compare the accessibility in a high density tokamak of a noncircular cross section with a tokamak of a circular cross section, the results are about the same when the ray is launched and propagates around the mid-plane, provided the noncircular

*This is a report of work sponsored by the Department of Energy under Contract No. DE-AC03-84ER53158.
†Permanent Address: Hunter College, City University of New York.

tokamak has up-down symmetry. It is well-known that a ray can access the highest accessible density if it propagates normal to magnetic field lines. In the projection on a poloidal plane, a ray accesses to the highest density if it is normal to equal density lines. This is the case if a ray lies in the mid-plane.

There are other restrictions to be considered for DIII-D; such as, the maximum available toroidal magnetic field is such that we have the fundamental resonance at the magnetic axis, and antennas should be placed at the weaker field side. Thus, the ordinary mode should be launched. If we launch waves at the mid-plane, the maximum plasma density for wave penetration and heating is the cutoff density ($n_e = 4.4 \times 10^{13}/\mathrm{cm}^{-3}$ for $f_\omega = 60$ GHz).

Now, consider an off-midplane launcher for a noncircular tokamak such as illustrated in Fig. 1. If we try to heat the center of the plasma from the launcher as illustrated in Fig. 1 (line A′), the peak plasma density should be $3 \times 10^{13}/\mathrm{cm}^{-3}$ or less. For a higher density, a ray cannot reach to the center nor the resonance layer as ray A. Because ray A crosses equal-density surfaces with angles much different from 90°, the ray turns back at a much lower density than the cutoff density. If a ray makes about 90° with equal-density surfaces in the region near the cutoff density such as ray B, it almost reaches to the cutoff layer, but may not reach to the resonance layer. Ray C, which has a slightly different injection angle from ray B, reaches to the resonance at a plasma density slightly lower than the cutoff density. However, even with this injection, if a plasma density becomes higher, this ray may turn back without reaching the resonance layer. If we try to heat an outer region and inject a ray in the direction D′, actual heating occurs at a further outer region. Thus, we must find out an optimum injection angle for plasmas to be heated. If the injection angle is fixed, we must produce a plasma in which peak density and profile are within certain ranges.

For the case of Fig. 2, in which the central density is $5.5 \times 10^{13}/\mathrm{cm}^{-3}$ and the density profile is approximately given by

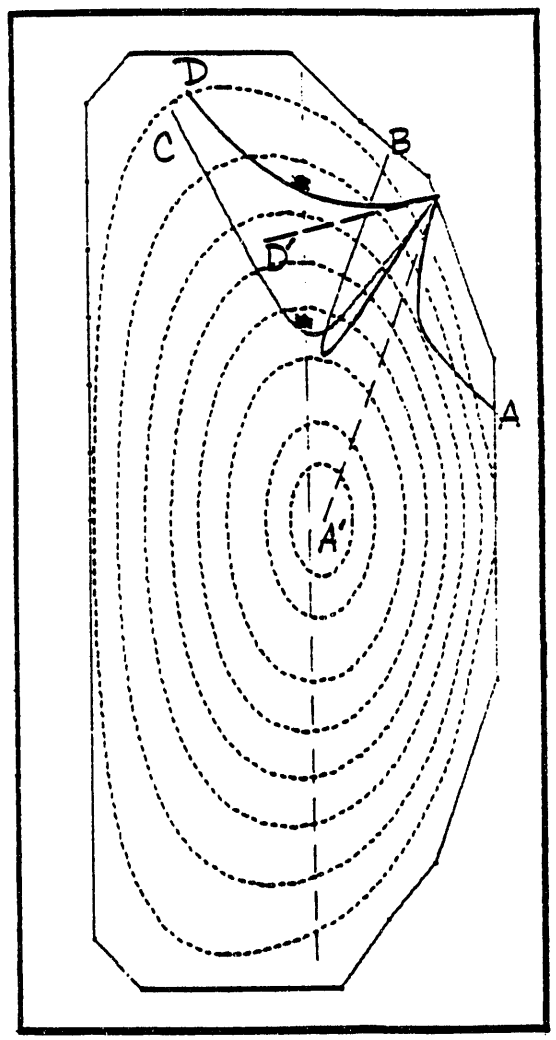


FIG. 1. Typical ray traces for an off-midplane launcher in a noncircular high density tokamak plasma.

$$n(z) = n_0 \left[1 - \left(\frac{z}{b}\right)^2\right]^{\alpha} \quad , \tag{1}$$

$$\alpha = 0.6 \quad ,$$

typical three rays are plotted. Ray A is tilted downward by 20° from the horizontal plane, B is 35°, and C is 40°. From this figure, we can expect that all rays pass the resonance if rays from an antenna are between 20° and 35°. But at the larger angle, only a fraction or none of the rays can pass the resonance. Assuming the opening

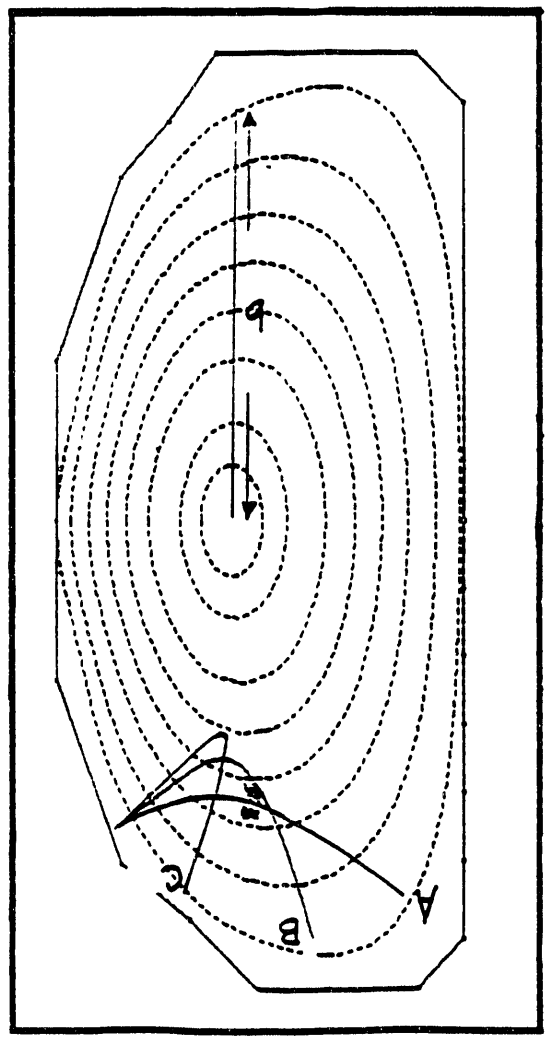


FIG. 2. Typical ray traces for $n_0 = 5.5 \times 10^{13}$ cm$^{-3}$.

of an antenna is 15° and the approximate density profile is given by Eq. (1) with various $n_0$ and $\alpha$, the absorption rate is shown in Table 1, assuming the central electron temperature of 2 keV. If the density is relatively low, a larger injection angle is probably more advantageous, because heating occurs relatively inside. But if the density is higher, a ray with a large angle cannot reach to the resonance, thus injection 20° ~ 35° gives better heating.

In conclusion, we need a detailed ray tracing study using the actual shape of a plasma if we have to launch waves which projections on a poloidal plane are not about

TABLE 1

ABSORPTION RATES FOR GIVEN DENSITY PROFILES

| $\theta$ | $n_0$ ($10^{13}/cm^{-3}$) | $\alpha$ | Absorption Rate (%) |
|---|---|---|---|
| 30° ~ 45° | 4.8 | 0.6 | 84 |
| | 5.0 | 0.7 | 78 |
| | 5.0 | 0.6 | 76 |
| | 5.5 | 0.7 | 49 |
| | 5.5 | 0.6 | 28 |
| | 6.0 | 1.0 | 62 |
| | 6.0 | 0.7 | 0 |
| | 6.5 | 1.0 | 0 |
| 20° ~ 35° | 5.5 | 0.7 | 72 |
| | 5.5 | 0.6 | 70 |
| | 6.0 | 1.0 | 78 |
| | 6.5 | 1.0 | 58 |

normal to the equal-density lines. If the experiment has some restrictions, as our DIII-D has, this kind of study may help designing experiments.

This is a report of work sponsored by the Department of Energy under Contract No. DE-AC03-84ER53158.

## Reference

[1] A.H. Kritz, H. Hsuan, A.C. Goldfinger, and D.B. Batchelor, in *Heating in Toroidal Plasmas* (Proc. 3rd Joint Varenna-Grenoble Int. Symposium, Grenoble, 1982), Vol. 2, 707 (1982).

# Simulation of the Effect of Electron Cyclotron Heating on Tearing Modes

E. Westerhof and W. Goedheer
*Association Euratom-FOM, FOM-Instituut voor Plasmafysica*
*Rijnhuizen, Nieuwegein, The Netherlands*

**ABSTRACT**

Transport code simulations of electron cyclotron heated discharges in TFR are presented. Special attention is paid to the influence of ECH on the behaviour of resistive MHD modes, as caused by changes of the current profile.

## I. INTRODUCTION

Electron cyclotron resonant heating experiments are in progress on the TFR tokamak using three 60 GHz gyrotrons [1]. The output power of each gyrotron is well over 200 kW and their pulselengths are limited to 100 ms. Introductory experiments were done with only one gyrotron at reduced power and pulselength, 100 kW (at the plasma) and 30 ms respectively. In these experiments a wide range of phenomena was studied [2]. One of these phenomena was MHD-activity. It was shown a.o. that heating just outside the q=2 surface stabilizes the (m=2, n=1) resistive tearing mode. Also active feedback control of this mode was done for the first time using electron cyclotron heating [2].

In this paper simulations of electron cyclotron heating in TFR are presented, which are performed with a version of the ICARUS [3] transport code. The beneficial effect of the well-localized electron cyclotron heating on the (m=2, n=1) tearing mode is shown and the dependence of this effect on the total absorbed power and the location of the electron cyclotron resonance is studied.

In the next two paragraphs a description is given of the models, that are used for the evaluation of the tearing mode evolution and of the power deposition of the electron cyclotron wave. Thereafter the results of the simulations are presented and their relation to the experimental result is discussed.

## II. THE TEARING MODE EVOLUTION

According to recent results from the quasilinear theory of tearing modes [4,5,6] there are three possible methods for stabilizing or diminishing tearing modes. Two of these, namely heating and current-drive inside the island directly affect the growth rate of the mode by changing locally the (m,n) component of the electric field. The third one: localized heating outside the resonant surface, only indirectly changes the growth of the mode through the induced changes in the current profile, thus changing 'delta prime', the stability parameter of the mode. In this paper only the latter effect is considered. The first two rely on poloidal variations of the electron temperature or current density and can only be accounted for in a 1-D transport code by making additional assumptions.

This leaves one with the following equation for the growth of a tearing mode with mode numbers (m,n) [6]

$$\dot{w}_{m,n} = 1.66\ \eta(r_s)\ \Delta'_{m,n}(w_{m,n}), \tag{1}$$

where $w_{m,n}$ is the total width of the (m,n)-islands, and $\eta(r_s)$ is the resistivity at the singular surface (defined by $q(r_s) = m/n$) and the factor 1.66 results from more detailed calculations [8] while $\Delta'_{m,n}(w_{m,n})$ is the change of the logarithmic derivative of the perturbed helical flux function $\psi_{m,n}$ over the entire island:

$$\Delta'_{m,n}(w_{m,n}) = \frac{\psi'_{m,n}(r_s + \tfrac{1}{2}w_{m,n}) - \psi'_{m,n}(r_s - \tfrac{1}{2}w_{m,n})}{\psi_{m,n}(r_s)} . \tag{2}$$

The perturbed helical flux function is given by the linearized equation of ideal MHD in the regions $r > r_s$ and $r < r_s$:

$$\frac{d^2}{dr^2}\psi_{m,n} + \frac{1}{r}\frac{d}{dr}\psi_{m,n} - \left[\frac{m^2}{r^2} + \frac{\mu_o \partial j_o/\partial r}{B_\theta - nrB_z/mR}\right]\psi_{m,n} = 0, \tag{3}$$

where $j_o$ is the current density (as it results from the transport code calculation), $B_\theta$ is the corresponding poloidal field, $B_z$ is the toroidal field and $\mu_o$ is the permeability of vacuum (all in S.I. units). Equation (3) determines $\psi_{m,n}$ in both regions up to a factor (which is proportional to the mode amplitude); together with the condition of continuity at $r=r_s$ this is sufficient to find $\Delta'$ from Eq. (2).

From Eq. (1) one sees that a saturated mode is found for $\Delta' = 0$. The size of the saturated island, $w_{sat}$, is thus given by the implicit equation

$$\Delta'(w_{sat}) = 0. \tag{4}$$

In Ref. 7 the resulting saturated island widths are shown to be in reasonable agreement with the results of a more detailed calculation [8].

At this stage we have to point to the following remark: stability or instability of a mode very sensitively depends on the singular term proportional to $\partial j_o/\partial r$ in Eq. (3); in a transport code, however, this term strongly depends on the assumptions made with regard to the resistivity. The uncertainties, in the experiments, about the resistivity are too large to permit a reliable prediction of (in-)stability of tearing modes, but it is meaningful to study the effect of profile changes due to, e.g., localized heating and its impact on an unstable mode. But caution remains necessary in the interpretation of the results of such a study.

## III. POWER DEPOSITION OF AN ELECTRON CYCLOTRON WAVE

In the experiments a wave is launched from the low-field side of the tokamak in the equatorial plane and perpendicular to the magnetic field. Wave polarization is in the ordinary mode. On the high-field side of the torus a collimating mirror, which conserves the mode polarization, is mounted to reflect the power which is not absorbed during the first pass at a toroidal angle of 20° in order to prevent reflection back into the launching system. In case of heating outside the q=2 surface the single-pass absorption in TFR is very low (i.e., less than 20%). Due to dispersion a large fraction of the remaining power will not reach the absorption layer in the second pass, but will only be absorbed after at least one additional reflection on the tokamak wall. This makes it virtually impossible to correctly predict the power deposition profile. For this reason the calculation is limited to the evaluation of the absorption during the first pass only and, for comparison with experiments, this absorbed power is identified with the injected power. To evaluate the first pass absorption a parallel beam having a finite vertical size is used. The power distribution inside the beam is taken to be parabolic, i.e.,

$$P_o(y) \sim \left(1 - (y/w)^2\right), \tag{5}$$

where y is the vertical coordinate, w is the half-width of the beam and $P_0(y)$ is taken to be the intensity of the beam integrated over the toroidal direction. The local power absorption in the poloidal cross-section of the tokamak then is given by

$$P_{abs}(x,y) = \alpha(x,y)\, e^{-\int_0^{s(x,y)} \alpha ds'}\, P_o(y), \tag{5}$$

where s is the spatial coordinate along the beam and $\alpha(x,y)$ is the local absorption coefficient, which is evaluated in the weakly relativistic limit for perpendicular propagation [9]. The power absorbed at any point of a flux surface spreads out very quickly over the entire flux surface leading to the following radial power deposition profile (cf. [11])

$$P_{ECH}(r) = \frac{1}{4\pi^2 R} \oint_0^{2\pi} d\theta\, P_{abs}(x,y), \tag{7}$$

where R is the major radius of the tokamak.

## IV. RESULTS OF THE SIMULATIONS

The effect of electron cyclotron heating on the (m=2, n=1) tearing mode is presented for three cases with only slightly different positions of the q=2 surface and the electron cyclotron resonance. The Ohmic target plasmas were simulated in such a way that they showed an unstable (m=2, n=1) tearing mode with a saturated width between 3 and 4 cm. In all three cases the same transport, average density and impurity content (O and Ni) was used. The relevant parameters are given in Table I.

Table I. Parameters common for all runs

| | | |
|---|---|---|
| major radius | R | 0.96 m |
| minor radius | a | 0.18 m |
| average density | $\langle n_e \rangle$ | $1.1 \cdot 10^{19}$ m$^{-3}$ |
| impurities | $n_O/n_e$ constant | 1 % |
| | $n_{Ni}/n_e$ constant | 2 ‰ |
| transport: | 'modified' ALCATOR/INTOR: | |
| | $n_e \chi_e$ | $(1.1 + 0.6\frac{r}{a})\, 10^{19}$ m$^{-1}$ s$^{-1}$; |
| | $D_e$ | $(0.5 - 0.4\frac{r}{a})\, \chi_e$; |
| | neo-classical thermal transport for the ions; | |
| | classical 'Spitzer' resistivity | |

For the Ohmic target plasmas only the total current, I, and the toroidal magnetic field, $B_\phi$, were varied in order to change the relative positions of the q=2 surface, $r_s$, and the position, $x_{cy}$, of the electron cyclotron resonance. In Table II these quantities are given for the three cases together with some characteristic parameters of the resulting target plasmas. The results of the simulation agree reasonably with the experimental observations on TFR in this regime.

Table II. Specific parameters for the ohmic target plasmas

| | Case I | Case II | Case III |
|---|---|---|---|
| $B_\phi$ | 2.43 T | 2.47 T | 2.47 T |
| I | 140 kA | 140 kA | 130 kA |
| $T_e(o)$ | 1050 eV | 1050 eV | 980 eV |
| $n_e(o)$ | $2.4 \cdot 10^{19}$ $m^{-3}$ | $2.4 \cdot 10^{19}$ $m^{-3}$ | $2.4 \cdot 10^{19}$ $m^{-3}$ |
| $\tau_E$ | 9 ms | 9 ms | 9 ms |
| $r_s$ | 14 cm | 14 cm | 13 cm |
| $x_{cy}$ | 13 cm | 15 cm | 15 cm |
| $w_{2/1,\,sat}$ | 3.4 cm | 3.5 cm | 3.4 cm |

The relative positions of $r_s$ and $x_{cy}$ indicate that the absorption occurs just inside $r_s$, just outside $r_s$ and somewhat further outside $r_s$, respectively. On these Ohmic target plasmas electron cyclotron pulses of 100 ms with 100, 200, 300, 400 and 500 kW total power and a beam (half-)width of 6 cm were applied. The resulting power deposition profile was centred around a radius equal to $x_{cy}$ with a width of 1 to 2 cm. The total amount of absorbed electron cyclotron power, which at high power levels increased considerably during the heating pulse, for cases II and III was 17, 36, 55 to 65, 75 to 100 and 95 to 150 kW, respectively, while for case I the total absorption was twice as high, the electron cyclotron resonance being further inside. In Fig. 1 the effect of these well-localized heating pulses on the width, $w_{2/1}$, of the island of the (m=2, n=1) tearing mode is shown. A large stabilizing effect is found for heating just outside the q=2 surface with a high total power absorption (Fig. 1b). Contrary to earlier results [4,10] this effect is found to be limited in time. In the next paragraph this result and further details will be discussed.

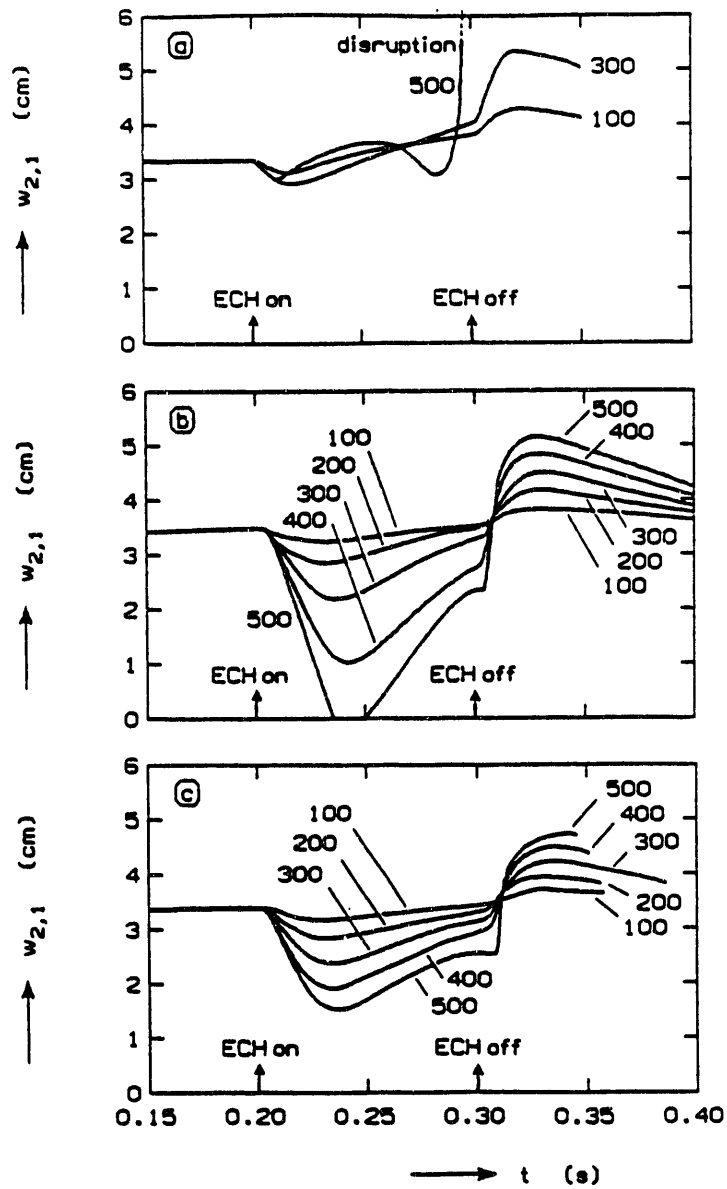


Fig. 1: The effect of ECH on the size of the (m=2, n=1) tearing mode. The effect of a 100 ms electron cyclotron heating pulse is shown:

a) for heating of the case I Ohmic target plasma with 100, 300 and 500 kW ECH. Really absorbed in the first pass is 30, 100 to 130 and 190 to 330 kW, respectively;

b) for heating of the case II Ohmic target plasma with 100, 200, 300, 400 and 500 kW ECH. Really absorbed in the first pass is 17, 36, 55 to 65, 75 to 100 and 95-150 kW, respectively;

c) for heating of the case III Ohmic target plasma. The launched and absorbed ECH powers are the same as quoted under b.

## V. DISCUSSION OF THE RESULTS

Figure 1 shows that the effect of the localized heating strongly depends on both the position of the heating and the effective heating power (i.e., the power which is absorbed in the plasma). While the effect of heating just inside the q=2 surface is small (Fig. 1a) heating up to 1 cm outside the q=2 surface can completely stabilize the (m=2, n=1) mode (Fig. 1b) if the absorbed power is around 100 kW (remember that the efficiency of single pass absorption is around 20 %). Heating about 1 cm further from the q=2 surface requires a considerably higher power to achieve the same effect (Fig. 1c).

All three cases show that the beneficial effect of the heating is only temporary. On a longer timescale the profiles become unstable again. For case I with 500 kW electron cyclotron heating power the island reaches an unrealistically large size just before the end of the pulse, which indicates the inevitable occurrence of a major disruption. This is caused by a slow global diffusion of the current from the centre outwards, which in the long run is destabilizing. This effect is illustrated in Fig. 2 where the current and temperature profiles for case II with 500 kW are shown before, after 10 ms of electron cyclotron heating and at the end of the electron cyclotron heating pulse. After 10 ms the change in the current profile is still reasonably localized and the radius of the q=2 surface is hardly changed. At the end of the pulse, however, the changes are global and much larger causing a significant increase in q on axis and an inward shift of the singular radius. This destabilizes the mode again.

All three cases also show that, when the heating is stopped, the mode shows an explosive growth. On a longer timescale, however, the plasma globally relaxes and returns to its initial steady state with a saturated island of the same width as before the heating.

Because of the uncertainties with regard to the current density and power disposition profile a detailed comparison with the experimental results is impossible. The timescales in the experiment [2], however, are about a factor of 2 faster than the ones shown in Fig. 1. This difference is within the uncertainty about the resistivity, which is sometimes claimed to be 2 or more times (neo-)classical. What one does see in the experiment, however, is that the effect can be only temporary: before the end of a 30 ms ECH pulse on a saturated mode the mode starts to grow again [2].

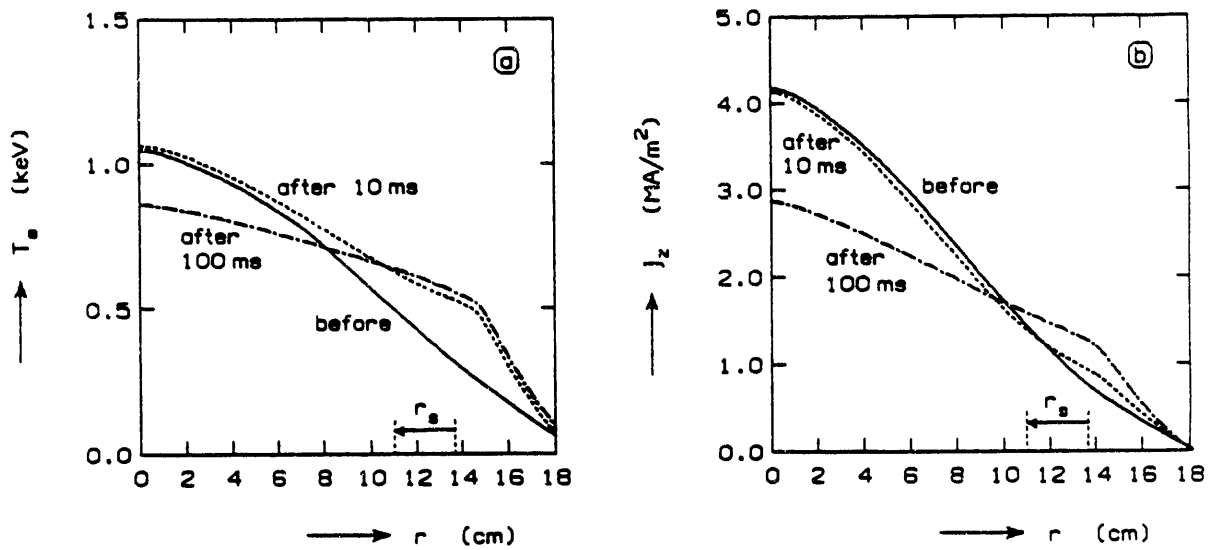


Fig. 2: The changes of the temperature and current density profile during the ECH pulse.

a) The temperature profiles of the case II plasma with 500 kW of ECH (95-150 kW really absorbed) just before ECH, after 10 ms of ECH and at the end of the 100 ms ECH pulse;

b) The corresponding current density profiles. The profile after 10 ms of ECH is already stable for the (m=2, n=1) tearing mode, but the mode can only decrease on a resistive timescale and lags behind. The profile at the end of the ECH pulse is unstable for the (m=2, n=1) tearing mode again due to the drop of $j_z(o)$ and the shift of the q=2 surface, $r_s$, as indicated in the figures.

As far as the amount of power necessary for complete stabilization is concerned, the experiment, in fact, showed complete stabilization with 100 kW injected into the plasma [2]. This probably corresponds to an absorbed power of 100 kW, since the power cannot easily escape from the vacuum vessel, so it eventually is absorbed around the EC resonance. This is consistent with the simulation which did show show the possibility of complete stabilization with ≈ 100 kW of actually absorbed power in a single pass.

## VI. CONCLUSIONS

This leads us to the following conclusions:

- Stabilization of the (m=2, n=1) tearing mode by means of ECH is possible in TFR as shown by both experiment and simulation.
- With long ECH pulses, however, the mode can become unstable again. This is because the amount of power necessary for stabilization is of the same order of magnitude as the Ohmic input power, thus leading to significant (destabilizing) global changes of the current density profile on a resistive timescale.
- The effect of ECH strongly depends on the relative location of the q=2 surface and the EC resonance. The effect is largest for heating just outside the q=2 surface.
- Detailed comparison of simulation and experimental results is hampered by the lack of knowledge of the resistivity (i.e., of the actual current profile) and of the true power deposition profile. This latter problem is due to the fact that single pass absorption around the q=2 surface is below 20 % in TFR.
- So far experiment and simulation are in reasonable agreement.

## ACKNOWLEDGEMENTS

Discussions with members of the TFR-Group and the FOM-ECRH-Team on both experiment and theory are gratefully acknowledged.

This work was performed under the Euratom-FOM association agreement with financial support from ZWO and Euratom.

## REFERENCES


1. R. Cano et al., 1984, in Proceedings of the 4th International Symposium on Heating in Toroidal Plasmas, Rome, March 21-28, 1984, Vol. II, p. 853.
2. FOM-ECRH Team & TFR-Group, in Proceedings of the 12th European Conference on Contr. Fusion and Plasma Physics, Budapest, 1985, Contributed papers, Vol. II, p. 60.
3. M. Watkins et al., 1976, in Methods in Computational Physics 16, Eds. J. Killeen et al., Academy press, New York.
4. Y. Yoshioka, S. Kinoshita and T. Kobayashi, 1984, Nucl. Fusion 24, 565.
5. A.H. Reiman, 1983, Phys. Fluids 26, 1338.
6. R.B. White et al., 1985, to be published in the Proceedings of the Workshop on Magnetic Reconnection and Turbulence, Cargèse (Corsica, France), July 7-13, 1985.
7. B. Carreras, B.V. Waddel and H.R. Hicks, 1979, Nucl. Fusion 19. 1423.
8. R.B. White et al., 1977, Phys. Fluids 20, 800.
9. M. Bornatici et al., 1985, Nucl. Fusion 23. 1153; and references therein.
10. V. Chan and G. Guest, 1982, Nucl. Fusion 22, 272.
11. R. Cano et al., 1983, rapport EUR-CEA-FC-1170.

# Velocity Space Diffusion of Electrons Induced by a Beam of Electron Cyclotron Waves of Finite Size in Toroidal Geometry

L. Demeio* and F. Engelmann
*Association Euratom-FOM, FOM-Instituut voor Plasmafysica*
*Rijnhuizen, Nieuwegein, The Netherlands*

**ABSTRACT**

Generalizing earlier results, the quasilinear diffusion tensor $\underline{\underline{D}}$ is derived for circulating electrons interacting with an electron cyclotron wave beam of finite size in a tokamak configuration. Two approaches are considered, the first starting from Vlasov's equation following the lines of standard quasilinear theory, the other using a test particle model. The result is applied to rediscuss the limitations of the quasi-uniform model commonly adopted.

## 1. INTRODUCTION

Velocity space diffusion of the electron distibution, induced by a wave field, has been extensively studied in the case of an infinite homogeneous plasma, immersed in a uniform static magnetic field (see, e.g., [1]). However, when RF power is injected into a toroidal plasma a somewhat different situation is encountered. In fact, the inhomogeneity of the magnetic field and the finite size of the wave beam modify the basic characteristics of the resonant interaction between particles and waves; in particular, the time of interaction which is infinite in a homogeneous system (neglecting collisions and radiation damping) is now finite, which leads to a broadening of the resonance of the wave-particle interaction.

The quasilinear diffusion tensor, as derived for a homogeneous system, has been applied by several authors (see, e.g., [2,3]) to the case of heating and current drive by means of electron cyclotron waves in a toroidal plasma by simply reducing the known expression by the ratio of the beam cross-section to the area of the flux surface concerned. More-

* Euratom fellow; Commission of the European Communities, Brussels, Belgium

over, the magnetic field is taken to be constant on a flux surface. As shown in [4] and discussed in more detail in this paper, this approach is not generally satisfactory. In fact, it appears that only for those flux surfaces whose minor radius r is much larger or much smaller than the linear dimension of the beam d, this simple model is applicable, while flux surfaces with r ≈ d are poorly described.

The aim of the present work is to reconsider the derivation of the diffusion tensor $\underline{\underline{D}}$ describing the time evolution of the electron distribution function for a non-uniform confining magnetic field and a non-uniform wave excitation. In particular, we refer to an axisymmetric toroidal plasma into which a beam of electron cyclotron waves of finite size is injected. Only the regions of velocity space corresponding to effectively freely circulating particles, with approximately constant parallel velocity, are considered.

Two different approaches are used:

(i) the diffusion equation for the electron distribution function is obtained from Vlasov's equation, following the lines of the standard derivation of quasilinear theory [1];

(ii) a test particle model is used, which describes the effect of many transits through the beam as a random walk in velocity space.

For simplicity, in both cases, the analysis is performed for successive transits through the beam being statistically independent although the effect of correlations between transits can be taken into account by a straightforward generalization of the model. The finiteness of the wave beam is taken into account in two different ways: either by introducing explicitly a finite wave-particle interaction time or by taking a wave spectrum appropriate to describe the finite beam width.

The expression obtained for the diffusion tensor $\underline{\underline{D}}$ is the same in all cases and provides a generalization of the result of Ref. 4, where only the perpendicular tensor component $D_{\perp\perp}$ was considered adopting a test particle model.

## 2. DERIVATION OF THE DIFFUSION TENSOR

### 2.1 Introductory remarks

For simplicity, we consider an axisymmetic toroidal magnetoplasma in which circular concentric magnetic surfaces are present, as illustrated in Fig. 1. The magnetic field is assumed to be nearly toroidal. The wave

beam is supposed to be symmetric with respect to the midplane of the torus, L and 2b being, respectively, its toroidal and vertical dimensions. Most of the discussion, however, applies more generally.

For the wave field, we take either a single mode

$$\tilde{E}\,(\mathbf{x},t) = E_{k_0}\, g(\theta)h(z)e^{i(\mathbf{k}_0.\mathbf{x}-\omega t)} + \text{c.c.} \tag{2.1}$$

with h(z) effectively describing the beam shape in the toroidal direction or alternatively

$$\tilde{E}(\mathbf{x},t) = g(\theta) \int_{-\infty}^{+\infty} dk_{\|}\, E_{\mathbf{k}}\, e^{i(\mathbf{k}\,.\,\mathbf{x}-\omega t)} + \text{c.c.} \tag{2.2}$$

where the finite beam size in toroidal direction is described via an appropriate wave spectrum $E(k_{\|})$. Here c.c. denotes the complex conjugate and $\mathbf{k}_0 \equiv \mathbf{n}k_{\|_0} + k_{\perp}\,(\mathbf{e}_1 \cos\psi + \mathbf{e}_2 \sin\psi)$ is the wave vector of a plane wave, the subscripts $\|$ and $\perp$ referring to parallel and perpendicular directions with respect to the static magnetic field $\mathbf{B}_0$ and ($\mathbf{n} \equiv \mathbf{B}_0/B_0$, $\mathbf{e}_1,\mathbf{e}_2$) forming a right-handed set of orthogonal unit vectors. The wave frequency $\omega$ is taken to be real. The function $g(\theta)$ describes the shape of the beam in the poloidal direction. The Fourier component $E_{\mathbf{k}}$ in (2.2) can be expressed by

$$E_{\mathbf{k}} = E_{\mathbf{k}_0}\, H(k_{\|}) \tag{2.3}$$

where $\mathbf{k} \equiv \mathbf{n}k_{\|} + k_{\perp}(\mathbf{e}_1 \cos\psi + \mathbf{e}_2 \sin\psi)$ and $H(k_{\|})$ is the Fourier transform of h(z). The quasilinear theory of uniform systems relies on distinguishing two different scales in the time dependence of the distribution function f and the amplitudes $\tilde{\mathbf{E}}$ and $\tilde{\mathbf{B}}$ of the electric and magnetic wave fields: a rapid oscillation and a slow variation of the equilibrium, a necessary condition being that $|\tilde{\mathbf{E}}|$, $|\tilde{\mathbf{B}}|$ are sufficiently small. In toroidal geometry an intermediate time scale appears, characterized, for example, by the time of revolution of a circulating particle around the torus, $\tau_c \equiv 2\pi R/|v_{\|}|$, where R is the major radius of the torus and $v_{\|}$ the component of the velocity vector parallel to the static magnetic field. Furthermore, since a wave beam of finite size is considered, one also has a transit time of a particle through the beam

$$\tau_F \equiv \frac{1}{|v_{\|}|} \int_{-\infty}^{+\infty} h(z')\, dz' \equiv \frac{L}{|v_{\|}|}\ ,$$

and an average time between successive transits through the beam, $\bar{\tau}_p \equiv \tau_F S/\sigma$, where $S = 4\pi^2 rR$ is the flux surface area, and $\sigma$ the area of that part of the flux surface which intersects with the beam. For $r > b$, one has $\sigma = 4Lr\arcsin(b/r)$, while for $r < b$ one obtains $\sigma = 2\pi rL$. The relation $\bar{\tau}_p >> \tau_F$, which expresses the smallness of the dimensions of the beam compared to the size of the system, will be assumed throughout. Both $\tau_F$ and $\bar{\tau}_p$ also are intermediate time scales. As a consequence, $v_\parallel$ can be considered to be constant over many transits of a particle through the wave beam.

### 2.2 Kinetic approach

Denoting with $f_0$ and $\bar{f}$, respectively, the slowly varying and the oscillating part of the electron distribution function, Vlasov's equation yields, in the usual way,

$$\partial f_0/\partial t = e/m < (\bar{E} + v \times \bar{B}/c) \cdot \partial \bar{f}/\partial v > . \tag{2.4}$$

and

$$d\bar{f}/\partial t\Big|_0 = e/m\ (\bar{E} + v \times \bar{B}/c) \cdot \partial f_0/\partial v . \tag{2.5}$$

Here, e and m are the charge and the mass of the electron, c the speed of light and $d/dt|_0 \equiv \partial/\partial t + v \cdot \nabla - (e/mc) v \times B_0 \cdot \partial/\partial v$ is the time derivative along the unperturbed particle orbit. The statistical average <...>, is assumed to have the property of annihilating all fast oscillating contributions. From Eqs. (2.4) and (2.5) one obtains

$$\partial f_0/\partial t = \partial/\partial v \cdot \underline{\underline{D}}(t) \cdot (\partial/\partial v) f_0, \tag{2.6}$$

where the diffusion tensor $\underline{\underline{D}}$ is given by

$$\underline{\underline{D}}(t) = \left(\frac{e}{m}\right)^2 [g(\theta)]^2 \sum_\ell [a_{\ell,k_0}\ h(z_0 + v_\parallel t) - \frac{i}{\omega}\frac{dh}{dt} \cdot c_{\ell,k_0}] \cdot$$
$$\cdot [\int_{-\infty}^{t} dt'\, h(z_0 + v_\parallel t') e^{-i\int_t^{t'} \Omega_{\ell,k_0} dt''} b_{\ell,k_0} - \frac{ih(z_0 + v_\parallel t)}{\omega} \cdot c_{\ell,k_0}]^* + c.c. \tag{2.7}$$

Here, $\Omega_{\ell,k_0} \equiv \omega - k_{\parallel_0} v_\parallel - \ell\omega_c$, $\omega_c \equiv |eB_0/mc|$ is the cyclotron frequency,

$$a_{\ell,k_0} = b_{\ell,k_0} - (\Omega_{\ell,k_0}/\omega)\, c_{\ell,k_0}, \quad c_{\ell,k_0} = \varepsilon_{\ell,k_0}[n(v_\perp/v_\parallel) - (v_\perp/v_\perp)],$$

$$b_{\ell,k_0} = \theta_{\ell,k_0}[n(v_\perp/v_\parallel)((\omega-\ell\omega_c)/\omega) + (v_\perp/v_\perp)(\ell\omega_c/\omega)],$$

$$\varepsilon_{\ell,k_0} = J_{\ell-1}E^-_{k_0}e^{i\psi} + J_{\ell+1}E^+_{k_0}e^{-i\psi}, \quad \theta_{\ell,k_0} = \varepsilon_{\ell,k_0} + (v_\parallel/v_\perp)J_\ell E''_{k_0},$$

where $J_\ell$ is the Bessel function of order $\ell$ and argument $k_\perp v_\perp/\omega_c$, $E^\pm_{k_0} = \frac{1}{2}(E^{(1)}_{k_0} \pm iE^{(2)}_{k_0})$ are the right-handed and left-handed polarizations of the electric field, and $E''_{k_0} = E_{k_0}\cdot n$. The explicit time dependence which appears in $\underline{\underline{D}}(t)$ refers to the intermediate time scale. The diffusion coefficient describing the motion of the equilibrium on the long time scale is given by

$$\underline{\underline{D}} = \frac{1}{\tau_c}\oint\frac{B(s)ds}{\oint B(s)ds}\int_{-\infty}^{+\infty}dt\,\underline{\underline{D}}(t) = \frac{4\pi^2}{\tau_c}\left(\frac{e}{m}\right)^2\oint\frac{B(s)ds}{\oint B(s)ds}\times$$

$$[g(s)]^2\sum_\ell|\Delta(\Omega_{\ell,k_0},s)|^2\,b_{\ell,k_0}b^*_{\ell,k_0}. \qquad (2.8)$$

where s denotes a coordinate along the circumference of the cross-section of the magnetic surface considered. The ideal resonance, which is present in uniform systems, is now replaced by

$$\Delta(\Omega,s) \equiv \frac{1}{2\pi}\int_{-\infty}^{+\infty}dt\,h(z_0 + v_\parallel t)\,e^{-i\int_0^t dt'\,\Omega(s,t')}, \qquad (2.9)$$

from which, in the limit of a homogeneous magnetic field and uniform wave excitation, the Dirac $\delta$-function is recovered.

When the finite beam size is introduced through the shape of the spectrum one finds

$$\underline{\underline{D}} = \frac{4\pi^2}{\tau_c}\left(\frac{e}{m}\right)^2\oint\frac{B(s)ds}{\oint B(s)ds}[g(s)]^2\sum_\ell\left|\int_{-\infty}^{+\infty}dk_\parallel\,e^{ik_\parallel z_0}H(k_\parallel)\Delta_\infty(\Omega_{\ell,k_0},s)\right|^2$$

$$\cdot\, b_{\ell,k_0}b^*_{\ell,k_0} \qquad (2.10)$$

with $\Delta_\infty(\Omega,s) \equiv \frac{1}{2\pi}\int_{-\infty}^{+\infty}dt\,e^{-i\int_0^t\Omega(s,t)dt'}$, which, after some algebra, can be proven to be equal to (2.8).

### 2.3 Test particle approach

At any transit through the wave beam, an electron suffers an increment $\Delta v$ in the velocity vector. Assuming that successive transits are statistically independent, the diffusion tensor $\underline{\underline{D}}$ is obtained by calculating

$$\underline{\underline{D}} = \int\frac{B(s)ds}{\oint B(s)ds}\,\frac{\langle\Delta v\,\Delta v\rangle}{2\tau_c}.$$

The increment $\Delta \mathbf{v}$ can be derived from the equation of motion for a single electron, regarding the effect of the wave as a perturbation on the basic cyclotron motion. Substituting the result in the expression for $\underline{\underline{D}}$, averaging over the Larmor period and the initial phases, and over the flux surface, expression (2.8) for the diffusion tensor is recovered. In a similar way, Eq. (2.10) is found when the finite beam size is described by a wave spectrum.

## 3. CONCLUSIONS AND DISCUSSION

In conclusion, all approaches considered yield the same expression for the diffusion tensor. The agreement between the two different ways of treating the finite beam size (i.e., finite interaction time and appropriate $k_{||}$ spectrum) is actually trivial, since the two cases are only formally different. On the other hand, the kinetic and the single particle approach, although aiming at describing the same physical process, rely on somewhat different concepts, so that the agreement of the results is not fully obvious.

Let us now discuss the properties of the diffusion tensor in some more detail. To obtain an explicit expression for the resonant function $|\Delta|^2$, we assume that, within the wave beam, the change of the cyclotron frequency $\omega_c$ along a field line, due to the rotational transform, is small and can be described by using the expansion $\omega_c(z) = \omega_c(z_0) + (d\omega_c/dz)_{z_0}(z - z_0)$. Note that this approximation is not valid in the special case of magnetic field lines crossing the equatorial plane while passing through the beam (i.e., for $\theta = s/r \simeq 0;\pi$). Putting $z = z_0 + v_{||} t$ we have $\omega_c(t) = \omega_c(0,\theta) + \text{sign}\,(v_{||} \sin\theta)(2\pi/\tau_B^2)t$. Simple geometrical considerations show that $\tau_B = R\{2\pi q/(r\omega_c|v_{||} \sin\theta|)\}^{1/2}$, where R is the distance of the point corresponding to $z_0$ from the major axis of the torus and $\omega_c \equiv \omega_c(0,\theta)$. The time $\tau_B$ is related to the variation of the magnetic field felt by a particle travelling along the field line considered and measures the duration of the resonant interaction of a particle with the wave during one transit through the beam.

With the special choice $h(z_0 + v_{||} t) = \exp\{-\pi(t/\tau_F)^2\}$ for the function describing the shape of the wave beam, we finally obtain

$$\left|\Delta(\Omega_{\ell,k_0},s)\right|^2 = \left(\frac{\tau_F}{2\pi}\right)^2 \left\{1 + \left(\frac{\tau_F}{\tau_B}\right)^4\right\}^{-1/2} e^{-\frac{(\bar{\Omega}_{\ell,k_0,\theta}\tau_F)^2/2\pi}{1 + (\tau_F/\tau_B)^4}} \tag{3.1}$$

where $\bar{\Omega}_{\ell,k_0,\theta} \equiv \omega - k_{||_0} v_{||} - \ell\omega_c(0,\theta(s))$. Two limiting cases can be distinguished. For $\tau_F \ll \tau_B$, the magnetic field variation felt by the

particle while passing through the wave beam is very small and the resonant interaction is effectively determined by the finite beam size, leading to a broadening of the resonance, with respect to the homogeneous case, $\delta\bar{\Omega} \approx 1/\tau_F$ consistent with the wave-particle interaction time being $\tau_F$. In the opposite limit, $\tau_F \gg \tau_B$, the effect of the magnetic field variation is strong, leading to an interaction time short compared to the transit time through the beam. Since the exact resonance $\Omega_{\ell,k_0} = 0$, for the field line considered, can be at any point within the beam and $\omega_c(z)$ varies along the field line by $\Delta\omega_c \approx 2\pi\tau_F/\tau_B^2$, the function $|\Delta|^2$ is large over the interval $\delta\bar{\Omega} \approx \tau_F/\tau_B^2$. Furthermore, the maximum of the diffusion tensor is smaller, by a factor $(\tau_B/\tau_F)^2 \ll 1$, than its value in the opposite limit.

With Eq. (3.1) one can estimate the validity of the simple flux surface averaging of the diffusion tensor, currently in use [2,3]. It is easy to see that, for $\tau_F \gg \tau_B$, the result given by the quasi-uniform model cannot be recovered, therefore, $\tau_F \ll \tau_B$ must be fulfilled. Moreover, $|\Delta|^2 \approx (\tau_F/2\pi)^2$ must be valid over the intersection of the flux surface with the wave beam, which requires $|\bar{\Omega}_{\ell,k_0}(\theta)\tau_F/\sqrt{2\pi}| \ll 1$ for all values of $\theta$ within the beam, i.e., the magnetic field may vary only very little in this range. This latter condition is often stronger than the former, $\tau_F \ll \tau_B$, in particular if the wave beam is around the equatorial plane, as considered here. It implies

$$\left(\frac{v_\parallel}{c}\right)^2 \{1 + [g(r)]^{-2}\} + \left(\frac{v_\perp}{c}\right)^2 \gg 1, \tag{3.2}$$

with $g(r) = (1/\sqrt{2\pi})(\omega_c L/c)(r/R)$ for $r \leq b$, and $g(r) = (1/\sqrt{2\pi})(\omega_c L/c)(r/R)\{1 - [1 - (b/r)^2]^{1/2}\}$ for $r > b$. The maximum of $g(r)$ is at $r = b$ and takes the value $g(b) = (1/\sqrt{2\pi})(\omega_c L/c)(b/R)$. Condition (3.2) can be satisfied only if $g(r) \ll 1$. The behaviour of $g(r)$, normalized to its maximum $g(b)$, is shown in Fig. 2. In most practical cases, $g(b) \approx 1$ or larger. E.g., for a small tokamak, like TFR, $g(b) \approx 3$, while in a larger device, assuming a well collimated beam, $g(b)$ can be somewhat smaller, but not less than one.

In conclusion, we can expect the simple quasi-uniform model to yield a good approximation only on the outermost flux surfaces and close to the magnetic axis; in fact, in both cases, the variation of the magnetic field over the beam aperture is small: because of the small curvature in the former case, and because of the small excursion perpendicular to the confining magnetic field in the latter. With regard to the outermost flux

surfaces and in the non-relativistic limit, this result has been given by Cairns and Lashmore-Davies [4]. If condition (3.2) is not satisfied, the diffusion, within the resonant range as following from the quasi-uniform model, tends to be weaker than this model would predict, while it may extend over a range that is wider. Effectively, the results obtained for $\underline{\underline{D}}$ indicate that a corrected quasi-uniform model in which only that part of the beam is taken into account which can resonantly interact with an electron of given velocity provides a fair approximation to the actual situation, as is physically intuitive. However, in addition the resonant range must be properly adjusted.

**ACKNOWLEDGEMENT.** This work was performed under the Euratom-FOM association agreement with finacial support from ZWO and Euratom.

**REFERENCES**

[1] Kennel C.F., Engelmann F., Phys. Fluids 9 (1966) 2377.
[2] Cordey J.G., Edlington T. Start D.F.H., Plasma Phys. 24 (1982) 73.
[3] Fidone I., Meyer R.L., Granata G., Phys. Fluids 26 (1983) 3292.
[4] Cairns R.A., Lashmore-Davies C.N., IVth Int. Symp. on ECE and ECRH, Rome, March 28-30 (1984), p. 72; Ed. by ENEA.

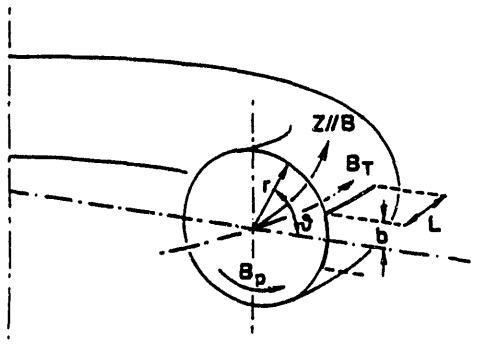


Fig.1: Geometry and coordinates.

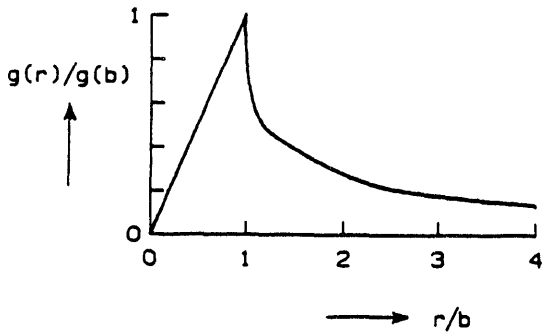


Fig.2: Schematical plot of the function g(r)/g(b) as defined in the text.

# Propagation of a Gaussian Wave Packet in an Absorbing Medium and Generalization of a Group Velocity

Masayoshi Tanaka
*Research Institute for Applied Mechanics,*
*Kyushu University, Kasuga, Fukuoka 816, Japan*

ABSTRACT

Propagation of a Gaussian wave packet in an absorbing medium is studied in order to shed a light on the physical basis of ray tracing in a plasma with the electron cyclotron absorption. Using the saddle point method, we obtain the propagation velocity for the maximum amplitude as

$$\frac{dx}{dt} = \frac{C}{\left(\frac{\partial n\bar{\omega}_s}{\partial \bar{\omega}_s}\right)' - \left(\frac{\partial n\bar{\omega}_s}{\partial \bar{\omega}_s}\right)''\left(\frac{\partial^2 n\bar{\omega}_s}{\partial \bar{\omega}_s^2}\right)' \Big/ \left(\left(\frac{\partial^2 n\bar{\omega}_s}{\partial \bar{\omega}_s^2}\right)'' + \frac{x_0}{x}\Delta^2\right)}$$

,which is reduced to the group velocity for the absorption free case. This velocity shows a good agreement with the numerical results and is considered as the generalized group velocity valid for an absorbing medium.

## I INTRODUCTION

A method for describing wave propagation in a plasma is based on the geometrical optics, in which the trajectories of waves are defined by the group velocity and the Hamiltonian equations are obtained for the trajectory and the wavenumber. Integrating these equations with appropriate dispersion relation, we can describe the wave propagation in the plasma.

As was pointed out by Brillouin and Sommerfeld,[1] however, an absorbing medium indicates the anomalous dispersion and the group velocity may become infinite in the absorption range of frequency. Similar results[2),3)] have been reported for a plasma with the electron cyclotron absorption. So far,a common understanding on the group velocity in an absorbing medium is that the concept of group velocity breaks down.

Recently there have been many attempts to describe a wave packet propagation in an absorbing medium. Among them, Gintzburg[4] proposed the group velocity in an absorbing medium as

$$\frac{dx}{dt} = \frac{C}{\left(\frac{\partial n\omega}{\partial \omega}\right)' - \left(\frac{\partial n\omega}{\partial \omega}\right)''^{2} \Big/ \left(\frac{\partial n\omega}{\partial \omega}\right)'}$$

On the other hand, Garrett and MuCumber[5] pointed out that under certain conditions the wave packet does propagate with the group velocity even it exceeds the light velocity. Crisp[6] proposed the wave packet deformation as a mechanism of such the anomalous propagation.

In experiments, direct observations of the wave packet have been made on semiconductors using the time of flight methods of laser pulses, which provide two seemingly contradictory results, i.e., in a spatially dispersive medium the pulse velocity slows down in the absorption range of frequency,[7] however, the pulse acceleration has been observed on a frequency dispersive

medium.[8] The latter is understood in terms of wave packet deformation due to absorption characteristic of the medium. Tanaka et al.[9] show the coexistence of both propagations in a Lorentz medium and also show that these are fundamental characteristic of wave packet propagation in an absorbing medium.

The problem of interest is to obtain the propagation velocity relevant to describe those various phenomena on the wave packet propagation in an absorbing medium. For this purpose we consider the propagation of a Gaussian wave packet travelling in a model medium with absorption and examine its asymptotic behaviour both theoretically and numerically. The saddle point method[10] is used in describing the wave packet and the propagation velocity for peak amplitude is derived as

$$\frac{dx}{dt} = \frac{C}{\left(\frac{\partial n\bar{\omega}_s}{\partial \bar{\omega}_s}\right)' - \left(\frac{\partial n\bar{\omega}_s}{\partial \bar{\omega}_s}\right)''\left(\frac{\partial^2 n\bar{\omega}_s}{\partial \bar{\omega}_s^2}\right)' \Big/ \left(\left(\frac{\partial^2 n\bar{\omega}_s}{\partial \bar{\omega}_s^2}\right)'' + \frac{x_0}{x}\Delta^2\right)}$$

, which coincides with the group velocity for an absorption free case. Numerical calculations show that the trajectory of the peak amplitude asymptotically approaches to that obtained by the above equation. It also reveals that in the early stage of flight the wave packet propagates backward direction. After a few tens of wavelength the backward components fully die out and then the wave packet propagates forward direction. The result is qualitatively understood in terms of the damping of Fourier component waves.

## II FORMULATION

### (i) The Saddle Point Method

One dimensional Propagation of a Gaussian wave packet is studied in a uniform electron Lorentz gas as a model medium of a plasma with absorption. The refractive index, which characterizes the wave packet propagation, is related to the dielectric coefficient of the medium as

$$n(\omega) = n'(\omega) + i\, n''(\omega) = \sqrt{\varepsilon(\omega)} \tag{1}$$

$$\varepsilon(\omega) = 1 + \frac{\omega_p^2}{\omega_0^2 - \omega^2 - 2i\rho\omega} \tag{2}$$

where $\omega_p$ and $\rho$ are an electron plasma frequency and a dissipation rate, respectively. A quantity $\omega_0$ is a resonance frequency of the medium at which the absorption takes place. Figure 1 shows the refractive index as a function of frequency. The medium exhibits anomalous dispersion and is highly dispersive around the resonance frequency.

The profile of the wave packet propagating in the medium (at time t and position x ) is expressed by the Fourier integral[11];

$$U(x,t) = \frac{1}{\sqrt{2\pi}} \int_{-\infty}^{\infty} d\omega\, e^{-i\omega t} \left[ A(\omega) e^{i\frac{n(\omega)\omega x}{c}} + B(\omega) e^{-i\frac{n(\omega)\omega x}{c}} \right] \tag{3}$$

We will consider a Gaussian modulated wave packet given by

$$U(0,t) = e^{-t^2/2\Delta^2} \cos\omega_c t \tag{4}$$

where $\Delta$ is the pulse width and $\omega_c$ is the frequency of carrier wave.

Taking a right-going wave (positive direction of x ) in eq.(3), we have

$$U(x,t) = \frac{1}{\sqrt{2\pi}} \int_{-\infty}^{\infty} d\omega\, A(\omega)\, e^{i\frac{n(\omega)\omega}{c}x - i\omega t} + c.c. \tag{5}$$

where $A(\omega)$ is given by

$$A(\omega) = \frac{\Delta}{4}\, e^{-\frac{1}{2}(\omega-\omega_c)^2\Delta^2} \tag{6}$$

The asymptotic form of the wave packet is obtained with an aid of the saddle point method. To make use of this method, $n(\omega)$ is analytically continued to a complex $\omega$-plane . Equation (5) is then re-written by

$$U(x,t) = \frac{\bar{\Delta}/4}{\sqrt{2\pi}} \int d\bar{\omega}\, e^{\frac{x}{x_0}P(\bar{\omega})} + c.c. \tag{7}$$

where $\bar{\omega} = \omega/\omega_0$, $x_0 = c/\omega_0$, and the $P(\bar{\omega})$ is given by

$$P(\bar{\omega}) = i\left(n(\bar{\omega})\bar{\omega} - \bar{\omega}\frac{ct}{x}\right) - \frac{1}{2}\frac{x_c}{x}(\bar{\omega}-\bar{\omega}_c)^2\bar{\Delta}^2 \qquad (8)$$

where $\bar{\omega}_c = \omega_c/\omega_0$, $\bar{\Delta} = \Delta\omega_0$ . A quantity $x/x_0$ is the propagation distance normalized by the wavelength in the vacuum. The asymptotic form of eq.(7) is determined by the saddle points of $P(\bar{\omega})$ , which is defined by

$$\bar{\omega}_s ; \quad \left.\frac{\partial P}{\partial \bar{\omega}}\right|_{\omega_s} = i\left(\frac{\partial n\bar{\omega}_s}{\partial \bar{\omega}_s} - \frac{ct}{x}\right) - \frac{x_0}{x}(\bar{\omega}_s - \bar{\omega}_c)\bar{\Delta}^2 = 0 \qquad (9)$$

The saddle points are usually complex quantities and the path of integration is deformed so as to pass through the saddle points. After an integration the wave packet is given by

$$U(x,t) = \sum_{\bar{\omega}_s} \frac{\bar{\Delta}/4}{\sqrt{\frac{x}{x_0}\left|\frac{\partial^2 P}{\partial \omega_s^2}\right|}} \; e^{\frac{x}{x_0}P(\bar{\omega}_s) + i\alpha_s} \qquad (10)$$

where $\alpha_s$ is the angle between the path of integration and the real axis at the saddle point. When more than one saddle points are present in the complex $\omega$-plane, eq.(10) is considered as a summation with respect to the saddle points.

(ii) Velocity of Peak Amplitude

Now we will derive the velocity of peak amplitude. The saddle point corresponding to the peak amplitude is determined by the zero of exponent of eq.(10):

$$R_e\left[\frac{\partial P(\bar{\omega}_s)}{\partial t}\right] = R_e\left[\frac{\partial P}{\partial t} + \frac{\partial P}{\partial \bar{\omega}_s}\frac{\partial \bar{\omega}_s}{\partial t}\right] = 0 \qquad (11)$$

Noting that $\partial P/\partial \bar{\omega}_s = 0$ , we obtain from the first term of eq.(11),

$$\omega_s'' = 0 \qquad \text{for peak amplitude.} \qquad (12)$$

After infinitesimal increment of time $t \to t+\delta t$, the position of the peak amplitude and the saddle point change their values as $x \to x+\delta x$, $\omega_s \to \omega_s+\delta\omega_s$. Since the saddle point must always satisfy eq.(9),

$$\frac{\partial}{\partial \bar{\omega}_s}\frac{\partial P}{\partial \bar{\omega}_s}\delta\bar{\omega}_s + \frac{\partial P}{\partial t\,\partial \bar{\omega}_s}\delta t + \frac{\partial P}{\partial x\,\partial \omega_s}\delta x = 0 \qquad (13)$$

Dividing the above equation with respect to $\delta t$ , we have

$$\frac{\partial P}{\partial x \partial \bar{\omega}_s} \frac{dx}{dt} + \frac{\partial^2 P}{\partial \bar{\omega}_s^2} \frac{d\bar{\omega}_s}{dt} = - \frac{\partial P}{\partial t \partial \bar{\omega}_s} \tag{14}$$

The real and imaginary part of this equation are

$$\left(\frac{\partial n \bar{\omega}_s}{\partial \omega_s}\right)'' \frac{dx}{dt} - x \left(\left(\frac{\partial^2 n \bar{\omega}_s}{\partial \bar{\omega}_s^2}\right)'' + \frac{x_0}{x} \Delta^2\right) \frac{d\bar{\omega}_s'}{dt} = 0 \tag{15}$$

$$\left(\frac{\partial n \bar{\omega}_s}{\partial \bar{\omega}_s}\right)' \frac{dx}{dt} + x \left(\frac{\partial^2 n \bar{\omega}_s}{\partial \bar{\omega}_s^2}\right)' \frac{d\bar{\omega}_s'}{dt} = C \tag{16}$$

where $\bar{\omega}_s'' = 0$ is used. Solving these equations in terms of dx/dt and $d\bar{\omega}_s'/dt$, we have the velocity of peak amplitude and the rate of change of the saddle point frequency along the trajectory;

$$\frac{dx}{dt} = \frac{C}{\left(\frac{\partial n \bar{\omega}_s}{\partial \bar{\omega}_s}\right)' - \left(\frac{\partial n \bar{\omega}_s}{\partial \bar{\omega}_s}\right)'' \left(\frac{\partial^2 n \bar{\omega}_s}{\partial \bar{\omega}_s^2}\right)' \Big/ \left(\left(\frac{\partial^2 n \bar{\omega}_s}{\partial \bar{\omega}^2}\right)'' + \frac{x_0}{x} \Delta^2\right)} \tag{17}$$

$$\frac{d\bar{\omega}_s'}{dt} = \frac{C/x}{\left(\frac{\partial^2 n \bar{\omega}_s}{\partial \bar{\omega}_s^2}\right)' + \left(\left(\frac{\partial^2 n \bar{\omega}_s}{\partial \bar{\omega}_s^2}\right)'' + \frac{x_0}{x} \Delta^2\right) \left(\frac{\partial n \bar{\omega}_s}{\partial \omega_s}\right)' \Big/ \left(\frac{\partial n \bar{\omega}_s}{\partial \bar{\omega}_s}\right)''} \tag{18}$$

When the absorption is negligibly small, $(\partial n\bar{\omega}_s/\partial\bar{\omega}_s)'' \approx 0$ , these equations are reduced to

$$\frac{dx}{dt} = \frac{c}{\dfrac{\partial n\bar{\omega}_c}{\partial\bar{\omega}_c}} \tag{19}$$

$$\frac{d\bar{\omega}_c}{dt} = 0 \tag{20}$$

which is a usual Hamiltonian system describing the wave trajectory in a homogeneous medium. Equation (19) is the group velocity.

Integrating the set of eqs.(17) and (18), we can determined the trajectory of peak amplitude for an absorbing medium.

## III RESULTS and DISCUSSION

The saddle points are numerically determined by eqs.(1),(2) and (9) and the wave packet is evaluated by substituting those saddle points into eq.(10). Figure 2 shows the time development of the wave packet observed at a fixed position for different carrier frequencies. The abscissa is normalized time $t/t_c$ where $t_c$ is the travelling time of a light pulse in the vacuum and the observation position is $x/x_0 = 120$ . The maximum amplitudes are normalized to unity. The width of the wave packet is $\bar{\Delta}$ = 50. When the carrier frequency is far from the frequency of absorption, the wave packet propagates without deformation. On the other hand ,when the carrier frequency

is near the frequency of absorption, the wave packet takes longer time to reach the observation point and exhibits the deformation from its initial wave form. The average propagation velocity determined by the travelling distance divided by its flight time of the peak amplitude, x/t , is plotted in Fig.3. A dashed line indicates the group velocity obtained from the dispersion relation and a dotted line the velocity given by Gintzburg. Although these velocities coincide with numerical results in the absorption free region, there is a remarkable deviation in the absorption range of frequency. This means that these velocity , group velocity and Gintzburg's velocity, no longer describe the propagation of the wave packet.

The trajectory of the wave packet can be determined by integrating eqs.(17) and (18) , which is shown by the solid line in Fig.4. The profiles of the wave packet observed at fixed positions are also shown in Fig.5. The carrier frequency is $\omega_c/\omega_0 = 1$ for both figures and the peak amplitudes are normalized to unity in Fig.5. In the short range of travelling distance, there is a small peak propagating backward and it damps out within a few tens of wavelength. After some critical distance forward-going peak appears and its trajectory asymptotically approaches to that obtained by eqs.(17)and (18). The wave packet in the initial stage of flight propagates backward direction.

The above results can be qualitatively understood in terms of Fourier component waves. Consider the wave packet with carrier frequency $\omega_c/\omega_c = 1$. Figure 6 shows the schematic of refractive index and the Fourier spectrum of the wave packet. A component wave in the anomalous dispersion region (denoted by $U_A$ ) may propagate backward direction, while a component wave in the normal dispersion region( denoted by $U_N$ ) may propagate forward direction. In the initial stage of flight the most part of wave energy locates in the anomalous dispersion region and so the wave packet as a whole propagates backward direction. However, the anomalous component fully die out within short

travelling distance Then the wave packet consists of those normal component and, thereafter, propagates forward direction.

It might be worth pointing out the mathematical difference between the saddle point method and the expansion approximation which is used in deriving the group velocity and the Gintzburg's velocity. To describe the wave packet, one have to evaluate the Fourier integral in which the integrand is highly oscillating function(see eq.(3)). The expansion approximation is so far used assuming a narrow frequency spread of the spectrum. However, the integrand is highly oscillating function and the contribution is not localized in the neighbourhood of the central region of the spectrum because of resultant cancellations of the integrand. Moreover, the medium is highly dispersive in the absorption range of frequency. The basic assumption that the contribution is localized does not always hold and therefore this approximation is inappropriate for this problem. In the saddle point method, however, the oscillation of the integrand can be suppressed by deforming the contour of the integral and one can evaluate the integral with desired accuracy. In addition this method has a great advantage that further assumption on the spectrum such as a narrow frequency spread is no need for evaluations.

When the absorption is negligibly small, one can easily verify that the saddle point corresponding to the peak amplitude is equal to the carrier wave frequency. Under these conditions there is no difference between the two methods and eq.(17) gives the group velocity, which is the reason why the group velocity and Gintzburg's velocity show a good agreement with numerical results for the absorption free region.

In summary, we study the propagation of wave packet in an absorbing medium. It turns out that the group velocity and Gintzburg's velocity fail in describing the propagation of wave packet in the absorption range of frequency. The velocity of peak amplitude is obtained within the framework of

the saddle point method. The numerical calculations reveals that the wave packet in the initial stage propagates backward and the trajectory asymptotically approaches to that obtained by eq.(17). This quantity, which is reduced to the group velocity for an absorption free case, is considered as a " generalized group velocity " valid for an absorbing medium.

## REFERENCES


1. L. Brillouin, Wave Propagation and Group Velocity (Academic, New York, 1960).
2. M. Tanaka, M. Fujiwara, and H. Ikegami, J. Phys. Soc. Jpn. 50, 1358 (1981).
3. C.Maroli and V. Petrillo, Plasma Physics 23, 671 (1981).
4. V. L. Gintzburg, The Propagation of Electromagnetic Waves in Plasma (Pergamon, Oxford, 1964) p.496
5. C. G. B. Garrett and D. E. McCumber, Phys. Rev. A 1, 305 (1970).
6. M. D. Crisp, Phys. Rev. A 4, 2104 (1971).
7. R. G. Ulbrich and G. W. Fehrenbach, Phys. Rev. Lett. 43, 963 (1979).
8. S. Chu and S. Wong, Phys. Rev. Lett 48, 738 (1982).
9. M. Tanaka, M.Fujiwara and H. Ikegami, Institute of Plasma Physics Report Nagoya University, IPPJ-710 1984, submitted to Phys. Rev. A
10. P. M. morse and H. Feshbach, Methods of Theorecical Physics (McGrow-Hill, New York, 1953) Part I, p.437.
11. J. D. Jackson, Classical Electrodynamics (John Wiley & Sons, New York, 1975) Chap. 7, p.331.

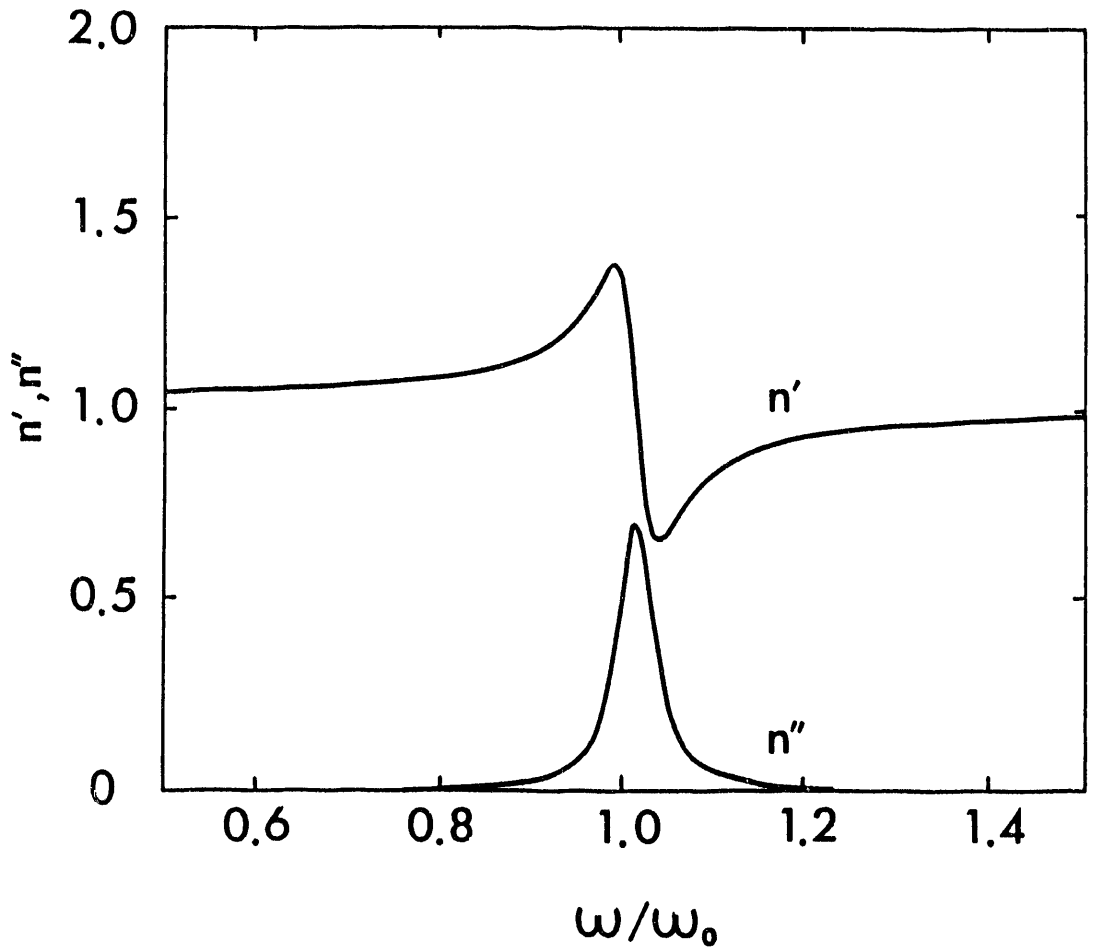


Fig.1 Refractive index as a function of frequency
$\omega_p / \omega_0 = 0.25, \quad \rho / \omega_0 = 0.02$

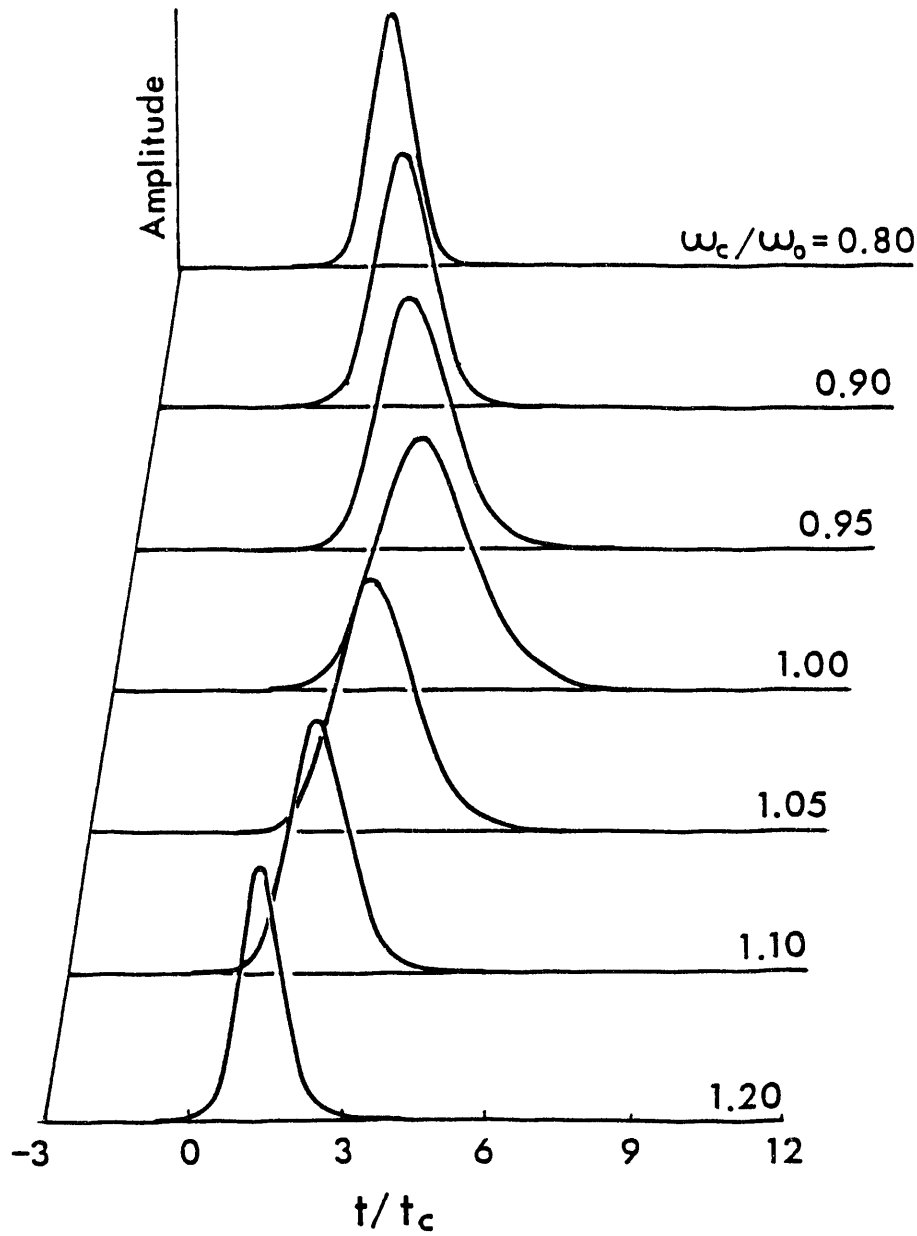


Fig.2 Time development of wave packets. The observation position is $x/x_0 = 120$. $\rho/\omega_0 = 0.02$, $\omega_p/\omega_0 = 0.25$

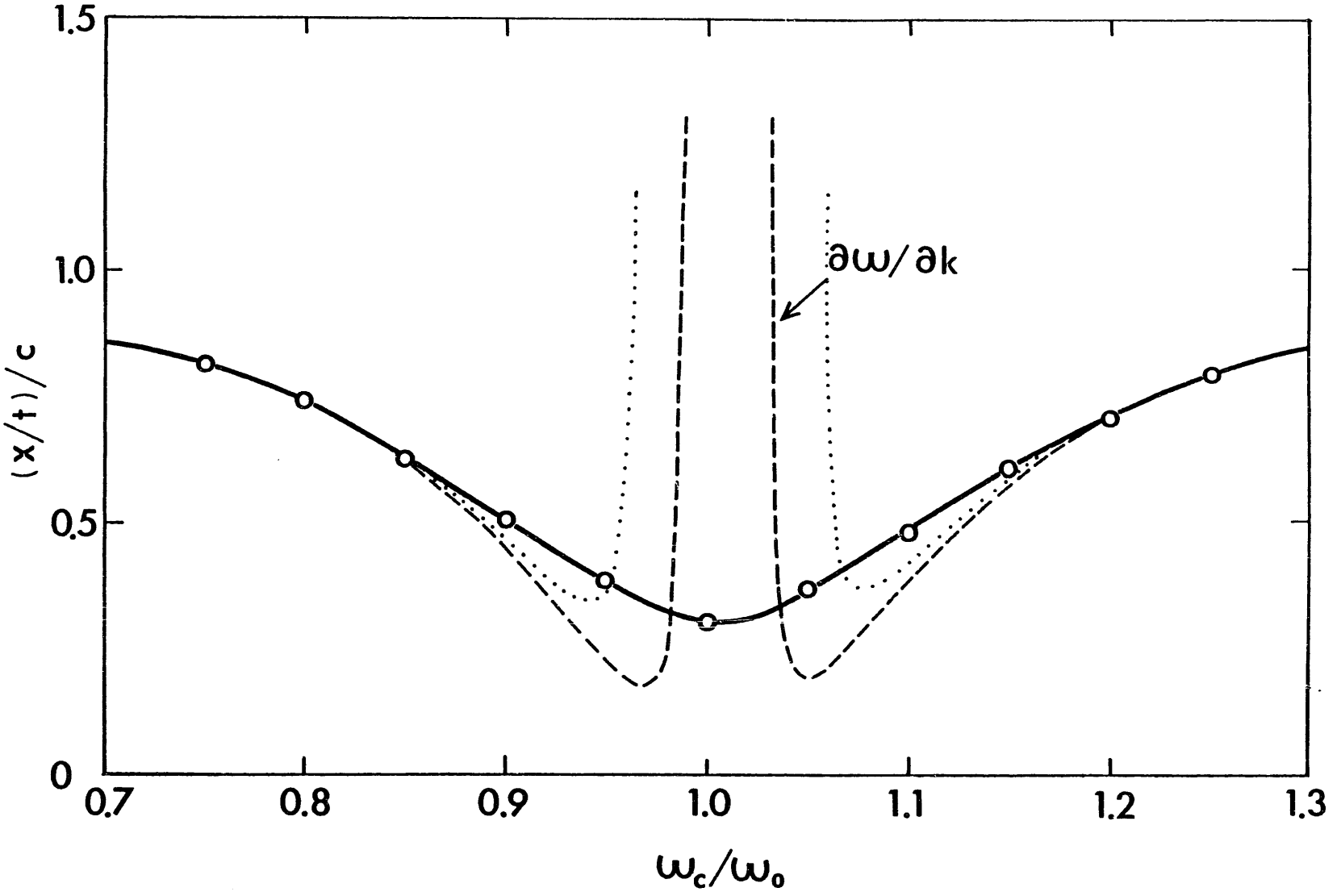


Fig.3 Velocity of wave packet as a function of carrier frequency. The group velocity is shown by the dashed line and Gintzburg's velocity the dotted line. $\rho/\omega_0 = 0.02$, $\omega_p/\omega_0 = 0.25$.

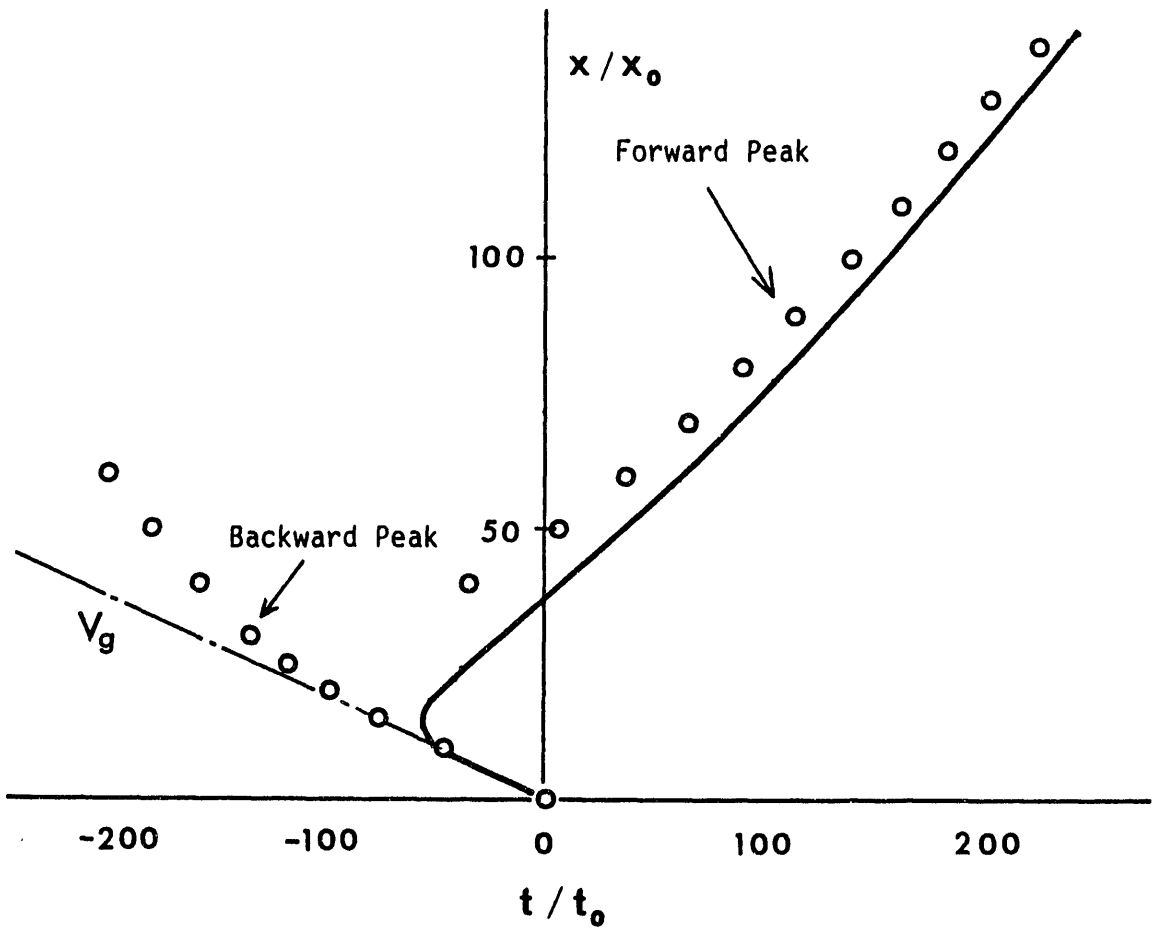


Fig.4 Trajectory of peak amplitude for absorption dominant case.
The solid line indicates the trajectory determined by eqs.(17) and (18).

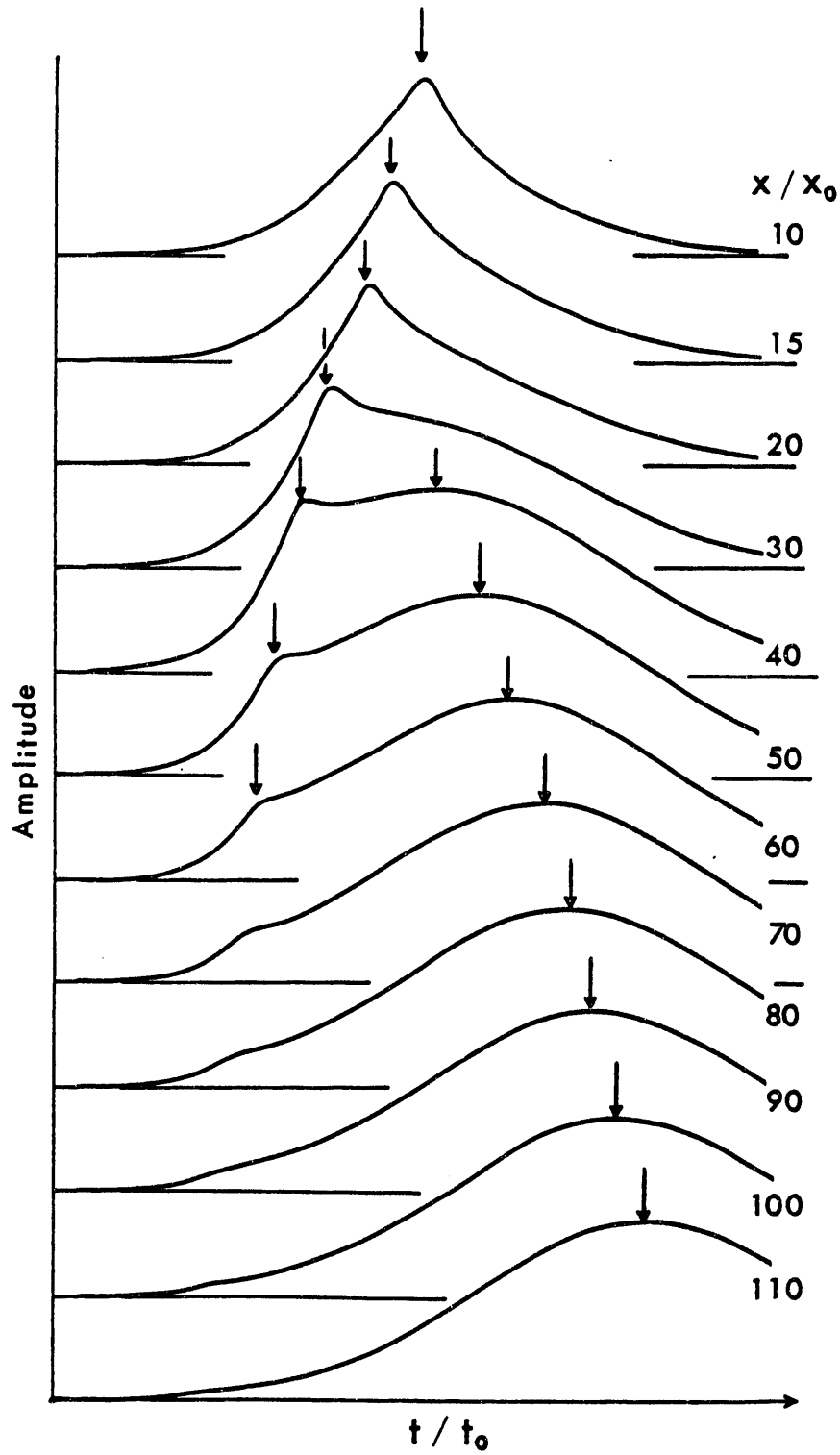


Fig.5 Time development of wave packets. The maximum amplitudes are normalized to unity. $\rho/\omega_0 = 0.02$, $\omega_p/\omega_0 = 0.1$

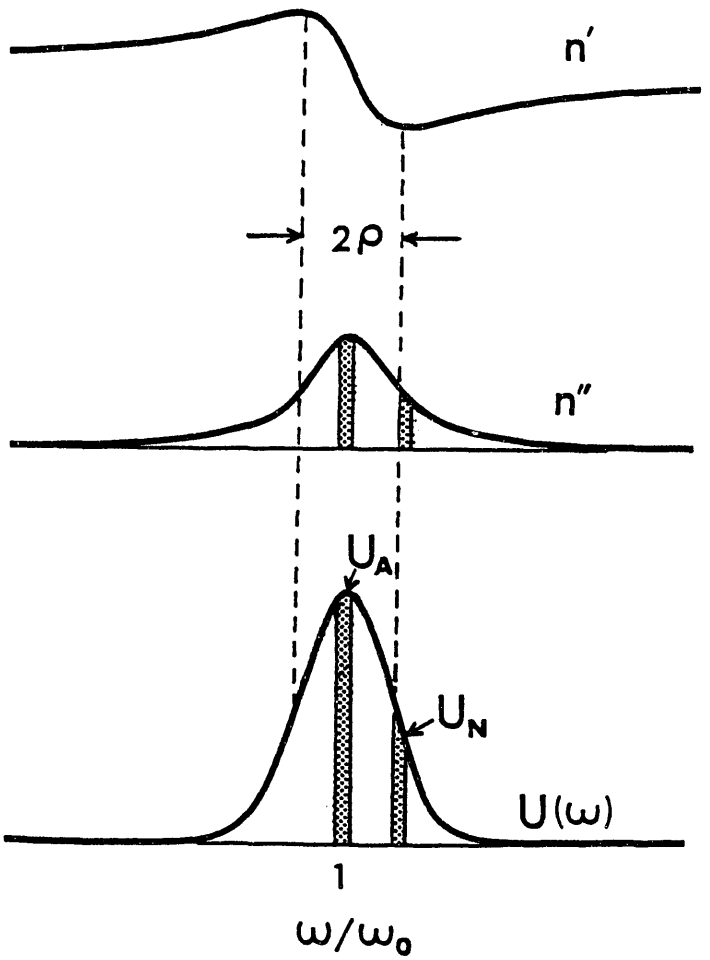


Fig.6 Schematic of refractive index of an absorbing medium and a Fourier spectrum of wave packet with a carrier frequency $\omega_c/\omega_0$ = 1.0.

# On the Application of Whistler Waves to Toroidal Discharges

C.N. Lashmore-Davies
*Cuylham Laboratory, Abingdon, Oxfordshire OX14 3DB, UK*
*(EURATOM/UKAEA Fusion Association)*

Abstract

The propagation of whistler waves in toroidal discharges is examined. It is shown that the whistler wave can propagate from the edge plasma of a toroidal discharge to its central regions provided the frequency is sufficiently below the electron cyclotron frequency and $n_\parallel$ is significantly larger than unity. The density to which the wave can propagate is controlled by $n_\parallel$. The possibility of driving a current in a reversed field pinch is considered. The power transfer between the whistler wave and the plasma is through electron Landau damping. In a tokamak the whistler wave can propagate to very high densities from the low field side e.g. for a magnetic field of 2.5 tesla and $n_\parallel \approx 8$ the wave could reach a density as high as $10^{21} m^{-3}$.

## 1. INTRODUCTION

Various plasma waves have been proposed for heating and non-inductive current drive in toroidal plasmas. It appears, however, that the whistler wave has not so far been considered. This may be because the whistler is usually thought of as propagating along the equilibrium magnetic field. In this paper we consider the propagation of a whistler wave across the magnetic field with a view to its application in both a reversed field pinch and a tokamak.

We shall consider the possibility of both heating and current drive by means of whistler waves in tokamaks. We shall also consider the possibility of driving the poloidal current required to produce the reversal of the toroidal magnetic field in a reversed field pinch. For the tokamak application the whistler wave is able to propagate to very high densities if a satisfactory antenna can be designed.

The whistler wave is similar to the lower hybrid wave in so far as it couples parallel energy to the electrons provided the wave frequency $\omega$ is

sufficiently below the electron cyclotron frequency $\Omega_e$. However, it also possesses properties which may enable it to couple to the electrons for both heating and current drive at higher densities where lower hybrid waves have been ineffective.

For the reversed field pinch application the poloidal current must be driven in the outer regions of the discharge. This will require the waves to couple to thermal electrons thus necessitating large values of $n_{\parallel}$. The pinch application is also analogous to controlling the current profile in tokamaks in that the current must be driven at a specified radial location.

## 2. THE PROPAGATION AND DAMPING OF WHISTLER WAVES

The whistler wave is supported by the electrons and propagates at frequencies up to the electron cyclotron frequency where the wave has a parallel resonance. For parallel propagation the wave is right hand circularly polarized and can propagate in plasmas of arbitrarily large density. However, for applications in toroidal experiments we need to consider the propagation of the whistler wave across the magnetic field. The case of oblique propagation is shown in figure 1, taken from Clemmow and Dougherty[1], where the square of the refractive index is plotted as a

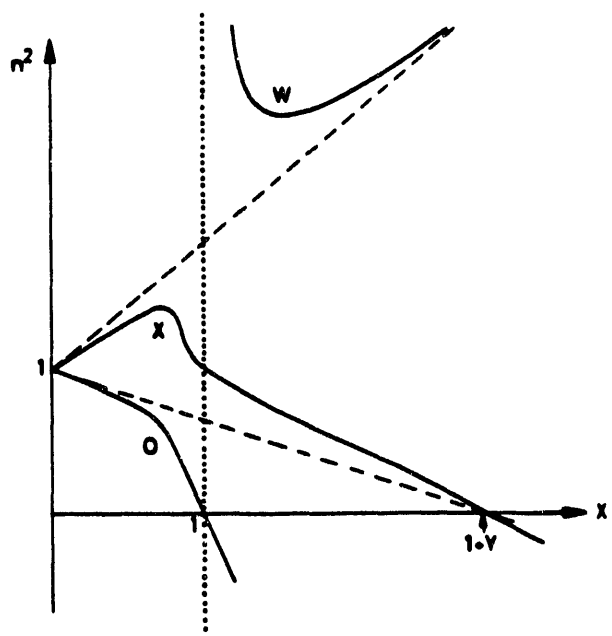


Figure 1. The variation of the refractive index squared as a function of plasma density ($X \equiv \omega^2_{pe}/\omega^2$) for fixed frequency. The full lines are for $\theta \neq 0$ and the broken lines for $\theta = 0$ where $\theta$ is the angle between the wave vector and the magnetic field. The dotted line is the plasma frequency line and $Y \equiv \Omega_e/\omega$.

function of density. The broken lines refer to the $\theta = 0$ case and the full lines to $\theta \neq 0$ where $\theta$ is the angle between the wave vector and the magnetic field. We shall be interested in the whistler branch, labelled W, which only exists for $Y \cos\theta > 1$, where $Y = \Omega_e/\omega$. For oblique propagation the waves are no longer circularly polarized and also possess a component of electric field parallel to the equilibrium magnetic field. The field polarizations given by the cold plasma model are

$$\frac{E_x}{E_y} = \frac{i\,\varepsilon_{xy}}{(\varepsilon_\perp - n^2)} \quad ; \quad \frac{E_\parallel}{E_y} = -\frac{n_\parallel n_\perp}{(\varepsilon_\parallel - n_\perp^2)} \tag{1}$$

where $n_\parallel \equiv ck_\parallel/\omega$, $n_\perp \equiv ck_\perp/\omega$ and $\varepsilon_\perp$, $\varepsilon_{xy}$ and $\varepsilon_\parallel$ are the elements of the cold plasma dielectric tensor.[1] In the above we have taken $\underset{\sim}{k} = (0, k_\perp, k_\parallel)$.

Let us now consider the propagation of the whistler wave across the magnetic field. This is done in the usual way by writing the cold plasma dispersion relation as

$$\varepsilon_\perp n_\perp^4 - \left[(\varepsilon_\perp - n_\parallel^2)(\varepsilon_\perp + \varepsilon_\parallel) - \varepsilon_{xy}^2\right] n_\perp^2 + \varepsilon_\parallel\left[(\varepsilon_\perp - n_\parallel^2)^2 - \varepsilon_{xy}^2\right] = 0 \tag{2}$$

and assuming $n_\parallel$ is fixed by the antenna whilst $n_\perp$ varies. For $\omega < \Omega_e$ and $n_\parallel > 1$ the above equation gives two cut-offs, $X = 1$ and $X = (Y-1)(n_\parallel^2-1)$. We shall only be interested in $n_\parallel > 1$ because this both singles out the whistler wave and makes it susceptible to electron Landau damping.

The flow of wave energy across the magnetic field will also be affected by the existence of a turning point where the perpendicular group velocity is zero. Such a point occurs when the two roots of equ.(2) are coincident. The condition for such a coincidence can be expressed in terms of the density parameter $X$ $(\equiv \omega_{pe}^2/\omega^2)$, thus

$$X = \frac{1}{4\,n_\parallel^2}\left[Y^2 n_\parallel^4 + 2(2 - Y^2)\, n_\parallel^2 + Y^2\right] \tag{3}$$

For $n_\parallel \gg 1$ this reduces to

$$X \simeq Y^2 n_\parallel^2/4 \tag{4}$$

This information is shown schematically in figures 2(a)-(c).

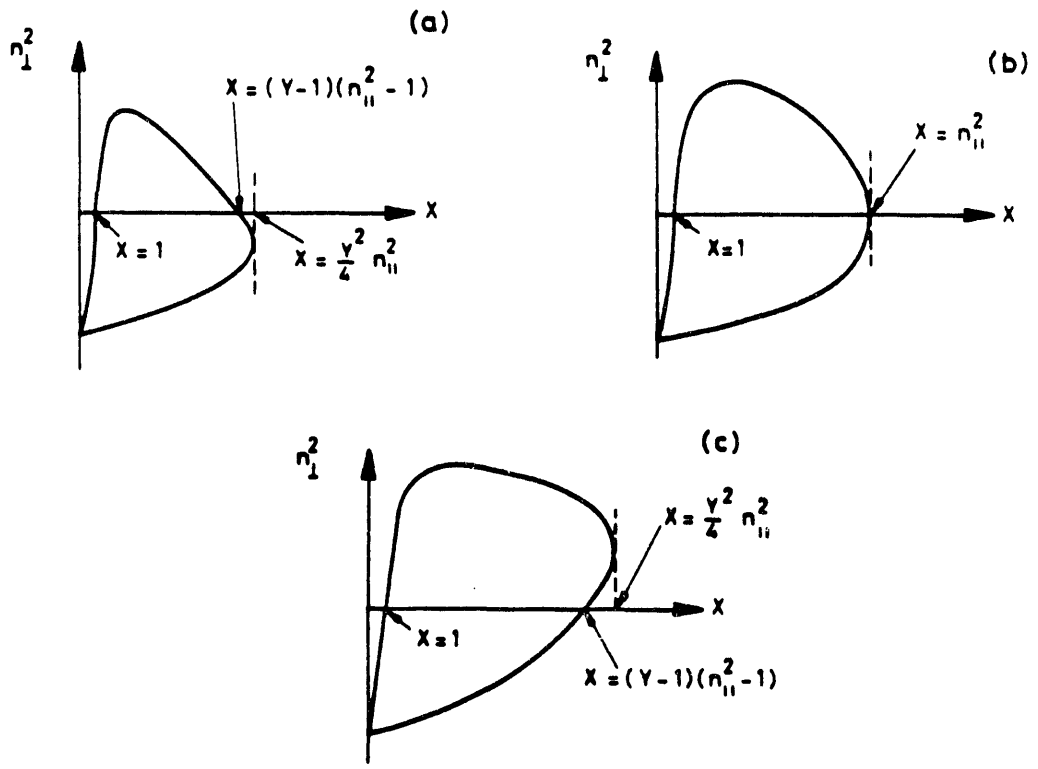


Figure 2. The variation of the perpendicular refraction index squared as a function of density, (a) $Y < 2$, (b) $Y = 2$ and (c) $Y > 2$.

The important point to note is that the localization of the wave in the perpendicular direction is controlled by $n_\parallel$. The wave is evanescent at the plasma edge but this evanescent region can be minimized by lowering the frequency. For $Y > 2$ a wave launched at the edge of a toroidal device will "bounce" between the two cut-offs reaching a maximum density at the turning point.

For $\omega \ll \Omega_e$, the whistler wave will not undergo cyclotron damping but will be subject to electron Landau damping. Under these conditions the only significant thermal correction is to $\varepsilon_\parallel$ which gives the following approximate expression for the imaginary part of $n_\perp$

$$\mathrm{Im}\, n_\perp \simeq \frac{i\delta\varepsilon_\parallel \{n_{\perp c}^2 (\varepsilon_\perp - n_\parallel^2) - (\varepsilon_\perp - n_\parallel^2)^2 + \varepsilon_{xy}^2\}}{\{4\, n_{\perp c}^3\, \varepsilon_\perp - 2\, n_{\perp c}[(\varepsilon_\perp - n_\parallel^2)(\varepsilon_\perp + \varepsilon_\parallel) - \varepsilon_{xy}^2]\}} \tag{5}$$

where $n_{\perp c}$ is the solution of the cold plasma dispersion relation and

$$\delta\varepsilon_\parallel \simeq \sqrt{\pi}\, \omega_{pe}^2\, u_o\, e^{-u_o^2} / k_\parallel^2\, v_{Te}^2 \tag{6}$$

where $u_o \equiv c/\sqrt{2}\, n_\parallel\, v_{Te}$.

## 3. WHISTLER DRIVEN CURRENTS IN A REVERSED FIELD PINCH.

Let us now apply the results of the previous section to the excitation of poloidal currents in a reversed field pinch. We shall consider the specific example of HBTX. In the vicinity of the toroidal field reversal point the electron temperature is approximately 100eV, the density $10^{19}$ $m.^{-3}$ and the poloidal magnetic field 0.15 tesla. As already mentioned, in order for the wave to drive a poloidal current we must choose an $n_\parallel$ such that the wave will damp on thermal electrons. Thus, for $n_\parallel = 20$ we obtain a ratio of phase velocity to thermal velocity of about 2.5. This is about the upper limit for the wave to couple to thermal electrons. It is also of interest to calculate the electric field polarization near the turning point. With the aid of the solution of the cold plasma dispersion relation, equation (2) and the expressions for the field polarizations we obtain

$$\frac{E_x}{E_y} \simeq 0.26i \quad \text{and} \quad \frac{E_\parallel}{E_y} = 0.34$$

where we have chosen the X parameter to be 850. We therefore see that the parallel electric field is of the same order as the perpendicular field. The theory of currents driven along the magnetic field due to the quasi-linear distortion of the parallel distribution function has been adequately described elsewhere [2, 3, 4]. Here, we apply the results of Cordey et al [4] to the present problem. These authors have computed the total current per unit power injected. Using their figure 1 we obtain for $u_o^2 = 6.4$

$$\frac{I}{P} = 0.067\text{amps/watt} \tag{7}$$

for the conditions relevant to the field reversal region of HBTX. Assuming that the poloidal current must produce a reverse field of 0.01 tesla and that the poloidal current is spread over a radial width of ~ 0.05m. about the reversal location we conclude that the required poloidal current is of the order of 40kA where we have taken the reversal to occur at a major radius of 0.8m.

With the aid of equation (12) we therefore conclude that the whistler wave power required to drive the field reversal is 600kW. For $Y > 2$, equation (7) shows that the whistler wave would not propagate beyond a density of $2 \times 10^{19}\ m^{-3}$ which is consistent with the wave energy only driving currents near the reversal point. The large value of $n_{\parallel}$ would guarantee that the whistler branch was excited, since no other wave has such a large value of n.

Two further points concern the choice of frequency and the method of launching. With regard to the frequency the only fundamental restriction is that it should be below the electron cyclotron frequency. Otherwise, from the point of view of the space available to the launching system the higher the frequency the better Thus, a frequency of 1.05 GHz would propagate above a density of $1.4 \times 10^{16}\ m^{-3}$ and a frequency of 2.1 GHz above $5.5 \times 10^{16}\ m^{-3}$.

The launching of a wave with such a large value of $n_{\parallel}$ (we assumed $n_{\parallel} \approx 20$) is evidently one of the main technical problems. Presumably a phased wave guide array similar to that used in lower hybrid heating could be used. The array would of course be arranged to couple to the poloidal electric field with the wave guide array turned on its side compared with the lower hybrid case. The coupling can be made from the low field side.

## 4. THE APPLICATION OF WHISTLER WAVES IN TOKAMAKS.

In view of the above discussion for pinches it is apparent that whistler waves might have some application in tokamaks. Since the magnetic field is much larger in a tokamak a frequency correspondingly lower than the electron cyclotron frequency would need to be chosen in order for the wave to propagate reasonably near the plasma edge. Thus, for a magnetic field of 2.5 tesla a frequency of 7GHz would propagate above a density of $6 \times 10^{17}\ m^{-3}$ and a frequency of 14GHz above $2.4 \times 10^{18}\ m^{-3}$.

The excitation of $n_{\parallel}$ well above $1 + (Y - 1)$ should ensure coupling to the whistler wave since the X - mode refractive index must be less than the above quantity.

Once launched, the whistler wave is able to propagate to higher densities depending on the value of $n_{\parallel}$. Thus for $n_{\parallel}$ values of 3, 6, and 8 a frequency of 7GHz and magnetic field of 2.5 tesla the densities at which the turning point occurs are $1.1 \times 10^{20}\ m.^{-3}$, $5.2 \times 10^{20}\ m.^{-3}$ and $9.4 \times 10^{20}\ m^{-3}$. Clearly, the whistler wave would easily penetrate to the centre of a high density tokamak.

Under such high density conditions the whistler wave would be able to heat the electrons by electron Landau damping. For a density of $10^{20}\ m.^{-3}$ a magnetic field of 2.5 tesla and $n_{\parallel}=8$ the electric field polarizations are

$$\frac{E_x}{E_y} \simeq 0.0044\ i \quad , \quad \frac{E_{\parallel}}{E_y} \approx 0.12$$

This polarization is therefore consistent with a strong interaction with thermal electrons. In order to appreciate the full potential of whistler wave heating a ray tracing analysis would need to be carried out. However, one advantage this scheme may have over lower hybrid heating is that since the frequency is well above the ion plasma frequency no transition from electron to ion coupling is to be expected, an effect which has complicated current drive and electron heating with lower hybrid waves.[5] At the high densities which are accessible to the whistler wave the ions would be heated indirectly, through collisions.

Current drive by means of whistler waves would of course be subject to the same density and temperature scalings as other schemes. However, due to its easy access to high density and the absence of any ion coupling it may offer advantages at the higher densities which have proved difficult for lower hybrid current drive. The possibility of influencing the current profile by choosing lower values of $n_{\parallel}$ as discussed for the reversed field pinch is more difficult in the tokamak case due to the much larger magnetic field. However, for a dense, hot tokamak it might be possible to position the turning point at specified radii off centre and to drive electron currents there. Again a detailed ray tracing study of this point needs to be carried out.

## 5. CONCLUSION

We have considered how the whistler wave may be coupled at the plasma edge (from the low field side) obliquely to the magnetic field so as to

reach the central regions of a toroidal discharge. A turning point which, for $n_{\parallel}^2 >> 1$, occurs at a density which is proportional to $n_{\parallel}^2$ was noted. This allowed the interesting application of driving the poloidal current in a reverse field pinch in the field reversal region and hence of supporting this reversal. The power required to do this was estimated to be approximately 600kW assuming a density and temperature in the reversal region of $10^{19}$ m.$^{-3}$ and 100eV. If the density in this region could be lowered or the temperature raised (or both!) then the required power would be less.

For the higher magnetic fields present in a tokamak we have also shown how the whistler wave could tunnel through the edge plasma to reach very high densities. The whistler wave is supported by the electrons and for $\omega << \Omega_e$ is damped by electron Landau damping due to the presence of a significant fraction of $E_{\parallel}$. In both pinch and tokamak applications large values of $n_{\parallel}$ are required to ensure coupling to the whistler wave, ~ 20 for the pinch and 3 - 8 for the tokamak. Thus, for a magnetic field of 2.5 tesla and a frequency of 7GHz a whistler wave would propagate for densities above $6 \times 10^{17}$ m.$^{-3}$ and would be able to reach densities between $10^{20}$ and $10^{21}$ m.$^{-3}$ depending on the value of $n_{\parallel}$.

## 6. ACKNOWLEDGEMENTS

I would like to thank Dr R.S.Pease for encouraging me to consider this problem and Drs P.Lallia and A.Newton for helpful discussions.

## 7. REFERENCES

[1] P.C.Clemmow and J.P.Dougherty, Electrodynamics of Particles and Plasmas, Addison - Wesley 1969, Chap. 5.
[2] N.J.Fisch, Phys Rev. Letters 41, 873 (1978)
[3] N.J.Fisch and C.F.F.Karney, Phys. Fluids, 24, 27 (1981).
[4] J.G.Cordey, T.Edlington and D.F.H.Start, Plasma Physics 24, 73 (1982).
[5] F.De Marco, F.Alladio, F.Crisanti et al Proc. 4th Int. Symposium on Heating in Toroidal Plasmas, Rome 1984 Ed. H.Knoepfel and E. Sindoni, Vol. I p. 546.

# GYROTRON DEVELOPMENT

# Varian Gyrotrons for Electron Cyclotron Heating Applications

H. Jory
*Varian Associates, Inc., Palo Alto, California 94303, USA*

Varian has developed and manufactured a wide range of high-power gyrotron oscillators for use in electron cyclotron heating applications in magnetic confinement fusion devices. Gyrotron oscillators capable of generating 200 kW CW have been developed at frequencies of 28 GHz, 35 GHz, 56 GHz, and 60 GHz. In addition, 200 kW, 40ms-100ms pulse tubes at 28 GHz, 53 GHz, 60 GHz, and 70 GHz have also been delivered to various fusion laboratories. Most recently, a 70 GHz, 200 kW CW tube has been designed and is currently being tested. The design of the different tubes will be discussed and recent operating experience with the various tubes will be summarized. Prospects for future millimeter wave power sources will also be outlined.

# Progress on the Varian 140 GHz Gyrotron

K. Felch
*Varian Associates, Inc., Palo Alto, California 94303, USA*

The development of 140 GHz gyrotron oscillators, capable of genera ting power levels of 100 kW CW, is currrently in progress at Varian. The tubes are designed for operation in the $TE^{o}_{031}$ cavity mode with the electron beam situated at the second radial maximum of the electric field in the cavity.

The first experimental 140 GHz tube employs a simple tapered $TE_{031}$ cavity, and a magnetron injection electron gun which has nonlaminar electron trajectories. Pulse tests on the tube have yielded power levels in excess of 100 kW with efficiencies of about 28% in the desired $TE^{o}_{031}$ mode at 140 GHz. Emission in the $TE^{o}_{231}$ mode at 137 GHz and the $TE^{o}_{621}$ mode at 161 GHz has been observed with similar power levels and efficiencies by tuning the gyrotron magnetic field. CW tests of the first tube are currently underway. Measurements of the power lost in the cavity walls and the temperature of the output window will be made as the tube is brought into full CW operation.

The results of the pulse and CW tests on the first tube will be presented and the salient features of succeeding experimental 140 GHz tubes will be summarized. In addition, the possibility of operating the tube up to power levels of 200 kW will be addressed.

* The 140 GHz gyrotron oscillator is being developed under contract with Lawrence Livermore National Laboratory, operated by the University of California for the U. S. Department of Energy, under Prime Contract W-7405-ENG-48.

# Varian Gyrotron Production and Reliability Improvement Progress

L.J. Craig
*Varian Associates, Inc., Palo Alto, California 94303, USA*

Varian has developed, manufactured and shipped more than 80 high power gyrotrons, 8 for use as design vehicles and 72 for electron cyclotron heating applications in magnetic confinement fusion devices. These microwave power sources operate at frequencies ranging from 28 GHz to 140 GHz, typically at 200 kW pulse or CW. The relatively small total number of gyrotrons made, their different frequencies and configurations, and the fact that they are more developmental than production devices makes for sparse failure rate data directly usable for reliability predictions. Nonetheless, gyrotron users are universally interested in quality performance, high reliability and long tube life, all at affordable prices. However, despite the seeming contradiction, there are some reliability improvements that can be incorporated to achieve extended MTBFs without greatly increasing the cost of these tubes. The approach to implementing these reliablity improvements will be presented.

# Research on High Power, CW Relevant Gyrotrons at the Naval Research Laboratory

**M.E. Read and R. Rhinewine**
*Naval Research Laboratory, Washington, D.C. 20375, USA*

The NRL program on high power gyrotron has focussed on the development of concepts for realization of megawatt gyrotons with frequencies in excess of 100 GHz and for use in lower power/frequency gyrotrons being developed in industry. In the first category fall the quasi-optical gyrotron and whispering gallery gyrotrons. In the second category are the complex cavity and $TE_{1,n}$ gyrotrons. Present emphasis is on the quasi-optical and $TE_{1,n}$ gyrotrons. These are discussed briefly below.

## Quasi Optical Gyrotron

The Quasi Optical gyrotron consists of an optical resonator with its axis aligned perpendicular to the direction of beam propagation (see Figure 1.) The resonator can be very large, with correspondingly large mirror surfaces, allowing ohmic losses to be kept low (< 1kW/cm) for even multimegawatt devices at frequencies above 100 GHz. In addition, the geometry allows seperation of the microwave output and the collector, thru avoiding conflict in dimensional requirements.

A QO gyrotron with a small cavity (mirror radius = 2.5 cm, separation = 4 cm, radius of curvature = 146 cm) has been operated at NRL and previously reported.[1]

At frequencies between 110-120 GHz, a maximum output efficiency of 11% was achieved and a maximum output power of 80 kW. Diffraction losses of 60% were calculated, indicating an electronic efficiency of 18%. Single mode operation was obtained as was expected since the spacing of the longitudinal modes $2c/\ell$ was approximately equal to the 3% bandwidth of the instability.

The large mirror system has been fabricated and is shown schematically in Figure 2. The output is coupled out via an azimuthal slot, with a coupling of approximately 1%. The output is focussed to a near Gausian beam by a cassegrain antenna. The electron beam is formed by a magnetron injection gun producing a 10A beam with an energy of 70 kev

Testing of the large mirror quasi-optical gyrotron is expected to begin in the spring of 1986.

## $TE_{1,3}$ Gyrotron

$TE_{1,n}$ Gyrotron modes appear useful in that the cavity can be configured to suppress other modes, thus allowing the use of high order modes. The suppression is accomplished by axial slots in the cavity.

For modes with $n \leq 3$, there is enough separation between the modes so that for beam voltages less than ~ 100kV, good single mode operation can be reasonably expected even without slots. As a first step in research on $TE_{1,n}$ modes, NRL has performed an experiment using the $TE_{1,3}$ mode.

### Description of the Experiment

The cavity used was essentially of conventional design, with a $.8^{o}$ input taper to improve efficiency and reduce mode conversion at the input. The length was approximately 2.4 cm, or 6.8 wavelengths. The output was formed by a double taper, which was used in place of a simple taper in order to reduce mode conversion.

The electron gun used was one that was originally designed[2] for use with a $TE_{0,1}$, 35 GHz gyrotron. In order to match the beam radius to that of the second radial peak of the $TE_{1,3}$ mode at 85 GHz, the magnetic field compression ratio was increased from 6.7 to 12. The resulting beam was modeled with a gun analysis code developed by Herrmannsfeldt[3]. The gun was modeled with a cathode voltage of -55 kV to -70 kV and beam currents of up to 10 A. With a ratio of perpendicular to parallel velocities of 1.5, a spread in parallel velocities of 5.8% was predicted. From previous cavity studies, this spread was not expected to significantly affect the gyrotron output.

The output window was of BeO, in a (circular) pillbox configuration. The thickness was 1 wavelength, having a calculated reflection of ~ 2% at 84.85 GHz and ~ 4% at 85.85 GHz.

Measurement of the frequency was made via a commercial wavemeter, with a resolution of approximately 10 MHz. Measurement of the power was made using a water calorimeter. This device was calibrated at 35 GHz (there being no source available at 85 GHz with adequate average power). This was not fully satisfactory, since the calibration apparently included losses of approximately 30%, which cannot be extrapolated to 85 GHz with any certainty. Therefore, the measurement of the output powers obtained are given as preliminary estimates.

### Experimental Results

Significant power was observed at 83 $\pm$ .2 GHz, 84.85 $\pm$ .05 GHz, and approximately 86.95 GHz. This is shown in Figure 3, as are the expected frequencies. The center group of frequencies correspond well to those expected for the $TE_{1,3,1}$ mode, and it was for this operating range that the highest power and most stable operation occurred. The upper frequency appears to coincide with the $TE_{1,3,3}$ mode. The selection of this mode over the $TE_{1,3,2}$ may have been due to a window resonance and/or gain in the output guide. (The uniform magnetic field extended for approximately 15 cm past the

end of the cavity output.) The origin of the lower band of frequencies is unclear. No radiation was observed corresponding to the $TE_{7,1}$ mode, as expected, because of poor coupling due to the beam. Somewhat surprising was the lack of power at 79.6 GHz, where the $TE_{3,2}$ mode was expected.

The currents for which strong radiation was observed, as a function of magnetic field, is shown in Figure 4. (The points are discrete only because they represent individual observations.) As can be seen and as expected, the 84.85 GHz points lie almost exclusively above the theoretically predicted starting currents for the $TE_{1,3,1}$ mode. (The starting currents and efficiencies discussed below were calculated by using a code in which the beam electron energies were numerically integrated along the particle orbits.)

The power observed at 84.85 GHz is shown in Figure 5, along with the theoretical prediction. A maximum power of 285 kW was observed, using the calorimeter discussed above. This is compared to a predicted power with a current of 10 A of 350 kW. For this frequency range, a maximum efficiency of 43% was observed, as compared to a theoretically predicted value of 50%. At 83 $\pm$ .2 GHz, and 86.85 GHz, typical powers were 50 and 150 kW, respectively.

## 10 MW Gyrotron

In addition to the 85 GHz device, a very high power $TE_{1,3}$ gyrotron is being developed to produce radiation at 10 GHz.[4] The specifications of the gyrotron are given in Table 1.

Because of the high voltage used ( ~ 240 kV), short cavities are required for good efficiency. The short interaction lengths result in relatively wide interaction bandwidths, and increased mode competition. To suppress the competition, in this case from the $TE_{3,2}$ mode, a cavity with 2 axial slots may be required. Such a cavity will be incorporated as a second stage in the development.

The electron gun, which is a single mode MIG, is shown schematically in Figure 6. The gyrotron as a whole is shown in Figure 7.

Testing of this device is expected to begin early in 1986.

## References

1. T.A. Hargreaves et. al. "Experimental Study of a Single Mode Quasi-Optical Gyrotron," Int. J. of Elect. 57, pp. 977 - 985 (1984).

2. J.L. Seftor, A.T. Drobot and K.R. Chu, "An Investigaion of a Magnetron Injection Gun Suitable for Use in Cyclotron Resonance Masers," IEEE Trans. Elect. Devices ED-26, pp. 1609-1616 (1979).

3. W.B. Herrmannsfeldt, SLAC Report-226, (1979).

4. M.E. Read and G. Bergeron III, "Design of a 10 GHz, 10 MW Gyrotron," NRL Report #5629 (1985).

TABLE 1

Summary of Gyrotron Designs

| | | $TE_{1,3}$ | $TE_{1,4}$ |
|---|---|---|---|
| Frequency | | 10 GHz | 10 GHz |
| Gun Voltage | | 240 kV | 240 kV |
| Beam Current | Nominal | 158 | 142 |
| | Maximum | 250 | 250 |
| Output Efficiency | | | |
| | at nominal current | 31%* | 28%** |
| | at maximum current | 33% | 30% |
| Output Power | | | |
| | at nominal current | 10 MW | 10 MW |
| | at maximum current | 14.7 MW | 16.9 MW |
| Polarization | | linear | |
| Pulse Length | | 1 μs - 100 μs | |
| Duty Cycle | | $\leq 10^{-3}$ | |
| Maximum Average Power | | 10 kW | |

* Includes the effects of mode competition, potential depression, and velocity spread.

** Includes the effects of potential depression. Velocity spread is expected to be unimportant. Mode competition will be severe without suppression.

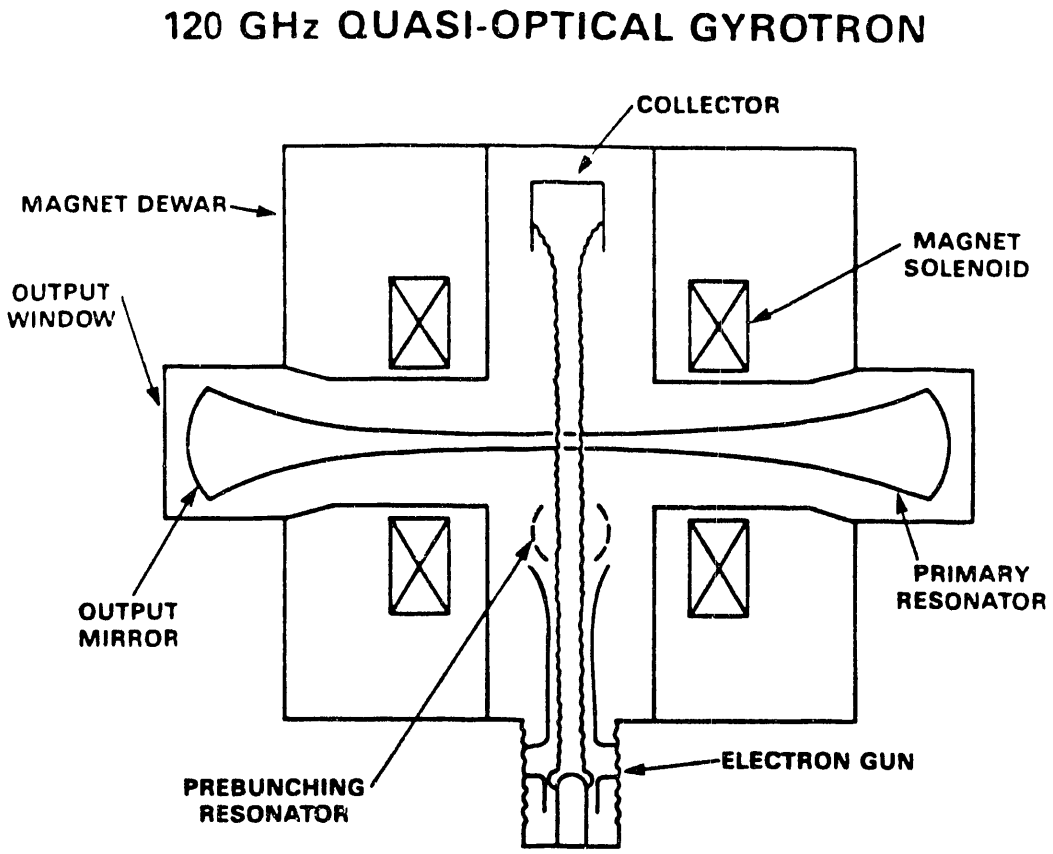


Figure 1. Schematic of the large cavity NRL quasi-optical gyrotron.

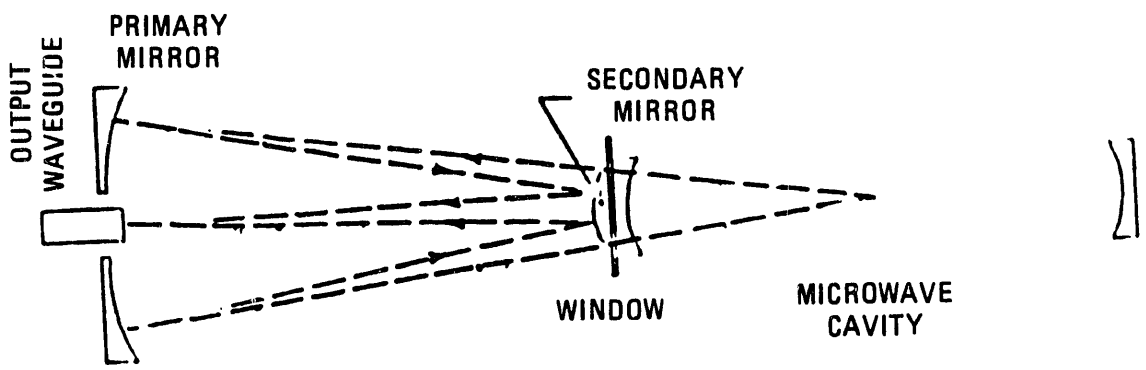


Figure 2. Schematic of the quasi-optical resonator and cassegrain output.

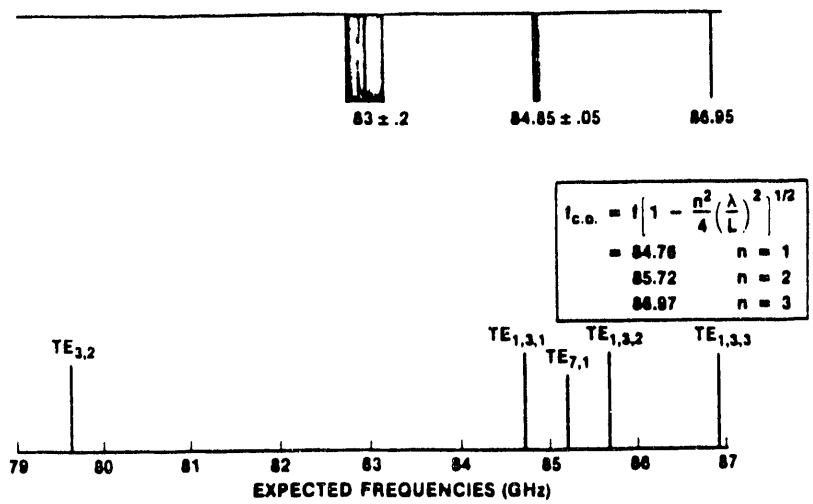


Figure 3. Measured frequencies compared to expected frequencies.

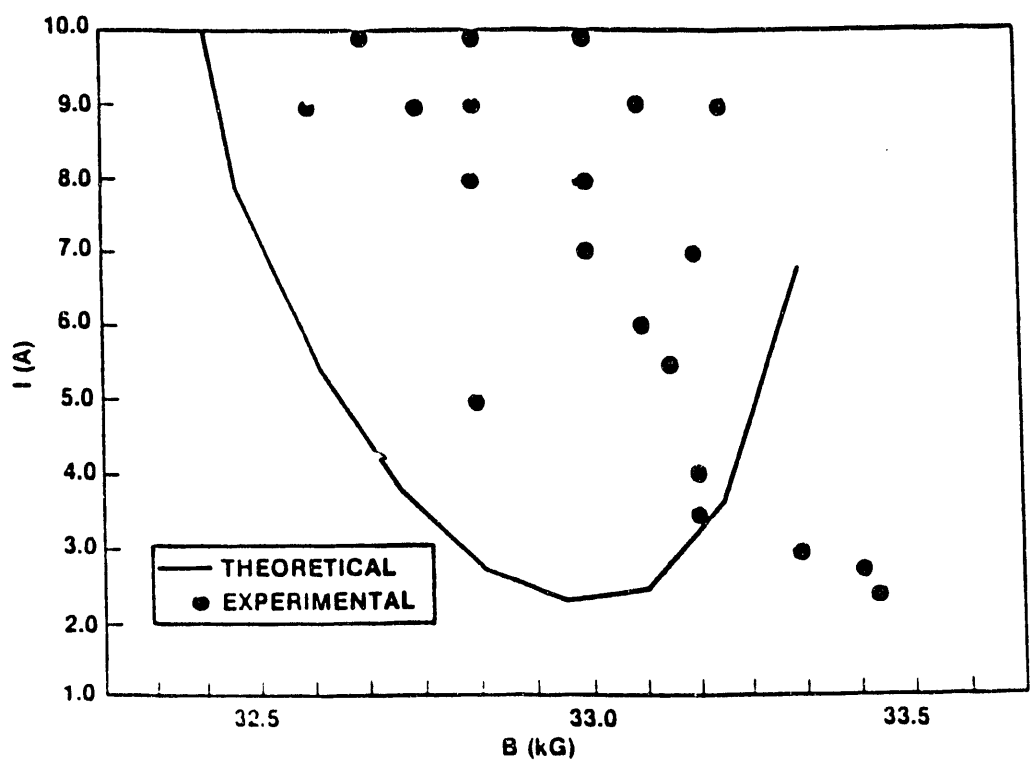


Figure 4. Current as a function of magnetic field. The theoretical curve is the starting current for the $TE_{1,3,1}$ mode.

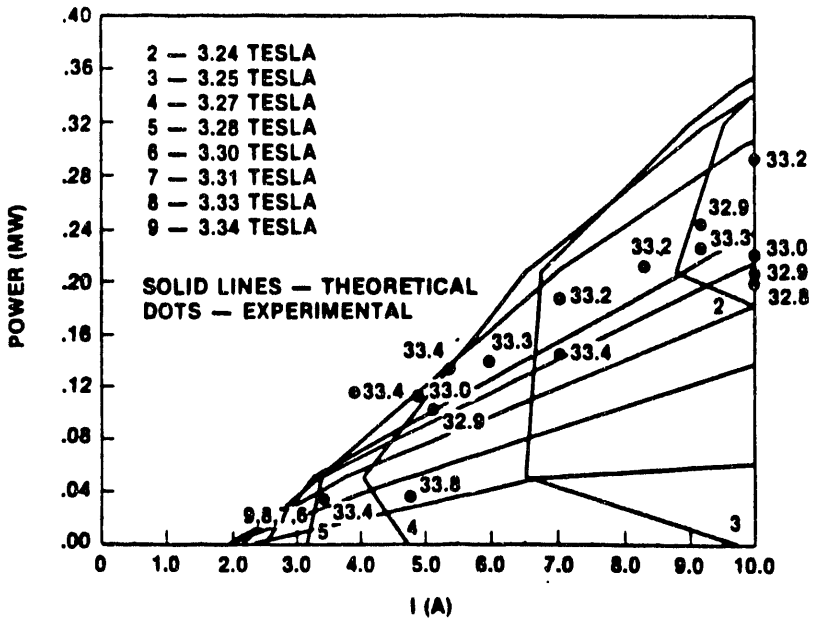


Figure 5. Power vs current at various magnetic fields. Experimental points are labeled in kG.

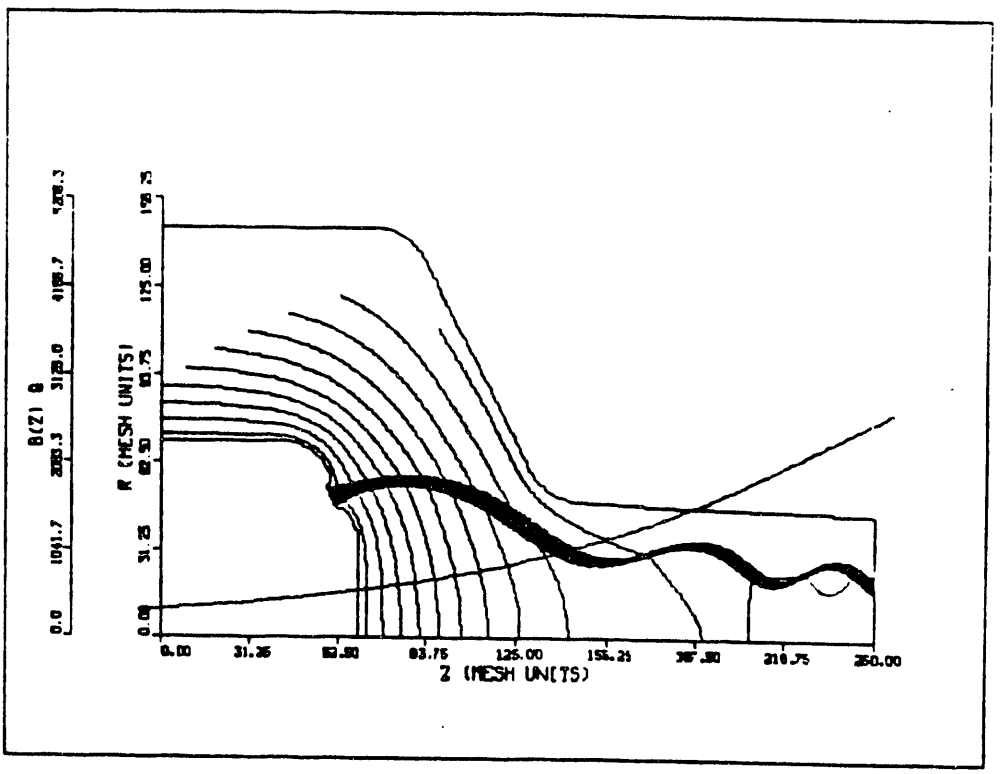


Figure 6. Schematic of the electron gun for the $TE_{1,3}$ 10 GHz gyrotron. (1mu = 1mm).

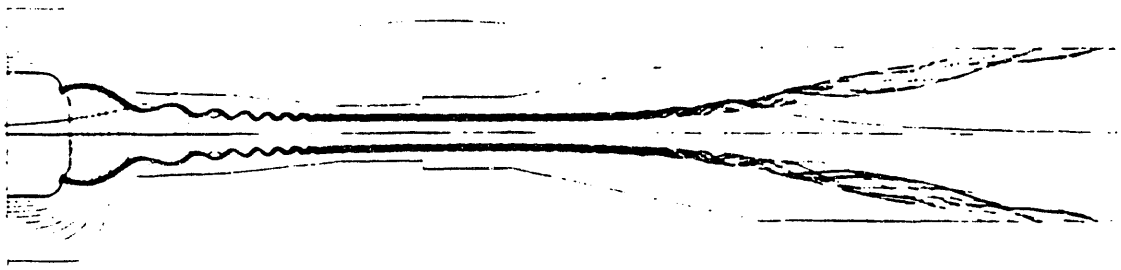

Figure 7. Schematic of the 10 MW gyrotron.

# Prospects for High Power Gyrotrons

K.E. Kreischer, B.G. Danly, H. Saito,[1] R.J. Temkin, and T.M. Tran[2]
*Plasma Fusion Center*
*Massachusetts Institute of Technology, Cambridge, Massachusetts 02139, USA*

ABSTRACT

In this paper, the prospects for high frequency gyrotrons capable of output powers in excess of 1 MW will be examined. Gyrotrons capable of such powers could dramatically reduce both the complexity and the cost per kilowatt of an ECRH system. A generalized design study of gyromonotrons has recently been completed that indicates that cw gyrotrons capable of MW powers and high efficiency are consistent with the technological constraints of the device. Among the constraints that were considered were ohmic losses in the cavity walls, voltage depression of the beam, and efficiency reduction due to space charge forces. The design parameters of 1 and 10 MW, 120 GHz monotrons have been determined. Both designs have total theoretical efficiencies in excess of 40%. It was found that, as the output power is increased, the cavity length and radius become comparable. As a result, megawatt gyrotrons may exhibit operating characteristics that are different than those of lower power devices.

Experimental research at MIT in support of the development of high power gyrotrons will be described. A gyrotron operating with a minimum diffractive Q cavity has recently been demonstrated. Quasioptical techniques have also been used to efficiently convert the output radiation of a gyrotron operating in a surface mode ($TE_{6,1,1}$) into a linearly polarized, Gaussian-like beam. Theoretical investigations of multiple cavity devices, such as gyrotwystrons and gyroklystrons, have also been conducted. An ECRH system based on megawatt gyrotrons will be described and compared with alternative plasma heating techniques.

[1] Permanent address: Institute of Space and Astronautical Science, Tokyo, Japan, 154
[2] Permanent address: CRPP, Association Euratom-Confederation Suisse, EPFL, 21, Av. des Bains, CH-1007 Lausanne, Switzerland

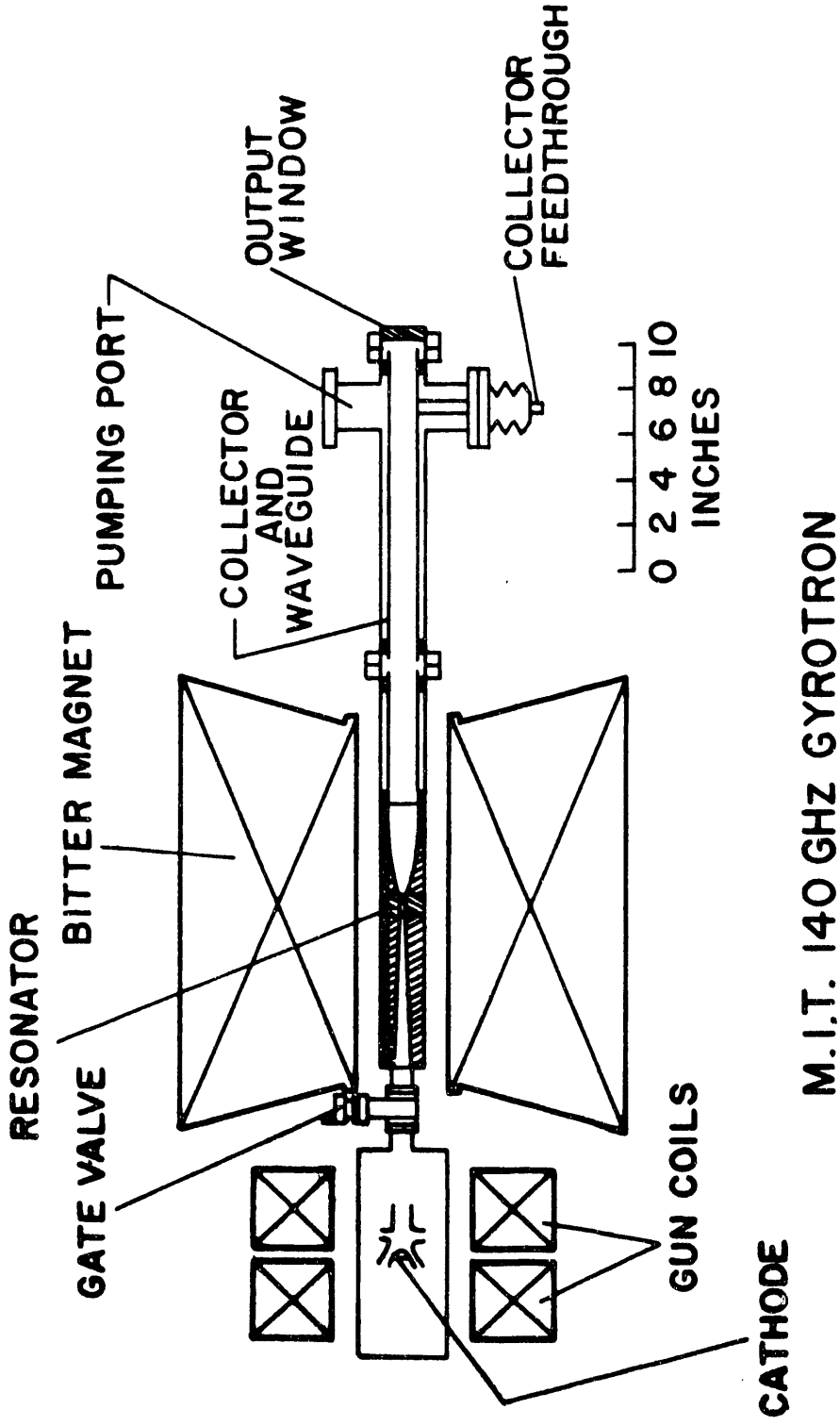


M.I.T. 140 GHz GYROTRON

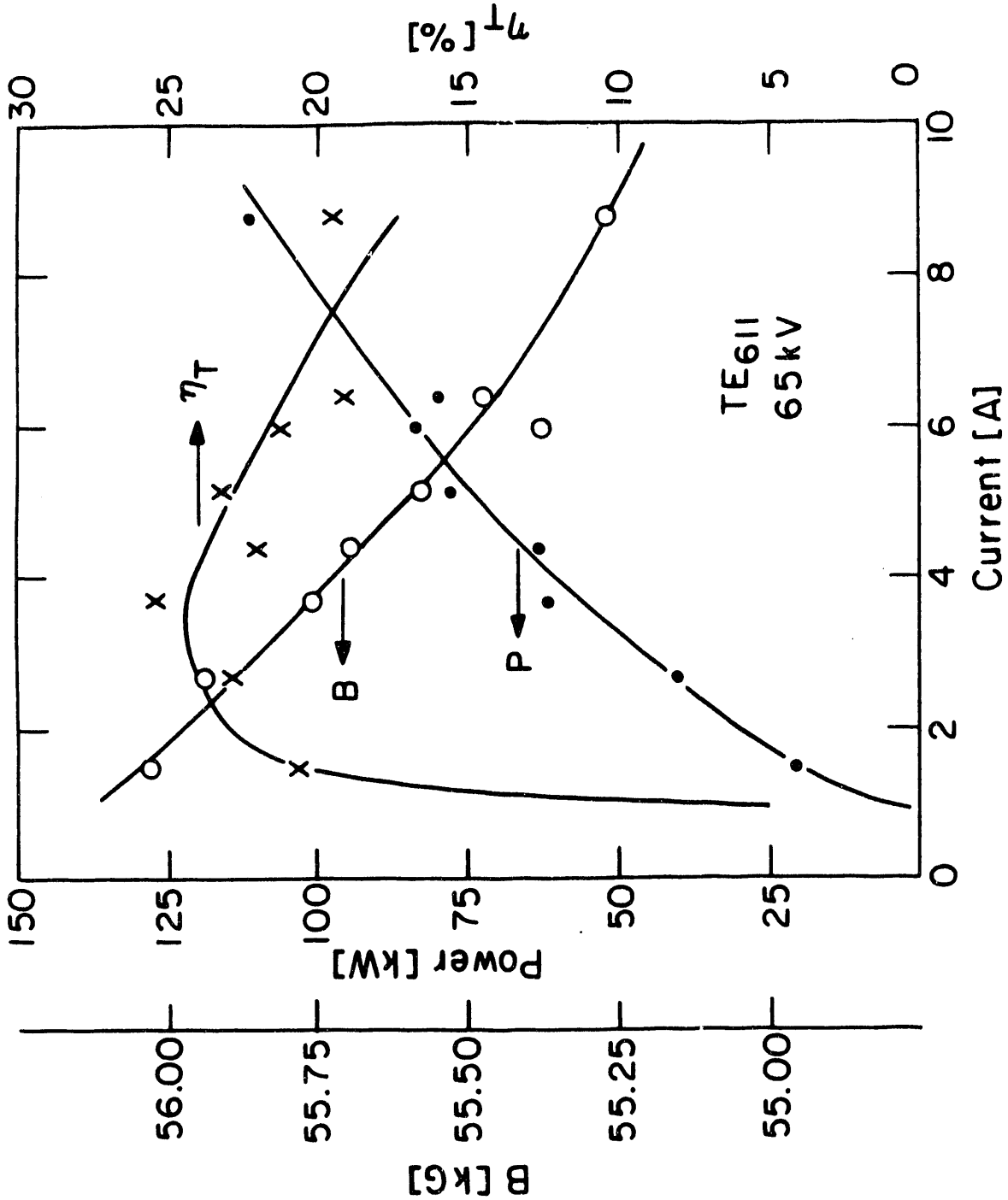
η⊥ [%]
30
25
20
15
10
5
0
η_T
B
P
TE611
65 kV
Current [A]
0
2
4
6
8
10
150
125
100
75
50
25
Power [kW]
56.00
55.75
55.50
55.25
55.00
B [kG]

# VLASOV COUPLER

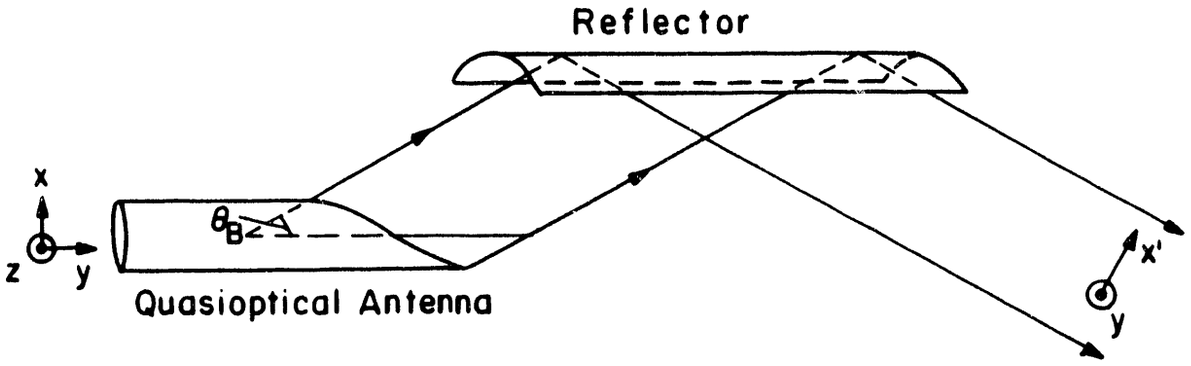


a. Side View

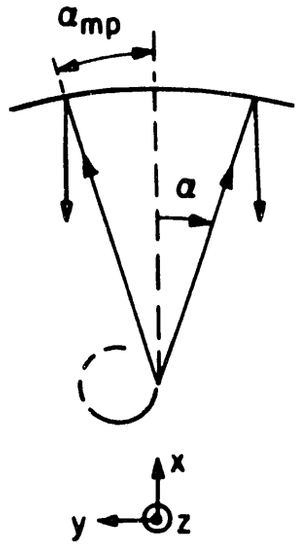


b. End View

## FAR FIELD PATTERN

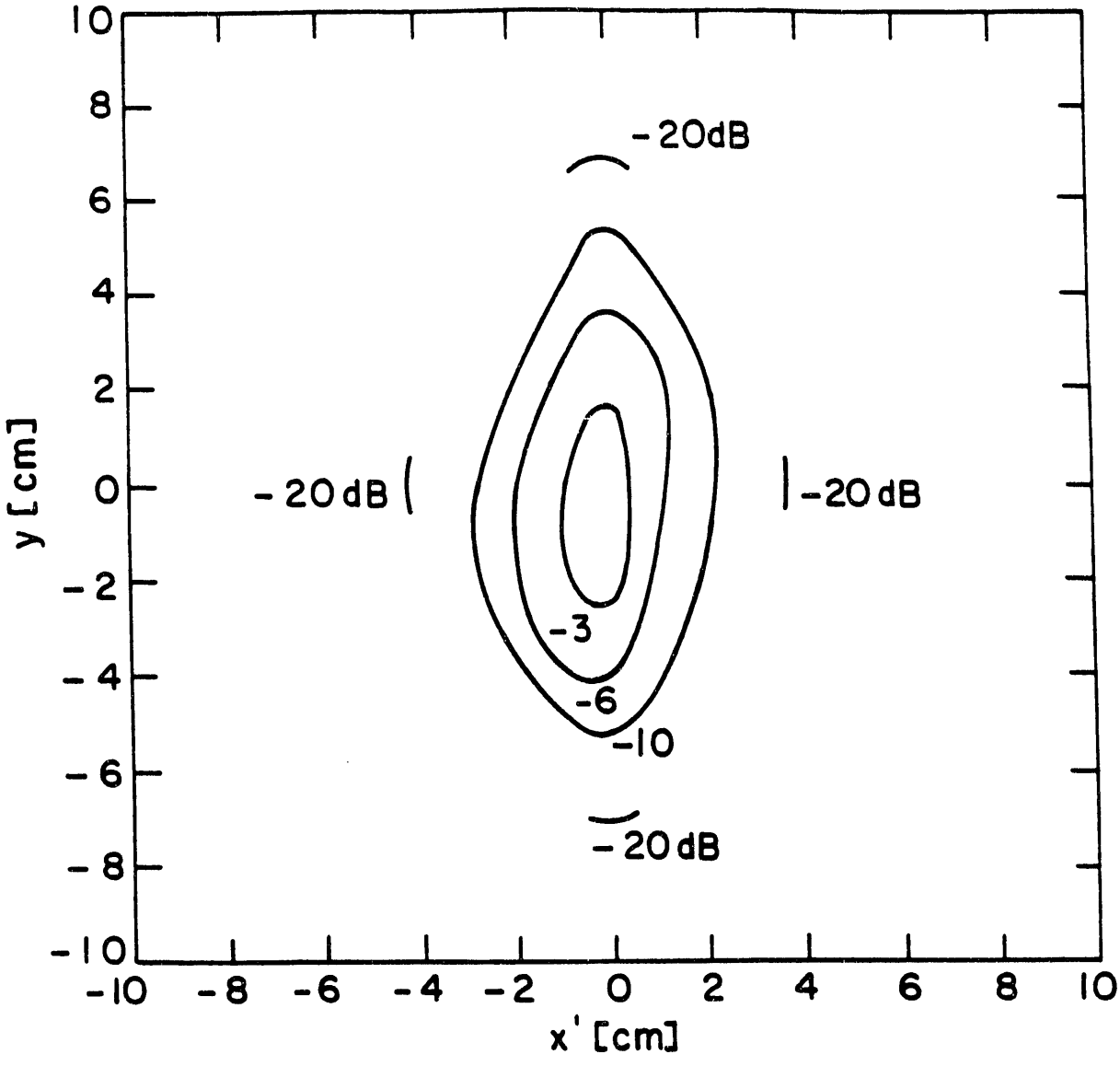

## 5-10 MW, 120 GHz Gyrotrons

- ECRH is an attractive heating technique

  Gyrotrons are isolated from reactor

  Local deposition of power

  Simple transmission system

  Efficient coupling to plasma

- Efficient, multi-megawatt operation is consistent with the major constraints of the beam and cavity

- Multi-megawatt gyrotrons appear competitive with alternative heating sources

  Low recirculating power

  Modular

  Simple launching structure

  Similar power supply

- Short pulse experiment is recommended to investigate unresolved issues (eg., mode competition)

| Parameter | Design Value |
|---|---|
| I (A) | 28.7 |
| $\eta_T$ (%) | 43.5 |
| $\beta_\perp$ | 0.44 |
| $\beta_\parallel$ | 0.22 |
| F | 0.091 |
| $\mu$ | 15.1 |
| Minimum $\nu_{mp}$ | 18.9 |
| $\Delta$ V/V (%) | 2.2 |
| $I_{MAX}$ (A) | 115 |
| $R_e$ (cm) | 0.60 |
| $\Delta_g/\lambda$ | 0.085 |
| $J_s$ (A/cm$^2$) | 1190 |
| $Q_T$ | 365 |
| $B_o$ (T) | 4.7 |

Table I. Design parameters for a 1 MW, 120 GHz, gyrotron with a symmetric Gaussian axial field profile and $V_c$=80 kV.

## TABLE II

## MODE CONVERTER PARAMETERS

| | $TE_{03} \rightarrow TE_{02}$ (AXISYMMETRIC) | $TE_{02} \rightarrow TE_{01}$ (AXISYMMETRIC) | $TE_{01} \rightarrow TE_{11}$ (WRIGGLE) |
|---|---|---|---|
| MAXIMUM DIA. | 0.5 INCH | 0.5 INCH | 0.5 INCH |
| BEAT $\lambda$ | 2.148 CM | 3.500 CM | 12.90 CM |
| BEAT AMPLITUDE | + 3.7% | + 6.4% | 4.1 - 8.5%* |
| # BEATS | 5 | 5 | 7.75 |
| TOTAL LENGTH | 10.74 CM | 17.50 CM | 99.98 CM |
| CONVER. EFF. (CALCULATED) | 99.0% | 99.8% | 97.9% |
| CONVER. EFF.* (MEASURED) | 85% | 95% | 99.9% |

*SEE TEXT.

# The 120 GHz Quasi-Optical Gyrotron at the Centre de Recherches en Physique des Plasmas

M.Q. Tran and the Quasi-Optical Gyrotron Development Group
*Centre de Recherches en Physique des Plasmas*
*Association Euratom/Confédération Suisse*
*Ecole Polytechnique Fédérale de Lausanne*
*21, Av. des Bains, CH-1007 Lausanne, Switzerland*

## I) INTRODUCTION

In the framework of the European programme on gyrotron development, the Association Switzerland/Euratom, in collaboration with the Electron Tubes Department EKR of BBC Brown, Boveri & Co. Ltd., is developing a quasi-optical gyrotron at 120 GHz and with a power level of about 200 kW. In this report, the status of the project and its major stages will be discussed.

## II) THE DEVELOPMENT PROGRAMME

In the fall of 1983, approval for the development of a 120 GHz, 200 kW quasi-optical gyrotron programme has been granted. Three different stages are foreseen.

- A first experiment shall be performed with a small (5 cm) quasi-optical resonator. Pulse lengths will be limited to less than 100 μs due to the excessive thermal loading on the mirror ($\gg$ 1.5 kW/cm$^2$). The short pulse length also allows us to use radiation cooled mirrors and collector.

- A larger resonator (36 cm) will then be tested. It will be water-cooled and designed to sustain pulses as long as 100 ms.

- Finally, in order to improve the efficiency, we shall implement a prebunching resonator to investigate the concept of the quasi-optical gyroklystron.

Global electronic efficiency of about 30% is expected in the first two stages, while it could reach 40% in a quasi-optical gyroklystron.

## III) DESIGN OF THE QUASI-OPTICAL GYROTRON

### a) Design consideration

The exploratory nature of the programme and the configuration of the resonator lend themselves to an approach using a test stand (Fig. 1) and not to the fabrication of successive generations of a prototype. The two main elements of the test stand are:

- a set of superconducting magnets consisting of a pair of split coils and a bucking coil with a warm bore and spacing;
- a large diameter (40 cm) vacuum vessel where different resonator configurations could be easily exchanged or modified.

In the design of all the components, the guidelines are their flexibility and the diagnostic possibility. The Electron Tubes Department of BBC is responsible for the design and manufacture of the magnetron injection gun, the beam duct, the resonator and the collector. Other components of the test stand (magnet [1], vacuum vessel) and the ancillary systems (high voltage (HV) power supply, HV modulator and regulator, liquid Helium liquefier-refrigerator) were subcontracted to European manufacturers. All the different items have been completed and commissioning is underway.

### b) Characteristics of the first stage quasi-optical gyrotron

A detailed technical description of the quasi-optical gyrotron can be found in reference [2]. We shall only recall here the most salient features of the devices.

The electron gun is a conventional triode magnetron injection gun, capable of delivering 10A at 70 kV. The beam radius at the resonator is 2 mm and the ratio $p_\perp/p_\parallel$ is about 1.5 at a compression ratio of 20. The high voltage insulation is provided by an $SF_6$ hood: It was also found that the temperature distribution along the various ceramic parts of the gun is adequate and thus no further cooling required.

The first resonator system is confocal and has a mirror separation of 5 cm. The Fresnel number N is 0.722, leading to a total diffraction loss of 2%. Variation of the mirror separation (± 5 mm) and centering of the resonator with respect to the electron beam axis is possible under high vacuum with a tolerance of a few microns. The power is coupled out by diffraction at the two mirror edges into a 2.5 inch diameter cylindrical waveguide.

The gyrotron operation depends critically on the magnetic field profile in the interaction region. The specification of the split coil system calls for the possibility of producing a field gradient of about 1% per cm in the interaction region [1]. The bucking coil carries two independent windings so that the field and its gradient at the cathode can be independently adjusted to optimize the ratio $p_\perp/p_\parallel$.

## IV) CONCLUSION

While the quasi-optical concept bears many promising advantages [3,4], its development is only at an early stage compared to the one of cylindrical cavity gyrotron. The design of our system is aimed principally towards the study of the key questions such as efficiency enhancement by the gyroklystron concept and longitudinal mode competition [5].

## Acknowledgements

This work is supported by Euratom-Fusion, the Swiss Commission pour l'Encouragement de la Recherche Scientifique, the Ecole Polytechnique Fédérale de Lausanne, and BBC Brown, Boveri and Company Limited, Baden. We would like to acknowledge the technical assistance of O. Schafheitle, C. Biolley, B. Zigerlig (BBC-EKR) and J.-M. Mayor and H. Ripper (CRPP).

* ALBERTI, S.; ISAAK, B.; LIETTI, A.; PERRENOUD, A.; TRAN, M.Q., Centre de Recherches en Physique des Plasmas, Ecole Polytechnique Fédérale de Lausanne, 21, Av. des Bains, 1007 Lausanne/Switzerland.

AEBERHARD, R.; GARDIOL, F.; SPHICOPOULOS, T., Laboratoire d'Electromagnétisme et d'Hyperfréquence, Ecole Polytechnique Fédérale de Lausanne, 24, Ch. de Bellerive, 1007 Lausanne/Switzerland.

HOLM, K.; KUSE, D.; MATHEWS, H.-G., BBC Brown, Boveri & Company, Limited, Electron Tubes Department (EKR), 5401 Baden/Switzerland.

## References

[1] Spoorenberg, C. et al., 9th Int. Conf. Magnet Techn., Zurich, 1985, Poster 2PG-03.

[2] Quasi-optical Gyroklystron Development Group EPFL/BBC, Design of a quasi-optical 120 GHz Gyrotron, Lausanne Report LRP 277/85.

[3] Hargreaves, T.A. et al., Int. J. Electronics 57 (1984) 977.

[4] Perrenoud, A. et al., Int. J. Electronics 57 (1984) 985.

[5] Bondeson, A. et al., Int. J. Infrared and Millimeter Waves 9 (1984) 309.

# DESIGN OF QUASI-OPTICAL GYROTRON TESTSTAND

[f = 120 GHz; P ≤ 200 kW; τ ≤ 100 μs]

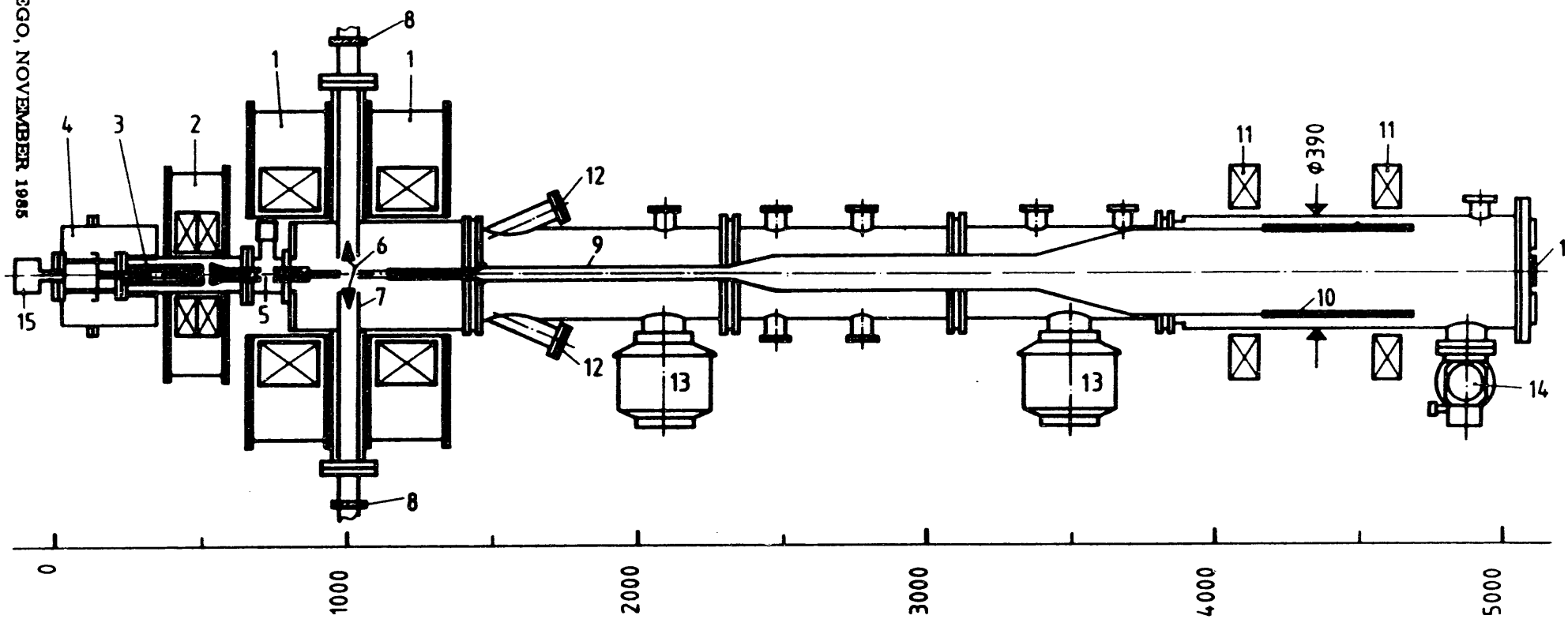


1. main magnet coils (sc)
2. gun magnet coils (sc)
3. electron gun (MIG)
4. $SF_6$-insulation hood
5. gate valve
6. mirror resonator
7. coupling tube
8. rf-window
9. beamduct
10. collector
11. collector coil
12. viewport
13. Ti-getterpump
14. turbopump
15. ion getterpump

FIG. 1

FIG. 2

THE SMALL RESONATOR SYSTEM

# Design and First Experimental Results of Components for ERCH at Thomson-CSF

A. Benshimhon, P. Garin, E. Jedar, G. Mourier, A. Thevenot
*Association Euratom-CEA sur la Fusion, DRFC, CEN*
*Boîte Postale No. 6, 92260 Fontenay-aux-Roses, France*

## 100 GHz Gyrotrons*

### Design

The main requirements are: 100 GHz, 200 kW min, 100 ms (CW in a subsequent stage), efficiency 30% min.

Tolerable cavity wall losses, the design of the gun (mirror ratio, cathode density), mode competition led us to a complex cavity $TE_{02}/TE_{04}$ with beam on second electric field maximum.

A $TE_{53}$ profiled cavity was also calculated.

The tube has a single disc window with peripheral cooling.

### Experimental Results

Three tubes were built with complex cavity. All delivered more than 200 kW, 35% efficiency $TE_{04}$ without spurious oscillation on $TE_{24}$ and probably less than 5% spurious mode.

One tube was tested up to 10 ms, 150 kW, and 20 ms, 100 kW without failure.

One tube was built with $TE_{53}$ cavity. It delivered more than 280 kW in short pulses (100 $\mu$s).

There is concern about beam interception, actual wall losses and window stresses.

## 60 GHz Transmission Lines**

Three transmission lines consisting in tapers, mode convertors ($TE_{02} \rightarrow TE_{01}$, $TE_{01} \rightarrow TE_{11}$), corrugated curves, mode filters, arc detectors were built.

They work satisfactorily on Tokamak de Fontenay aux Roses with Varian gyrotrons: 3×220 kW were injected in plasma for 100 ms pulses.

* Work sponsored by Euratom
** Work sponsored by CEA

# ECH SYSTEMS AND WAVEGUIDE DEVELOPMENT

# Technical Aspects of the Joint FOM/CEA ECH Experiment on TFR

A.G.A. Verhoeven, A.F. van der Grift, J. de Hoop,
M. van der Kaay, L. Kroonenburg, A.B. Sterk
*Association Euratom-FOM, FOM-Instituut voor Plasmafysica*
*Rijnhuizen, Nieuwegein, The Netherlands*
and
J.P. Crenn, L. Rebuffi, B. Tournesac
*Association Euratom-CEA sur la Fusion, DRFC, CEN*
*Boîte Postale No. 6, 92260 Fontenay-aux-Roses, France*

## 1. ABSTRACT

For electron cyclotron resonance heating, three 60 GHz gyrotrons each capable to deliver over 200 kW of microwave output power are in use since September 1985 on the TFR tokamak at Fontenay-aux-Roses.

Recent technical improvements on the high-voltage power supply, on electronic systems used to modulate the RF-power, injected into the plasma, and on the transmission line systems are described.

## 2. INTRODUCTION

An electron cyclotron heating experiment on the TFR tokamak has been undertaken by the EUR-FOM and the EUR-CEA Associations. The main physical aims of this experiment are: local heating of the bulk electrons, experimental investigation of a proposed current drive scheme by EC-waves, plasma formation and control of MHD-instabilities [1,2]. The installation of the ECH-system on TFR started in January 1984. The first gyrotron arrived at FaR in September 1984. It unfortunately broke down during the final acceptance test because of too long "idling" (beam current without RF-output, see chapter 5). Beam deposit tests have been done on the second gyrotron in November 1984 to try to understand the reason of the failure and to take protective measures. In February 1985 all three gyrotrons were accepted and was the system ready for pulsing.

The transmission line system, built by Thomson CSF is made up of three transmission lines, each connecting one gyrotron to the same TFR port [3]. Similar transmission lines were manufactured already for ECH experiments [4,5,6]. Presently, two microwave beams are launched perpendicularly to the toroidal magnetic field and one with an angle of 16° (limited by the TFR geometry) with respect to the others. The length of each transmission line is about 15 m. The complete system is operating since September 1985. The 3 gyrotrons deliver each around 220 kW RF-power during a 100 ms pulse.

## 3. POWER SUPPLY

The high-voltage power supply of the 3 gyrotrons is a transformer-rectifier unit delivered by Alsthom, France. This transformer-rectifier, connected to the 20 kV network, enables the delivery of a voltage up to 100 kV during a pulsed current of 40 A [7].

A modulator-regulator unit, supplied by Universal Voltronics Co., U.S.A., delivers 80 kV to each of the gyrotrons. A series tube stabilizes the output voltage within ± 0.25% of the desired value and enables to pulse the gyrotron collector-cathode voltage. In case of a fault at the output of the modulator-regulator the series tube will interrupt the output current within a few microseconds. If the fault does not disappear an ignitron crowbar will short-circuit the high voltage power supply.

For each of the gyrotrons a separate anode-modulating system consists of a zener stabilizer fed from the collector voltage (see Fig. 3.1). Two pulse tetrodes across the zener-stack are short-circuiting the zeners in case no gyrotron output is required. The foreseen way of operating the gyrotrons was to switch the first tube in order to raise the anode voltage of the gyrotron to a level just below the RF-output condition at almost full beam-current: the RF-standby situation. By switching the second tube the anode voltage should step to a higher level to obtain optimal oscillating conditions. However, very soon after the beginning of the experiments it became clear that the time during which the beam is switched on but the gyrotron is not generating RF-output, had to be restricted severely (see chapter 5). This "IDLING"-time is now limited by means of a protection system.

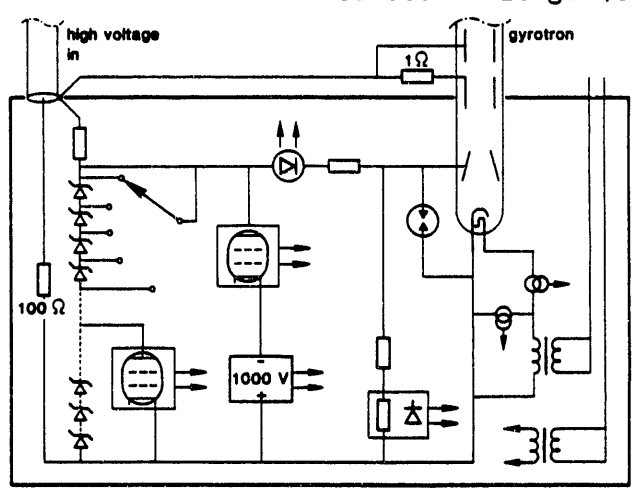

Fig. 3.1 The anode modulating system

Due to warming up of the zener diodes, a slight variation of the anode voltage (< 1%) has been observed. To avoid this, the zener diodes were replaced by temperature compensated zenerdiodes. Further a power mosfet was placed in parallel to each of these zenerdiodes. In this situation only 1 mA is flowing through the zeners and therefore the warming up is drastically limited. As a consequence the series resistor of the zener stack could be decreased from 2MΩ to 400 kΩ. As a result the rise time of the anode voltage is decreased. A reduction of the delay time between triggering of the first anode tetrode and full RF-output power from approximately 225 μs to 80 μs has been obtained. This enables a faster reaction to trigger signals. The "idling"-time is also reduced for each pulse because the no-RF-time is shorter and therefore the number of pulses (from zero to full RF-power) can be increased. The risetime of the RF-power is further decreased from 10 μs to 4 μs. The anode voltage variation decreased to 0.1% and ensured a more stable RF-output.

## 4. CONTROL AND DATA ACQUISITION

The status of all important control units and security circuits is transferred by means of fibre optic links to a microprocessor system. When all the units are ready the microprocessor enables the start of the Time Sequence Generator (TSG). The TSG supplies timing pulses - with a resolution of 1 μs - to the power supply, to the modulator, and to each of the anode voltage switches separately. For conditioning of the gyrotrons it is possible to pulse with a duty cycle of 1%. For pulses to the plasma the TSG is either triggered at a preset time after the start of the TFR plasma or at the moment a trigger-signal is received from the plasma.

To measure fast varying signals CAMAC analog-to-digital converters, are used. A PDP11/23+ computer system is used to process this data and for communication with the TFR-SOLAR computer. For direct communication between the laboratory in Holland and the computer at the experiment in France a switched package data network (Datanet 1 - Transpac) is used. Inside a screened cage most of the electronic protection systems are housed, e.g. the Arc detector Interrupt Module (AIM). The coupling to the gyrotron installation is by means of fibre optics to avoid electromagnetic interference.

The inputs for the AIM are four arc detectors and one reflected RF power signal from each of the transmission lines. As soon as one of the inputs is active, the gyrotron will shut down within 2 μs. After a short clearing time the gyrotron is switched on again. In case of a new fault it is switched off again. This goes on for a preset number of times. In case more gyrotrons are in use simultaneously, only the faulty one is switched off [8].

## 5. BEAM DEPOSIT TEST

The first gyrotron was accepted at Varian's factory in June 1984. However, at the end of the final acceptance test at Fontenay-aux-Roses, witnessed by the manufacturers test-engineer the gyrotron broke down. A hole was burned in the collector wall. This happened after seven pulses of 100 ms each, during which the beam-current was switched on but no RF-radiation was emitted. This is the so-called "idling"-mode. The explanation of this breakdown is most probably as follows: If the gyrotron is operated in the "normal" RF-producing mode, the energy of all the electrons is almost the same (~ 80 keV). After interacting with the RF-field the energy of the electrons will vary a lot more and therefore the electron beam will be spread over an appreciable length in the collector. The spread-out of the deposition depends on the profile of the magnetic field of the superconducting coils (I1, I2 and bucking coil I5, see Fig. 5.2). To protect the output window permanent magnets (nr. 8 and 9, see Fig. 5.2) are placed around the collector and very strong permanent magnets (nr. 6 and 7) close to the window, to bend the last existing electrons to the wall.

If no RF is generated the spread of the electron energy is much less and therefore a more localised deposition of the electron beam can be expected. Furthermore, the normal RF output power of approx. 220 kW has to be dissipated as well.

Extensive beam deposit tests have been performed on the second gyrotron, in collaboration with the manufacturer. By measuring the temperature as a function of time at several places on the collector wall, (using a curve of the thermal capacitance as a function of position at the collector) it was possible to determine the power deposited per $cm^2$. These tests were done with 10 ms-pulses with collector cooling switched off. Measurements were taken at six places in the length of the gyrotron, and on four circular positions (north, east, south and west, where east is the direction in which the electrons are bend by the permanent magnets). The result was a prohibitively high energy density of more than 2 $kW/cm^2$ in the east direction, close to the window.

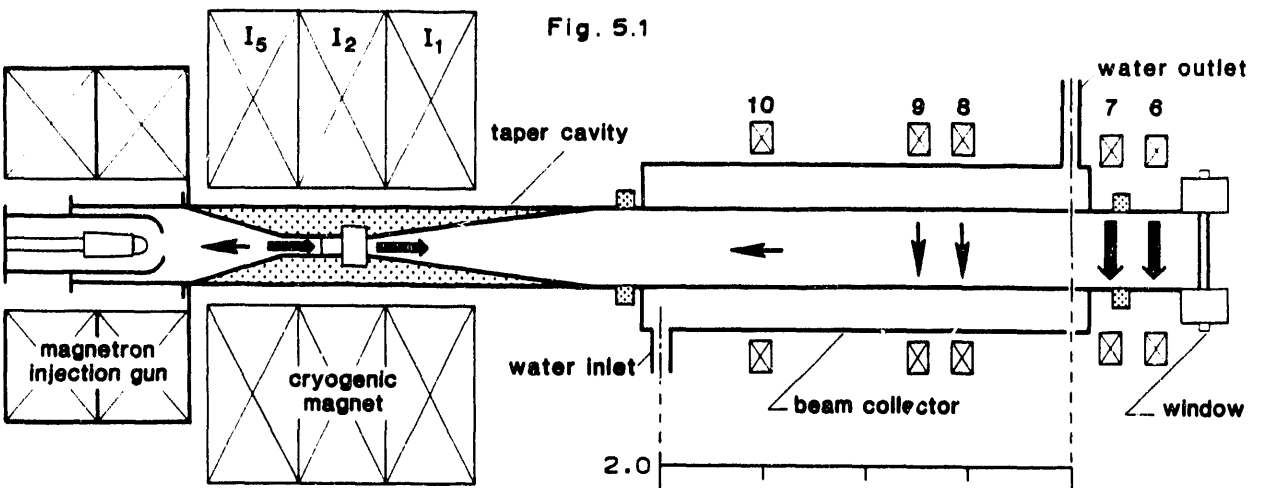


Fig. 5.1

After installing an extra solenoid (nr. 10 in Fig. 5.1) with a current of 1.5 A and a magnetic field opposite to the main coils 1 and 2 the tests were executed again.

This resulted in Fig. 5.2 where the deposited energy density is given as a function of position at the collector. Although the energy density at the right hand side of this figure is reduced, it is still very high. Because of the position of the collector cooling water outlet it was not possible to measure further to the right where the maximum power density might be suspected. Close to the window the power density at the east side of the collector is for the "idling" situation almost twice as high compared with the "RF-on" situation (see Fig. 5.2).

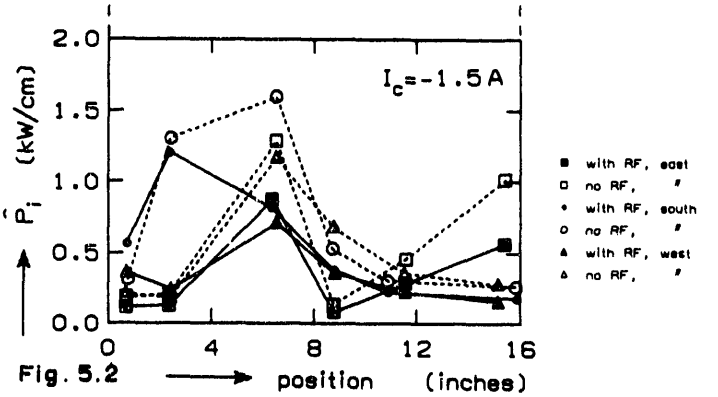


Fig. 5.2

From these tests Varian concluded that is is necessary to limit the idling time to 30 ms. An electronic protecting unit is now in use, which normally limits the idling time to 3 ms.

## 6. GYROTRON OPERATION

The RF power of the gyrotrons has been measured as a function of magnet currents, beam current and anode voltage, through a waterload mounted directly on top of the gyrotron. During normal operation the ECH power is calculated from the beam- and magnet currents using the measurements.

Since the idling time is limited the gyrotrons are usually pulsed by switching on and off completely - RF-power 0% or 100% - . Another possibility is to have the step in the anode voltage reduced to e.g. 1 kV (see Fig. 6.1). In this case the RF power can be modulated between any desired percentage and the full level for modulating frequencies up to 50 kHz. A 50 Hz ripple during low-RF is caused by the filament-supply and the very steep RF-power vs. anode voltage characteristic. To achieve a very high modulating frequency it is possible to switch on the anode voltage again before it is completely switched off. This enables a modulation of the RF-power from 0 to 100% with a frequency up to 100 kHz. Even higher frequencies are possible when modulating less than 100% RF-power.

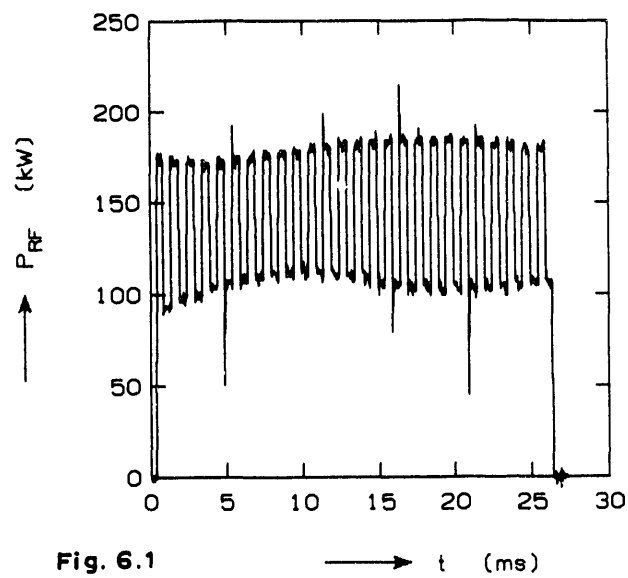


Fig. 6.1

## 7. MHD-FEEDBACK CONTROL UNIT

Local heating outside the q = 2 surface can suppress the m = 2 mode activity. In mode control experiments on TFR with one gyrotron a feedback system was used that switches on the gyrotron in case the MHD-activity, as derived from a set of Mirnov coils, surpasses a certain level [1,2]. To enhance and improve this feedback system a new control unit is being designed and will be installed in November 1985. The unit functions as follows (see Fig. 7.1).

The signal from the plasma is transferred into an optical signal with a frequency proportional to the degree of disturbance. At the first pulse the first gyrotron will start transmitting RF power into the plasma. In case the mode is suppressed, the gyrotron will be switched off. If the mode activity remains higher than a certain threshold, the second gyrotron will be switched on automatically. A very high disturbance will switch on the third gyrotron as well. An anode feedback control is built in to switch over to the next gyrotron either in case the 100 ms limit is reached or the gyrotron is switched off because of another interrupting action.

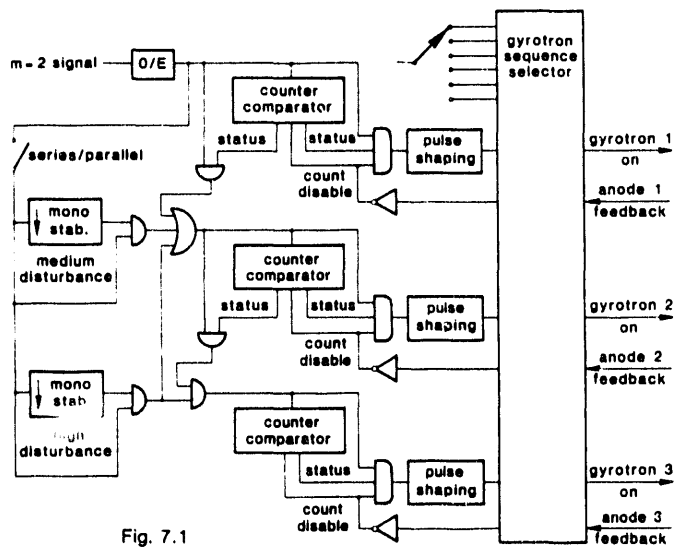

Fig. 7.1

## 8. TRANSMISSION LINE SYSTEM

The output power of the gyrotron is delivered in an oversized vertical cylindrical waveguide, mainly in the TE02 mode. The best physical conditions for the absorption call for a linearly polarized beam, i.e. the TE11 mode, to be coupled to the ordinary mode into the plasma. The mode conversion is made in two steps, first TE02 to TE01 to minimize the losses, then, close to the end of the line TE01 to TE11. The sequence of waveguide components in a line is listed in Table I. Note that there are slight differences in sequence and performances, compared to what has been previously reported [9]. Each line has the same components but straight waveguide lengths and bend angles are different.

### 8.1 Components

The characteristics of the main components are given in this section.

8.1.1 Waveguide tapers: Their shapes are optimized to get a rejection of 33 dB on spurious mode (TE01 and TM11). The TE02 and TE11 tapers are respectively 800 and 1300 mm long.

8.1.2 Mode converters: The theoretical efficiencies and lengths for the TE02 to TE01 and TE01 to TE11 mode converters are 98% for 6 λB and 96% for 8 λB respectively, λB being the beat wavelength of the two considered modes.

TABLE 1

From the output of the gyrotron: TE02 mode, ϕ 63.5 mm each line is made up of the following components:

| | |
|---|---|
| Arc detector | Corrugated bend |
| Bellow | TE01 bidirectional coupler |
| Four holes coupler | Bellow |
| Resistive filter | Arc detector |
| Taper 63.5 to 27.8 mm | DC break |
| TE02 bidirectional coupler | TE01 to TE11 mode converter |
| Corrugated bend | Taper 27.8 to 63.5 mm |
| TE02 to TE01 mode converter | Arc detector |
| Arc detector | Vacuum window |
| Straight waveguide | Waveguide antenna |

8.1.3 Bidirectional couplers: The two selective couplers, respectively in the main TE02 and TE01 modes, are used to interrupt the microwave beam in case of a too high level of reflected power and to tune the gyrotrons to an optimal mode purity using the backward wave output signal. Because of a too large value of coupled non circular spurious modes, the TE01 bidirectional coupler cannot be used to measure the incident power (see chapter 6).

The coupling coefficient is about 60 dB, and the directivity more than 20 dB. The spurious mode rejection, depending upon modes in the lines, is more than 30 dB for unwanted circular modes.

8.1.4 Resistive mode filters: Only one resistive mode filter, close to the gyrotron and made of silicon carbide as absorbing wall material, is used for the time being. Its attenuations for the TE02, TE11 and TM12 modes are 0.12 dB, 1.65 dB and 4 dB respectively. The second one, in silicon carbide as well, but with a 27.8 mm diameter, was first inserted between both bends. Internal arcs occurred, preventing to enlarge 200 kW power pulses beyond 30 ms. The same phenomena has been observed with all three lines. This type of filter has been removed. A stainless steel smooth waveguide of 2 meter long is mounted in one line and causes no problems anymore. A carbon filter will be tested soon.

8.1.5 Corrugated bends: The TE02 bends are 2.70 m long and have angles between 101° and 118°. The TE01 bends are 1.80 m long with angles between 20° and 64°. Corrugations and curvature shapes are optimized for mode conversion losses less than 0.1 dB.

8.1.6 Vacuum windows: The Varian beryllium oxyde vacuum windows are designed for the TE11 mode at 60 GHz. Cold tests have been carried out in order to measure the transmission coefficient. This coefficient varies with the frequency. On the other hand, all three gyrotrons do not emit their power at the same frequency. We choose the windows in order to match them with the gyrotrons. In the operating frequency bandwidth, the transmitted power is more than 97%.

## 8.2 Antenna system

The antenna system, presently made of a circular waveguide, launches the TE11 mode from the low-field side of the torus. In the near future it is foreseen to use as antenna a straight wall corrugated TE11 to HE11 converter. Anyway, in the case of TFR, as shown in [10], the HE11 mode would not improve very much the polarization and the pattern compared to the TE11 mode. Two types of reflector have been mounted on the inner wall of the torus. The first was a smooth roof-top mirror angled at $\pm$ 10° with respect to the toroidal magnetic field. The second, a corrugated surface twist reflector, with an angle of 10°, converts the beam fraction which is not absorbed by the plasma from the O-mode to the X-mode polarization. Behind this mirror, a system of three circular waveguides will be installed to measure the incident beam intensity and polarization.

## 8.3 Radiometer

To obtain maximum performances from the gyrotrons, a fine control of the magnet currents is necessary. The signals from the bidirectional couplers and a radiometer (Fig. 8.3.1) are used to monitor the tuning of the tubes.

A signal extracted from the transmission line is mixed to a signal delivered by a local source oscillating at a frequency close to that of the gyrotron. The beat signal is then sent into a frequency spectrum analyzer. The optimal tuning, corresponding to a minimum number of arcs, is obtained when the frequency spectrum analyzer gives only one spectral line.

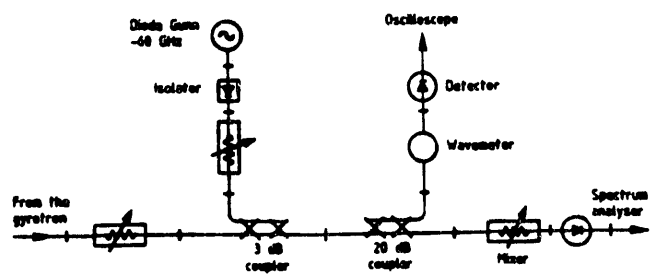


Fig. 8.3.1

## 8.4 Experimental results

Cold tests at works have been carried out, on all three lines, without the vacuum windows. Overall efficiencies, $\eta$ = output power in TE11 mode/input power in TE02 mode, of about 85% ± 4% have been measured.

The far-field pattern of the TE11 mode radiated at the exit of the line has been measured in the E plane and is shown in Fig. 8.4.1. The result shows that spurious modes, mainly in side-lobes, are not very important. On site, high power tests have been performed. Different line configurations have been tested:

- in a temporary assembly, into a water load, with and without the vacuum windows,
- in the final assembly, including the windows, with the vacuum chamber of the TFR tokamak as a load.

The following comments can be made:

- full performances can be obtained only with a very sharp tuning of the gyrotrons,
- under the same conditions, normal air in the line allows to reach higher performances than nitrogen gas.
- mode contents investigations have been carried out using thermal paper. Only qualitative information can be obtained.

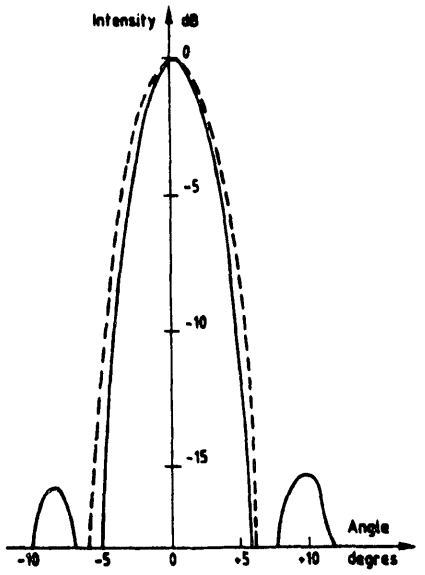


Fig. 8.4.1 : Far field pattern of the $TE_{11}$ mode at the exit of the transmission line
Full line : Experimental curve
Dotted line : Theoretical curve

## REFERENCES


[1] FOM-ECRH Team and TFR Group, 12th Conf. on Contr. Fus. and Plasma Phys., Budapest, 2-6 Sept. 1985, pp 60-63, Volume II.

[2] FOM-ECRH Team and TFR Group, 5th Int. Workshop on ECE and ECH. San Diego, 9-12 Nov. 1985. (Paper at this conference.)

[3] E. Jedar et al. 8ème Colloque Optique Hertzienne et Diélectrique, Grenoble, 16-18 Sept. 1985.

[4] H. Hsuan et al. Proc. 4th Int. Symp. on Heating in Toroidal Plasmas. Rome, 21-18 March 1984, pp. 853-864.

[5] C.P. Moeller et al. Proc. 4th Int. Symp. on Heating in Toroidal Plasmas, Rome, 21-18 March 1984, pp. 1454-1460.

[6] M. Thumm et al., Proc. 4th Int. Symp. on Heating in Toroidal Plasmas, Rome, 21-28 March 1984, pp. 1461-1468.

[7] A.M. van Ingen et al. Proc. 13th Symp. on Fusion Techn., Varese, 24-28 Sept. 1984, pp 805-809.

[8] J.W. L'Ami et al. Proc. 13th Symp. on Fusion Techn., Varese, 24-28 Sept. 1984, pp 1097-1102.

[9] R. Cano et al. Proc. 13th Symp. on Fusion Techn., Varese, 24-28 Sept. 1984, pp 611-616.

[10] L. Rebuffi, Course and Workshop on Appl. of RF Waves to Tokamak Plasmas, Varenna, September 1985.

ACKNOWLEDGEMENTS

The FOM activities were performed under the EURATOM-FOM Association agreement with financial support from ZWO and Euratom.

# Microwaves for ECRH in Milano C.N.R. Laboratory

S. Cirant and G. Falciasecca*
*Instituto di Fisica del Plasma*
*Associazione EURATOM-CNR, Milano, Italy*

Asymmetric modes can be generated in a circular oversized waveguide carrying circular eletric modes by reflections from a non-ideal load and by conversion at non perfect transitions or inhomogeneities along the line itself; even a small amount of power in these unwanted modes can lead to an improper operation of the gyrotron and lower the power capability of the whole system, so they must be suppressed by mode selective filters.

The stronger finite resistivity effect on the attenuation for all non circular $TE_{o,q}$ modes is the basis on which resistive wall mode filters used in ECH experiments (1) are built.

A different approach relies on the deposition of a thin layer of lossy dielectric on the inside surface of the guide metallic wall; again $TE_{o,q}$ modes are uneffected while the attenuation of all the other modes is significantly increased (2).

The highest attenuation coefficient for some non $TE_{o,q}$ modes has been obtained with circumferentially corrugated stainless steel filters (3) in which those modes are converted into surface waves, heavily dumped by the specific wall structure.

The helix waveguide approach (4) analyzed here has at least one advantage over all the other methods in the sense that the power into non $TE_{o,q}$ modes is not resistively dumped at the waveguide walls but it is lost by radiation from the leaky guiding structure; thermal loading of the inner surface with possible breakdown problems is then avoided. Furthermore it is not mode selective; the attenuation coefficient is substantial for all non circular electric modes, even if it can be lower than that of the corrugated filter for some specific modes.

The helix waveguide can be described (5) by a cylindrical surface with infinite conductivity along the helix and zero conductivity perpendicularly to it; the surface is surrounded by an infinite medium characterized by a dielectric constant which can have a finite imaginary part; by imposing the proper boundary conditions a characteristic equation can be derived (6):

$$J_p'^2(k_0a)+i\frac{\varepsilon k_0}{k_1}J_p'(k_0a)J_p(k_0a) - \frac{p^2\bar{\beta}_2^2}{k_2^2a^2}J_p^2(k_0a)+\frac{p\bar{\beta}\,tg\alpha}{\pi a/\lambda_0}J_p^2(k_0a) = 0$$

*Dipartimento di Elettronica, Informatica e Sistemistica, Universita di Bologna, Bologna, Italy.

where $k_0^2 = \omega^2 \varepsilon_0 \mu_0 - \beta^2$ ; $\varepsilon = \varepsilon' - i\varepsilon''$ is the dielectric constant of the jacket material; $k^2 = \omega^2 \varepsilon_0 \mu_0 \varepsilon - \beta^2$; a is the radius of the winding and $\alpha$ the pitch angle.

Assuming the pitch angle to be negligible the characteristic equation can be solved with $\varepsilon' = 4$ (fiberglass impregnated with epoxy resins) and $a/\lambda_0 = 2.96$. The real and imaginary part of the normalized phase constants relative to some of the most important modes are shown in Figs. 1a,1b. Allowing the tg$\delta$ of the jacket material to be in the order of $10^{-2}$ it turns out that $\varepsilon''$ is much less than unity and a minimum $\bar{\beta}''$ of the order of $10^{-3}$ is to be expected, which gives an attenuation constant $\beta'' \cong 6$ dB/m, confirmed by the measure of the insertion loss for the $TE_{11}$ mode.

Both straight waveguide sections and the $TE_{02}$ - $TE_{01}$ mode converter (Fig. 2) have been built with this technique, with a total length of 2 m and an overall attenuation for non circular electric modes in the order of 12 dB at least.

The predicted behaviour of the 5 $\lambda_b$ mode converter, 6.42% ripple amplitude, is shown in Figs. 5-6; the measure of the gain in the conversion with increasing the converter length is shown in Fig. 7.

Mode purity and its measure is always a matter of concern in transmission lines for E.C.H.; in the following a method to quantitatively measure the power in circular electric modes at the end of a line powered by a gyrotron is discussed. If conducting sheets are radially inserted equally spaced in a circular waveguide a new set of modes is generated; the number of sheets can be made high enough to put in cut-off all modes allowed in the circular waveguide apart from the circular electric ones.

In each one of the equal sectors in which the guide is divided the new boundary conditions define the new set of modes:

$$TM_{p,q} \qquad p = r\,K/2 \qquad r = 1, 2, \ldots.$$

$$TE_{p,q} \qquad p = r\,K/2 \qquad r = 0, 1, 2, \ldots$$

correspondingly $\beta^2 = \omega^2 \varepsilon_0 \mu_0 - (\chi'_{pq}/a)$ and $\beta^2 = \omega^2 \varepsilon_0 \mu_0 - (\chi_{pq}/a)$ , where $\chi$ and $\chi'$ are respectively the q-th roots of the Bessel function of order p and its derivative. If K is even the allowed modes have their counterpart with those in the empty guide, while if K is odd a new set of modes is generated.

We have built a component with 8 sectors about 30 $\lambda_0$ long, which is in cut-off for all the following empty waveguide modes:

$$TE_{p,q} \qquad p \neq 0, 4, 8, 16 \quad ; \quad p \geqq 17$$

$$TM_{p,q} \qquad p \neq 4,8 \quad ; \quad p \geqq 16$$

In practice all spurious modes of interest are reflected at this mode selective mismatch placed at the end of the line before the water load, their power being dumped by the distributed filtering of the helix waveguide sections.
The insertion loss of this component has been measured at full gyrotron's power to be 11%, $\pm$5%; on the other hand low power tests have shown that this component doesn't affect the radiation pattern of the $TE_{01}$ mode (Fig. 3) and it can be concluded that the final polarizing antenna used to launch O-waves into the plasma is illuminated mostly with a $TE_{01}$ mode, the spurious mode content being in the order of 10%.
The Wengenroth-extended polarizing antenna (Fig. 4) is composed by ten flat corrugated mirrors arranged in order to approximate a parabolic surface; the resulting half maximum beam-widths are 6.8° and 9.2° respectively in the E and H planes; the cross polarization is at least 20 dB down, giving an efficiency in converting the waveguide $TE_{01}$ mode into a single polarized beam in excess of 95% (Fig. 8).
Future work will consider a mode selective sectoral mismatch for all non-circular electric modes, bends in a corrugated waveguide carrying a $TE_{02}$ mode, mode selective directional couplers, improved versions of the polarizing antenna and the study of a 140 GHz transmission line.
As far as the very high frequency development program is concerned firstly the possibility of building $TE_{01}$ - $TE_{11}$ mode converters in a small radius evacuated waveguide will be evaluated, the potentialities of gaussian beam propagation will be explored and the limits will be investigated in launch pure gaussian beams with high efficiency by polarizing reflectors.

## References


1) C.P. Moeller et al., Components and transmission system for ECH , 4th Int. Symp. on Heating in Toroidal Plasmas, Rome, 1984;
2) H.G. unger, Lined waveguide, Bell Syst. Tech. J. 41,745, 1962;
3) M. Thumm et al, ECRH System for linearly polarized plasma irradiation in the $HE_{11}$ mode at 28 and 70 GHz, 4th Int. Symp. on Heating in Toroidal Plasmas, Rome, 1984;
4) L. Argenti et al., Effects of ECW in injection in the THOR tokamak plasma, XII Eur. Conf. on Controlled Fusion and Plasma Physics, p. 300, Budapest 1985;
5) R.A. Waldron et al., Normal modes of helix waveguide, Marconi Rev. 28, 29 1965;
6) R.A. Waldron, Theory of guided electromagnetic waves, Van Nostrand, London,1969.

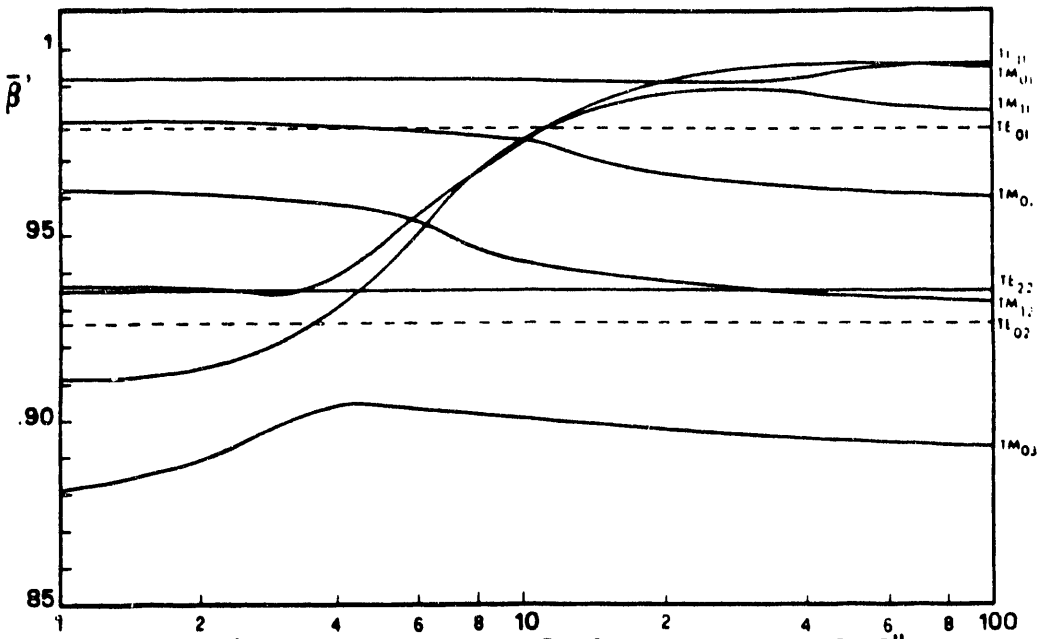


Fig.1a - Real part of the normalized phase constant. $\varepsilon'=4$

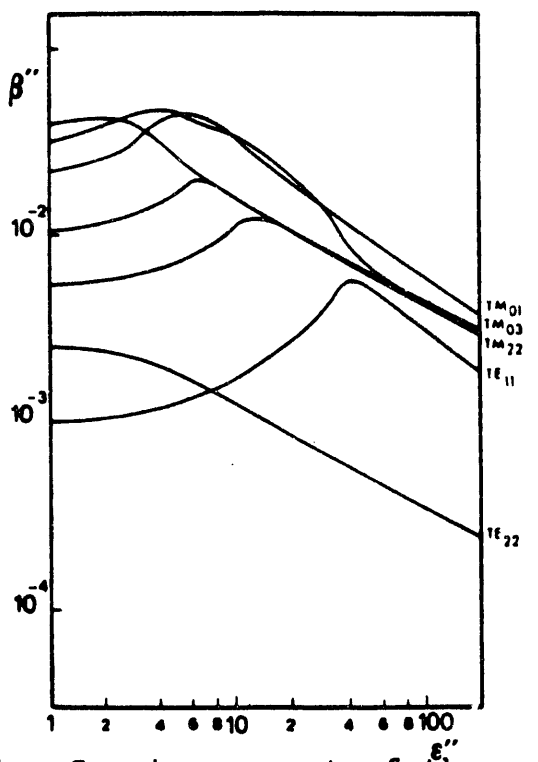


Fig.1b - Imaginary part of the normalized phase constant. $\varepsilon'=4$

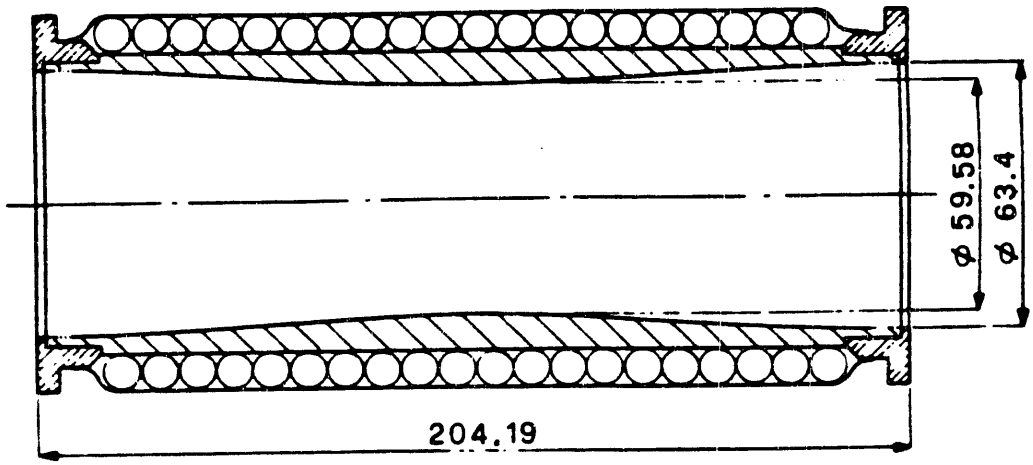


Fig.2 - One section of the helix waveguide mode converter

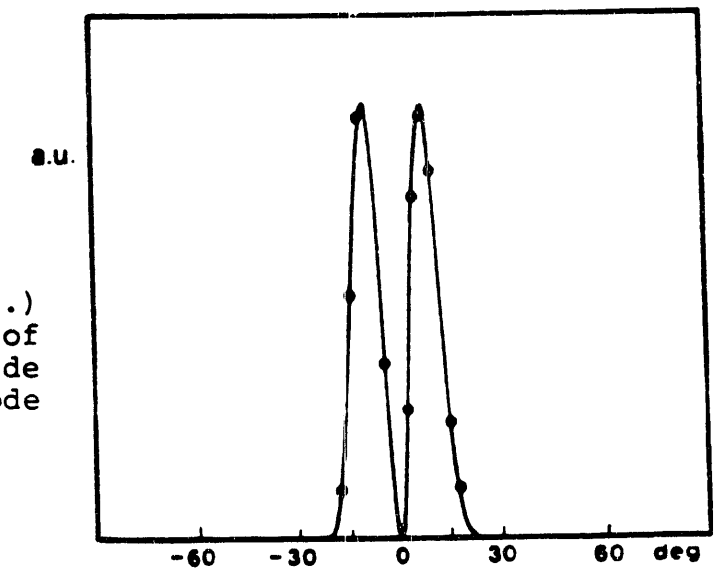


Fig.3 - Measured (.) radiation pattern of a sectored waveguide carrying a $TE_{01}$ mode

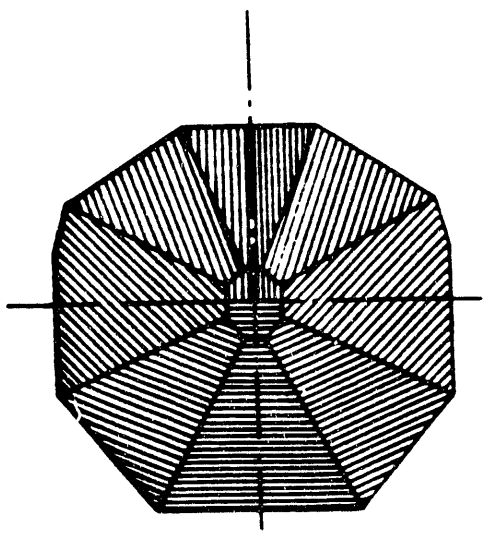

Fig.4 - Front view of the Wengenroth-extended antenna

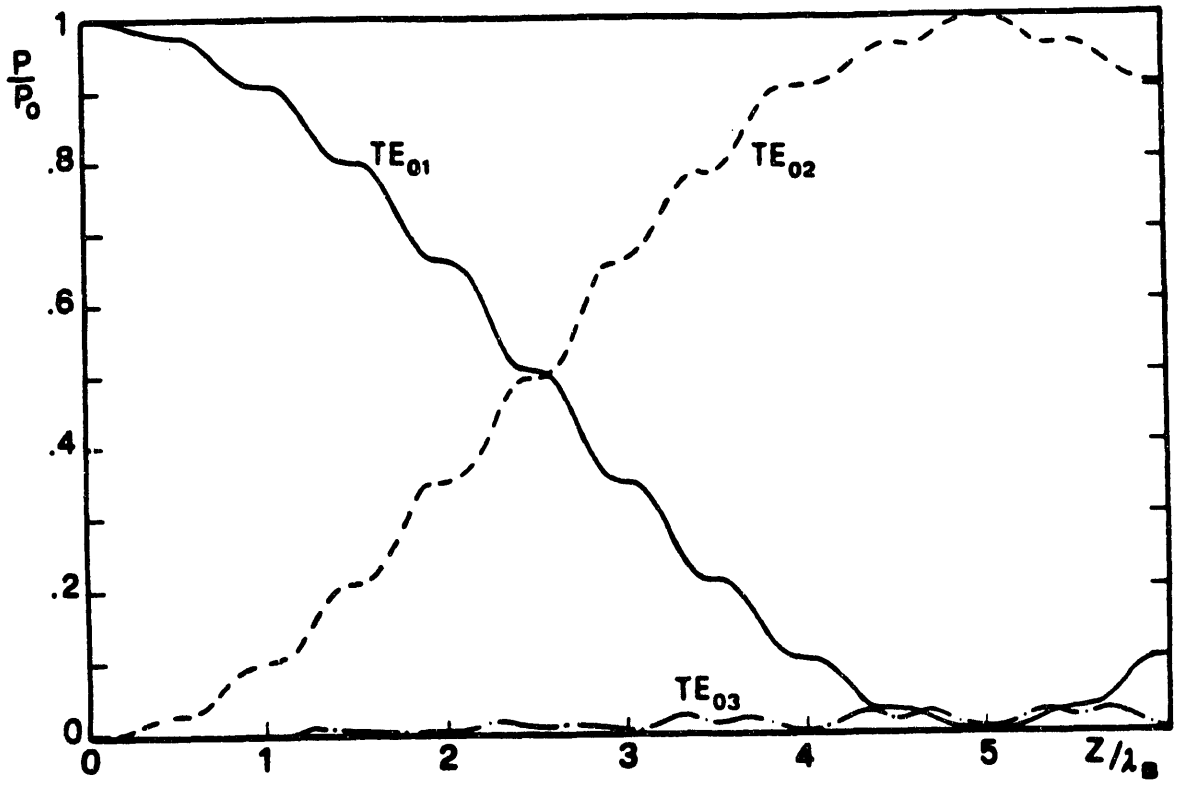


Fig. 5 - Converter efficiency vs. length. 100% $TE_{01}$

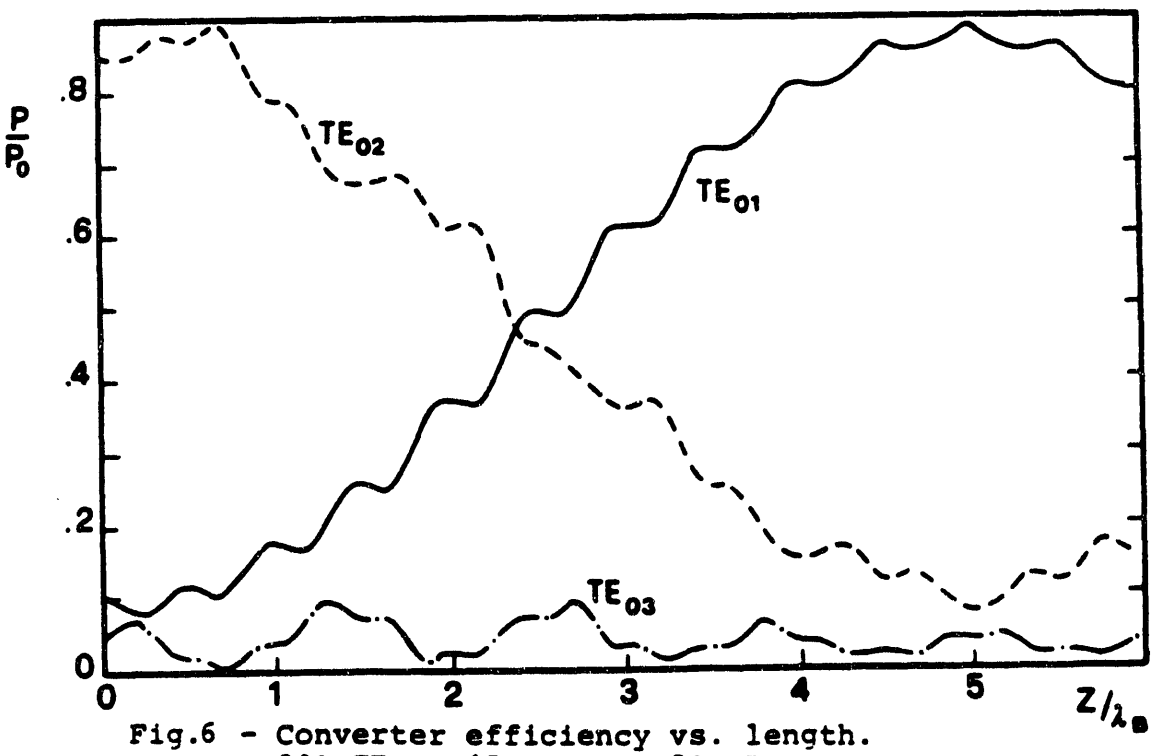


Fig.6 - Converter efficiency vs. length.
80% $TE_{02}$ 15% $TE_{01}$ 5% $TE_{03}$

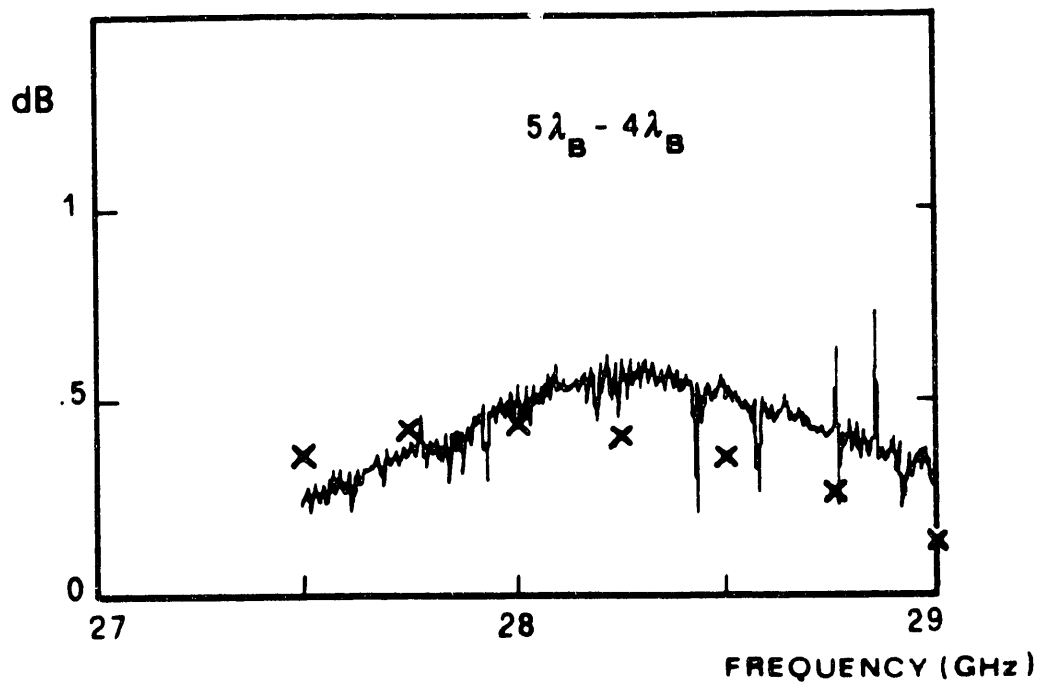


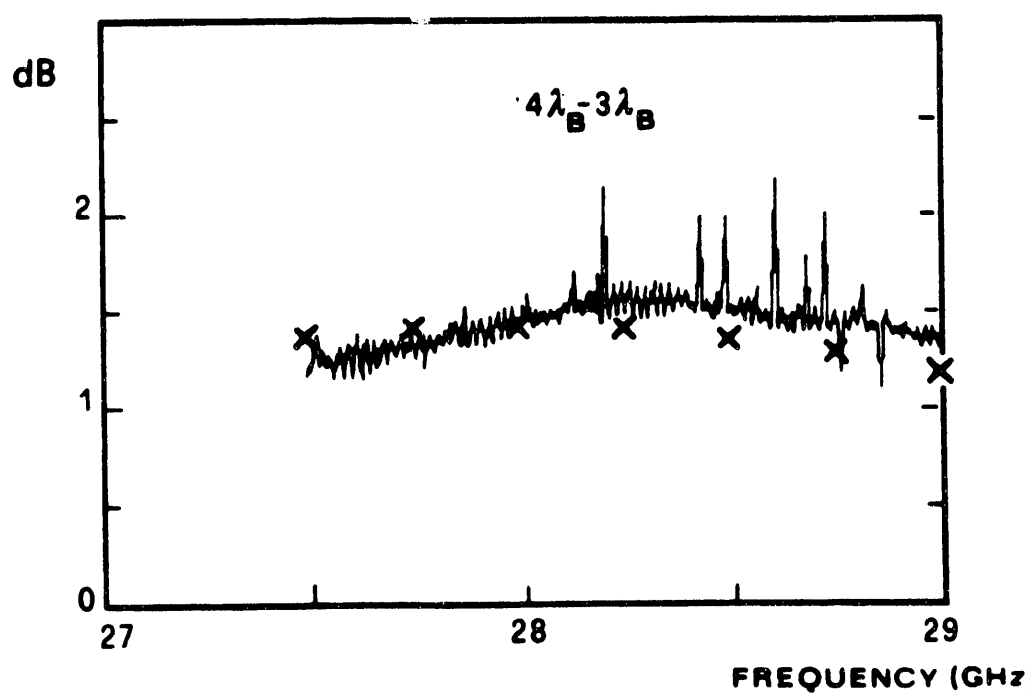


Fig.7 - Theoretical (x) and experimental conversion gain obtained adding one element to the converter length.

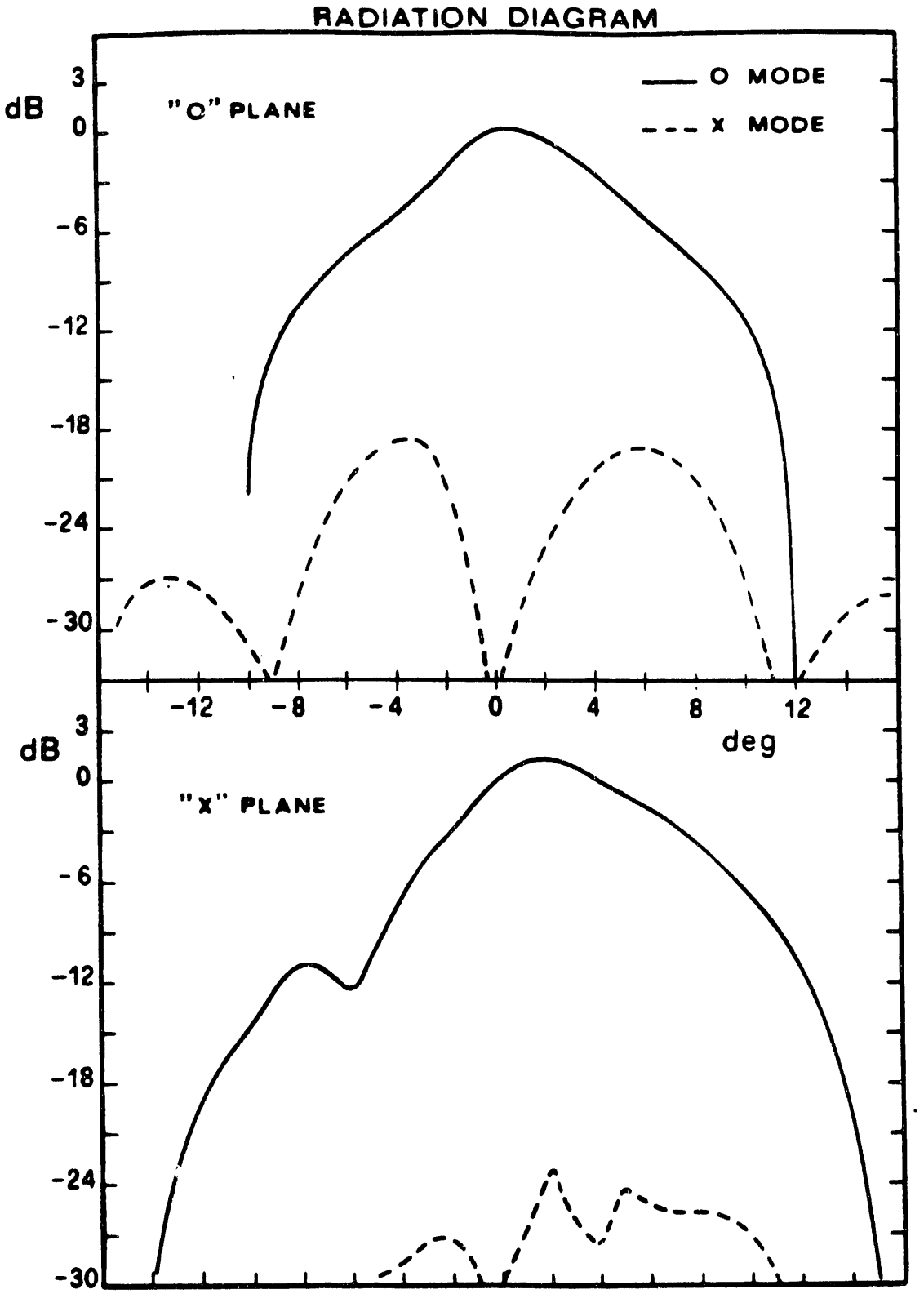


Fig.8 - Wengenroth extended polarizing antenna radiation diagram.

# Optimization of Wall Perturbations in Rippled Wall Mode Converters for Overmoded Circular Waveguide

M. Thumm, G.A. Müller, R. Wilhelm
*Institut für Plasmaforschung, Universität Stuttgart*
*D-7000 Stutgart 80, Federal Republic of Germany*

ABSTRACT

Considerable improvement (higher efficiency, shorter length) of periodic-perturbation mode converters for overmoded circular high-power waveguides has been accomplished by changing the perturbation period of the wall slightly from the beat wavelength between the input and the desired output mode combined with superimposing additional, phase-matched, small perturbations, whose periods correspond to the beat wavelengths between the input and output mode and their related, strongest coupled unwanted modes, respectively. Numerical calculations and measurements on optimization of wall perturbations in TE0n-to-TE0,n-1 mode converters and TE01-to-TE11 transducers for the 1 MW-ECRH system (five 200 kW/70 GHz-transmission lines with cw capability) at the Garching WENDELSTEIN VII-AS stellarator are reported. In the case of TE02-to-TE01 transformation a maximum theoretical efficiency of $\eta$ = 99.7% (99.5 ± 0.5% measured with an 8-period converter, transducer length L = 0.87 m, average inner radius $a_o$ = 13.9 mm) was achieved by means of rippled wall mode converters with axisymmetric radius perturbations (superposition of a second harmonic period to the main period). Conventional TE02-to-TE01 mode converters with simple perturbation structures exhibit conversion efficiencies of approximately 99%. More significant is the obtainable efficiency improvement in the case of TE01-to-TE11 mode conversion in transducers with constant diameter and periodically perturbed curvature (in one plane). The multimode calculations show that the efficiency $\eta$ = 86.2% (undesired modes: 6.9% TE01, 4.8% TE12, 0.7% TE21; 1.4% ohmic skin losses) of a simple 8-period 70 GHz transducer (cos-shaped perturbation, L = 2.49 m, $a_o$ = 13.9 mm) can be raised up to 97.4% (unwanted modes: 0.6% TE01, 0.4% TE12, 0.1% TE21; 1.5% attenuation; L = 2.53 m, two additional periods). The experimentally determined TE01-to-TE11 conversion efficiency is (97.2 ±0.5)%.

## 1. Introduction

Gyrotron oscillator tubes are efficient sources of high-power millimeter wave radiation for plasma start-up and electron cyclotron resonance heating (ECRH) of plasmas in thermonuclear fusion research. Their output, however,

is in an unpolarized circular electric TE0n waveguide mode (predominantly TE02 at frequencies between 28 GHz and 70 GHz) that is not convenient because of its undesirable hollow conical radiation pattern. Efficient plasma heating requires an axisymmetric, narrow, pencil-like millimeter wave beam with well-defined polarization as produced by the TE11 mode (or better HE11 hybrid mode) at an open-ended, oversized circular waveguide antenna [1,2]. Thus, it is desirable to transform the gyrotron output to TE11 or ideally HE11. Due to the high frequencies and high power levels involved, the mode conversion must take place in highly overmoded waveguide.

In oversized circular waveguide a selective transformation of one specific mode into another can be achieved by means of suited periodic perturbation structures of the inner waveguide wall under the condition that the geometric period $\lambda_W$ of the wall perturbations and the unperturbed wave numbers $\beta_n$ and $\beta_m$ of the considered modes have to satisfy the resonance relationship $\Delta\beta(n,m)=\beta_n-\beta_m=2\pi/\lambda_B=2\pi/\lambda_W$ (constructive interference); $\lambda_B$ is the beat wavelength of the two modes [3-5]. An axisymmetric structure preserves the azimuthal mode number while a fluted structure can change both radial and azimuthal mode numbers. In the case where the waveguide distortions are small, reflections are negligible in overmoded waveguide and the perturbation structure as well as the converter length necessary for almost complete conversion and low level of undesired modes can be deduced from coupled-mode differential equations for the complex forward-travelling amplitudes [4,5].

In a serpentine TE01-to-TE11 transducer the unwanted TE12 wave is also strongly coupled to the TE01 input mode because $\Delta\beta(01,12)$ is close to $\Delta\beta(01,11)$. In addition, the TE21 mode is tightly coupled to the arising TE11 mode. In order to get sufficient discrimination against these modes it is necessary to increase the number N of geometric periods to ten [5]. The rather significant ohmic attenuation of the TE11 mode ultimately limits the efficiency. Moreover, the bandwidth of high-N number periodic-perturbation type mode converters is inherently narrow.

The efficiency of rippled wall mode converters with simple perturbation profile (pure cos-or sin-shape, constant maximum amplitude, number of periods is an integer) depends on the starting phase of the wall distortions [6]. It can be further improved by:

- tapering of the maximum perturbation amplitude [7],
- proper placement of "phase delay" sections of straight waveguide [5],
- appropriate truncation of the last converter period [7],

in order to reduce the amplitudes of unwanted modes in the interior and at the output of the converter, respectively.

It is shown that the decisive improvement (higher efficiency while length is simultaneously reduced) can be obtained by the combined application of:

(1) slightly changed perturbation period ($\lambda_W \approx \lambda_B$) resulting in a continuous phase re-matching within the converter [5,6,8],
(2) superposition of additional, phase-matched, small perturbations to the main wall distortion, whose geometric periods correspond to the beat wavelengths between the input and output mode and their related, strongest coupled undesired modes, respectively [8].

This work reports computations and measurements on optimization of wall perturbations in TE0n-to-TE0,n-1 mode converters and TE01-to-TE11 transducers at 70 GHz for 200 kW transmission lines of the 1 MW-ECRH system on the

WENDELSTEIN VII-AS stellarator at Garching. The numerically optimized mode converters were manufactured and after that tested at low-power levels by means of far-field radiation pattern measurements, by determination of insertion losses through two back-to-back converters using frequency sweeping and phase shifting techniques, and with a novel device which measures the spectrum of axial wavenumbers in overmoded waveguide [10]. This wavenumber spectrometer consists of a leaky-wave antenna structure in the waveguide wall and of a movable receiver antenna system with high directivity.

## 2. TE01-to-TE11 Mode Converter

Conversion of the circular symmetric TE01 mode to the almost linearly polarized TE11 mode is achieved by a non-axisymmetric mode transducer with constant radius ($a_0$ = 13.9 mm, 200 kW transmission line) and periodically perturbed curvature in one plane ($\Delta m = 1$) [4,5]. The general expression for the waveguide radius coordinate of the actual improved transformers is given by:

$$a(z,\phi)=a_0[1+[\varepsilon_{11}\cos(\Delta\beta_W(01,11)\cdot z)-\varepsilon_{12}\sin(\Delta\beta_W(01,12)\cdot z) -\varepsilon_{21}\sin(\Delta\beta_W(11,21)\cdot z)]\cos\phi] \quad (1)$$

where $\phi$ is the azimuthal angle with $\phi = 0,\pi$ in the plane of the wiggles. The E-field plane of the TE11 mode is perpendicular to this plane.

Six coupled modes were included in the theoretical analysis: TE01, TE11, TE12, TE21, TM11 and TM21. Ohmic attenuation and possible ellipticity coupling, introduced by the manufacturing procedure, are included in the coupling matrices. The influence of TM11 and TM21 turned out to be negligible because there is a continuous and coherent conversion and reconversion (with no change in phasing) between TE01 and the degenerate TM11 mode and because the TM21 mode is only weakly coupled. The coupling coefficients of the desired TE01/TE11-curvature coupling, of the unwanted TE01/TE12-coupling (more important in the first half of the transducer), and of the TE11/TE21-coupling (more important in the second half) are given in Tab. I together with the corresponding differences of the phase constants.

| coupled modes | curvature coupling coefficients [$m^{-1}$] | difference of unperturbed wavenumbers [$m^{-1}$] | slightly changed $\Delta\beta_W$-values [$m^{-1}$] |
|---|---|---|---|
| TE01,TE11 | $C(01,11)=3.76\cdot\kappa(z)$ | $\Delta\beta(01,11)=20.15$ | $\Delta\beta_W(01,11)=19.87$ |
| TE01,TE12 | $C(01,12)=6.18\cdot\kappa(z)$ | $\Delta\beta(01,12)=24.91$ | $\Delta\beta_W(01,12)=24.84$ |
| TE11,TE21 | $C(11,21)=6.07\cdot\kappa(z)$ | $\Delta\beta(11,21)= 9.59$ | $\Delta\beta_W(11,21)= 9.94$ |

Tab.I: Curvature coupling coefficients, differences $\Delta\beta$ of unperturbed phase constants and slightly changed $\Delta\beta_W$-values of major coupled modes in smooth-walled circular waveguide ($a_0$=13.9 mm) at 70 GHz. $\kappa(z)$ is the curvature distribution along the bent waveguide.

The optimum number of perturbations is determined by the need for limiting the conversion to unwanted modes as well as by limitations on the conversion rate to the desired mode. This depends on the various values of $|C(n,m)/\Delta\beta(n,m)|$ for the different modes [5]. The TE01 mode is also strongly coupled to the unwanted TE12 mode because $\Delta\beta(01,11)$ is quite close to $\Delta\beta(01,12)$ and $C(01,12) > C(01,11)$. In addition, the TE21 wave is tightly coupled to the generated TE11 mode (large value of $C(11,21)/\Delta\beta(11,21)$). In

order to get an efficiency of approximately 93% it turned out to be necessary to increase the number N of periods in a rotatable converter (ordinary or extraordinary ECR-wave irradiation) with simple cos-shaped perturbation to ten [5]. The overall length of this converter is L = 3.12 m ($a_o$ = 13.9 mm; $\varepsilon_{11}$ = 0.049 $\varepsilon_{12} = \varepsilon_{21}$ = 0; $\Delta\beta(01,11)$ = 20.15 $m^{-1}$). The results of numerical computations and the geometrical data of such a simple cos-shaped 70 GHz TE01-to-TE11 mode transducer with eight geometrical periods (N = 8) are summarized in Tab. II and the calculated normalized power in each mode as a function of z along the converter is plotted in Fig. 1a. The conversion efficiency is quite low ($\eta$ = 86.2%) and the levels of unwanted modes are rather high. The multimode calculations show that the conversion efficiency can be improved to $\eta$ = 94.0% by a 1.6% increase in the perturbation period ($\Delta\beta_W$ = 19.87 $m^{-1}$) which reduces the unwanted TE12 mode level and causes a continuous re-matching of the required phase difference between the TE01 and TE11 modes [5] resulting in a reduction of the remaining TE01 mode content from 6.9% to 0.9% (see Tab. II and Fig. 1b). The power levels in undesired modes are further reduced (Fig. 1c) by superimposing two additional, phase-matched (-sin) small perturbations, which periods correspond to the beat wavelengths between TE01 and TE12 ($\Delta\beta_W(01,12)$ = 24.84 $m^{-1}$) and between TE11 and TE21 ($\Delta\beta_W(11,21)$ = 9.94 $m^{-1}$). In this case eight main TE01/TE11-periods correspond to ten TE01/TE12-periods and to four TE11/TE21-periods ($8\cdot\Delta\beta_W(01,11) = 10\cdot\Delta\beta_W(01,12) = 4\cdot\Delta\beta_W(11,21)$, see Tab. I). The theoretical conversion efficiency of this improved TE01-to-TE11 mode converter is $\eta$ = 97.4% (including ohmic attenuation of 1.4% in Cu-waveguide).

| perturbation | single cos-perturbation | single cos-perturbation and phase re-matching | 3 phase-matched perturbations and phase re-matching |
|---|---|---|---|
| $\varepsilon_{11}$ | 0.0594 | 0.0594 | 0.0594 |
| $\varepsilon_{12}$ | 0 | 0 | 0.0044 |
| $\varepsilon_{21}$ | 0 | 0 | 0.0094 |
| length L(m) | 2.49 | 2.53 | 2.53 |
| TE01 | 0.069 | 0.009 | 0.006 |
| TE11 | 0.862 | 0.940 | 0.974 |
| TE12 | 0.048 | 0.029 | 0.004 |
| TE21 | 0.007 | 0.007 | 0.001 |
| $P_{SUM}$ | 0.986 | 0.985 | 0.985 |

Tab.II: Geometrical data, computed normalized output mode levels and transmission efficiencies ($P_{SUM}$) of 8-period TE01-to-TE11 mode converters ($a_o$ = 13.9mm, 70 GHz) with simple cos-shaped and improved perturbation structures.

The optimum mode transducer was fabricated by direct machining on a numerical lathe and assembled from eight individual sections. According to the numerical calculations the influence of the tiny ellipticity, introduced by this convenient manufacturing procedure, turned out to be negligible. Fig. 2 shows measured far-field E- and H- planes as well as cross-polar (XP 45°) patterns of the TE11 mode generated from a pure TE01 input mode (see section 3). The agreement of the power distributions with theoretical ones ( dashed curves) is good and consistent with the calculated efficiency. This far-field radiation pattern measurement together with insertion loss measurements using a second converter (and re-conversion multimode calculations) and measurements with the $k_z$-spectrometer revealed a measured efficiency of $\eta_{exp}$=(97.2 ± 0.5)% which is in excellent agreement with the predicted value.

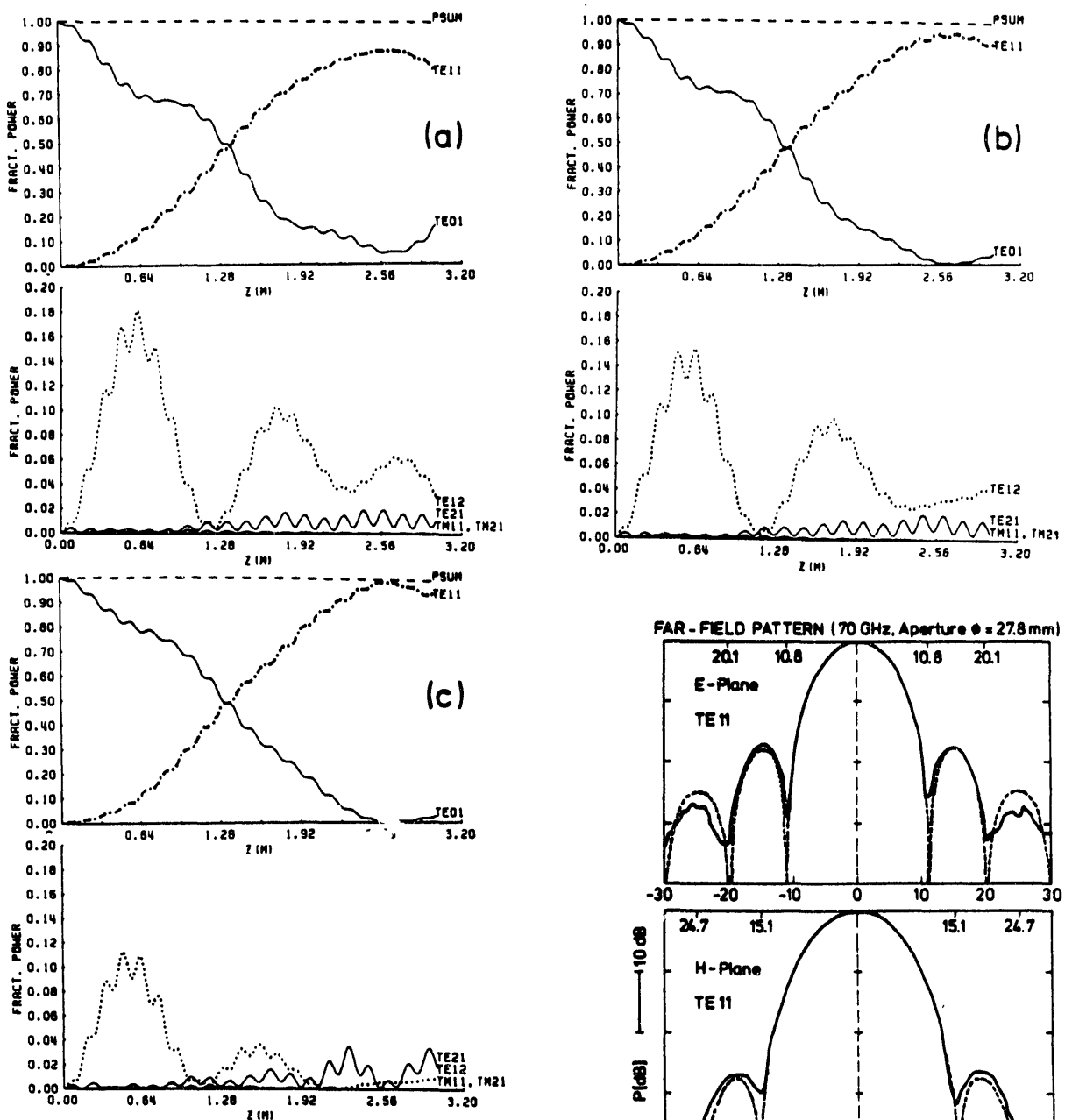


Fig. 1: Calculated fractional power in each mode along 70 GHz TE01-to-TE11 converters ($a_o$ = 13.9 mm, 8 geometrical periods).
(a) simple cos-shaped perturbation
(b) as (a) but slightly changed period
(c) slightly changed period and superposition of 3 different periodic perturbations.

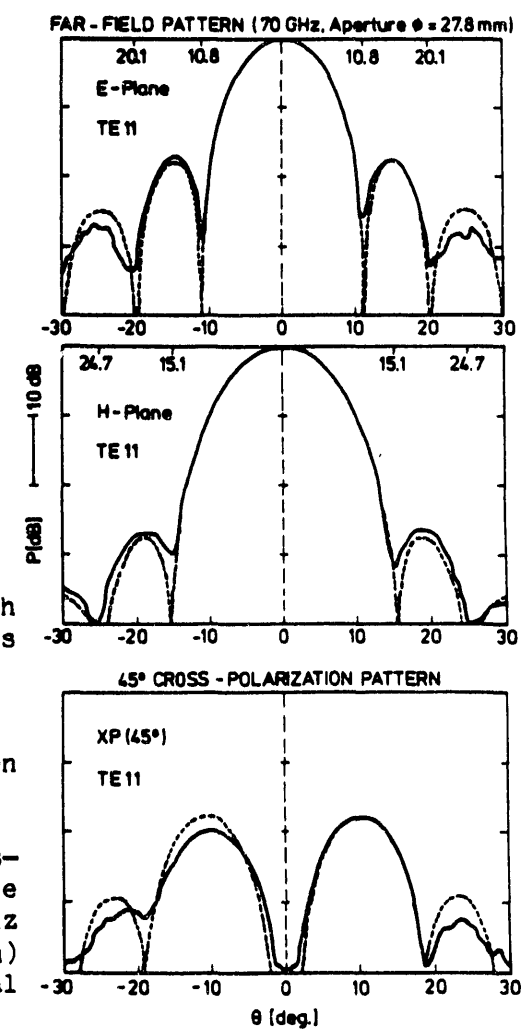


Fig. 2: Measured E- and H- plane and cross-polarization (XP) far-field patterns of the TE11 mode generated by the improved 70 GHz TE01-to-TE11 mode converter ($a_o$ = 13.9 mm) from a pure TE01 input mode. The theoretical patterns are superimposed (dashed curves).

The numerical optimization calculations showed that TE01-to-TE11 conversion efficiencies of 97% to 98% can also be achieved with considerably shorter serpentine converters ($N \geq 4$). Such short transducers have not been realized mechanically because of the following reasons:

(1) perturbation amplitudes ≥1.9 mm (length of one converter section: 316mm) could not be manufactured by direct machining on a lathe,

(2) short converters exhibit higher levels of unwanted modes in their interior which might cause arcing during long-pulse high-power operation, especially if the gyrotron emits spurious asymmetric modes or if there are backward travelling asymmetric modes produces by reflections.

## 3. TE0n-to-TE0,n-1 Mode Converters

Mode transducers with axisymmetric, periodic radius perturbations ($\Delta m = 0$) convert TE0n into TE0,n-1 power, provided that the converter radius is approximately periodic with the beat wavelength $\lambda_B(n,n-1)$ of the two modes. Efficiency optimization is studied by numerically solving the coupled-mode differential equations for all propagating TE0n modes in the waveguide ($a_o$ = 13.9 mm). Ohmic attenuation is included in the analysis. In the case of TE02-to-TE01 transformation conversion efficiencies $\eta \geq 99\%$ are obtainable with simple cos-shaped perturbations. However, high efficiency mode transducers for higher order circular electric modes require more complicated perturbation structures. As an example, results of calculations for improved 8-main period TE03-to-TE02 and TE02-to-TE01 transducers for the conversion of the output mode mixture of VARIAN 70 GHz gyrotrons (92% to 95% TE02, the remaining power being distributed between TE03 and TE01 [6]) into the basic TE01 mode are summarized in Tab. III along with measured values (low-power measurements) and the geometrical converter data. The waveguide radius of these improved mode converters is given by:

$$a(z)=a_o[1-\varepsilon_{01}\cos(\Delta\beta_W(n,n-1)\cdot z)-\varepsilon_{02}\cos(2\cdot\Delta\beta_W(n,n-1)\cdot z)]/(1-\varepsilon_{01}-\varepsilon_{02}). \quad (2)$$

The major period $\lambda_W(n,n-1) = 2\pi/\Delta\beta_W(n,n-1)$ of the wall perturbations differs slightly from $\lambda_B(n,n-1)$ resulting in a reduction of the remaining TE01 mode content. The superposition of a small amount of the phase matched (-cos) second harmonic perturbation ($2\cdot\Delta\beta_W(n,n-1) = \Delta\beta_W(n+1,n)$) reduces the amplitudes of the undesired modes TE0,n+1 and TE0,n-2 at the converter output.

These improved mode transducers were manufactured by direct machining on a numerically controlled lathe and assembled from eight individual sections. In both cases measured and predicted conversion efficiencies are in excellent agreement. Fig. 3 shows a series of far-field patterns measured by

| mode | TE03-to-TE02 converter (L=449 mm) $\varepsilon_{01}$ = 0.0237 calculated | $\varepsilon_{02}$ = 0.0020 measured | TE02-to-TE01 converter (L=872 mm) $\varepsilon_{01}$ = 0.0401 calculated | $\varepsilon_{02}$ = 0.0050 measured |
|---|---|---|---|---|
| TE01 | 0.002 | 0.005 | $\eta_o$ = 0.997 | 0.995±0.005 |
| TE02 | $\eta_o$ = 0.992 | 0.990±0.007 | 0 | 0 |
| TE03 | 0.001 | 0 | 0.001 | 0.003 |
| TE04 | 0.002 | 0.002 | 0 | 0 |
| $P_{SUM}$ | 0.997 | | 0.998 | |

Tab.III: Geometrical data, computed and measured conversion and transmission efficiencies and normalized spurious mode levels at the output of improved 8-period TE03-to-TE02 and TE02-to-TE01 converters ($a_o$ = 13.9 mm) at 70 GHz.

adding 1 to 8 TE01–to–TE02 mode transducer sections,each being $\lambda_W$ long. Complete power transfer is achieved for $L = 8 \cdot \lambda_W$. In Fig. 4 the measured far-field radiation patterns of the TE02 and TE03 modes successively produced from a pure TE01 input mode are plotted. The agreement of these patterns with those that were computed is good and consistent with the calculated efficiencies. Fig. 5 shows the corresponding $k_z$–spectra measured with the wavenumber spectrometer. In the case of the TE02–to–TE01 transformation theoretical conversion efficiencies $\eta \geq 99\%$ were also obtained with considerably shorter improved converters ($N \geq 2$). The number $N = 8$ of main periods was chosen because one geometrical period of such a transducer converts 3 to 4%, which is the expected power level of TE03 and TE01 modes emitted by the gyrotron. A phase–locked gyrotron mode mixture containing ≈ 93% TE02, ≈ 3.5% TE03, and ≈ 3.5% TE01 may be cleaned without power losses by using one section of the TE03–to–TE02 transformer at a specified axial position of the longitudinal beat structure in the waveguide (phase–matching at the converter input). The resulting TE02/TE01 mode composition can finally be converted into an almost pure TE01 mode by using only seven sections of the TE02–to–TE01 converter. The measured overall conversion efficiency is (99 ± 1)%.

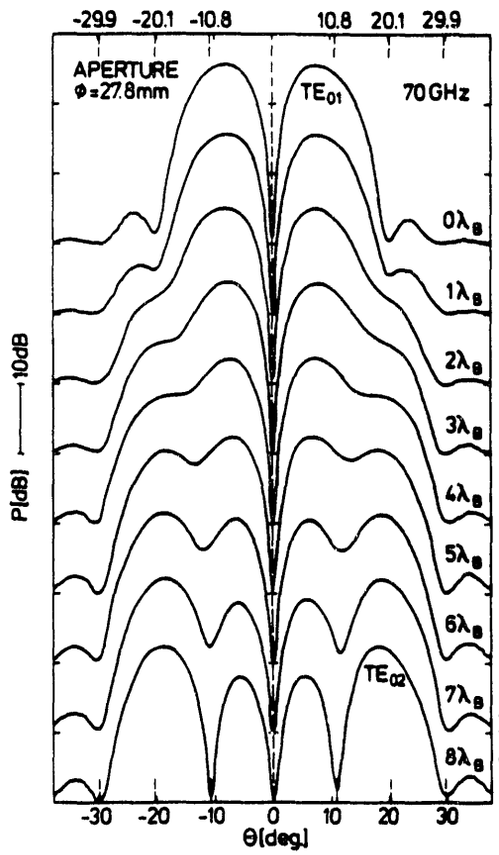


Fig.3: Series of measured far–field pattern produced by 1 to 8 periods (each being $\lambda_W$ long) of the improved 70 GHz TE01–to–TE02 transducer ($a_o$=13.9 mm).

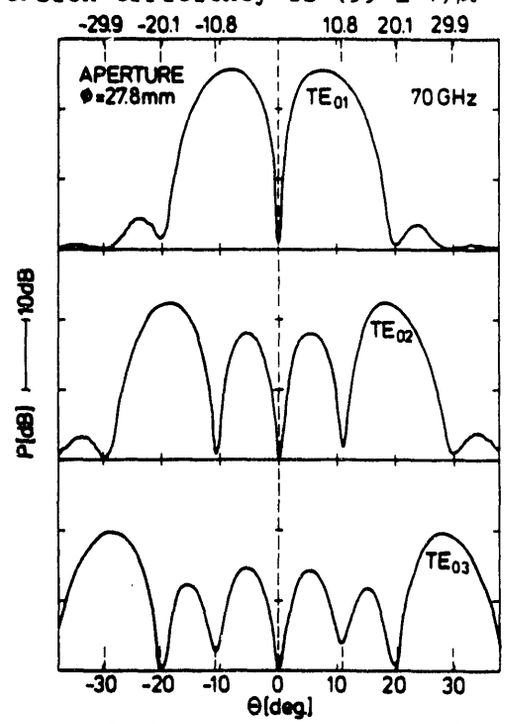


Fig.4: Measured far–field pattern of the TE02 and TE03 modes successively generated from a pure TE01 input mode at 70 GHz ($a_o$=13.9 mm).

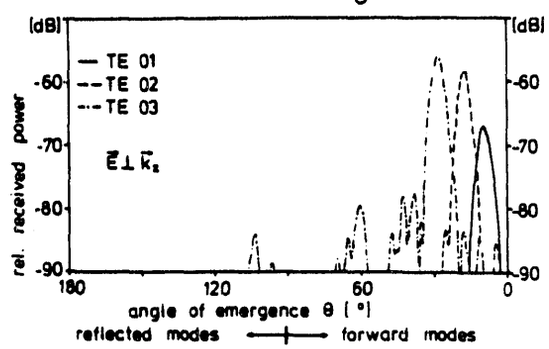


Fig.5: Spectrum of the TE01 mode and of the TE02 and TE03 modes successively generated by improved mode transducers and measured with a $k_z$–spectrometer.

## 4. Conclusions

Considerably higher efficiencies of rippled wall mode converters for oversized circular waveguide have been achieved by changing the perturbation period of the wall slightly from the beat wavelength between the input and the desired output mode and by superimposing additional, phase-matched, small perturbations, whose periods correspond to the beat wavelengths between the desired modes and their strongest coupled unwanted modes. In the case of TE02-to-TE01 and TE03-to-TE02 transformation with improved 8-period transducers theoretical efficiencies of 99.7% (99.5 ± 0.5% measured) and 99.2% (99.0 ± 0.7% measured) where obtained at 70 GHz and $a_o$ = 13.9 mm. The corresponding values for mode converters with simple perturbation structure are 99.0% and 98.5%, respectively [5]. More significant is the achievable efficiency improvement in the case of serpentine TE01-to-TE11 mode transducers. The multimode calculations show that the efficiency $\eta$ = 92.5% (undesired modes: 2.8% TE01, 2.1% TE12, 0.5% TE21, 1.9% ohmic attenuation) of a simple 10-period 70 GHz transducer (cos-shaped perturbation, L = 3.12 m, $a_o$ = 13.9 mm) can be increased to 97.4% (unwanted modes: 0.6% TE01, 0.4% TE12, 0.1% TE21, 1.5% attenuation) with an improved 8-period converter (superposition of 3 different perturbation periods, L = 2.53 m, $a_o$ = 13.9 mm). The measured value of (97.2 ± 0.5)% is in excellent agreement with the predicted one.By the use of these improved periodic-perturbation mode converters together with optimized corrugated TE11-to-HE11 mode transducers [6] the overall transmission efficiency of the 70 GHz mode converter system for ECRH on the W VII-AS stellarator in the desired polarization ($\Sigma$TE0n-to-HE11 conversion including attenuation) is determined to be 95%. The accomplished improvement compared to the W VII-A mode transducer system [6] is 4%. The choice of the number of converter periods is rather conservative because large perturbation amplitudes in serpentine TE01-to-TE11 transformers cannot be manufactured by direct machining on a lathe and because very short converters exhibit higher levels of undesired modes in their interior which might be the reason for arcing in the waveguide during long-pulse high-power operation.

## References


[1] Wilhelm, R., V. Erckmann, G. Janzen, W. Kasparek, G. Müller, E. Räuchle P.G. Schüller, K. Schwörer, M. Thumm, W VII-A Team, Plasma Physics and Controlled Fusion, 26 (1984) 1433.

[2] Erckmann, V., G. Janzen, W. Kasparek, G.A. Müller, P.G. Schüller, K. Schwörer, M. Thumm, R. Wilhelm, W VII-A Team, Proc. 12th European Conf. on Controlled Fusion and Plasma Physics, Budapest (1985), Part I, 385.

[3] Kovalev, N.F., I.M. Orlowa, M.I. Petelin, Radio Phys. Quant. Electronics, 11 (1969) 449.

[4] Moeller, C., Int. J. Electronics, 53 (1982) 587.

[5] Thumm, M., Int. J. Electronics, 57 (1984) 1225.

[6] Thumm, M., V. Erckmann, G. Janzen, W. Kasparek, G. Müller, P.G. Schüller, R. Wilhelm, Int.J.Infrared and Millimeter Waves, 6 (1985) 459

[7] Trulsen, J., P. Woskoboinikow, R. Temkin, BAPS, 29 (1984) 1254.

[8] Thumm, M., Proc. 15th European Microwave Conference, Paris (1985) 790.

[9] Kasparek, W., G.A. Müller, "A Novel Device for Multimode Analysis in Oversized Waveguides",10th Int. Conf. on Infrared and Millimeter Waves, Lake Buena Vista (Orlando), USA (1985).

[10] Sturm, H., M. Thumm, "Optimized Overmoded TE01-to-TM11 Mode Converters for High-Power Millimeter Wave Applications at 70 and 140GHz",10th Int. Conf. on Infrared and Millimeter Waves, Lake Buena Vista, USA (1985).

# Mode Converters for Generating the $HE_{11}$ (Near-Gaussian) Mode from Gyrotron $TE_{0N}$ Modes at 140 GHz

Manfred Thumm and Helga Sturm
*Institut für Plasmaforschung, Universität Stuttgart*
*D-7000 Stuttgart 80, Federal Republic of Germany*

ABSTRACT

Efficient plasma heating by ECR-wave irradiation requires axisymmetric, narrow, pencil-like millimeter wave beams with well-defined polarization. The linearly polarized Gaussian-like HE11 mode satisfies these conditions best. This quasi-optical hybrid mode can be generated from TE0n gyrotron mode compositions by the two multi-step mode conversion processes: (1) ΣTE0n to TE01 to TE11 to HE11 or (2) ΣTE0n to TE01 to TM11 to HE11. The first scheme has the advantage that the converters can all be made without bends, allowing an arbitrary choice and fast change of the polarization plane. The second scheme does not exhibit this advantage, but it is more suitable for high power 140 GHz transmission lines (large waveguide diameter) because efficient TE01-to-TM11 transducers can be made considerably shorter than serpentine TE01-to-TE11 mode converters. This paper presents computations on mode converter systems of both types at 140 GHz (I.D.= 27.8 mm for 200 kW transmission lines, I.D.=40.0 mm for 500 kW transmission lines). The structure of wall perturbations (superposition of 2 or 3 different periods) in the rippled wall mode converters and the curvature distribution in the bent smooth-walled TE01-to-TM11 mode transducers were optimized by numerically solving the corresponding coupled-mode differential equations. Computer-aided optimization of circumferentially corrugated mode converters has been achieved with a scattering matrix code employing the modal field expansion technique (Modular Analysis Concept: MAC). In all cases the predicted overall efficiency of the complete mode converter system from ΣTE0n (predominantly TE03) to HE11 in the desired mode is approximately 90% to 92% (ohmic attenuation is included). First low-power measurements on the efficiency of a 140 GHz TE01-to-TM11 mode transducer ($a_0$ = 13.9 mm) are in excellent agreement with the predicted value of 95.2% (including ohmic attenuation).

## 1. Introduction

High-power gyrotrons have been used very successfully for plasma start-up and subsequent electron cyclotron resonance heating (ECRH) of stellarator

and tokamak plasmas as well as for plasma production in industrial processes (e.g. isotope separation). High-frequency millimeter waves ($f \approx 140$ GHz) are required in order to achieve reactor relevant plasma densities ($n_{eo} \geq 2 \cdot 10^{20} m^{-3}$) and optimum magnetic confinement conditions ($B_o \approx 5$ T). Commercial gyrotrons launch mixtures of circular electric TE0n modes (mainly TE02 at frequencies between 28 and 70 GHz, and in the near future TE03 at 140 GHz [1] and TE04 at 100 GHz [2]) into a highly overmoded circular waveguide (Int. Diameter $D=2a_o=63.5$ mm). In particular, the TE01 mode is appropriate for power transmission through long runs of straight circular waveguide because of its low ohmic attenuation. However, TE0n modes are unpolarized and produce an undesirable conical radiation pattern with no energy content on the axis. Efficient ECRH requires an axisymmetric, narrow, pencil-like beam with well-defined polarization. The almost perfectly linearly polarized Gaussian-like HE11 hybrid mode, radiated from an open-ended, circumferentially corrugated, oversized circular waveguide, satisfies these conditions best [3,4]. This mode is ideal for quasi-optical propagation and launching by the use of focussing mirrors and polarization twist reflectors. The HE11 mode can be generated from TE0n gyrotron modes by the two multistep mode conversion sequences: (1) TE0n→TE01→TE11→HE11 [4] or (2) TE0n→TE01→TM11→HE11 [3]. The first scheme, which uses the TE11 mode as polarized intermediate mode, has the advantage that the converters can all be made without bends allowing an arbitrary choice and fast change of the polarization plane by simply rotating the TE01-to-TE11 converter around its axis. However, the present paper shows that the second scheme is more suitable for high-power 140 GHz transmission lines because efficient TE01-to-TM11 transducers (bent smooth-walled waveguides) can be made half as long as the corresponding serpentine TE01-to-TE11 mode converters, which must be made very long to suppress the undesired TE12- and TE21-modes [5] (beat wavelengths scale with $a_o^2 f$). Moreover, due to the relatively large number of coupling periods the TE01-to-TE11 transducer bandwidth is inherently narrower than that of the TE01-to-TM11 transformer. The TE11-to-HE11 converter bandwidth is also reduced, relative to that of the TM11-to-HE11 transformer, by the need to start the corrugation depth at $\lambda/2$ in the former [3,6].

This paper reports computations on 140 GHz mode converter systems of both types for future 200 kW transmission lines ($D=27.8$mm) as well as for 500 kW transmission lines ($D \approx 40.0$ mm) and first measurements on a 140 GHz TE01-to-TM11 transducer.

## 2. ΣTE0n-to-TE01 Mode Conversion

Mode transducers with axisymmetric, periodic radius perturbations ($\Delta m=0$) convert TE0n into TE0,n-1 power in both conversion schemes, provided the converter radius is periodic with the beat wavelength $\lambda_B(n,n-1)$ of the two modes [5,7]. Efficiency optimization is studied by numerically solving the corresponding coupled-mode differential equations. Modes up to TE08 are included. The waveguide radius is approximately given by

$$a(z)=a_o[1-\varepsilon_o\cos(2\pi z/\lambda_W(n,n-1))]/(1-\varepsilon_o). \qquad (1)$$

The optimum wavelength $\lambda_W(n,n-1)$ of the wall perturbations differs slightly from $\lambda_B(n,n-1)$ resulting in a reduction of the remaining TE0n mode content [8]. The efficiencies $\eta_o$ were further improved by superimposing small amounts of additional, phase matched, higher harmonics on the wall structure

in order to reduce the amplitudes of the undesired modes TE0,n+1 and TE0,n−2 at the converter output [8,9]. Results of optimization calculations for several single-step 200 kW TE0n-to-TE0,n−1 mode transducers (n=2–6) at 140 GHz ($a_0$ = 13.9 mm) are summarized in Tab. I. The numerical computations show that the number N of main coupling periods of the various mode transducers may be somewhat reduced without substantial reduction of the conversion efficiency. In the case of TE02-to-TE01 transformation efficiencies of approximately 99% can be achieved with merely 2 or 3 periods.

The frequency sensitivity of rippled wall mode transducers is discussed in [7]. The conversion efficiency $\eta$ is approximately given by $\eta = \eta_0/(1+\delta^2)$, where $\delta = 2N(\Delta f/f_0)$. Numerically deduced bandwidth factors $1/(1+\delta^2)$ for the various mode transformers at a typical gyrotron frequency deviation of 0.3% are also given in Tab. I. TE03 or higher TE0n gyrotron modes (e.g. TE04) can be converted to the basic TE01 mode by cascading the corresponding single-step mode transducers resulting in a total conversion efficiency of 98.9% or 97.7%, respectively; ohmic losses are included (Cu-waveguide). Direct TE03-to-TE01 conversion is impossible, because $\lambda_B(3,1) = \lambda_B(3,4)$ [5], whereas a TE04-to-TE01 conversion efficiency of 97.7% was also achieved by using a direct TE04-to-TE01 mode transformer (N=46, $\varepsilon_0$=0.0173, L=1.95 m). However, the bandwidth of such a high N-number converter is inherently narrow ($1/(1+\delta^2)$=0.929 for $\Delta f/f_0$=0.3%).

| Modes: TE0n→TE0,n−1 | TE06→TE05 | TE05→TE04 | TE04→TE03 | TE03→TE02 | TE02→TE01 |
|---|---|---|---|---|---|
| Converter length L | 797 mm | 862 mm | 945 mm | 1073 mm | 1352 mm |
| Number of periods N | 14 | 12 | 10 | 8 | 6 |
| Perturbation $\varepsilon_0$ | 0.0063 | 0.0089 | 0.0137 | 0.0238 | 0.0535 |
| Conv. efficiency $\eta_0$ | 0.983 | 0.986 | 0.988 | 0.992 | 0.997 |
| Transm. efficiency | 0.994 | 0.995 | 0.997 | 0.998 | 0.999 |
| Unwanted-mode levels TE0,n+1 | 0.006 | 0.004 | 0.005 | 0.002 | 0.002 |
| TE0,n−2 | 0.005 | 0.005 | 0.004 | 0.004 | – |
| $1/(1+\delta^2)$ | 0.992 | 0.994 | 0.996 | 0.998 | 0.999 |

Tab.I: Geometrical converter data, calculated conversion and transmission efficiencies, unwanted-mode levels and bandwidth factors (0.3% frequency deviation) of 140 GHz TE0n-to-TE0,n−1 mode converters (n=2–6, $a_0$=13.9 mm).

Phase-locked gyrotron TE0n-mode mixtures may be cleaned without power losses by using appropriate and matched TE0n-to-TE0,n−1 transformer sections at specified axial positions of the longitudinal beat structure in the waveguide (phase-matching at the converter input) [5]. One period of a 6-, 8- or 10-period transducer converts 6.7%, 3.8% or 2.4%, respectively.

For a given number N of periods, the ratio of the coupling coefficient $C_{n,n'}$ between TE0n and TE0n' modes for a radius change and the difference $\Delta\beta_{n,n'} = 2\pi/\lambda_B(n,n')$ of the unperturbed wavenumbers remains constant. As a result the efficiencies of 140 GHz TE0n-to-TE0,n−1 transducers with $a_0$=20.0 mm are almost the same.

## 3. TE01-to-TE11-to-HE11 Mode Conversion Sequence

In the TE01-to-TE11-to-HE11 mode conversion scheme a non-axisymmetric mode transducer with constant radius and periodically perturbed curvature in one plane ($\Delta m=1$) transfers the unpolarized TE01 mode to the almost linearly polarized TE11 mode [5,7]. The radius coordinate in a rotatable converter with simple cos-shaped perturbation is given by

$$a(z,\phi)=a_0[1+\varepsilon_1\cos(2\pi z/\lambda_B(01,11))\cos\phi], \qquad (2)$$

where $\phi$ is the azimuthal angle with $\phi=0,\pi$ in the plane of the wiggles. The polarization of the TE11 mode is perpendicular to this plane. Six coupled modes are included in the theoretical analysis: TE01, TE11, TE12, TE21, TM11 and TM21. According to the multimode computations the conversion efficiency $\eta_0=81.6\%$ (unwanted modes: 9.7% TE01, 4.6% TE12, and 0.6% TE21; ohmic attenuation in Cu-waveguide: 3.5%) of an eight-period 200 kW converter ($a_0=13.9$ mm, $L=5.03$ m, $\varepsilon_1=0.0594$) can be improved to almost 90.8% by a 1.6% increase of the perturbation period ($\lambda_W=1.016\cdot\lambda_B(01,11)$) which reduces the remaining TE01 mode content and the level of the undesired TE12 mode [5]. The decisive improvement of the efficiency up to $\eta_0=95\%$ is achieved by superimposing two additional, phase-matched, small perturbations, which periods correspond to the beat wavelengths between the TE01 input mode and TE12 and the TE11 output mode and TE21, respectively [9]. Such improved per-

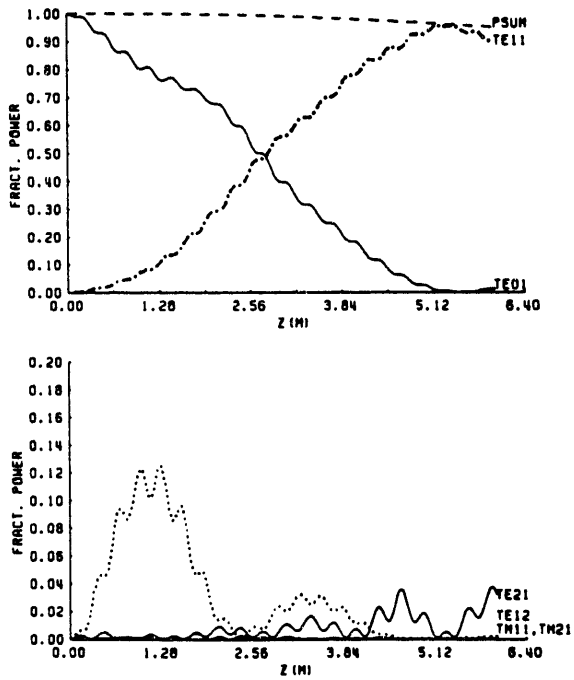


Fig. 1:
Calculated fractional power in desired and unwanted modes as a function of z along the optimum 200 kW TE01-to-TE11 mode converter (L = 5.12 m, $a_0$ = 13.9 mm).

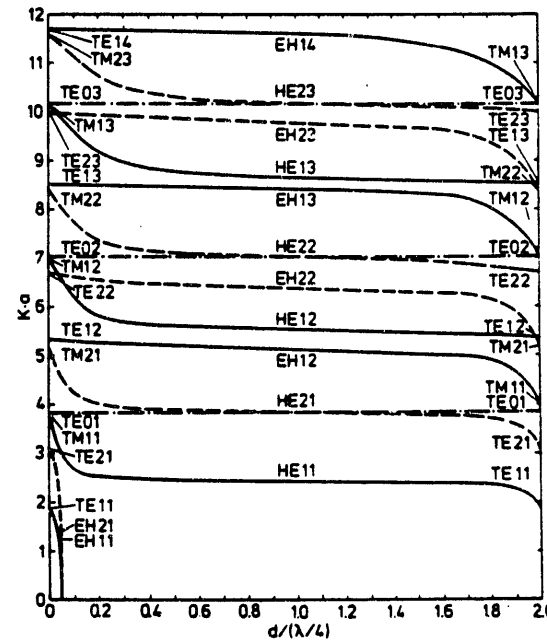


Fig. 2:
Eigenvalues K·a of the characteristic equation versus normalized electrical slot depth $d/(\lambda/4)$ for various modes in circumferentially corrugated waveguide with inner radius $a_0$ = 13.9 mm at 140 GHz ($k\cdot a$ = 40.78).

turbation structures result in a minimization of the TE12 and TE21 mode levels at the converter output. Fig.1 shows the calculated normalized power in each mode as a function of z along the optimum TE01-to-TE11 transducer. At the converter output (L=5.12m) the input TE01 mode is converted to the TE11 mode with an efficiency of $\eta_o$ = 95.0% (unwanted modes: 1.0% TE01, 0.1% TE12, 0.1% TE21; ohmic attenuation: 3.8%). However, the corresponding 8-main period serpentine converter for a 500 kW transmission line ($a_o$=20.0 mm) becomes impractically long (L=10.6 m, $\eta_o$=93.5%, 5.3% ohmic losses in Cu) because beat wavelengths scale with $a_o^2$.

Adiabatic TE11-to-HE11 mode conversion is achieved in a straight, circumferentially corrugated, waveguide section in which the electrical depth of the annular slots gradually decreases from an initial value of almost $\lambda/2$ ($\lambda=2\pi/k$ is the free-space wavelength) to a final slot depth of approximately $\lambda/4$ (Fig.2) [6]. Unwanted mode conversion is associated primarily with the entirely cross-polarized EH12 mode. Computer-aided optimization of converter length, shape of corrugations, and slot depth profile along the converter is obtained with a scattering matrix formalism employing the modal field expansion technique: Modular Analysis Concept (MAC) [10]. An optimized non-linear profile of the mechanical slot depth is absolutely necessary for achieving a mode purity of almost 99% and cross-polar levels lower than -28 dB with a converter length of L=0.74 m for $a_o$=13.9 mm and L=1.06 m with $a_o$=20.0 mm. Slot width and slot pitch are chosen to be 0.35 mm and 0.7 mm, respectively. The calculated return losses are lower than -56 dB. The optimum slot depth profile is very close to that of constant coupling along the converter [3] and decreases slowest at the converter input where the coupling coefficient for hopping to the TM11-to-EH12 conversion branch is largest.

## 4. TE01-to-TM11-to-HE11 Mode Conversion Sequence

In an alternative two-step mode conversion process the HE11 mode is generated from TE01 using TM11 instead of TE11 as intermediate polarized mode. First, a smooth circular waveguide is bent with an optimized curvature distribution at a proper angle to convert virtually all of the TE01 power to TM11 which is polarized perpendicularly to the plane of bend. Power is continously coupled from TE01 to TM11 along the converter because TE01 and TM11 are degenerated in smooth-walled circular waveguides (same propagation constants). A waveguide bend of angle

$$\theta_c = k_{01} \cdot \lambda / (2\sqrt{2} \cdot a_o) \qquad (3)$$

will convert all the power from one mode to the other [3,11]; $k_{01}$=3.8317 is the first root of the Bessel-function $J_o' = -J_1$. The bend must be long enough to avoid unintentional mode conversion to unwanted modes, but ought to be as short as possible to minimize ohmic (wall) losses from the high-loss TM11 mode. Bent 140 GHz TE01-to-TM11 mode converters with $a_o$=13.9mm and $a_o$=20.0mm were optimized by means of numerical integration of the coupled-mode equations for the six coupled modes: TE01, TM11, TE11, TE12, TE21 and TM21 (ellipticity coupling is included in the coupling matrices). Due to the multimode coupling, the conversion angle $\theta_c$ depends on the curvature distribution and differs by a small amount from the value calculated with (3). In both cases, the lowest spurious mode levels together with highest transmission efficiency (shortest arc length $L_c$) were achieved using sinusoidal curvature distribution instead of constant curvature as used in [3]. This is

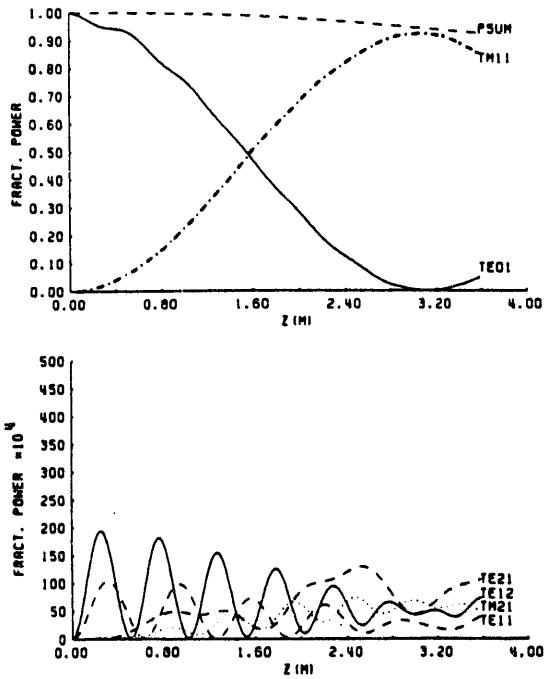


Fig. 3:
Calculated fractional power in desired and unwanted modes as a function of z along 140 GHz TE01-to-TM11 mode converter with $a_o$=13.9mm and constant curvature.

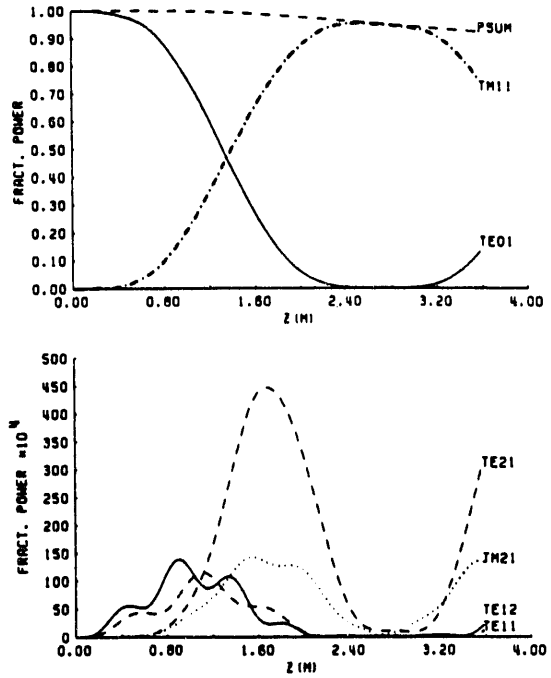


Fig. 4:
Calculated fractional power in desired and unwanted modes as function of z along 140 GHz TE01-to-TM11 mode converter with $a_o$=13.9mm and optimum, sinusoidal curvature distribution.

| CURVATURE DISTRIBUTION | CONSTANT | | SINUSOIDAL | |
|---|---|---|---|---|
| waveguide radius $a_o$ | 13.9 mm | 20.0 mm | 13.9 mm | 20.0 mm |
| conversion angle $\theta_c$ | 12.02° | 8.34° | 12.5° | 8.66° |
| arc length $L_c$ | 3.05 m | 6.09 m | 2.49 m | 5.04 m |
| NORMALIZED POWER LEVELS | | | | |
| TE01 | 0.0015 | 0.0017 | 0.0008 | 0.0004 |
| TM11 | 0.9252 | 0.9036 | 0.9524 | 0.9352 |
| TE11 | 0.0025 | 0.0034 | 0.0001 | 0.0001 |
| TE12 | 0.0045 | 0.0050 | 0.0001 | 0.0001 |
| TE21 | 0.0048 | 0.0053 | 0.0025 | 0.0043 |
| TM21 | 0.0065 | 0.0070 | 0.0016 | 0.0022 |
| TRANSMITTED POWER $P_{SUM}$ | 0.9450 | 0.9260 | 0.9575 | 0.9423 |

Tab.II: Geometrical data, normalized power levels at the output and transmission efficiency $P_{SUM}$ of bent 140 GHz TE01-to-TM11 mode converters with constant and sinusoidal curvature distribution and waveguide radii of $a_o$=13.9 mm and $a_o$=20.0 mm, respectively.

obvious from the comparison of the calculated normalized power in each mode as a function of z along the 200 kW converters as plotted in Figs. 3–4. In Tab.II the calculated data of the two optimum 140 GHz TE01–to–TM11 transducers with sinusoidal curvature distribution are compared with the corresponding data of constant curvature transformers. The bandwidth factor of the optimum mode converters with sinusoidal curvature distribution is 0.998 (0.2% reduction of the efficiency) at a frequency deviation of 0.3%.

The 200 kW TE01–to–TM11 converter ($a_o$=13.9 mm) was fabricated by bending commercially available C76 waveguide in a preassembled frame with a shape defining the curve. Fig.5 shows a photograph of the mode transducer. According to the multimode calculations the influence of the measured ellipticity (≤0.02 mm) on the conversion efficiency turned out to be negligible. Fig. 6 shows the measured 140 GHz TM11–mode pattern (E–plane). This far–field pattern measurement together with insertion loss measurements through two back–to–back converters, using phase shifting and frequency sweeping techniques, delivered an experimental conversion efficiency of (95.0±1.0)% which is in good agreement with the predicted one.

TM11–to–HE11 conversion is achieved adiabatically in a straight circumferentially corrugated waveguide section by non–linearly tapering the corrugation depth from 0 to nominally $\lambda/4$ (Fig.2). This transducer has to be long enough (L=0.84 m for $a_o$=13.9 mm and L=1.2 m for $a_o$=20.0 mm; sloth width = tooth width = 0.35 mm) in order to suppress mode hopping to the TE11–EH11 surface mode branch as well as to the TE12–EH12 mode branch [3]. The theoretical conversion efficiency is around 98.5%. The slot depth increases slowest at the converter input where coupling to both unwanted mode branches is strongest.

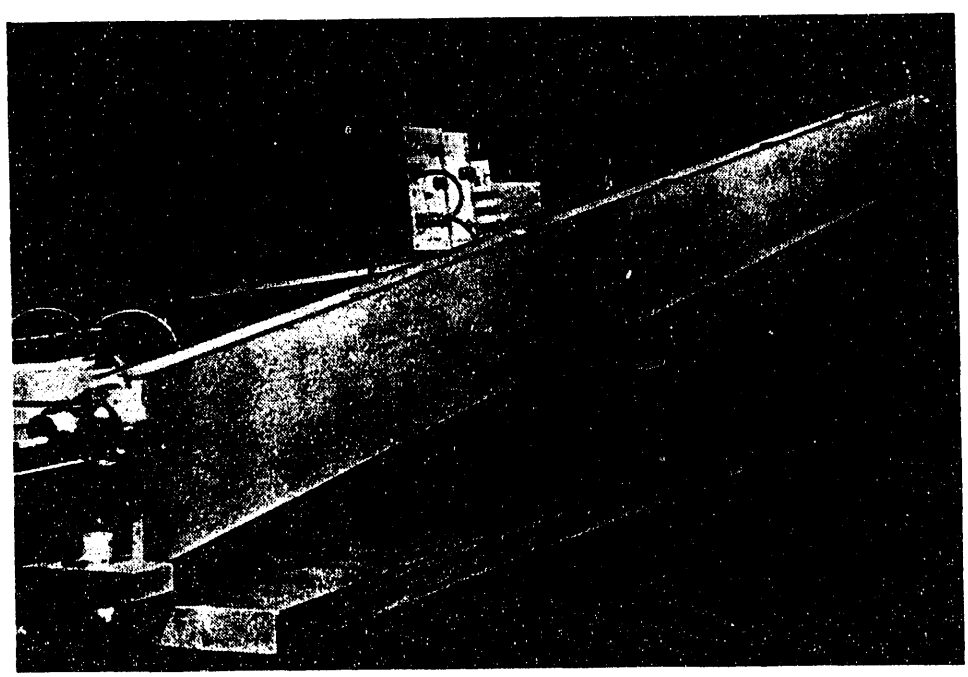

Fig. 5:
A photograph of the 140 GHz TE01–to–TM11 mode converter (arc length $L_c$=2.49m conversion angle $\theta_c$=12.5°, sinusoidal curvature distribution) for a 200 kW transmission line ($a_o$=13.9 mm).

Fig. 6:
Measured E-plane far-field pattern of the TM11 mode generated by the 200 kW TE01-to-TM11 mode converter (linear scale, low-power measurement).

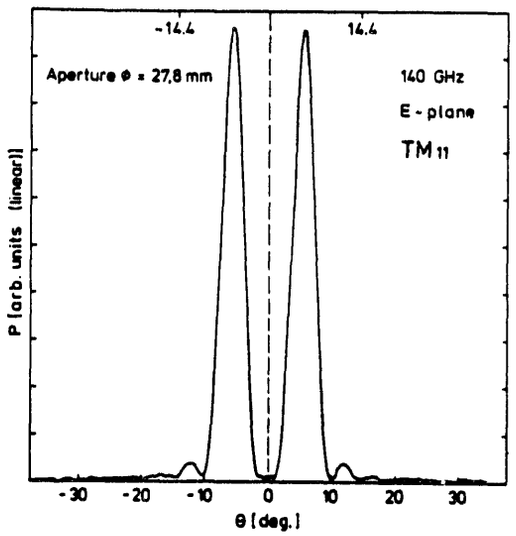


## 5. Conclusions

Optimization calculations on the two multi-step mode conversion sequences: (1) TE0n to TE01 to TE11 to HE11 and (2) TE0n to TE01 to TM11 to HE11 for generating the quasi-optical HE11 hybrid mode from gyrotron TE0n modes at 140 GHz are presented. TE03 or higher TE0n gyrotron modes are converted to the basic TE01 mode by cascading the corresponding single-step TE0n-to-TE0,n-1 mode transducers resulting in high conversion efficiencies and fairly broad bandwidths. The second conversion scheme is more suitable for 500kW transmission lines ($a_0$ = 20.0 mm) because bent TE01-to-TM11 transducers can be made considerably shorter than serpentine TE01-to-TE11 mode transformers. In both conversion sequences the predicted overall efficiency of the complete mode converter system (from ΣTE0n to HE11) in the desired mode is approximately 92% for a 200 kW transmission line (I.D. = 27.8 mm) and 90% for a 500 kW transmission system (I.D. = 40.0 mm). First low-power measurements on the efficiency of a 140 GHz TE01-to-TM11 mode converter ($a_0$=13.9mm) are in excellent agreement with the theoretical value.

## References


[1] Felch, K.,"Progress on the Varian 140 GHz Gyrotron", EC-5 Int. Workshop on ECE and ECRH and Gyrotron User / Developer Meeting, San Diego, 1985

[2] Grivet, P., Mourier, G., Proc. 15th European Microwave Conference, Paris, 1985, 3

[3] Doane, J.L., Int. J. Electronics, 53, 573, 1982; IEEE MTT-32, 1362,1984

[4] Erckmann, V., Janzen, G., Müller, G.A., Schüller, P.G., Thumm, M., Wilhelm, R., Proc.5th Top.Conf. on RF Plasma Heating, Madison,1983,209

[5] Thumm, M., Int. J. Electronics, 57, 1225, 1984

[6] Thumm, M., Int. J. Infrared and Millimeter Waves, 6, 577, 1985

[7] Moeller, C., Int. J. Electronics 53, 587, 1982

[8] Thumm, M., Proc. 15th European Microwave Conference, Paris, 1985, 790

[9] Thumm, M., Müller, G.A., Wilhelm, R., "Optimization of Wall Perturbations in Rippled Wall Mode Converters for Overmoded Circular Waveguide", EC-5 Int. Workshop on ECE and ECRH and Gyrotron User / Developer Meeting, San Diego, 1985

[10] Kühn, E., Hombach, V., IEE Conf.Publ., 219 (ICAP 83), 1983, Part 1, 127

[11] Miller, S.E., Proc. IRE, 40, 1104, 1952

# Methods of Designing Higher Efficiency, Shorter Length Periodic-Perturbation Mode Converters for Over-Moded Waveguides*

R.J. Vernon, U. Rhee, and K. Audenaerde†
*University of Wisconsin, Madison, Wisconsin 53706, USA*

Abstract

Gyrotrons currently in use typically have circular-waveguide microwave outputs in the $TE_{01}$ or $TE_{02}$ modes which are not efficient for plasma heating. Periodic perturbation type mode converters have been successfully used to convert these outputs to a $TE_{11}$ or $HE_{11}$ mode which have more efficient plasma heating characteristics. Methods are discussed by which the efficiency and power handling capability of these mode converters can be increased while their length is simultaneously reduced. The mode converter's bandwidth is also usually increased. These improvements are accomplished by

1) changing the perturbation period slightly from the beat wavelength between the input and the desired output mode,
2) appropriate placement of "phase delay" sections of waveguide,
3) varying the perturbation amplitude along the length of the converter,

and 4) choosing the profile of the perturbation period to further reduce the coupling to unwanted modes.

A mode converter system which can produce any output "polarization" of a $TE_{11}$ or $HE_{11}$ mode from linear to left- or right-hand circularly polarized is also discussed.

*This work was supported by the U.S. Dept. of Energy through Contract DE-AC02-83ER52093.

† Present address: State University of New York at New Paltz.

Gyrotrons currently in use typically have circular-waveguide microwave outputs in the $TE_{01}$ or $TE_{02}$ modes which are not efficient for plasma heating. Periodic perturbation type mode converters have been successfully used to convert these outputs to a $TE_{11}$ or $HE_{11}$ mode which have more efficient plasma heating characteristics. Methods are discussed in this paper by which the efficiency and power handling capability of these mode converters can be increased while their length is simultaneously reduced. (Here efficiency is defined as the ratio of the power output in the desired mode to the total input power, taking into account attenuation. We will assume single mode inputs initially but extend the discussion to multimode inputs later.) The mode converter's bandwidth is also usually increased by these methods.

The type of mode converter system for which these components are intended is shown in Fig. 1 which is drawn for a 60 GHz gyrotron with a $TE_{02}$ mode output in a 2-1/2" circular waveguide. The first mode converter in this system is a $TE_{02}$ - $TE_{01}$ converter of the varying radius type; the second is a $TE_{01}$ - $TE_{11}$ converter of the curving axis or serpentine type. The design techniques used to improve the efficiency of these converters apply to both cases (and to periodic perturbation mode converters in general). However since the improvement is most striking for the $TE_{01}$ - $TE_{11}$ mode converters we will concentrate on this type as an example. Previous designs of this type of $TE_{01}$ - $TE_{11}$ converter use a periodic cosinusoidal variation of the circular waveguide axis with the period being the beat wavelength, $\lambda_B$, between the $TE_{01}$ and $TE_{11}$ modes. Moeller [1] used a converter $6\lambda_B$ long with a diameter of 0.75" achieving an efficiency of 92%. Thumm [2] used a converter $10\lambda_B$ long with a diameter of 1.094" achieving an efficiency of 92.5%.

We have made the following design modifications for these kinds of converters using only four periods in a 1.094" diameter waveguide:

1) Alter the period to account for the effect of the presence of unwanted "secondary" modes. It is also often of benefit to alter the period slightly from one cycle to the next.
2) Insert sections of straight waveguide to adjust the relative phases of the important modes so that coupling to unwanted modes is minimized.
3) Alter the amplitude of the perturbation from period to period to maximize the converter efficiency.
4) Choose the profile of the perturbation period to further reduce the coupling to unwanted modes.

Figure 2 shows a schematic diagram of such a four-period converter, designed for 60 GHz operation, with an approximately 7% increase in the perturbation period, a single flat section, and circle segments for the curvature profile. Figure 3 shows a graph of the power-normalized amplitude of the $TE_{01}$ and $TE_{11}$ modes and six spurious modes for the case of a four-period converter of the simple design (completely periodic with a period of $\lambda_B$) while Fig. 4 shows the same mode amplitudes for the modified design. Here the fraction of power in any given mode at a given value of z can be found by squaring the amplitude at that position. Ohmic losses are taken into account by including attenuation in the amplitude propagation constants. The perturbation amplitude is made smaller in the first and fourth periods where the coupling to the unwanted $TE_{12}$ and $TE_{21}$ modes is high. The length of the period is also varied slightly from one period to the next. The efficiency is only about 63% for the simple design but is 98.3% for the modified design.

Decreasing the number of periods using these design techniques allows for a shorter device with less loss for the same diameter or a larger diameter device giving greater power handling capability. If the shorter device option

is chosen this design modification also gives a broader bandwidth. This is shown in Fig. 5 which gives the efficiency of a) the improved four cycle design discussed above, b) a similar design using constant amplitude perturbations and one straight section, and completely periodic c) six, d) five, and e) four-cycle designs. Notice that although the efficiency of the completely periodic designs increases with the number of cycles, N, at the design frequency, the bandwidth decreases as N increases.

We have required that the input and output apertures for the $TE_{01}$ - $TE_{11}$ mode converter are centered on and perpendicular to the same axis. This allows for the rotation of the mode converter, and consequently the polarization of the output $TE_{11}$ mode, to any desired orientation. This, in conjunction with the elliptical-guide polarization converter, can give any desired polarization output from linear to circular with either sense of rotation.

The same form of design modification has been implemented for a four-cycle varying-radius $TE_{02}$ - $TE_{01}$ mode converter. The difficulties here with spurious modes are much less severe and previous designs had already achieved a very high efficiency of about 99% using 6 cycles with a total converter length of 59.4 cm (Thumm [2]) and 5 cycles with a total length of 48 cm (Moeller [1]). Our $TE_{02}$ - $TE_{01}$ converter design has only four cycles, is only 40 cm long, and has a predicted efficiency of 99.4%. It uses two straight sections in otherwise constant period and amplitude perturbations. Figure 6 shows the power normalized amplitude of the only five modes which can propagate in the structure ($TE_{01}$, $TE_{02}$, $TE_{03}$, $TE_{04}$, and $TE_{05}$) as a function of position. It has an efficiency of 99.4% when ohmic losses are included. This efficiency may be increased by 0.2 - 0.3% if a slight variation in the perturbation amplitude is included in the design. However, this small improvement

may not warrant the additional complication in the design. The simple, completely periodic, beat-wavelength-period design for the $TE_{02}$-$TE_{01}$ mode converter has the an efficiency of 97.3% so the improvement is not nearly as dramatic as for the case of the $TE_{01}$-$TE_{11}$ converter discussed above.

Generally the output power of a gyrotron is not purely in a single mode but may contain a few percent of its output power in other modes. If the first mode converter following the gyrotron has been optimized for a single mode input, the presence of other modes will normally decrease the converter's efficiency. For the case of a gyrotron producing mainly a $TE_{02}$ mode with a few percent $TE_{01}$ mode, the efficiency can be increased to single mode levels by adjusting the phase of the input $TE_{01}$ mode relative to the $TE_{02}$ mode and adjusting the lengths of the two flat-section inserts. It is more difficult to compensate for the effects of a few percent of $TE_{03}$ mode (or other $TE_{0n}$ mode $n > 3$) in this way. However such a mode component may be largely converted to the $TE_{02}$ mode by a short (only about 5 cm for the $TE_{03}$ mode case) single-cycle converter which would have at its output only a few tenths of a percent of any such $TE_{0n}$ mode. Thus by simple modifications to the same converter (no refabrication is necessary), it may be adapted to high efficiency operation for an input with several percent power in the $TE_{01}$ and/or $TE_{03}$ (or $TE_{0n}$, $n > 3$).

References

[1] C. Moeller, Mode Converters Used in the Doublet III ECH Microwave System, Int. J. Electronics, 53, pp. 587-593, 1982.

[2] M. Thumm, High-Power Millimeter-Wave Mode Converters in Overmoded Circular Waveguide Using Periodic Wall Perturbations, Int. Symposium on Gyrotron Development, Lausanne, Switzerland, July 4-6, 1984.

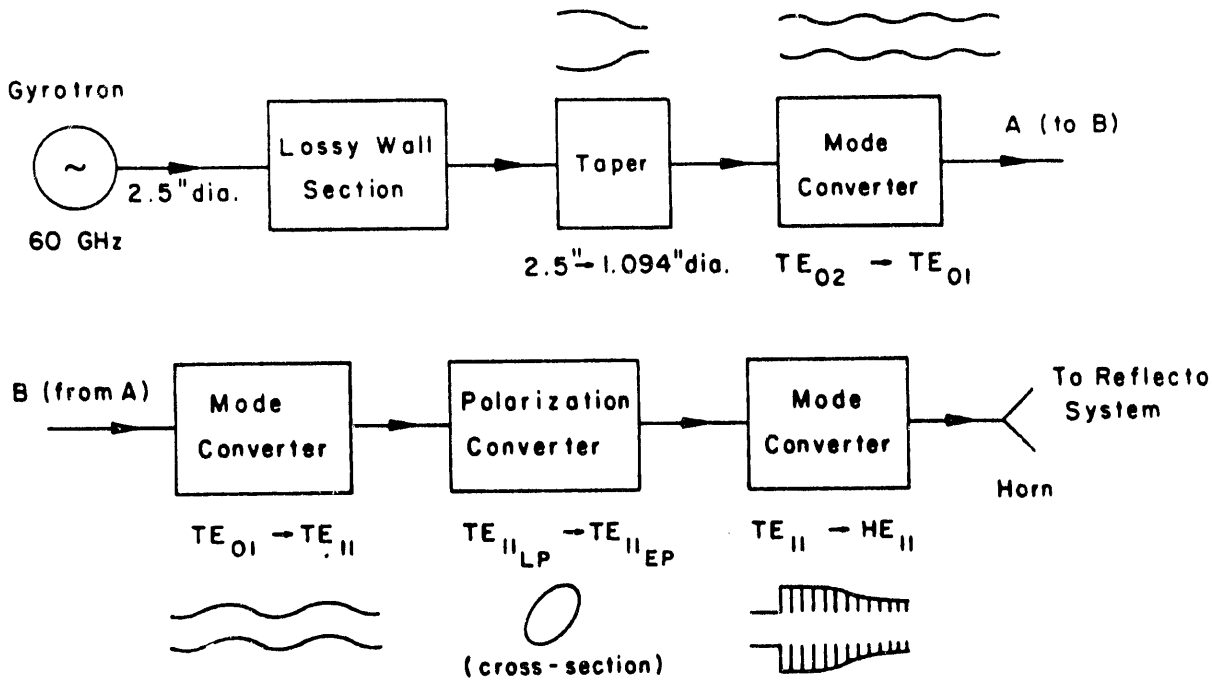


Fig. 1. A $TE_{02}$-$HE_{11}$ mode converter system. After the 2.5"-to-1.094" taper, all components but the polarization converter use a 1.094" diameter waveguide. The polarization converter may have a minimum diameter slightly less than 1.094".

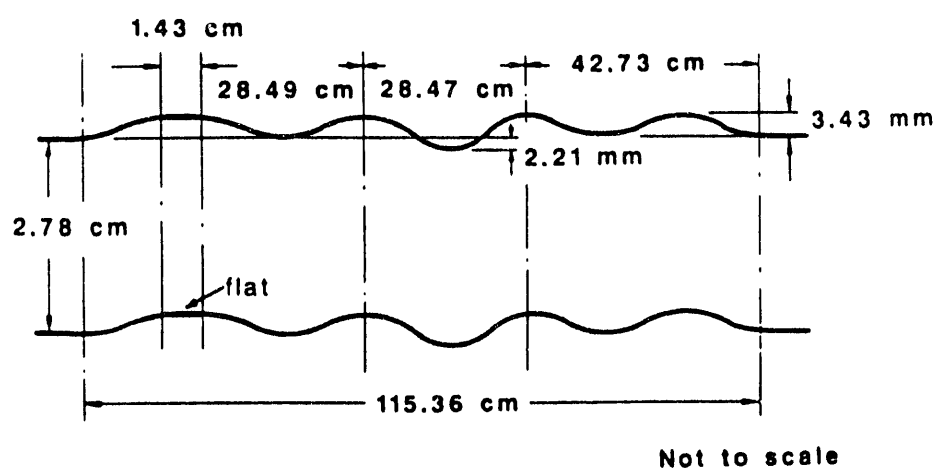


Fig. 2. Drawing of the modified-design $TE_{01}$-$TE_{11}$ mode converter. The vertical scale is exaggerated.

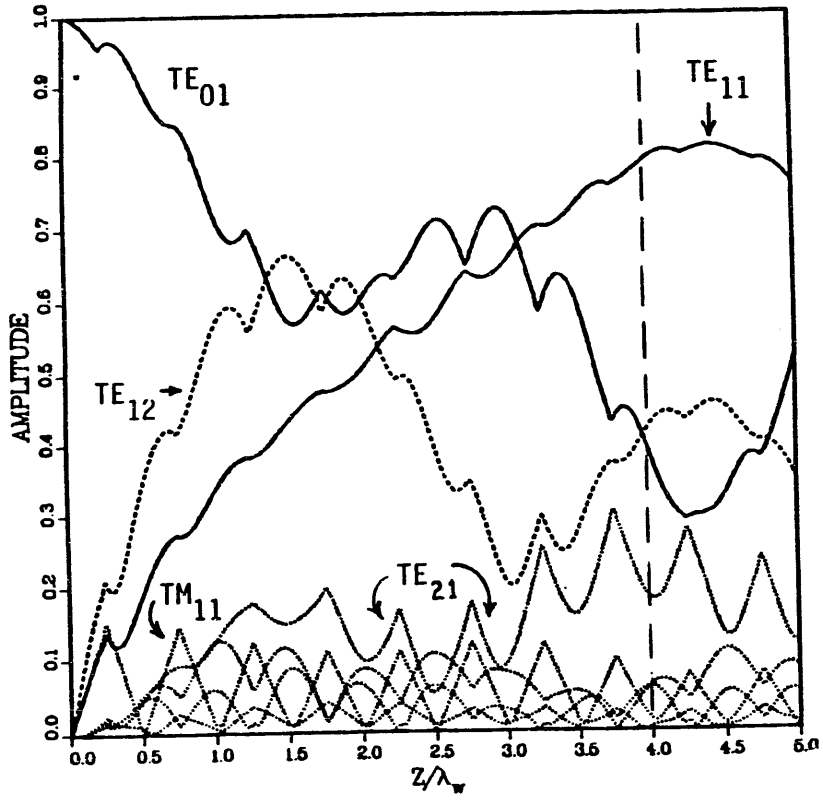


Fig. 3. Graph of power-normalized amplitude versus distance of the eight largest modes in a four-cycle completely-periodic $TE_{01}$-$TE_{11}$ mode converter with a period of $\lambda_B$. The modes considered are the $TE_{01}$, $TE_{11}$, $TE_{12}$, $TE_{21}$, $TM_{11}$, $TE_{02}$, and $TM_{21}$.

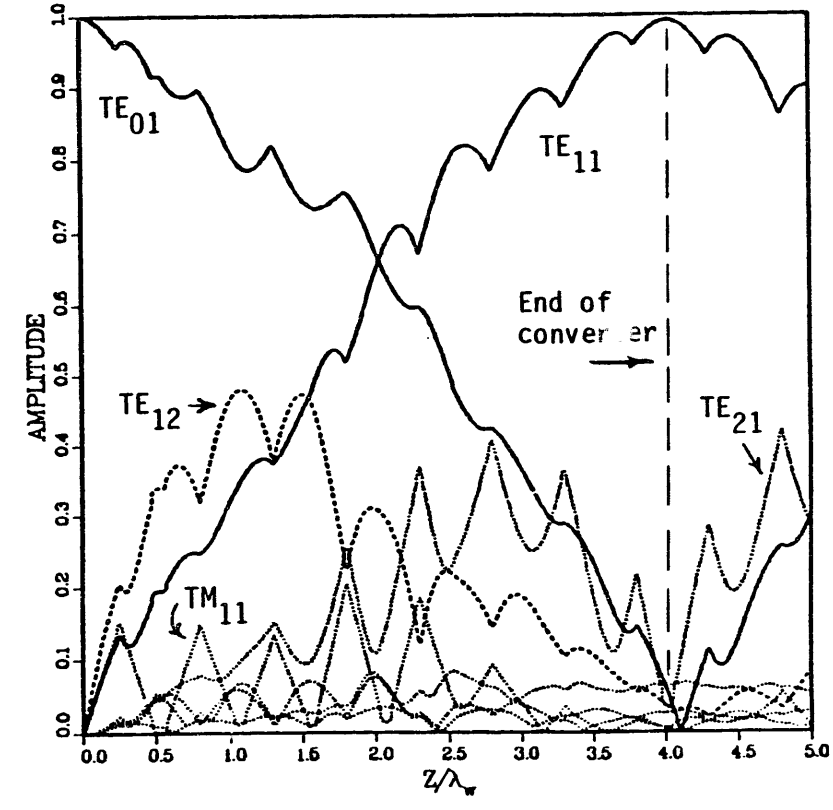


Fig. 4. Graph of power-normalized amplitude versus distance of the eight largest modes in the modified $TE_{01}$-$TE_{11}$ mode converter shown in Fig. 2. The modes considered are the $TE_{01}$, $TE_{11}$, $TE_{12}$, $TE_{21}$, $TM_{11}$, $TE_{22}$, $TE_{02}$, and $TM_{21}$.

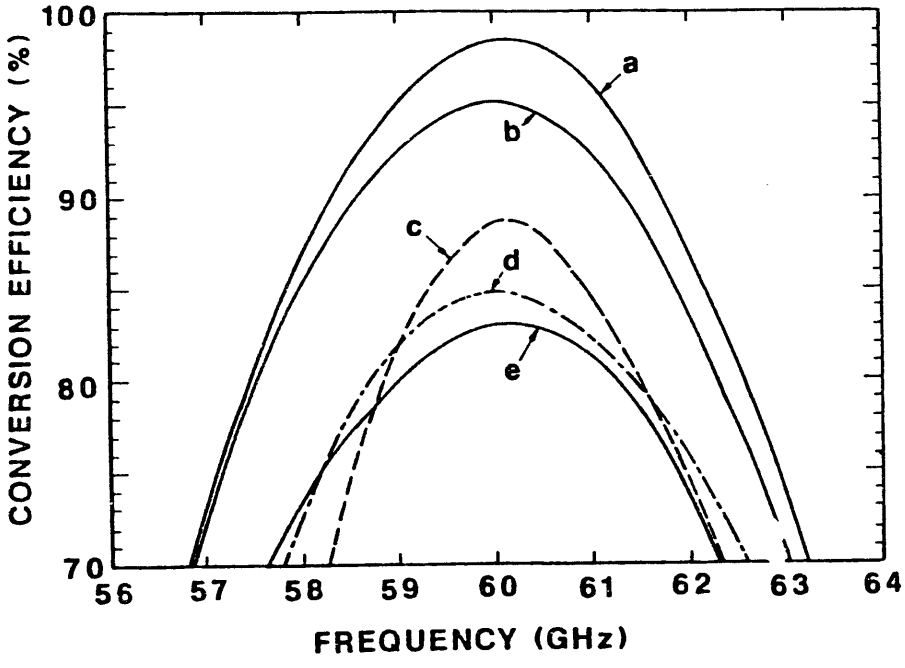


Fig. 5. Graph of conversion efficiency versus frequency for five different $TE_{01}$-$TE_{11}$ mode converters, all in 1.094" diameter waveguide: a) the improved four-period design; b) same as a) but with constant amplitude and period of perturbation but one flat section; c) six-cycle, d) five-cycle, and e) four-cycle completely periodic designs.

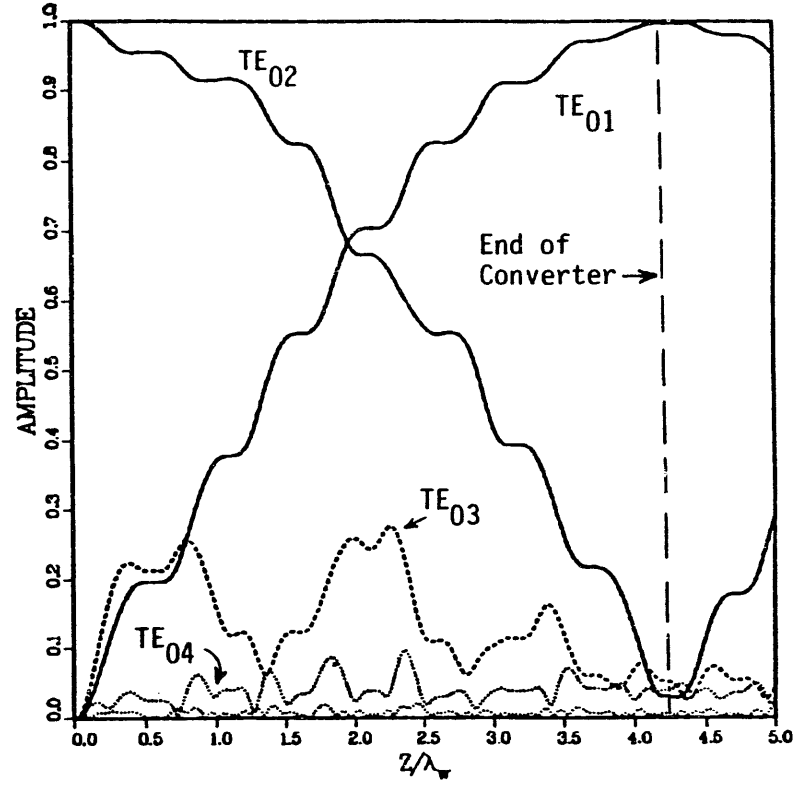


Fig. 6. Graph of power-normalized amplitude versus distance for all five excited modes in the $TE_{02}$-$TE_{01}$ mode converter. The modes are the $TE_{0n}$ modes, n=1 to 5.

# Waveguide Elliptic Polarizers for ECH at Down Shifted Frequencies on PLT

J.L. Doane
*Princeton Plasma Physics Laboratory, Princeton, New Jersey 08544, USA*

## Abstract

ECH experiments on PLT with resonance frequencies of 80-90 GHz at the plasma center use 60 GHz extraordinary mode (X-mode) propagation at 30° from the toroidal field. Efficient excitation of this mode requires elliptic polarization of the incident wave at the plasma edge. On PLT the elliptic polarization is achieved outside the vacuum vessel in an elliptically deformed section of circular waveguide propagating TM11, a mode that is intermediate between TE01 and HE11 (which has an ideal radiation pattern). The squeeze and orientation of the TM11 polarizer are adjusted to compensate both for the birefringence of a corrugated bend propagating HE11 and for a flat mirror inside PLT that reverses the sense of rotation of the polarization.

## Introduction

Since generating high power at millimeter-wave frequencies generally becomes more difficult as the frequency is increased, an electron cyclotron heating (ECH) scheme that reduces the required frequency would appear attractive. For electron temperatures and densities typical of present large tokamaks, large absorption due to energetic electrons can theoretically occur over short path lengths at relatively low frequencies [1]. For example, with cyclotron resonance frequencies of 140 and 80 GHz at the center of TFTR and PLT, respectively, virtually complete absorption not too far from the plasma center should be achievable with incident power at around 100 and 60 GHz.

Optimum absorption at such down shifted frequencies requires propagation of the extraordinary mode (X-mode) at an angle relative to the toroidal magnetic field [1]. Efficient excitation of this mode requires, in turn, elliptic polarization of the incident wave at the plasma edge.

Previously, for a different application involving X-mode propagation on Doublet III, the required elliptical polarization was achieved by using grooved mirrors at the end of waveguides propagating a linearly-polarized TE11 mode [2]. Focusing twist reflectors with curved grooves of varying depth have been used on TMX-U to generate a linearly polarized wave from an incident TE01 mode [3] and could in principle generate elliptical polarization as well. These grooved devices generally must be located inside the vacuum vessel.

ECH on PLT uses waveguide mode converters to generate the ideal HE11 mode, which generates a free-space gaussian mode at the open ended corrugated waveguide inside PLT (see Fig. 1). Elliptical polarization of HE11 is

achieved by suitably squeezing a section of waveguide outside PLT propagating the TM11 mode, which is intermediate in the mode conversion process from TE01 to HE11 [4]. Since TE01 is unpolarized and corrugated waveguide propagating HE11 is not birefringent under elliptical deformation [5], the desired polarization conversion must be done on the TM11 mode.

## Design

As is well known, smooth-wall circular waveguide propagating the dominant TE11 mode becomes birefringent when deformed elliptically: the E-field component along the minor axis undergoes more phase shift than the component along the major axis [6]. Circular polarizers using this effect are available commercially for frequencies up to the lower millimeter-wave range [7]. Since TE11 is commonly generated from TE01 in overmoded waveguide systems for ECH ([2], [8]), the required elliptical polarization could also be generated by squeezing a section propagating TE11. As discussed below, however, the birefringence for TE11 is much smaller than for the TM11 mode used on PLT.

In general, if the radius of deformed circular waveguide is written in cylindrical coordinates as

$$a(z) = a_0 + \sum_{\ell=1} a_\ell(z) \sin\ell\phi \qquad (1)$$

then incident $TE^s_{pm}$ or $TM^s_{pm}$ modes with radial electric fields varying transversely as $E^s_r \sim \sin p\phi$ will be coupled to $TE^c_{qm}$ and $TM^c_{qm}$ modes with $E^c_r \sim \cos q\phi$, where $\ell = p-q$. This relation also holds if $q < 0$; hence an $a_{2p}(z)$ deformation causes coupling of the two independent polarizations of $TE_{pm}$ or $TM_{pm}$ (see Fig 2). This coupling may be used to describe the birefringence [9].

If the integral of the deformation satisfies

$$|K| \int_{-L/2}^{L/2} a_{2p}(z)dz = \pi/4 \quad , \qquad (2)$$

where K is the relevant coupling coefficient, then an incident $TE_{pm}$ or $TM_{pm}$ mode with fixed polarization can be converted to rotating polarization and vice versa [9]. When p = 1, the rotating polarization is called circular polarization.

The coupling coefficient K in Eq. (2) varies approximately as $\lambda/a_0^3$ for large $a_0/\lambda$ and is $-j1.44$ in.$^{-2}$ for TM11 at 60 GHz in WC109 waveguide ($2a_0$ = 1.094 in.). The coupling coefficient for TE11 in this case is $+j0.60$, or 2.4 times smaller. The sign difference corresponds to opposite signs for the birefringence.

To avoid coupling to unwanted modes, the polarization converter must not be too short and the deformation should vary smoothly. For a TM11 polarization converter, TE31 is the most important unwanted mode, because the phase velocities of these two modes are very close. Also important is coupling to TE11.

The results of numerical integration of the coupled mode equations are shown in Figs. 3-5. The incident mode is linearly polarized in the vertical direction and the elliptical deformation is oriented as in Fig. 2. A smooth cosine-squared variation for the magnitude of the deformation along the converter is suitable for minimizing spurious mode generation and is easily approximated in practice.

For the circular polarizer of Figs. 3 and 4, the output power should ideally be divided equally between the horizontally and vertically polarized components and the relative phase should be 90°. The latter requirement can be satisfied at relatively short converter lengths; the former requires a converter length of 15 to 20 inches for TM11 and at least 30 inches for TE11. The much larger spurious mode generation in the TE11 converter for a given length is caused by the need to increase the magnitude of the distortion to compensate for the much lower coupling coefficient K.

To rotate the polarization of a linearly polarized mode by 90° requires a doubling of the distortion integral in Eq. (2) to $\pi/2$. This corresponds to a phase shift of 180° between the components parallel and perpendicular to the ellipse major axis (see Fig. 2). As shown in Fig. 5, a vertically polarized TM11 mode can be well converted to horizontal polarization in a elliptically deformed waveguide 25 to 30 inches long. For the PLT configuration, the desired elliptical polarization required a distortion integral of $0.41\pi$ (see discussion below); hence a length of 28 inches for the distortion was chosen to insure low spurious mode generation.

## Fabrication

To generate an elliptic deformation that is smoothly varying and zero at each end, the fixture shown in Fig. 6 was convenient. Two thick aluminum plates squeezed by a bolt at $z = 0$ and restrained at each end generated an $a_2(z)$ variation approximately equal to $\cos^2(\pi z/L)$. The waveguide was standard WC109, with an initial O.D. of approximately 1.222 in. Before assembly into the frame, the waveguide was annealed with a hand-held torch enough to allow squeezing in place without excess torque but not so much as to make the waveguide flatten out under the squeeze. The diameter squeeze at the center needed to produce a TM11 circular polarizer was about .085 in., in close agreement with Eq. (2) and the coupling coefficient cited above. The average diameter decreased by less than .005 in. at the center and should cause no significant mode conversion.

## Measurement

The TM11 polarization converter was placed between the TE01 to TM11 and TM11 to HE11 converters described in Ref. 4. The major and minor axes were oriented at 45° from the direction of polarization of the field incident from the TE01 to TM11 converter. A small aperture linearly polarized receiving horn was located 24 inches from the open end of the TM11 to HE11 converter.

To facilitate finding the optimum squeeze of the polarization converter, and also to verify the sense of rotation of the polarization, a low-power rotatable polarizer with parallel plate waveguides [10] could be placed in front of the receiving horn. The phase shift between field components parallel and perpendicular to the plates was 90°. When this polarizer was

used, a glass lens was placed between it and the open-ended TM11 to HE11 converter to collimate the beam at the polarizer. The parallel plates were oriented at 45 degrees from the vertical (Fig. 7), and the TM11 polarization converter was squeezed until the field at the receiving horn was linearly polarized (as determined by rotating the horn). The TM11 polarization converter was then a circular polarizer; the measured sense of rotation agreed with the theory.

The radiation field was then checked without the parallel plate polarizer and collimating lens. The peak-to-peak variation in the field received by the linearly polarized horn as the latter was rotated was only 0.6 dB. The measured radiation patterns for various orientations of the horn were almost identical, and the sidelobes were at least 23 dB down.

In the waveguide leading to the top port of PLT there is a 90° bend in the HE11 mode (see Fig. 1). This bend is also birefringent due to a difference in one of the modes coupled by the bend: either TE01 or TM02 for H and E plane bends, respectively. To measure the birefringence, a 90° bend was placed after the TM11 polarizer and the TM11 to HE11 converter. The rotatable parallel plate polarizer and the rotatable receiving horn were used to analyze the elliptic polarization radiated from the bend. From this analysis it was determined that the E-field component perpendicular to the plane of the bend was delayed in phase by approximately 59° relative to the component in the plane of the bend. This agreed well with a relative phase shift of 56° predicted by numerical integration of the coupled wave equations, assuming an effective corrugation depth of 0.7 $\lambda/4$.

We now adjusted the TM11 polarization converter to compensate for the birefringence of the 90° HE11 bend (item D in Fig. 1), the 102° orientation of this bend (see Fig. 1), and the reversal of the sense of rotation of the polarization at the flat mirror (item H in Fig. 1). Theoretically, the squeeze axis of the polarization converter should be changed from 45° to 26° from the vertical, and the squeeze increased to increase the relative phase shift of the field components parallel and perpendicular to the major axis of the deformation ellipse from 90° (for the circular polarizer) to 147.5°.

This adjustment should have given left handed elliptical polarization before the mirror with a 1.2 ratio of the magnitudes of the electric field components perpendicular and parallel to the toroidal field $B_T$. In the laboratory, using the set-up shown in Fig. 8, the proper orientation of the elliptical polarization was observed, and the ratios of the field component magnitudes was measured to be approximately 1.3. This still should provide a good match at the plasma edge to an extraordinary wave propagating at a 30° angle relative to $B_T$ (Fig. 1) (see, for example, Ref. 11, section 1.4).

## Acknowledgments

The author acknowledges helpful discussions with E. Mazzucato, M.A. Goldman, and H. Hsuan, and the help of J. Boychuk, S. Luyber, and E. Hall in fabricating the TM11 polarization converter.

This work was supported by U.S. Department of Energy Contract No. DE-AC02-76-CHO-3073.

## References


[1] E. Mazzucato, I. Fidone, G. Giruzzi, and V. Krivenski, Report PPPL-2229, Princeton Plasma Physics Laboratory, June 1985; also to be published in Nuclear Fusion.

[2] C.P. Moeller, R. Prater, and S.H. Lin, Proceedings of the Fourth International Symposium on Heating in Toroidal Plasmas, Rome, Italy, 1984, pp. 1454-1460.

[3] B.W. Stallard, F.E. Coffield, B. Felker, J. Taska, T.E. Christensen, N.C. Gallagher, Jr., and D.W. Sweeney, Proceedings of EC-4 Workshop, Rome, Italy, 1984, pp. 107-113.

[4] J.L. Doane, Int. J. Electronics, 53 (1982) 573.

[5] P.J.B. Clarricoats, A.D. Olver, C.G. Parini, and G.T. Poulton, Proc. Fifth European Microwave Conference, Hamburg, 1975, pp. 56-60.

[6] P.I. Sandsmark, IRE Trans. on Microwave Theory and Techniques, MTT-3 (1955) 15.

[7] For example, Systron Donner Model 930 Circular Waveguide Polarizers.

[8] M. Thumm, V. Erckmann, G. Janzen, W. Kasparek, G. Müller, P.G. Schüller, and R. Wilhelm, Int. J. Infrared and Millimeter Waves, 6 (1985) 459.

[9] J.L. Doane, "Propagation and Mode Coupling in Corrugated and Smooth-Wall Circular Waveguides," in K.J. Button, ed., Infrared and Millimeter Waves, Vol. 13, Academic Press, 1985.

[10] A.H.F. van Vliet and Th. de Graauw, Int. J. Infrared and Millimeter Waves, 2 (1981) 465-477.

[11] M.A. Heald and C.B. Wharton, Plasma Diagnostics with Microwaves, Wiley, New York, 1965.

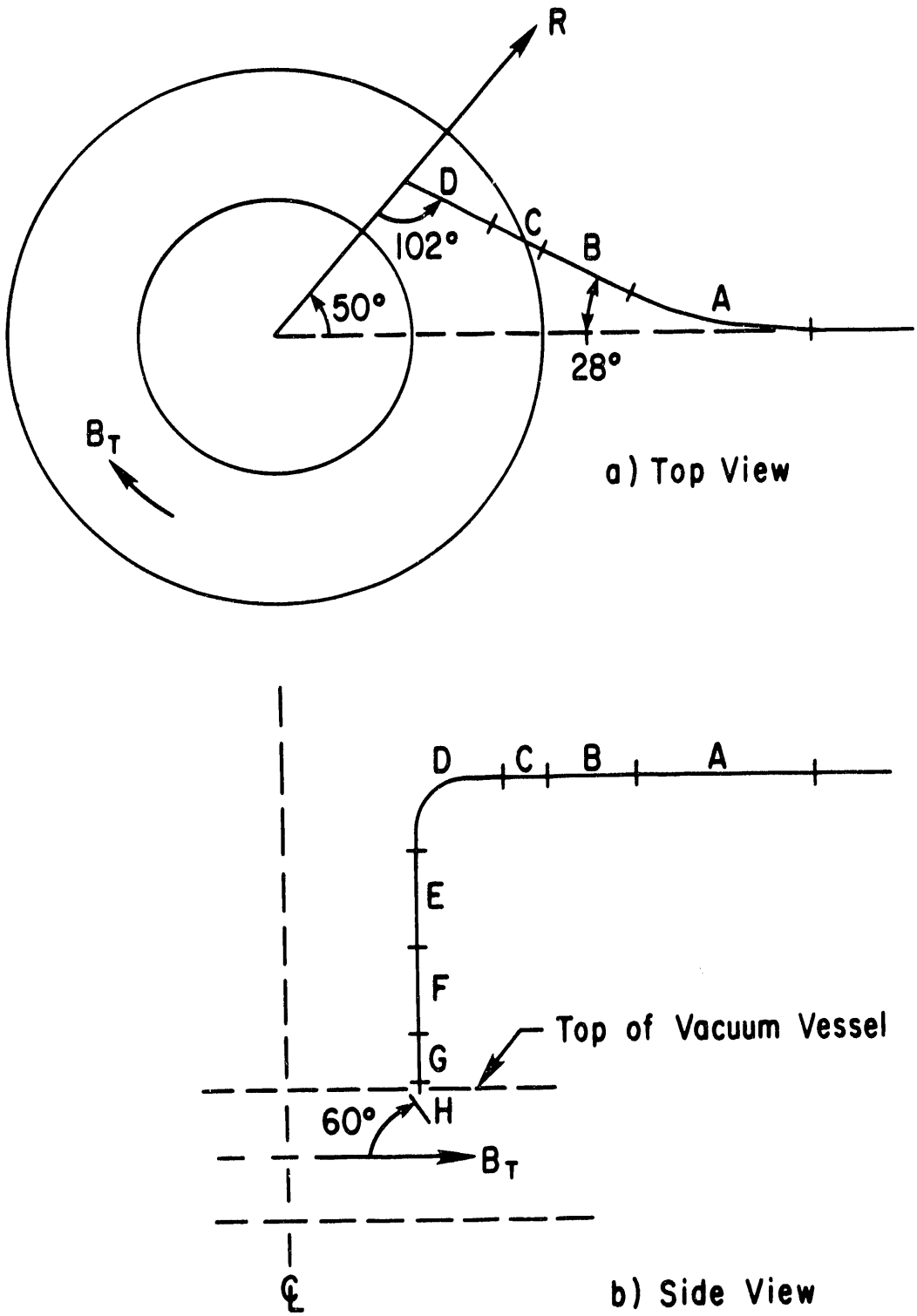


Fig. 1. Schematic of top launch on PLT. A: TE01-TM11 mode converter; B: TM11 polarization converter; C: TM11-HE11 mode converter; D: HE11 bend; E: straight corrugated waveguide; F: corrugated taper from 1.094 to 2.5 inch I.D.; G: window; H: smooth mirror at end of 2.5 inch I.D. corrugated waveguide.

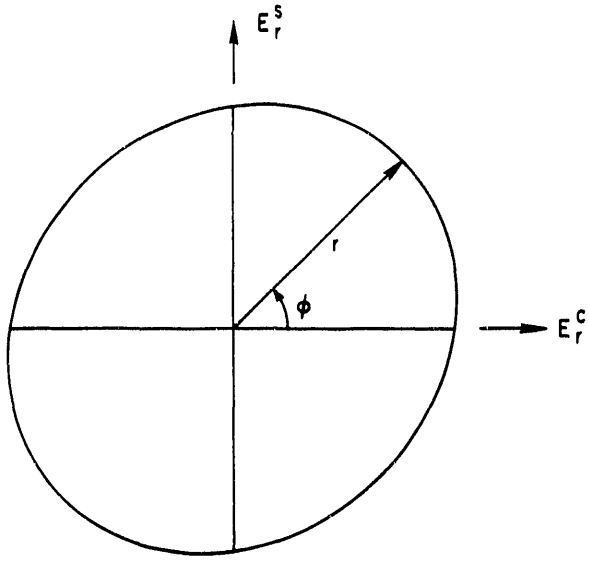


Fig. 2. A 2-foil (elliptical) deformation $a_2$ oriented to couple the horizontally and vertically polarized components of a $TE_{1m}$ or $TM_{1m}$ mode.

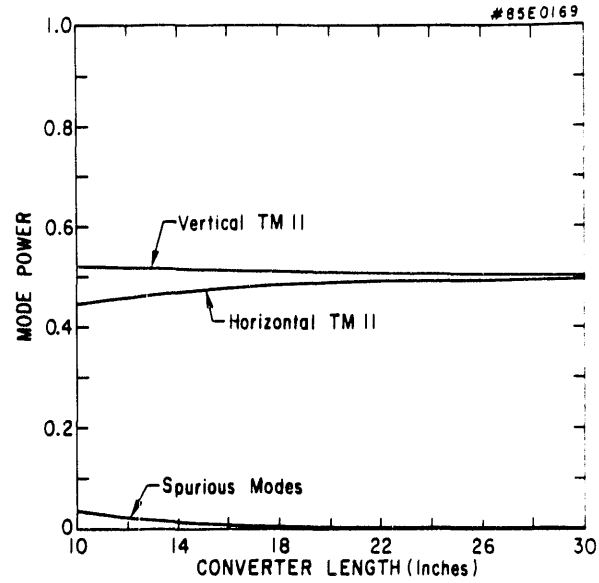


Fig. 3. Effect of TE11, TE12, TE31, and TM31 spurious modes on a TM11 circular polarizer at 60 GHz in 1.094 in. I.D. waveguide. The magnitude of the elliptical distortion, oriented as in Fig. 2, with a cosine squared variation along the converter, is adjusted for each length to produce circular polarization at the output in the absence of spurious modes. The input is vertically polarized.

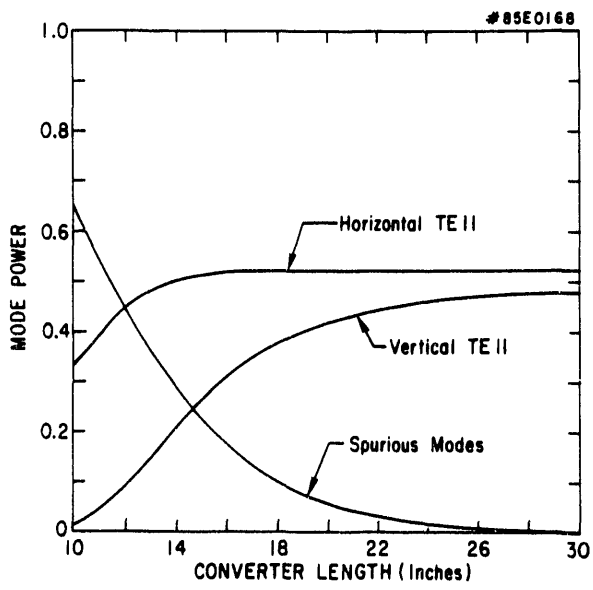


Fig. 4. Effect of TE12, TM11, TE31, and TM31 spurious modes on a TE11 circular polarizer with a vertically polarized input. Parameters same as Fig. 3.

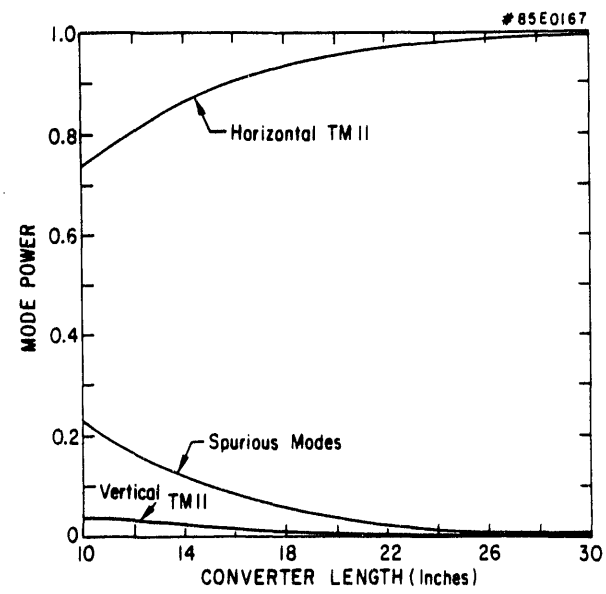


Fig. 5. Effect of TE11, TE12, TE31, and TM31 spurious modes on a converter to rotate the polarization of a linearly polarized incident TM11 mode by 90°. Parameters same as Fig. 3.

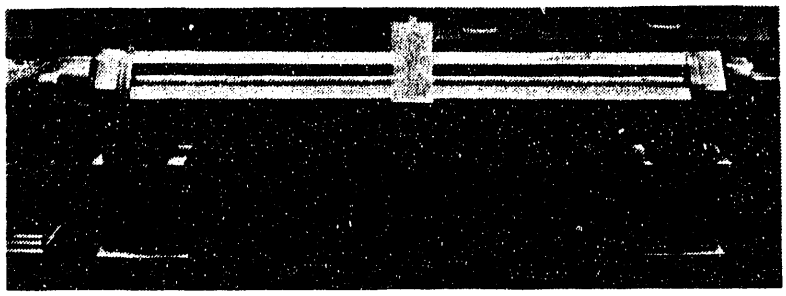

Fig. 6. TM11 polarization converter in squeeze frame. Overall length: 32 inches.

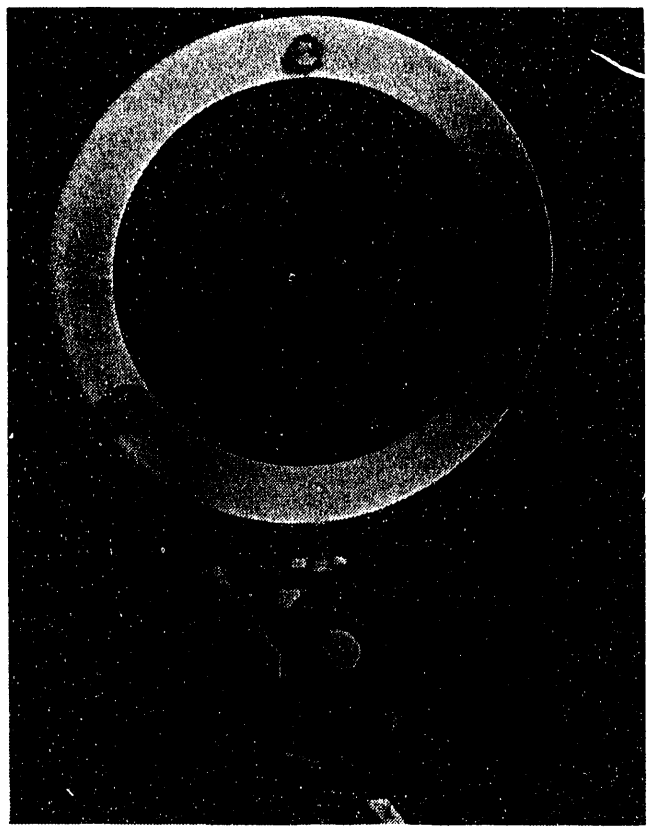

Fig. 7. Parallel plate polarizer

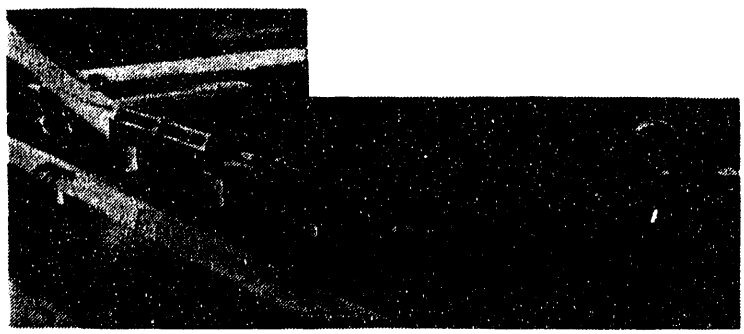

Fig. 8. Laboratory setup for analysis of elliptical polarization following components A thru D connected as in Fig. 1.

# Pure Mode Swept Frequency $TE_{02}$ Measurements in 6.35 cm Circular Waveguide*

T.S. Bigelow, T.L. White, and H.D. Kimrey
*Oak Ridge National Laboratory, Oak Ridge, Tennessee 37831, USA*

**Abstract**

A mode transducer was developed which generates high purity (> 99%) $TE_{02}$ mode in small diameter (1.64 cm) circular waveguide. The device works from 52-62 GHz which allows relatively wideband, accurate swept frequency measurements of insertion and return loss in this mode. $TE_{01}$ to $TE_{02}$ insertion loss for the device is approximately 0.2 dB and the $TE_{01}$ mode rejection from the $TE_{02}$ port is 15 dB. A 2- degree linear taper is used to connect to 6.35 cm diameter waveguide. Mode purity of the $TE_{02}$ mode after this taper is > 98%. Some typical measurements of waveguide components as well as a description of the device will be presented.

*Research sponsored by the Office of Fusion Energy, U. S. Department of Energy, under Contract No. DE-AC05-84OR21400 with Martin Marietta Energy Systems, Inc.

Waveguide development work is currently underway at ORNL for the Advanced Toroidal Facility (ATF) ECH System. The initial capabilities of the system will be 200 kW CW at 53.2 GHz. ATF is capable of running steady-state at 1T and less than 5-sec at 2T, however, plans call for initial operation of less than 5 sec pulses with a central magnetic field of 1T. In this mode, heating will be from NBI and the ECH system will be used for plasma startup only.

The proposed waveguide system is actually quite simple as shown in Fig. 1. The entire waveguide length will have a diameter of 6.35 cm and will be under vacuum. The waveguide will propagate the $TE_{02}$ mode generated by the gyrotron. Two bends are required for top launch on the ATF device. These bends will be optimized miter bends which are currently under development. Mode conversion into a Gaussian beam will occur at the launcher which will be a Vlasov type with a polarization rotating reflector.

To facilitate testing and optimize the performance of components under development, a mode transducer to generate pure $TE_{02}$ mode was developed. This transducer converts an input $TE_{01}$ mode (generated by commercially available $TE_{10}$ to $TE_{01}$ transducers) into a high purity $TE_{02}$ mode (> 99%) over a frequency range of 52-62 GHz. The wide bandwidth and small size of this transducer make it quite useful for testing in swept frequency laboratory setups. It will also be useful for testing and alignment of the installed waveguide system on ATF.

The mode transducer consists of a step in waveguide diameter to a larger diameter guide. This diameter step with an incident $TE_{01}$ mode excites a composite $TE_{01}$ - $TE_{02}$ waveguide (plus some evanescent modes) as described in Marcatili.[1] This composite wave is converted entirely into $TE_{02}$ mode by a coaxial waveguide section which has phase shifting inserts.

Adjustment of the transducer is performed using the radiation pattern technique. A computer program was written for calculating patterns for composite modes which provides insight into mode content for a particular positioning of the coaxial converter

section. The presence of non-circular mode impurities such as $TE_{11}$ and $TE_{12}$ indicate a tilting or offset of the converter. The presence of $TE_{01}$ circular mode is best determined by the relative height of the inner and outer peak as shown in Fig. 2. The exact pattern for small apertures (ka ≤ 1-2) is not accurately given by simple far-field integration of the aperture fields.[2] A more accurate determination of mode purity can be made by using waveguide spacers of several lengths after the transducer and checking for consistency in the measured pattern. This is shown in Fig. 2 where at least one beat wavelength of the $TE_{01}$ and $TE_{02}$ mode is scanned through. The change in height of the inner peak is ≈ < .5dB which, based on computer code predictions, indicates a mode purity of 99%. This process can of course be repeated at any frequency of interest to determine the bandwidth of the device.

A back-to-back swept frequency insertion loss measurement of two transducers is shown in Fig. 3. There the normalized reference line corresponds to the $TE_{01}$ transducers (and mode absorber) alone. In the frequency range that applies (≈ 52-62 GHz) the two transducer insertion loss is .5 dB or less, of which ≈ .2 dB could be accounted for by reflections from device (≃ -15 dB return loss each).

There are several components that can be tested in $TE_{02}$ mode for insertion loss. Using these transducers, components such as miter bends, mode absorbers, other mode converters, and directional couplers can be easily tested. This testing can be done in 6.35 cm waveguide by tapering carefully from the transducer output (1.64 cm). A pair of 2° linear tapers was constructed for this purpose. It was determined (using the pattern method) that these tapers produced ≈ 5% $TE_{01}$ mode plus some $TE_{03}$ mode.

Since the transducers are not matched perfectly for $TE_{01}$ mode and $TE_{03}$ is cutoff in the taper, there is the possibility of trapped mode resonances which will cause spikes in swept frequency measurements. To reduce this problem and increase accuracy, good wideband tapers are required and any component to be tested should be low in mode conversion. The spikes can be averaged out somewhat by matching the electrical

length of the component with a section of plain waveguide for the reference and using the normalizing features of a scalar network analyzer to subtract out the spikes. Presumably, the remaining signal is close to the true value in the region of the spike. In some cases the level of spikes can be reduced further by adding a high frequency FM component to the sweep oscillator signal. This FM tends to average out the high Q trapped mode resonances when multiple sweeps are averaged. An example of an insertion loss measurement is shown in Fig. 3. Here, a Titanium Dioxide lined waveguide mode absorber (12" long) is measured for insertion loss. As desired, the insertion loss is low – approximately .1 dB. This same measurement setup has been quite useful in studying optimized miter bends for use on ATF.

Swept frequency return loss measurements can be made through the $TE_{02}$ transducer using a directional coupler in the rectangular waveguide source line. Unfortunately, without some reflection cancellation technique, this setup is limited to - 15 dB return loss or worse due to reflections off the mode transducer itself. Nevertheless, the resonant frequency of a single disc window was verified using this technique. Further improvements in this technique could come from tuning of the $TE_{02}$ transducer and improvement of the tapers.

An equally useful application for the mode transducer is in testing of launchers designed for the $TE_{02}$ mode. In this case measurements are made at a single frequency anywhere in the transducer passband. The entire launcher for ATF when completed will be tested using this transducer.

By increasing the transducer converter section and the diameter step ratio, it is possible to build a $TE_{01}$ to $TE_{03}$ transducer that will probably have similar performance characteristics to this device. This principle could be extended to higher order circular electric modes, however, the complexity of adjustment will probably make $TE_{04}$ or higher impractical.

## REFERENCES


[1] Marcatili, E. A., "A Circular Electric Hybrid Junction and Some Channel Dropping Filters," Bell System Tech. J, January 1961, pp. 185-196.

[2] Collin, R. E. and Zucker, F. J., "Antenna Theory Part 1," McGraw Hill, New York, p. 631.

ORNL-DWG 84-3382A FED

# MICROWAVE HEATING SYSTEM FOR THE ADVANCED TOROIDAL FACILITY (ATF)

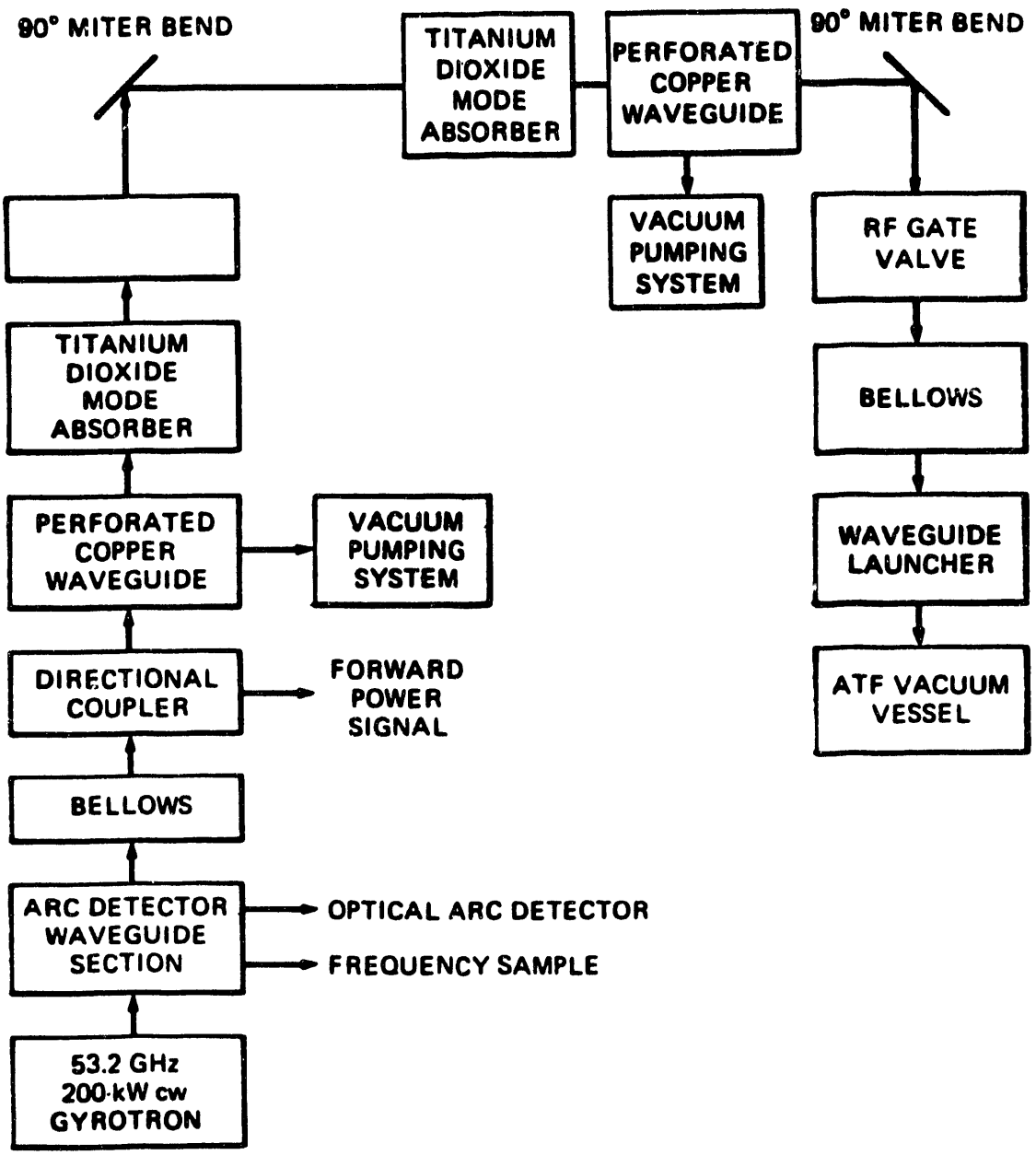


FIG. 1

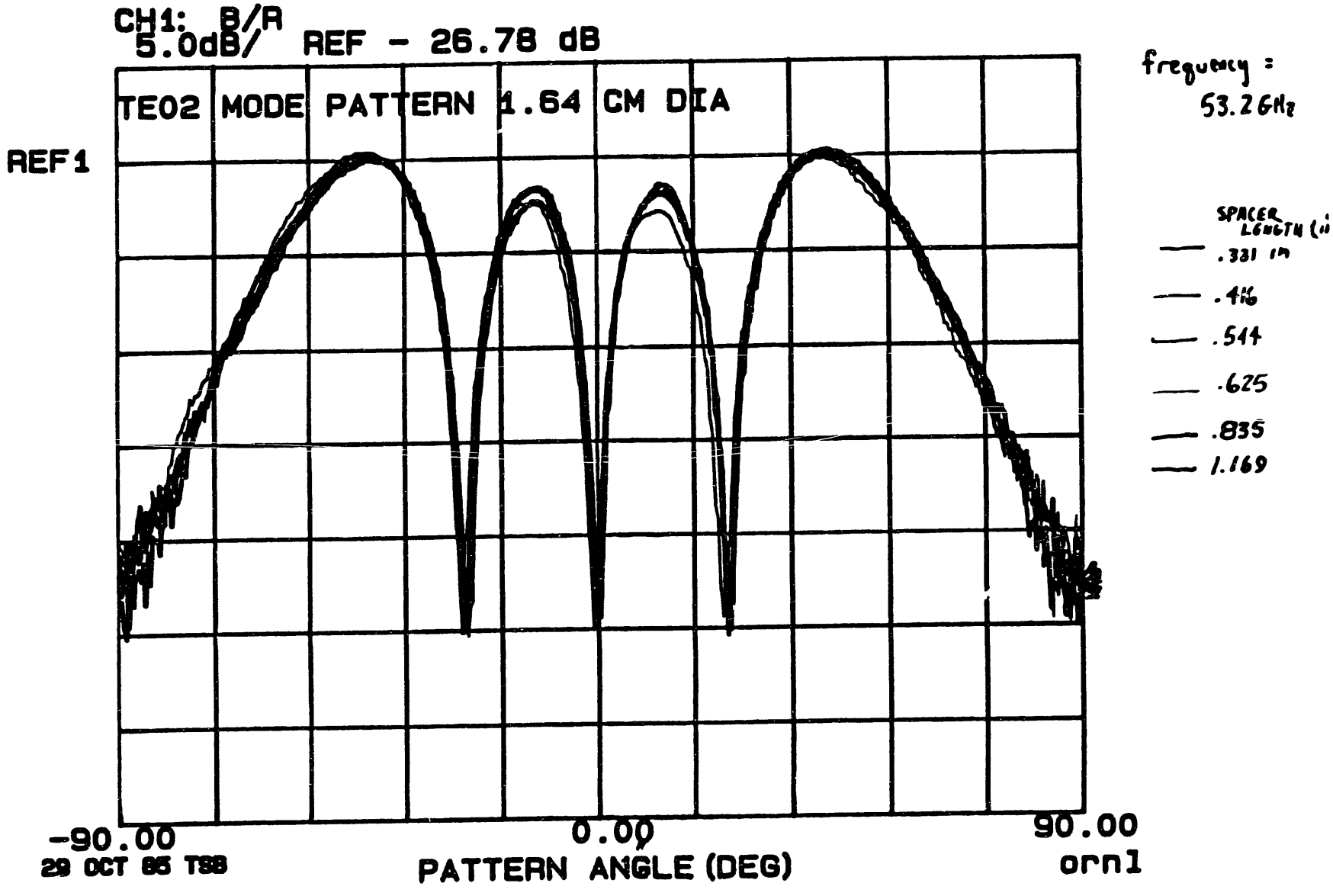


FIG. 2 Transducer Antenna Pattern with Several Spacer Lengths

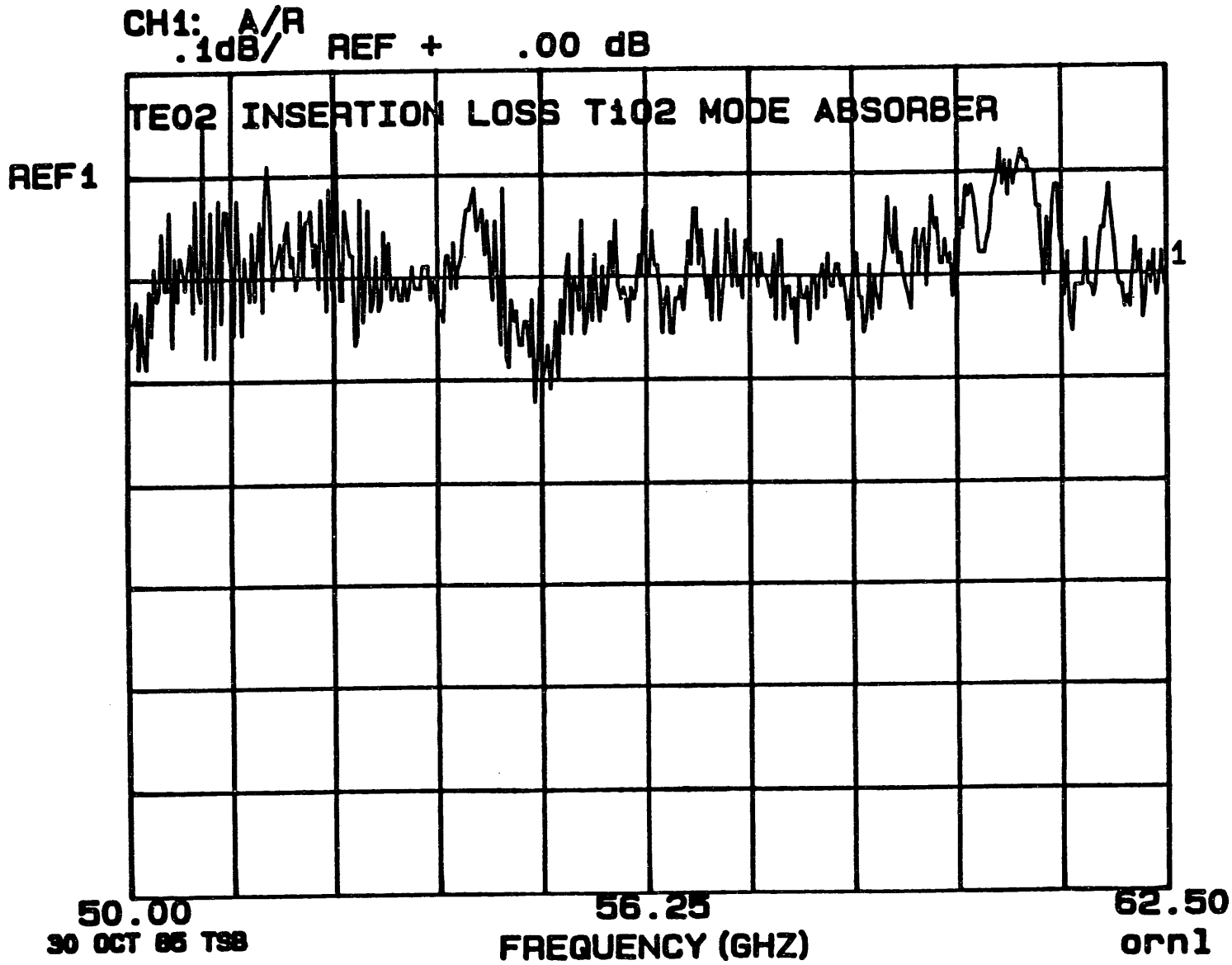


Fig. 3 Swept Frequency Insertion Loss of 12 inch $Ti_{02}$ Mode Absorber

# Author Index


A
Ainsworth, N.R. — 135
Airoldi, A. — 10
Alcock, M.W. — 181
Alper, B. — 135
Arunasalam, V. — 18
Atkinson, D. — 135
Audenaerde, K. — 337

B
Baker, E.A.M. — 3, 65
Bartlett, D.V. — 3, 10, 65
Bell, R. — 45
Benshimhon, A. — 300
Bigelow, T.S. — 353
Blewett, S.G.F. — 135
Bornatici, M. — 88, 123
Boyd, D.A. — 18, 77
Brusati, M. — 10

C
Campbell, D.J. — 3, 65
Cavallo, A. — 45
Chan, V.S. — 233
Cirant, S. — 313
Collins, P.R. — 135
Costley, A.E. — 3, 65
Craig, L.J. — 277
Crenn, J.P. — 303
Cutler, M.P. — 18

D
Danly, B.G. — 286
de Esch, H.P.L. —154
de Hoop, J. — 303
Dellis, A.N. —135,181
Demeio, L. — 97, 238
Doane, J.L. — 345

E
Edlington, T. — 135
Efthimion, P.C. — 18
Engelmann, F. — 97, 238

F
Falciasecca, G. — 313
Felch, K. — 276

G
Garin, P. — 300
Goedheer, W. — 228
Guss, W.C. — 189

H
Hartfuß, H.J. — 37, 145
Harvey, R.W., — 223
Hoekzema, J.A. — 154
Hosea, J. — 45
Hughes, M. — 181
Hsu, J.Y. — 105
Hsuan, H. — 213

J
Jedar, E. — 300
Jory, H. — 275

K
Kiff, M.G. — 3
Kimrey, H.D. — 353
Kissel, S.E. — 3, 65
Kreischer, K.E. — 286
Kritz, A.H. — 213, 223
Kroonenburg, L. — 303

L
Lashmore-Davies, C.N. — 105, 264
Lee, P. — 196
Lieber, A.J. —168, 196
Lloyd, B. — 135
Lohr, J. — 56

M
Ma, F. — 135
Maaßberg, H. — 145
Manuel, M.E. — 189
Matsuda, K. — 213, 223
McCarthy, M.P. — 18
McNeill, D. — 45
Moeller, C. — 56
Moss, D.G. — 65
Mourier, G. — 300
Müller, G.A. — 321
Myer, R. — 189

N
Neill, G.F. — 3
Niestadt, R.M. — 65
Nowak, S. — 10

O
O'Brien, M.R. — 135, 181
Orefice, A. — 10
Oyevarr, Th. — 65

P
Parham, B.J. — 135
Piekaar, H.W. — 65
Polman, R.W. — 154
Pradhan, A.K. — 196
Prater, R. — 56, 168

R
Ramponi, G. — 10
Rasmussen, D.A. — 18
Read, M.E. — 278
Rebuffi, L. — 303
Rhee, U. — 337
Rhinewine, R. — 278
Riviere, A.C. — 135, 181
Roach, P.F. — 3
Robinson, D.C. — 135, 181
Ruffina, U. — 88, 123

S
Saito, H. — 286
Schrader, W.J. — 154
Sillen, R.M.J. — 113
Smith, D.K. — 189
Start, D.F.H. — 135
Stauffer, F.J. — 18
Sterk, A.B. — 303
Sturm, H. — 329

T
Tanaka, M. — 246
Taylor, G. — 18
Temkin, R.J. — 286
Thevenot, A. — 300
Thumm, M. — 321, 329
Todd, T.N. — 135, 181
Tournesac, B. — 303
Tran, M.Q. — 294
Tran, T.M. — 286
Tubbing, B.J.D. — 65
Tutter, M. — 37, 145

V
van der Grift, A.F. — 303
van der Kaay, M. — 303
Verhoeven, A.G.A. — 303
Vernon, R.J. — 337

W
Westerhof, E. — 88, 228
White, T.L. — 353
Wilgen, J. — 18
Wilhelm, R. — 321

Y
Yueming, X. — 196

# END

DATE
FILMED
11/6/92